

豊田工業大学

文部科学省私立大学戦略的研究基盤形成支援事業

先進触媒開発研究センター

(2015年度～2019年度)

研究成果報告書

2020年5月

目次

I. 豊田工業大学 「先進触媒開発研究センター」 研究成果報告書 概要

II. 研究報告

1. 高活性光触媒の光励起ダイナミクス

山方 啓 (量子界面物性研究室)

2. キャリア選択型太陽電池を用いた水素生成

大下 祥雄 (半導体研究室)

3. 高活性電極触媒の開発に向けたナノ炭素材料の適用

原 正則・吉村 雅満 (表面科学研究室)

4. 熱的プロセスによるバイオマスからの水素製造と安全利用技術

武野 計二 (熱エネルギー工学研究室)

5. 新規な金属クラスターの発生法と触媒機能

本山 幸弘 (触媒有機化学研究室)

6. 放射光 X 線および中性子回折技術に基づく合成高分子の結晶構造解析：

田代 孝二 (田代孝二特任教授研究室)

Part 1

I. 豊田工業大学 「先進触媒開発研究センター」

研究成果報告書 概要

法人番号	231023
プロジェクト番号	S1511022

**平成 27 年度～平成 31 年度「私立大学戦略的研究基盤形成支援事業」
研究成果報告書概要**

- 1 学校法人名 トヨタ学園 2 大学名 豊田工業大学
- 3 研究組織名 先進触媒開発研究センター
- 4 プロジェクト所在地 愛知県名古屋市天白区久方 2-12-1 豊田工業大学内
- 5 研究プロジェクト名 水素原子・分子の活用技術革新のための先進触媒の研究
- 6 研究観点 研究拠点を形成する研究

7 研究代表者

研究代表者名	所属部局名	職名
本山 幸弘	大学院工学研究科	教授

- 8 プロジェクト参加研究者数
- 8
- 名

- 9 該当審査区分
- 理工・情報
- 生物・医歯
- 人文・社会

10 研究プロジェクトに参加する主な研究者

研究者名	所属・職名	プロジェクトでの研究課題	プロジェクトでの役割
本山 幸弘	大学院 工学研究科・教授	高機能担持型金属ナノ粒子触媒の 開発	プロジェクト統括・ 金属ナノ粒子触媒の創製
大下 祥雄	大学院 工学研究科・教授	新規太陽電池開発と化学物質に よる水素貯蔵に関する研究	新規太陽電池開発と 水素貯蔵化合物の探索
吉村 雅満	大学院 工学研究科・教授	炭素材料への元素ドーピング手 法の開発	表面局所構造解析
田代 孝二	大学院 工学研究科・教授	触媒・有機化合物および高分子 複合体の静的・動的構造解析	触媒・有機化合物および高 分子複合体の静的・動的構造の 解明
山方 啓	大学院 工学研究科・准教授	水素製造用水分解光触媒の 開発	水分解機構の解明と新規触媒 開発
原 正則	大学院 工学研究科・准教授	燃料電池用電極触媒の 開発と評価	炭素材料の分光評価
武野 計二	大学院 工学研究科・教授	水素のバイオマスからの製造およ び高圧水素の利用	バイオマスからの触媒的水素 製造手法の開発
張 振中	大学院 工学研究科・ ポスドクラル研究員	担持型金属ナノ粒子の 触媒反応開発	担持型金属ナノ粒子の 触媒機能評価

新

変更前の所属・職名	変更(就任)後の所属・職名	研究者氏名	プロジェクトでの役割
山梨大学 燃料電池ナノ 材料研究センター・ 特任助教	大学院工学研究科・准教授	原 正則	炭素材料の分光評価

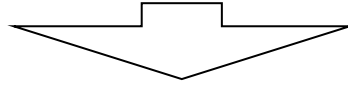
(変更の時期:平成 28 年 4 月 1 日)

法人番号	231023
プロジェクト番号	S1511022

旧

プロジェクト外での研究課題	所属・職名	研究者氏名	プロジェクトでの役割
担持型金属ナノ粒子の触媒反応開発	大学院工学研究科・ポスドクラル研究員	細川 さとみ	担持型金属ナノ粒子の触媒機能評価

(変更の時期:平成 29 年 4 月 30 日)



新

変更前の所属・職名	変更(就任)後の所属・職名	研究者氏名	プロジェクトでの役割
九州大学大学院理学研究院・学術研究員	大学院工学研究科・ポスドクラル研究員	張 振中	担持型金属ナノ粒子の触媒機能評価

(変更の時期:平成 29 年 4 月 1 日)

新

変更前の所属・職名	変更(就任)後の所属・職名	研究者氏名	プロジェクトでの役割
大学院工学研究科・教授	大学院工学研究科・教授	武野 計二	バイオマスからの触媒的水素製造手法の開発

(変更の時期:平成 30 年 5 月 1 日)

法人番号	231023
プロジェクト番号	S1511022

11 研究の概要(※ 項目全体を10枚以内で作成)

(1) 研究プロジェクトの目的・意義及び計画の概要

【目的】

本プロジェクトでは、各人がこれまでに蓄積してきた研究実績を融合させ、水素を中心とする炭素、窒素、酸素、ケイ素との元素間結合の活性化と切断・生成反応の高度制御を「デザインされた高機能金属触媒」により達成することで、低炭素社会を支える再生可能エネルギーの有効活用と有用物質の効率的な合成プロセスの構築を目ざす。

【意義】

資源や環境の保全とエネルギー確保の観点から、水素の発生・活用技術の高度化と水素に関連する物質製造工程の革新が急務である。本研究は水素と触媒を鍵に、物質合成とエネルギー技術を有機的に繋ぐことで水素の発生と活用の技術の革新を目指しており、水素社会に向けた水素の需給システムの進化と、元素戦略に立脚した水素を用いる物質変換・合成技術の発展への寄与が期待できる。

【計画の概要】

「水素」原子や分子の発生と利活用に関する主要課題の解決を目指す。特に、水素に関連する「触媒」技術に焦点を絞り、

I-A) 水分解光触媒の動作機構の解明と高度化、

I-B) 太陽電池を電源とする水の電気分解で生じた水素の貯蔵と再放出の制御や水電解および燃料電池の電極触媒の開発、

II) 水素関連化合物における多重結合の「還元」を制御し、物質の変換や合成反応の効率を格段に高める高機能触媒の開発を行う。

[年次計画概要]

1 年目: (I-A) 可視光吸収型光触媒の高度化と光吸収特性の検討;

(I-B) 水分解用高効率太陽電池デバイスの開発;

(II) 窒素ドープ炭素材料およびそれらを担体とする金属担持被毒触媒の合成と解析

2 年目: (I-A) 光励起キャリア再結合の機構解明と速度制御;

(I-B) 直列型水分解システムの構築と化合物探索

(II) 被毒触媒の各種水素化反応における触媒機能評価と触媒の再設計

3 年目: (I-A) 触媒の再設計; (I-B) システム改良と触媒探索;

(II) 官能基選択的水素化反応の実現

4 年目: (I-A) 電子-正孔分離機構解析と p-n 接合型触媒創製;

(I-B) 触媒合成法とシステム構築の技術の検討

(II) ヒドロシランによる低反応性化合物用の触媒探索と高活性触媒反応の構築

5 年目: 各研究課題の達成度の見極めと最終調整, およびプロジェクトの総括

法人番号	231023
プロジェクト番号	S1511022

(2) 研究組織

最終的には、本学にあるすべての分野(物質・電子・機械)に属する6研究室の7名の教員(当初は物質・電子の2分野:5名)が「先端触媒開発研究センター」を形成し、基礎科学研究から応用開発研究までを有機的な連携体制により推進する。これらに加え、学内外の関連する教員からも適宜協力を得て研究代表者が統括して実施している。また、各担当教員の指導の下で博士研究員や大学院生、学部4年生の30名ほどが研究に参加している。研究設備としては、参加教員の保有する分析機器の相互利用に加え、本学の施設である「共同利用クリーンルーム」も利用している。

また、東京大学大学院の堂免一成教授ならびに九州大学大学院の徳永信教授に外部評価委員をお願いし、適宜助言を頂いている。

(3) 研究施設・設備等

核磁気共鳴装置 (JEOL JMN-ECZ400R)
 元素分析装置 (PerkinElmer 2400 II)
 グローブボックス (MBRAUN Labster 1200/780 W)
 赤外分光装置 (ブルカーオプティクス社・Vertex80)
 ナノ欠陥イメージング装置 (堀場製作所・ZAT)
 原子層堆積装置 (Ultratech Savannah G2 S100)

(4) 研究成果の概要 ※下記、13及び14に対応する成果には下線及び*を付すこと。

【水分解光触媒の開発】

＜優れた成果が上がった点＞

光触媒を用いると、太陽エネルギーを用いて水から水素を製造することが可能となる。しかし、この光触媒を工業的に用いるためには、その活性を飛躍的に向上させる必要がある。光触媒としては、一般に金属酸化物や金属酸窒化物などの粉末が用いられる。粉末の表面には欠陥が多数有り、この欠陥が活性を低下させる最大の原因であると従来考えられてきた。しかし、粉末の欠陥は光励起電子と正孔の再結合速度の遅延に役立つと共に、光触媒活性の向上にも役立つ場合があることを発見^{*44,52}した。この発見は、より高性能な光触媒の設計に役立つ極めて重要な成果であると考えている。従来の光触媒開発は、表面欠陥を少なくする方向で研究が進められてきた。しかし、活性を向上するためには設計思想を180度変えなければいけないということである。実際に光触媒粒子に意図的に欠陥を導入することで、光触媒の活性や反応選択性が変化することを実証^{*11,12}した。

＜課題となった点＞

表面欠陥は再結合速度を遅くし、光触媒活性の向上に役に立つ場合があることを明らかにしたが、すべての欠陥が活性向上に役立つわけではない。事実、 SrTiO_3 の場合、表面欠陥はナノ秒領域以降に残存する光励起キャリアの数を増加させるが、ピコ秒領域における再結合速度は欠陥によって加速することを明らかにした。このように欠陥には再結合を促進する効果と抑制する二つの効果があることを明らかにした。しかし、この相反する効果がどのような理由によって発現するのか不明である。例えば WO_3 の場合、欠陥は再結合速度を速くする効果の方が大きい、 Ga_2O_3 では再結合が遅くなる効果の方が大きい。欠陥の構造や組成だけではなく、材料によっても効果が異なる。この効果の違いを明らかにすることができれば、より普遍的な原理の発見に繋がると期待される。

＜自己評価の実施結果と対応状況＞

中間評価の段階では、いくつかの光触媒材料において、欠陥が光触媒活性向上に役立つ可能性があることを報告した。しかし、その後、この研究を様々な光触媒材料に発展させた結

法人番号	231023
プロジェクト番号	S1511022

果、欠陥が活性向上に役立つ場合とむしろ活性を低下させる場合があり、この違いには、ある法則性があることが分かってきた。

<外部(第三者)評価の実施結果と対応状況>

フェムト秒から秒の時間領域で可視から中赤外域の過渡吸収スペクトルを測定することで、光触媒中に生成した電子や正孔の動きを独立に評価できる分析手法を開発し、反応機構解明に役立つことが評価された。その後、さらに実験装置と解析手法を改良し、異種接合界面における界面電荷分離過程や反応過程を明らかにすることができるようになった。また、ピコ秒領域における発光寿命も過渡吸収測定と同じ実験条件で測定することが可能になり、複雑な構造を有する光触媒粒子の中における複雑なキャリアの動きをさらに詳しく解析することが可能になった。

<研究期間終了後の展望>

欠陥には光触媒活性の向上に役立つ場合と活性を低下させる場合があることを明らかにした。今後はこのメカニズムを明らかにする。最近の計算化学の進歩によって、複雑な欠陥における電子状態を予測することが可能になりつつある。今後は、計算グループとも積極的に共同研究を行うことで実験と理論の両面から欠陥を解析し、より高い性能を有する光触媒設計に貢献したい。

<研究成果の副次的効果>

独自の分光分析技術を用いて、水を分解する光触媒のメカニズムを調べる研究の過程で、この手法が発光材料や色素太陽電池や有機太陽電池の開発にも役立つことが明らかになった。異分野の研究者との交流も活発になり、より大きな研究ネットワークの構築に役立った。

【水素の貯蔵と放出用の高機能触媒開発】

<優れた成果が上がった点>

将来の脱炭素社会の実現に対して、再生可能エネルギーである太陽電池で発電した電気を用いて水を分解し水素を得、その水素を分子に付加して貯蔵し、必要に応じて燃料電池を用いてその分子に貯蔵されている水素を取り出して用いて発電するシステムの実現を目標に研究を進めてきた。従来の太陽電池により得られる電位差は、結晶シリコン太陽電池で0.7V以下である。それに対し、本研究では水を分解するに有効な特に高い電圧の実現を目指して、キャリア選択型結晶シリコン太陽電池、さらには本太陽電池をベースとした多接合型太陽電池の開発を進めてきた。一方、水の電気分解で得られた水素を自然由来の分子の形で貯蔵する触媒、必要に応じてその分子から水素を取り出して発電する触媒としての金属担持ポリシリコンなどの材料探索を行ってきた。結果として、高い電圧が得られる太陽電池の実現と、電気分解で得られた水素の分子への付加、付加した分子を用いての燃料電池による発電などの原理実証を行い、提案システムの有効性を示した。

<課題となった点>

太陽電池を用いた発電時に、電極が水と反応し劣化する問題が生じた。いくつかの改善策を検討してきたが、長期安定性が太陽電池の一つの課題である。また、触媒においては過還元の抑制と効率的な還元の両立がいまだ課題である。

<自己評価の実施結果と対応状況>

太陽電池材料や太陽電池構造を総合的に幅広く研究している機関は、本学以外には国内外において稀有である。本目的に適したキャリア選択型シリコン太陽電池を試作する工程を確立し、幅広い検討を行ってきた。特に、本目的のキャリア選択型太陽電池用の電極材料として、酸化チタンや安定性向上のためにタンタルをドーピングした酸化チタン材料を開発^{*国際²}

法人番号	231023
プロジェクト番号	S1511022

するなど、多くの重要な結果が得られている。また、水分解により得られた水素を効率的にキノン系分子に添加できること^{*国際¹}を示すなど、水素付加および取り出しの実験においても一定の成果を示すことができた。

<外部(第三者)評価の実施結果と対応状況>

従来と比較して高効率で太陽光を電気に変換し、かつ、その時の電圧が高いpn接合を有しない新たなキャリア選択型の太陽電池の研究、ならびに水素原子の分子保存に関する研究結果に関しては、高く評価されている。

<研究期間終了後の展望>

太陽電池に関しては、より高い電圧発生が期待されるキャリア選択型シリコン太陽電池をベースとしたタンデム太陽電池の開発を進める。タンデム太陽電池においては、異なる材料の太陽電池をシリコン太陽電池の上に積層する。このとき、発電時には、多くの光が上層の太陽電池により吸収されるため、下層の結晶シリコン太陽電池における発電時の電流が低下する。このような低照度下においても高い電圧を維持するには、今まで以上に結晶シリコン表面の保護効果を高める必要がある。そのための方策を検討することが重要である。一方、分子における水素の着脱に関しては、より効率的な水素の付加や取り出しに適した触媒の探索や、保存用の分子としてより汎用性の高いものを探索する必要がある。

<研究成果の副次的効果>

得られた結果は単に太陽電池に関するものではなく、光触媒など他の研究にも広く波及する成果である。プロジェクトを通じたこのような異分野との交流を通じて、今回得られた結果が広く触媒分野における知見を深めることに貢献することが期待される。

【水電解および燃料電池の電極触媒の開発】

<優れた成果が上がった点>

水電解用のアノード触媒(酸素発生反応(OER)触媒)である IrO₂ 触媒の高活性化のため、ナノ炭素材料(グラフェンやカーボンナノチューブ)を担体に用い、IrO₂ 触媒のナノ粒子化による比表面積の向上により、担体の無い既存触媒の 10 倍以上まで触媒の OER 質量活性を向上させることに成功^{*3}した。さらに触媒の比活性を向上させる目的で、担体であるグラフェンへの窒素やホウ素のドーピングや IrO₂ ナノ粒子を RuO₂ との合金化により IrO₂ の電子状態を修飾することで、活性をさらに 10 倍以上向上させることに成功^{*2}した。このように、ナノ粒子化による比表面積向上と電子状態修飾による比活性向上の相乗効果により、触媒活性を既存触媒から2桁向上することに成功した。水素を燃料に用いた直接形燃料電池のアノード触媒の開発では、窒素やホウ素をドーピングしたグラフェンが高活性を示すこと^{*国際⁸,国内⁷}を見出した。これより、異種元素で修飾したナノ炭素材料が非金属の電極触媒として有望であることを明らかにした。

<課題となった点>

水電解のアノード触媒は、高電位・高電流に対する耐性が必要となるため、IrO₂ 以外の金属を使用することが困難である。そのため、IrO₂ を電子的に修飾することにより、触媒活性を向上する必要がある。また、酸化耐性があり高導電性の材料が必要とされる。本研究では、窒素とホウ素を共ドーピングすることにより、担体の一部を耐久性の高い BN シートで置き換えることで、IrO₂ 触媒活性の向上に対する寄与を維持しつつ、担体の耐久性向上にも成功した。

<自己評価の実施結果と対応状況>

中間審査では、ナノ炭素担体を適用することで、IrO₂ 触媒のナノ粒子化による比表面積と触媒活性の向上に成功しており、更なる触媒活性向上には、IrO₂ 触媒の比活性を向上させることが求められていた。中間審査以降、担体であるグラフェンへの異種元素ドーピングにより、IrO₂

法人番号	231023
プロジェクト番号	S1511022

触媒ナノ粒子の電子状態を修飾する技術を確立することにより、さらに高活性な触媒を開発することに成功した。

<外部(第三者)評価の実施結果と対応状況>

外部評価(中間審査)では、欠陥を導入したグラファイトを用いた電極触媒の開発とその高活性化には、試行錯誤的なスクリーニングに頼るのではなく、詳細な反応機構の解明が必要であると指摘を受けた。本研究では、反応物(H₂O および吸着 OH)との結合形成に関与する要素として、Ir の電子状態を評価することで、触媒の電子状態変化が触媒活性向上の指針となることを示した。

<研究期間終了後の展望>

再生可能エネルギーの有効利用に向けた、固体高分子形水電解槽による余剰電力を活用した水素製造装置の開発において、電力ロスの大いアノード触媒の高活性化に成功した。開発した触媒を用いることにより、貴金属である Ir の触媒使用量を低減しつつ、エネルギー変換効率の大幅な向上が期待される。今後は、固体高分子形水電解槽の実セルを用い、新規触媒の実用に向けた触媒開発を進める。

<研究成果の副次的効果>

本研究では、担体の修飾により担持された酸化物触媒の電子状態の制御とそれに伴う触媒の高活性化が可能であることを明らかにした。これにより、高活性触媒の開発における担体の重要性を示すことができ、外部資金の獲得に繋がった。今後、ナノ構造の制御が容易なナノ炭素材料のさらなる用途の拡大が期待できる。

【バイオマスからの触媒的水素製造手法の開発】

<優れた成果が上がった点>

木本類や草本類などのバイオマスの利用促進には、ガス化(H₂ や CO 製造)や液化による減容化が必須とされる。これまでのガス化反応速度の計測や解析は、バイオマスの加熱や H₂O との反応における共存ガスの影響が考慮されていないが、部分酸化ガス化炉では CO₂ が高濃度で共存しているため、本研究ではバイオマスの熱分解を CO₂ の存在下で行わせ、生成したチャーの性状およびガス化反応性を調べた。ラマン分光や質量分析を用いた熱分解ガスの分析結果などから、バイオマスチャー作製を CO₂ 雰囲気で行う事で、反応率が低い低温範囲から水素転換ガス化反応が起こり易いチャーが生成すること、更に低温反応性の違いは官能基に依存すること*^{国内⁵}を初めて明らかにした。

水素は単位体積当たりの発熱量が他の可燃性気体と比較して小さいため(メタンの約 1/3、プロパンの約 1/8)、燃料として使用する場合には高圧貯蔵が必須である。水素の利用として必須な、高圧水素の噴出時の着火について、最大よどみ圧力を 14 MPa として水素噴流における衝撃波構造と着火特性の関係を実験的に調査した。その結果、ノズル出口以降に衝撃波が生じない適正膨張の場合に保炎に必要な最小流量が最大になるなど、衝撃波構造が着火に及ぼす影響を明らかにした*⁵。

<課題となった点>

CO₂ の存在下で乾留されたバイオマスは低温でのガス化反応性が高くなるとの知見は得られたものの、官能基が影響している化学的機構までは言及されていない。これには原子吸光など官能基の同定が可能な計測法を用いた多くの実験データが必要である。

高圧水素の利用に関しては、ノズル下流における衝撃波の構造と着火・保炎の関係が明確にされたが、その機構を説明するには速度場の計測が必要である。

<自己評価の実施結果と対応状況>

法人番号	231023
プロジェクト番号	S1511022

バイオマスのガス化反応はこれまで数多くの研究が成されてきたが、乾留時の共存ガスの影響については、ほとんど研究例が報告されていなかった。今回 CO₂ の存在下で乾留を行い、生成チャーの低温域でのガス化反応性が向上するとの新しい知見を得た。

<研究期間終了後の展望>

課題となった点にも記した通り、バイオマスのガス化に関する興味深い現象が得られたものの、その化学的メカニズムは明確にされておらず、今後原子吸光分析法などを用い明確にする計画である。高圧水素の利用に関しても、衝撃波の下流の流れについてPIV法を用いた計測を行い、着火・保炎の機構について明確にする。

<研究成果の副次的効果>

高圧水素の利用についての成果は、JAEA(日本原子力研究開発機構)における水素安全研究に活用できる。

【高機能触媒による水素化およびヒドロシリル化反応の開発】

<優れた成果が上がった点>

活性炭担持パラジウム触媒にヒドロシランを作用させると、アミド化合物の脱酸素型還元反応を穏和な条件下で進行させるほど高活性な可溶性の金属クラスターが生成することから、この活性種の応用について検討した。その結果、活性炭担持パラジウムだけでなく安価な塩化パラジウムでも土居用の活性種が発生すること、さらに通常困難な 4 級炭素-酸素結合、特に *tert*-ブチル-酸素結合を穏和な条件下で切断可能なことを見出し、新規な *tert*-基の脱保護手法の開発に成功^{*4}した。

既に炭素ナノ繊維存在下、0価の白金オレフィン錯体に常温・常圧で水素を接触させると、高活性な白金クラスターが系中で発生することを見出していた。そこで反応条件を精査した結果、安価な活性炭でも同様にクラスターが生成し、常温・常圧で多様な官能基を有する芳香族化合物の環水素化が進行^{*国内^{11,13}}することを見出した。

さらに従来用いてきた炭素材料に替わり金属酸化物を担体として用いると、特殊な化学選択性を有する金属クラスターが生成することを見出した。すなわち、カルボニル化合物の中で通常では反応しやすいアルデヒドやケトンは全く水素化されず、イミンが選択的に水素で還元できる。この特長を利用して、カルボニル化合物をアルキル化剤として用いるアミンの還元的 *N*-アルキル化を、常温・常圧の穏和な条件下、両試剤を化学量論量用いるという高効率・高選択的な反応として実現^{*国内¹²,国際²}した。

<課題となった点>

極めて微小で高活性な金属クラスター種の発生手法を幾つか開発することに成功し、これらが従来のクラスターとは異なる触媒活性や化学選択性を示すことを明らかにした。しかし、触媒機能とクラスターサイズの相関が触媒設計において重要であるが、そのサイズや分散度が未だに不明な場合が多いことから、サイズ制御法の確立が喫緊の課題である。

<自己評価の実施結果と対応状況>

中間評価の段階では、担体を高価で自作が必要な炭素ナノ繊維から安価で大量合成が可能な炭素材料などへの変換、さらにクラスターサイズをより小さくすることによる高活性化、を目標としていた。これらにおいて、反応条件を再検討することでクラスター前駆体の候補を拡張しつつ、新たな発生法ならびに担体への担持手法を構築することができ、市販の活性炭や金属酸化物などへの転換を実現すると共に、担体特有の化学選択性の賦与にも成功した。

<外部(第三者)評価の実施結果と対応状況>

外部評価(中間審査)では、従来還元が難しいカルボン酸アミドの還元や、中および大員環

法人番号	231023
プロジェクト番号	S1511022

ラクトンからの部分還元体であるラクツールや脱酸素型還元体である環状エーテルへの新規な変換手法の開発が評価された。その後、特に後者については、これらの触媒的な変換手法を用いることで、天然物や医薬品合成に適用できることを実証した。

<研究期間終了後の展望>

この研究期間では、金属種としてパラジウムを中心に詳細な検討や機構解析、さらには実践的な触媒的合成反応への展開を図ってきた。しかしヒドロシランによる微小な可溶性金属クラスターの発生は、ルテニウム、ロジウム、白金でも確認できている。同様に金属酸化物上への他の金属種のクラスター形成も一部で確認されている。そこで今後は、金属種の拡張、また、担体として各種炭素材料や金属酸化物へと展開して一連の担持型金属クラスターのライブラリを構築し、それらの担体-金属種-活性の相関を精査していく予定である。

<研究成果の副次的効果>

本研究で得られた成果は、単に有機合成用の触媒としての利用だけではなく、同様の金属クラスターを活用しているエレクトロニクス、環境、バイオ、医療、材料開発などへの応用展開も可能と考えられることから、その波及効果は広範な分野に及ぶものと期待される。

【原子間力顕微鏡を用いた触媒担持メカニズムの分子レベル評価】

<優れた成果が上がった点>

水電解におけるアノード触媒である IrO_2 のサイズは、炭素材料上に担持することで数 nm 程度になり、サイズ効果や実効表面積の増大によって触媒の活性が向上することが報告されている。 IrO_2 が炭素表面にどのように担持されているかについては、光電子分光法(XPS)や電子顕微鏡(TEM)を用いることにより、炭素との結合状態や分散性をマクロ的に調べることで分析可能である。触媒効果の観点から考えると、触媒粒子のサイズや位置制御はその性能に大きな影響を与えることから極めて重要である。今回、高品質の単層グラフェンに対し故意に欠陥を導入し、その表面を分子レベルで評価した上で、欠陥表面が IrO_2 の担持メカニズムに与える影響を、原子間力顕微鏡(AFM)を用いて詳細に調べることに成功した。結果として、欠陥導入により形成されるグラフェンのナノレベルの空洞構造のエッジ部分に IrO_2 が核成長し、欠陥密度が大きいほど IrO_2 の粒子サイズが小さくなるという極めて重要な結果が示された。

<課題となった点>

モデル表面として選んだ炭素材料であるグラフェンには、高品質と大面積化が必要となる。グラフェンの化学気相成長合成の実験条件(合成温度、原料ガス分量)を最適化し、かつ転写方法(バブル法)を工夫することにより、mm オーダーの高品質グラフェンの形成に至った。一方、 IrO_2 の担持法として、今回水熱合成法を用いたが、グラフェンの平面構造を維持した状態で微粒子担持するために、水熱反応条件をよりマイルドに最適化する必要があった。これについては加熱温度や時間などを細かく制御することにより実現し、最終的に欠陥を導入したグラフェン上へグラフェンの初期構造を維持したまま微粒子を担持することに成功した。

<自己評価の実施結果と対応状況>

上記のようにグラフェン形成方法、欠陥導入プロセスの適切な選択(オゾン処理)、及び担持法の改良により、担持メカニズムを分子レベルで解明することに成功した。今後は水電解としての実触媒機能との対応を明らかにする必要がある。

<外部(第三者)評価の実施結果と対応状況>

分子レベルの材料評価技術は触媒反応プロセスを解明する上で重要であり、原子レベルで観察できる原子間力顕微鏡を駆使することにより、触媒の担持プロセスを明らかにすることができた。

法人番号	231023
プロジェクト番号	S1511022

<研究期間終了後の展望>

本研究から、欠陥導入量により触媒サイズを制御することが可能となったので、今後はアノード触媒としての実評価を行う必要がある。本研究で明らかにした微粒子形成メカニズムは活性炭素など一般的な炭素材料にも適用可能であり、触媒サイズの最適化により、高効率、かつ非常に安価な触媒開発に繋がると考えられる。

<研究成果の副次的効果>

本研究のようなモデル表面を用いた分子レベルでの触媒担持メカニズムの報告例は極めて少なく、本研究の波及成果は多大なものと考えられる。実際に、本研究期間中に、複数の企業からの多くの分析依頼があり、その中でいくつかの共同研究に至っている。

【触媒・有機化合物および高分子錯体の静的・動的構造解析】

<優れた成果が上がった点>

X線結晶構造解析に中性子結晶構造解析を結合させることで、ポリジアセチレン高分子の巨大単結晶においてX線と中性子(N)の精密結晶構造解析に成功するとともに、両者の差として、分子鎖に沿った結合電子密度分布の定量的評価に成功^{*30,33}した。この快挙は、1世紀にもわたる高分子科学の歴史の中で初めてのものである。

また、従来はポリビニルアルコールおよびそのヨウ素錯体についてX線構造解析結果を正解と思い込まれてきたが、今回新たに測定した中性子データを全く説明できないことが判った。「構造の乱れ」という新たな概念を導入することで、このX線と中性子回折データ解析の矛盾を解消することに成功^{*国内³⁹}すると共に、ポリビニルアルコールのヨウ素錯体形成機構についての具体的描像^{*国内³⁹}を与えることができた。

<課題となった点>

電子密度分布の解析精度を高める解析技術の開発、および、これまで常識とされてきた構造を否定するに足る高信頼性の実験データを如何に集積するかが課題であった。最先端の放射光および中性子(J-PARC)の利用が問題解決につながった。

<自己評価の実施結果と対応状況>

再生可能エネルギーを利用した水素の製造・貯蔵法・新活用法の探索を目指した本プロジェクトの対象の一つに高分子材料を含めている。しかし、高分子材料における水素の役割を明らかにするためには、水素原子の位置や運動性、電子との相関など、高分子物質としてこれまで殆ど不可能と諦観されてきた課題に挑戦せねばならない。そこで高分子物質の構造物性相関を原子さらには電子レベル、つまり量子レベルから、どこまで精度高く明確に出来るかに焦点をあてた。その結果、幾つかの高分子において密度汎関数法に基づく量子化学計算結果とほぼ完全に一致するまでに至った。

<外部(第三者)評価の実施結果と対応状況>

外部評価(中間審査)では、汎用の高分子ヨウ素錯体の詳細な構造解析に成功したことから、その生成機構や構造に関する新たな知見となったことが評価された。その後、この最先端の量子ビームシステムを利用して、様々な高分子化合物の結合電子密度分布状態の解析にも適用できることを実証した。

<研究期間終了後の展望>

X線結晶構造解析に中性子結晶構造解析を結合させたシステムは、高分子物質の構造物性相関の基礎となる「結合に関与する電子密度分布」の定量評価に有効なことを実証した。この成功により、一般の高分子物質についても電子レベルからの検討が可能になると期待できる。

法人番号	231023
プロジェクト番号	S1511022

＜研究成果の副次的効果＞

今回の成果は、これまで殆ど諦観されてきた「高分子および高分子＝無機錯体における構造物性相関の量子レベルからの解明」に必要な、「水素原子および結合電子に関する構造情報の獲得」を呈示した初めての成功例であり、今後は「量子高分子科学」といった新しい学問体系を構築する最初の一步であると確信する。

＜外部(第三者)評価の実施結果と対応状況＞

全体としては、中間報告時に外部評価委員 2 名からプロジェクト全体の評価をお願いし、両氏からの評価は概ね良好であった。特に本プロジェクトにおける基礎研究と応用研究の融合において高い評価を受けていたことから、残りの2年間では、これまで以上に基礎から応用までをバランスよく、さらに研究を加速させるとともに、本研究成果を基盤とするプロジェクト終了後の新たな方向性についても議論を開始し、外部資金への申請等も積極的に行っている状況であり、本学の新たな研究基盤が着実に形成されているものと考えている。

12 キーワード(当該研究内容をよく表していると思われるものを8項目以内で記載してください。)

- | | | |
|--------------------|------------------------|-----------------|
| (1) <u>水分解光触媒</u> | (2) <u>キャリア選択型太陽電池</u> | (3) <u>燃料電池</u> |
| (4) <u>炭素材料</u> | (5) <u>金属ナノ粒子</u> | (6) <u>還元反応</u> |
| (7) <u>元素ドーピング</u> | (8) <u>分子間相互作用</u> | |

法人番号	231023
プロジェクト番号	S1511022

13 研究発表の状況(研究論文等公表状況。印刷中も含む。)

上記、11(4)に記載した研究成果に対応するものには*を付すこと。

<雑誌論文>

【水分解光触媒の開発】

- 1 K. Kawashima, M. Hojamberdiev, H. Wagata, K. Yubuta, J. J. M. Vequizo, A. Yamakata, S. Oishi, K. Domen, K. Teshima, “NH₃-Assisted Flux-Mediated Direct Growth of LaTiO₂N Crystallites for Visible-Light-Induced Water Splitting”, *J. Phys. Chem. C* **2015**, *119*, 15896-15904.
- 2 M. Hojamberdiev, K. Yubuta, J. J. M. Vequizo, A. Yamakata, S. Oishi, K. Domen, K. Teshima, “NH₃-Assisted Flux Growth of Cube-like BaTaO₂N Submicron Crystals in a Completely Ionized Nonaqueous High-Temperature Solution and Their Water Splitting Activity”, *Cryst. Growth Des.* **2015**, *15*, 4663–4671.
- 3 A. Yamakata, Y. Ham, M. Kawaguchi, T. Hisatomi, J. Kubota, Y. Sakata, K. Domen, “Morphology-sensitive trapping states of photogenerated charge carriers on SrTiO₃ particles studied by time-resolved visible to Mid-IR absorption spectroscopy: The effects of molten salt flux treatments”, *J. Photochem. Photobiol. A-Chem.* **2015**, *313*, 168-175.
- 4 A. Yamakata, J. J. M. Vequizo, H. Matsunaga, ”Distinctive Behavior of Photogenerated Electrons and Holes in Anatase and Rutile TiO₂ Powders”, *J. Phys. Chem. C* **2015**, *119*, 24538-24545.
- 5 Y. Ham, T. Hisatomi, Y. Goto, Y. Moriya, Y. Sakata, A. Yamakata, J. Kubota, K. Domen, “Flux-mediated doping of SrTiO₃ photocatalysts for efficient overall water splitting”, *J. Mater. Chem. A* **2016**, *4*, 3027-3033.
- 6 M. Hojamberdiev, H. Wagata, K. Yubuta, K. Kawashima, J. J. M. Vequizo, A. Yamakata, S. Oishi, K. Domen, K. Teshima, “KCl Flux-Induced Growth of Isometric Crystals of Cadmium-Containing Early Transition-Metal (Ti⁴⁺, Nb⁵⁺, and Ta⁵⁺) Oxides and Nitridability to Form Their (Oxy)nitride Derivatives under an NH₃ Atmosphere For Water Splitting Application”, *Appl. Catal. B-Environ.* **2016**, *182*, 626-635.
- 7 A. Yamakata, M. Kawaguchi, R. Murachi, M. Okawa, I. Kamiya, “Dynamics of Photogenerated Charge Carriers on Ni- and Ta-Doped SrTiO₃ Photocatalysts Studied by Time-Resolved Absorption and Emission Spectroscopy”, *J. Phys. Chem. C* **2016**, *120*, 7997-8004.
- 8 R. Kuriki, H. Matsunaga, T. Nakashima, K. Wada, A. Yamakata, O. Ishitani, K. Maeda, ”Nature-Inspired, Highly Durable CO₂ Reduction System Consisting of a Binuclear Ruthenium(II) Complex and an Organic Semiconductor Using Visible Light”, *J. Am. Chem. Soc.* **2016**, *138*, 5159-5170.
- 9 山方啓, 「酸化チタン光触媒のキャリアーダイナミクスー粉末におけるアナターゼとルチルの特異的な挙動ー」, *光化学* **2016**, *47*, 25-32.
- 10 J. J. M. Vequizo, M. Yokoyama, M. Ichimura, A. Yamakata, “Enhancement of Photoelectrochemical Activity of SnS Thin-film Photoelectrodes using TiO₂, Nb₂O₅, and Ta₂O₅ Metal Oxide Layers”, *Appl. Phys. Express* **2016**, *9*, 067101.
- 11 Y. Sakata, Y. Miyoshi, T. Maeda, K. Ishikiriya, Y. Yamazaki, H. Imamura, Y. Ham, T. Hisatomi, J. Kubota, A. Yamakata, K. Domen, “Photocatalytic Property of Metal ion Added SrTiO₃ to Overall H₂O splitting”, *Appl. Catal. A- Gen.* **2016**, *521*, 227-232. (*11)
- 12 M. Hojamberdiev, M. F. Bekheet, E. Zahedi, H. Wagata, J. J. M. Vequizo, A. Yamakata, K. Yubuta, A. Gurlo, K. Domen, K. Teshima, “The contrasting effect of the Ta/Nb ratio in (111)-layered B-site deficient

法人番号	231023
プロジェクト番号	S1511022

- hexagonal perovskite $\text{Ba}_5\text{Nb}_{4-x}\text{Ta}_x\text{O}_{15}$ crystals on visible-light-induced photocatalytic water oxidation activity of their oxynitride derivatives”, *Dalton Trans.* **2016**, 45, 12559-12568. (*12)
- 13 J. J. M. Vequizo, H. Matsunaga, T. Ishiku, S. Kamimura, T. Ohno, A. Yamakata, “Trapping-Induced Enhancement of Photocatalytic Activity on Brookite TiO_2 Powders: Comparison with Anatase and Rutile TiO_2 Powders”, *ACS Catalysis*, **2017**, 7, 2644-2651.
- 14 A. Nakada, S. Nishioka, J. J. M. Vequizo, K. Muraoka, T. Kanazawa, A. Yamakata, S. Nozawa, H. Kumagai, S. Adachi, O. Ishitani, K. Maeda, “Solar-driven Z-scheme water splitting using tantalum/nitrogen co-doped rutile titania nanorod as an oxygen evolution photocatalyst”, *J. Mater. Chem. A*, **2017**, 5, 11710-11719.
- 15 M. Hojamberdiev, M. F. Bekheet, J. N. Hart, J. J. M. Vequizo, A. Yamakata, K. Yubuta, A. Gurlo, M. Hasegawa, K. Domen, K. Teshima, “Elucidating the Impact of A-Site Cation Change on Photocatalytic H_2 and O_2 Evolution Activities of Perovskite-Type LnTaON_2 ($\text{Ln} = \text{La}$ and Pr)”, *Phys. Chem. Chem. Phys.*, **2017**, 19, 22210-22220.
- 16 M. Hojamberdiev, M. F. Bekheet, J. N. Hart, J. J. M. Vequizo, A. Yamakata, K. Yubuta, A. Gurlo, M. Hasegawa, K. Domen, K. Teshima, “Cation-dependent restructure of the electric double layer on CO-covered Pt electrodes: Difference between hydrophilic and hydrophobic cations”, *J. Electroanal. Chem.*, **2017**, 800, 19-24.
- 17 K. Wada, C. S. K. Ranasinghe, R. Kuriki, A. Yamakata, O. Ishitani, K. Maeda, “Interfacial Manipulation by Rutile TiO_2 Nanoparticles to Boost CO_2 Reduction into CO on a Metal-Complex/Semiconductor Hybrid Photocatalyst”, *ACS Appl. Mater. Interfaces*, **2017**, 9, 23869–23877.
- 18 J. J. M. Vequizo, S. Kamimura, T. Ohno, A. Yamakata, “Oxygen Induced Enhancement of NIR Emission in Brookite TiO_2 Powders: Comparison with Rutile and Anatase TiO_2 Powders”, *Phys. Chem. Chem. Phys.*, **2018**, 20, 3241-3248.
- 19 C. S. K. Ranasinghe, A. Yamakata, “Structural Changes of Water Molecules during Photoelectrochemical Water Oxidation on TiO_2 Thin Film Electrodes”, *Phys. Chem. Chem. Phys.*, **2018**, 20, 3388-3394.
- 20 M. Hojamberdiev, K. Kawashima, M. Kumar, A. Yamakata, K. Yubuta, A. Gurlo, M. Hasegawa, K. Domen, K. Teshima, “Engaging the Flux-Grown $\text{La}_{1-x}\text{Sr}_x\text{Fe}_{1-y}\text{Ti}_y\text{O}_3$ Crystals in Visible-Light-Driven Photocatalytic Hydrogen Generation”, *Int. J. Hydrogen Energy*, **2018**, 42, 27024-27033.
- 21 J. J. M. Vequizo, M. Hojamberdiev, K. Teshima, A. Yamakata, “Role of CoOx Cocatalyst on Ta_3N_5 Photocatalysts Studied by Transient Visible to Mid-Infrared Absorption Spectroscopy”, *J. Photochem. Photobiol. A: Chemistry*, **2018**, 358, 315-319.
- 22 C. S. K. Ranasinghe, J. J. M. Vequizo, A. Yamakata, “Fabrication of Highly Active Transparent TiO_2 Thin Films by Atomized Spray Pyrolysis Deposition for Photoelectrochemical Water Oxidation”, *J. Photochem. Photobiol. A: Chemistry*, **2018**, 358, 320-326.
- 23 K. Maeda, D. An, C. S. K. Ranasinghe, T. Uchiyama, R. Kuriki, T. Kanazawa, D. Lu, S. Nozawa, A. Yamakata, Y. Uchimoto, O. Ishitani, “Characterization of silver species on graphitic carbon nitride nanosheets as promoters for photocatalytic carbon dioxide reduction under visible light with a mononuclear ruthenium(II) complex”, *J. Mater. Chem.*, **2018**, in press.
- 24 T. Oshima, T. Ichiba, K. S. Qin, K. Muraoka, J. J. M. Vequizo, K. Hibino, R. Kuriki, S. Yamashita, K. Hongo, T. Uchiyama, K. Fujii, D. Lu, R. Maezono, A. Yamakata, H. Kato, K. Kimoto, M. Yashima, Y. Uchimoto, M. Kakihana, O. Ishitani, H. Kageyama, K. Maeda, “Undoped Layered Perovskite Oxynitride

法人番号	231023
プロジェクト番号	S1511022

- Li₂LaTa₂O₆N for Photocatalytic CO₂ Reduction with Visible Light”, *Angew. Chem. Int. Ed.*, **2018**, in press.
- 25 Z. Lian, M. Sakamoto*, H. Matsunaga, J. J. Vequizo, A. Yamakata, M. Haruta, H. Kurata, W. Ota, T. Sato, T. Teranishi, “Near Infrared Light Induced Plasmonic Hot Hole Transfer At a Nano-Heterointerface”, *Nat. Commun.*, **2018**, in press.
- 26 A. Miyoshi, J. J. M. Vequizo, S. Nishioka, Y. Kato, M. Yamamoto, S. Yamashita, T. Yokoi, A. Iwase, S. Nozawa, A. Yamakata, T. Yoshida, K. Kimoto, A. Kudo, K. Maeda, “Nitrogen/fluorine-codoped rutile titania as a stable oxygen-evolution photocatalyst for solar-driven Z-scheme water splitting”, *Sustainable Energy & Fuels*, **2018**, 2, 2025–2035.
- 27 A. Yamakata, J. J. M. Vequizo, “Curious Behaviors of Photogenerated Electrons and Holes at the Defects on Anatase, Rutile, and Brookite TiO₂ Powders: A Review,” *J. Photochem. Photobiol. C-Photochem. Rev.*, **2018**, in press.
- 28 G. Hasegawa, M. Tanaka, J. J. M. Vequizo, A. Yamakata, H. Hojo, M. Kobayashi, M. Kakihana, M. Inada, H. Akamatsu, K. Hayashi, “Sodium Titanium Oxide Bronze Nanoparticles Synthesized via Concurrent Reduction and Na⁺-doping into TiO₂(B),” *Nanoscale*, **2018**, 11, 1442–1450.
- 29 K. Okuno, H. Kato, J. J. M. Vequizo, A. Yamakata, H. Kobayashi, Ma. Kobayashi, M. Kakihana, “Expansion of the Photoresponse Window of a BiVO₄ Photocatalyst by Doping with Chromium(VI),” *RCS Adv.*, **2018**, 8, 38140–38145.
- 30 C. Tsounis, R. Kuriki, K. Shibata, J. J. M. Vequizo, D. Lu, A. Yamakata, O. Ishitani, R. Amal, K. Maeda, “Copolymerization Approach to Improving Ru(II)-Complex/C₃N₄ Hybrid Photocatalysts for Visible-Light CO₂ Reduction,” *ACS Sus. Chem. Eng.*, **2018**, 6, 15333–15340.
- 31 A. Nakada, R. Kuriki, K. Sekizawa, S. Nishioka, J. J. M. Vequizo, T. Uchiyama, N. Kawakami, D. Lu, A. Yamakata, Y. Uchimoto, O. Ishitani, K. Maeda, “Effects of Interfacial Electron Transfer in Metal Complex–Semiconductor Hybrid Photocatalysts on Z–Scheme CO₂ Reduction under Visible Light,” *ACS Catal.* **2018**, 8, 9744–9754.
- 32 S. Komatsuda, Y. Asakura, J. J. M. Vequizo, A. Yamakata, S. Yin, “Enhanced Photocatalytic NO_x Decomposition of Visible-Light Responsive F-TiO₂/(N,C)-TiO₂ by Charge Transfer Between F-TiO₂ and (N,C)-TiO₂ through Their Doping Levels,” *Appl. Catal. B Environ.*, **2018**, 238, 358–364.
- 33 M. Hojamberdiev, Y. Cai, J. J. M. Vequizo, M. Mansoob Khan, R. Vargas, K. Yubuta, A. Yamakata, K. Teshima, M. Hasegawa, “Binary Flux-Promoted Formation of Trigonal ZnIn₂S₄ Layered Crystals Using ZnS-Containing Industrial Waste and Their Photocatalytic Performance for H₂ Production,” *Green Chem.*, **2018**, 20, 3845–3856.
- 34 R. Kuriki, C. S. K. Ranasinghe, Y. Yamazaki, A. Yamakata, O. Ishitani, K. Maeda, “Excited-State Dynamics of Graphitic Carbon Nitride Photocatalyst and Ultrafast Electron Injection to a Ru(II) Mononuclear Complex for Carbon Dioxide Reduction,” *J. Phys. Chem. C*, **2018**, 122, 16795–16802.
- 35 S. Nishioka, J. Hyodo, J. J. M. Vequizo, S. Yamashita, H. Kumagai, K. Kimoto, A. Yamakata, Y. Yamazaki, K. Maeda, “Homogeneous Electron Doping into Non-Stoichiometric Strontium Titanate Improves Its Photocatalytic Activity for Hydrogen and Oxygen Evolution,” *ACS Catal.* **2018**, 8, 7190–7200.
- 36 T. Iihoshi, T. Ohwaki, J. J. M. Vequizo, A. Yamakata, “Improvement of photocatalytic activity under visible-light irradiation by heterojunction of Cu ion loaded WO₃ and Cu ion loaded N-TiO₂,” *Appl. Catal.*

法人番号	231023
プロジェクト番号	S1511022

- B Environ.*, **2019**, *248*, 249–254.
- 37 Z. Lian, M. Sakamoto, J. J. M. Vequizo, C. S. K. Ranasinghe, A. Yamakata, T. Nagai, K. Kimoto, Y. Kobayashi, N. Tamai, T. Teranishi, “Plasmonic p–n Junction for Infrared Light to Chemical Energy Conversion,” *J. Am. Chem. Soc.*, **2019**, *141*, 2446–2450.
- 38 M. Sakamoto, T. Kawawaki, M. Kimura, J. J. M. Vequizo, H. Matsunaga, C. S. K. Ranasinghe, A. Yamakata, H. Matsuzaki, A. Furube, T. Teranishi, “Clear and Transparent Nanocrystals for Infrared-Responsive Carrier Transfer,” *Nat. Commun.* **2019**, *10*, 406–412.
- 39 K. Shibata, K. Kato, C. Tsounis, T. Kanazawa, D. Lu, S. Nozawa, A. Yamakata, O. Ishitani, K. Maeda*, “Synthesis of Copolymerized Carbon Nitride Nanosheets from Urea and 2-Aminobenzonitrile for Enhanced Visible-Light CO₂ Reduction with a Ruthenium(II) Complex Catalyst”, *Solar RRL*, **2019**, 1900461.
- 40 A. Nakada, H. Suzuki, J. J. M. Vequizo, K. Ogawa, M. Higashi, A. Saeki, A. Yamakata, H. Kageyama, R. Abe, “Fe/Ru Oxide as Versatile and Effective Cocatalyst for Boosting Z-Scheme Water Splitting: Suppressing Undesirable Backward Electron Transfer”, *ACS Appl. Mater. Interfaces*, **2019**, *11*, 45606-45611.
- 41 N. Hirayama, H. Nakata, H. Wakayama, S. Nishioka, T. Kanazawa, R. Kamata, Y. Ebato, K. Kato, H. Kumagai, A. Yamakata, K. Oka, K. Maeda, “Solar-Driven Photoelectrochemical Water Oxidation over an n-Type Lead-Titanium Oxyfluoride Anode”, *J. Am. Chem. Soc.*, **2019**, *141*, 17158-17165.
- 42 J. J. M. Vequizo, S. Nishioka, Y. Yamazaki, K. Maeda, A. Yamakata, “Crucial impact of reduction on the photocarriers dynamics on SrTiO₃ powders studied by transient absorption spectroscopy”, *J. Mater. Chem. A.*, **2019**, *7*, 26139-26146.
- 43 Y. Hiramachi, H. Fujimori, A. Yamakata, Y. Sakata, “Achievement of High Photocatalytic Performance to BaTi₄O₉ toward Overall H₂O Splitting”, *ChemCatChem*, **2019**, *11*, 6213-6217.
- 44 K. Kato, J. Jiang, Y. Sakata, A. Yamakata, “Effect of Na-doping on Electron Decay kinetics in SrTiO₃ Photocatalyst”, *ChemCatChem*, **2019**, *11*, 6349-6354. (*44)
- 45 S. Nishioka, K. Yanagisawa, D. Lu, J. J. M. Vequizo, A. Yamakata, K. Kimoto, M. Inada, K. Maeda, “Enhanced water splitting through two-step photoexcitation by sunlight using tantalum/nitrogen-codoped rutile titania as a water oxidation photocatalyst”, *Sustain. Ener. Fuels*, **2019**, *3*, 2337-2346.
- 46 K. Muraoka, J. J. M. Vequizo, R. Kuriki, A. Yamakata, T. Uchiyama, D. Lu, Y. Uchimoto, O. Ishitani, K. Maeda, “Oxygen-Doped Ta₃N₅ Nanoparticles for Enhanced Z-Scheme Carbon Dioxide Reduction with a Binuclear Ruthenium(II) Complex under Visible Light”, *ChemPhotoChem*, **2019**, *3*, 1027-1033.
- 47 Y. Luo, S. Suzuki, Z. Wang, K. Yubuta, J. J. M. Vequizo, A. Yamakata, H. Shiiba, T. Hisatomi, K. Domen, K. Teshima, “Construction of Spatial Charge Separation Facets on BaTaO₂N Crystals by Flux Growth Approach for Visible-Light-Driven H₂ Production”, *ACS Appl. Mater. Interfaces*, **2019**, *11*, 22264-22271.
- 48 F. Amano, M. Nakata, J. J. M. Vequizo, A. Yamakata, “Enhanced Visible Light Response of TiO₂ Codoped with Cr and Ta Photocatalysts by Electron Doping”, *ACS Appl. Energy Mater.*, **2019**, *2*, 3274-3282.
- 49 P.-H. Hung, J. J. M. Vequizo, R.-A. Wu, A. Yamakata, W. J. Tseng, “Effect of CuFe₂O₄ ferrite on photocatalysis and carrier dynamics of electrospun α -Fe₂O₃ nanofibers by time-resolved transient absorption spectroscopy”, *Ceram. Int.*, **2019**, *45*, 15676-15680.
- 50 M. Takagi, M. Kawaguchi, A. Yamakata, “Enhancement of UV-responsive photocatalysts aided by visible-light responsive photocatalysts: role of WO₃ for H₂ evolution in CuCl”, *Appl. Catal. B: Environ.*, **2020**, *263*, 118333.
- 51 J. Lim, H. Kim, J. Park, G. Moon, J. J. M. Vequizo, A. Yamakata, J. Lee, W. Choi, “How g-C₃N₄ Works and

法人番号	231023
プロジェクト番号	S1511022

- Is Different from TiO₂ as Environmental Photocatalyst: Mechanistic View”, *Environ. Sci. Technol.*, **2020**, *54*, 497-506.
- 52 A. Yamakata, C. S. K. Ranasinghe, N. Hayashi, K. Kato, J. J. M. Vequizo, “Identification of Individual Electron- and Hole-Transfer Kinetics at CoO_x/BiVO₄/SnO₂ Double Heterojunctions”, *ACS Appl. Energy Mater.*, **2020**, *3*, 1207-1214. (*52)
- 53 C. Noda, Y. Asakura, K. Shiraki, A. Yamakata, S. Yin, “Synthesis of Three-component C₃N₄/rGO/C-TiO₂ Photocatalyst with Enhanced Visible-light Responsive Photocatalytic deNO_x Activity”, *Chem. Eng. J.*, **2020**, *390*, 124616.
- 54 T. Kanazawa, K. Kato, R. Yamaguchi, T. Uchiyama, D. Lu, S. Nozawa, A. Yamakata, Y. Uchimoto, K. Maeda, “Cobalt Aluminate Spinel as a Cocatalyst for Photocatalytic Oxidation of Water: Significant Hole-Trapping Effect”, *ACS Catalysis*, **2020** *10*, 4960-4966.
- 55 K. Kato, A. Yamakata ”Defect-induced Acceleration and Deceleration of Photocarrier Recombination in SrTiO₃ Powders”, *J. Phys. Chem. C*, *in press*.
- 56 H. Wakayama, K. Kato, K. Kashihara, T. Uchiyama, A. Miyoshi, H. Nakata, D. Lu, K. Oka, A. Yamakata, Y. Uchimoto, K. Maeda, ”Activation of a Pt-loaded Pb₂Ti₂O_{5.4}F_{1.2} photocatalyst by alkaline chloride treatment for improved H₂ evolution under visible light”, *J. Phys. Chem. A*, *in press*.
- 57 S. Chen, J. J. M. Vequizo, T. Hisatomi, M. Nakabayashi, L. Lin, Z. Wang, A. Yamakata, N. Shibata, T. Takata, T. Yamada. K. Domen, “Efficient photocatalytic hydrogen evolution on single-crystalline metal selenide particles with suitable cocatalysts”, *Chem. Sci.*, *in press*.

【水電解および燃料電池の電極触媒の開発】

- 1 M. Hara, R. Badam, K. De Silva, H.-H. Huang, M. Yoshimura, “Fabrication and Evaluation of Nanocarbon supported Iridium Oxide catalysts for Water Electrolysis”, *PGIS research Congress 2017*, **2017**, *4*, 125.
- 2 M. Hara, R. Badam, G. J. Wang, H.-H. Huang, M. Yoshimura, “Synthesis and Evaluation of Iridium Oxide Nanoparticle Catalysts Supported on Nitrogen-Doped Reduced Graphene Oxides”, *ECS transactions*, **2018**, *85*, 27-35. (*2)
- 3 R. Badam, M. Hara, H.-H. Huang, M. Yoshimura, “Synthesis and Electrochemical Analysis of Novel IrO₂ Nanoparticle Catalysts Supported on Carbon Nanotube for Oxygen Evolution Reaction”, *Int. J. Hydrogen Energy*, **2018**, *43* 18095–18104.(*3)
- 4 D. Yoneda, S. Suzuki, S. Hiramoto, Y. Matsuoka, M. Hara, M. Yoshimura, “Growth of vertically-aligned carbon nanotubes on graphite for electric double-layer capacitors”, *Mater. Research Express*, **2019**, *6*, 086322.

【バイオマスからの触媒的水素製造手法の開発】

- 1 S. Yamamoto, R. Sakatsume, K. Takeno, “Blow-off process of highly under-expanded hydrogen non-premixed jet flame”, *Int. J. Hydrogen Energy*, **2018**, *43*, 5199-5205.
- 2 K. Okabayashi, K. Tagashira, K. Kawazoe, K. Takeno, M. Asahara, A. K. Hayashi, M. Komori, “Non-steady characteristics of dispersion and ignitability for high-pressurized hydrogen jet discharged from a pinhole” *Int. J. Hydrogen Energy*, **2019**, *44*, 9071-9079.
- 3 N. Qadi, K. Takeno, A. Mosqueda, M. Kobayashi, Y. Motoyama, K. Yoshikawa, “Effect of Hydrothermal Carbonization Conditions on the Physicochemical Properties and Gasification Reactivity of Energy Grass”, *Energy Fuels*, **2019**, *33*, 6436-6443.

法人番号	231023
プロジェクト番号	S1511022

- 4 N. Qadi, M. Kobayashi, K. Takeno, “Influence of torrefaction after densification on the fuel characteristics and the inherited gasification kinetics of Erianthus arundinaceus energy grass”, *Environmental Progress and Sustainable Energy*, **2019**, 38, 1-11.
- 5 K. Takeno, S. Yamamoto, R. Sakatsume, S. Hirakawa, H. Takeda, V. Shentsov, D. Makarov, V. Molkov, “Effect of shock structure on stabilization and blow-off of hydrogen jet flames”, *Int. J. Hydrogen Energy*, **2020**, 45, 10145-10154.(*5)

【高機能触媒による水素化およびヒドロシリル化反応の開発】

- 1 S. Hosokawa, K. Teramoto, Y. Motoyama, “Palladium on Carbon-Catalyzed Silane-Reduction of Tertiary Carboxamides: Soluble Palladium Colloids are an Active Catalyst Species”, *ChemistrySelect* **2016**, 1, 2594-2602.
- 2 Y. Motoyama, K. Morii, S. Ishizuka, S. Inomoto, Z. Zhang, S.-H. Yoon, “Specific Inhibition of the Hydrogenolysis of Benzylic C–O Bond Using Palladium Nanoparticles Supported on Nitrogen-Doped Carbon Nanofiber”, *ChemCatChem* **2018**, 10, 505-509.
- 3 S. Hosokawa, M. Toya, A. Noda, M. Morita, T. Ogawa, Y. Motoyama, “Catalytic Silane-Reduction of Carboxylic Esters and Lactones: Selective Synthetic Methods to Aldehydes, Lactols, and Ethers via Silyl Acetal Intermediates”, *ChemistrySelect* **2018**, 3, 2958-2961.
- 4 T. Ikeda, Z. Zhang, Y. Motoyama, “Hydrosilane-Promoted Facile Deprotection of *tert*-Butyl Groups in Esters, Ethers, Carbonates, and Carbamates”, *Adv. Synth. Catal.* **2019**, 361, 673-677. (Selected as a Very Important Publication)(*4)
- 5 N. Qadi, K. Takeno, A. Mosqueda, M. Kobayashi, Y. Motoyama, K. Yoshikawa, “Effect of Hydrothermal Carbonization Conditions on the Physicochemical Properties and Gasification Reactivity of Energy Grass”, *Energy Fuels* **2019**, 33, 6436-6443.

【原子間力顕微鏡を用いた触媒担持メカニズムの分子レベル評価】

- 1 A. Okada, Y. Nakata, K. Minou, M. Yoshimura, K. Kadono, “Effect of solvent evaporation temperature on the structure of two-dimensional melamine networks on Au(111)”, *Jpn. J. Appl. Phys.* **2016**, 55, 125001.
- 2 Y. You, J. Deng, X. Tan, N. Gorjizadeh, M. Yoshimura, S. C. Smith, V. Sahajwalla, R. K. Joshi, “On the mechanism of gas adsorption for pristine, defective and functionalized graphene”, *Phys. Chem. Chem. Phys.* **2017**, 19, 6051-6056.
- 3 A. Okada, S. Hara, M. Yoshimura, “Atomistic study of comblike structure on the MoO₂/Mo(110) surface by scanning tunneling microscopy and density functional theory calculations”, *Jpn. J. Appl. Phys.* **2017**, 56, 095501.
- 4 S. Suzuki, Y. Terada, M. Yoshimura, “Suppression of Graphene Nucleation by Turning Off Hydrogen Supply Just before Atmospheric Pressure Chemical Vapor Deposition Growth”, *Coatings* **2017**, 7, 206.
- 5 Y. Hashimoto, S. Katafuchi, M. Yoshimura, T. Hara, Y. Hara, M. Hamagaki, “Effect of low-energy nitrogen ion treatment of highly ordered pyrolytic graphite on oxygen reduction reaction activity”, *Nanomaterials and Nanotechnology* **2017**, 7, 1-8. (*5)
- 6 R. Badam, M. Hara, H.-H. Huang, M. Yoshimura, “Synthesis and Electrochemical Analysis of Novel IrO₂ Nanoparticle Catalysts Supported on Carbon Nanotube for Oxygen Evolution Reaction”, *Int. J. Hydrogen Energy*, **2018**, 43 18095–18104.

法人番号	231023
プロジェクト番号	S1511022

- 7 H.-H. Huang, R. Joshi, K. De Silva, R. Badam, M. Yoshimura, “Fabrication of Reduced Graphene Oxide Membranes for Water Desalination”, *J. Membrane Sci.*, **2019**, 572, 12–19.
- 8 H. Huang, K. De Silva, G. Kumara, M. Yoshimura, “Structural Evolution of Hydrothermally Derived Reduced Graphene Oxide”, *Scientific Report*, **2019**, 8, 6849–6857.
- 9 D. Yoneda, S. Suzuki, S. Hiramoto, Y. Matsuoka, M. Hara, M. Yoshimura, “Growth of vertically-aligned carbon nanotubes on graphite for electric double-layer capacitors”, *Mater. Research Express*, **2019**, 6, 086322.

【触媒・有機化合物および高分子錯体の静的・動的構造解析】

- 1 D. Xu, Y. Bin, K. Tashiro, “Detailed analysis of temperature dependences of spherulite morphology and crystallite orientation of poly(vinylidene fluoride) via a combinatorial method”, *J. Polym. Sci., Part B: Polym. Phys.*, **2015**, 53, 253-261.
- 2 K. Tokumitsu, T. Matuura, S. Kawasaki, K. Tashiro, “A Study on Crystallization Behavior for Poly(Lactic Acid) in Addition of Cardo Materials”, *J. Soc. Mat. Sci., Jpn.*, **2015**, 64, 1-6.
- 3 K. Tashiro, H. Kitai, S. M. Saharin, A. Shimazu, T. Itou, “Quantitative Crystal Structure Analysis of Poly(vinyl Alcohol)-Iodine Complexes on the Basis of 2D X-ray Diffraction, Raman Spectra, and Computer Simulation Techniques”, *Macromolecules*, **2015**, 48, 2138-2148.
- 4 P. Jariyasakoolroj, K. Tashiro, W. Hai, H. Yamamoto, W. Chinsirikul, N. Kerddonfag, S. Chirachanchai, “Isotropically small crystalline lamellae induced by high biaxial-stretching rate as a key microstructure for super-tough polylactide film”, *Polymer*, **2015**, 68, 234-245.
- 5 P. Nimmanpipug, T. Laosombat, V. Sanghiran Lee, S. Vannarat, S. Chirachanchai, J. Yana, K. Tashiro, “Proton transfer mechanism of 1,3,5-tri(2-benzimidazolyl) benzene with a unique triple-stranded hydrogen bond network as studied by DFT-MD simulations”, *Chem. Eng. Sci.*, **2015**, 137, 404-411.
- 6 J. Yana, S. Chirachanchai, C. Jarumaneeroj, V. S. Lee, K. Kodchakorn, K. Tashiro, P. Nimmanpipug, “DFT Study of Proton Transfer in Methyl Urocanate and Butyl Urocanate”, *Macromolecular Symposia*, **2015**, 354, 99-103.
- 7 S. Kummara, K. Tashiro, T. Monma, K. Horita, “Isotope Effect on the Melt–Isothermal Crystallization of Polyoxymethylene D/H Random Copolymers and D/H Blend Samples”, *Macromolecules*, **2015**, 48, 8070-8081.
- 8 S. Kummara, K. Tashiro, “Phenomenological study of the isotope effect on the equilibrium melting point of polymer crystal”, *Polymer*, **2015**, 80, 138-145.
- 9 S. M. Saharin, T. Takahama, S. Nonogaki, K. Saito, K. Tashiro, “Effect of OH Segmental Length on the Iodine Complex Formation of Ethylene-Vinyl Alcohol Random Copolymers”, *Macromolecules*, **2015**, 48, 8867-8876.
- 10 P. Tanphibal, K. Tashiro, S. Chirachanchai, “Molecular assembly of highly symmetric molecules under a hydrogen bond framework controlled by alkyl building blocks: a simple approach to fine-tune nanoscale structures”, *Soft Matter*, **2016**, 12, □486-491.
- 11 S. M. Saharin, T. Takahama, S. Nonogaki, K. Saito, K. Tashiro, “The effect of counter cation species on the formation of various crystal forms and their phase transition behavior of poly(vinyl alcohol)-iodine complex”, *Polymer*, **2016**, 89, 81-93.

法人番号	231023
プロジェクト番号	S1511022

- 12 J. Hu, K. Tashiro, “Relation between higher-order structure and crystalline phase transition of oriented isotactic polybutene-1 investigated by temperature-dependent time-resolved simultaneous WAXD/SAXS measurements”, *Polymer*, **2016**, *90*, 165-177.
- 13 H. Wang, K. Tashiro, “Reinvestigation of Crystal Structure and Intermolecular Interactions of Biodegradable Poly(3-Hydroxybutyrate) α -Form and the Prediction of Its Mechanical Property”, *Macromolecules*, **2016**, *49*, 581-594.
- 14 K. Tashiro, J. Hu, H. Wang, M. Hanesaka, S. Alberto, “Refinement of the Crystal Structures of Forms I and II of Isotactic Polybutene-1 and a Proposal of Phase Transition Mechanism between Them”, *Macromolecules*, **2016**, *49*, 1392-1404.
- 15 T. Yoshioka, K. Tashiro, N. Ohta, “Molecular Orientation Enhancement of Silk by the Hot-Stretching-Induced Transition from α -Helix-HFIP Complex to β -Sheet”, *Biomacromolecules*, **2016**, *17*, 1437-1448.
- 16 S. Kummara, K. Tashiro, “Isotope effect on the structural evolution process in the isothermal crystallization phenomenon of polyoxymethylene”, *Polymer*, **2016**, *90*, 76-88.
- 17 P. Tanphibal, K. Tashiro, S. Chirachanchai, “Constructiong π -Electron-Conjugated Diarylbutadiyne-Based Polydiacetylene under Molecular Framework Controlled by Hydrogen Bond and Side-Chain Substituent Position”, *Macromol. Rapid Commun.*, **2016**, *37*, 685-690.
- 18 J. Hu, K. Tashiro, “Time-Resolved Imaging of the Phase Transition in the Melt-Grown Spherulites of Isotactic Polybutene-1 as Detected by the Two-Dimensional Polarized IR Imaging Technique”, *J. Phys. Chem., B*, **2016**, *120*, 4689-4698.
- 19 T. Takahama, S. M. Saharin, K. Tashiro, “Details of the intermolecular interactions in poly(vinyl alcohol)-iodine complexes as studied by quantum chemical calculations”, *Polymer*, **2016**, *99*, 566-579.
- 20 H. Yamamoto, K. Tashiro, K. Ishino, M. Takahashi, R. Endo, M. Asada, Y. Li, K. Katsube, T. Ishii, , “Crystal structures and phase transition behavior of Poly(nonamethylene terephthalamide) and its model compounds”, *Polymer*, **2017**, *116*, 378-394.
- 21 T. Yoshioka, K. Tashiro, N. Ohta, “Observation of Water-Stimulated Supercontraction of Uniaxially-Oriented Poly(vinyl Alcohol) and the Related Hierarchical Structure Change Revealed by the Time-Resolved WAXD/SAXS Measurements”, *Macromolecules*, **2017**, *50*, 2803-2813.
- 22 H. Wang, J. Zhang, K. Tashiro, Phase Transition Mechanism of Poly(L-Lactic Acid) among the α , δ , and β Forms On the Basis of the Reinvestigated Crystal Structure of the β Form, *Macromolecules*, **2017**, *50*, 3285-3300.
- 23 M. Ishinabe, Y. Yamashita, K. Tsutsumiuchi, K. Tashiro, K. Imaeda, M. Kawamura, “Effect of Crystal Status Transformation on the Thermal Shrinkage Characteristics and Extensional Characteristics of Acetaldehyde Solvent-Induced Crystallization PET Film”, *Trans. Mat. Res. Soc. Japan*, **2017**, *42*, 97-101.
- 24 K. Tashiro, N. Kouno, H. Wang, H. Tsuji, “Crystal Structure of Poly(lactic acid) Stereocomplex: Random Packing Model of PDLA and PLLA Chains As Studied by X-ray Diffraction Analysis”, *Macromolecules*, **2017**, *50*, 8048–8065.
- 25 K. Tashiro, H. Wang, N. Kouno, J. Koshobu, K. Watanabe, “Confirmation of the X-ray-Analyzed Heterogeneous Distribution of the PDLA and PLLA Chain Stems in the Crystal Lattice of Poly(lactic acid) Stereocomplex on the Basis of the Vibrational Circular Dichroism IR Spectral Measurement”,

法人番号	231023
プロジェクト番号	S1511022

- Macromolecules*, **2017**, *50*, 8066–8071.
- 26 W. Mengfan, K. Tashiro, Y. Ozaki, “Reinvestigation of the β -to- α Crystal Phase Transition of Poly(butylene adipate) by the Time-Resolved X-ray Scattering and FTIR Spectral Measurements in the Temperature Jump Process”, *Macromolecules*, **2017**, *50*, 3883-3889.
- 27 X. Zhang, L. Santonja-Blasco, K. B. Wagener, E. Boz, M. Tasaki, K. Tashiro, R. G. Alamo, “Infrared Spectroscopy and X-ray Diffraction Characterization of Dimorphic Crystalline Structures of Polyethylenes with Halogens Placed at Equal Distance along the Backbone”, *J. Phys. Chem. B*, **2017**, *121*, 10166-10179.
- 28 T. Yoshioka, T. Kameda, K. Tashiro, N. Ohta, A. K. Schaper, “Transformation of Coiled α -Helices into Cross- β -Sheets Superstructure”, *Biomacromolecules*, **2017**, *18*, 3892-3903.
- 29 M. A. Barique, E. Tsuchida, A. Ohira, K. Tashiro, “Effect of Elevated Temperatures on the States of Water and Their Correlation with the Proton Conductivity of Nafion”, *ACS Omega*, **2018**, *3*, 349-360.
- 30 K. Tashiro, K. Kusaka, T. Hosoya, T. Ohhara, M. Hanesaka, Y. Yoshizawa, H. Yamamoto, N. Niimura, I. Tanaka, K. Kurihara, R. Kuroki, T. Tamada, “Structure Analysis and Derivation of Deformed Electron Density Distribution of Polydiacetylene Giant Single Crystal by the Combination of X-ray and Neutron Diffraction Data”, *Macromolecules*, **2018**, *51*, 3911-3922. (*30)
- 31 M. Tosaka, K. Tashiro, “Crystal Polymorphism and Structure Models of Poly(dimethylsiloxane),” *Polymer*, **2018**, *153*, 507–520.
- 32 K. Tashiro, H. Yamamoto, K. Sugimoto, “Study of Phase Transition and Ultimate Mechanical Properties of Orthorhombic Polyoxymethylene Based on the Refined Crystal Structure,” *Polymer*, **2018**, *153*, 474–484.
- 33 K. Tashiro, “Quantitative Evaluation of Deformed Electron Density Distribution of Polydiacetylene Crystal on the Basis of the Organized Combination of X-ray and Neutron Diffraction Data,” *MLF Annual Report 2017. Vol. 2: Materials and Life Science Experimental Facility, Research and Development Highlights*, **2019**, 26–28.(*33)
- 34 K. Tashiro, H. Yamamoto, K. Funaki, J. Hu, “Synchrotron Microbeam X-ray Scattering Study of the Crystallite Orientation in the Spherulites of Isotactic Poly(butene-1) Crystallized Isothermally at Different Temperatures”, *Polym. J.*, **2019**, *51*, 143–153.
- 35 K. Tashiro, T. Yoshioka, H. Yamamoto, H. Wang, E. M. Woo, K. Funaki, H. Murase, “Relationship Between Twisting Phenomenon and Structural Discontinuity of Stacked Lamellae in the Spherulite of Poly(ethylene adipate) as Studied by the Synchrotron X-ray Microbeam Technique,” *Polym. J.*, **2019**, *51*, 131-141.
- 36 K. Tashiro, H. Yamamoto, K. Sugimoto, T. Takahama, M. Tanaka, M. Hasegawa, “Experimental Determination of the Geometrical Relation between Monomer and Polymer Species of 2,5-Distyrylpyrazine Single Crystal in the Topotactic Photoinduced Polymerization Reaction,” *Macromolecules*, **2019**, 2189–2202.
- 37 K. Tashiro, M. Gakhutishvili, “Crystal Structure of Cellulose-Iodine Complex,” *Polymer*, **2019**, *171*, 140–148.
- 38 S. Phongtamrug, K. Tashiro, “X-ray Crystal Structure Analysis of Poly(3-hydroxybutyrate) β -Form and the Proposition of a Mechanism of the Stress-Induced α -to- β Phase Transition,” *Macromolecules*, **2019**, *52*, 2995–3009.
- 39 T. Yoshioka, T. Tsubota, K. Tashiro, A. Jouraku, T. Kameda, “A Study of the Extraordinarily Strong and

法人番号	231023
プロジェクト番号	S1511022

Tough Silk produced by Bagworms”, *Nat. Commun.*, **2019**, *10*, 1469–1479.

40 K. Tashiro, H. Yamamoto, “Structural Evolution Mechanism of Crystalline Polymers in the Isothermal Melt-Crystallization Process: A Proposition Based on Simultaneous WAXD/SAXS/FTIR Measurements”, *Polymers*, **2019**, *11*, 1316-1340.

41 K. Tashiro, M. Gakhutishvili, “Crystal Structure of Cellulose-Iodine Complex”, *Polymer*, **2019**, *171*, 140-148.

42 Y. Kawahara, T. Yoshioka, H. Minami, N. Kuwabara, K. Tashiro, “Forcibly Spinning Using Bombyx Mori Silkworm Anesthetized by the Water Narcosis Treatment”, *J. Natural Fibers*, **2019** (<https://doi.org/10.1080/15440478.2019.1623750>).

43 K. Kodchakorn, P. Nimmanpipug, S. Phongtamrug, K. Tashiro, “pH-induced conformational changes in histamine in the solid state”, *RSC Advances*, **2019**, *9*, 19375-19389.

44 C. Li, J. Hu, K. Tashiro, Z. Ren, S. Yan, “Synthesis and Cyclization-induced Charge Transfer of Rectangular Bisterthiophenesiloxanes”, *Chem. Eur. J.*, 10.1002/chem.201903462 (2019).

45 D. Tahara, T. H. Ninh, H. Yamamoto, K. Tashiro, “Metropolis Monte Carlo Simulation of Two-Dimensional Small-Angle X-ray Scattering Patterns of Oriented Polymer Materials”, *Macromolecules*, **2020**, *53*, 276-287.

<図書>

【水分解光触媒の開発】

- 1 山方啓, 「光半導体による水分解の反応機構 時間分解分光測定を用いた光触媒のキャリアダイナミクス」, 光触媒/光半導体を利用した人工光合成—最先端科学から実装技術への発展を目指して—, 第3編, (株)エヌ・ティー・エス, **2017**, 第5章, pp. 158-167 (分担執筆; 章著) .
- 2 A. Yamakata, “Behavior of Charge Carriers at the Defects on Powder Photocatalysts -Time-resolved Visible to mid-IR Absorption Study-”, Understanding Charge transfer Processes on Metal Oxide Surfaces through Laser Flash Photolysis Analysis (Editor: Prof. D. Bahnemann), Pan Stanford Publishing, Singapore, **2018**. (分担執筆; 章著) .

【触媒・有機化合物および高分子錯体の静的・動的構造解析】

- 1 田代孝二, 「日本の高分子科学技術史第2巻 (高分子学会編)」, 研究史2 「高分子科学の発展を支えた分析器の進歩 (概観)」, **2016**, s8-s11.
- 2 K. Tashiro, “Microscopically Viewed Relationship Between Structure and Mechanical Property of Crystalline Polymers: An Important Guiding Principle for the Development of Super Fibers”, in “High-Performance and Specialty Fibers” (The Society of Fiber Science and Technology, Japan), **2016**, Chapter 6, pp. 95-108.
- 3 K. Tashiro, “Progress in Structure Analysis Techniques of Fibers”, in “High-Performance and Specialty Fibers” (The Society of Fiber Science and Technology, Japan), **2016**, Chapter 2, p. 21-47.

<学会発表>

国内

【水分解光触媒の開発】

- 1 山方啓, Y. Ham, 久富隆史, 久保田純, 堂免一成, 「時間分解可視中赤外分光測定でみた光触媒

法人番号	231023
プロジェクト番号	S1511022

- のキャリアダイナミクス」, 2015 年光化学討論会 (大阪) **2015** (9/11).
- 2 J. J. M. Vequizo, A. Yamakata, “Dynamics of photocarriers in anatase and rutile TiO₂ photocatalysts studied by transient absorption spectroscopy from visible to mid-IR region”, 第116回触媒討論会 (三重) **2015** (9/16).
 - 3 松永大典, 山方啓, 「フェムト秒時間分解分光法を用いた光触媒のキャリアダイナミクス」, 第 116 回触媒討論会 (三重) **2015** (09/17)
 - 4 J. J. M. Vequizo, A. Yamakata, M. Hojamberdiev, K. Yubuta, S. Oishi, K. Domen, K. Teshima, “Dynamics of Photogenerated Charge Carriers in Metal Nitride Photocatalysts Studied by Time-Resolved Absorption Spectroscopy”, 第 25 回日本 MRS 年次大会 (横浜) **2015** (12/09).
 - 5 松永大典, 山方啓, 「フェムト秒時間分解分光を用いた可視光照射下の光触媒のキャリアダイナミクス」, 第25回日本MRS年次大会 (横浜) **2015** (12/09).
 - 6 松永大典, J. J. M. Vequizo, 山方啓, 「酸化チタン光触媒のフェムト秒時間分解分光測定」, 第 15 回日本表面科学会中部支部学術講演会 (名古屋) **2015** (12/19).
 - 7 J. J. M. Vequizo, A. Yamakata, “Time-resolved Spectroscopic Analysis of the Dynamics of Charge Carriers in Metal Nitride Photocatalysts”, 「スマートエネルギー技術研究センター」第 7 回シンポジウム (名古屋) **2016** (2/04).
 - 8 J. J. M. Vequizo, A. Yamakata, M. Hojamberdiev, H. Wagata, K. Kawashima, K. Yubuta, S. Oishi, K. Domen, K. Teshima, “Transient Absorption Spectroscopic Analysis of the Dynamic of Photocarriers in Metal OxyNitrides Photocatalysts”, 第 16 回先端フォトンテクノロジー研究センターシンポジウム (名古屋) **2016** (3/04).
 - 9 山方啓, 「粉末系光触媒のキャリアダイナミクス」, 第 16 回先端フォトンテクノロジー研究センターシンポジウム (名古屋) **2016** (3/04).
 - 10 松永大典, J. J. M. Vequizo, 山方啓, 「フェムト秒時間分解分光法を用いた TiO₂ 光触媒のキャリアダイナミクス触媒のキャリアダイナミクス」, 第 16 回先端フォトンテクノロジー研究センターシンポジウム (名古屋) **2016**, (3/04).
 - 11 村知良亮, 山方啓, 「複合型触媒のキャリアダイナミクス」, 第 16 回先端フォトンテクノロジー研究センターシンポジウム (名古屋) **2016** (3/04).
 - 12 J. J. M. Vequizo, 松永大典, 山方啓, 横野照尚, 「ブルックライト酸化チタンのキャリアダイナミクス」, 第 35 回光がかかわる触媒化学シンポジウム (東京) **2016** (6/10).
 - 13 西岡駿太, 兵頭潤次, 山方啓, 山崎仁丈, 前田和彦, 「酸素欠陥濃度を制御した不定比 SrTiO_{3-δ} の水分解光触媒活性」, 第 35 回光がかかわる触媒化学シンポジウム (東京) **2016** (6/10).
 - 14 松永大典, J. J. M. Vequizo, 山方啓, 「フェムト秒時間分解分光法を用いた TiO₂ 粉末と単結晶のキャリアダイナミクス」, 2016 年光化学討論会 (東京) **2016** (9/7).
 - 15 山方啓, J. J. M. Vequizo, 松永大典, 「時間分解可視赤外分光法を用いた粉末酸化チタンのキャリアダイナミクス」, 第 10 回分子科学討論会 2016 (神戸) **2016** (9/13).
 - 16 西岡駿太, 兵頭潤次, 山方啓, 山崎仁丈, 前田和彦, 「酸素欠損型不定比 SrTiO_{3-δ} の水分解光触媒活性」, 第 118 回触媒討論会 (盛岡) **2016** (9/21).
 - 17 C. S. K. Ranasinghe, 山方啓, “Transient Absorption Study of Photogenerated Charge Carriers in Electrochemical Systems”, 第 118 回触媒討論会 (盛岡) **2016** (9/22).
 - 18 栗木亮, 松永大典, 中島拓哉, 山方啓, 石谷治, 前田和彦, 「有機半導体と金属錯体との複合体を

法人番号	231023
プロジェクト番号	S1511022

光触媒とした可視光駆動型 CO₂ 還元光触媒反応」, 第 118 回触媒討論会 (盛岡) **2016** (9/22).

19 J. J. M. Vequizo, 山方啓, M. Hojamberdiev, K. Kawashima, H. Wagata, K. Yubuta, S. Oishi, 堂免一成, K. Teshima, “Transient Visible to Mid-IR Absorption Spectroscopic Analysis of the Dynamics of Photocarriers in Metal Nitride/Oxynitride Photocatalysts”, 第 118 回触媒討論会 (盛岡) **2016** (9/22).

20 山方啓, 「半導体光触媒の光励起ダイナミクス」, 第 2 回 半導体による太陽光-水素エネルギー変換技術研究会 (名古屋) **2016** (10/13). (招待講演).

21 C. S. K. Ranasinghe, A. Yamakata, 「柔らかな固液界面における化学反応ダイナミクス -TiO₂ 光電極における光励起ダイナミクス-」, 新学術領域研究 柔らかな分子系 第 4 回公開シンポジウム (名古屋) **2016** (10/27).

22 松永大典, 山方啓, 「柔らかな固液界面における化学反応ダイナミクス -フェムト秒時間分解分光法による光触媒の光励起ダイナミクス-」, 新学術領域研究 柔らかな分子系 第 4 回公開シンポジウム (名古屋) **2016** (10/27).

23 C. S. K. Ranasinghe, A. Yamakata, “Photogenerated Electron-Hole Dynamics in BiVO₄ Based Photoelectrodes”, 「スマートエネルギー技術研究センター」 第 8 回シンポジウム (名古屋) **2016** (11/18).

24 J. J. M. Vequizo, H. Matsunaga, A. Yamakata, T. Ohno, “Dynamics of Photocarriers of Brookite TiO₂ Photocatalyst Studied by Transient Absorption and Emission Spectroscopy”, 「スマートエネルギー技術研究センター」 第 8 回シンポジウム (名古屋) **2016** (11/18).

25 松永大典, 山方啓, 「フェムト秒時間分解分光法による酸化チタン光触媒のキャリアダイナミクス」, 2016 年電気化学会北海道支部・東海支部合同シンポジウム「インテリジェント電気化学の新潮流」(札幌) **2016** (11/23).

26 山方啓, 「時間分解分光測定を利用した金属微粒子を担持した光触媒のキャリアダイナミクス」, 第 36 回表面科学学術講演会 (名古屋) **2016** (11/30), (依頼講演).

27 J. J. M. Vequizo, 松永大典, S. Okamura, T. Ohno, 山方啓, “Transient Absorption and FT-IR Analysis of the Carrier Dynamics of TiO₂ Photocatalysts”, 第 36 回表面科学学術講演会 (名古屋) **2016** (11/30).

28 松永大典, J. J. M. Vequizo, 山方啓, 「フェムト秒時間分解分光測定を用いた光触媒のキャリアダイナミクス」, 第 36 回表面科学学術講演会 (名古屋) **2016** (11/30).

29 山方啓, 「新しい分光技術を利用した光触媒反応の機構解明」, 『山口大学 光・エネルギー研究センターシンポジウム 光科学が生み出す新しい世界-光制御と分光技術の最前線-』, 山口大学常盤キャンパス (山口) **2016** (12/14), (招待講演).

30 C. S. K. Ranasinghe, A. Yamakata, “Behaviors of Photogenerated Electrons and Holes in SnO₂/BiVO₄/CoO_x Heterojunctions”, 第 16 回日本表面科学会中部支部 学術講演会 (名古屋) **2016** (12/17).

31 松永大典, J. J. M. Vequizo, 山方啓, 「フェムト秒時間分解分光測定を用いた酸化チタン表面欠陥におけるキャリアダイナミクス」, 第 16 回日本表面科学会中部支部 学術講演会 (名古屋) **2016** (12/17), (講演奨励賞).

32 山方啓, 「光励起キャリアーの動きとエネルギー制御」, JST さきがけ「光エネルギーと物質変換」第 3 期研究者研究成果報告会 (東京) **2017** (1/28).

法人番号	231023
プロジェクト番号	S1511022

- 33 C. S. K. Ranasinghe, A. Yamakata, “Time-resolved Absorption Study on the Behavior of Photogenerated Charge Carriers in Visible-Light Active Photoelectrochemical Systems”, 「スマートエネルギー技術研究センター」第9回シンポジウム (名古屋), **2017** (1/30).
- 34 J. J. M. Vequizo, H. Matsunaga, A. Yamakata, T. Ohno, “Photodynamics of Anatase, Rutile and Brookite TiO₂ Powders Studied by Transient Absorption Spectroscopy”, 「スマートエネルギー技術研究センター」第9回シンポジウム (名古屋) **2017** (1/30).
- 35 C. S. K. Ranasinghe, A. Yamakata, “Enhancement of Photocatalytic Activity in BiVO₄ Based Visible Active Photoanodes”, 先進触媒開発研究センター 第1回シンポジウム (名古屋) **2017** (3/10).
- 36 J. J. M. Vequizo, H. Matsunaga, A. Yamakata, T. Ohno, “Distinctive Behavior of Photocarriers in TiO₂ Powders (Anatase, Rutile, and Brookite) Studied by Transient Absorption Spectroscopy”, 先進触媒開発研究センター 第1回シンポジウム (名古屋) **2017** (3/10).
- 37 山方啓, 「半導体光触媒の光励起ダイナミクス」, 先進触媒開発研究センター 第1回シンポジウム (名古屋) **2017** (3/10).
- 38 松永大典, J. J. M. Vequizo, 山方啓, 「フェムト秒時間分解分光法による単結晶と粉末 TiO₂ の光励起キャリアの挙動とエネルギー状態」, 先進触媒開発研究センター 第1回シンポジウム (名古屋) **2017** (3/10).
- 39 R. Kuriki, A. Yamakata, O. Ishitani, K. Maeda, “Visible-light-driven photocatalytic CO₂ reduction reaction using hybrid with an organic semiconductor and a Ru(II) binuclear complex”, 日本化学会第97春季年会 (千葉) **2017** (3/18).
- 40 石山翔太, 張仕麒, 横川俊哉, 山方啓, 酒多喜久, 「Ca イオンを添加した Ga₂O₃ の H₂O 完全分解反応に対する光触媒特性」, 第119回触媒討論会 (東京) **2017** (3/22).
- 41 山方啓, 「金属酸窒化物複合アニオン型光触媒のキャリアーダイナミクス」, 新学術領域研究 (平成28~32年度) 複合アニオン化合物の創製と新機能 第2回トピカル会議 (機能) (宮城) **2017** (8/7), (招待講演).
- 42 R. Kuriki, A. Yamakata, O. Ishitani, K. Maeda, “Development of hybrid photocatalysts for visible-light CO₂ reduction using carbon nitride and a binuclear Ru(II) complex”, 2017年光化学討論会 (宮城) **2017** (9/4).
- 43 C. S. K. Ranasinghe, A. Yamakata, “Fabrication of Highly Efficient TiO₂ Photoanodes by Atomized Spray Pyrolysis Deposition”, 2017年光化学討論会 (宮城) **2017** (9/4).
- 44 J. J. M. Vequizo, S. Ishiyama, Y. Sakata, A. Yamakata, “Dynamics of Photocarriers in Metal Ion Doped Ga₂O₃ Photocatalysts Studied by Transient Absorption Spectroscopy”, 2017年光化学討論会 (宮城) **2017** (9/4).
- 45 石山翔太, 横川俊哉, 山方啓, 酒多喜久, 「金属イオン添加 Ga₂O₃ 光触媒の H₂O 完全分解反応に対する光触媒特性」, 第120回触媒討論会 (愛媛) **2017** (9/13).
- 46 汪雨濃, J. J. M. Vequizo, 岡崎めぐみ, 前田和彦, 山方啓, 「コバルト酸化物を担持した酸化チタンのキャリアーダイナミクス」, 第120回触媒討論会 (愛媛) **2017** (9/13).
- 47 C. S. K. Ranasinghe, A. Yamakata, “Behavior of Photogenerated Charge Carriers in SnO₂/BiVO₄/CoO_x Heterostructure Studied by Transient Absorption Spectroscopy”, 第120回触媒討論会 (愛媛) **2017** (9/14).

法人番号	231023
プロジェクト番号	S1511022

- 48 J. J. M. Vequizo, S. Ishiyama, Y. Sakata, A. Yamakata, “Effects of Metal Ion-Doping on Ga₂O₃ Photocatalysts Studied by Transient Absorption Spectroscopy”, 第 120 回触媒討論会 (愛媛) **2017** (9/14).
- 49 山方啓, J. J. M. Vequizo, 石山翔太, 酒多喜久, 「金属イオンをドーピングした Ga₂O₃ の光励起ダイナミクス」, 第 11 回分子科学討論会 (宮城) **2017** (9/16).
- 50 C. S. K. Ranasinghe, A. Yamakata, “Transient Absorption Study of Photogenerated Charge Carriers in Electrochemical Systems”, スマートエネルギー技術研究センター 第 10 回シンポジウム (名古屋) **2017** (10/13).
- 51 J. J. M. Vequizo, C. S. K. Ranasinghe, S. Ishiyama, Y. Sakata, A. Yamakata, “Effects of Surface Modification on Powder Photocatalysts Studied by Transient Absorption Spectroscopy”, スマートエネルギー技術研究センター 第 10 回シンポジウム (名古屋) **2017** (10/13).
- 52 山方啓, 「超高活性 Ga₂O₃ 系水分解光触媒の反応機構」, スマートエネルギー技術研究センター 第 10 回シンポジウム (名古屋) **2017** (10/13).
- 53 兵頭潤次, 西岡駿太, 熊谷啓, 前田和彦, J. J. M. Vequizo, 山方啓, 山崎仁丈, 「酸素空孔濃度および電子濃度を制御した SrTiO₃ における光触媒特性 - 欠陥化学と光化学反応 -」, 第 43 回固体イオニクス討論会 (山形) **2017** (12/5).
- 54 K. Muraoka, J. J. M. Vequizo, A. Yamakata, O. Ishitani, K. Maeda, “Oxygen-Doped Ta₃N₅ as a Building Block for Z-scheme CO₂ Reduction with a Binuclear Ru(II) Complex Workable under a Wide Range of Visible Light”, 日本化学会第 98 春季年会 (千葉) **2018** (3/21).
- 55 T. Ohwaki, A. Yamakata, J. J. M. Vequizo, T. Itohoshi, “Improvement of photocatalytic activity under visible light irradiation by composite with Cu/WO₃ and Cu/N-TiO₂”, 日本化学会第 98 春季年会 (千葉) **2018** (3/21).
- 56 T. Oshima, K. Muraoka, J. J. M. Vequizo, S. Yamashita, A. Yamakata, K. Kimoto, O. Ishitani, K. Maeda, “Synthesis and photocatalytic activity of a layered perovskite oxynitride Li₂LaTa₂O₆N”, 日本化学会第 98 春季年会千葉) **2018** (3/21).
- 57 栗木亮, C. S. K. Ranasinghe, 山方啓, 石谷治, 前田和彦, 「C₃N₄ の光励起キャリアダイナミクスと錯体触媒への電子移動過程の観察」, 第 121 回触媒討論会東京) **2018** (3/22).
- 58 山方啓, J. J. M. Vequizo, 「時間分解分光測定を利用した高活性光触媒の反応機構解明」, 日本セラミックス協会 第 31 回秋季シンポジウム (名古屋) **2018** (9/5) (依頼講演).
- 59 小松田紫央, 朝倉裕介, J. J. M. Vequizo, 山方啓, 殷シュウ, 「ソルボサーマル反応をベースとした光触媒コンポジットの合成と活性向上」, 日本セラミックス協会 第 31 回秋季シンポジウム (名古屋) **2018** (9/5).
- 60 A. Miyoshi, J. J. M. Vequizo, S. Nishioka, S. Yamashita, A. Iwase, S. Nozawa, A. Yamakata, K. Kimoto, A. Kudo, K. Maeda, “Synthesis of nitrogen/fluorine codoped rutile TiO₂ photocatalyst and its application for Z-scheme water splitting,” 2018 年光化学討論会 (兵庫) **2018** (9/5).
- 61 J. J. M. Vequizo, F. Amano, A. Yamakata, “Dynamics of photocarriers in reduced TiO₂ studied by transient visible to mid-IR absorption spectroscopy,” 2018 年光化学討論会 (兵庫) **2018** (9/7).

法人番号	231023
プロジェクト番号	S1511022

- 62 山方啓, J. J. M. Vequizo, 岡村翔, 白木恭平, 「光触媒粒子における電子のトラップ過程と蓄積過程」, 第 12 回分子科学討論会 (福岡) **2018** (9/11).
- 63 J. J. M. Vequizo, S. Ishiyama, Y. Sakata, A. Yamakata, “Impact of Cocatalyst on the Dynamics of Photocarriers in Ga₂O₃ Powders Studied by Time-Resolved Absorption Spectroscopy,” 第 122 回触媒討論会 (函館) **2018** (9/26).
- 64 山方啓, J. J. M. Vequizo, M. Hojamberdiev, S. Chen, 手島勝弥, 堂免一成, 「金属酸窒化物光触媒における光励起キャリアの過渡吸収」, 第 122 回触媒討論会 (函館) **2018** (9/26).
- 65 J. J. M. Vequizo, S. Tsuboi, S. Ishiyama, Y. Sakata, A. Yamakata, “Electron Transfer to Water Molecules on Rh-loaded Ga₂O₃ Photocatalysts,” グリーン電子素子・材料研究センター 最終年度シンポジウム (名古屋) **2018** (11/2).
- 66 山方啓, 「過渡吸収分光測定を用いた光触媒粒子の光励起ダイナミクス」, 第 49 回中部化学関係学協会支部連合秋季大会 (名古屋) **2018** (11/4) (依頼講演).
- 67 山方啓, 「ポンププローブ法による界面ダイナミクス」, 2018 年電気化学会関東支部セミナー 先端計測技術による電極界面分析の新展開 (東京) **2018** (11/9) (招待講演).
- 68 山方啓, 「高活性光触媒の実現を目指した新しい分光測定技術の開発」, 第 11 回ワークショップ 固体材料合成および評価技術の新展開 (宮城) **2018** (11/12) (基調講演).
- 69 山方啓, J. J. M. Vequizo, 石山翔太, 酒多喜久, 「超高活性 Ga₂O₃ 系水分解光触媒の光励起ダイナミクス」, 表面・界面スペクトロスコピー2018 (茨城) **2018** (12/1).
- 70 山方啓, 「時間分解分光測定による高活性光触媒反応のメカニズム解明」, 熊本大学工学部研究セミナー (熊本) **2018** (12/5) (招待講演).
- 71 山方啓, 「高性能光触媒の設計を目指した反応機構の解明」, 中央大学理工学部・研究セミナー (東京) **2019** (1/22) (招待講演).
- 72 奥野和哉, J. J. M. Vequizo, 山方啓, 垣花真人, 加藤英樹, 「BiVO₄ 光触媒へのボールミ処理効果」, 第 123 回触媒討論会 (大阪) **2019** (3/20).
- 73 小川幹太, 中田明伸, 鈴木肇, 富田修, 東正信, 山方啓, 佐伯昭紀, 阿部竜, 「各種助触媒担持による層状酸ハロゲン化物光触媒の水分解活性向上」, 第 123 回触媒討論会 (大阪) **2019** (3/20).
- 74 西岡駿太, 兵頭潤次, J. J. M. Vequizo, 山下俊介, 熊谷啓, 木本浩司, 山方啓, 山崎仁丈, 前田和彦, 「酸素分圧制御下で合成した不定比 SrTiO_{3-δ} の光触媒活性への電子ドーピング効果」, 第 123 回触媒討論会 (大阪) **2019** (3/21).
- 75 山方啓, 「時間分解分光測定を利用した粉末光触媒のキャリアダイナミクス」, 第 38 回光がかかわる触媒化学シンポジウム, (名古屋) **2019** (6/21).
- 76 山方啓, 小川貴史, 白木恭平, 小川幹太, 桑原彰秀, 阿部竜, 陰山洋, 「ビスマス系酸ハロゲン化物光触媒の光励起ダイナミクス」, 2019 年光化学討論会, (名古屋) **2019** (9/10).
- 77 加藤康作, 姜君哲, 酒多喜久, 山方啓, 「チタン酸ストロンチウムのキャリアダイナミクス」, 2019 年光化学討論会, (名古屋) **2019** (9/12).
- 78 柴田健吾, 加藤康作, 山方啓, 石谷治, 前田和彦, 「C₃N₄ 共重合体による CO₂ 還元光触媒反応の高活性化」, 第 124 回触媒討論会, (長崎) **2019** (9/18).
- 79 小川幹太, 富田修, 立川貴士, 山方啓, 阿部竜, 「光励起キャリアの有効利用による層状酸ハロゲン化物光触媒の水素生成活性向上」, 第 124 回触媒討論会, (長崎) **2019** (9/18).

法人番号	231023
プロジェクト番号	S1511022

- 80 加藤康作, 姜君哲, 酒多喜久, 山方啓, 「不純物をドーブしたチタン酸ストロウムの過渡吸収測定」, 第 124 回触媒討論会, (長崎) **2019** (9/19).
- 81 白木恭平, 井上直洋, 山方啓, 「金属微粒子を担持した酸化チタンの可視光励起ダイナミクス」, 第 124 回触媒討論会, (長崎) **2019** (9/19).
- 82 林成希, 山方啓, 「酸化チタン光電極の表面修飾効果」, 第 124 回触媒討論会, (長崎) **2019** (9/19).
- 83 J. Jiang, H. Fujimori, A. Yamakata, Y. Sakata, “Preparation of High Active SrTiO₃ to photocatalytic overall H₂O splitting by doping Na ion” , 第 124 回触媒討論会, (長崎) **2019** (9/20).
- 84 山方啓, 小川貴史, 白木恭平, 小川幹太, C. S. K. Ranasinghe, 桑原彰秀, 阿部竜, 陰山洋, 「ピスマス系酸ハロゲン化物のアニオン欠陥準位」, 第 124 回触媒討論会, (長崎) **2019** (9/20).
- 85 加藤康作, 山方啓, 「不純物をドーブした SrTiO₃ の光励起キャリアダイナミクス」, 豊田工業大学スマートエネルギー研究センターシンポジウム, (名古屋) **2019** (11/21).
- 86 坪井翔哉, 山方啓, 「酸化タングステン微粒子の光励起キャリアの挙動」, 豊田工業大学スマートエネルギー研究センターシンポジウム, (名古屋) **2019** (11/21).
- 87 白木恭平, 山方啓, 「Pt 担持 TiO₂における可視光照射時の光励起キャリアダイナミクス」, 豊田工業大学スマートエネルギー研究センターシンポジウム, (名古屋) **2019** (11/21).
- 88 林成希, 山方啓, 「酸化チタン多層電極の活性評価」, 豊田工業大学スマートエネルギー研究センターシンポジウム, (名古屋) **2019** (11/21).
- 89 山方啓, 「レーザー分光を用いた光触媒反応機構の解明」, 第 29 回キャラクタリゼーション講習会「触媒および表面の解析に役立つキャラクタリゼーションの基礎と実際」, (富山) **2019** (11/21).
- 90 加藤康作, 山方啓, 「SrTiO₃の光励起キャリアダイナミクスにおける Na ドープの効果」, 第 13 回表面・界面スペクトロスコーピー2019, (東京) **2019** (12/6).
- 91 山方啓, 「酸ハロゲン化物光触媒の光励起キャリアダイナミクス」, 第 13 回 表面・界面スペクトロスコーピー2019, (東京) **2019** (12/6).
- 92 加藤康作, 山方啓, 「Na をドーブしたチタン酸ストロンチウムの光励起キャリアダイナミクス」, 豊田工業大学 先進触媒開発研究センター 最終年度シンポジウム, (名古屋) **2020** (3/5).
- 93 山方啓, 「高活性光触媒の光励起ダイナミクス」, 豊田工業大学 先進触媒開発研究センター 最終年度シンポジウム, (名古屋) **2020** (3/5).
- 94 坪井翔哉, 山方啓, 「WO₃内励起キャリアの挙動の粒子サイズ依存性」, 豊田工業大学 先進触媒開発研究センター 最終年度シンポジウム, (名古屋) **2020** (3/5).
- 95 白木恭平, 山方啓, 「Pt 担持 TiO₂におけるキャリアダイナミクス」, 豊田工業大学 先進触媒開発研究センター 最終年度シンポジウム, (名古屋) **2020** (3/5).
- 96 林成希, 山方啓, 「酸化チタン二層電極の表面修飾効果」, 豊田工業大学 先進触媒開発研究センター 最終年度シンポジウム, (名古屋) **2020** (3/5).
- 97 金澤知器, 内山智貴, 内本喜晴, 野澤俊介, 山方啓, 前田和彦, 「半導体光触媒を用いた水の酸化反応を促進する CoAlO_x 複合酸化物助触媒の開発」, 日本化学会第 100 春季年会, (千葉) **2020** (3/24).
- 98 A. Miyoshi, J. J. M. Vequizo, S. Nishioka, S. Yamashita, S. Nozawa, A. Kuwabara, A. Yamakata, K. Kimoto, K. Maeda, “Visible light Z-scheme water splitting using nitrogen/fluorine

法人番号	231023
プロジェクト番号	S1511022

codoped rutile TiO_2 as O_2 evolution photocatalyst”, 日本化学会第 100 春季年会, (千葉)2020 (3/25).

- 99 若山晴輝, 平山直樹, 中田博子, 加藤康作, 山方啓, 岡研吾, 前田和彦, 「酸フッ化物 $\text{Pb}_2\text{Ti}_2\text{O}_5.4\text{F}_{1.2}$ へのアルカリ処理と光触媒活性への影響」, 日本化学会第 100 春季年会, (千葉) 2020 (3/25).
- 100 海野優樹, 平町雄一, 藤森宏高, 山方啓, 酒多喜久, 「トンネル構造を有するチタン混合酸化物光触媒の H_2O 分解反応に対する特性」, 日本化学会第 100 春季年会, (千葉) 2020 (3/26).

【水素の貯蔵と放出用の高機能触媒開発】

- 1 磯貝勇樹, 神岡武文, リ ヒュンジュ, 小島信晃, 大下祥雄, 「反応性プラズマ蒸着プロセスの影響によるライフタイム変化」, 第 14 回次世代の太陽光発電システムシンポジウム(名古屋), 2017.

【水電解および燃料電池の電極触媒の開発】

- 1 原正則, Kanishka De Silva, Hsin-Hui Huang, 吉村雅満, 「 IrO_2 担持グラフェン触媒による水電解反応の評価」, 第 36 回表面科学学術講演会 (名古屋) 2016, 1Ga03 (11/29) .
- 2 Badam Rajashekar, Kanishka De Silva, 原正則, 吉村雅満, 「 IrO_2 /carbon NanoHybrid as Efficient Oxygen Evolution Reaction Catalysts」, 第 16 回日本表面科学会中部支部学術講演会 (名古屋) 2016, 12 (12/17) .
- 3 原正則, Badam Rajashekar, Kanishka De Silva, Hsin-Hui Huang, 吉村雅満, 「 IrO_2 担持グラフェン触媒上における酸素発生反応の電気化学特性評価」, 第 64 回応用物理学会春季学術講演会(横浜) 2017, 14p-P4-23 (3/14) .
- 4 Badam Rajashekar, Hsin-Hui Huang, 原正則, 吉村雅満, 「 IrO_2 Decorated Functionalized Acetylene Black as Highly Efficient Oxygen Evolution Reaction Catalysts」, 電気化学会第 84 回大会 (東京) 2017, 1K17 (3/25) .
- 5 Rajashekar Badam, Wang Guan Jhong, Hsin-Hui Huang, 原正則, 吉村雅満, 「 IrO_2 Decorated Nitrogen Doped Graphene Electrocatalysts for Efficient Oxygen Evolution Reaction」, 電気化学会第 85 回大会 (東京) 2018, S11-1014 (3/9) .
- 6 原正則, Rajashekar Badam, Hsin-Hui Huang, 吉村雅満, 「酸素発生反应用 IrRuO_x / Graphene 触媒の合成と特性評価」, 第 65 回応用物理学会春季学術講演会 (東京) 2018, 17p-202-14 (3/17) .
- 7 原正則, R. Badam, H.-H. Huang, 吉村雅満, 「グラフェン上におけるキノン分子の酸化反応の活性評価」, 第 79 回応用物理学会秋季学術講演会 (名古屋) 2018, 18p-PB3-53 (9/18).(*国内 7)
- 8 P. Joshi, R. Badam, H.-H. Huang, M. Hara, M. Yoshimura, ” Effect of Nitrogen Doping Amount on Electrocatalytic Activity of IrO_2 on Nitrogen-doped Graphene for Excellent Oxygen Evolution Reaction” , 第 65 回応用物理学会春季学術講演会 (東京) 2018, 20a-PB9-5 (9/20).
- 9 米田大祐, 鈴木誠也, 原正則, 吉村雅満, 「電気二重層キャパシタ用カーボンナノチューブ/グラファイト複合電極の作製」, 2018 年電気化学会秋季大会 (金沢) 2018, 1D14 (9/25).
- 10 原正則, 「固体高分子燃料電池内部の反応挙動のその場観察」, 実用エネルギー材料開発のためのオペランド解析研究会 (名古屋) 2019 (1/31).
- 11 原正則, 池田義仁, 吉村雅満, 「電気二重層キャパシタ用カーボンナノチューブ/Cu 電極の作製と評価」, 第 66 回応用物理学会春季学術講演会 (東京) 2019, 10p-PB5-26 (3/10).

法人番号	231023
プロジェクト番号	S1511022

- 12 P. Joshi, H.-H. Huang, M. Hara, M. Yoshimura, "Evaluation of IrO₂ Activity as an Electrocatalyst for Oxygen Evolution Reaction by Heteroatom doped Reduced Graphene Oxide", 第 66 回応用物理学会春季学術講演会 (東京) **2019**, 10a-W521-11 (3/10).
- 13 原正則, P. Joshi, H.-H. Huang, 吉村雅満, 「水電解アノード用の新規触媒 IrRuO_x 合金ナノ粒子担持グラフェンの合成」, 電気化学会 第 86 回大会 (京都) **2019**, 2A01 (3/28).
- 14 原正則, 池田義仁, 吉村雅満, 「垂直配向カーボンナノチューブを用いた電気二重層キャパシタ用電極の作製」, 2019 年電気化学会秋季大会 (甲府) **2019**, 1G04 (9/5).
- 15 P. Joshi, H.-H. Huang, M. Hara, M. Yoshimura, "Enhance the Electrocatalytic Activity of IrO₂ via Boron-doping of Carbon Support", 2019 年電気化学会秋季大会 (甲府) **2019**, 2G03 (9/6).
- 16 原正則, P. Joshi, H.-H. Huang, 吉村雅満, 「異種元素ドーピンググラフェン上に担持した IrRuO_x 触媒の合成と活性評価」, 第 80 回応用物理学会秋季学術講演会 (札幌) **2019**, 18p-E308-16 (9/18).
- 17 原正則, 「ナノカーボン担体を用いた新規水電解触媒の開発」, 第 30 回電解プロセス研究会 (大阪) **2019** (9/27).
- 18 原正則, 吉村雅満, 「カーボンナノチューブ/ Cu 電極の Li イオンキャパシタ性能評価」, 第 67 回応用物理学会春季学術講演会 (東京) **2020** (3/12-15).
- 19 R. Yadav, M. Hara, P. Joshi, M. Yoshimura, "Effect of Nitrogen-Doping in Graphene on the Performance as a Supercapacitor Electrode", 電気化学会 第 87 回大会 (名古屋) **2020** (web 討論会, 3/17-19).
- 20 P. Joshi, H.-H. Huang, M. Hara, M. Yoshimura, "Heteroatom (B/N) Codoped Graphene as IrO₂ catalyst Support for Oxygen Evolution Reaction", 電気化学会 第 87 回大会 (名古屋) **2020** (web 討論会, 3/17-19).

【バイオマスからの触媒的水素製造手法の開発】

- 1 武野計二, 石田真也, 高野孝義, 「金属接触部位の表面微細形状と熱抵抗の関係」, 日本機械学会年次大会 (関西大学) **2018** (9/10).
- 2 川ノ上弘規, 武山周介, 長田和也, 林紘啓, 武野計二, 「高粘性液体の噴霧におけるノズル内キャビテーションの観察」, 第 56 回燃焼シンポジウム (堺市) **2018** (11/14).
- 3 平川栞, 武田大樹, 坂爪亮, 山本昌平, 武野計二, 「高圧水素噴出火炎におけるノズルのスロート勾配と吹き飛び特性の関係」, 第 56 回燃焼シンポジウム (堺市) **2018** (11/14).
- 4 K. Takeno, N. Qadi, S. Kosaka, M. Kobayashi, "Gasification of Energy Grass Pretreated with Densification and Torrefaction", Fifty-sixth Combustion Symposium of Japan (Sakai, Japan), **2018** (11/14).
- 5 小阪信一郎, 武野計二, ナシム キャディ, 「草本系バイオマスの CO₂ 雰囲気における乾留およびチャーのガス化反応特性」, 第 57 回燃焼シンポジウム (札幌) **2019** (11/20). (*国内 5)
- 6 武山周介, 武野計二, 川ノ上弘規, 「高粘性液体の噴霧におけるノズル内キャビテーションの影響」, 第 57 回燃焼シンポジウム (札幌) **2019** (11/20).
- 7 武田大樹, 武野計二, 平川栞, 山本昌平, 木戸ひかる, 「高圧水素噴流火炎における衝撃波構造の保炎への影響」, 第 57 回燃焼シンポジウム (札幌) **2019** (11/20).

法人番号	231023
プロジェクト番号	S1511022

- 8 幅田恒平, 武野計二, 山本昌平, 「可燃性予混合気の熱面発火における金属表面粗さの影響」, 第 57 回燃焼シンポジウム (札幌) **2019** (11/21).
- 9 武山周介, 武野計二, 川ノ上弘規, 「高粘性液体の噴霧における矩形ノズル内キャビテーションの観察」, 第 28 回 微粒化シンポジウム (山口大学) **2019** (12/22).
- 10 N. Qadi, K. Takeno, Y. Motoyama, “Effect of Hydrothermal Carbonization Temperature on the Gasification Kinetics of Hydrochar Produced from Energy Grass Biomass”, 豊田工業大学 先進触媒開発研究センター 最終年度シンポジウム (名古屋) **2020**, P-10.
- 11 S. Kosaka, N. Qadi, K. Takeno, “CO₂ Gasification of Char Produced from the Devolatilization of Energy Grass Biomass under CO₂”, 豊田工業大学 先進触媒開発研究センター 最終年度シンポジウム (名古屋) **2020**, P-11.
- 12 武田大樹, 武野計二, 木戸ひかる, 「高圧水素噴出時の着火特性」, 豊田工業大学 先進触媒開発研究センター 最終年度シンポジウム (名古屋) **2020**, P-12.

【高機能触媒による水素化およびヒドロシリル化反応の開発】

- 1 森井昂至, 井本聡, 細川さとみ, 本山幸弘, 「窒素含有炭素ナノ繊維担持 Pd ナノ粒子による芳香族ケトンの選択的水素化反応」, 第 46 回中部化学関係学協会支部連合秋季大会 (津) **2015**, 2P70.
- 2 寺本一季, 細川さとみ, 本山幸弘, 「活性炭担持パラジウム触媒による新規なアミド化合物のシラン還元反応」, 第 46 回中部化学関係学協会支部連合秋季大会 (津) **2015**, 2P69.
- 3 細川さとみ, 寺本一季, 本山幸弘, 「パラジウム触媒を用いたカルボニル化合物の簡便な還元法」, 日本プロセス化学会 2016 サマーシンポジウム (名古屋) **2016**, 2P-15.
- 4 寺本一季, 細川さとみ, 本山幸弘, 「パラジウム触媒によるアミド化合物のシラン還元: 反応機構の解析」, 第 47 回中部化学関係学協会支部連合秋季大会 (豊橋) **2016**, 1P-06.
- 5 本山幸弘, 「パラジウム触媒による新規なアミド化合物のシラン還元反応」, 豊田工業大学 先進触媒開発研究センター 第 1 回シンポジウム (名古屋).
- 6 細川さとみ, 寺本一季, 本山幸弘, 「活性炭担持パラジウムとヒドロシランによるアミド化合物の脱酸素型還元反応」, 豊田工業大学 先進触媒開発研究センター 第 1 回シンポジウム (名古屋) **2017**, P-2.
- 7 寺本一季, 細川さとみ, 本山幸弘, 「コロイド型パラジウム触媒によるアミド化合物のシラン還元反応」 豊田工業大学 先進触媒開発研究センター 第 1 回シンポジウム (名古屋) **2017**, P-3.
- 8 石塚翔也, 本山幸弘, 「窒素含有炭素ナノ繊維担持 Pd ナノ粒子による選択的水素化反応」, 豊田工業大学 先進触媒開発研究センター 第 1 回シンポジウム (名古屋) **2017**, P-4.
- 9 戸谷元紀, 細川さとみ, 本山幸弘, 「環状エステルの新規な選択的シラン還元反応の開発」, 第 48 回中部化学関係学協会支部連合秋季大会 (岐阜) **2017**, 2PC08.
- 10 石塚翔也, 森井昂至, 張振中, 本山幸弘, 「窒素含有炭素ナノ繊維担持パラジウムナノ粒子による選択的水素化反応の開発」, 第 48 回中部化学関係学協会支部連合秋季大会 (岐阜) **2017**, 2PC10.
- 11 大西健太, 本山幸弘, 「白金サブナノクラスター触媒による芳香族化合物の環水素化反応」, 第 50 回中部化学関係学協会支部連合秋季大会 (松本) **2019**, 2P33.
- 12 Z. Zhang, T. Ikeda, H. Murayama, M. Tokunaga, T. Honma, Y. Motoyama, “Anchored Molecular Palladium-Generated Clusters for Reductive *N*-Alkylation of Amines with Carbonyl Compounds under Atmospheric Hydrogen”, 豊田工業大学 先進触媒開発研究センター 最終年度シンポジウ

法人番号	231023
プロジェクト番号	S1511022

ム (名古屋) 2020, P-8.

- 13 大西健太, 本山幸弘, 「白金クラスター触媒による芳香族化合物の環水素化反応」, 豊田工業大学 先進触媒開発研究センター 最終年度シンポジウム (名古屋) 2020, P-9.
- 14 本山幸弘, 「新規な金属クラスターの発生法と触媒機能」, 豊田工業大学 先進触媒開発研究センター 最終年度シンポジウム (名古屋) .

【原子間力顕微鏡を用いた触媒担持メカニズムの分子レベル評価】

- 1 甲斐鈴菜, 原民夫, 原正則, 吉村雅満, 「大気圧プラズマによる欠陥導入 HOPG の触媒活性の評価」, 第 64 回応用物理学会春季学術講演会 (横浜) 2017, 14p-P4-22 (3/14) .
- 2 原正則, R. Badam, H. -H. Huang, 吉村雅満, 「グラフェン上におけるキノン分子の酸化反応の活性評価」, 第 79 回応用物理学会秋季学術講演会 (名古屋) 2018, 18p-PB3-53 (9/18).
- 3 P. Joshi, R. Badam, H. -H. Huang, M. Hara, M. Yoshimura, ” Effect of Nitrogen Doping Amount on Electrocatalytic Activity of IrO₂ on Nitrogen-doped Graphene for Excellent Oxygen Evolution Reaction” , 第 65 回応用物理学会春季学術講演会 (東京) 2018, 20a-PB9-5 (9/20).
- 4 米田大祐, 鈴木誠也, 原正則, 吉村雅満, 「電気二重層キャパシタ用カーボンナノチューブ/グラファイト複合電極の作製」, 2018 年電気化学会秋季大会 (金沢) 2018, 1D14 (9/25).
- 5 原正則, 「固体高分子形燃料電池内部の反応挙動のその場観察」, 実用エネルギー材料開発のためのオペランド解析研究会 (名古屋) 2019 (1/31).
- 6 原正則, 池田義仁, 吉村雅満, 「電気二重層キャパシタ用カーボンナノチューブ/Cu 電極の作製と評価」, 第 66 回応用物理学会春季学術講演会 (東京) 2019, 10p-PB5-26 (3/10).
- 7 P. Joshi, H. -H. Huang, M. Hara, M. Yoshimura, ” Evaluation of IrO₂ Activity as an Electrocatalyst for Oxygen Evolution Reaction by Heteroatom doped Reduced Graphene Oxide” , 第 66 回応用物理学会春季学術講演会 (東京) 2019, 10a-W521-11 (3/10).
- 8 原正則, P. Joshi, H. -H. Huang, 吉村雅満, 「水電解アノード用の新規触媒 IrRuO_x 合金ナノ粒子担持グラフェンの合成」, 電気化学会 第 86 回大会 (京都) 2019 , 2A01 (3/28).
- 9 原正則, 池田義仁, 吉村雅満, 「垂直配向カーボンナノチューブを用いた電気二重層キャパシタ用電極の作製」, 2019 年電気化学会秋季大会 (甲府) 2019, 1G04 (9/5).
- 10 P. Joshi, H. -H. Huang, M. Hara, M. Yoshimura, “Enhance the Electrocatalytic Activity of IrO₂ via Boron-doping of Carbon Support” , 2019 年電気化学会秋季大会 (甲府) 2019, 2G03 (9/6).
- 11 原正則, P. Joshi, H. -H. Huang, 吉村雅満, 「異種元素ドーピンググラフェン上に担持した IrRuO_x 触媒の合成と活性評価」, 第 80 回応用物理学会秋季学術講演会 (札幌) 2019, 18p-E308-16 (9/18).
- 12 原正則, 吉村雅満, 「カーボンナノチューブ/ Cu 電極の Li イオンキャパシタ性能評価」, 第 67 回応用物理学会春季学術講演会 (東京) 2020 (3/12-15).
- 13 R. Yadav, M. Hara, P. Joshi, M. Yoshimura, “Effect of Nitrogen-Doping in Graphene on the Performance as a Supercapacitor Electrode” , 電気化学会 第 87 回大会 (名古屋) 2020 (web 討論会, 3/17-19).
- 14 P. Joshi, H. -H. Huang, M. Hara, M. Yoshimura, “Heteroatom (B/N) Codoped Graphene as IrO₂ catalyst Support for Oxygen Evolution Reaction” , 電気化学会 第 87 回大会 (名古屋) 2020 (web 討論会, 3/17-19).

法人番号	231023
プロジェクト番号	S1511022

【触媒・有機化合物および高分子錯体の静的・動的構造解析】

- 1 田代孝二, 山元博子, 王海, 太田昇, 「透過赤外・放射光広角小角 X 線散乱同時時間分解測定に基づくイソタクティックポリプロピレンのメルト等温結晶化過程における構造発展追跡」, 高分子学会予稿集 (神戸), **2016**, 65, 1Pc029.
- 2 吉岡太陽, 亀田恒徳, 田代孝二, 「シルク繊維の引張り過程における構造変化と力学挙動の関係」, 高分子学会予稿集 (神戸), **2016**, 65, 1Pc039.
- 3 吉岡弥生, 田代孝二, 「ナノファイバー状芳香族ポリアミドの形成過程における構造変化」, 高分子学会予稿集 (神戸), **2016**, 65, 1Pf076.
- 4 田代孝二, S. M. Saharin, 高濱智彦, 「ポリビニルアルコール・ヨウ素錯体の新しい結晶型の検出と構造転移機構」, 高分子学会予稿集 (神戸), **2016**, 65, 1Ph032.
- 5 田代孝二, S. Kumbara, 「一連の D/H ランダム共重合体を用いたポリオキシメチレンのメルト等温結晶化速度のスケーリング」, 高分子学会予稿集 (神戸), **2016**, 65, 1Pg037.
- 6 田代孝二, H. Jian, 「イソタクティックポリブテン-1 の II 型-I 型結晶相転移機構解明」, 繊維学会年次大会 (東京), **2016**, 1C05.
- 7 吉岡太陽, 亀田恒徳, 田代孝二, 「応力ひずみ特性の異なる二種類のシルクの延伸時構造変化の比較から考えるシルクの構造と物性の関係性」, 繊維学会年次大会 (東京), **2016**, 2C16.
- 8 河原豊, 藤井秀彰, 吉岡太陽, 田代孝二, 渡邊千咲, 玉田靖, 「樹状構造を発現した液状絹エアロゲルの水溶性」, 繊維学会年次大会 (東京), **2016**, 2C016.
- 9 高濱智彦, 田代孝二, 「PVA-ヨウ素錯体の構造と形成機構に関する量子化学的検討」, 高分子計算機科学研究会 (東京), **2016** (招待講演).
- 10 田原大輔, 田代孝二, 「力学変形過程におけるエラストマーの高次構造変化: モンテカルロシミュレーション法に基づく 2 次元広角小角 X 線散乱図形実測データの再現」, 高分子討論会予稿集 (神奈川), **2016**, 65, 1H15.
- 11 田代孝二, 山元博子, 田原大輔, W. Hai, 吉岡太陽, 「高分子の熔融等温結晶化における構造発展過程と中間相の役割」, 高分子討論会予稿集 (神奈川), **2016**, 65, 1H12.
- 12 田代孝二, 「高分子・ヨウ素錯体の結晶構造と相互作用」, 高分子討論会予稿集 (神奈川), **2016**, 65, 1H11.
- 13 田代孝二, 高濱智彦, 「種々の高分子・ヨウ素錯体の結晶構造解析と分子間相互作用」, 日本結晶学会 (茨城), **2016**, p. 33.
- 14 山元博子, 田代孝二, 浅田光則, 勝部勝義, 「ポリノナメチレンテレフタルアミドとそのモデル化合物の結晶相転移挙動」, 東海支部若手繊維研究会 (岐阜), **2016**, P. 7.
- 15 山元博子, 田代孝二, 浅田光則, 勝部勝義, 「ポリノナメチレンテレフタルアミドとそのモデル化合物の結晶相転移挙動」, 東海支部若手繊維研究会 (岐阜), **2016**, P. 7.
- 16 田代孝二, 山元博子, 杉本邦久, 長谷川正木, 「ジスチリルピラジンモノマー及びポリマー単結晶の X 線構造解析の成功と光固相重合反応機構の確立」, 高分子学会年次大会 (名古屋), **2018**, 67, 1Pe033 (5/23-25).
- 17 田代孝二, 山元博子, 杉本邦久, 「放射光 X 線構造解析および密度汎関数法による熱力学関数計算に基づくポリオキシメチレン直方晶-三方晶結晶相転移機構の検討」, 高分子学会年次大会 (名古屋), **2018**, 67, 1Pd036 (5/23-25).

法人番号	231023
プロジェクト番号	S1511022

- 18 田代孝二, W. Mengfan, 「配向非晶ポリ酢酸ビニル試料における結晶様ヨウ素錯体の生成」, 高分子学会年次大会(名古屋), 2018, 67, 1Pf034 (5/23-25).
- 19 田代孝二, 山元博子, 青山光輝, 関口博史, 岩本裕之, 「放射光広角・小角 X 線散乱および透過赤外スペクトルの同時時間分解測定に基づくポリフッ化ビニリデン階層構造の高電場印加下での挙動」, 高分子学会年次大会(名古屋), 2018, 67, 1Pc037 (5/23-25).
- 20 高濱智彦, 田代孝二, 「ポリビニルアルコール=ヨウ素錯体における水素結合と赤外スペクトル—量子化学計算に基づく検討—」, 高分子学会年次大会(名古屋), 2018, 67, 1Pf032 (5/23-25).
- 21 田原大輔, 田代孝二, 「実測広角・小角 X 線散乱データのコンピューターシミュレーション技法に基づく高分子 3 次元高次構造解析の展開」, 高分子学会年次大会(名古屋), 2018, 67, 1Pe027 (5/23-25).
- 22 田代孝二, 「ポリ乳酸の結晶相転移に関する構造科学的考察」, 高分子学会討論会(札幌), 2018, 67(2), ROMBUNNO. 2Y04 (9/12-14).
- 23 田代孝二, 高濱智彦, W. MengFan, 「ポリビニルアルコールおよび関連高分子のヨウ素錯体についての構造科学的考察」, 高分子学会討論会(札幌), 2018, 67(2), ROMBUNNO. 2Q07 (9/12-14).
- 24 田代孝二, 高濱智彦, W. MengFan, 「高分子—ヨウ素錯体の構造形成機構と分子間相互作用に関する量子化学的考察」, 高分子学会討論会(札幌), 2018, 67(2), ROMBUNNO. 2K16 (9/12-14).
- 25 吉岡太陽, 亀田恒徳, 田代孝二, 「放射光 X 線解析から分かってきたシルクの高タフネス性発現における階層的構造の役割」, 高分子学会討論会(札幌), 2018, 67(2), ROMBUNNO. 2I10 (9/12-14).
- 26 田代孝二, 山元博子, 日下勝弘, 「X 線および中性子回折データの組み合わせによる合成高分子の結合電子密度分布の実験的評価と密度汎関数法による検討」, 日本中性子化学会第 18 回年会(茨城), 2018, P2-15 (12/4-5).
- 27 MengFan Wang, 田代孝二, 「非晶性ポリ酢酸ビニルが形成する結晶性ヨウ素錯体の構造化学的検討」, 第 32 回東海支部若手繊維研究会(名古屋), 2018, P-1 (12/8).
- 28 田代孝二, 山元博子, 吉岡太陽, 船城健一, E. M. Woo, 「高分子球晶の不連続構造とラメラねじれとの関わり」, 第 32 回日本放射光学会年会・放射光科学合同シンポジウム(福岡), 2019, 1C002 (1/9-11).
- 29 田代孝二, 「高分子の結晶相転移と階層構造変化」, 名古屋大学放射光シンポジウム(名古屋), 2019, (招待講演).
- 30 山元博子, 船城健一, 増永啓康, 田代孝二, Eamor M Woo, 「ポリエチレン球晶におけるラメラねじれ構造の再検討」, 第 68 回高分子年次大会(大阪) 2019.
- 31 田代孝二, 増永啓康, 加部泰三, 「広角 X 線回折測定用「穴あき」光子計数型検出器を導入した高分子階層構造研究のための WAXD/SAXS 同時測定システム構築」, 第 68 回高分子年次大会(大阪) 2019.
- 32 W. MengFan, 高濱智彦, 田代孝二, 「非晶性ポリ酢酸ビニルの結晶性ヨウ素錯体形成に関する構造科学的検討」, 第 68 回高分子年次大会(大阪) 2019.
- 33 田代孝二, 高濱智彦, W. MengFan, 「ポリビニルアルコール偏光板におけるヨウ素錯体の構造に関する考察」, 第 68 回高分子年次大会(大阪) 2019.
- 34 山元博子, 船城健一, 増永啓康, E. M. Woo, 田代孝二, 「ポリエチレン球晶の階層構造とラメラねじれ現象との関連性」, 第 68 回高分子討論会(福井) 2019.
- 35 田代孝二, 田原大輔, S. Phongtamrug, 「ポリ-3-ヒドロキシブチラート $\alpha \rightarrow \beta$ 相転移における構

法人番号	231023
プロジェクト番号	S1511022

造変化：WAXS/SAXS 測定およびモンテカルロシミュレーションに基づく考察」, 第 68 回高分子討論会 (福井) **2019**.

- 36 田代孝二, 山元博子, 井口正俊, 増永啓康, 加部泰三, 「天然ゴムラテックスの引っ張り歪誘起結晶化現象に関する構造科学的考察」, 第 68 回高分子討論会 (福井) **2019**.
- 37 田代孝二, 高濱智彦, W. MengFan, 「ポリビニルアルコール=ヨウ素錯体型偏光板の内部構造」, 第 68 回高分子討論会 (福井) **2019**.
- 38 S. Kummara, 田代孝二, 「ナイロン 6 の X 線結晶弾性率と応力不均一分布」, 第 69 回高分子年次大会 (福岡) **2020**.
- 39 田代孝二, 日下勝弘, 山元博子, 田中伊知朗, 大原高志, 玉田太郎, 「X 線および中性子回折データの統合的解析に基づくポリビニルアルコールおよびヨウ素錯体の結晶構造への乱れ概念導入」, 第 69 回高分子年次大会 (福岡) **2020**. (*国内 39)

国際会議

【水分解光触媒の開発】

- 1 J. J. M. Vequizo, H. Matsunaga, A. Yamakata, “Distinctive photocatalytic activities of polycrystalline anatase and rutile TiO₂ studied by transient absorption spectroscopy”, 2015 International Conference on Applied Materials and Optical Systems (ICAMOS), (Cavite, Philippines), **2015** (10/22).
- 2 A. Yamakata, “Behaviors of Photogenerated Charge Carriers in Single-Crystalline and Polycrystalline Powder SrTiO₃”, 2015 EMN Meeting on Photocatalysis (Energy Materials Nanotechnology), (New York, Las Vegas, USA), **2015** (11/23) (招待講演).
- 3 A. Yamakata, M. Kawaguchi, J. Kubota, K. Domen, “Time-resolved visible to mid-IR absorption study on the behavior of photogenerated electrons and holes in LaTiO₂N visible light responsive water splitting photocatalysts”, Pacificchem 2015 (Hawaii, USA), **2015** (12/16).
- 4 J. J. M. Vequizo, A. Yamakata, “Dynamics of photocarriers in SrTiO₃ studied by transient absorption spectroscopy: Elucidation of the effects of defects”, Pacificchem 2015 (Hawaii, USA), **2015** (12/17).
- 5 A. Yamakata, “Behavior of Photogenerated Electrons and Holes on Anatase and Rutile TiO₂ Powders”, Collaborative Conference on 3D and Materials Research (CC3DMR) 2016 (Incheon, South Korea), **2016** (6/22), (招待講演).
- 6 A. Yamakata, “Curious Behaviors of Photogenerated e⁻ and h⁺ in Anatase and Rutile TiO₂ Powders”, IKM International Symposium on Pure & Applied Chemistry (ISPAC) 2016 (Kuching, Malaysia), **2016** (8/17), (招待講演) .
- 7 C. S. K. Ranasinghe, A. Yamakata, “Time-resolved IR absorption study of photogenerated charge carrier dynamics in BiVO₄/SnO₂ and BiVO₄/CoOx heterojunctions”, 4th Conference on Sri Lanka - Japan Collaborative Research - 2016 (SLJCR-2016) (Kandy, Sri Lanka), **2016** (8/20).
- 8 J. J. M. Vequizo, A. Yamakata, M. Hojamberdiev, K. Kawashima, H. Wagata, K. Yubuta, S. Oishi, K. Domen, K. Teshima, “Dynamics of Photocarriers of Metal Nitrides/Oxynitrides Studied by Transient Absorption Spectroscopy: Controlling the Effects of Defects”, 2016 International Conference on Materials Science and Nanotechnology (ICMSN) (Dumaguete City, Philippines), **2016** (10/21).
- 9 J. J. M. Vequizo, H. Matsunaga, T. Ohno, A. Yamakata, “Dynamics of Photocarriers of Brookite TiO₂ Studied by Spectroscopic Techniques: A Comparison with Anatase and Rutile TiO₂ Photocatalysts”, 第 26 回日本 MRS 年次大会, (神奈川), **2016** (12/20), (招待講演).

法人番号	231023
プロジェクト番号	S1511022

- 10 A. Yamakata, J. J. M. Vequizo, H. Matsunaga, "Behavior of photogenerated electrons and holes at the defects on anatase and rutile TiO₂ powders studied by transient absorption spectroscopy from visible to mid-IR region", 2017 International Conference on Artificial Photosynthesis (ICARP 2017), (Kyoto), 2017,(3/2-5).
- 11 J. J. M. Vequizo, H. Matsunaga, S. Kamimura, T. Ohno, A. Yamakata, "Photodynamics of Brookite TiO₂ Photocatalyst Studied by Time-resolved Vis to mid-IR Absorption Spectroscopy", Artificial Photosynthesis (ICARP 2017): Faraday Discussion, (Kyoto), **2017** (3/2-5).
- 12 S. Nishioka, J. Hyodo, A. Yamakata, Y. Yamazaki, K. Maeda, "Photocatalytic Activity of Oxygen Deficient SrTiO₃-□ Prepared by Reduced Atmosphere Calcination", 16th Korea-Japan Symposium on Catalysis & 3rd International Symposium of Institute for Catalysis , Kaderu 2.7, (Hokkaido, Japan), **2017** (5/15).
- 13 C. S. K. Ranasinghe, A. Yamakata, "Behavior of Photogenerated Charge Carriers in BiVO₄ Based Heterojunctions", 16th Korea-Japan Symposium on Catalysis & 3rd International Symposium of Institute for Catalysis , Kaderu 2.7, (Hokkaido, Japan), **2017** (5/15).
- 14 J. J. M. Vequizo, S. Ishiyama, Y. Sakata, A. Yamakata, "Dynamics of Photocarriers in Ga₂O₃-based Photocatalyst Studied by Transient Absorption Spectroscopy", 16th Korea-Japan Symposium on Catalysis & 3rd International Symposium of Institute for Catalysis , Kaderu 2.7, (Hokkaido, Japan), **2017** (5/15).
- 15 K. Maeda, A. Nakada, K. Ishimaki, J. J. M. Vequizo, A. Yamakata, O. Ishitani, "Water Splitting and CO₂ Fixation on Visible-Light-Responsive Rutile TiO₂-based Photocatalysts", 16th Korea-Japan Symposium on Catalysis & 3rd International Symposium of Institute for Catalysis , Kaderu 2.7, (Hokkaido, Japan), **2017** (5/17).
- 16 A. Yamakata, J. J. M. Vequizo, H. Matsunaga, "Difference in the Behavior of Photogenerated Electrons and Holes on Anatase and Rutile TiO₂ Powders", 16th Korea-Japan Symposium on Catalysis & 3rd International Symposium of Institute for Catalysis , Kaderu 2.7, (Hokkaido, Japan), **2017** (5/17).
- 17 A. Yamakata, "Behaviors of Photogenerated Electrons and Holes in Photoelectrochemical Interfaces", International Symposium on Pure & Applied Chemistry (ISPAC) 2017, (Ho Chi Minh City, Vietnam), **2017** (6/8), (招待講演).
- 18 A. Yamakata, "Reaction dynamics at the liquid/solid soft-interfaces", KAKENHI International Symposium on "Studying the Function of Soft Molecular Systems", (Hokkaido, Japan), **2017** (6/27), (招待講演).
- 19 K. Ishikiriyama, Y. Goto, T. Hisatomi, T. Yokogawa, A. Yamakata, Y. Sakata, K. Domen, "Effects of the Preparation Methods of Na ion Doped SrTiO₃ to the Photocatalytic Property of Overall H₂O Splitting", 13th European Congress on Catalysis (EUROPACAT 2017), (Florence, Italy), **2017** (8/28).
- 20 S. Ishiyama, S. Zhang, A. Yamakata, T. Yokogawa, Y. Sakata, "Influences of the Metal Ion Addition to Ga₂O₃ to the Photocatalytic Property of Overall H₂O Splitting", 13th European Congress on Catalysis (EUROPACAT 2017) (Palazzo Congressi, Florence, Italy) **2017** (08/28).
- 21 J. J. M. Vequizo, A. Yamakata, "Impact of Metal Ion Doping on Ga₂O₃ Photocatalysts Studied by Transient Absorption Spectroscopy", 2017 ASEAN Conference on Advanced Functional Materials and Nanotechnology (ASEAN-AFMN), (Cebu City, Philippines), **2017** (10/19), (招待講演).
- 22 A. Yamakata, "Mechanism of Photocatalytic Reactions on TiO₂ Powders", 19th SPVM National Physics Conference, 2017 ASEAN Conference on Advanced Functional Materials and Nanotechnology (ASEAN-AFMN), and 5th International Meeting on Complex Systems (IMCS), (Cebu City, Philippines),

法人番号	231023
プロジェクト番号	S1511022

- 2017 (10/21), (Plenary 基調講演)
- 23 P.-H. Hung, J. J. M. Vequizo, A. Yamakata, W. J. Tseng, “Carrier Dynamics on TiO₂ Powders Studied by Time-Resolved IR Absorption Spectroscopy”, 6th International Symposium on Advanced Ceramics and Technology for Sustainable Energy Applications toward a Low Carbon Society (ACTSEA 2017), (Kaohsiung, Taiwan), **2017** (11/1).
- 24 J. J. M. Vequizo, H. Matsunaga, T. Ohno, A. Yamakata, “Trapping States and Behavior of Photocarriers in Brookite TiO₂ Powders Studied by Transient Absorption and Emission Spectroscopies”, The 6th Toyota RIKEN International Workshop 2017 (Aichi, Japan), **2017** (11/11).
- 25 A. Yamakata, “Behaviors of Electrons and Holes in Photocatalysts Studied by Time-resolved Visible to Mid-IR Absorption Spectroscopy”, International Conference on Photochemistry and Its Applications (ICPA 2017) (Kottayam, Kerala, India), **2017** (11/11), (招待講演).
- 26 A. Yamakata, J. J. M. Vequizo, H. Matsunaga, “Behaviors of Photogenerated Electrons and Holes on TiO₂ Powder Photocatalysts”, The 22nd International Conference on Semiconductor Photocatalysis and Solar Energy Conversion (SPASEC-22) (Florida, USA), **2017** (11/14) (招待講演).
- 27 A. Yamakata, “Principal Difference in the Behaviors of Photogenerated e⁻ and h⁺ in Anatase and Rutile TiO₂ Powders”, 東京大学第5回伊藤国際学術研究センター会議 (IIRC5) – Forefront of Molecular Dynamics at Surfaces and Interfaces: From a single molecule to catalytic reaction – (東京), **2017** (11/21).
- 28 A. Yamakata, J. J. M. Vequizo, “Trapping-Induced Enhancement of Photocatalytic Activity on TiO₂ Powders”, International Congress on Pure & Applied Chemistry (ICPAC) 2018 (Siem Reap, Cambodia), **2018** (3/7), (招待講演 Symposium Award 受賞講演).
- 29 A. Yamakata, “How the Defects Affects the Photocatalytic Activity on Powder and Single crystalline TiO₂,” International Conference on Ceramic Materials and Components for Energy and Environmental Applications (CMCEE-12) (Singapore), **2018** (7/23), (招待講演).
- 30 A. Yamakata, J. J. M. Vequizo, Y. Sakata, “Defects Induced Enhancement of Ga₂O₃ Based Photocatalysts Studied by Time-Resolved Absorption Spectroscopy,” 2018 International Symposium on Advancement and Prospect of Catalysis Science & Technology (Sydney, Australia), **2018** (7/26), (招待講演).
- 31 A. Yamakata, J. J. M. Vequizo, “The Role of Powder Defects for Efficient Photocatalytic Reactions,” The 22nd International Conference on Photochemical Conversion and Storage of Solar Energy (IPS-22) (Hefei, China), **2018** (8/1), (基調講演).
- 32 J. J. M. Vequizo, S. Ishiyama, Y. Sakata, A. Yamakata, “Remarkable Activity Enhancement of Ca and Zn Doped Ga₂O₃ Photocatalysts Studied by Transient Absorption Spectroscopy,” The 22nd International Conference on Photochemical Conversion and Storage of Solar Energy (IPS-22) (Hefei, China), **2018** (8/1).
- 33 A. Yamakata, J. J. M. Vequizo, “Effects of Surface Defects on Powder Photocatalysts Studied by Time-resolved Visible to Mid-IR Absorption Spectroscopy,” International Workshop on Water Splitting: Challenges and Opportunity (Xi’an, China), **2018** (8/4), (招待講演).
- 34 T. Oshima, K. Muraoka, J. J. M. Vequizo, S. Yamashita, A. Yamakata, K. Kimoto, O. Ishitani, K. Maeda, “Synthesis of 2D perovskite oxynitride Li₂LaTa₂O₆N and the photocatalytic performance for CO₂ reduction,” The 8th Tokyo Conference on Advanced Catalytic Science and Technology (TOCAT8) (横浜), **2018** (8/8).
- 35 S. Nishioka, J. Hyodo, J. J. M. Vequizo, S. Yamashita, H. Kumagai, K. Kimoto, A. Yamakata, Y. Yamazaki, K. Maeda, “Effects of electron doping with oxygen defect introduction on photocatalytic hydrogen/oxygen evolution activity of non-stoichiometric SrTiO_{3-δ},” The 8th Tokyo Conference on Advanced Catalytic

法人番号	231023
プロジェクト番号	S1511022

- Science and Technology (TOCAT8) (横浜), **2018** (8/8).
- 36 K. Muraoka, J. J. M. Vequizo, A. Yamakata, O. Ishitani, K. Maeda, “Oxygen-doped Ta₃N₅ modified with a Ru(II) binuclear complex having the ability to reduce CO₂ under a wide range of visible light,” The 8th Tokyo Conference on Advanced Catalytic Science and Technology (TOCAT8) (横浜), **2018** (8/8).
- 37 A. Miyoshi, Y. Kato, J. J. M. Vequizo, S. Yamashita, S. Nozawa, A. Yamakata, T. Yoshida, K. Kimoto, K. Maeda, “Nitrogen/fluorine codoped rutile titanium(IV) oxide as a visible-light-driven photocatalyst for water oxidation,” The 8th Tokyo Conference on Advanced Catalytic Science and Technology (TOCAT8) (横浜), **2018** (8/8).
- 38 R. kuriki, A. Yamakata, O. Ishitani, K. Maeda, “Photocatalytic CO₂ reduction under visible light using carbon nitride and a binuclear Ru(II) complex,” The 8th Tokyo Conference on Advanced Catalytic Science and Technology (TOCAT8) (横浜), **2018** (8/8).
- 39 A. Yamakata, J. J. M. Vequizo, “Behavior of Photogenerated Charge Carriers on Highly Efficient Photocatalysts,” The 8th Advanced Functional Materials and Devices (AFMD 2018) (Leuven, Belgium), **2018** (8/18), (招待講演).
- 40 A. Yamakata, J. J. M. Vequizo, “Time-resolved Absorption Study on the Behavior of Photogenerated Electrons and Holes in Highly Active Photocatalysts,” Functional Ceramics forum for the upcoming Annual Materials Science Conference (Taichung, Taiwan), **2018** (11/17), (招待講演).
- 41 A. Yamakata, “Curious Behavior of Photogenerated Electrons and Holes in Single-crystalline and Powder Photocatalysts,” Research Seminar at National Chung Hsing University (Taichung, Taiwan), **2018** (11/19), (招待講演).
- 43 A. Yamakata, “Time-Resolved Visible to mid-IR Absorption Study of Photodynamics on Powder Photocatalysts,” Research Seminar at National Chiao Tung University (Hsinchu, Taiwan), **2018** (11/20), (招待講演).
- 44 A. Yamakata, “Curious Behaviors of Photogenerated Charge Carriers at the Defects on Powder Photocatalysts,” International Workshop on Crystalline Materials and Applications (IWCMA-2019) (Chennai, India), **2019** (1/3), (基調講演).
- 45 A. Yamakata, J. J. M. Vequizo, S. Ishiyama, T. Hiramane, Y. Sakata, “Defects for the Enhancement of Photocatalytic Activity”, International Conference on Photocatalysis and Photoenergy 2019 (ICoPP2019), (Incheon, Korea), **2019** (5/24), (招待講演).
- 46 T. Ogawa, A. Yamakata, A. Kuwabara, “Density Functional Studies of Electron Trapping Behaviors in Photocatalytic Materials”, The 6th International Symposium on Advanced Microscopy and Theoretical Calculations (AMTC6), (名古屋), **2019**, (6/14).
- 47 A. Yamakata, J. J. M. Vequizo, H. Matsunaga, “Trapping of Photogenerated Electrons at the Defects on Anatase and Rutile TiO₂”, The 6th International Symposium on Advanced Microscopy and Theoretical Calculations (AMTC6), (名古屋), **2019**, (6/14).
- 48 A. Yamakata, J. J. M. Vequizo, “Behaviour of Photogenerated Charge Carriers at the Defects on Photocatalysts”, The First Symposium on Photo (electro) catalysis (SOP-1), (Beijing, China), **2019**, (6/23) (招待講演).
- 49 Y. Hiramachi, H. Fujimori, M. Yoshida, A. Yamakata, Y. Sakata, “Improvement of the photocatalytic property of BaTi₄O₉ to the overall H₂O splitting”, The 8th Asia Pacific Congress on Catalysis (APCAT-8), (Bangkok, Thailand), **2019** (8/5).
- 50 J. Jiang, H. Fujimori, M. Yoshida, A. Yamakata, Y. Sakata, “Preparation of High Active SrTiO₃ to overall H₂O splitting by doping Na ion”, The 8th Asia Pacific Congress on Catalysis (APCAT-8), (Bangkok,

法人番号	231023
プロジェクト番号	S1511022

- Thailand), **2019** (8/5).
- 51 A. Yamakata, J. J. M. Vequizo, S. Ishiyama, T. Hiramane, Y. Sakata, “Mechanism of highly efficient Ga₂O₃ based photocatalysts studied by time-resolved absorption spectroscopy”, The 8th Asia Pacific Congress on Catalysis (APCAT-8), (Bangkok, Thailand), **2019** (8/5).
- 52 A. Yamakata, “Impurity Induced Enhancement of Photocatalytic Activity on Ga₂O₃”, International Congress on Pure & Applied Chemistry (ICPAC) Yangon 2019, (Yangon, Myanmar), **2019**, (8/7) (招待講演).
- 53 A. Yamakata, “Enhancement of photocatalytic activity of Ga₂O₃ based photocatalysts studied by time-resolved absorption spectroscopy”, The 24th International Conference on Semiconductor Photocatalysis and Solar Energy Conversion (SPASEC-24), (Ontario, Canada), **2019**, (10/14) (招待講演).
- 54 A. Yamakata, J. J. M. Vequizo, “Charge Carrier Dynamics on Powder Photocatalysts Studied by Time-resolved Visible to Mid-IR absorption Spectroscopy”, International Conference on Photochemistry and Sustainable Energy (ICPSE 2019), (Kelala, India), **2019**, (10/19) (招待講演).
- 55 Y. Lu, A. Yamakata, T. Watanabe, “Evaluation of NaTaO₃ photocatalyst synthesized from various route by time-resolved absorption and emission spectroscopy”, The 13th Pacific Rim Conference of Ceramic Societies (PACRIM13), (沖縄), **2019**, (10/28).
- 56 K. Ogawa, A. Nakada, H. Suzuki, O. Tomita, A. Yamakata, A. Saeki, H. Kageyama, R. Abe, “Flux Synthesis of Layered Perovskite Oxyhalide Bi₄NbO₈Cl Photocatalyst for Efficient Water Oxidation Under Visible Light”, The 13th Pacific Rim Conference of Ceramic Societies (PACRIM13), (沖縄), **2019**, (10/28).
- 57 A. Yamakata, J. J. M. Vequizo, S. Ishiyama, T. Hiramane, Y. Sakata, “Enhancement of photocatalytic activity of Ga₂O₃ by impurity doping”, The 13th Pacific Rim Conference of Ceramic Societies (PACRIM13), (沖縄), **2019**, (10/29) (招待講演).
- 58 K. Sano, F. Kuttassery, A. Yamakata, B. Ohtani, T. Shimada, H. Tachibana, T. o Ishida, S. Takagi, H. Inoue, “Synthesis and Identification of Titanium Oxide Nanoparticle for Molecular Catalyst Sensitized Artificial Photosynthesis Systems”, 3rd International Solar Fuels Conference (ISF-3) / International Conference on Artificial Photosynthesis-2019 (ICARP2019), (広島), **2019**, (11/20-24).
- 59 A. Yamakata, J. J. M. Vequizo, Y. Sakata, “Defects-induced enhancement of photocatalytic activity of Ga₂O₃ studied by time-resolved visible to mid-IR absorption spectroscopy”, The 36th International Japan-Korea Seminar on Ceramics (JK-Ceramics 36), (鳥取), **2019**, (11/22) (招待講演).
- 60 A. Yamakata, “Behavior of Photogenerated Charge Carriers on Powder Photocatalysts”, Materials Research Meeting 2019 (MRM2019), (神奈川), **2019**, (12/11) (招待講演).

【水素の貯蔵と放出用の高機能触媒開発】

- 1 Y. Isogai, T. Kamioka, H. Lee, N. Kojima, Y. Ohshita, “Influence of ITO-RPD Process on Effective Minority Carrier Lifetime in Reactive Plasma Deposited ITO/SiO₂/Si Structure”, The 27th Photovoltaic Science and Engineering Conference (PVSEC-27), 2018.
- 2 Y. Ohshita, H. Machida, T. Takada, A. Ogura, “Solar energy storage system with recycled hydrogen carriers”, E-MRS (Strasbourg, France), **2017**.(*国外 2)
- 3 Y. Ohshita, H. Lee, T. Kamioka, N. Usami, “Effects of Surface Doping of Si Absorbers on the Performance of Carrier Selective Contact”, MRS fall meeting (Boston USA), **2018**.(*国外 3)

法人番号	231023
プロジェクト番号	S1511022

【水電解および燃料電池の電極触媒の開発】

- 1 M. Hara, B. Rajashekar, K. De Silva, H.-H. Huang, M. Yoshimura, “Fabrication and characterization of IrO₂ / nano-carbon catalysts”, The 52nd Fullerenes-Nanotubes-Graphene General symposium(Tokyo) **2017**, 3-8(3/3).
- 2 B. Rajashekar, K. De Silva, M. Hara, M. Yoshimura, “IrO₂/carbon Nano Hybrids as Efficient Oxygen Evolution Reaction Catalysts”, FiMPART’17 (Bordeaux, France) **2017**, F3 (7/11).
- 3 M. Hara, B. Rajashekar, K. De Silva, H.-H. Huang, M. Yoshimura, “Fabrication and Evaluation of Nanocarbon supported Iridium Oxide catalysts for Water Electrolysis”, PGIS research Congress 2017 (Peradeniya, Sri Lanka) **2017**, ID50 (9/9).
- 4 B. Rajashekar, M. Hara, H.-H. Huang, M. Yoshimura, “IrO₂ Based Modified Graphene Materials as Efficient Oxygen Evolution Reaction Catalysts”, The 8th International Symposium on Surface Science (ISSS-8) (Ibaraki) **2017**, 6PN-72 (10/26).
- 5 M. Hara, B. Rajashekar, H.-H. Huang, M. Yoshimura, “Synthesis of Novel IrRuO_x / Graphene Catalyst for Oxygen Evolution Reaction”, The 54th Fullerenes-Nanotubes-Graphene General symposium(Tokyo) **2018**, 1P-26(3/10).
- 6 M. Hara, R. Badam, G. J. Wang, H.-H. Huang, M. Yoshimura, “Synthesis and Evaluation of Iridium Oxide Nanoparticle Catalysts Supported on Nitrogen-Doped Reduced Graphene Oxides”, 233rd Electrochemical Society (Seattle USA) **2018**, I03-1664(5/14).
- 7 P. Joshi, R. Badam, H.-H. Huang, M. Hara, M. Yoshimura, “Design and Evaluation of IrO₂ on Nitrogen-doped Reduced Graphene Oxide as an Electrocatalyst for Oxygen Evolution Reaction”, ACSIN-14 & ICSPM26 (Sendai) **2018** (10/23).
- 8 M. Hara, P. a Joshi, H.-H. Huang, M. Yoshimura, “Synthesis of Heteroatom-doped Graphene as Active Catalysts for Hydroquinones Oxidation Reaction”, The 56th Fullerenes-Nanotubes-Graphene General symposium (Tokyo) **2019**, No. 1-8 (3/2).(*国際 8)
- 9 M. Hara, P. Joshi, H.-H. Huang, M. Yoshimura, “Synthesis and Evaluation of Novel Iridium Ruthenium Oxide Catalysts Supported on Reduced Graphene Oxide for Oxygen Evolution Reaction”, 235rd Electrochemical Society (Dallas USA) **2019**, I03-1664 (5/27).
- 10 R. Yadav, M. Hara, P. Joshi, M. Yoshimura, “Zinc Oxide Nanoparticles Decorated on Nitrogen-Doped Graphene Sheets as Advanced Supercapacitor Electrode”, The 57th Fullerenes-Nanotubes-Graphene General Symposium (Nagoya) **2019**, No. 2P-25 (9/4).
- 11 S. Ogawa, S. Suzuki, M. Hara, M. Yoshimura, “Preparation of IrO₂ nanoparticles on CVD graphene by hydrothermal method”, The 57th Fullerenes-Nanotubes-Graphene General symposium (Nagoya) **2019**, No. 3P-27 (9/5).
- 12 P. Joshi, R. Yadav, Y. Matsuoka, M. Hara, M. Yoshimura, “B,N-codoped Reduced Graphene Oxide as a Support for IrO₂ as Active OER Electrocatalyst”, The 57th Fullerenes-Nanotubes-Graphene General symposium (Nagoya) **2019**, No. 3P-28 (9/5).
- 13 P. Joshi, H.-H. Huang, M. Hara, M. Yoshimura, “Boron doped Reduced Graphene Oxide as a Catalyst Support for Oxygen Evolution Reaction”, ICSPM 27 (Shizuoka) **2019**, S4-7 (12/5).
- 14 M. Hara, P. Joshi, M. Yoshimura, “Development of novel iridium oxide catalysts supported on modified nanocarbons for oxygen evolution reaction”, FiMPART 2019 (Ahmedabad India) **2019**, B3-2 (12/17)(招

法人番号	231023
プロジェクト番号	S1511022

待講演).

- 15 R. Yadav, P. Joshi, M. Hara, M. Yoshimura, "Evaluation of various nitrogen -doping in graphene on the performance as a supercapacitor electrode", The 58th Fullerenes-Nanotubes-Graphene General symposium (Tokyo) **2020**, No. 1P-5 (3/15).
- 16 P. Joshi, R. Yadav, Y. Matsuoka, M. Hara, M. Yoshimura, "Heteroatom -doped Nanocarbons as Active Support for IrO₂ as an OER Electrocatalyst", The 58th Fullerenes-Nanotubes-Graphene General symposium (Tokyo) **2020**, No. 2P-27 (3/16).

【高機能触媒による水素化およびヒドロシリル化反応の開発】

- 1 S. Hosokawa, K. Teramoto, Y. Motoyama, "Facile Silane-Reduction of Tertiary Carboxamides by Using Palladium on Carbon Catalyst", The 13th International Kyoto Conference on New Aspects of Organic Chemistry (IKCOC-13) (Kyoto) **2015**, PB(C)-32.
- 2 T. Ikeda, Z. Zhang, Y. Motoyama, "Hydrosilane-Promoted Facile Deprotection of *tert*-Butyl Groups in Esters, Ethers, Carbonates, and Carbamates", The 4th International Symposium on Process Chemistry (ISPC 2019) (Kyoto) **2019**, 1P-52.

【原子間力顕微鏡を用いた触媒担持メカニズムの分子レベル評価】

- 1 R. Kai, M. Hara, M. Yoshimura, "Catalytic Activity of Defective Highly Oriented Pyrolytic Graphite Modified by Hydrogen Plasma", 25th International Colloquium on Scanning Probe Microscopy (Shizuoka) **2017**, S4-49 (12/7).
- 2 P. Joshi, R. Badam, H.-H. Huang, M. Hara, M. Yoshimura, "Design and Evaluation of IrO₂ on Nitrogen-doped Reduced Graphene Oxide as an Electrocatalyst for Oxygen Evolution Reaction", ACSIN-14 & ICSPM26 (Sendai) **2018** (10/23).
- 3 H.-H. Huang, K. De Silva, M. Yoshimura, "Kelvin Probe Force Microscopy Study of 2D Graphene-Based Sheets", ACSIN-14 & ICSPM26 (Sendai) **2018** (10/22).
- 4 H.-H. Huang, L.-W. Su, K. De Silva, M. Yoshimura, "Graphene/Layered Double Hydroxide Composite for Ion Sieving", ACSIN-14 & ICSPM26 (Sendai) **2018** (10/23).
- 5 M. Hara, P. a Joshi, H.-H. Huang, M. Yoshimura, "Synthesis of Heteroatom-doped Graphene as Active Catalysts for Hydroquinones Oxidation Reaction", The 56th Fullerenes-Nanotubes-Graphene General symposium (Tokyo) **2019**, No. 1-8 (3/2).
- 6 M. Hara, P. Joshi, H.-H. Huang, M. Yoshimura, "Synthesis and Evaluation of Novel Iridium Ruthenium Oxide Catalysts Supported on Reduced Graphene Oxide for Oxygen Evolution Reaction", 235rd Electrochemical Society (Dallas USA) **2019**, I03-1664 (5/27).
- 7 R. Yadav, M. Hara, P. Joshi, M. Yoshimura, "Zinc Oxide Nanoparticles Decorated on Nitrogen-Doped Graphene Sheets as Advanced Supercapacitor Electrode", The 57th Fullerenes-Nanotubes-Graphene General Symposium (Nagoya) **2019**, No. 2P-25 (9/4).
- 8 S. Ogawa, S. Suzuki, M. Hara, M. Yoshimura, "Preparation of IrO₂ nanoparticles on CVD graphene by hydrothermal method", The 57th Fullerenes-Nanotubes-Graphene General symposium (Nagoya) **2019**, No. 3P-27 (9/5).
- 9 P. Joshi, R. Yadav, Y. Matsuoka, M. Hara, M. Yoshimura, "B,N-codoped Reduced Graphene Oxide as a Support for IrO₂ as Active OER Electrocatalyst", The 57th Fullerenes-Nanotubes-Graphene General

法人番号	231023
プロジェクト番号	S1511022

symposium (Nagoya) **2019**, No. 3P-28 (9/5).

- 10 P. Joshi, H.-H. Huang, M. Hara, M. Yoshimura, “Boron doped Reduced Graphene Oxide as a Catalyst Support for Oxygen Evolution Reaction”, ICSPM 27 (Shizuoka) **2019**, S4-7 (12/5).
- 11 M. Hara, P. Joshi, M. Yoshimura, “Development of novel iridium oxide catalysts supported on modified nanocarbons for oxygen evolution reaction”, FiMPART 2019 (Ahmedabad India) **2019**, B3-2 (12/17)(招待講演).
- 12 R. Yadav, P. Joshi, M. Hara, M. Yoshimura, “Evaluation of various nitrogen -doping in graphene on the performance as a supercapacitor electrode”, The 58th Fullerenes-Nanotubes-Graphene General symposium (Tokyo) **2020**, No. 1P-5 (3/15).
- 13 P. Joshi, R. Yadav, Y. Matsuoka, M. Hara, M. Yoshimura, “Heteroatom -doped Nanocarbons as Active Support for IrO₂ as an OER Electrocatalyst”, The 58th Fullerenes-Nanotubes-Graphene General symposium (Tokyo) **2020**, No. 2P-27 (3/16).

【触媒・有機化合物および高分子錯体の静的・動的構造解析】

- 1 K. Tashiro, “Novel Concepts in the Study of Phase Transition and Crystallization Phenomenon of Polymers Viewed from the Wide Hierarchical Points”, MACRO2017, Trivandrum (India) **2017** (Invited Lecture).
- 2 K. Tashiro, “A new aspect of crystal phase transition and its relation with the hierarchical structure change of crystalline polymers”, Pure and Applied Chemistry International Conference 2017 (Bangkok) (Plenary Lecture).
- 3 K. Tashiro, “Hierarchical Structure of Polymer Spherulites Detected by Synchrotron X-ray Microbeam and 2D FTIR Spectral Techniques,” The International Conference on Advanced and Applied Petroleum, Petrochemicals, and Polymers 2018 (Bangkok, Thailand), **2018** (12/18–20), (基調講演).
- 4 K. Tashiro, “Development of Simultaneous Measurement System of FTIR, WAXD and SAXS Data for the Study of Hierarchical Structure Change of Polymers Subjected to the Various External Fields,” 2018 Synchrotron Radiation in Polymer Science (2018 SRPS: SRPS VII) (Gyeongju, Korea), **2018** (9/4–7), (招待講演).
- 5 K. Tashiro, “Structure and Phase Transitions of Biodegradable Polyesters”, International Association of Applied Materials Award (Orland, USA), **2019**(招待講演).
- 6 S. Phongtamrug, K. Tashiro, “Hierarchical Structure Change in the Stress-induced α -to- β Phase Transition of Highly-Oriented Poly(3-hydroxybutyrate)”, International Conference of BioPolymers (Bangkok, Thailand), **2019**(招待講演).

法人番号	231023
プロジェクト番号	S1511022

シンポジウム・学会等の実施状況、インターネットでの公開状況等

<既に実施しているもの>

- ・第1回シンポジウム 2017.3.10 開催
- ・最終年度シンポジウム 2020.3.5(新型コロナウイルスのため要旨集のみ発行)
- ・論文および学会発表リスト (大学 HP)
website: <https://www.toyota-ti.ac.jp/advancedcatalysis/index.html>

・プレスリリース:

農業・食品産業技術総合研究機構と豊田工業大学(田代孝二特任教授)

「ミノムシの紡ぐ絹糸が世界最強たる理由の構造科学的解明に成功」;同時プレスリリース
(2019.4.2)

SPring-8

「次世代構造材料として期待されるミノムシの糸の強さの秘密を構造科学的に解明」
BL40B2(構造生物学 II) (2019.4.15)

<これから実施する予定のもの>

- ・上記最終年度シンポジウムの代替として, 2020 年度中に開催予定

14 その他の研究成果等

特に無し

法人番号	231023
プロジェクト番号	S1511022

15 「選定時」及び「中間評価時」に付された留意事項及び対応

<「選定時」に付された留意事項>

「拠点としての特徴を明確にして研究を進めていただきたい」

<「選定時」に付された留意事項への対応>

本学は「先端ハイブリッド工学」という独自の理念の下に、小規模大学の利点を活かして複数の分野の有機的結合を重視した研究体制の確立と推進に取り組んでおり、光と物質科学を基盤とした新素材・素子の開発研究とエネルギー分野への展開を重点目標のひとつとしている。

本研究拠点は発足当初、物質工学と電子工学に属する 5 研究室の協力体制であったが、その後、3分野の残りの1つである機械工学の研究室にも参加して頂き、再生可能エネルギーとして注目されているバイオマスの高効率エネルギー変換に関する課題をプラスすることで、全学的な体制で“水素の発生・活用技術の高度化とエネルギー蓄積や水素に関連する物質製造工程の革新を「先進触媒」により実現するための拠点”へと成長した。

このように「水素」と「触媒」を基軸として、本学における 3 分野が有機的に結びついた中核となる研究拠点として、これらに関する基礎学術の確立と産業応用へ展開を加速すべく注力している。

<「中間評価時」に付された留意事項>

特に無し

<「中間評価時」に付された留意事項への対応>

法人番号	231023
プロジェクト番号	S1511022

年度・区分	支出額	内 訳						備考
		法人負担	私学助成	共同研究機関負担	受託研究等	寄付金	その他()	
平成27年度	施設	0						
	装置	0						
	設備	104,401	34,800	69,601				
	研究費	37,286	19,091	18,195				
平成28年度	施設	0						
	装置	0						
	設備	19,915	6,639	13,276				
	研究費	30,215	18,059	12,156				
平成29年度	施設	0						
	装置	0						
	設備	0						
	研究費	46,793	28,325	18,468				
平成30年度	施設	0						
	装置	0						
	設備	0						
	研究費	33,051	18,251	14,800				
平成31年度	施設	0						
	装置	0						
	設備	0						
	研究費	28,090	13,693	14,397				
総額	施設	0	0	0	0	0	0	0
	装置	0	0	0	0	0	0	0
	設備	124,316	41,439	82,877	0	0	0	0
	研究費	175,435	97,419	78,016	0	0	0	0
総計	299,751	138,858	160,893	0	0	0	0	

法人番号

231023

17

《施設》(私学助成を受けていないものも含め、使用している施設をすべて記載してください。)(千円)

施設の名 称	整備年度	研究施設面積	研究室等数	使用者数	事業経費	補助金額	補助主体
触媒有機化学研究室・実験室	昭和56年度	199m ²	1	16	不明	0	
量子界面物性研究室・実験室	平成7年度	247m ²	1	15	不明	0	
表面科学研究室・実験室	平成7年度	343m ²	1	10	不明	0	

※ 私学助成による補助事業として行った新增築により、整備前と比較して増加した面積

0 m²

《装置・設備》(私学助成を受けていないものは、主なもののみを記載してください。)(千円)

装置・設備の名称	整備年度	型番	台数	稼働時間数	事業経費	補助金額	補助主体
(研究装置) なし							
(研究設備) デジタル核磁気共鳴装置	27		1	2,800 h	47,952	31,968	私学助成
全自動元素分析装置	27		1	980 h	13,996	9,331	私学助成
フーリエ変換型赤外分光装置	27		1	2,520 h	12,495	8,330	私学助成
ナノ欠陥イメージング装置	27		1	2,800 h	21,999	14,666	私学助成
グローブボックス	27		1	2,100 h	7,959	5,306	私学助成
薄膜製造装置	28		1	1,400 h	19,915	13,276	私学助成
(情報処理関係設備) なし							

18 研究費の支出状況

(千円)

年 度	平成 27 年度		
小 科 目	支 出 額	積 算 内 訳	
		主 な 使 途	金 額
教 育 研 究 経 費 支 出			
消 耗 品 費	12,644	試薬、溶媒、光学部品	12,644
光 熱 水 費	5,302	電気代	5,302
通 信 運 搬 費	9	ガス容器処分代	9
印 刷 製 本 費	591	研究成果報告書印刷代	591
旅 費 交 通 費	585	学会発表にかかる旅費	585
賃 借 料	10	学外研究施設利用料金	10
報 酬・委 託 料	11	装置調整代	11
諸 会 費	15	学会参加費	15
修 繕 費	7,643	装置保守費	7,643
出 版 物 費	359	論文別刷代	359
計	27,169		27,169
ア ル パ イ ト 関 係 支 出			
人 件 費 支 出 (兼務職員)	0		0
教育研究経費支出 計	0		0
設 備 関 係 支 出(1個又は1組の価格が500万円未満のもの)			
教育研究用機器備品	7,100		7,100
図 書	32		32
計	7,132		7,132
研 究 ス タ ッ フ 関 係 支 出			
リサーチ・アシスタント			
ポスト・ドクター	2,985		2,985
研究支援推進経費			
計	2,985		2,985
ア ル パ イ ト 関 係 支 出			
人 件 費 支 出 (兼務職員)	824		824
教育研究経費支出 計	824		824
設 備 関 係 支 出(1個又は1組の価格が500万円未満のもの)			
教育研究用機器備品	10,440		10,440
図 書	50		50
計	10,490		10,490
研 究 ス タ ッ フ 関 係 支 出			
リサーチ・アシスタント			
ポスト・ドクター	4,278		4,278
研究支援推進経費			
計	4,278		4,278

年 度		平成 29 年度		法人番号	231023
小 科 目	支 出 額	積 算 内 訳			
		主 な 使 途	金 額	主 な 内 容	
教 育 研 究 経 費 支 出					
消 耗 品 費	9,023	試薬、溶媒、光学部品	9,023	試薬、溶媒、光学部品	
光 熱 水 費	3,384	電気代	3,384	電気代	
通 信 運 搬 費	11	宅配便代	11	宅配便代	
印 刷 製 本 費	0		0		
旅 費 交 通 費	2,599	学会発表にかかる旅費	2,599	学会発表にかかる旅費	
賃 借 料	41	学外研究施設利用料金	41	学外研究施設利用料金	
報 酬・委 託 料	55	試料測定依頼	55	試料測定依頼	
修 繕 費	1,251	実験装置修理	1,251	実験装置修理	
諸 会 費	491	学会・講演会参加費	491	学会・講演会参加費	
出 版 物 費	15	研究資料代	15	研究資料代	
損 害 保 険 料	5	海外出張付帯保険	5	海外出張付帯保険	
計	16,875				
ア ル パ イ ト 関 係 支 出					
人 件 費 支 出 (兼務職員)	167		167		
教育研究経費支出 計	167		167		
設 備 関 係 支 出(1個又は1組の価格が500万円未満のもの)					
教育研究用機器備品 図 書	21,045		21,045		
計	21,045		21,045		
研 究 ス タ ッ フ 関 係 支 出					
リサーチ・アシスタント ポスト・ドクター	8,706		8,706	外国2人	
研究支援推進経費 計	8,706		8,706		

年 度		平成 30 年度			
小 科 目	支 出 額	積 算 内 訳			
		主 な 使 途	金 額	主 な 内 容	
教 育 研 究 経 費 支 出					
消 耗 品 費	8,812	試薬、溶媒、光学部品	8,812	試薬、溶媒、光学部品	
通 信 運 搬 費	80	宅配便代	80	宅配便代	
印 刷 製 本 費	0		0		
旅 費 交 通 費	1,853	学会発表にかかる旅費	1,853	学会発表にかかる旅費	
報 酬・委 託 料	100	講師謝礼	100	講師謝礼	
出 版 物 費	61	論文掲載料	61	論文掲載料	
雑 費	0		0		
修 繕 費	3,788	実験装置修理	3,788	実験装置修理	
諸 会 費	422	学会・講演会参加費	422	学会・講演会参加費	
計	15,116		15,116		
ア ル パ イ ト 関 係 支 出					
人 件 費 支 出 (兼務職員)	0		0		
教育研究経費支出 計	0		0		
設 備 関 係 支 出(1個又は1組の価格が500万円未満のもの)					
教育研究用機器備品 図 書	17,892		17,892		
計	17,935		17,935		
研 究 ス タ ッ フ 関 係 支 出					
リサーチ・アシスタント ポスト・ドクター					
研究支援推進経費 計	0				

		法人番号		231023	
年 度	平成 31 年度				
小 科 目	支 出 額	積 算 内 訳			
		主 な 使 途	金 額	主 な 内 容	
教 育 研 究 経 費 支 出					
消 耗 品 費	10,101	試薬、溶媒、光学部品	10,101	試薬、溶媒、光学部品	
光 熱 水 費	0		0		
通 信 運 搬 費	7	宅配便代	7	宅配便代	
印 刷 製 本 費	0		0		
旅 費 交 通 費	2,821	学会発表にかかる旅費	2,821	学会発表にかかる旅費	
賃 借 料	0		0		
報 酬 ・ 委 託 料	1,431	試料加工依頼	1,431	試料加工依頼	
修 繕 費	933	実験装置修理	933	実験装置修理	
諸 会 費	895	学会・講演会参加費	895	学会・講演会参加費	
出 版 物 費	2	研究資料代	2	研究資料代	
雑 費	125	海外出張付帯保険	125	海外出張付帯保険	
計	16,315		16,315		
ア ル パ イ ト 関 係 支 出					
人 件 費 支 出 (兼務職員)	0		0		
教 育 研 究 経 費 支 出 計	0		0		
設 備 関 係 支 出(1個又は1組の価格が500万円未満のもの)					
教 育 研 究 用 機 器 備 品 図 書	11,775		11,775		
計	11,775		11,775		
研 究 ス タ ッ フ 関 係 支 出					
リサーチ・アシスタント					
ポスト・ドクター	0		0		
研究支援推進経費					
計	0		0		

Part 2

II. 研究報告

1. 高活性光触媒の光励起ダイナミクス

山方 啓

(量子界面物性研究室)

2. キャリア選択型太陽電池を用いた水素生成

大下 祥雄

(半導体研究室)

3. 高活性電極触媒の開発に向けたナノ炭素材料の適用

原 正則・吉村 雅満

(表面科学研究室)

高活性光触媒の光励起ダイナミクス

豊田工業大学大学院工学研究科 山方 啓

一般に触媒には単結晶より粉末が好んで用いられる。これは、粉末表面に多数存在する欠陥は化学反応を促進するからである。しかし、光触媒の場合、欠陥は再結合を促進する場として忌み嫌われてきた。しかし、それは本当だろうか。筆者らは、欠陥に捕捉された電子の動きを解析できる独自の分光装置を開発し、欠陥における光励起キャリアーの動きを調べてきた。本稿では、その詳細を解説する。

1. 緒言

エネルギー問題や環境問題を解決するために、太陽エネルギーを用いて水から水素を製造し、有害汚染物質を無害物質へと分解できる光触媒が注目されている。この光触媒反応のメカニズムは、平たく言えば太陽電池を用いた水や化学物質の電気分解と同じである。しかし、光触媒が太陽電池よりも優れている点は、半導体材料の“粉末”をそのまま利用できることである。粉末は単結晶材料などに比べて圧倒的に安いコストで製造することができる。しかし、最大の問題点は粉末の表面には多くの欠陥が存在することである。粉末を光触媒に利用した場合、これらの欠陥は光励起キャリアーの再結合を促進し、光触媒活性を低下させる最大の原因であると考えられてきた。しかし、光触媒には依然として粉末が好んで用いられている。この矛盾を理解するためには、粉末欠陥における光励起キャリアーの挙動を実際に観察する必要がある。それは、光触媒反応の量子効率、光励起キャリアーの再結合失活速度と反応分子への電荷移動速度の比で決まるからである。光励起キャリアーの寿命を測定するためには、時間分解分光測定が有用である。しかし、従来一般的な時間分解分光装置では可視領域、あるいは赤外領域しか測定ができないため、伝導帯電子と欠陥に捕捉されたトラップ電子を区別することができなかった。そこで、著者は測定波長範囲を赤外から近紫外域まで拡張し、さらに時間分解能も秒からフェムト秒まで拡張した装置を開発した¹⁾。この装置により、伝導帯電子とトラップ電子、さらにトラップ正孔を区別することが可能になり、欠陥だらけの粉末特有の光励起キャリアーの挙動を調べることが可能になった。

筆者らは、これまでにこの装置を用いて様々な粉末

光触媒の欠陥に捕捉された光励起キャリアーの動きを調べてきた。その結果、これまでの予想に反して粉末に多数存在する欠陥は再結合を抑制する効果があり、光触媒活性の向上に役立つ場合があることを発見した。例えば、 SrTiO_3 の単結晶と粉末を比較したところ、確かに粉末の場合、大部分のキャリアーは欠陥に捕捉される。しかし、光励起キャリアーの再結合寿命は単結晶よりも粉末の方がむしろ長くなることを見いだした²⁾。さらに、 TiO_2 のアナターゼとルチル³⁾、ブルッカイト⁴⁾と $\text{TiO}_2(\text{B})$ ⁵⁾の酸化還元活性の違いは、結晶相に依存した欠陥準位の深さの違いで説明できることを明らかにした。また、粉末にフラックス処理^{6,7)}やドーピング^{8,9)}、表面処理^{1,10)}を施すと欠陥準位や再結合速度が変化し、光触媒活性もまた変化することを明らかにした。本稿では、これらの結果について詳しく解説する。

2. レーザー分光を用いた電子トラップ準位の計測

光触媒に光を照射して生成したキャリアーの挙動を調べるためには、パルスレーザーを用いた時間分解分光測定が有効である。光励起キャリアーによる光吸収過程を Fig. 1 に示すが、伝導帯に励起された伝導帯電子は、主に中赤外域に吸収を与える¹¹⁾。この吸収はバンド内遷移に帰属され、右肩上がりで構造がないという特徴を有している。一方、欠陥にトラップされた電子は、トラップ準位から伝導帯への遷移に帰属される吸収を主に可視から近赤外域に与える。そして、この吸収端のエネルギーから、伝導帯の下からトラップ準位の上端までの深さを大まかに見積もることができる。一方、トラップ正孔は多くの触媒においてバンドギャップよりも若干長波長側の可視域に吸収を与えることが報告されている¹⁾。したがって、近紫外から中赤外域の時間分解吸収分光測定を行うことで伝導帯電子とトラップ電子、トラップ正孔のエネルギー状態や減衰過程を区別して独立に調べることができる¹⁾。

このような時間分解分光測定は、自作の装置を用いて行っている¹⁾。詳しい装置の説明はここでは省略するが、マイクロ秒から秒の領域の時間分解測定には、ハロゲンランプやグローバーなどの連続光源と分散型分光器、オシロスコープを利用している。また、これよりも速い過程は、フェムト秒レーザーを用いたポン

プローブ法を用いている。そして、これらの装置を組み合わせることで、可視から中赤外領域の過渡吸収測定をフェムト秒から秒の時間領域で行うことができる。また、測定には粉末光触媒を CaF_2 板に固定したものを利用するが、これは赤外光を良く透過するので、赤外域の測定は透過配置で行う。しかし、可視から近赤外域の光は散乱されるので、この領域では、拡散反射配置で行っている。

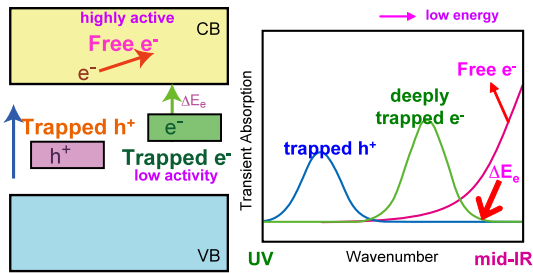


Fig. 1 Typical transient absorption spectra of free, trapped electrons and holes generated by band-gap photoexcitation of photocatalysts.

3. 欠陥ばかりの粉末と単結晶の違い

3. 1 SrTiO_3 単結晶の光励起キャリアーの挙動

まず、光触媒として最も良く用いられる材料の一つである SrTiO_3 の単結晶 (100 面) に紫外光レーザーパルス (355 nm, 6 ns) を照射し、透過配置で測定した過渡吸収スペクトルを Fig. 2(A) に示す²⁾。バンドギャップを励起すると、 25000 cm^{-1} から 2500 cm^{-1} にかけて右肩上がりの単調な吸収が観察された。赤外域にかけて強く観察されるこのような単調な吸収は、 TiO_2 ¹²⁾ の他 NaTaO_3 ¹³⁾ などで観察され、Fig. 1 で説明したように、伝導帯に励起された自由電子に帰属される。また、 2500 cm^{-1} (0.2 eV) 付近に吸収ピークが観察されるが、これは伝導帯から約 0.2 eV 程度の浅い準位に捕捉された電子の寄与が一部含まれることを示唆している。しかしながら、可視から近赤外域には、何も吸収ピークが観察されていない。これらの結果は、欠陥が少ないと推察される単結晶の場合、光励起電子の大部分は、伝導帯電子や浅いトラップ電子として残存することを意味している。しかし、問題は再結合速度が速いことである。 2500 cm^{-1} の吸収強度の減衰曲線を Fig. 2(A) の挿入図に示すが、伝導帯電子や浅いトラップ電子は、光照射 100 ns 以内にほぼ完全に再結合消滅してしまう。そして、気相に酸素やメタノール蒸気を導入しても、減衰速度は全く変化しない。これは、単結晶の場合、光励起電

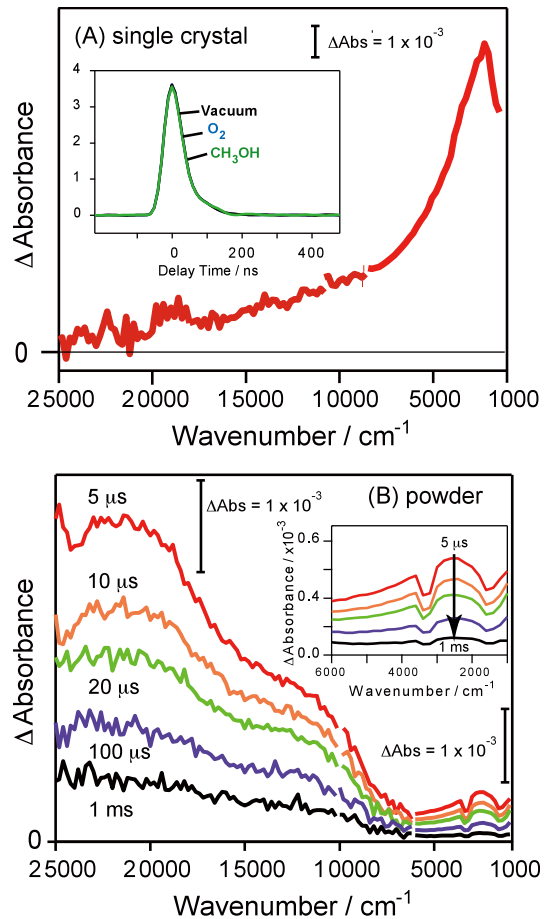


Fig. 2 Transient absorption spectra of single crystalline (A) and powder SrTiO_3 (B). The inset of (A) shows decay curves measured at 2500 cm^{-1} in vacuum, 10 Torr O_2 and MeOH vapor.

子と正孔はいずれも気相に導入した分子と反応しないことを意味している。この原因は、単結晶は表面積が小さく反応分子の吸着量が少ないことに加えて、光励起キャリアーの寿命が 100 ns と短いことが上げられる。つまり、単結晶の場合、大部分の電子は伝導帯電子や浅いトラップ電子として残存するにもかかわらず、寿命が短いので吸着分子と反応する確率が極めて小さいことが分かった。

3. 2 SrTiO_3 粉末の光励起キャリアーの挙動

次に、 SrTiO_3 粉末 (Aldrich 社 : 粒径 100 nm) における光励起キャリアーの挙動を調べた。その結果を Fig. 2(B)²⁾ に示すが、スペクトルの形状は単結晶とは全く異なることが分かる。粉末の場合にも単結晶の場合と同様に、 4000 cm^{-1} 以下に伝導帯電子や浅いトラップ電子に帰属される右肩上がりの吸収が観察されている。しかし、それよりさらに強い吸収ピークが 22000 cm^{-1} と 11000 cm^{-1} 付近に観測されている。これらの二つのピ

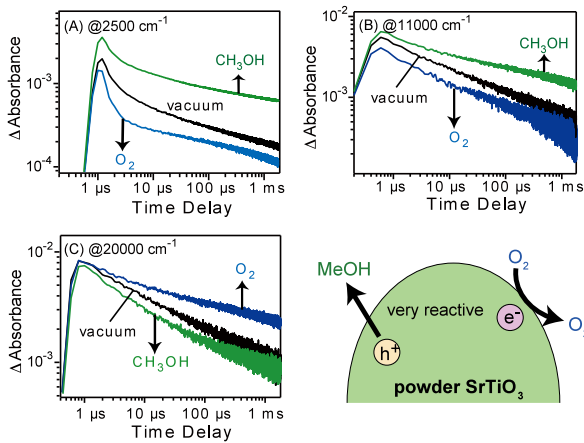


Fig. 3 Reactivity of photogenerated electrons and holes in powder SrTiO₃ measured at 2500 cm⁻¹ (A), 11000 cm⁻¹ (B), and 20000 cm⁻¹ (C) exposed with O₂ and MeOH vapor.

ークは単結晶では観察されていないことから、先に述べたように、粒子の欠陥に深くトラップされた電子、あるいはトラップ正孔に帰属される。そして、注目すべきは、これらの吸収は照射後 1 ms 経過しても残存していることである。この結果は、粉末の場合、大部分の光励起キャリアーはマイクロ秒領域において欠陥にトラップされているが、単結晶に比べて長い寿命を有していることを意味している。従来欠陥は再結合を促進すると考えられてきた。しかし、この実験結果は、欠陥は再結合をむしろ抑制する効果があることを意味している。欠陥にキャリアーがトラップされると、キャリアーの移動度が低下し、電子と正孔が衝突する確率が低下する。その結果、再結合が遅くなると解釈できる。

しかし、問題はこれらの長い寿命を有するトラップキャリアーが反応活性を有するか否かである。そこで、これらの光励起キャリアーの反応活性を調べるために、気相に反応ガスを導入して減衰過程を調べた。Fig. 3(A)に示すように、2500 cm⁻¹の吸収は、酸素を導入すると減衰速度が速くなる。この結果は、伝導帯電子は酸素と反応することを意味している¹⁴⁾。一方、メタノールを導入すると電子の減衰速度が遅くなった。これは正孔がメタノールと反応消費されることで電子の寿命を延ばすからである¹⁵⁾。同様な結果は、11000 cm⁻¹の吸収を与えるトラップ電子でも観測された (Fig. 3(B))。一方、20000 cm⁻¹の場合には (Fig. 3(C))、2500 cm⁻¹や 11000 cm⁻¹とは正反対に、減衰速度は酸素の導入で遅くなり、メタノールの導入で速くなった。これらの結果は、20000 cm⁻¹の吸収強度は正孔の数を反映することを意味している。いずれにしても、これらの

結果は、粉末の場合、大部分の光励起キャリアーは欠陥に捕捉されているが、反応活性を維持していることが分かった。つまり、粉末欠陥は再結合速度を抑制し、光触媒活性の向上に役立っていることが分かった。

4. 欠陥準位の違いで決まる酸化チタン光触媒活性の違い

4. 1 アナターゼ、ルチル、ブルッカイト、TiO₂(B)の過渡吸収スペクトルの違い

SrTiO₃の単結晶と粉末の違いから、欠陥に光励起キャリアーがトラップされると再結合速度が遅くなり、光触媒活性の向上に役立つ場合があることを見いだした。しかし、例えば電子トラップ準位が深くなると、正孔の寿命は長くなるが、電子の反応活性は低下する。したがって、電子と正孔が共に反応消費されなくてはならない定常反応活性はいつも向上するとは限らない。よって、粉末によってトラップ準位の深さがどの程度であるのか、そしてその深さはどのような要因で決まるのか、これを明らかにする必要がある。筆者らは、TiO₂の場合、同じ酸素欠陥に由来する欠陥準位でも、この深さは結晶相に依存し、これが光触媒活性の結晶相依存性を支配していることを明らかにした。ここでは、この結晶相依存性について詳しく調べた結果を述べる。

TiO₂には、アナターゼとルチル、ブルッカイトの他、近年ブロンズ型構造を有する TiO₂(B)が新しい材料として注目されている。一般に、光触媒には前の2つが良く用いられ、アナターゼはルチルよりも光触媒活性が高く、特に水や酸素の還元の高い活性があることが知られている。一方、ルチルはアナターゼより水の酸化に高い活性を有している。そして、これらの光触媒活性が違うメカニズムを調べる研究が長年行われてきた。しかし、その根本的な違いはまだ十分に解明されていない。そこで本研究では、これらの材料における電子と正孔の挙動を調べた³⁾。

まず、アナターゼ粉末 (触媒学会の参照触媒 TIO-10) に紫外光レーザーパルスを照射して測定した過渡吸収スペクトルを Fig. 4(A)に示す³⁾。25,000~6,000 cm⁻¹にブロードな吸収が観測された。これらの吸収は酸素やメタノールガスを導入した実験により、トラップ正孔とトラップ電子の寄与が混合したものに帰属された。しかし、4,000 cm⁻¹以下には伝導帯電子に帰属される強い吸収が観測されている。この伝導帯電子による吸収強度は、トラップ電子やトラップ正孔の和よりも圧倒的

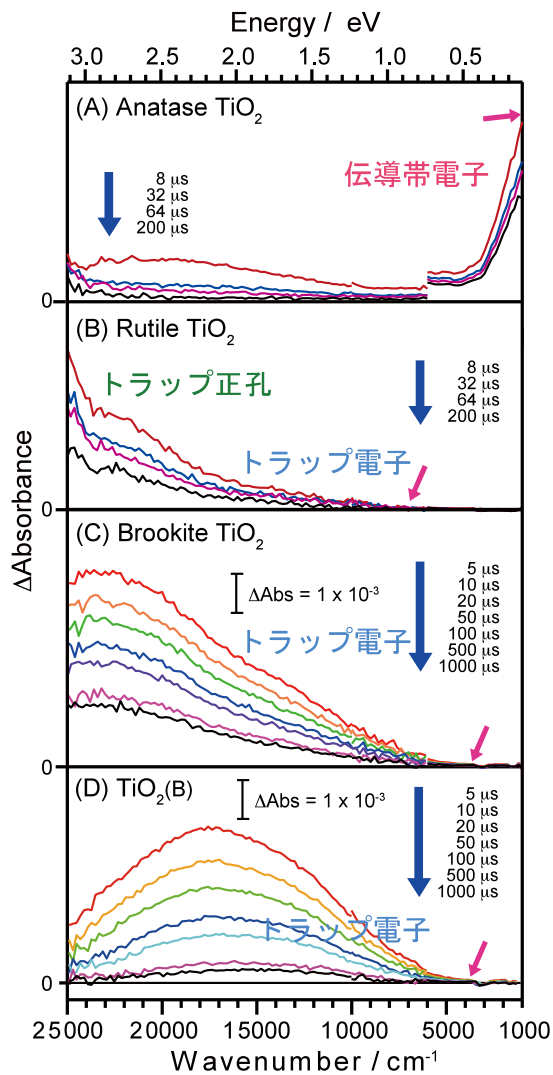


Fig. 4 Transient absorption spectra of anatase (A), rutile (B), brookite (C) and TiO₂(B) (D) powder photocatalysts.

に強い。つまり、アナターゼの場合、一部トラップ電子は存在するものの、大部分の電子はマイクロ秒領域でも伝導帯電子として残存することが分かった。また、この吸収は $1,000 \text{ cm}^{-1}$ ($\sim 0.1 \text{ eV}$) まで観察されることから、この吸収がトラップ電子によるものだと仮定してもその深さは 0.1 eV より浅いことを意味している (Fig. 5)。このような浅いトラップ電子や伝導帯電子はエネルギーが高いため、高い反応活性を有する。そして、実際に酸素を導入すると容易に反応することが確認された。このように、伝導帯電子が長い寿命を有するため、アナターゼは高い還元活性を有することが分かった。

次に、ルチル粉末 (触媒学会参照触媒 TIO-6) を用いて同様な実験を行った³⁾。過渡吸収スペクトルを Fig. 4(B) に示すが、スペクトルの形状は、アナターゼ粉末とは全く異なることが分かった。 $25,000 \text{ cm}^{-1}$ から $7,000 \text{ cm}^{-1}$ にかけて吸収強度はなだらかに減少し、 $22,000 \text{ cm}^{-1}$

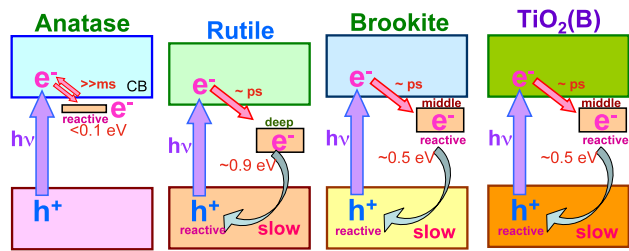


Fig. 5 Electron trapping states of anatase, rutile, brookite and TiO₂(B) powder photocatalysts.

と $13,000 \text{ cm}^{-1}$ 付近にブロードな吸収ピークが観察されている。これらの吸収は酸素やメタノールガスを導入した実験により、それぞれトラップ正孔とトラップ電子に帰属された。そして、最も大きな違いはアナターゼ粉末で強く現れた $4,000 \text{ cm}^{-1}$ 以下の吸収がほとんど観察されないことである。この結果は、ルチル粉末の場合、大部分の電子はマイクロ秒領域では欠陥に捕捉されており、伝導帯電子の残存数がアナターゼ粉末と比べて極端に少ないことを意味している。すなわち、ルチルの還元活性が低い原因は、反応活性が高い伝導帯電子や浅いトラップ電子の残存数が少ないからであると説明することができる。なお、 $13,000 \text{ cm}^{-1}$ にピークを与えるトラップ電子の吸収端は $\sim 7,000 \text{ cm}^{-1}$ (0.9 eV) に観察された。よって、このルチルの電子トラップ準位は伝導帯の下から約 0.9 eV のところにあると推察することができる (Fig. 5)。

一方、ルチルはアナターゼよりも高い酸化活性を有していることが報告されている。これは、マイクロ秒領域における正孔の残存数の違いで説明できる。正孔の吸収はいずれも $22,000 \text{ cm}^{-1}$ 付近に出現する。 Fig. 4(A) と Fig. 4(B) において、この強度を比較すると、アナターゼよりもルチルの方が5倍以上大きい。つまり、正孔の残存数はアナターゼよりもルチルの方が多いことがわかる。実際にこのトラップ正孔は気相に導入したメタノールなどと反応することが確認されており、よってルチルは高い酸化活性を有すると考えることができる。ルチルの正孔の残存数が多い原因は、ルチルの電子トラップ準位がアナターゼよりも深いことで説明できる。前述したように、ルチルの場合大部分の電子は深い欠陥準位に捕捉されている。電子が深くトラップされると、動きが遅くなり、正孔と衝突する確率が低下する。そのため再結合が抑制され、正孔の寿命は長くなる。つまり、電子トラップ準位の深さは電子の反応活性だけではなく、正孔の残存数に支配される酸

化活性も支配することが分かった。

次に、ブルッカイト粉末（九州工業大学・横野照尚教授よりご提供）の測定を行った⁴⁾。結果を Fig. 4(C) に示すが、過渡吸収スペクトルの形状はルチル型に非常によく似ており、 25000 cm^{-1} から 3000 cm^{-1} にかけて吸収強度はなだらかに減少し、 22000 cm^{-1} 付近にブロードな吸収ピークが観察されている。これらの吸収は酸素やメタノールガスを導入した実験により、いずれもトラップ電子による吸収が支配的であることが分かった。しかし、ルチルと異なる点は、トラップ電子の吸収端が、約 4000 cm^{-1} (0.5 eV) 付近にあり、トラップ準位がルチルよりも浅いことである (Fig. 5)。よって、電子の反応活性はルチルよりも高いことが推察される。実際にアセトアルデヒドの分解反応において、活性はアナターゼ>ブルッカイト>ルチルとなり、ブルッカイトはルチルよりも高い反応活性を示した。

また $\text{TiO}_2(\text{B})$ についても同様な測定を行った⁵⁾。その結果、Fig. 4(D) に示すように、 25000 cm^{-1} から 3000 cm^{-1} にかけてブロードな吸収が観察された。これらの吸収は酸素やメタノールガスを導入した実験により、いずれもトラップ電子に帰属された。そして、トラップ電子の吸収端が、約 4000 cm^{-1} (0.5 eV) 付近にあり、電子トラップ準位の深さはブルッカイトと同様に 0.5 eV 程度であることが分かった。

5. 表面形態の制御とドーピングによる欠陥準位の変化と制御

5. 1 フラックス処理による表面形態の制御とトラップ準位の変化

粉末の表面構造は極めて複雑である。綺麗な単結晶面が出ている場合もあれば、いびつで構造が特定できないこともある。よって、同じ組成の粉末でも粉末の形態によって欠陥の数が異なり、電子や正孔のトラップ状態が異なることが推察される。したがって、粒子の表面形態を制御すれば欠陥構造も制御でき、光触媒活性も制御できると考えられる。一般に、金属酸化物などの粉末を NaCl や KCl などの熔融塩中で加熱すると、再結晶化が促進され、綺麗な結晶が生成する^{16,17)}。この操作をフラックス処理と呼ぶが、ここでは、このフラックス処理によって粉末の形態と光励起キャリアーの動きがどのように変化するかを調べた。

この実験では、和光純薬社製の SrTiO_3 粉末を用い、これを 1100°C の SrCl_2 熔融塩中で10時間加熱処理した（東京大学・堂免一成教授よりご提供）⁶⁾。まず、こ

れらの粉末の走査型電子顕微鏡 (SEM) 写真を Fig. 6 の挿入図に示すが、フラックス処理前の粉末は、小さな一次粒子が不規則に凝集した二次粒子で構成されることが分かる。しかし、 SrCl_2 と SrTiO_3 の混合比 ($\text{FLUX}=\text{SrCl}_2/\text{SrTiO}_3$) を 0.1 から 1 に増加させながらフラックス処理するにつれて、きれいな立方体の結晶ができることが分かる。つまり、フラックス処理を行うことで結晶性が良く欠陥の少ない結晶を調製できることが分かった。

これらの試料の過渡吸収スペクトルを測定した結果を Fig. 6⁶⁾ に示す。Fig. 6(A) をみると、フラックス処理前の粉末の吸収スペクトルの形状は、Fig. 1 に示した単結晶はおろか、Aldrich 社の粉末とも全く異なることが分かった。 4000 cm^{-1} 以下の吸収と 20000 cm^{-1} 付近の吸収がほとんど観察されず、 11000 cm^{-1} 付近に一本だけピークが現れる。この吸収はメタノールの導入と酸素の導入に対して共に増加したので、トラップ電子とトラップ正孔の両方の寄与が含まれることが分かった⁶⁾。

次に、フラックス処理 ($\text{FLUX}=0.1$) を行くと、スペ

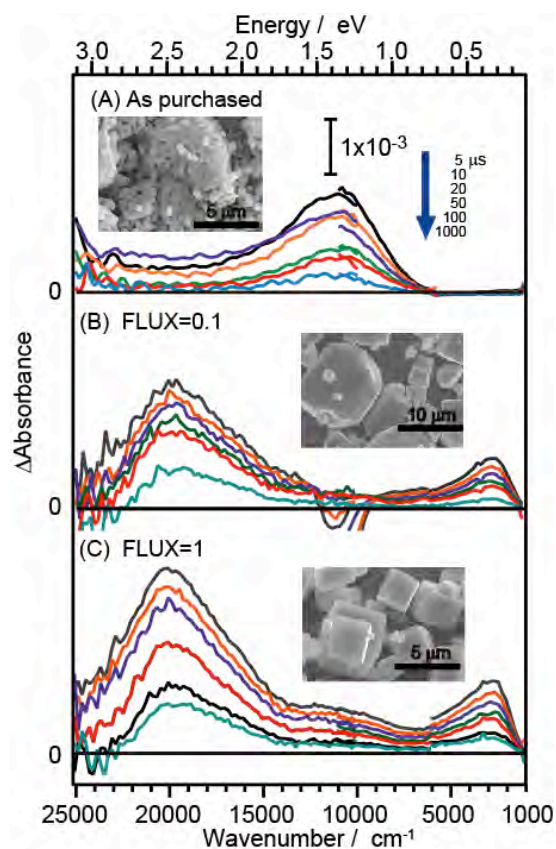


Fig. 6 Transient absorption spectra of flux-treated SrTiO_3 powder photocatalysts. The amount of flux ($\text{FLUX}=\text{SrCl}_2/\text{SrTiO}_3$) was varied from 0.1 to 1.

クトルの形状が劇的に変わった。フラックス処理前に観察されていた 11000 cm^{-1} の吸収強度が減少し、これがあたかも二つに分かれたかのように 20000 cm^{-1} と 2500 cm^{-1} に新しいピークが出現した。さらに FLUX=1 まで増やすと、これらの二つの吸収強度が共に増加した。これらの2つの吸収は、Aldrich 社の粉末の場合と同じように、気相に酸素やメタノールを導入してその減衰速度を比較することで、それぞれ正孔と電子に帰属された⁶⁾。フラックス処理によるこれらのスペクトル形状の変化は粒子の形態変化と関係があると考えられる。フラックス処理前は、表面が凸凹しており、粒界や欠陥の存在が顕著である。よって、光励起キャリアはこれらの欠陥に捕捉されやすいと考えられる。しかし、フラックス処理すると、一次粒子がはぐれはじめ、粒界が減少すると共に表面がフラットになる。つまり、フラックス処理により表面欠陥が低減するので深いトラップ電子が減少し、浅いトラップ電子や伝導帯電子の数が増えると予想することができる。

実際に紫外光を用いた水分解反応による水素生成活性を調べると、フラックス処理前には活性がほとんどゼロであったが、処理することによって FLUX=0.1 のとき 6 mmol/h 、FLUX=1 のとき 40 mmol/h と増加した。これは、フラックス処理によって光励起キャリアを深く捕捉する粒界やいびつな欠陥が低減し、反応活性を示す浅いトラップキャリアが増加したためと解釈できる。

5. 2 表面修飾によるトラップ準位の変化

一般に光触媒に水素発生を促進する Pt や酸素発生を促進する CoO_x などの助触媒を担持すると活性が向上する。これは、これらの助触媒がそれぞれ電子と正孔を捕集し、水素発生や酸素発生に必要な過電圧を減少させるためであると考えられている。しかし、我々は、一連の研究の中で CoO_x 助触媒は正孔を捕捉する効果があるが、それに加えて電子トラップ準位を浅くする効果があることを見いだした。そこで、ここでは、これらの助触媒の担持効果を詳しく調べた。

本研究では、まず LaTiO_2N を用いた¹⁾。これは 600 nm 以下の可視光を吸収し、水の酸化活性が極めて高い光触媒である。この光触媒に Pt を担持しても水素生成活性はそれほど向上しない。しかし、 CoO_x を担持すると、酸素生成の量子効率約 30% にまで向上する。そこで、本研究では LaTiO_2N への Pt や CoO_x の担持効果を調べた。

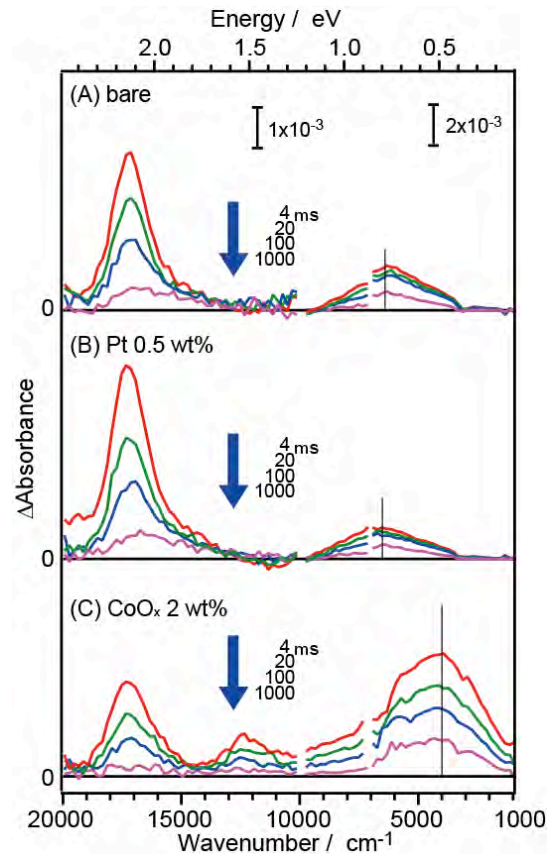


Fig. 7 Transient absorption spectra of bare and Pt- or CoO_x -loaded LaTiO_2N photocatalysts.

まず何も担持しない LaTiO_2N に 355 nm の紫外光パルス照射して測定した過渡吸収スペクトルを測定した¹⁾。Fig. 7(A)に示すように、 LaTiO_2N のバンドギャップを励起すると、 17000 と 6000 cm^{-1} ブロードな過渡吸収ピークが観測された。これらの吸収は酸素やメタノールの導入試験により、それぞれトラップ正孔とトラップ電子に帰属された。注目すべきは、 LaTiO_2N の場合、 SrTiO_3 やアナターゼ型 TiO_2 で強く観察された伝導帯電子がほとんど存在せず、大部分の電子は深くトラップされていることである。この原因は、 LaTiO_2N の調製方法にあると考えている。一般に、酸窒化物は、前駆体となる金属酸化物をアンモニアガス中で加熱して窒化する。つまり、還元雰囲気下で加熱して調製するので、電子を深くトラップする酸素欠陥がしやすいと考えられる。

次に、Pt 助触媒の担持効果を調べた。Fig. 7(B)に示すように、Pt を担持すると 6000 cm^{-1} の強度が若干減少し、逆に 17000 cm^{-1} の強度が若干増加している。この結果は、 LaTiO_2N から Pt に電子が移動し、これによって LaTiO_2N 中に存在する正孔の寿命は長くなることを意味している。しかし、この助触媒への電子移動量は

これまでに報告してきたTiO₂やNaTaO₃などと比べて非常に小さい。これは、LaTiO₂Nの場合、電子は深くトラップされており、移動度が小さいのでPtに移動しにくいと考えている。実際に、LaTiO₂NにPtを担持しても水素生成活性はそれほど向上しない。これはPtへの電子移動量が少ないためと考えられる。

次にCoO_xの担持効果を調べた。Fig. 7(C)に測定した過渡吸収スペクトルを示すが、CoO_xを担持すると、17000 cm⁻¹の正孔による吸収強度が減少し、逆に5000 cm⁻¹のトラップ電子による吸収強度が増加した。これらの結果は、CoO_xを担持すると、LaTiO₂N中の正孔の濃度が減少し、電子の数が増加することを示している。また、CoO_xを担持すると、12500 cm⁻¹に新しい吸収ピークが出現する。この吸収は、Co(III)による吸収に帰属されるが、これはCoO_xが正孔を捕捉すると、一部のCo(II)がCo(III)に酸化したことを意味している。

ここで注目すべきことは、CoO_xを担持すると、トラップ電子の吸収ピークが6000から5000 cm⁻¹に長波長シフトすることである。この長波長シフトは、伝導帯から電子が存在するトラップ準位までの深さが浅くなることを示唆している。先に述べたように、LaTiO₂Nの場合、大部分は酸素欠陥に起因する深い欠陥準位に電子がトラップされている。CoO_xを担持すると、この表面欠陥にCoO_xが配位することで酸素欠陥の構造が変化すると考えている。このような電子トラップ準位の変化は、LaTiO₂NではなくFig. 8に示すようにTa₃N₅ (信州大学・M. Hojamberdiev 准教授よりご提供)でも

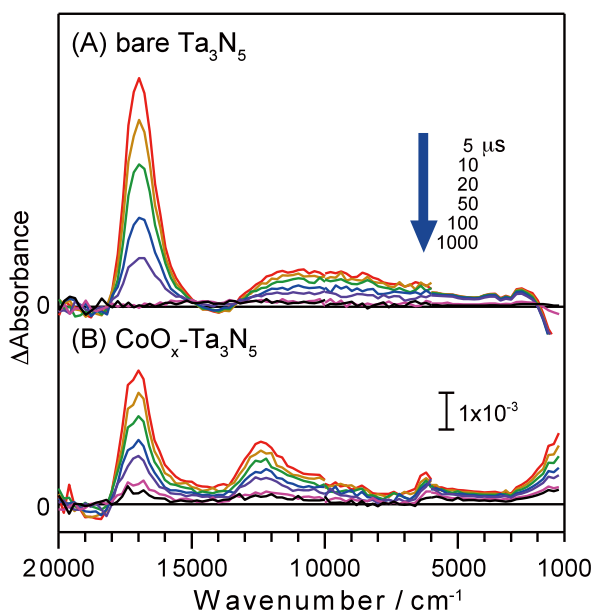


Fig. 8 Transient absorption spectra of bare and CoO_x-loaded Ta₃N₅ photocatalysts.

観察された¹⁰。Ta₃N₅の場合、13000~3000 cm⁻¹に深いトラップ電子の吸収が観測されている。しかし、CoO_xを担持すると、3000 cm⁻¹以下に伝導帯電子や浅いトラップ電子に帰属される吸収が出現する。この結果はCoO_xがTa₃N₅の酸素欠陥準位を変化させることを意味しており、LaTiO₂Nよりもより浅い準位に変えることを意味している。

5. 3 ドーピングによるトラップ準位の変化

電子トラップとして働く酸素欠陥はドーピングによっても防ぐことができる。例えば、窒素ドープ酸化チタン(TiO₂:N)はドープしたN³⁺がO²⁻に置き換わるが、このときチャージバランスを保つため、酸素欠陥ができやすい。そのため、N³⁺をドープする際にFを共ドープすると酸素欠陥ができにくくなることが予想される。そこで、TiO₂にN³⁺とFを共ドープして、過渡吸収スペクトルを測定した⁹。

まず、ルチル型TiO₂:N (東京工業大学・前田和彦准教授よりご提供)に紫外光を照射して測定すると、トラップ電子に帰属される吸収ピークが7000 cm⁻¹付近に観察された (Fig. 9(A)). 次に、ドーピングの際にフッ素の前駆体 (NH₄)₂TiF₆ を混入し、その混入量をC=0からC=1, C=50へ増やしていくと、挿入図のよう

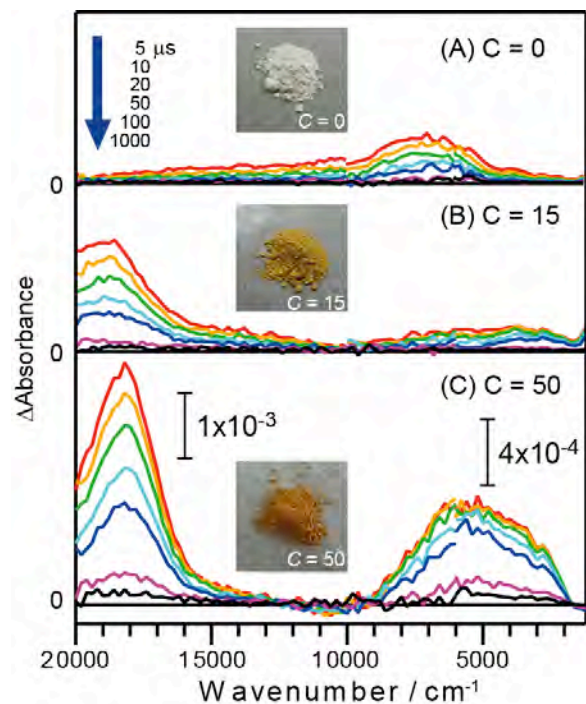


Fig. 9 Transient absorption spectra of rutile TiO₂:N photocatalysts co-doped with F. The amount of fluoride precursor was changed from C=0 to C=50.

に色がより濃い茶色っぽくなり、ドーピングがされやすくなるのが分かる。実際にこれらの試料の過渡吸収スペクトルを測定した結果が Fig. 9(B)と Fig. 9(C)である。C=15 では、 7000 cm^{-1} 付近に観察された深いトラップ電子の吸収が減少し、ブロードなピークが 3000 cm^{-1} 付近へと低波数側にシフトしている。この結果は、Fの共ドーピングによって酸素欠陥の生成が抑制されたことを示唆している。また、Fの共ドーピングによって反応活性の高いトラップ正孔に帰属される吸収が $20000\sim 10000\text{ cm}^{-1}$ に出現した。次に、フッ素の添加量をさらに C=50 に増やすと、このトラップ正孔の吸収は増える。しかし、逆にトラップ電子のピークは 5000 cm^{-1} 付近にシフトし、C=15 で観察された $3000\sim 1000\text{ cm}^{-1}$ 付近の伝導帯電子や浅いトラップ電子が減少した。これは、フッ素を過剰に添加すると再び欠陥準位が形成されることを意味している。実際に Z-スキーム型での水分解の定常反応活性も C=15 が最も高い活性を有する。これはトラップ正孔の残存量と、電子トラップ準位の深さの兼ね合いで決まる結果であると考えられる。

6. おわりに

本稿では、様々な粉末系光触媒材料に光を照射して生成した光励起キャリアーのトラップ状態について調べた結果についてまとめた。バンドギャップを励起して測定したスペクトルの形状をみて分かるように、同じ組成の材料でも試料の形態や結晶相によって吸収スペクトルの形状は全く異なる。特に、欠陥の少ない単結晶の場合には、伝導帯電子の吸収が強く観察される。一方、粉末の場合には、大部分の光励起キャリアーは欠陥に捕捉されていることが分かった。しかし、光励起キャリアーの再結合寿命は単結晶より桁違いに長い。電子が欠陥に捕捉されると、動きが遅くなるので正孔と衝突する確率が減少し、正孔の寿命は長くなる。よって、電子トラップ準位の深さは、電子の反応活性だけではなく酸化活性をも支配する重要な要因である。そして、大変興味深いことに、表面欠陥準位は表面処理やドーピングによって変化する。欠陥構造のわずかな変化が、光励起キャリアーのエネルギー状態に大きな摂動を与える。近紫外から中赤外域の時間分解分光測定を利用すると、欠陥における光励起キャリアーの挙動を詳しく調べることができる。今後、欠陥構造とトラップ準位の関係をより正確に予測できることが可能になると、この情報はより高い活性を有する光触媒

の設計に役立つかもしれない。欠陥ばかりの粉末の表面構造は極めて複雑である。しかし、まだまだ謎に満ちあふれたやりがいのある研究対象である。

7. 謝辞

本稿で解説した研究内容は、堂免一成教授（東京大学）、酒多喜久教授（山口大学）、手嶋勝弥教授（信州大学）、前田和彦准教授（東京工業大学）および豊田工業大学、東京大学、東京工業大学の研究員、学生との共同研究の成果である。この場を借りて関係者に感謝する。

文 献

- 1) A. Yamakata, M. Kawaguchi, N. Nishimura, T. Minegishi, J. Kubota, and K. Domen, *J. Phys. Chem. C*, **118**, 23897 (2014).
- 2) A. Yamakata, J. J. M. Vequizo, and M. Kawaguchi, *J. Phys. Chem. C*, **119**, 1880 (2015).
- 3) A. Yamakata, J. J. M. Vequizo, and H. Matsunaga, *J. Phys. Chem. C*, **119**, 24538 (2015).
- 4) J. J. M. Vequizo, H. Matsunaga, T. Ishiku, S. Kanimura, T. Ohno, and A. Yamakata, *ACS Catal.*, **7**, 2644 (2017).
- 5) G. Hasegawa, M. Tanaka, J. J. M. Vequizo, A. Yamakata, H. Hojo, M. Kobayashi, M. Kakihana, M. Inada, H. Akamatsu, and K. Hayashi, *Nanoscale*, **11**, 1442 (2019).
- 6) A. Yamakata, H. Yeilin, M. Kawaguchi, T. Hisatomi, J. Kubota, Y. Sakata, and K. Domen, *J. Photochem. Photobiol. A-Chem.*, **313**, 168 (2015).
- 7) M. Hojamberdiev, K. Yubuta, J. J. M. Vequizo, A. Yamakata, S. Oishi, K. Domen, and K. Teshima, *Cryst. Growth Des.*, **15**, 4663 (2015).
- 8) A. Yamakata, M. Kawaguchi, R. Murachi, M. Okawa, and I. Kamiya, *J. Phys. Chem. C*, **120**, 7997 (2016).
- 9) A. Miyoshi, J. J. M. Vequizo, S. Nishioka, Y. Kato, M. Yamamoto, S. Yamashita, T. Yokoi, A. Iwase, S. Nozawa, A. Yamakata, T. Yoshida, K. Kimoto, A. Kudo, and K. Maeda, *Sustain. Energ. Fuels*, **2**, 2025 (2018).
- 10) J. J. M. Vequizo, M. Hojamberdiev, K. Teshima, and A. Yamakata, *J. Photochem. Photobiol. A-Chem.*, **358**, 315 (2018).
- 11) J. I. Pankove: *Optical Processes in Semiconductors*.

Dover, New York, (1975).

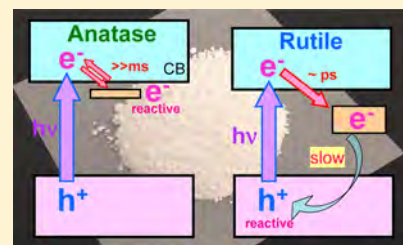
- 12) A. Yamakata, T. Ishibashi, and H. Onishi, *Chem. Phys. Lett.*, **333**, 271 (2001).
- 13) A. Yamakata, T. Ishibashi, H. Kato, A. Kudo, and H. Onishi, *J. Phys. Chem. B*, **107**, 14383 (2003).
- 14) A. Yamakata, T. Ishibashi, and H. Onishi, *J. Phys. Chem. B*, **105**, 7258 (2001).
- 15) A. Yamakata, T. Ishibashi, and H. Onishi, *J. Phys. Chem. B*, **106**, 9122 (2002).
- 16) Y. Miseki, K. Saito, and A. Kudo, *Chem. Lett.*, **38**, 180 (2009).
- 17) H. Kato, M. Kobayashi, M. Hara, and M. Kakihana, *Catal. Sci. Technol.*, **3**, 1733 (2013).

Distinctive Behavior of Photogenerated Electrons and Holes in Anatase and Rutile TiO₂ Powders

Akira Yamakata,^{*,†,‡} Junie Jhon M. Vequizo,[†] and Hironori Matsunaga[†][†]Graduate School of Engineering, Toyota Technological Institute, 2-12-1 Hisakata, Tempaku, Nagoya 468-8511, Japan[‡]Precursory Research for Embryonic Science and Technology (PRESTO), Japan Science and Technology Agency (JST), 4-1-8 Honcho Kawaguchi, Saitama 332-0012, Japan

S Supporting Information

ABSTRACT: TiO₂ powders have been widely used for photocatalysts; however, why anatase shows higher activity than rutile has been a long-standing question. Here, we have elucidated the difference in the behavior of photogenerated electrons and holes by time-resolved visible to mid-IR absorption spectroscopy. In anatase TiO₂, a considerable number of free electrons survive longer than 1 ms, but they are deeply trapped within a few picoseconds in the case of rutile TiO₂. The longer lifetime of free electrons is responsible for the higher activity for reduction processes on anatase TiO₂. However, deep electron trapping in rutile TiO₂ elongates lifetime of holes and promotes multihole processes such as water oxidation. However, the low reactivity of deeply trapped electrons fails to increase the overall activity. These peculiar behaviors of electrons and holes are induced by defects on the powder particles and less sensitive to the physical properties such as particle size and specific surface area.



1. INTRODUCTION

Photocatalysts have attracted considerable attention due to their potential application to the water-splitting reaction and degradation of pollutants using solar energy. TiO₂ is one of the most often used materials for photocatalysts because it is nontoxic and chemically stable during photocatalytic reactions.^{1–6} For TiO₂, anatase and rutile are the primary crystal structures, and their differences in photocatalytic activity have been well studied. In many photocatalytic reactions, anatase TiO₂ has a higher activity than rutile TiO₂. It is often proposed that this difference arises from the higher activity for the reduction of O₂, since O₂ anion radicals promote the oxidation of organic molecules.^{7–9} Anatase TiO₂ also has a higher activity than rutile TiO₂ for water reduction reactions. However, in water oxidation, rutile TiO₂ has a much higher activity than anatase TiO₂.^{7,10,11} Despite many reports discussing the differences in photocatalytic activity between anatase and rutile TiO₂, the principal reason for the difference in photocatalytic activity has not yet been fully elucidated. This fundamental information is indispensable, not only for the better understanding of the mechanism but also for the further development of highly efficient photocatalysts. The photocatalytic activity is determined by the energy states of the charge carriers as well as their behavior, so differences in the behavior of photogenerated electrons and holes should be investigated in detail.

Time-resolved absorption spectroscopy from the visible to mid-IR region is a powerful method of studying the behavior of photogenerated charge carriers. Especially in the visible to near-IR (NIR) region, holes and deeply trapped electrons give characteristic absorption peaks, so spectroscopy has been applied to investigate the behavior of deeply trapped electrons and holes in photocatalysts such as TiO₂,^{12–17} α -Fe₂O₃,^{18,19}

and LaTiO₂N.²⁰ On the other hand, free electrons excited into the conduction band (CB) and shallowly trapped electrons in the midgap states have structureless broad absorptions in the mid-IR region.²¹ These electrons are more reactive than deeply trapped electrons. Therefore, time-resolved measurements were performed to study the behavior of free and/or shallowly trapped electrons in TiO₂,^{21–26} NaTaO₃,²⁷ GaN,²⁸ LaTiO₂N,²⁹ and SrTiO₃.^{30–32} However, simultaneous measurements in the visible to mid-IR region (400 nm to 10 μ m) that covers energies from 0.1 to 3.1 eV provide more useful information regarding not only the decay kinetics but also the energy states of trapped charge carriers. By using this method, we have elucidated that the behavior of photogenerated charge carriers on single crystals and powder particles are totally different.^{31,32} Powders are richer in defects than single crystals,³³ and we found that most of charge carriers are trapped at the defects of the powder, but their lifetimes are much longer than that in defect-free single crystals. The defects are believed to accelerate the recombination but instead decelerate the recombination; i.e., defects on powder particles rather work positively to enhance the overall photocatalytic activity.

In the present work, we have elucidated the differences in the behavior of electrons and holes in polycrystalline anatase and rutile TiO₂ powders by time-resolved visible to mid-IR absorption spectroscopy. In the case of defect-free single crystalline TiO₂, several papers have been already reported that the recombination in anatase TiO₂ is slower than in rutile TiO₂.^{34–36} However, we found that the behaviors of charge

Received: September 22, 2015

Revised: October 7, 2015

Published: October 8, 2015

carriers in defect-rich powders are totally different from those in single crystals (Figure S1).³² Since photocatalysts are often used in powder form, the behaviors of charge carriers on the powder should be elucidated. We found that free electrons survive for longer than 1 ms in anatase TiO₂ powders, but they are deeply trapped within a few picosecond in the case of rutile TiO₂ powders. The deep electron trapping in rutile TiO₂ prevents recombination and elongates the lifetime of holes. These curious behaviors of charge carriers are less sensitive to the physical properties such as particle size and specific surface area and determine the distinctive photocatalytic activities of anatase and rutile TiO₂ powders. The detailed mechanism that determines the substantial difference in the photocatalytic activities of anatase and rutile TiO₂ powders will be discussed based on the behavior of charge carriers.

2. EXPERIMENTAL SECTION

Femtosecond time-resolved visible to mid-IR absorption measurements were performed using a pump–probe method based on a femtosecond Ti:sapphire laser system (Spectra-Physics, Solstice & TOPAS prime; duration 90 fs; repetition rate 1 kHz), as reported in our previous paper.²⁹ Briefly, a 350 nm pulse was utilized to excite the photocatalysts, and 22 000 cm⁻¹ (455 nm), 14 300 cm⁻¹ (700 nm), and 2000 cm⁻¹ (5 μm) pulses were used for the probe light. In the mid-IR region, the probe light transmitted from the sample was detected by an MCT array detector (Infrared Systems Development Corporation, 128 Ch, 6000–1000 cm⁻¹). On the other hand, in the visible to NIR region, the diffuse reflected probe light from the sample was detected by a photomultiplier (Hamamatsu Photonics, H5784-03, 25 000–143 00 cm⁻¹). The NIR detection was limited up to 14 300 cm⁻¹ by the sensitivity of the photomultiplier.

Microsecond time-resolved visible to mid-IR absorption measurements were performed by the custom-built spectrometers, as reported in our previous paper.²⁹ Briefly, in the mid-IR region (6000–1000 cm⁻¹), probe light emitted from an MoSi₂ coil was focused on the sample, and the transmitted light was introduced to a grating spectrometer. The monochromated light was detected by an MCT detector (Kolmar), and the output electric signal was amplified with an ac-coupled amplifier (Stanford Research Systems, SR560, 1 MHz). In the visible to NIR region (25 000–6000 cm⁻¹), a halogen lamp (50 W) and Si or InGaAs photodiodes were utilized for the probe light and detectors, and the experiments were performed in reflection mode. In each experiment, a 355 nm UV pulse from an Nd:YAG laser (Continuum, Surelite I; duration 6 ns; power 0.5 mJ; repetition rate 10–0.01 Hz) was used to excite the band gap of the photocatalysts. The time resolution of the spectrometers was limited to 1–2 μs by the bandwidth of the amplifier.

In the experiments, two anatase TiO₂ powders, TIO-1(A) (particle size: 21 nm; specific surface area: 73 m² g⁻¹) and TIO-10(A) (size: 15 nm; surface area: 100 m² g⁻¹), and two rutile TiO₂ powders, TIO-3(R) (size: 40 nm; surface area: 40 m² g⁻¹), and TIO-6(R) (size: 15 nm; surface area: 100 m² g⁻¹), supplied by the Catalysis Society of Japan were used without further treatment. Each TiO₂ powder was fixed on a circular CaF₂ plate with density of 3 mg cm⁻¹ and placed in the closed IR cell. The measurements were performed either in vacuum or in the presence of O₂²² or MeOH^{23,24} vapor at room temperature.

3. RESULTS AND DISCUSSION

3.1. Behavior of Photogenerated Charge Carriers in Polycrystalline Anatase TiO₂ Powders. Transient absorption spectra of anatase TIO-10(A) induced by 355 nm laser pulse irradiation are shown in Figure 1a. After band gap

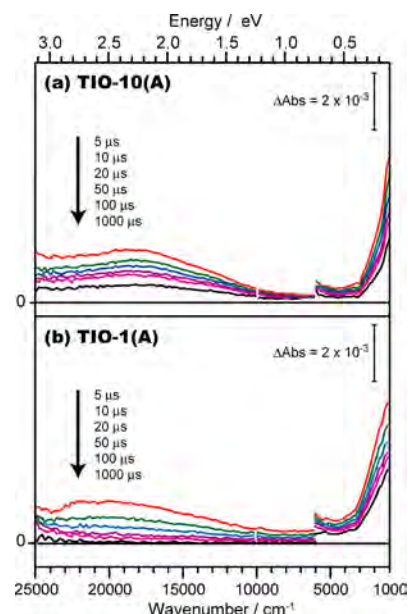


Figure 1. Transient absorption spectra of anatase TiO₂: (a) TIO-10(A) and (b) TIO-1(A) irradiated by UV laser pulses (355 nm, 6 ns duration, 0.5 mJ per pulse, and 5 Hz).

photoexcitation, a broad absorption was observed over the entire wavenumber region from 25 000 to 1000 cm⁻¹ (400 nm to 10 μm) that could be divided into two features: a broad absorption from 25 000 to 13 000 cm⁻¹ and another from 4000 to 1000 cm⁻¹ of which the intensity increased with decreasing wavenumber. The monotonic absorption below 4000 cm⁻¹ was assigned to the intraband transition of free electrons in CB or the direct transition of shallowly trapped electrons from the midgap states to the CB.²¹ The depth of the electron trap was estimated to be smaller than 0.1 eV, as strong absorption was observed even at the low wavenumber limit of 1000 cm⁻¹ (~0.1 eV).²¹ This value is small enough for the thermal equilibrium with the free electrons. Therefore, both contributions of free and shallowly trapped electrons are involved in the absorption intensity below 4000 cm⁻¹. On the other hand, the broad absorption spanning from 25 000 to 13 000 cm⁻¹ was ascribed to absorption by trapped electrons and/or holes.^{21–26} The detailed assignment of the absorption is possible by observing the decay curves in the presence of reactant molecules.

The decay processes of transient absorption in TIO-10(A) were further examined in the presence and absence of O₂ and CH₃OH vapor. As shown in Figure 2, changes in the intensity at 2000, 18 000, and 22 000 cm⁻¹ were measured. For the absorption at 2000 cm⁻¹, the decay was accelerated at 0–1 ms and decelerated after 1 μs by exposure to O₂ and CH₃OH vapor, respectively. Because these molecules capture electrons and holes, respectively, the results suggest that the absorption intensity at 2000 cm⁻¹ reflects the number of electrons.^{21,22,27,32} On the other hand, the absorption at 18 000 cm⁻¹ exhibited a different trend: the absorption intensity increased with exposure to CH₃OH, suggesting that the intensity at 18 000

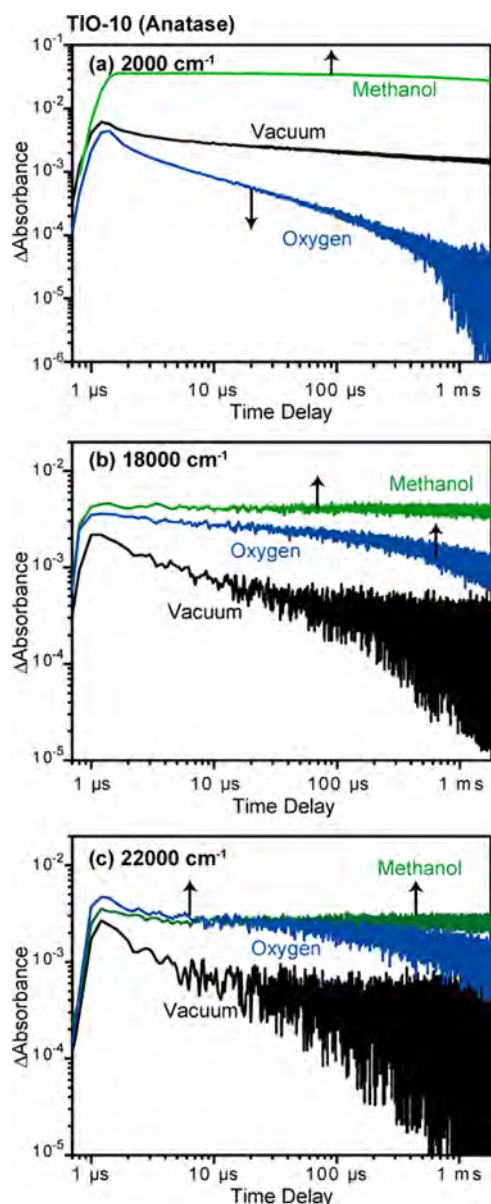


Figure 2. Decay curves of transient absorption by anatase TiO₂-10(A) irradiated by UV laser pulses (355 nm and 0.5 mJ per pulse) probed at 2000 (a), 18 000 (b), and 22 000 cm⁻¹ (c) in a vacuum, 20 Torr of O₂, and CH₃OH.

cm⁻¹ reflects the number of electrons. However, exposure to O₂ also increased the absorption intensity higher than that in a vacuum. This result suggests that the absorption at 18 000 cm⁻¹ also reflects the number of holes; i.e., the intensity at 18 000 cm⁻¹ reflects both electrons and holes. This assignment was justified by simple numerical simulations (see the Supporting Information Figure S3), and a similar behavior was observed for SrTiO₃ powders.³¹

For the decays at 22 000 cm⁻¹, the results were very similar to those at 18 000 cm⁻¹, and the intensity increased by exposure to either O₂ or CH₃OH (Figure 2c). These results confirm that the transient absorption at 22 000 cm⁻¹ reflects the number of both electrons and holes. It has been reported that trapped holes and electrons in anatase exhibit very broad absorption at 450–550 nm (22 000–18 000 cm⁻¹) and 650–770 nm (15 000–13 000 cm⁻¹), respectively.^{12–15} These absorption peaks are broad and overlapping, making it very

difficult to distinguish them. Our results are consistent with the reports that the absorptions at 22 000 and 18 000 cm⁻¹ arise from a mixture of trapped electrons and holes.

The same results were obtained on another anatase TiO₂ powder, TIO-1(A). The absorption intensity of TIO-1(A) at 18 000 cm⁻¹ was slightly smaller than that of TIO-10(A) (Figure 1b), but the spectral shape was essentially the same with that of TIO-10(A). The similar decay curves were also observed at 2000, 18 000, and 22 000 cm⁻¹ upon exposure to O₂ and CH₃OH (Figure S2). These results confirm that the energy states and the behaviors of charge carriers in TIO-10(A) and TIO-1 (A) are similar, indicating that they are less sensitive to the differences in physical properties such as particle size and specific surface area.

3.2. Behavior of Photogenerated Charge Carriers in Polycrystalline Rutile TiO₂ Powders. The behavior of photogenerated charge carriers in rutile TiO₂ powder was also examined by observing the transient absorption spectra after band gap excitation. As shown in Figure 3a, the spectral shape

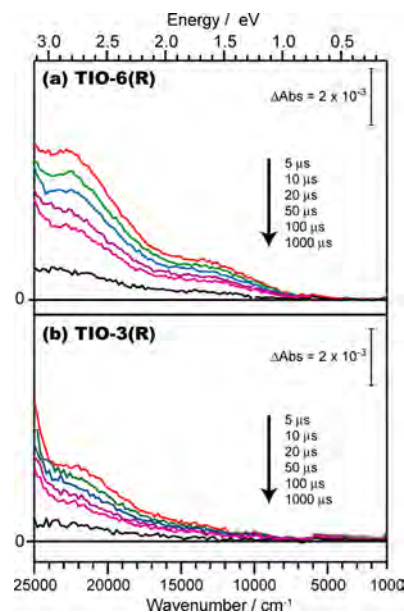


Figure 3. Transient absorption spectra of rutile TiO₂: (a) TIO-6(R) and (b) TIO-3(R) irradiated by UV laser pulses (355 nm, 6 ns duration, 0.5 mJ per pulse, and 5 Hz).

of TIO-6(R) was completely different from those observed for anatase TiO₂ powders (TIO-1(A) and TIO-10(A)), where the absorption intensity increased with increasing wavenumber from 1000 to 25 000 cm⁻¹. There were broad peaks at 22 000 cm⁻¹ (455 nm) and 13 000 cm⁻¹ (769 nm), but the absorption in the mid-IR region (<4000 cm⁻¹) was negligibly small compared to that of anatase TiO₂. These results confirm that the number of free or shallowly trapped electrons surviving in TIO-6(R) on the microsecond time scale was much smaller than that in anatase TiO₂.

The decay processes of photogenerated charge carriers in TIO-6(R) were further examined. As shown in Figure 4b, the intensity at 13 000 cm⁻¹ increased within 1 μs after exposure to CH₃OH. This result suggests that the absorption at 13 000 cm⁻¹ reflects the number of trapped electrons. However, exposure to O₂ gas did not change the intensity. This indicates that the trapped electrons, which cause the absorption at 13 000 cm⁻¹, are not reactive with O₂.

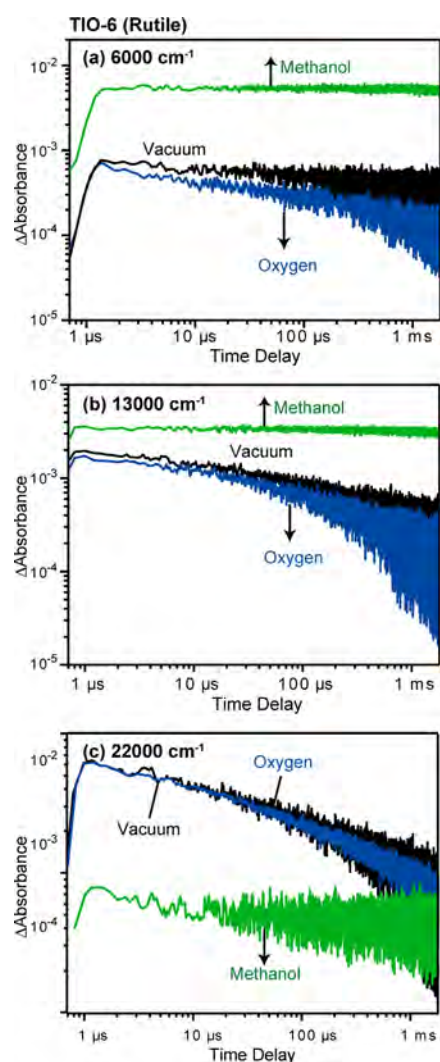


Figure 4. Decay curves of transient absorption by rutile TIO-6(R) irradiated by UV laser pulses (355 nm and 0.5 mJ per pulse) probed at 6000 (a), 13 000 (b), and 22 000 cm^{-1} (c) in a vacuum, 20 Torr of O_2 , and CH_3OH .

For the absorption intensity at 22 000 cm^{-1} (Figure 4c), the opposite behavior was observed: it decreased within 1 μs after exposure to CH_3OH . This suggests that this absorption intensity reflects the number of holes. However, the intensity did not change upon exposure to O_2 , which again confirms that the electrons generated in rutile TiO_2 are not consumed by O_2 .

We further examined the reactivity of photogenerated electrons by observing the intensity change at 6000 cm^{-1} (Figure 4a) because the intensity at 2000 cm^{-1} was negligible. We expected that the absorption at 6000 cm^{-1} would reflect the number of more shallowly trapped electrons than those responsible for the absorption at 13 000 cm^{-1} . However, the intensity was not so affected by exposure to O_2 again, although the intensity increased within 1 μs after exposure to CH_3OH . Therefore, it is concluded that trapped electrons that survive for microseconds have less reactivity with the exposed O_2 .

These results are consistent with those deduced from the shapes of the transient absorption spectra (Figure 3a), of which most of the electrons in the rutile were deeply trapped, so the reactivity was lower than that of free or shallowly trapped electrons generated in anatase TiO_2 . The depth of the electron traps in rutile TiO_2 can be deduced from the transient

absorption spectra observed at 18 000–7000 cm^{-1} . From the onset of absorption at 7000 cm^{-1} (~ 0.9 eV), the lower limit of the electron trap depth was estimated to be ~ 0.9 eV, suggesting that the electron traps in rutile TiO_2 are much deeper than those in anatase TiO_2 (< 0.1 eV). In addition, similar results were obtained in another rutile powder, TIO-3(R) (Figure 3b and Figure S2), regardless of the differences in physical properties such as particle size and specific surface area as in the case of anatase TiO_2 powders.

3.3. Differences in the Behavior of Photogenerated Electrons and Holes in Anatase and Rutile TiO_2 Powders from Femtoseconds to Milliseconds. The decay process of photogenerated charge carriers in anatase and rutile TiO_2 powders was further investigated by comparing the decay curves obtained in Figures 2 and 4 as well as Figure S2. The transient absorptions at 2000, 13 000, and 22 000 cm^{-1} for each sample are summarized in Figure 5. It is evident from Figure 5a that the lifetime of free electrons in anatase TiO_2 is longer than that in rutile TiO_2 , where the absorption intensity at 2000 cm^{-1} decreases in the order TIO-10(A) $>$ TIO-1(A) $>$ TIO-3(R) $>$ TIO-6(R). However, in the case of deeply trapped electrons at 13 000 cm^{-1} (Figure 5b), the order is opposite to that of free

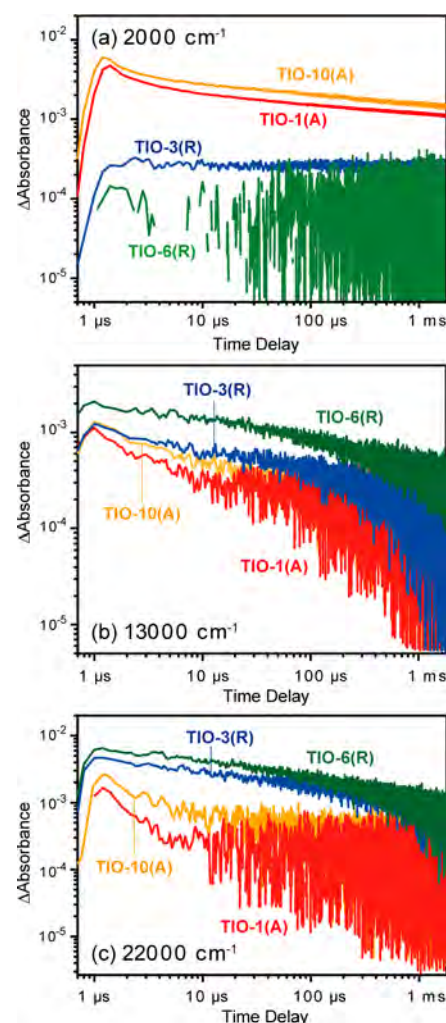


Figure 5. Decay curves of transient absorption by electrons and holes in TIO-1(A), TIO-10(A), TIO-3(R), and TIO-6(R), measured in a vacuum. The decay curves were probed at 2000 (a), 13 000 (b), and 22 000 cm^{-1} (c).

electrons, where the lifetime is longer in rutile than in anatase TiO_2 : TIO-6(R) > TIO-3(R) > TIO-10(A) > TIO-1(A). For trapped holes at $22\,000\text{ cm}^{-1}$, the order is also opposite to that of free electrons, and the lifetime is longer in rutile TiO_2 than in anatase TiO_2 . This is the same sequence as that of trapped electrons: TIO-6(R) > TIO-3(R) > TIO-10(A) > TIO-1(A) (Figure 5c). It is noted that the actual number of trapped electrons (holes) in anatase is much lower than that estimated from the absorption intensity at $13\,000\text{ cm}^{-1}$ ($22\,000\text{ cm}^{-1}$) because the holes (electrons) are involved in the absorption intensity at $13\,000\text{ cm}^{-1}$ ($22\,000\text{ cm}^{-1}$).

The initial decay process for free electrons in rutile TiO_2 was further examined using femtosecond time-resolved visible to mid-IR absorption spectroscopy. Figure 6 shows the intensity

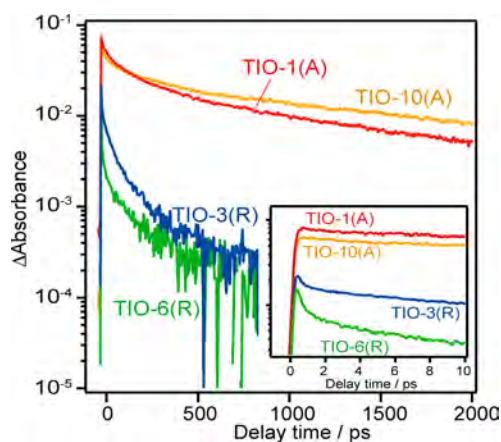


Figure 6. Decay curves of free electrons in polycrystalline anatase and rutile TiO_2 samples measured in vacuum at 2000 cm^{-1} .

changes at 2000 cm^{-1} for rutile TiO_2 (TIO-3(R) and TIO-6(R)) and anatase TiO_2 (TIO-1(A) and TIO-10(A)) excited by a 350 nm laser pulse. The number of free electrons in anatase TIO-1(A) and TIO-10(A) did not decrease very much from 0 to 10 ps but decreased rapidly in both rutile TIO-3(R) and TIO-6(R) from 0 to 2 ps. As a result, the number of free electrons surviving in TIO-1(A) and TIO-10(A) at 1000 ps is 100 times more than that in TIO-3(R) and TIO-6(R). In order to show the electron decay process more clearly, the normalized absorbance changes at $22\,000$, $14\,300$, and 2000 cm^{-1} are displayed in Figure 7. In TIO-1(A) and TIO-10(A), the rate of free-electron decay (2000 cm^{-1}) was comparable to that of trapped electrons ($14\,300\text{ cm}^{-1}$) and holes ($22\,000\text{ cm}^{-1}$). In TIO-3(R) and TIO-6(R), the decay rate of trapped electrons ($14\,300\text{ cm}^{-1}$) is slightly slower than that of holes ($22\,000\text{ cm}^{-1}$), but the rate of free-electron decay (2000 cm^{-1}) was significantly higher than that of trapped electrons and holes. These results confirm that the rapid decay of free electrons in rutile TiO_2 was not due to faster recombination but to rapid trapping at defects, because the decays of trapped electron and hole were much slower than that for the free electrons: the direct recombination of free electrons with holes cannot be a dominant process since the decay curve of free electrons is far from that of holes. When free electrons are deeply trapped at defects, the electron mobility decreases, thereby reducing the probability that the electrons will encounter with holes.^{37–40} As a result, the lifetimes of holes in rutile TiO_2 becomes longer than in anatase TiO_2 , in which more mobile free electrons are present.

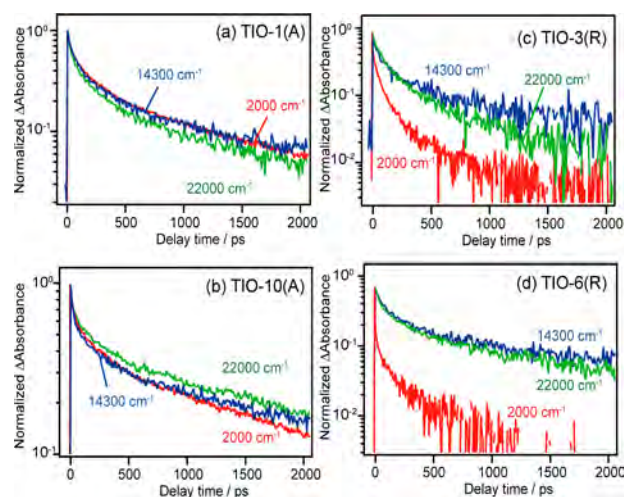


Figure 7. Normalized transient decays of electrons and holes in TIO-1(A), TIO-10(A), TIO-3(R), and TIO-6(R), measured in a vacuum and probed at 2000 , $14\,300$, and $22\,000\text{ cm}^{-1}$.

3.4. Trapping of Charge Carriers and Effects on the Steady-State Photocatalytic Activity.

The trapping of photogenerated charge carriers in TiO_2 particles has been studied by EPR,⁴¹ FT-IR,^{42–44} and photoluminescence (PL) spectroscopy.^{45–48} In the case of anatase TiO_2 powder, it has been reported that Ti^{3+} at an oxygen vacancy acts as a deep electron trap, but these electron traps are limited in number, so most of the electrons are not deeply trapped.⁴¹ Steady-state FT-IR measurements, which enable the detection of free electrons, support the EPR studies, indicating that free electrons have a longer lifetime and are the dominant carriers in anatase TiO_2 .^{42–44} PL measurements provide further information about the trapping of charge carriers.^{45–48} It is proposed that photogenerated electrons are deeply trapped in rutile than in anatase TiO_2 , since they show emission peak at 840 and $\sim 500\text{ nm}$, respectively.^{45,46} However, PL measurement alone cannot categorically determine whether the red-shift is due to the deep trapping of electrons or holes. As a result, an alternate conclusion was proposed^{47,48} where the NIR emission in rutile is not due to the deep trapping of electrons, but to deep trapping of holes although the peak was located at the same position (840 nm). Therefore, for the precise interpretation, other experimental supports are necessary.

Theoretical calculations provide a detailed picture of the defects on anatase and rutile TiO_2 .^{49–54} It is reported that excess electrons are trapped at the defects such as oxygen vacancy and Ti interstitials as Ti^{3+} with structural relaxation (polaron formation). The atomic displacement of the lattice via electron trapping is larger on rutile than on anatase, and hence the stabilization energy of the electron trapping in rutile defects is much larger than that of anatase. The detailed value depends on the calculation method, but the depths of the electron trap in anatase TiO_2 tend to be much shallower than in rutile TiO_2 .^{49–54} For example, they are estimated to be 0.8 – 1 and 0 – 0.2 eV for rutile and anatase, respectively.⁵² As a result, electrons in rutile are heavily localized with hopping transport, but those in anatase are delocalized with conduction-band-like electron transport.⁵⁴ These reports support our experimental results where photogenerated electrons are deeply trapped in rutile defects and elongate the lifetime of holes.

The difference in photocatalytic activity between anatase and rutile TiO_2 powders can be reasonably explained by the results

obtained in this work. The higher photocatalytic activity for the reduction of anatase is often proposed to be responsibly due to the higher position of the CB in anatase TiO₂ than in rutile TiO₂. However, our experimental results clearly demonstrate that the difference in the depth of the electron trap is mainly responsible. In the case of anatase TiO₂, the electron traps are shallower than 0.1 eV, so these electrons are in equilibrium with free electrons. Furthermore, their lifetime is longer than 1 ms. Therefore, the electrons in anatase TiO₂ are highly reactive. However, in rutile TiO₂, the electron traps are much deeper (~0.9 eV), and most of the free electrons are quickly trapped at these defects within a few picoseconds. As a result, only a trace amount of free or shallowly trapped electrons survive in microsecond time scales. These results confirm that the difference in the reduction activities of anatase and rutile TiO₂ is caused by the longer lifetime of free electrons in anatase TiO₂ than that in rutile TiO₂.

In the case of photocatalytic oxidation, a clear difference was observed in the lifetime of holes, where it was much longer in rutile TiO₂ than in anatase TiO₂. The lifetime of holes is important for the higher activity, especially for multihole processes such as water oxidation; hence, rutile TiO₂ has a higher activity than anatase TiO₂. Under steady-state condition, photogenerated electrons are accumulated in the particles by filling the midgap states from deeper to shallower. These accumulated electrons in the shallow traps are reactive for water reduction, and hence rutile TiO₂ can split water in the absence of sacrificial reagents.¹¹ However, when the electrons are accumulated in the particles, the recombination with holes is accelerated.⁵⁵ As a result, the overall photocatalytic activity is not increased for many photocatalytic reactions. In the case of anatase TiO₂, photogenerated electrons are reasonably reactive even in the absence of electron accumulation; therefore, anatase TiO₂ exhibits higher activity in many photocatalytic reactions.

4. CONCLUSION

In this work, we have clearly elucidated the principal mechanism that determines the difference in photocatalytic activities of anatase and rutile TiO₂ powders. The biggest difference is the depth of the electron traps at powder defects, which were estimated to be <0.1 and >0.9 eV, respectively. In anatase TiO₂ particles, free and shallowly trapped electrons are in equilibrium and have a lifetime longer than 1 ms. These electrons are highly reactive, so anatase TiO₂ has a higher activity for photocatalytic reduction. On the contrary, free electrons in rutile TiO₂ are deeply trapped within a few picoseconds, and only a trace amount of free electrons survives for 1 ms. The deeply trapped electrons are less reactive, so rutile TiO₂ has a lower activity for reduction. However, this deep electron trapping acts to prevent recombination, extending the lifetimes of holes. The longer lifetime of holes promotes photocatalytic oxidation, especially for multihole processes such as water oxidation. Accumulation of electrons in rutile TiO₂ particles enables the water reduction, but it accelerates the recombination. As a result, the overall photocatalytic activity is not increased for many photocatalytic reactions. In anatase TiO₂, electrons and holes are both reactive, so anatase TiO₂ exhibits a higher photocatalytic activity than rutile TiO₂ in many photocatalytic reactions. These peculiar behaviors of charge carriers are induced by defects on the powder particles and less sensitive to the physical properties such as particle size and specific surface area. These insights offer lucid understanding of the catalytic mechanisms

in anatase and rutile TiO₂ and can further be useful for the development of highly active photocatalysts based on TiO₂ materials.

■ ASSOCIATED CONTENT

Supporting Information

The Supporting Information is available free of charge on the ACS Publications website at DOI: 10.1021/acs.jpcc.5b09236.

Recombination kinetics in single-crystalline TiO₂, decay curves for anatase TIO-1(A) and rutile TIO-3(R) powders, numerical simulations, and decay curves in the picoseconds region (PDF)

■ AUTHOR INFORMATION

Corresponding Author

*E-mail: yamakata@toyota-ti.ac.jp (A.Y.).

Notes

The authors declare no competing financial interest.

■ ACKNOWLEDGMENTS

This work was supported by the PRESTO/JST program "Chemical Conversion of Light Energy". The authors acknowledge Grants-in-Aid for Specially Promoted Research (No. 23000009) and Basic Research (B) (No. 23360360) from the Ministry of Education, Culture, Sports, Science, and Technology (MEXT) of Japan. The authors also thank the Nippon Sheet Glass Foundation and the Nagai Foundation for Science and Technology.

■ REFERENCES

- (1) Fujishima, A.; Honda, K. Electrochemical Photolysis of Water at a Semiconductor Electrode. *Nature* **1972**, *238*, 37–38.
- (2) Kamat, P. V. Photochemistry on Nonreactive and Reactive (Semiconductor) Surfaces. *Chem. Rev.* **1993**, *93*, 267–300.
- (3) Linsebigler, A. L.; Lu, G. Q.; Yates, J. T. Photocatalysis on TiO₂ Surfaces - Principles, Mechanisms, and Selected Results. *Chem. Rev.* **1995**, *95*, 735–758.
- (4) Hagfeldt, A.; Gratzel, M. Light-induced Redox Reactions in Nanocrystalline Systems. *Chem. Rev.* **1995**, *95*, 49–68.
- (5) Hoffmann, M. R.; Martin, S. T.; Choi, W. Y.; Bahnemann, D. W. Environmental Application of Semiconductor Photocatalysis. *Chem. Rev.* **1995**, *95*, 69–96.
- (6) Ma, Y.; Wang, X.; Jia, Y.; Chen, X.; Han, H.; Li, C. Titanium Dioxide-Based Nanomaterials for Photocatalytic Fuel Generations. *Chem. Rev.* **2014**, *114*, 9987–10043.
- (7) Ohno, T.; Haga, D.; Fujihara, K.; Kaizaki, K.; Matsumura, M. Unique Effects of Iron(III) Ions on Photocatalytic and Photoelectrochemical Properties of Titanium Dioxide. *J. Phys. Chem. B* **1997**, *101*, 6415–6419.
- (8) Ohno, T.; Sarukawa, K.; Matsumura, M. Photocatalytic Activities of Pure Rutile Particles Isolated from TiO₂ Powder by Dissolving the Anatase Component in HF Solution. *J. Phys. Chem. B* **2001**, *105*, 2417–2420.
- (9) Jia, J. G.; Ohno, T.; Matsumura, M. Efficient Dihydroxylation of Naphthalene on Photoirradiated Rutile TiO₂ Powder in Solution Containing Hydrogen Peroxide. *Chem. Lett.* **2000**, 908–909.
- (10) Abe, R.; Sayama, K.; Domen, K.; Arakawa, H. A New Type of Water Splitting System Composed of Two Different TiO₂ Photocatalysts (Anatase, Rutile) and a IO³⁻/I⁻ Shuttle Redox Mediator. *Chem. Phys. Lett.* **2001**, *344*, 339–344.
- (11) Maeda, K. Direct Splitting of Pure Water into Hydrogen and Oxygen Using Rutile Titania Powder as a Photocatalyst. *Chem. Commun.* **2013**, *49*, 8404–8406.
- (12) Bahnemann, D.; Henglein, A.; Lilie, J.; Spanhel, L. Flash-Photolysis Observation of the Absorption-Spectra of Trapped Positive

Holes and Electrons in Colloidal TiO₂. *J. Phys. Chem.* **1984**, *88*, 709–711.

(13) Bahnemann, D. W.; Hilgendorff, M.; Memming, R. Charge Carrier Dynamics at TiO₂ Particles: Reactivity of Free and Trapped Holes. *J. Phys. Chem. B* **1997**, *101*, 4265–4275.

(14) Yoshihara, T.; Katoh, R.; Furube, A.; Tamaki, Y.; Murai, M.; Hara, K.; Murata, S.; Arakawa, H.; Tachiya, M. Identification of Reactive Species in Photoexcited Nanocrystalline TiO₂ Films by Wide-wavelength-Range (400–2500 nm) Transient Absorption Spectroscopy. *J. Phys. Chem. B* **2004**, *108*, 3817–3823.

(15) Tamaki, Y.; Furube, A.; Murai, M.; Hara, K.; Katoh, R.; Tachiya, M. Direct Observation of Reactive Trapped Holes in TiO₂ Undergoing Photocatalytic Oxidation of Adsorbed Alcohols: Evaluation of the Reaction Rates and Yields. *J. Am. Chem. Soc.* **2006**, *128*, 416–417.

(16) Meekins, B. H.; Kamat, P. V. Role of Water Oxidation Catalyst IrO₂ in Shuttling Photogenerated Holes Across TiO₂ Interface. *J. Phys. Chem. Lett.* **2011**, *2*, 2304–2310.

(17) Wang, X. L.; Kafizas, A.; Li, X. O.; Moniz, S. J. A.; Reardon, P. J. T.; Tang, J. W.; Parkin, I. P.; Durrant, J. R. Transient Absorption Spectroscopy of Anatase and Rutile: The Impact of Morphology and Phase on Photocatalytic Activity. *J. Phys. Chem. C* **2015**, *119*, 10439–10447.

(18) Barroso, M.; Cowan, A. J.; Pendlebury, S. R.; Gratzel, M.; Klug, D. R.; Durrant, J. R. The Role of Cobalt Phosphate in Enhancing the Photocatalytic Activity of alpha-Fe₂O₃ toward Water Oxidation. *J. Am. Chem. Soc.* **2011**, *133*, 14868–14871.

(19) Barroso, M.; Mesa, C. A.; Pendlebury, S. R.; Cowan, A. J.; Hisatomi, T.; Sivula, K.; Gratzel, M.; Klug, D. R.; Durrant, J. R. Dynamics of Photogenerated Holes in Surface Modified Alpha-Fe₂O₃ Photoanodes for Solar Water Splitting. *Proc. Natl. Acad. Sci. U. S. A.* **2012**, *109*, 15640–15645.

(20) Singh, R. B.; Matsuzaki, H.; Suzuki, Y.; Seki, K.; Minegishi, T.; Hisatomi, T.; Domen, K.; Furube, A. Trapped State Sensitive Kinetics in LaTiO₂N Solid Photocatalyst with and without Cocatalyst Loading. *J. Am. Chem. Soc.* **2014**, *136*, 17324–17331.

(21) Yamakata, A.; Ishibashi, T.; Onishi, H. Time-Resolved Infrared Absorption Spectroscopy of Photogenerated Electrons in Platinized TiO₂ Particles. *Chem. Phys. Lett.* **2001**, *333*, 271–277.

(22) Yamakata, A.; Ishibashi, T.; Onishi, H. Water- and Oxygen-Induced Decay Kinetics of Photogenerated Electrons in TiO₂ and Pt/TiO₂: A Time-Resolved Infrared Absorption Study. *J. Phys. Chem. B* **2001**, *105*, 7258–7262.

(23) Yamakata, A.; Ishibashi, T.; Onishi, H. Electron- and Hole-Capture Reactions on Pt/TiO₂ Photocatalyst Exposed to Methanol Vapor Studied with Time-Resolved Infrared Absorption Spectroscopy. *J. Phys. Chem. B* **2002**, *106*, 9122–9125.

(24) Yamakata, A.; Ishibashi, T.; Onishi, H. Effects of Water Addition on the Methanol Oxidation on Pt/TiO₂ Photocatalyst Studied by Time-Resolved Infrared Absorption Spectroscopy. *J. Phys. Chem. B* **2003**, *107*, 9820–9823.

(25) Heimer, T. A.; Heilweil, E. J. Direct Time-Resolved Infrared Measurement of Electron Injection in Dye-Sensitized Titanium Dioxide Films. *J. Phys. Chem. B* **1997**, *101*, 10990–10993.

(26) Yamakata, A.; Ishibashi, T.; Onishi, H. Microsecond Kinetics of Photocatalytic Oxidation on Pt/TiO₂ Traced by Vibrational Spectroscopy. *Chem. Phys. Lett.* **2003**, *376*, 576–580.

(27) Yamakata, A.; Ishibashi, T.; Kato, H.; Kudo, A.; Onishi, H. Photodynamics of NaTaO₃ Catalysts for Efficient Water Splitting. *J. Phys. Chem. B* **2003**, *107*, 14383–14387.

(28) Yamakata, A.; Yoshida, M.; Kubota, J.; Osawa, M.; Domen, K. Potential-Dependent Recombination Kinetics of Photogenerated Electrons in n- and p-Type GaN Photoelectrodes Studied by Time-Resolved IR Absorption Spectroscopy. *J. Am. Chem. Soc.* **2011**, *133*, 11351–11357.

(29) Yamakata, A.; Kawaguchi, M.; Nishimura, N.; Minegishi, T.; Kubota, J.; Domen, K. Behavior and Energy States of Photogenerated Charge Carriers on Pt- or CoO_x-loaded LaTiO₂N Photocatalysts:

Time-resolved Visible to mid-IR Absorption Study. *J. Phys. Chem. C* **2014**, *118*, 23897.

(30) Furuhashi, K.; Jia, Q.; Kudo, A.; Onishi, H. Time-Resolved Infrared Absorption Study of SrTiO₃ Photocatalysts Codoped with Rhodium and Antimony. *J. Phys. Chem. C* **2013**, *117*, 19101.

(31) Yamakata, A.; Yeilin, H.; Kawaguchi, M.; Hisatomi, T.; Kubota, J.; Sakata, Y.; Domen, K. Morphology-sensitive Trapping States of Photogenerated Charge Carriers on SrTiO₃ Particles Studied by Time-resolved Visible to Mid-IR Absorption Spectroscopy: the Effects of Molten Salt Flux Treatments. *J. Photochem. Photobiol., A* **2015**, DOI: 10.1016/j.jphotochem.2015.05.016.

(32) Yamakata, A.; Vequizo, J. J. M.; Kawaguchi, M. Behavior and Energy State of Photogenerated Charge Carriers in Single-Crystalline and Polycrystalline Powder SrTiO₃ Studied by Time-Resolved Absorption Spectroscopy in the Visible to Mid-Infrared Region. *J. Phys. Chem. C* **2015**, *119*, 1880–1885.

(33) Jupille, J.; Thornton, G. *Defects at Oxide Surfaces*; Springer: Switzerland, 2015.

(34) Xu, M. C.; Gao, Y. K.; Moreno, E. M.; Kunst, M.; Muhler, M.; Wang, Y. M.; Idriss, H.; Woll, C. Photocatalytic Activity of Bulk TiO₂ Anatase and Rutile Single Crystals Using Infrared Absorption Spectroscopy. *Phys. Rev. Lett.* **2011**, *106*, 138302.

(35) Luttrell, T.; Halpegamage, S.; Tao, J.; Kramer, A.; Sutter, E.; Batzill, M. Why is Anatase a Better Photocatalyst than Rutile?—Model Studies on Epitaxial TiO₂ Films. *Sci. Rep.* **2014**, *4*, 4043.

(36) Ozawa, K.; Emori, M.; Yamamoto, S.; Yukawa, R.; Yamamoto, S.; Hobara, R.; Fujikawa, K.; Sakama, H.; Matsuda, I. Electron-Hole Recombination Time at TiO₂ Single-Crystal Surfaces: Influence of Surface Band Bending. *J. Phys. Chem. Lett.* **2014**, *5*, 1953–1957.

(37) Nelson, J. Continuous-Time Random-Walk Model of Electron Transport in Nanocrystalline TiO₂ Electrodes. *Phys. Rev. B: Condens. Matter Mater. Phys.* **1999**, *59*, 15374–15380.

(38) Nelson, J.; Haque, S. A.; Klug, D. R.; Durrant, J. R. Trap-Limited Recombination in Dye-Sensitized Nanocrystalline Metal Oxide Electrodes. *Phys. Rev. B: Condens. Matter Mater. Phys.* **2001**, *63*, 205321.

(39) Barzykin, A. V.; Tachiya, M. Mechanism of Charge Recombination in Dye-Sensitized Nanocrystalline Semiconductors: Random Flight Model. *J. Phys. Chem. B* **2002**, *106*, 4356–4363.

(40) Tachiya, M.; Seki, K. Theory of Bulk Electron-Hole Recombination in a Medium with Energetic Disorder. *Phys. Rev. B: Condens. Matter Mater. Phys.* **2010**, *82*, 085201.

(41) Berger, T.; Sterrer, M.; Diwald, O.; Knozinger, E.; Panayotov, D.; Thompson, T. L.; Yates, J. T. Light-Induced Charge Separation in Anatase TiO₂ Particles. *J. Phys. Chem. B* **2005**, *109*, 6061–6068.

(42) Szczepankiewicz, S. H.; Moss, J. A.; Hoffmann, M. R. Slow Surface Charge Trapping Kinetics on Irradiated TiO₂. *J. Phys. Chem. B* **2002**, *106*, 2922–2927.

(43) Connor, P. A.; Dobson, K. D.; McQuillan, A. J. Infrared Spectroscopy of the TiO₂/Aqueous Solution Interface. *Langmuir* **1999**, *15*, 2402–2408.

(44) Sezen, H.; Buchholz, M.; Nefedov, A.; Natzeck, C.; Heissler, S.; Di Valentin, C.; Woll, C. Probing Electrons in TiO₂ Polaronic Trap States by IR-Absorption: Evidence for the Existence of Hydrogenic States. *Sci. Rep.* **2014**, *4*, 3808.

(45) Shi, J.; Chen, J.; Feng, Z.; Chen, T.; Lian, Y.; Wang, X.; Li, C. Photoluminescence Characteristics of TiO₂ and Their Relationship to the Photoassisted Reaction of Water/Methanol Mixture. *J. Phys. Chem. C* **2007**, *111*, 693–699.

(46) Wang, X.; Feng, Z.; Shi, J.; Jia, G.; Shen, S.; Zhou, J.; Li, C. Trap States and Carrier Dynamics of TiO₂ Studied by Photoluminescence Spectroscopy under Weak Excitation Condition. *Phys. Chem. Chem. Phys.* **2010**, *12*, 7083–7090.

(47) Knorr, F. J.; Mercado, C. C.; McHale, J. L. Trap-State Distributions and Carrier Transport in Pure and Mixed-Phase TiO₂: Influence of Contacting Solvent and Interphasial Electron Transfer. *J. Phys. Chem. C* **2008**, *112*, 12786–12794.

(48) Knorr, F. J.; Zhang, D.; McHale, J. L. Influence of TiCl_4 Treatment on Surface Defect Photoluminescence in Pure and Mixed-phase Nanocrystalline TiO_2 . *Langmuir* **2007**, *23*, 8686–8690.

(49) Na-Phattalung, S.; Smith, M. F.; Kim, K.; Du, M. H.; Wei, S. H.; Zhang, S. B.; Limpijumnong, S. First-Principles Study of Native Defects in Anatase TiO_2 . *Phys. Rev. B: Condens. Matter Mater. Phys.* **2006**, *73*, 125205.

(50) Finazzi, E.; Di Valentin, C.; Pacchioni, G. Nature of Ti Interstitials in Reduced Bulk Anatase and Rutile TiO_2 . *J. Phys. Chem. C* **2009**, *113*, 3382–3385.

(51) Di Valentin, C.; Pacchioni, G.; Selloni, A. Reduced and n-Type Doped TiO_2 : Nature of Ti^{3+} Species. *J. Phys. Chem. C* **2009**, *113*, 20543–20552.

(52) Mattioli, G.; Filippone, F.; Alippi, P.; Bonapasta, A. A. Ab Initio Study of the Electronic States Induced by Oxygen Vacancies in Rutile and Anatase TiO_2 . *Phys. Rev. B: Condens. Matter Mater. Phys.* **2008**, *78*, 241201.

(53) Mattioli, G.; Alippi, P.; Filippone, F.; Caminiti, R.; Bonapasta, A. A. Deep versus Shallow Behavior of Intrinsic Defects in Rutile and Anatase TiO_2 Polymorphs. *J. Phys. Chem. C* **2010**, *114*, 21694–21704.

(54) Spreafico, C.; VandeVondele, J. The Nature of Excess Electrons in Anatase and Rutile from Hybrid DFT and RPA. *Phys. Chem. Chem. Phys.* **2014**, *16*, 26144–26152.

(55) Yamakata, A.; Ishibashi, T.; Onishi, H. Effects of Accumulated Electrons on the Decay Kinetics of Photogenerated Electrons in Pt/ TiO_2 Photocatalyst Studied by Time-Resolved Infrared Absorption Spectroscopy. *J. Photochem. Photobiol., A* **2003**, *160*, 33–36.

Trapping-Induced Enhancement of Photocatalytic Activity on Brookite TiO₂ Powders: Comparison with Anatase and Rutile TiO₂ Powders

Junie Jhon M. Vequizo,[†] Hironori Matsunaga,[†] Tatsuya Ishiku,[‡] Sunao Kamimura,[‡] Teruhisa Ohno,^{*,‡} and Akira Yamakata^{*,†,§}

[†]Graduate School of Engineering, Toyota Technological Institute, 2-12-1 Hisakata, Tempaku, Nagoya 468-8511, Japan

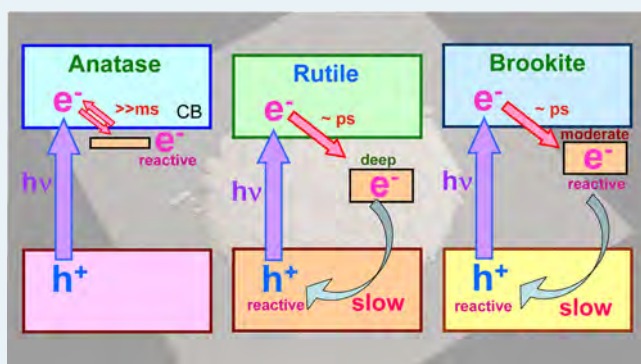
[‡]Department of Materials Science, Faculty of Engineering, Kyushu Institute of Technology, 1-1 Sensui-cho, Tobata-ku, Kitakyushu, Fukuoka, 804-8550, Japan

[§]Precursory Research for Embryonic Science and Technology (PRESTO), Japan Science and Technology Agency (JST), 4-1-8 Honcho Kawaguchi, Saitama 332-0012, Japan

Supporting Information

ABSTRACT: Brookite TiO₂ is a promising material for active photocatalysts. However, the principal mechanism that determines the distinctive photocatalytic activity between anatase, rutile, and brookite TiO₂ has not yet been fully elucidated. Therefore, in this work, we studied the behavior of photogenerated electrons and holes in these TiO₂ powders by using femtosecond to millisecond time-resolved visible to mid-IR absorption spectroscopy. We found that most of the photogenerated electrons in brookite TiO₂ are trapped at powder defects within a few ps. This electron trapping decreases the number of surviving free electrons, but it extends the lifetime of holes as well as the trapped electrons because the probability of electrons to encounter holes is decreased by this electron-trapping. As a result, the number of surviving holes increases, which is beneficial for photocatalytic oxidation. In contrast, the reactivity of electrons is decreased to some extent by trapping, but they still remain active for photocatalytic reductions. Electron trapping also takes place on anatase and rutile TiO₂ powders, but the trap-depth in anatase is too shallow to extend the lifetime of holes and that of rutile is too deep than the thermal energy (kT) at room temperature for the electron-consuming reactions. As a result of the moderate depth of the electron trap in brookite, both electrons and holes are reactive for photocatalytic reductions and oxidations. These results have clearly demonstrated that the presence of an appropriate depth of the electron trap can effectively contribute to enhance the overall photocatalytic activity.

KEYWORDS: TiO₂ photocatalysts, photogenerated charge carriers, surface-defects, charge trapping, recombination, time-resolved absorption spectroscopy



1. INTRODUCTION

Photocatalysts have attracted higher interest due to their potential applications for water-splitting reaction and degradation of pollutants by using solar energy. TiO₂ is one of the most widely used materials for photocatalysis, primarily because of its abundance and high chemical stability.^{1–5} There are three polymorphs in the crystal structure of TiO₂: anatase, rutile, and brookite. The photocatalytic activity of anatase and rutile TiO₂ has been well-studied; however, there have been relatively fewer studies on brookite TiO₂ because the synthesis of pure brookite powder is technically difficult. However, the recent development of an improved synthesis method has prompted more studies of brookite TiO₂, which is now attracting considerable attention for application not only to photocatalysts^{6–15} but also to perovskite solar cells.¹⁶ Brookite TiO₂ demonstrates superior

performance for several photocatalytic reactions than anatase and rutile TiO₂.^{6–15} Despite these promising reports on brookite TiO₂, the principal difference in the behavior of photogenerated electrons and holes in these polymorphs is not fully elucidated yet. Photocatalytic activity is determined by the behavior of photogenerated electrons and holes, and hence, the photodynamical processes on brookite TiO₂ powders have been examined by Cargnello et al.;¹⁷ however, the details have not yet been fully elucidated. For the further application of TiO₂ as a light-energy conversion material, the differences in

Received: January 13, 2017

Revised: March 3, 2017

Published: March 6, 2017

the photodynamical processes among anatase, rutile, and brookite should be elucidated.

Time-resolved absorption spectroscopy is useful to study the behavior of photogenerated charge carriers on photocatalysts. Because free electrons in the conduction band and shallowly trapped electrons in midgap states give structureless broad absorption in mid-IR region,^{18,19} time-resolved mid-IR absorption spectroscopy is used to investigate the behaviors of free and shallowly trapped electrons in TiO₂,^{20–22} NaTaO₃,^{23,24} SrTiO₃,²⁵ and GaN,²⁶ etc. On the other hand, deeply trapped electrons and holes give absorption in visible to near-IR region, the time-resolved visible to NIR spectroscopy have been used to investigate the behaviors of holes and deeply trapped electrons in TiO₂,²⁷ Fe₂O₃,²⁸ LaTiO₂N,²⁹ and so on. However, when the absorption measurements from visible to mid-IR region are combined, it becomes more powerful: we can envisage full behaviors of photogenerated charge carriers. It enables not only the individual observation of free and deeply trapped electrons and holes but also information about the depth of the electron traps. Reactivity of electrons depends on the depth of the trap; therefore, the information on the energy states of charge carriers is important to discuss the reactivities of charge carriers. Recently, we have developed new spectrometers to measure the transient absorption spectra from visible to mid-IR region with femtosecond to millisecond time resolution,³⁰ and we demonstrated the feasibility to elucidate the behaviors of electrons and holes in LaTiO₂N,³⁰ SrTiO₃,^{31,32} and TiO₂³³ photocatalysts.

By using time-resolved absorption spectroscopies, the difference in the behaviors of photogenerated charge carriers on anatase and rutile TiO₂ has been well-studied.^{19,21,27,33–37} In the case of single-crystalline TiO₂, it is reported that anatase TiO₂ shows higher activity than rutile TiO₂³⁸ and that the electron–hole pair recombination is faster in rutile than in anatase.^{39,40} However, recently we found that the results are not always the same in the case of powder.³³ Certainly, the lifetime of electrons and holes in the picosecond region is longer in anatase than in rutile, but the amount of long-lived species in the microsecond to millisecond region is much larger in rutile than in anatase.³³ Consistent results have been reported for holes in anatase and rutile TiO₂ films, and the results revealed that regardless of the difference in the morphologies, the lifetime of holes is longer in rutile TiO₂ than in anatase TiO₂, indicating a strong dependence on the phase.^{41,42} We elucidated that these curious behaviors in powder TiO₂ come from the difference in the depth of electron trap between anatase and rutile; they are estimated to be <0.1 eV and >0.9 eV, respectively.³³ The depth of the electron trap depends on how the defects stabilize the trapped electrons through polaron formation.^{43–45} Theoretical calculations predicted stabilization energies of 0.8–1 eV and 0–0.2 eV for rutile and anatase, respectively.^{43–45} Electron-trapping at the defects somehow reduces the reactivity of electrons, but it also positively works in elongating the lifetime of holes. The extent of reactivity reduction depends on the electron trap-depth. Electrons in shallower traps can still participate in the reduction reaction such as oxygen reduction, but those in deeper traps hardly facilitate reduction.^{30–32} However, of equal importance is the increase of the number of long-lived holes, which is beneficial for photocatalytic oxidations, especially for multihole processes such as water oxidation. The activity in the steady-state reaction is determined by the competition between the positive and negative effects of electron trapping, and therefore,

an appropriate electron trap depth is strictly important to obtain maximum activity.

In this work, the behavior of photogenerated electrons and holes in brookite TiO₂ powders was investigated by using time-resolved visible to mid-IR absorption spectroscopy. We found that most of the free electrons are trapped at the powder defects within a few picoseconds after the band gap photoexcitation. The results are very similar to those of rutile; however, the depth of the electrons trap is shallower than that of rutile but deeper than that of anatase TiO₂ powders. This moderate depth of the electron trap induces several characteristic behaviors of photogenerated electrons and holes compared to those of anatase and rutile TiO₂ powders. The distinctive photocatalytic activity of brookite TiO₂ powders is discussed on the basis of the behaviors of photogenerated electrons and holes.

2. EXPERIMENTAL SECTION

In the experiments, two different brookite TiO₂ powders, as-synthesized fine crystals (specific surface area: 45 m²/g)¹⁵ and a commercial powder (Kojundo Chemicals, Ltd., specific surface area: 22.7 m²/g) were investigated. As-synthesized brookite TiO₂ was prepared by hydrothermal synthesis method as reported previously by one of our coauthors (Ohno et al.).¹⁵ Briefly, 12.5 mmol of amorphous titanium hydroxide particles dispersed in 40 mL of H₂O₂ (30%) were used as starting precursors, and then 10 mL of ammonia and glycolic acid were added. The mixture solution was stirred for 6 h at constant temperature of 60 °C, after which an orange-colored gel compound was obtained. The gel was then dispersed in deionized water, and the pH was adjusted to 10 by adding ammonia. The volume of the solution was adjusted using deionized water until it reached 50 mL, and this final mixture solution was subjected to hydrothermal treatment at 200 °C for 48 h. After the treatment, the residue was washed with deionized water and dried under reduced pressure at 60 °C for 12 h. On the other hand, “commercial” brookite TiO₂ powders purchased from Kojundo Chemical Ltd. was used as-received. Anatase (TIO-1) and rutile (TIO-3) TiO₂ powders supplied by the Catalysis Society of Japan were also used for the comparison. These TiO₂ powders were fixed separately on CaF₂ plate with a density of 3 mg cm⁻¹, and then were placed in a tightly closed sample cell. The TiO₂ powders were fixed on the CaF₂ by dropping and drying the TiO₂ aqueous suspension.

The microsecond time-resolved visible to mid-IR absorption measurements were performed by using the laboratory-built spectrometers as described in our previous papers.^{19,30} Briefly, in the mid-IR region (6000–1000 cm⁻¹), the measurement was carried out in transmission mode, wherein the probe light emitted from a MoSi₂ coil was focused on the sample, and then the transmitted light was introduced to the grating spectrometer. The monochromated light was then detected by an MCT detector (Kolmar), and the output electric signal was amplified with AC-coupled amplifier (Stanford Research Systems, SR560, 1 MHz). In the visible to NIR region (25 000–6000 cm⁻¹), the experiments were performed in the reflection mode, wherein the probe light that comes from the halogen lamp (50 W) was focused on the sample and detected using Si or InGaAs photodiodes. In each experiment, the pump UV (355 nm) laser pulses that originated from a Nd:YAG laser (Continuum, Surelite I, duration: 6 ns, power: 0.5 mJ, repetition rate: 10–0.01 Hz) were utilized to excite the TiO₂ samples. The time resolution of the spectrometers was limited

to 1–2 μs by the bandwidth of the amplifier. To determine the decay processes and reactivity of photogenerated charge carriers, the measurements were performed in vacuum, or in the presence of 20 Torr O_2 gas or MeOH vapor at room temperature.^{21,22}

Femtosecond time-resolved visible to mid-IR absorption measurements were performed by utilizing a pump–probe technique based on a femtosecond Ti:sapphire laser system (Spectra Physics, Solstice and TOPAS prime, duration: 90 fs, repetition rate: 1 kHz) as described in our previous paper.³⁰ In this experiment, a 350 nm pulse was utilized for excitation of the photocatalysts, and 22 000 cm^{-1} (455 nm), 14 300 cm^{-1} (700 nm), and 2000 cm^{-1} (5 μm) pulses were used for the probe light. In the mid-IR region, the probe light transmitted from the sample was detected by an MCT array detector (Infrared Systems Development Corporation, 128 Ch, 6000–1000 cm^{-1}). On the other hand, in the visible to NIR region, the diffuse reflected probe light was detected by photomultiplier (Hamamatsu Photonics, H5784–03, 25 000–14 300 cm^{-1}). The detection of the NIR is limited only up to 14 300 cm^{-1} by the sensitivity of the photomultiplier. To obtain the absorbance change with a better signal-to-noise ratio, pump pulses were chopped with a 500 Hz optical chopper, and the signal acquisition was carried out on a shot-by-shot basis at a rate of 1 kHz. The decay curves were obtained at 0.1 or 5 ps intervals and averaged over 2000 scans for one point.

The photocatalytic activities of commercial and as-synthesized brookite, anatase and rutile TiO_2 powder samples were assessed by decomposition of acetaldehyde following the similar procedure reported in the previous work.⁷ Briefly, 100 mg of TiO_2 powder was diffused on a glass dish, which was put in a 125 cm^3 Tedlar bag. After cleaning the catalysts by irradiating UV light for 2–3 days until no CO_2 was detected from contaminants, 500 ppm of gaseous acetaldehyde was introduced into the Tedlar bag. The composition of the gaseous constituents inside the Tedlar bag was N_2 (79%), O_2 (21%), CO_2 (<0.1 ppm), and acetaldehyde (500 ppm) with ca. 30% relative humidity. After the acetaldehyde had reached adsorption equilibrium, the photoirradiation was carried at room temperature. An emitted light with a wavelength of ca. 365 nm (intensity = 0.1 mW cm^{-2}) from the light emitting diode (Nichia, NCCU033) was used as the photoirradiation source. The acetaldehyde and carbon dioxide (CO_2) concentrations were then respectively measured using gas chromatography (Shimadzu, GC-8A, FID detector).

3. RESULTS AND DISCUSSION

3.1. Transient Absorption Spectra of Brookite TiO_2 Powders. We first measured the transient absorption (TA) spectra of as-synthesized brookite TiO_2 powders. The SEM (Figure S1) and TEM (Figure S2) images of the powders clearly demonstrate that fine crystals were obtained, and characteristic peaks of brookite crystal were observed in the XRD pattern (Figure S3). The TA spectra measured after 355 nm laser pulse irradiation (6 ns duration, 5 Hz, 0.5 mJ cm^{-2}) are shown in Figure 1a. A broad absorption was observed over the entire wavenumber region from 25 000 to 3000 cm^{-1} (400 nm to 3.3 μm). Two broad absorption peaks appeared at 22 000 and 13 000 cm^{-1} , and these were both assigned to deeply trapped electrons, as will be discussed later. It is notable that the absorption intensity below 3000 cm^{-1} was very little. This result suggests that the number of surviving free electrons was very small since a strong structureless absorption should be

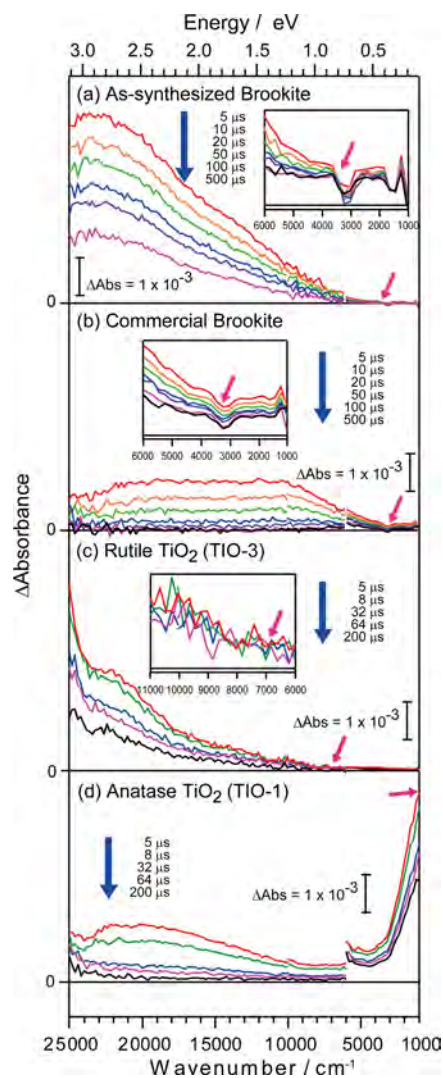


Figure 1. Transient absorption spectra of (a) as-synthesized brookite TiO_2 powder and (b) commercial brookite TiO_2 powder excited by UV laser pulses (355 nm, 6 ns duration, 0.5 mJ per pulse, and 5 Hz) in vacuum. Also shown are transient absorption spectra of rutile (c) and anatase TiO_2 powders (d) after band gap excitation. The red arrows indicate the adsorption edge of the trapped electrons. The insets show the enlarged spectra in IR region.

present below 3000 cm^{-1} if free electrons exist:¹⁹ this means that most of the electrons were already trapped at defects in microsecond region.

In order to understand the general features of brookite TiO_2 powders, another powder, purchased from Kojundo-Chemicals, Ltd., was examined. The obtained SEM image (Figure S1) shows that small particles aggregated to form larger secondary particles (around a few microns). The absorption intensity of the commercial powder (Figure 1b) at 25 000–10 000 cm^{-1} is smaller than that of as-synthesized brookite TiO_2 powders (Figure 1a), but the shape of TA spectrum at 10 000–1000 cm^{-1} is very similar, where the intensity <3000 cm^{-1} is also very small. These results confirm that most of the photogenerated electrons in brookite TiO_2 powders are trapped at defects. The depth of the electron trap can be estimated from the absorption edge of the trapped electrons. In the case of as-synthesized brookite TiO_2 powders, the absorption edge is positioned at $\sim 3500 \text{ cm}^{-1}$ ($\sim 0.4 \text{ eV}$), so the depth was estimated to be ~ 0.4

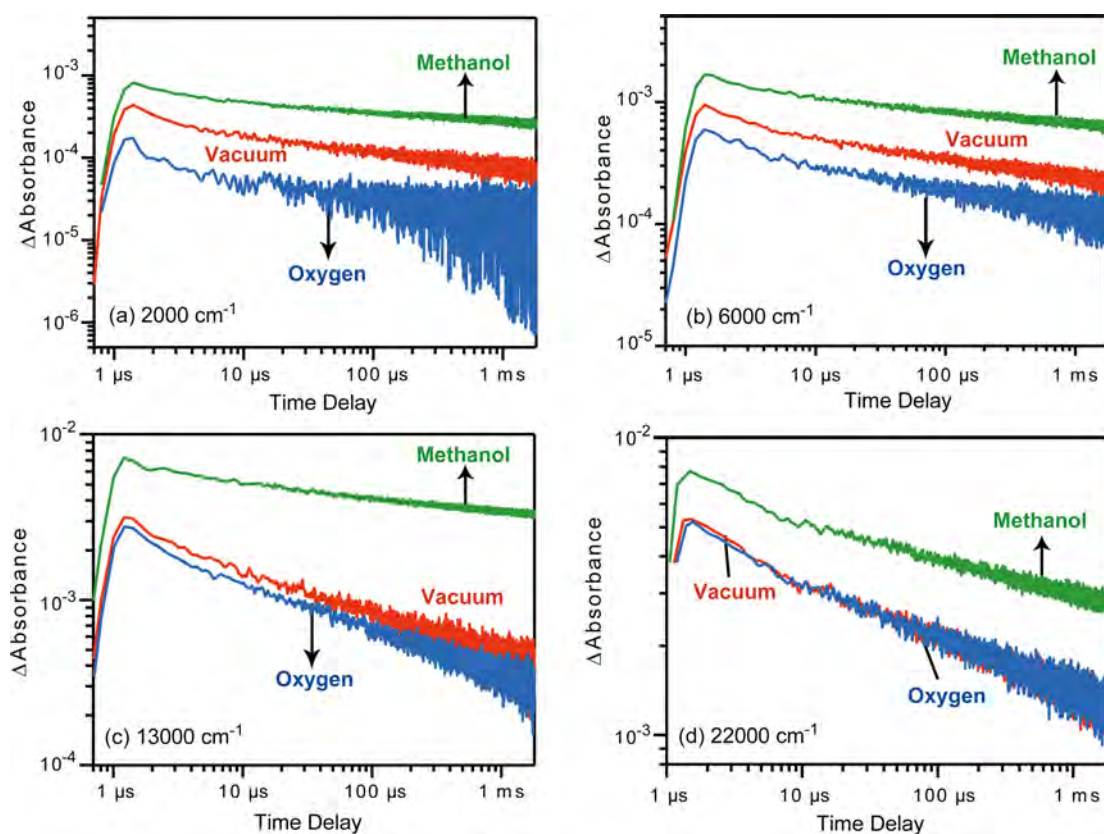


Figure 2. Decay curves of transient absorption of as-synthesized brookite TiO_2 powder irradiated by UV laser pulses (355 nm and 0.5 mJ per pulse) probed at 2000 cm^{-1} (a), 6000 cm^{-1} (b), 13000 cm^{-1} (c), and 22000 cm^{-1} (d) in vacuum, 20 Torr O_2 , and CH_3OH .

eV. This value is similar to that of commercial brookite TiO_2 powders, for which the absorption edge is located at $\sim 3500\text{ cm}^{-1}$. These results suggest that the depth of the electron trap is similar for all brookite TiO_2 powders, and is not very sensitive to the morphology or particle size of the powder.

Similarly shaped transient absorption spectra to those of brookite TiO_2 powders were observed for rutile TiO_2 powders, which are reported in our previous paper.³³ The spectra of rutile TiO_2 powders were again measured and displayed in Figure 1c. In these spectra, the absorption intensity of deeply trapped electrons ($>7000\text{ cm}^{-1}$) is higher than that of free and shallowly trapped electrons ($<3000\text{ cm}^{-1}$). In the case of rutile TiO_2 powders, the depth of the electron trap was estimated to be $\sim 0.9\text{ eV}$ from the absorption edge at $\sim 7000\text{ cm}^{-1}$ ($\sim 0.9\text{ eV}$).³³ This result is in contrast to that of anatase TiO_2 particles (Figure 1d), for which the intensity of free and shallowly trapped electrons ($<3000\text{ cm}^{-1}$) is much larger than that of deeply trapped electrons ($>7000\text{ cm}^{-1}$). In this case, free and shallowly trapped electrons are dominant. The depth of the electron-trap is estimated to be much shallower than 0.1 eV , because strong absorption was observed even at the low wavenumber limit at 1000 cm^{-1} (0.1 eV).³³ When the depth is comparable to the thermal energy at room temperature ($kT \sim 0.03\text{ eV}$), free electrons and shallowly trapped electrons are thermally equilibrated, and it is difficult to distinguish each other. These results indicate that the electron traps in TiO_2 powders grow deeper in the order: rutile $>$ brookite $>$ anatase.

3.2. Behavior of Photogenerated Charge Carriers in the Presence and Absence of Reactant Molecules. The decay processes of transient absorption in as-synthesized brookite TiO_2 particles were further examined in the presence

and absence of reactant molecules. As shown in Figure 2a, the intensity at 2000 cm^{-1} decreased within $2\text{ }\mu\text{s}$ of exposure to O_2 gas. This result suggests that the absorption at 2000 cm^{-1} reflects the number of surviving electrons, since adsorbed O_2 consumes electrons and accelerates electron decay.²¹ However, exposure to MeOH vapor increased the absorption intensity, indicating that holes are consumed by MeOH and that the hole-consuming reaction prevents recombination and extends the lifetime of electrons.²²

The absorption intensities at 6000 , 13000 , and 22000 cm^{-1} behaved similarly to that at 2000 cm^{-1} (Figure 2b, 2c, and 2d, respectively): the intensities increase and decrease by the exposure to MeOH vapor and O_2 , respectively; however, the influence of the O_2 becomes smaller and smaller with increasing the wavenumber. These results confirm that the transient absorption observed in Figure 1a mainly reflects the number of electrons, but the reactivity becomes smaller and smaller as the wavenumber becomes larger (the depth of the electron trap becomes larger). In addition, the absolute absorption intensity is larger in the order: $22000 > 13000 > 6000 \gg 2000\text{ cm}^{-1}$. This result implies that the number of deeply trapped electrons is larger than that of shallowly trapped electrons.

It is noted that the reduction of O_2 by photogenerated electrons is not so simple. The redox potentials for single-electron transfer as $\text{O}_2 + \text{e}^- \rightarrow \text{O}_2^-$ and $\text{O}_2 + \text{H}^+ + \text{e}^- \rightarrow \text{HO}_2$ are -0.284 and -0.046 V vs NHE, respectively, and these potentials are comparable or slightly higher than the CBM of anatase TiO_2 ($\sim -0.26\text{ V}$ vs NHE). This means that even for the anatase TiO_2 , the electrons have unfavorable energies to react with O_2 when they are trapped at the defects. For the same reason, the free electrons and trapped electrons in rutile

TiO₂ as well as the trapped electrons in brookite TiO₂ cannot react with O₂. The chemisorption of O₂ on the TiO₂ surface could perturb the electronic structure of adsorbed O₂ and can reduce the energy for the electron transfer, but it is well-known that multielectron transfer processes more readily take place than the single-electron transfer. For example, it is reported that multielectron reduction of O₂ (e.g., O₂ + 2H⁺ + 2e⁻ → H₂O₂, + 0.682 V vs NHE; O₂ + 4H⁺ + 4e⁻ → 2H₂O, + 1.23 V vs NHE) proceed on WO₃ photocatalysts, where the CBM is located at +0.5 eV vs NHE.⁴⁶ Therefore, it is plausible that these multielectron transfers would take place on TiO₂ particles with the aid of surface OH groups and/or small amount of chemisorbed/physisorbed H₂O. The mechanism is not simple, but the reaction does proceed.

In the commercial brookite TiO₂ powders, the absorption intensity at 2000 and 6000 cm⁻¹ also reflects the number of electrons, as shown in Figure S4. However, the absorption intensities at 13 000 and 22 000 cm⁻¹ reflect the number of both electrons and holes, as the intensity was increased by exposure to both O₂ and MeOH. This result initially seems confusing but as we reported previously,⁴⁷ if a particular absorption reflects the number of both electrons and holes, then the intensity will increase when either an electron- or hole-consuming reaction takes place. These results demonstrate that the trapped holes provide an absorption band at 22 000 and 13 000 cm⁻¹ for commercial brookite TiO₂ powders. In the case of as-synthesized brookite TiO₂, the absorption by holes might be also mixed at 22 000 and 13 000 cm⁻¹, but its contribution is much smaller than that by electrons. These results suggest that the holes are deeply trapped in the commercial powders, but not in the as-synthesized powders. It is often proposed that the surface OH groups and surface lattice oxygen species work as hole-trapping sites, and they are easily formed on rough surfaces.^{3,4} As seen from SEM and TEM images in Figure S1 and S2, the surface of as-synthesized brookite TiO₂ powders is very smooth but that of commercial is very rough. Therefore, it is expected that the signal intensity of trapped holes is more intense in the latter powder than that of former powders. Similarly, the absorption of trapped holes is absent from the visible to mid-IR region in the case of bulk single crystals such as SrTiO₃.³¹ Therefore, similar results can be expected for fine single-crystal brookite TiO₂ particles.

3.3. Deep Electron Trapping at Defects in Brookite TiO₂ Powders. In order to further examine the electron trapping process, the decay processes in the picosecond region were further studied using femtosecond laser systems. The normalized decay curves measured at 2000, 14 300 (700 nm), and 22 000 (455 nm) cm⁻¹ are shown in Figure 3. As shown in the figure, the rate of decay of free electrons (2000 cm⁻¹) is much faster than that of deeply trapped electrons (22 000 and 14 300 cm⁻¹) at 0–800 ps. This indicates that the free electrons are deeply trapped at 0–800 ps. The initial decay processes at 0–12 ps (inset figure) provide more detailed information: the number of free electrons increases within 0.5 ps but rapidly decreases from 0.5–2 ps. On the other hand, the number of deeply trapped electrons (14 300 and 22 000 cm⁻¹) increases more slowly, and it takes ~2 ps to reach the maximum. The decrease in free electrons and increase in deeply trapped electrons are well-correlated, suggesting that most of the free electrons excited in the CB are trapped within a few picoseconds. As a result, the number of surviving electrons at 2000 ps is larger in the order of the order of deeply trapped electrons (22 000 cm⁻¹) > trapped electrons (14 300 cm⁻¹) > free

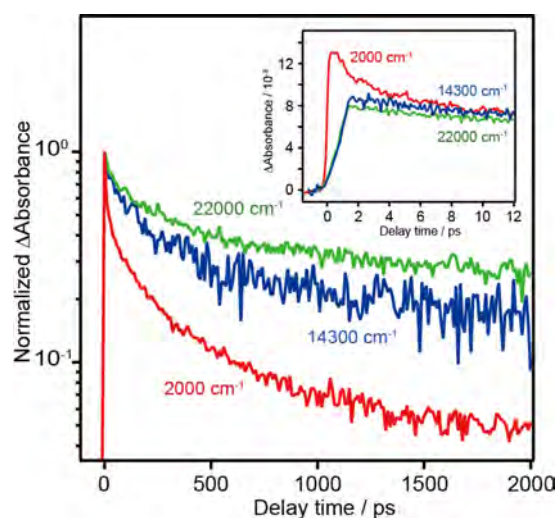


Figure 3. Decay curves of free electrons (2000 cm⁻¹) and deeply trapped electrons (14 300 and 22 000 cm⁻¹) in as-synthesized brookite TiO₂ powders measured by UV laser pulse irradiation (350 nm and 6 μJ per pulse, 500 Hz) in vacuum.

electrons (2000 cm⁻¹). This order is consistent with observations in the microsecond region (Figure 1a), where the intensity at 22 000 cm⁻¹ is larger than those at 14 300 and 2000 cm⁻¹. This confirms that the rate of decay of deeply trapped electrons is much slower than that of free electrons, and the number of carriers surviving in the microsecond region is determined by the picosecond-scale dynamics.

Similar results were observed for commercial brookite TiO₂ powders (Figure S5): the decay of free electrons is much faster than those of deeply trapped electrons and holes, giving absorption bands at 14 300 and 22 000 cm⁻¹. These results confirm that the electron-deep-trapping process was not sensitive to the differences in particle size and surface morphology. This rapid electron-trapping is also observed in rutile TiO₂ powders but not in anatase TiO₂ powders, as reported in our previous paper.³³

Here, we found that the depth of the electron-trap is different among anatase, rutile, and brookite TiO₂ powders. This difference comes from the difference in the “softness” of the defects that traps the electrons. It is reported that the origin of the electron trap is a defect such as an oxygen vacancy or Ti-interstitial.^{43–45} The Ti⁴⁺ around the defects capture electrons to form Ti³⁺ with structural deformation. The depth of the electron trap depends on how the defects stabilize the trapped electrons through structural relaxation (polaron formation).^{43–45} In other words, as the lattice of a particle becomes more deformed, the trapped electrons become increasingly stabilized. Theoretical calculations predicted stabilization energies of 0.8–1 eV and 0–0.2 eV for rutile and anatase, respectively.^{43–45} For brookite TiO₂, we could not find any theoretical papers simulating the electron trapping at the defects, but oxygen vacancies and Ti-interstitials should similarly trap the electrons. Experimentally, we estimated the depth of the electron trap to be ~0.4 eV from the absorption edge (~3500 cm⁻¹) of the transient absorption in Figure 1. This depth is deeper than that of anatase (<0.1 eV) but shallower than that of rutile (~0.9 eV), as described in the previous section.

3.5. Photocatalytic Activity of Brookite TiO₂: Differences from Anatase and Rutile TiO₂. Photocatalytic

activities of the TiO₂ powders for the decomposition of acetaldehyde were evaluated after 24 h as shown in Figure 4. In

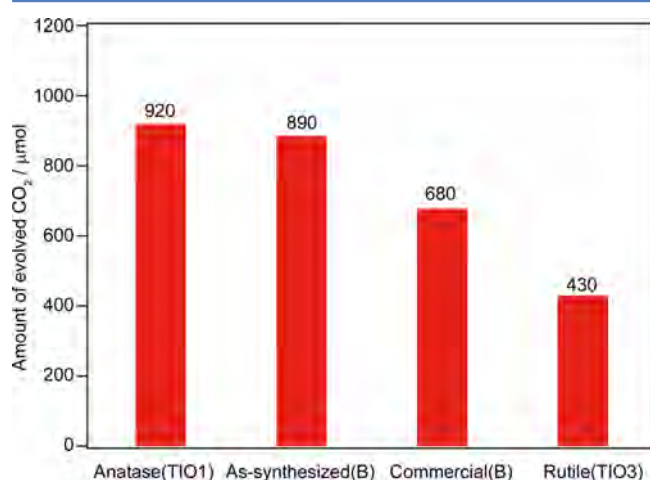


Figure 4. Photocatalytic activity of TiO₂ powders for the decomposition of acetaldehyde. The amount of evolved CO₂ gas after 24 h under UV light irradiation (365 nm, 0.1 mW cm⁻²) is shown.

this experiment, the amount of evolved CO₂ gas was measured under UV light irradiation. It is shown that the activity is higher in the order: anatase (TiO1) \approx as-synthesized brookite > commercial brookite > rutile TiO₂ powders (TiO3). We have reported in the previous paper⁷ that the as-synthesized brookite TiO₂ powders shows higher activity than anatase TiO₂ powders (Ishiraha Sangyo Co. Ltd., ST-01). In the present experiment, the anatase TiO₂ powders (TiO-1) and the as-synthesized brookite TiO₂ powders show comparable activity. This discrepancy might come from the difference in the degree of crystallinity of ST-01 and TiO1. The relative surface areas of ST-01 and TiO1 are about 300 and 70 m² g⁻¹. The crystallinity of TiO₂ powders are strongly correlated with the amount of oxygen defects of them because a low crystallinity induces formation of oxygen defects in the lattice of TiO₂. Oxygen defect plays a role of a recombination center between electrons and holes resulting in the decrease of photocatalytic activity.

In order to further discuss the difference in photocatalytic activity for these TiO₂ powders, the decay processes of photogenerated charge carriers in brookite TiO₂ powders were compared with those in anatase and rutile TiO₂ powders. As shown in Figure 5a, the number of surviving free electrons (2000 cm⁻¹) in the microsecond region is larger in the order: anatase > brookite > rutile. The number of surviving trapped electrons giving the absorption at 13 000 cm⁻¹ (Figure 5b) at 100 μs is different from that of free electrons, where it is larger in the order: as-synthesized brookite > rutile > anatase > commercial brookite. In the case of holes, we could not directly estimate the number of surviving holes in as-synthesized brookite, but it is expected to be the largest because the same number of holes with that of trapped electrons should be surviving to maintain charge balance. The absorption intensity at 22 000 cm⁻¹ mainly reflects the number of trapped holes for rutile TiO₂³³ but it is the mixture of electrons and holes for anatase³³ and commercial brookite TiO₂. Therefore, the number of surviving holes is larger in the order: as-synthesized brookite > rutile > commercial brookite \geq anatase TiO₂ powders.

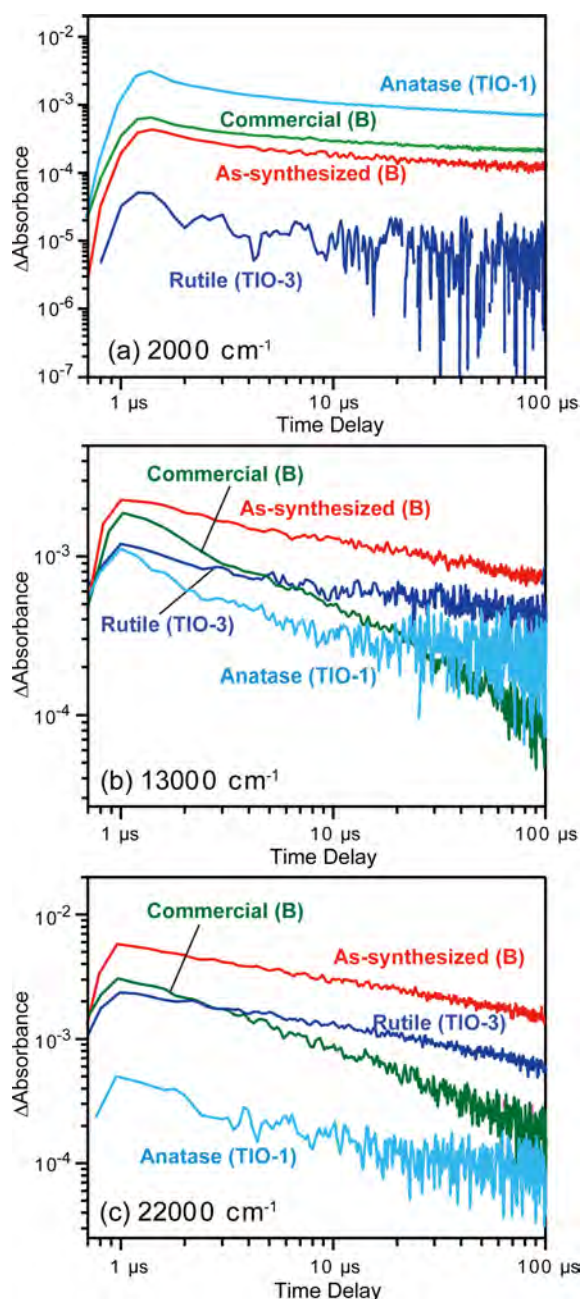


Figure 5. Decay curves of transient absorption measured at (a) 2000, (b) 13 000, and (c) 22 000 cm⁻¹ in vacuum. As-synthesized and commercial brookite, anatase (TiO-10), and rutile (TiO-6) TiO₂ powders were irradiated by UV laser pulses (355 nm, 6 ns duration, and 0.5 mJ per pulse).

The steady-state photocatalytic reactions proceed via the combination of reductions and oxidations, therefore, both reactivity of electrons and holes are important. There is no doubt that the free electrons are much reactive than the deeply trapped electrons. Most of the free electrons in brookite TiO₂ powders are trapped at the defects; however, the as-synthesized brookite TiO₂ powders still show comparable activity with that of anatase TiO₂ powders. The plausible reason for this distinctive activity of as-synthesized brookite TiO₂ is its larger number of surviving holes compared to that in anatase TiO₂ powders. In many photocatalytic reactions, holes usually have sufficient energy to oxidize many reactants. Furthermore, the

hole-consuming reactions proceed faster than the electron-consuming reactions,^{21,22} and therefore, increasing the number of surviving holes has a direct positive effect on photocatalytic oxidations. The as-synthesized brookite TiO₂ powders have the largest number of surviving holes; hence, this catalyst can have highest activity for photocatalytic oxidations. However, as mentioned above, the reactivity of electrons is also important for the steady-state reactions because without electron-consuming reactions, the electrons are overaccumulated in the particles and then accelerate the recombination with holes. As a result, the number of surviving holes decreases, and hence, the overall photocatalytic activity is not increased. In the case of anatase TiO₂, the number of surviving free electrons is the highest, and therefore, it is expected to exhibit higher photocatalytic activity in spite of smaller number of surviving holes. It is noted that the as-synthesized brookite and anatase TiO₂ showed comparable photocatalytic activity, but the mechanism that justifies this result is different. Certainly, electron trapping decreases the reactivity of electrons, but it is still beneficial to increase the lifetime of holes. Our findings reveal that rutile has longer lifetime of holes; however, the depth of the electron-trap (~0.9 eV) is too deep compared to that of brookite (~0.4 eV) and anatase (<0.1 eV). This indicates that brookite TiO₂ has moderate depth of the electron-trap. In addition, both trapped electrons and holes in brookite TiO₂ have reasonable reactivities. These are the reasons why brookite shows high activity contrary to that expected from the shorter-lifetime of free electrons.

We find that defects could work positively for the photocatalytic reactions. Recently, Dai et al. reported⁴⁸ that photocatalytic activity can be enhanced by fabricating defects on Bi₂MoO₆ crystals. They proposed that the defects are beneficial for increasing the number of long-lived charge carriers. In addition, Sakata et al. also succeeded in breaking the world record of quantum efficiency for pure water splitting reaction and obtained 71% by loading surface defects on Ga₂O₃ photocatalysts.⁴⁹ The property of the defects intentionally introduced on Bi₂MoO₆ and Ga₂O₃ is different from that of intrinsic native defects on TiO₂. Nevertheless, these reports support that fabrication of “appropriate defects” is beneficial to further enhance the photocatalytic activities.

4. CONCLUSIONS

In this work, we found that brookite TiO₂ powders have moderate depth of the electron-trap that can promote both of photocatalytic oxidations and reductions. In principle, the electron-trapping at powder defects decreases the reactivity of electrons but retards the electron–hole pair recombination to elongate the lifetime of holes. The depth on rutile is too deep for the electron-induced reductions, but that on anatase is too shallow to elongate the lifetime of holes. In the case of brookite TiO₂, electrons are trapped at moderate depths, which can effectively promote both photocatalytic reductions and oxidations. Powder defects work positively and negatively on the lifetime and reactivity of charge carriers, respectively. Therefore, appropriate depth of electron-trapping is necessary to maximize the overall photocatalytic activity.

■ ASSOCIATED CONTENT

Supporting Information

The Supporting Information is available free of charge on the ACS Publications website at DOI: 10.1021/acscatal.7b00131.

SEM and TEM images, XRD patterns, decay curves for commercial brookite TiO₂, laser-power dependence, steady-state IR spectra (PDF)

■ AUTHOR INFORMATION

Corresponding Authors

*E-mail: tohno@che.kyutech.ac.jp.

*E-mail: yamakata@toyota-ti.ac.jp.

ORCID

Akira Yamakata: 0000-0003-3179-7588

Notes

The authors declare no competing financial interest.

■ ACKNOWLEDGMENTS

This work was supported by the PRESTO/JST program “Chemical Conversion of Light Energy”, the Grant-in-Aid for Basic Research (B) (No. 16H04188) and Scientific Research on Innovative Areas (Area 2503; No. 16H00852), and the Strategic Research Infrastructure Project of MEXT.

■ REFERENCES

- (1) Fujishima, A.; Honda, K. *Nature* **1972**, *238*, 37–38.
- (2) Kamat, P. V. *Chem. Rev.* **1993**, *93*, 267–300.
- (3) Linsebigler, A. L.; Lu, G. Q.; Yates, J. T. *Chem. Rev.* **1995**, *95*, 735–758.
- (4) Hoffmann, M. R.; Martin, S. T.; Choi, W. Y.; Bahnemann, D. W. *Chem. Rev.* **1995**, *95*, 69–96.
- (5) Ma, Y.; Wang, X.; Jia, Y.; Chen, X.; Han, H.; Li, C. *Chem. Rev.* **2014**, *114*, 9987–10043.
- (6) Ohtani, B.; Handa, J.; Nishimoto, S.; Kagiya, T. *Chem. Phys. Lett.* **1985**, *120*, 292–294.
- (7) Murakami, N.; Kamai, T.-a.; Tsubota, T.; Ohno, T. *Catal. Commun.* **2009**, *10*, 963–966.
- (8) Augugliaro, V.; Loddo, V.; Lopez-Munoz, M. J.; Marquez-Alvarez, C.; Palmisano, G.; Palmisano, L.; Yurdakal, S. *Photochem. Photobiol. Sci.* **2009**, *8*, 663–669.
- (9) Kandiel, T. A.; Feldhoff, A.; Robben, L.; Dillert, R.; Bahnemann, D. W. *Chem. Mater.* **2010**, *22*, 2050–2060.
- (10) Magne, C.; Cassaignon, S.; Lancel, G.; Pauporte, T. *ChemPhysChem* **2011**, *12*, 2461–2467.
- (11) Zhang, L.; Menendez-Flores, V. M.; Murakami, N.; Ohno, T. *Appl. Surf. Sci.* **2012**, *258*, 5803–5809.
- (12) Liu, L.; Zhao, H.; Andino, J. M.; Li, Y. *ACS Catal.* **2012**, *2*, 1817–1828.
- (13) Kandiel, T. A.; Robben, L.; Alkaim, A.; Bahnemann, D. *Photochemical & Photobiological Sciences* **2013**, *12*, 602–609.
- (14) Li, Z.; Cong, S.; Xu, Y. *ACS Catal.* **2014**, *4*, 3273–3280.
- (15) Ohno, T.; Higo, T.; Saito, H.; Yuajn, S.; Jin, Z.; Yang, Y.; Tsubota, T. *J. Mol. Catal. A: Chem.* **2015**, *396*, 261–267.
- (16) Kogo, A.; Sanehira, Y.; Ikegami, M.; Miyasaka, T. *Chem. Lett.* **2016**, *45*, 143–145.
- (17) Cargnello, M.; Montini, T.; Smolin, S. Y.; Priebe, J. B.; Delgado Jaen, J. J.; Doan-Nguyen, V. T.; McKay, I. S.; Schwalbe, J. A.; Pohl, M.-M.; Gordon, T. R.; Lu, Y.; Baxter, J. B.; Bruckner, A.; Fornasiero, P.; Murray, C. B. *Proc. Natl. Acad. Sci. U. S. A.* **2016**, *113*, 3966–3971.
- (18) Pankove, J. I. *Optical Processes in Semiconductors*; Dover: New York, 1975.
- (19) Yamakata, A.; Ishibashi, T.; Onishi, H. *Chem. Phys. Lett.* **2001**, *333*, 271–277.
- (20) Heimer, T. A.; Heilweil, E. J. *J. Phys. Chem. B* **1997**, *101*, 10990–10993.
- (21) Yamakata, A.; Ishibashi, T.; Onishi, H. *J. Phys. Chem. B* **2001**, *105*, 7258–7262.
- (22) Yamakata, A.; Ishibashi, T.; Onishi, H. *J. Phys. Chem. B* **2002**, *106*, 9122–9125.

- (23) Yamakata, A.; Ishibashi, T.; Kato, H.; Kudo, A.; Onishi, H. *J. Phys. Chem. B* **2003**, *107*, 14383–14387.
- (24) Maruyama, M.; Iwase, A.; Kato, H.; Kudo, A.; Onishi, H. *J. Phys. Chem. C* **2009**, *113*, 13918–13923.
- (25) Furuhashi, K.; Jia, Q.; Kudo, A.; Onishi, H. *J. Phys. Chem. C* **2013**, *117*, 19101–19106.
- (26) Yamakata, A.; Yoshida, M.; Kubota, J.; Osawa, M.; Domen, K. *J. Am. Chem. Soc.* **2011**, *133*, 11351–11357.
- (27) Yoshihara, T.; Katoh, R.; Furube, A.; Tamaki, Y.; Murai, M.; Hara, K.; Murata, S.; Arakawa, H.; Tachiya, M. *J. Phys. Chem. B* **2004**, *108*, 3817–3823.
- (28) Barroso, M.; Cowan, A. J.; Pendlebury, S. R.; Gratzel, M.; Klug, D. R.; Durrant, J. R. *J. Am. Chem. Soc.* **2011**, *133*, 14868–14871.
- (29) Singh, R. B.; Matsuzaki, H.; Suzuki, Y.; Seki, K.; Minegishi, T.; Hisatomi, T.; Domen, K.; Furube, A. *J. Am. Chem. Soc.* **2014**, *136*, 17324–17331.
- (30) Yamakata, A.; Kawaguchi, M.; Nishimura, N.; Minegishi, T.; Kubota, J.; Domen, K. *J. Phys. Chem. C* **2014**, *118*, 23897–23906.
- (31) Yamakata, A.; Vequizo, J. J. M.; Kawaguchi, M. *J. Phys. Chem. C* **2015**, *119*, 1880–1885.
- (32) Yamakata, A.; Kawaguchi, M.; Murachi, R.; Okawa, M.; Kamiya, I. *J. Phys. Chem. C* **2016**, *120*, 7997–8004.
- (33) Yamakata, A.; Vequizo, J. J. M.; Matsunaga, H. *J. Phys. Chem. C* **2015**, *119*, 24538–24545.
- (34) Bahnemann, D.; Henglein, A.; Lilie, J.; Spanhel, L. *J. Phys. Chem.* **1984**, *88*, 709–711.
- (35) Bahnemann, D. W.; Hilgendorff, M.; Memming, R. *J. Phys. Chem. B* **1997**, *101*, 4265–4275.
- (36) Meekins, B. H.; Kamat, P. V. *J. Phys. Chem. Lett.* **2011**, *2*, 2304–2310.
- (37) Wang, X. L.; Kafizas, A.; Li, X. O.; Moniz, S. J. A.; Reardon, P. J. T.; Tang, J. W.; Parkin, I. P.; Durrant, J. R. *J. Phys. Chem. C* **2015**, *119*, 10439–10447.
- (38) Ahmed, A. Y.; Kandiel, T. A.; Oekermann, T.; Bahnemann, D. J. *J. Phys. Chem. Lett.* **2011**, *2*, 2461–2465.
- (39) Xu, M. C.; Gao, Y. K.; Moreno, E. M.; Kunst, M.; Muhler, M.; Wang, Y. M.; Idriss, H.; Woll, C. *Phys. Rev. Lett.* **2011**, *106*, 138302.
- (40) Luttrell, T.; Halpegamage, S.; Tao, J.; Kramer, A.; Sutter, E.; Batzill, M. *Sci. Rep.* **2014**, *4*, 1–8.
- (41) Sachs, M.; Pastor, E.; Kafizas, A.; Durrant, J. R. *J. Phys. Chem. Lett.* **2016**, *7*, 3742–3746.
- (42) Kafizas, A.; Wang, X. L.; Pendlebury, S. R.; Barnes, P.; Ling, M.; Sotelo-Vazquez, C.; Quesada-Cabrera, R.; Li, C.; Parkin, I. P.; Durrant, J. R. *J. Phys. Chem. A* **2016**, *120*, 715–723.
- (43) Na-Phattalung, S.; Smith, M. F.; Kim, K.; Du, M. H.; Wei, S. H.; Zhang, S. B.; Limpijumnong, S. *Phys. Rev. B: Condens. Matter Mater. Phys.* **2006**, *73*, 125205.
- (44) Mattioli, G.; Filippone, F.; Alippi, P.; Bonapasta, A. A. *Phys. Rev. B: Condens. Matter Mater. Phys.* **2008**, *78*, 241201.
- (45) Spreafico, C.; VandeVondele, J. *J. Phys. Chem. Chem. Phys.* **2014**, *16*, 26144–26152.
- (46) Abe, R.; Takami, H.; Murakami, N.; Ohtani, B. *J. Am. Chem. Soc.* **2008**, *130*, 7780–7781.
- (47) Yamakata, A.; Yeilin, H.; Kawaguchi, M.; Hisatomi, T.; Kubota, J.; Sakata, Y.; Domen, K. *J. Photochem. Photobiol., A* **2015**, *313*, 168–175.
- (48) Dai, Z.; Qin, F.; Zhao, H. P.; Ding, J.; Liu, Y. L.; Chen, R. *ACS Catal.* **2016**, *6*, 3180–3192.
- (49) Sakata, Y.; Hayashi, T.; Yasunaga, R.; Yanaga, N.; Imamura, H. *Chem. Commun.* **2015**, *51*, 12935–12938.

Defect-Induced Acceleration and Deceleration of Photocarrier Recombination in SrTiO₃ Powders

Kosaku Kato and Akira Yamakata*

Cite This: <https://dx.doi.org/10.1021/acs.jpcc.0c03369>

Read Online

ACCESS |



Metrics & More

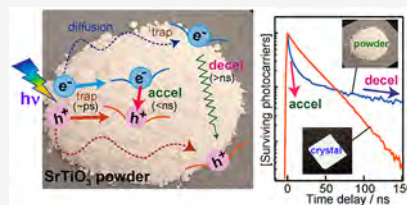


Article Recommendations



Supporting Information

ABSTRACT: Defects in powders play key roles in photocatalysis since they sometimes accelerate but other times prevent the recombination of photocarriers. However, how to differentiate the roles, as well as their actual effects, is still unclear. Here, we found that defects have dual properties: initially they accelerate recombination, but later they prevent it. These two contradictory properties are differentiated by whether electrons and holes are trapped in the vicinity or far away from each other. Just after photoirradiation, defects prevent carrier diffusion to keep them closer, resulting in accelerating recombination. However, once the carriers can escape from the initial trapping, they can spread and be trapped far away. These trapped carriers have to travel long distances by repeatedly hopping and tunneling; hence, the carrier lifetime becomes longer. The fate of carriers is determined by how they escape the initial trapping by using excess energy after photoexcitation; i.e., control of this process is the key to improving the photocatalytic activity.



1. INTRODUCTION

Hydrogen gas is an eco-friendly energy resource because it can be obtained from water and does not emit carbon dioxide when used as a fuel. Photocatalytic water splitting is a superior method of producing hydrogen gas because it is driven by abundant solar energy.^{1–9} When photocatalysts are illuminated by light with greater photon energy than their band gap, electrons and holes are excited. Some of them move to the surface and participate in the photocatalytic reaction, but others undergo electron–hole recombination without contributing to the reaction. To increase the efficiency of photocatalytic reactions, it is important to reveal the dynamics of photoexcited charge carriers. There are numerous reports on how photocarriers behave in many kinds of semiconductors.^{10–12} However, most of these reports involve defect-free systems such as single crystals (SC). On the other hand, photocatalysts are usually used in powder form due to their low cost and large surface area. Powders possess a lot of defects on the surface that trap charge carriers, and it has been widely believed that these defects work as electron–hole recombination centers. In fact, there are numerous reports that the lifetime of photogenerated charge carriers becomes shorter on introducing defects into a crystal.^{13–15} However, recently it was reported that photocarriers in defect-rich SrTiO₃ (STO) powder had longer lifetimes than those in defect-free SC STO,¹⁶ and defects can enhance the photocatalytic activities.¹⁷ These reports seem to contradict each other and imply that defects have properties of both accelerating and decelerating recombination. However, when and how the defects act to either accelerate or decelerate recombination have not been fully elucidated yet.

In this work, we have investigated the effects of defects on electron–hole recombination kinetics by comparing defect-free SC-STO and powder-STO. Femtosecond to microsecond time-

resolved absorption spectroscopy (TAS) and picosecond time-resolved photoluminescence (PL) measurements were employed to elucidate the behavior and energy state of photo-generated charge carriers. We found that in the case of defect-free SC most of the photogenerated charge carriers survived as free and/or shallowly trapped carriers and hardly recombined in the picosecond region. Contrarily, in the case of powder STO, most of the carriers were trapped at defects within ~30 ps, and a portion of them recombined in the picosecond region. However, once the charge carriers escaped from the initial picosecond-recombination process, they had longer lifetimes, surviving into the millisecond region. These results indicate that the defects have dualistic properties; initially they accelerate recombination, but later they prevent recombination. The detailed mechanism is discussed based on the results of time-resolved TAS and PL measurements.

2. EXPERIMENTAL SECTION

In the experiment, an undoped single crystal STO (Shinkosha, 110 orientation, 10 × 10 × 0.5 mm³) and a commercial polycrystalline powder (Aldrich Chemical Co., particle size of ~100 nm) were used. For the transient absorption (TA) measurements of powder STO, the powder was fixed on a CaF₂ plate at a density of 1.5 g cm⁻². For the time-resolved PL

Received: April 16, 2020

Published: April 24, 2020

measurement, STO pellets were fabricated by pressing the powder (~ 20 mg, ~ 5 mm in diameter, ~ 0.1 mm in thickness).

The transient absorption measurements were performed with the spectrometers described in the previous reports.^{18,19} For microsecond region measurements, samples were excited by the third harmonics of a Nd:YAG laser (Continuum, Surelite II; 355 nm wavelength, 6 ns duration, 0.5 mJ pulse energy, 5 Hz repetition rate). As a probe light, the light from a halogen lamp was used in the visible (25000 – 10000 cm^{-1}) and near-IR (10000 – 6000 cm^{-1}) regions, while the light from a MoSi₂ coil was used in the mid-IR region (6000 – 1000 cm^{-1}). The transmitted or diffuse reflected probe light was monochromated by a spectrometer and detected by a Si, InGaAs, and MCT detector in the visible, near-IR, and mid-IR region, respectively. The output electric signal was amplified by AC-coupled voltage amplifiers (NF Corporation, NF5307, 10 MHz bandwidth; Stanford Research Systems, SR560, 1 MHz bandwidth). The bandwidth of the amplifiers limited the time resolution of this system to 20 ns at best.

The femtosecond to picosecond TA measurements were performed by using a femtosecond Ti:sapphire laser system (Spectra-Physics, Solstice & TOPAS Prime; 90 fs duration; 1 kHz repetition rate). 355 nm pulses (1 and 6 μJ pulse⁻¹) were used to excite the samples. The 20000 cm^{-1} (500 nm), 11000 cm^{-1} (909 nm), and 2000 cm^{-1} (5 μm) pulses were used as the probe light and detected by a photomultiplier tube, InGaAs, and MCT detector, respectively. The delay between the pump and probe pulse was changed by a linear motorized stage (SIGMA KOKI, SGSP46-500(X)). The time resolution of the measurements was 0.1 ps.

For the subnanosecond TA measurements, the above-described femtosecond TA system was used. However, the third harmonic of a Nd:YVO₄ laser (InnoLas Laser, Picolo-1; 1 kHz repetition rate, 800 ps duration, 355 nm with 6 and 1 μJ pulse energy) was used to excite the samples. These two laser systems were temporarily synchronized, and the intervals between pump and probe pulses were controlled by a digital delay generator (Stanford Research Systems, DG535). The time resolution of the measurements was 800 ps.

For the time-resolved PL measurement, the samples were excited by 355 nm femtosecond pulses (90 fs duration, 6 and 1 μJ pulse⁻¹) from the laser system described above. The emitted light was collected by an off-axis parabolic mirror, dispersed in wavelength with a polychromator, and then detected by a streak camera (Hamamatsu, C14831-130). The time resolution was ~ 30 ps and 3 ns in the measurement time range of 1.5 and 100 ns, respectively.

3. RESULTS AND DISCUSSION

3.1. Transient Absorption Spectra of Photocarriers in Single Crystal and Powder SrTiO₃. We first measured the transient absorption spectrum of SC STO to investigate the effects of defects on the behaviors of photoexcited carriers. When the sample was irradiated by 355 nm pulse, a broad absorption appeared from 25000 to 1000 cm^{-1} (Figure 1a). The absorption intensity increased monotonically with decreasing wavenumber, which is characteristic of the intraband transition of free electrons in the conduction band (CB).^{12,18} A small peak appeared at around 2400 cm^{-1} , and this is ascribed to the electrons in polaronic states.^{20,21} These results confirm that most of the electrons survive as free electrons in the CB and/or shallowly trapped in the polaronic state. In addition, it is noted

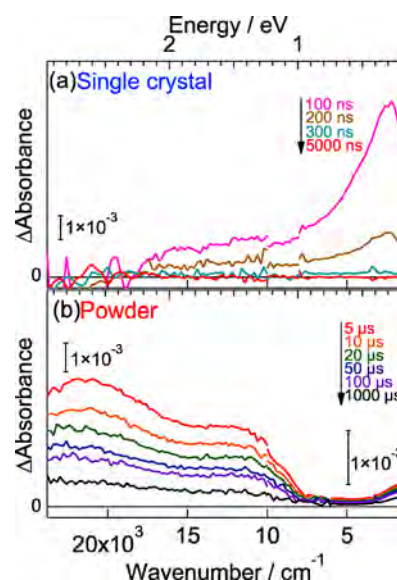


Figure 1. Transient absorption spectra of SrTiO₃ irradiated by UV laser pulses (355 nm, 6 ns duration, 0.5 mJ/pulse, and 5 Hz): (a) single crystal (110) and (b) powder.

that most of the charge carriers disappeared within 300 ns due to recombination.

In the case of powder STO (Figure 1b), the shape of the spectrum is totally different from that of SC: the absorption of free electrons and/or shallowly trapped electrons appears at <4000 cm^{-1} , but additional strong absorptions appear at ~ 22000 and ~ 11000 cm^{-1} . These absorptions are assigned to trapped holes and trapped electrons from reaction with O₂ and methanol, respectively.^{22–26} These results show that in the case of powder most of the photogenerated charge carriers are trapped at defects, but these carriers survive into the millisecond region since strong absorption is still observed even at 1 ms (Figure 1b).

3.2. Initial Trapping Kinetics of Photocarriers in SrTiO₃ Studied by Femtosecond Transient Absorption Spectroscopy. To further examine the initial decay kinetics of photocarriers, we measured the temporal profiles of the transient absorption from the femtosecond and nanosecond regions (Figure 2). In the case of SC-STO, all the absorption intensities measured at 20000, 11000, and 2000 cm^{-1} behaved similarly and reached their maximum values within 1 ps (Figure 2a). These absorptions hardly decayed in the picosecond region (Figure 2b), but the intensity decreased to $<1/100$ the original value by 150 ns (Figure 2c). The lifetimes of charge carriers were estimated by multiexponential curve fitting, and the derived values are summarized in Table S1. In the case of the absorption at 2000 cm^{-1} , two components were necessary, estimated as $\tau_1 = 6.7$ ns (17%) and $\tau_2 = 28.9$ ns (83%). As will be discussed later, the former is ascribed to radiative recombination and the latter is nonradiative recombination. Similar results were obtained for absorption at 11000 cm^{-1} ($\tau_1 = 7.6$ ns and $\tau_2 = 30.9$ ns) and 20000 cm^{-1} ($\tau_1 = 4.6$ ns and $\tau_2 = 25.2$ ns). For all three absorptions, regardless of the observed wavenumbers, these two components are essentially consistent within experimental error ($\tau_1 = 4$ – 8 ns, $\tau_2 = 25$ – 28 ns). Hence, these results confirm that these absorptions can be ascribed to identical free and/or shallowly trapped electrons, since these electrons give very broad absorption spanning from mid-IR to the visible region as shown in Figure 1a.

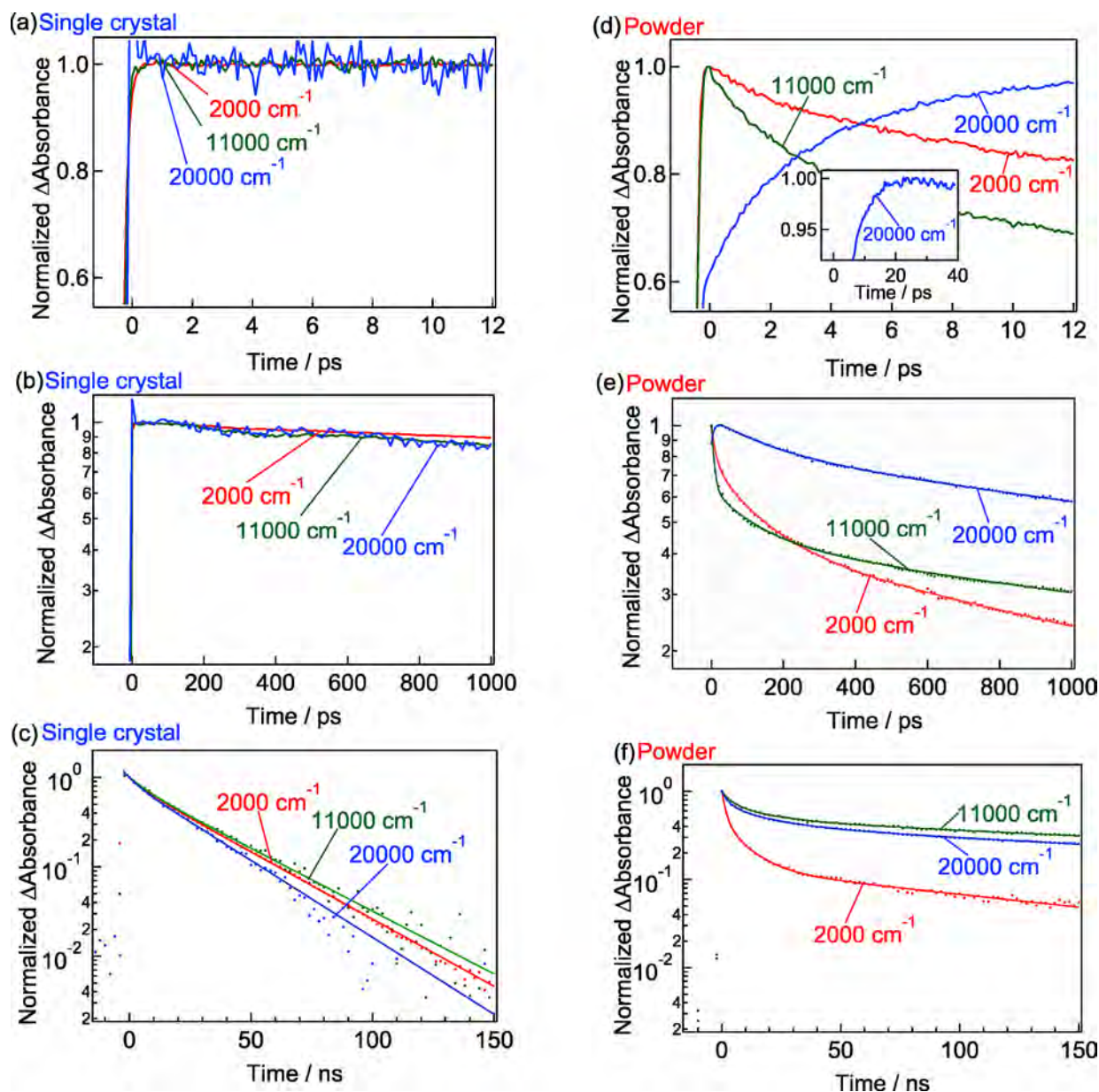


Figure 2. Decay curves of normalized transient absorptions measured at 20000, 11000, and 2000 cm^{-1} for single-crystal SrTiO_3 (a–c) and powder SrTiO_3 (d–f). Multiexponential curve-fitting results are also shown in (c, e, f). The obtained parameters are summarized in Tables S1, S3, and S4. The sample was excited by a 6 μJ , 355 nm laser pulse at 500 Hz with 90 fs duration for (a, b, d, e) and 800 ps duration for (c, f) with the same energy.

However, in the case of powders, free and/or shallowly trapped electrons (2000 cm^{-1}) decayed rapidly even within a few picoseconds (Figure 2d). Furthermore, the trapped electrons (11000 cm^{-1}) decrease more rapidly than free electrons. As reported previously,²⁷ the electron trapping at the defects in Na-doped STO increases the number of trapped electrons at 11000 cm^{-1} , but the intensity rather decreased. These results indicate that the recombination and the electron trapping take place in a few picoseconds region, and the trapped electrons recombine with holes more readily than free electrons. However, in the nanoseconds region (Figure 2f), the decay of free electrons, trapped electrons, and trapped holes decelerates (Figure 2f). As a result, their lifetimes become longer than those in SC. The decay kinetics of charge carriers in powder is more complex than in SC. Tentatively, these decay curves were fitted with multiexponential functions, and it was shown that more than six components were necessary to reproduce the decay

curves satisfactorily (Tables S2 and S3). This complexity comes from the recombination kinetics involving multiple trapping and detrapping cycles, as will be described later.

On the contrary, the decay of trapped holes on powders (20000 cm^{-1}) exhibits more complex behavior (Figures 2d–f): the absorption intensity gradually increases until $\sim 20 \text{ ps}$ (inset of Figure 2d). This time for the maximum becomes faster from ~ 100 to $\sim 20 \text{ ps}$ as the laser power increased from 1 to 6 μJ pulse as shown in Figure S1. These slow increases are ascribed to the accumulation of trapped carriers at the defects. With regard to the defects, there are several types whose depths are different, such as oxygen vacancies, Ti interstitials, surface hydroxyl groups, terminal and bridge oxygen ions, and so on.^{28–32} Among these traps, the charge carriers would hop over these sites until reaching to thermal equilibrium. The mobility of these trapped charge carriers should be small; hence, they will require some time for thermalization to occur.

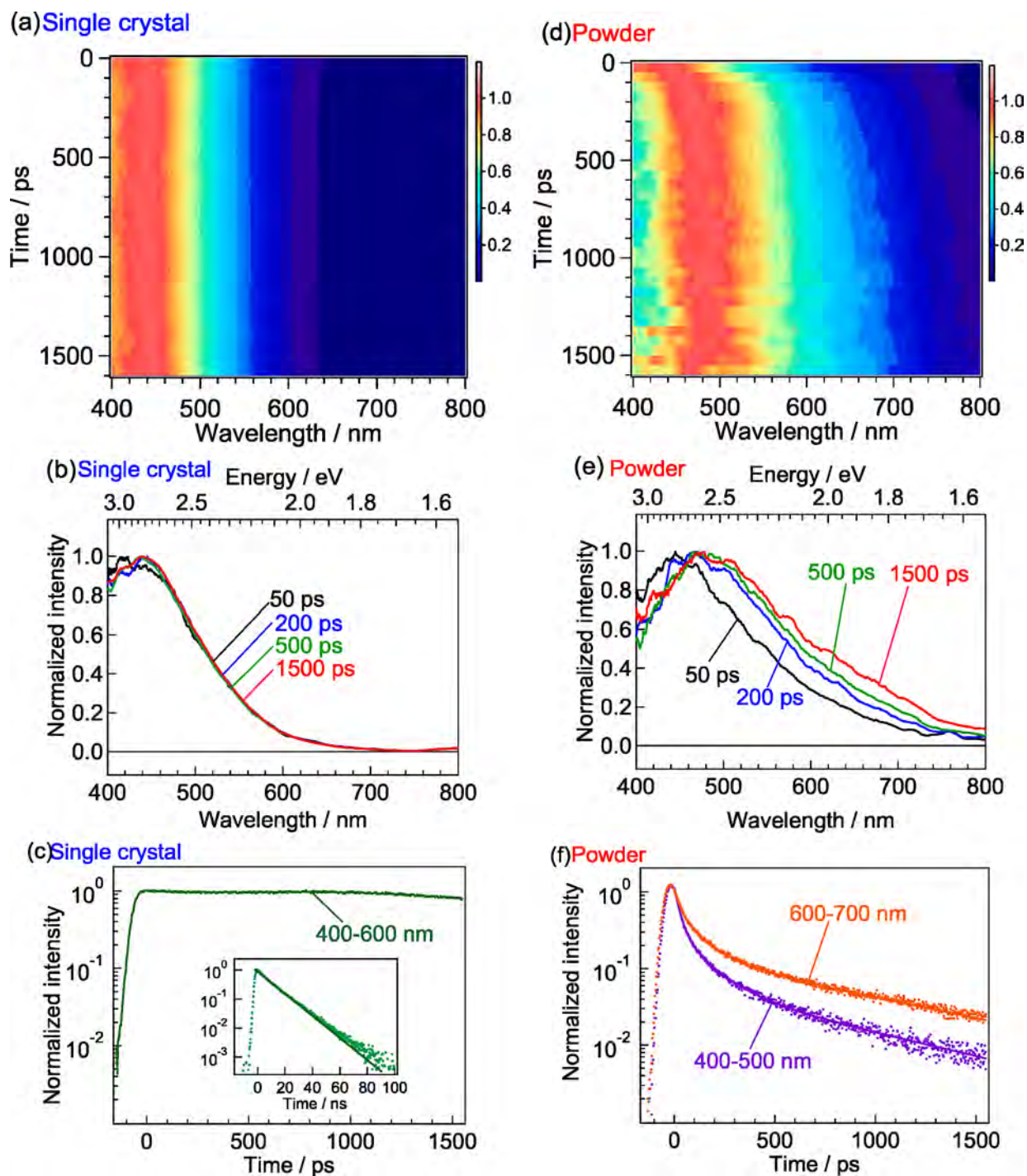


Figure 3. Image plot of time-resolved photoluminescence emitted from (a) single-crystal SrTiO₃ and (d) powder SrTiO₃, normalized to the maximum value. Photoluminescence spectra emitted from (b) single crystal and (e) powder. (c) Temporal profiles of the photoluminescence from single-crystal SrTiO₃ averaged between 400 and 600 nm. The inset shows the profiles until 100 ns after excitation. (f) Temporal profiles of the photoluminescence from powder SrTiO₃ averaged at 400–500 and 600–700 nm. The samples were excited by 355 nm laser pulses (90 fs duration, 6 μ J pulse⁻¹).

3.3. Difference of Radiative Recombination of Charge Carriers between the Single Crystal and Powder SrTiO₃.

The charge trapping process by defects was further investigated by measuring time-resolved PL spectra emitted from SC-STO after 355 nm laser pulse irradiation. As shown in Figure 3a, the emission peak measured at 0 ps is located at \sim 440 nm, and this peak position did not change up to 1500 ps. To illustrate the spectral shapes more clearly, the normalized PL spectra measured at 50, 200, 500, and 1500 ps are shown in Figure

3b, but the spectral shape is identical from 0 to 1500 ps. This emission is from the shallowly trapped photocarriers.³³ The lifetime of the PL was estimated from the temporal profiles of the averaged emission intensities between 400 and 600 nm (Figure 3c), and the decay curve was reproduced well by a single-exponential formula. The time constant was estimated to be $\tau_{\text{PL}} = 11.5 \pm 0.1$ ns, and this value seems to be little slower than that of the first component of the TA decay (Table S1, $\tau_1 = 5$ –8 ns). This result indicates that some little faster nonradiative decay

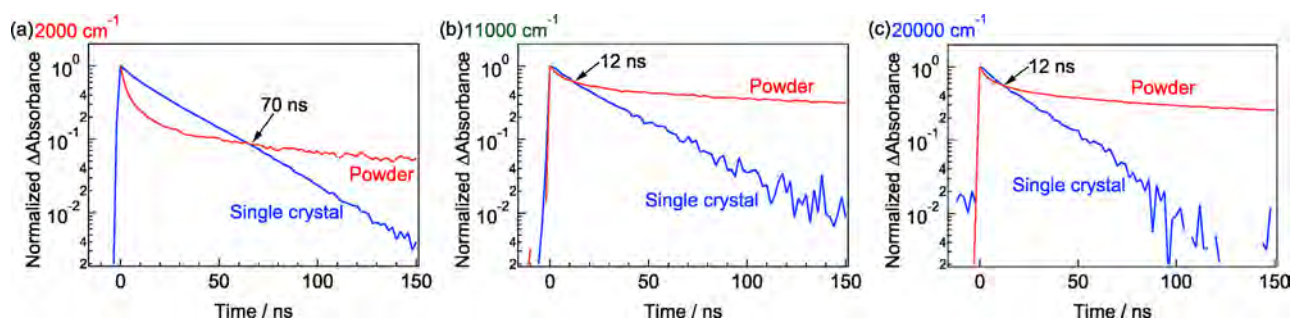


Figure 4. Decay curves of transient absorption measured at (a) 2000, (b) 11000, and (c) 20000 cm^{-1} for single-crystal and powder SrTiO_3 . The sample was excited by 355 nm laser pulse (800 ps duration, $6 \mu\text{J pulse}^{-1}$).

Scheme 1. Schematic Representation of the Acceleration and Deceleration of Photocarrier Recombination by the Defects on Powder SrTiO_3

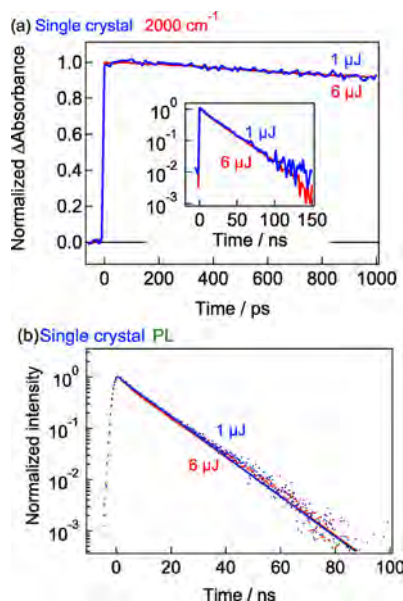
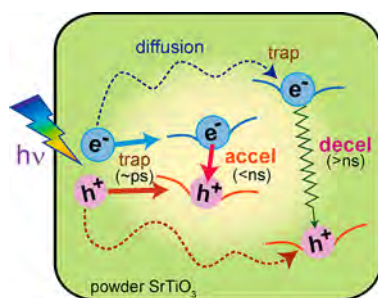


Figure 5. (a) Decay curves of normalized transient absorptions measured at 2000 cm^{-1} for single-crystal SrTiO_3 excited by 355 nm laser pulses with 90 fs duration. The inset shows those excited by 355 nm laser pulses with 800 ps duration. (b) Decay curves of normalized PL for single-crystal SrTiO_3 excited by 355 nm laser pulse (90 fs duration). Single-exponential curve-fitting results are also shown in (b). The obtained parameters are summarized in Table S2.

component is involved in the TA decay. However, the time resolution of the PL measurement is only ~ 3 ns in this region; hence, more precise experiments are necessary for the further analysis.

By contrast, the PL spectrum of the powder is totally different from that of the SC (Figure 3d). Just after the photoirradiation

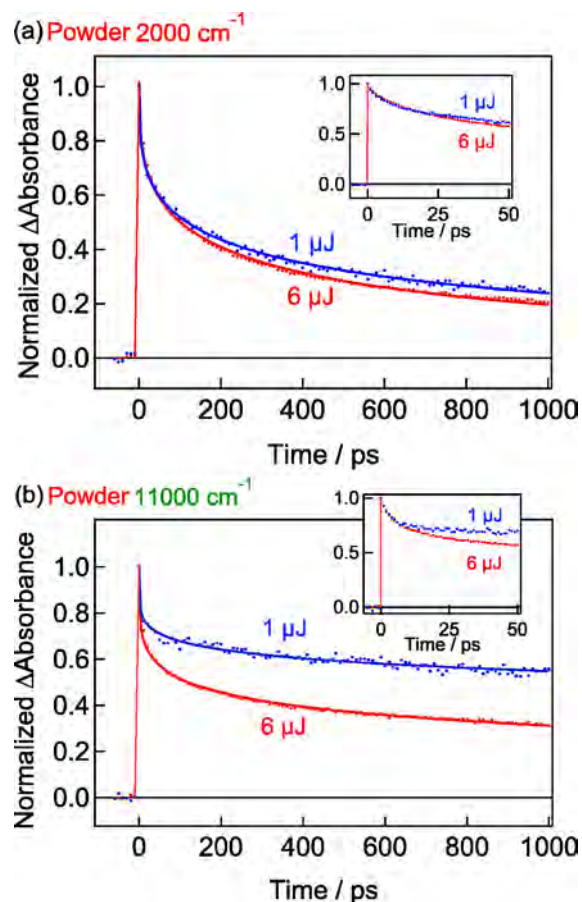


Figure 6. Decay curves of normalized transient absorptions measured at (a) 2000 and (b) 11000 cm^{-1} for powder SrTiO_3 excited by 355 nm laser pulse (90 fs duration). Stretched-exponential curve-fitting results are also shown. The obtained parameters are summarized in Tables S6 and S7.

(~ 0 ps), the peak position in the powder was located at the same position as in the SC (~ 440 nm). However, it gradually redshifted from 440 to 500 nm over a period of hundreds of picoseconds (Figure 3d,e). This result suggests that radiative recombination initially proceeds from the free and/or shallowly trapped carriers but gradually changes to deeply trapped charge carriers. In addition, Figure 3f shows that the decay of the 600–700 nm emission was slower than that at 400–500 nm. These results confirm that the radiative recombination of deeply trapped carriers is much slower than that of shallowly trapped carriers; i.e., powder defects decelerate the recombination.

3.4. Mechanism of the Formation of Long-Lived Photocarriers in Powders. To further examine the influence of the defects on the electron-decay kinetics, the decay curves of free electrons (2000 cm^{-1}) in SC and powder were compared (Figure 4a). The results show that the decay in SC is simple, but that in powder gradually slowed down, with several decay components (Table S3 and Table S4). As a result, the lifetime of free electrons in SC is longer than in powder in the early time region ($<70\text{ ns}$), but the situation is reversed after 70 ns . Similar results were also observed for the trapped electrons and trapped holes (Figure 4b,c), but the crossing point occurs earlier, at $\sim 12\text{ ns}$. This result confirms that the lifetime of photoexcited carriers in powder is shorter in a few nanoseconds region, but longer in the nanoseconds to milliseconds region. This means that the defects in powders have two effects: one is the acceleration of recombination and the other is deceleration of recombination in early and later time regions, respectively.

These contradictory dualistic effects can be explained as follows (Scheme 1). In the early time region, especially in the picoseconds region, powder defects accelerated the recombination. This is due to charge trapping at the defects. Just after the photoirradiation, the charge carriers have excess energy to diffuse into the bulk and the surface. However, there are numerous number of defects in powders, and the charge carriers will be trapped at these defects and diffusion will be prevented, keeping them closer together. In the few picoseconds region, the charge separation is not great enough; hence, electrons and holes will be captured when in the vicinity of one another. These closely trapped electrons/holes can hop to approach each other; hence, recombination will be accelerated in the picosecond region as shown in Scheme 1. In this way, the defects on powders can accelerate the recombination, especially in the picosecond region where the charge separation is not great enough to prevent it.

However, once the charge carriers can escape from the initial recombination process, they can diffuse and become separated by greater distances. Then they can occasionally be captured by traps far away from one another. In this case, the trapped carriers have to travel a long distance by repeated hopping or tunneling to get closer, so that recombination takes a long time. Hence, the lifetime of charge carriers in powders becomes longer than in SC, especially after the nanosecond region. The laser-power dependence also supported this mechanism. As shown in Figure 5, in the case of SC, no power dependence was observed in decay kinetics of both TA and PL: the decay curves measured at 1 and $6\text{ }\mu\text{J pulse}^{-1}$ are completely overlapping each other. This result suggests that the recombination proceeds in the first-order kinetics, which is often observed at low laser power excitation.²¹ However, in the case of powders, significant power dependence was observed: the decay of electrons becomes faster as the laser power increased from 1 to $6\text{ }\mu\text{J}$ as shown in Figure 6 and S1. Furthermore, the difference in deeply trapped electrons is larger than that in free and/or shallowly trapped electrons. These decay curves were well reproduced by the stretched exponential decay ($y = A \exp[-(x/\tau)^\beta]$) rather than second-order decay kinetics ($y = A c_0 / (k c_0 x + 1)$) as shown in Figure S2. The former is applicable to the recombination processes where the multiple trapping and detrapping cycles are involved,^{34,35} and the latter is for the bimolecular recombination of free carriers.^{36,37} These results support that the decelerated decay after nanosecond region is due to the trapping of charge carriers.

4. CONCLUSION

In conclusion, we found that the powder defects have dualistic properties of accelerating and decelerating electron–hole pair recombination. Just after photoirradiation, the defects trap the charge carriers and prevent their diffusion. As the electrons and holes remain in the vicinity of one another, recombination will be accelerated. However, once the photogenerated carriers escape from the initial trapping and recombination processes, they can spread by diffusion and become trapped far away from one another. In such case, the probability that electrons and holes meet will be reduced so that the lifetime of carriers becomes longer. These two contradictory effects are differentiated by whether electrons and holes are trapped in the same vicinity or far away one another. The fate of carriers is determined by how they can escape the initial trapping process by using the excess energy gained after photoirradiation. In fact, the longer lifetime of photocarriers is important to increase the photocatalytic activity, since the probability of carriers to meet with the reactant molecules increases as the lifetime of carriers becomes longer.^{16,17,27,38,39} Therefore, the control of this initial trapping process is the key to further improving the photocatalytic activity.

■ ASSOCIATED CONTENT

Supporting Information

The Supporting Information is available free of charge at <https://pubs.acs.org/doi/10.1021/acs.jpcc.0c03369>.

Fitting parameters of the decay curves, pump-pulse energy dependence (PDF)

■ AUTHOR INFORMATION

Corresponding Author

Akira Yamakata – Graduate School of Engineering, Toyota Technological Institute, Nagoya 468-8511, Japan; Cooperative Research Fellow, Institute for Catalysis, Hokkaido University, Sapporo 001-0021, Japan; orcid.org/0000-0003-3179-7588; Email: yamakata@toyota-ti.ac.jp

Author

Kosaku Kato – Graduate School of Engineering, Toyota Technological Institute, Nagoya 468-8511, Japan; orcid.org/0000-0002-9977-7439

Complete contact information is available at: <https://pubs.acs.org/doi/10.1021/acs.jpcc.0c03369>

Notes

The authors declare no competing financial interest.

■ ACKNOWLEDGMENTS

This work was supported by a Grant-in-Aid for Basic Research (B) (19H02820), Early-Career Scientists (20K15386), Scientific Research on Innovative Areas (Mixed Anion: 19H04708, Light-Energy Conversion: 20H05117), the Strategic Research Infrastructure Project of MEXT, and the Cooperative Research Program of Institute for Catalysis, Hokkaido University (17A1001).

■ REFERENCES

(1) Yao, T.; An, X.; Han, H.; Chen, J. Q.; Li, C. Photoelectrocatalytic Materials for Solar Water Splitting. *Adv. Energy Mater.* **2018**, *8*, 1800210.

- (2) Osterloh, F. E. Inorganic Materials as Catalysts for Photochemical Splitting of Water. *Chem. Mater.* **2008**, *20*, 35–54.
- (3) Kudo, A.; Miseki, Y. Heterogeneous Photocatalyst Materials for Water Splitting. *Chem. Soc. Rev.* **2009**, *38*, 253–278.
- (4) Xing, J.; Fang, W. Q.; Zhao, H. J.; Yang, H. G. Inorganic Photocatalysts for Overall Water Splitting. *Chem. - Asian J.* **2012**, *7*, 642–657.
- (5) Ismail, A. A.; Bahnemann, D. W. Photochemical Splitting of Water for Hydrogen Production by Photocatalysis: A Review. *Sol. Energy Mater. Sol. Cells* **2014**, *128*, 85–101.
- (6) Jafari, T.; Moharrer, E.; Amin, A. S.; Miao, R.; Song, W.; Suib, S. L. Photocatalytic Water Splitting - The Untamed Dream: A Review of Recent Advances. *Molecules* **2016**, *21*, 900.
- (7) Takata, T.; Domen, K. Particulate Photocatalysts for Water Splitting: Recent Advances and Future Prospects. *ACS Energy Lett.* **2019**, *4*, 542–549.
- (8) Wang, Z.; Li, C.; Domen, K. Recent Developments in Heterogeneous Photocatalysts for Solar-Driven Overall Water Splitting. *Chem. Soc. Rev.* **2019**, *48*, 2109–2125.
- (9) Zhang, H.; Chen, G.; Bahnemann, D. W. Photoelectrocatalytic Materials for Environmental Applications. *J. Mater. Chem.* **2009**, *19*, 5089–5121.
- (10) *Handbook of Optical Constants of Solids*; Palik, E. D., Ed.; Academic Press: 1985.
- (11) Cardona, M. Optical Properties and Band Structure of SrTiO₃ and BaTiO₃. *Phys. Rev.* **1965**, *140*, A651–A655.
- (12) Pankove, J. I. *Optical Processes in Semiconductors*; Dover books explaining science and mathematics; Dover: 1975.
- (13) Bemski, G. Recombination Properties of Gold in Silicon. *Phys. Rev.* **1958**, *111*, 1515–1518.
- (14) Curtis, O. L.; Cleland, J. W.; Crawford, J. H. Radiation-Induced Recombination Centers in Germanium. *J. Appl. Phys.* **1958**, *29*, 1722–1729.
- (15) Glaenger, R. H.; Wolf, C. J. Recombination in Gamma-Irradiated Silicon. *J. Appl. Phys.* **1965**, *36*, 2197–2201.
- (16) Yamakata, A.; Vequizo, J. J. M.; Kawaguchi, M. Behavior and Energy State of Photogenerated Charge Carriers in Single-Crystalline and Polycrystalline Powder SrTiO₃ Studied by Time-Resolved Absorption Spectroscopy in the Visible to Mid-Infrared Region. *J. Phys. Chem. C* **2015**, *119*, 1880–1885.
- (17) Vequizo, J. J. M.; Matsunaga, H.; Ishiku, T.; Kamimura, S.; Ohno, T.; Yamakata, A. Trapping-Induced Enhancement of Photocatalytic Activity on Brookite TiO₂ Powders: Comparison with Anatase and Rutile TiO₂ Powders. *ACS Catal.* **2017**, *7*, 2644–2651.
- (18) Yamakata, A.; Ishibashi, T. A.; Onishi, H. Time-Resolved Infrared Absorption Spectroscopy of Photogenerated Electrons in Platinized TiO₂ Particles. *Chem. Phys. Lett.* **2001**, *333*, 271–277.
- (19) Yamakata, A.; Kawaguchi, M.; Nishimura, N.; Minegishi, T.; Kubota, J.; Domen, K. Behavior and Energy States of Photogenerated Charge Carriers on Pt- or CoOx -Loaded LaTiO₂N Photocatalysts: Time-Resolved Visible to Mid-Infrared Absorption Study. *J. Phys. Chem. C* **2014**, *118*, 23897–23906.
- (20) Frederikse, H. P. R.; Thurber, W. R.; Hosler, W. R. Electronic Transport in Strontium Titanate. *Phys. Rev.* **1964**, *134*, A442–A445.
- (21) Yasuda, H.; Kanemitsu, Y. Dynamics of Nonlinear Blue Photoluminescence and Auger Recombination in SrTiO₃. *Phys. Rev. B: Condens. Matter Mater. Phys.* **2008**, *77*, 193202.
- (22) Yamakata, A.; Yeilin, H.; Kawaguchi, M.; Hisatomi, T.; Kubota, J.; Sakata, Y.; Domen, K. Morphology-Sensitive Trapping States of Photogenerated Charge Carriers on SrTiO₃ Particles Studied by Time-Resolved Visible to Mid-IR Absorption Spectroscopy: The Effects of Molten Salt Flux Treatments. *J. Photochem. Photobiol., A* **2015**, *313*, 168–175.
- (23) Yamakata, A.; Ishibashi, T. A.; Onishi, H. Water- and Oxygen-Induced Decay Kinetics of Photogenerated Electrons in TiO₂ and Pt/TiO₂: A Time-Resolved Infrared Absorption Study. *J. Phys. Chem. B* **2001**, *105*, 7258–7262.
- (24) Yamakata, A.; Ishibashi, T. A.; Onishi, H. Electron- and Hole-Capture Reactions on Pt/TiO₂ Photocatalyst Exposed to Methanol Vapor Studied with Time-Resolved Infrared Absorption Spectroscopy. *J. Phys. Chem. B* **2002**, *106*, 9122–9125.
- (25) Henderson, M. A. A Surface Science Perspective on TiO₂ Photocatalysis. *Surf. Sci. Rep.* **2011**, *66*, 185–297.
- (26) Chen, T.; Feng, Z.; Wu, G.; Shi, J.; Ma, G.; Ying, P.; Li, C. Mechanistic Studies of Photocatalytic Reaction of Methanol for Hydrogen Production on Pt/TiO₂ by in Situ Fourier Transform IR and Time-Resolved IR Spectroscopy. *J. Phys. Chem. C* **2007**, *111*, 8005–8014.
- (27) Kato, K.; Jiang, J.; Sakata, Y.; Yamakata, A. Effect of Na-Doping on Electron Decay Kinetics in SrTiO₃ Photocatalyst. *ChemCatChem* **2019**, *11*, 6349.
- (28) Hoffmann, M. R.; Martin, S. T.; Choi, W.; Bahnemann, D. W. Environmental Applications of Semiconductor Photocatalysis. *Chem. Rev.* **1995**, *95*, 69–96.
- (29) Salvador, P. On the Nature of Photogenerated Radical Species Active in the Oxidative Degradation of Dissolved Pollutants with TiO₂ Aqueous Suspensions: A Revision in the Light of the Electronic Structure of Adsorbed Water. *J. Phys. Chem. C* **2007**, *111*, 17038–17043.
- (30) Ji, Y.; Wang, B.; Luo, Y. Location of Trapped Hole on Rutile-TiO₂ (110) Surface and Its Role in Water Oxidation. *J. Phys. Chem. C* **2012**, *116*, 7863–7866.
- (31) Thompson, T. L.; Yates, J. T. Monitoring Hole Trapping in Photoexcited TiO₂ (110) Using a Surface Photoreaction. *J. Phys. Chem. B* **2005**, *109*, 18230–18236.
- (32) Pan, X.; Yang, M. Q.; Fu, X.; Zhang, N.; Xu, Y. J. Defective TiO₂ with Oxygen Vacancies: Synthesis, Properties and Photocatalytic Applications. *Nanoscale* **2013**, *5*, 3601–3614.
- (33) Kanemitsu, Y.; Yamada, Y. Light Emission from SrTiO₃. *Phys. Status Solidi B* **2011**, *248*, 416–421.
- (34) Nelson, J.; Haque, S. A.; Klug, D. R.; Durrant, J. R. Trap-Limited Recombination in Dye-Sensitized Nanocrystalline Metal Oxide Electrodes. *Phys. Rev. B: Condens. Matter Mater. Phys.* **2001**, *63*, 205321.
- (35) Barzykin, A. V.; Tachiya, M. Mechanism of Charge Recombination in Dye-Sensitized Nanocrystalline Semiconductors: Random Flight Model. *J. Phys. Chem. B* **2002**, *106*, 4356–4363.
- (36) Furube, A.; Asahi, T.; Masuhara, H.; Yamashita, H.; Anpo, M. Charge Carrier Dynamics of Standard TiO₂ Catalysts Revealed by Femtosecond Diffuse Reflectance Spectroscopy. *J. Phys. Chem. B* **1999**, *103*, 3120–3127.
- (37) Schneider, J.; Nikitin, K.; Wark, M.; Bahnemann, D. W.; Marschall, R. Improved Charge Carrier Separation in Barium Tantalate Composites Investigated by Laser Flash Photolysis. *Phys. Chem. Chem. Phys.* **2016**, *18*, 10719–10726.
- (38) Bacha, A. U. R.; Nabi, I.; Fu, Z.; Li, K.; Cheng, H.; Zhang, L. A Comparative Study of Bismuth-Based Photocatalysts with Titanium Dioxide for Perfluorooctanoic Acid Degradation. *Chin. Chem. Lett.* **2019**, *30*, 2225–2230.
- (39) Sun, N.; Qu, Y.; Yang, C.; Yang, Z.; Yan, R.; E, W.; Zhang, Z.; Li, Z.; Li, H.; Khan, I.; Sun, R.; Jing, L.; Fu, H. Efficiently Photocatalytic Degradation of Monochlorophenol on In-Situ Fabricated BiPO₄/β-Bi₂O₃ Heterojunction Microspheres and O₂-Free Hole-Induced Selective Dechlorination Conversion with H₂ Evolution. *Appl. Catal., B* **2020**, *263*, 118313.

NOTE ADDED AFTER ASAP PUBLICATION

This article published with errors in the Supporting Information, where the inset of Figure S1 is missing, and its Figure caption is not correct. The corrected file published May 8, 2020.

Identification of Individual Electron- and Hole-Transfer Kinetics at $\text{CoO}_x/\text{BiVO}_4/\text{SnO}_2$ Double Heterojunctions

Akira Yamakata,^{*,†,‡,ⓑ} Chandana Sampath Kumara Ranasinghe,[†] Naruki Hayashi,[†] Kosaku Kato,^{†,ⓑ} and Junie Jhon M. Vequizo^{†,§}

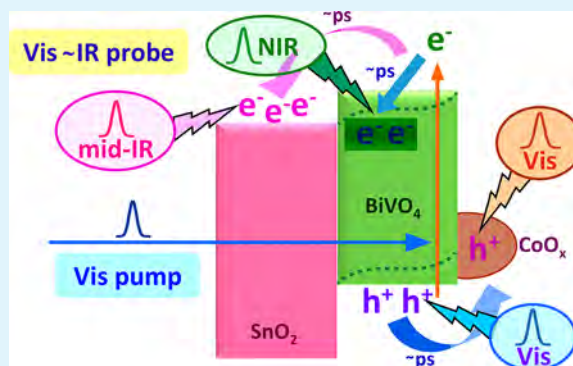
[†]Graduate School of Engineering, Toyota Technological Institute, 2-12-1 Hisakata, Tempaku, Nagoya 468-8511, Japan

[‡]Cooperative Research Fellow, Institute for Catalysis, Hokkaido University, Hokkaido 001-0021, Japan

Supporting Information

ABSTRACT: The fabrication of heterojunctions with different band gap semiconductors is a promising approach to increase photoelectrochemical (PEC) activity. The PEC activity is determined by the charge separation; hence, the behaviors of charge carriers at the junctions should be elucidated. However, it has been quite challenging since the distinction of carriers located in different layers has been extremely hard. In this work, we succeeded in the identification of the individual electron- and hole-transfer kinetics at $\text{CoO}_x/\text{BiVO}_4/\text{SnO}_2$ double heterojunctions by measuring transient absorption (TA) from the visible to mid-IR region: we found that the absorption peaks of electrons and holes depend on the materials. From the change in spectral shape after the selective photoexcitation of BiVO_4 , it was confirmed that electrons excited in the BiVO_4 rapidly transferred to the SnO_2 layer after ~ 3 ps, but the holes remained in the BiVO_4 and further transferred to CoO_x in a few picoseconds. As a result, recombination of charge carriers was suppressed and 2.4 and 3.6 times a large amount of carriers are surviving at $5 \mu\text{s}$ on $\text{BiVO}_4/\text{SnO}_2$ and $\text{CoO}_x/\text{BiVO}_4/\text{SnO}_2$, respectively, compared to bare BiVO_4 . For such picosecond-rapid and effective charge separation, the previously well proposed sole intralayer or interlayer charge separation mechanism is not enough. Hence the synergetic effect of these two mechanisms, the band-bending-assisted charge transfer across the heterojunction, is proposed. The enhanced PEC activity of $\text{CoO}_x/\text{BiVO}_4/\text{SnO}_2$ electrodes was reasonably explained by this synergistic charge separation kinetics. This fundamental knowledge of charge carrier dynamics will be beneficial for the design of superior solar energy conversion systems.

KEYWORDS: photoelectrodes, heterojunction, photogenerated charge carriers, charge-trapping, recombination, time-resolved absorption spectroscopy



1. INTRODUCTION

Photoelectrochemical (PEC) water splitting reactions are attractive methods for establishing artificial photosynthesis without any burden to the environment. From the discovery of H_2 and O_2 evolution from TiO_2 photoelectrodes,¹ many metal oxide-based semiconductors have been utilized for photoelectrodes.^{2–7} Among them, BiVO_4 is currently the most promising material for visible-light-responsive photoelectrodes,^{8–20} since it has a band gap of 2.4 eV and a suitable valence band maximum (VBM) for water oxidation.⁸ However, the rapid recombination and the low mobilities of carriers for the effective reactions present obstacles. The efficiency of the PEC system is mostly determined by the recombination processes of photogenerated charge carriers, so efficient charge separation is essential to prevent recombination. Fabrication of heterojunctions with different band gap materials is the most effective method of enhancing charge separation.²¹ Therefore, many heterostructures, such as $\text{SnO}_2/\text{BiVO}_4$,^{12–16,20} $\text{BiVO}_4/\text{WO}_3$,^{17,18,22,23} $\text{BiVO}_4/\text{SnO}_2/\text{WO}_3$,¹² $\text{BiVO}_4/\text{CoO}_x$,^{19,24–26}

and $\text{BiVO}_4/\text{CoPi}$,^{24,27} have been developed. However, correlating the enhanced photocatalytic performance with the behavior of photogenerated charge carriers using spectroscopic techniques is still not yet fully established. For the design of superior heterojunctions, the behavior of photogenerated electrons and holes at the junctions should be elucidated.

Transient absorption spectroscopy (TAS) is a powerful method for the study of charge carrier dynamics. Trapped holes give characteristic absorption in the visible region; hence, vis-TAS has been performed for TiO_2 ,^{28–32} Fe_2O_3 ,^{33,34} and BiVO_4 ,^{18,35–40} etc. On the other hand, free and shallowly trapped electrons give structureless broad absorption signals in the IR region,⁴¹ so IR-TAS has been applied to study the electron-decay kinetics of TiO_2 ,^{29,42,43} BiVO_4 ,^{38,44} SrTiO_3 ,³¹ and GaN ,⁴⁵ etc. These works have successfully elucidated the

Received: November 19, 2019

Accepted: December 23, 2019

Published: December 23, 2019

photodynamics of semiconductor photocatalysts and PEC systems; however, the method is not yet sufficient to elucidate the intricate charge carrier interactions at the heterojunctions.

The formation of heterojunctions strongly affects the lifetime of photogenerated charge carriers. To date, at least two different mechanisms have been considered.^{26,46} Barroso et al.,³³ for instance, proposed that the extended lifetime of holes inferred from TAS experiment on CoPi/hematite electrodes is ascribed to enhanced upward band-bending. On the other hand, Grigioni et al.^{37,44} and Loiodice et al.¹⁸ suggested a different mechanism on the BiVO₄/WO₃ system; in particular, the charge transfer is found to take place across the junction as evidenced from their TAS findings. In effect, the lifetimes of electrons and holes become longer by forming the heterojunction. However, the interpretations do not coincide; one is ascribed to the intralayer charge separation in the original layer, and the other is the interlayer charge separation across the heterojunction. Although the mechanism could be different by the material combination, the problems come from the lack of information about the exact location of accumulated electrons and holes as well as their distributions in the heterojunctions: the spectral information given by the wavelength-limited conventional TAS is not enough for the detailed analysis.

In this work, we succeeded in elucidating the individual electron- and hole-transfer kinetics at intricate heterojunctions such as CoO_x/BiVO₄/SnO₂ by measuring TAS from the visible to mid-IR region. This measurement enabled the distinction between electrons and holes located in SnO₂, BiVO₄, and CoO_x. By analyzing the changes in the spectral shape of CoO_x/BiVO₄/SnO₂, we obtained explicit evidence of the electron transfer from BiVO₄ to SnO₂ as well as hole transfer from BiVO₄ to CoO_x taking place in a few picoseconds after selective photoexcitation of the BiVO₄. On the basis of the kinetic and quantitative analysis of the charge separation, the mechanism of rapid and effective charge separation was unraveled. The band-bending not only enhances the intralayer charge separation but also accelerates the interlayer charge transportation. The synergistic band-bending-assisted charge transportation across the junctions is projected as the main reason for such effective charge separation.

2. EXPERIMENTAL SECTION

BiVO₄-based thin films were fabricated on FTO substrates (2 cm × 1 cm, Sigma-Aldrich) or on bare CaF₂ circular plates (Pier Optics) by spray pyrolysis deposition (SPD) following the reported procedure in the literature.^{20,27} The active area of photoelectrodes was 1 cm². To deposit the SnO₂ layer, a precursor solution consisting of 30 mM SnCl₄·5H₂O (Kanto Chemicals Co., Inc.) dissolved in ethanol (20 mL; Amakasu Chemical Industries) was sprayed onto the FTO substrate at 450 °C (at a spray rate of 5 mL min⁻¹). The as-deposited SnO₂ thin film was then annealed at 450 °C in ambient air for 30 min. A BiVO₄ layer was subsequently deposited on the annealed SnO₂ layer by spraying (rate, 2 mL min⁻¹) a precursor solution [10 mM Bi(NO₃)₃ (Sigma-Aldrich) and 10 mM NH₄VO₃ (Kanto Chemicals)] dissolved in a mixture of acetic acid (30 mL; Kanto Chemicals) and ethanol (70 mL). After depositing the BiVO₄ layer, the resulting BiVO₄/SnO₂/FTO heterostructure was further annealed at 450 °C in air for 30 min. A 40 mM amount of Co(NO₃)₂ (Wako Pure Chemical Industries, Ltd.) dissolved in ethanol (40 mL) was used as precursor for CoO_x deposition, which was carried out by spraying the precursor solution onto the BiVO₄/SnO₂/FTO at a rate of 5 mL min⁻¹ at 450 °C, followed by annealing in air at 450 °C for 30 min. The thicknesses of the FTO, SnO₂, and BiVO₄ are estimated to be ~600, ~100–300, and ~400–800 nm, respectively (Figure S3). For transient absorption

measurements, these thin films (SnO₂, BiVO₄, CoO_x, BiVO₄/SnO₂, and CoO_x/BiVO₄/SnO₂) were prepared on CaF₂ substrates in the same experimental procedure.

Photoelectrochemical measurements were carried out using a three-electrode system consisting of Ag/AgCl, Pt sheet, and the photoelectrodes prepared on FTO substrates. A 0.1 M potassium phosphate (K₂HPO₄ + KH₂PO₄, Wako Chemicals) aqueous solution (pH = 7.0) was used as the electrolyte. Prior to photoelectrochemical measurement, the solution was deaerated by Ar gas purging for 20 min. The applied potential was linearly scanned from -0.5 to +1.0 V vs Ag/AgCl at a rate of 10 mV s⁻¹. The photoelectrodes was irradiated from the FTO/glass side with a 455 nm cw-light (50 mW, Thorlabs M45SL3).

Microsecond transient absorption measurements were performed from the visible to mid-IR region (25000–1000 cm⁻¹) using a custom-built original spectrometer, as reported in our previous work.⁴⁷ Briefly, IR light irradiated from an MoSi₂ coil and visible to near-IR (NIR) light from a halogen lamp were used as probe lights in the mid-IR (6000–1000 cm⁻¹) and visible to NIR regions (25000–6000 cm⁻¹), respectively. The transmitted light from the sample was monochromated using a spectrometer furnished with optical gratings. In the visible to NIR region, the monochromated light was detected by Si and InGaAs photodetectors, while, in the mid-IR region, it was detected by MCT (Kolmar). The electrical signal was amplified using an AC-coupled amplifier (SR560, Stanford Research Systems). The signal was then monitored and recorded using an oscilloscope (LeCroy, WaveRunner 44Xi). As pump laser pulses, 355 nm pulses (0.5 mJ pulse⁻¹) and 480 nm pulses (5 mJ pulse⁻¹) from a Nd:YAG laser system (Continuum, Surelite I and Surelite OPO; duration, 6 ns; repetition rate, 5–0.01 Hz) were used. For the transient absorption spectra, the decay curves were measured at every 200 cm⁻¹ interval at 5 Hz laser pulse irradiation and reconstructed to the spectra. For the quantitative analysis of the distribution of charge carriers in each layer, the decay curves were measured precisely by reducing the repetition rate of the laser to 1–0.01 Hz.

Ultrafast transient visible to mid-IR absorption measurements were performed using a femtosecond Ti-sapphire laser system (Spectra-Physics, Solstice and TOPAS prime and TOPAS NDFG; duration, 90 fs; repetition rate, 1 kHz).⁴⁷ In the mid-IR region, the transmitted light from the sample was detected using an MCT array detector (128 ch, Infrared System Development). In the visible and NIR regions, the transmitted light was detected using a photomultiplier and InGaAs detectors. To excite the band gap of the BiVO₄ layer in the BiVO₄/SnO₂ and CoO_x/BiVO₄/SnO₂ heterojunctions, 480 nm laser pulses (8 μJ pulse⁻¹) were used, and the transient absorptions at 20000 (500 nm), 12000 (833 nm), 6000 (1667 nm), and 2000 cm⁻¹ (5000 nm) were measured. All transient absorption measurements were performed in vacuum without any externally applied potential.

3. RESULTS AND DISCUSSION

3.1. Photoelectrochemical Activity of CoO_x/BiVO₄/SnO₂ Heterojunctions. The photoelectrochemical response of the fabricated electrodes was measured under 455 nm visible light irradiation (Figure 1). In the case of bare BiVO₄/FTO, the anodic photocurrent for water oxidation was observed above ~0.0 V. The amplitude of this oxidation current increased as the applied potential became more positive, and reached 0.21 mA cm⁻² at 1.0 V. When an SnO₂ layer was added between the BiVO₄ and the FTO, the photocurrent increased to 0.51 mA cm⁻² at 1.0 V with a 2.4-fold enhancement compared to bare BiVO₄. The energy of the irradiated light (455 nm, ~2.7 eV) was too low to excite the band gap of SnO₂ (~3.8 eV), so the bare SnO₂ electrode showed a negligible photocurrent (not shown). The enhancement of photoelectrochemical activity of BiVO₄ by the addition of SnO₂ layer is reported in the literature,^{12–16,20}

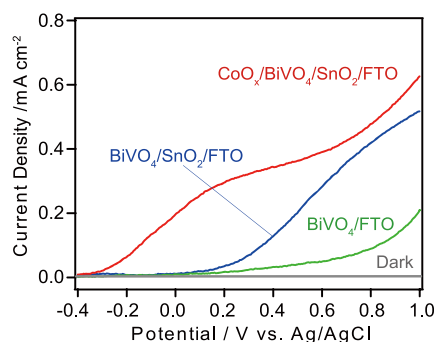


Figure 1. Photoelectrochemical response of bare BiVO_4 , $\text{BiVO}_4/\text{SnO}_2$, and $\text{CoO}_x/\text{BiVO}_4/\text{SnO}_2$ thin film electrodes fabricated on FTO glass under 455 nm (50 mW cm^{-2}) light irradiation in 0.1 M potassium phosphate (pH = 7.0). The dark current for $\text{CoO}_x/\text{BiVO}_4/\text{SnO}_2$ is also shown.

and the reasonable results were also obtained in our experiments.

After loading CoO_x particles on the BiVO_4 side of $\text{BiVO}_4/\text{SnO}_2/\text{FTO}$, the onset potential shifted from 0.0 to -0.3 V (Figure 1). The anodic photocurrent further increased, reaching 0.62 mA cm^{-2} at $+1.0 \text{ V}$, indicating a 3.1-fold increase compared to that of bare BiVO_4 . The negative shift of the onset potential and the activity enhancement by loading CoO_x on BiVO_4 were reported in the literature,^{24–26,48} and similar and consistent results were obtained in this experiment.

3.2. Transient Absorption Spectra of Electrons and Holes in Bare SnO_2 and Bare BiVO_4 . In order to elucidate the mechanism of the activity enhancement of $\text{CoO}_x/\text{BiVO}_4/\text{SnO}_2$ heterojunctions, we first measured the transient absorption spectra of electrons and holes in bare SnO_2 and bare BiVO_4 layers after 355 nm UV pulse irradiation. In this experiment, we first used well characterized commercial SnO_2 powder (Kojundo Chemical Laboratory) and laboratory-synthesized BiVO_4 powder^{49,50} and compared them with the fabricated thin films. In the case of bare SnO_2 powder (Figure 2A), a broad absorption was observed below 6000 cm^{-1} , wherein the absorption intensity increased with decreasing wavenumber. This absorption is ascribed to free electrons and/or shallowly trapped electrons,^{41,51} since the decay was decelerated by the exposure to CH_3OH but little accelerated by the exposure to O_2 gas as shown in Figure 2B.⁴³ In contrast, no absorption signal was observed at $25000\text{--}5000 \text{ cm}^{-1}$. These results indicate that most of the electrons survive as free or shallowly trapped electrons, and the number of deeply trapped electrons in bare SnO_2 is negligibly small. Trapped holes should be present in SnO_2 , but no signal was detected up to 25000 cm^{-1} . If trapped holes were present, a signal above 25000 cm^{-1} ($<400 \text{ nm}$) would be expected, since the trapped holes often provide absorption near the band gap, especially in the UV to visible region.^{29,33,34,36,38,40,47} It is noted that the similar shaped transient absorption spectra were also observed for SnO_2 thin film fabricated by splay pyrolysis (Figure S10A).

In the case of bare BiVO_4 powder (Figure 3B), the shape of the absorption spectra was totally different from that of SnO_2 : sharp and very broad absorption bands were observed at 20400 and $18000\text{--}3000 \text{ cm}^{-1}$, respectively. The absorptions at ~ 20000 and $\sim 6000 \text{ cm}^{-1}$ are assigned to trapped holes and trapped electrons, since these decays were accelerated and decelerated by the exposure to HCOOH , respectively (Figure 3B,C). In this case, HCOOH worked as a more effective hole-

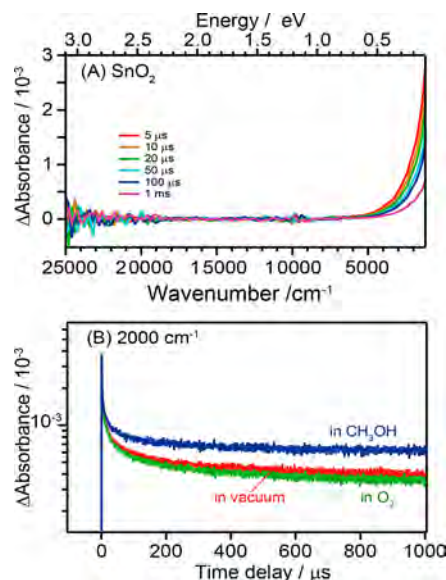


Figure 2. (A) Transient absorption spectra of SnO_2 powder measured after UV laser pulse irradiation (355 nm, 6 ns duration, $0.5 \text{ mJ pulse}^{-1}$, and 5 Hz repetition rate) in vacuum. (B) Decay curves measured at 2000 cm^{-1} after UV laser pulse irradiation (355 nm, $0.5 \text{ mJ pulse}^{-1}$, and 1 Hz repetition rate) in vacuum and in 20 Torr CH_3OH and O_2 gases.

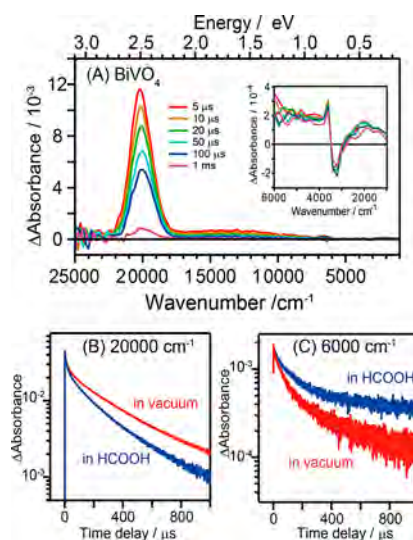


Figure 3. (A) Transient absorption spectra of BiVO_4 powder measured after UV laser pulse irradiation (355 nm, 6 ns duration, $0.5 \text{ mJ pulse}^{-1}$, and 5 Hz repetition rate) in vacuum. The negative band centered at $\sim 3200 \text{ cm}^{-1}$ is due to the desorption of adsorbed water by the laser irradiation. (B) Decay curves measured at 20000 cm^{-1} in vacuum and in 20 Torr HCOOH gas. (C) Decay curves measured at 6000 cm^{-1} in vacuum and in 20 Torr HCOOH gas. These decay curves were measured after UV laser pulse irradiation (355 nm, $2.5 \text{ mJ pulse}^{-1}$, and 1 Hz repetition rate).

scavenger than CH_3OH . It is noted that similar shaped transient absorption spectra were observed for BiVO_4 films fabricated by splay pyrolysis (Figure S10B). In each case, free and shallowly trapped electrons were absent in BiVO_4 .

These results confirm that the spectral profiles and peak positions of electrons and holes are different between SnO_2 and BiVO_4 . Therefore, we can study the electron- and hole-

transfer processes at the heterojunctions by analyzing the spectral changes measured from the visible to mid-IR region.

3.3. Transient Absorption Spectra of $\text{CoO}_x/\text{BiVO}_4/\text{SnO}_2$ Heterojunctions Induced by Charge Transfers from the BiVO_4 Layer. In order to investigate the charge-transfer processes from BiVO_4 to other layers, the BiVO_4 layer was selectively photoexcited by 480 nm (20833 cm^{-1}) pulse. First, the photoresponses of bare SnO_2 , bare CoO_x , and bare BiVO_4 under 480 nm pump pulse irradiation were measured (Figure 4). For the bare SnO_2 layer, negligibly small absorption

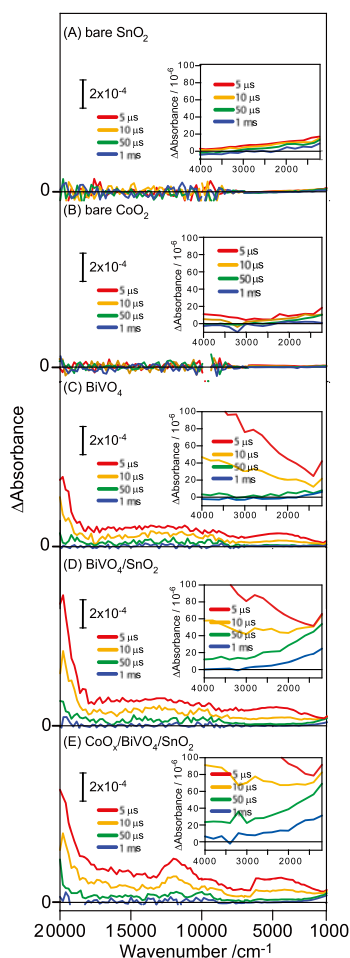


Figure 4. Transition absorption spectra of bare SnO_2 (A), bare BiVO_4 (B), bare CoO_x (C), $\text{BiVO}_4/\text{SnO}_2$ (D), and $\text{CoO}_x/\text{BiVO}_4/\text{SnO}_2$ (E) after visible laser pulse irradiation (480 nm, 6 ns duration, 5 mJ pulse $^{-1}$, and 5 Hz repetition rate) in vacuum. The laser pulses were irradiated from the CaF_2 plate side.

was observed over the entire region from 20000 to 1000 cm^{-1} (Figure 4A), because the 480 nm light was not energetic enough to excite the band gap of SnO_2 (3.8 eV). For the CoO_x , the absorption was also negligible (Figure 4B), either because the lifetime of photogenerated charge carriers was too short or because the amount of loaded CoO_x was very small. In the case of bare BiVO_4 , almost identical spectra as compared to those measured by 355 nm excitation (Figure S10B) were observed, with a sharp peak and a very broad absorption at 20000–18000 and 18000–3000 cm^{-1} , respectively (Figure 4C). These results suggest that the absorption spectra of electrons and holes in bare BiVO_4 do not differ with changes in the pump pulse energy from 355 to 480 nm.

However, when an SnO_2 layer was fabricated under the BiVO_4 layer, the spectral shape changed from that of bare BiVO_4 (Figure 4D). The similar shaped transient absorption was observed at 20000–4000 cm^{-1} , but a characteristic absorption of free electrons increased in intensity at 4000–1000 cm^{-1} . Since the electrons in BiVO_4 do not absorb below 4000 cm^{-1} (Figures 4C and S10B) and the 480 nm pulse hardly excites the SnO_2 layer (Figure 4A), this result strongly supports that part of the electrons excited in the BiVO_4 layer is transferred to the SnO_2 layer. This process is energetically favorable since the conduction band minimum (CBM) of SnO_2 is lower than that of BiVO_4 ,^{13,16,52} as shown in Figure 5. On the contrary, the valence band maximum of SnO_2 is lower than that of BiVO_4 ,⁵² so the holes remained in the BiVO_4 layer.^{13,16}

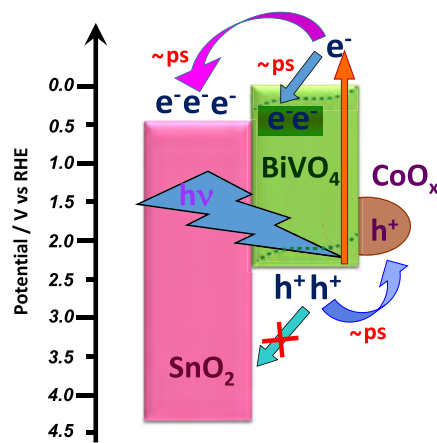


Figure 5. Schematic band alignment of the $\text{CoO}_x/\text{BiVO}_4/\text{SnO}_2$ heterojunction. The BiVO_4 layer was excited by visible laser pulses through the SnO_2 layer. The possible electron- and hole-transfer processes are shown. The band alignment was determined by the Mott–Schottky plot (Figure S5).

By loading CoO_x particles on $\text{BiVO}_4/\text{SnO}_2$ (Figure 4E), the spectral shape was further changed. The absorption intensity at $\sim 20000 \text{ cm}^{-1}$ slightly decreased, but that at $< 3000 \text{ cm}^{-1}$ increased. Furthermore, the absorption intensity at 12000 cm^{-1} was increased by CoO_x loading. This absorption was assigned to the d–d transition of Co^{3+} formed by the hole capture of Co^{2+} .^{33,47,53} These results reveal that holes generated in BiVO_4 were transferred from BiVO_4 to CoO_x , and the lifetime of electrons in BiVO_4 becomes longer, as demonstrated for $\text{LaTiO}_2\text{N}^{47}$ and Ta_3N_5 powders.⁵⁴

3.4. Electron- and Hole-Transfer Kinetics at the $\text{CoO}_x/\text{BiVO}_4/\text{SnO}_2$ Heterojunctions. The detailed charge-transfer processes at the $\text{CoO}_x/\text{BiVO}_4/\text{SnO}_2$ heterojunctions were studied by measuring the decay curves of electrons and holes. In the case of bare BiVO_4 (Figure 6A), the decay of free electrons at 2000 cm^{-1} consisted of at least two components: first, more than 50% of the electrons decayed within 5 ps, and second, the number of remaining electrons gradually decreased after 5 ps. The fast component can be ascribed to electron-trapping at the defects as reported by Suzuki et al.,³⁸ because the number of counteractive holes does not decrease, as shown in the inset of Figure 6G.

When an SnO_2 layer was fabricated under the BiVO_4 layer, the decay of free electrons decelerated significantly after ~ 3 ps (inset of Figure 6A). As a result, more than 10 times as many

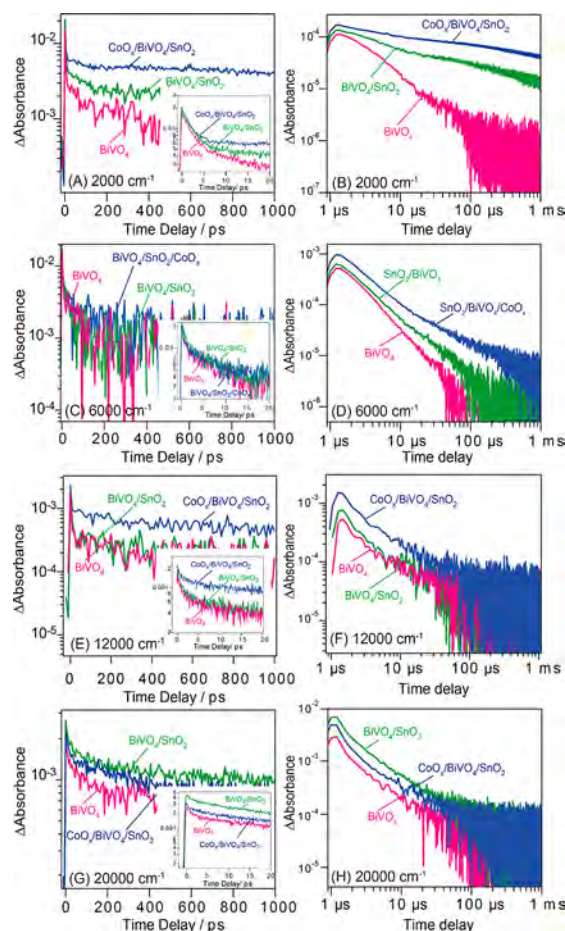


Figure 6. Decay of free electrons (2000 cm^{-1}), trapped electrons (6000 cm^{-1}), and hole in CoO_x (12000 cm^{-1}), trapped holes (20000 cm^{-1}) in bare BiVO_4 , $\text{BiVO}_4/\text{SnO}_2$, and $\text{CoO}_x/\text{BiVO}_4/\text{SnO}_2$ in the picosecond (A, C, E, and G) and microsecond (B, D, F, and H) regions. The 480 nm laser pulses were irradiated from the CaF_2 plate side.

free electrons survive to $100\ \mu\text{s}$ compared to bare BiVO_4 (Figure 6B). These results indicate that the electron transfer from BiVO_4 to SnO_2 proceeds after $\sim 3\text{ ps}$.

The loading of CoO_x further extended the lifetime of electrons in SnO_2 (Figure 6A), and more than 50 times as many electrons survive to $100\ \mu\text{s}$ compared to bare BiVO_4 (Figure 6B). Furthermore, the decay of holes at 20000 cm^{-1} (Figure 6G) was accelerated and the intensity of Co(III) at 12000 cm^{-1} (Figure 6E) increases by the CoO_x loading.^{47,54} These results confirm that hole transfer from BiVO_4 to CoO_x takes place within a few picoseconds.

By the numerical analysis of the TA intensities of Figure 6, the distribution of electrons and holes accumulated in BiVO_4 , SnO_2 and CoO_x can be estimated. The detailed method is described in the Supporting Information, and the results are summarized in Table 1. It is shown that $\sim 46\%$ of electrons moved from BiVO_4 to the SnO_2 at $5\ \mu\text{s}$ by fabricating an SnO_2

layer under BiVO_4 , and the total number of electrons and holes increased by 2.4-fold compared to bare BiVO_4 .

When CoO_x was loaded on $\text{BiVO}_4/\text{SnO}_2$, $\sim 58\%$ of holes generated in BiVO_4 were captured by CoO_x and $\sim 39\%$ of electrons moved from the BiVO_4 to the SnO_2 layer. As a result, a 3.6-fold larger number of electrons and holes are surviving at $5\ \mu\text{s}$. These results clearly show that the lifetime of charge carriers becomes longer by the formation of $\text{CoO}_x/\text{BiVO}_4/\text{SnO}_2$ double heterojunctions.

3.5. Mechanism of Rapid and Effective Charge Separation at the Heterojunction. For the charge separation mechanism at the heterojunctions, intralayer band-bending and interlayer charge-transfer mechanisms are proposed as described in the Introduction. These two mechanisms are distinguishable by thorough analysis of the number of surviving electrons and holes in BiVO_4 . When the intralayer charge separation is dominant, the number of both electrons and holes in BiVO_4 should be increased. In stark contrast, when the interlayer charge separation is superior, the number of either electrons or holes should be increased but the counter carrier, hole or electron, should be decreased. Hence, the numbers of surviving carriers summarized in Table 1 are further compared.

In the case of $\text{BiVO}_4/\text{SnO}_2$, it is shown that the number of both electron and hole in BiVO_4 was increased 1.3- and 2.4-fold by the attachment of SnO_2 , indicating that the intralayer band-bending model is mainly responsible. Since the CBM of SnO_2 is lower than that of BiVO_4 , the formation of downward band-bending can be expected as shown in Figure 5.⁵⁵ In addition, the interlayer charge separation also takes place in the picosecond region as evident in Figure 6A, which resulted in $\sim 45\%$ of electrons in BiVO_4 being transferred to the SnO_2 layer. These results indicate that the downward band-bending enhances both the intralayer charge separation and interlayer electron transportation to SnO_2 .

When CoO_x was loaded on $\text{BiVO}_4/\text{SnO}_2$, the number of electrons remaining in BiVO_4 increased by 1.7 ($=2.2/1.3$)-fold but that of holes remaining in BiVO_4 decreased to 0.6 ($=1.5/2.4$). These results indicate that the interlayer charge separation is responsible. However, the question is, why is the electron transfer to SnO_2 accelerated even after $\sim 3\text{ ps}$ (inset of Figure 6A)? The distance between CoO_x and SnO_2 is much longer than 100 nm ($400\text{--}800\text{ nm}$, Figure S3); hence, it should take more than 100 ns for the electrons to travel from the vicinity of the CoO_x to the SnO_2 layer only by the diffusion. The diffusion coefficient of electrons in BiVO_4 is too small ($\sim 1.2 \times 10^{-7}\text{ m}^2\text{ s}^{-1}$);⁵⁶ hence, the long-range electric field force such as the band-bending effects should be considered. It is reported that the upward band-bending is formed at $\text{CoO}_x/\text{BiVO}_4$ ⁵⁵ which promotes not only the intralayer charge separation in the BiVO_4 layer but also the electron transfer from BiVO_4 to SnO_2 . In addition, the hole transfer to CoO_x can also be accelerated due to this band-bending. These synergistic intralayer and interlayer charge separations at the $\text{CoO}_x/\text{BiVO}_4/\text{SnO}_2$ heterojunctions effec-

Table 1. Relative Number of Electrons and Holes Surviving at $5\ \mu\text{s}$ Estimated from TA Signals in Figure 6 & Table S1

	$[\text{e}^-]$ in BiVO_4	$[\text{h}^+]$ in BiVO_4	$[\text{e}^-]$ in SnO_2	$[\text{h}^+]$ in CoO_x	total $[\text{e}^-]$ or $[\text{h}^+]$
bare BiVO_4	1.0	1.0			1.0
$\text{BiVO}_4/\text{SnO}_2$	1.3 ± 0.1 (54%)	2.4 ± 0.3 (100%)	1.1 ± 0.4 (46%)		2.4
$\text{CoO}_x/\text{BiVO}_4/\text{SnO}_2$	2.2 ± 0.1 (61%)	1.5 ± 0.2 (42%)	1.4 ± 0.6 (39%)	2.1 ± 0.6 (58%)	3.6

tively suppress the recombination, which resulted to a 3.5-fold increase of charge carriers that are surviving at 5 μ s compared to bare BiVO₄.

However, the problem is that even for such rapid electron transfer to SnO₂, ~60% of electrons still remained in the BiVO₄ layer. As such, expeditious electron-trapping at the defects proceeds with the electron transfer at a comparable rate and this would make the charge transfer to SnO₂ inefficient. Moreover, trapping surely decreases the mobility of electrons, making them scarcely transfer to the SnO₂ layer. In effect, electrons are accumulated intensely in the BiVO₄ layer. As a consequence, the recombination with holes in BiVO₄ is accelerated and eventually decreases the photocatalytic activity.³² We have proposed previously that electron-trapping at the defects in powder photocatalysts remarkably works to prevent electron–hole recombination and hence it boosts the photocatalytic activity. In contrast, for photoelectrochemical (PEC) systems, electron-trapping at one layer prohibits the interlayer charge separation that would result in undesirable electron–hole recombination. Thus, enhancing the activity essentially requires that the defects on each layer should be minimized to allow faster and more efficient charge transfer across all of the layers. Doping⁵⁰ of transition metals on BiVO₄ is one of the effective strategies to reduce the defects such as oxygen vacancies, and hence, it will be also beneficial to increase the photoelectrochemical activity.

4. CONCLUSION

In this work, we have demonstrated that the transient absorption (TA) measurement from the visible to mid-IR region is powerful for elucidating the complex charge carrier dynamics at the double heterojunctions. For CoO_x/BiVO₄/SnO₂, we found that the electrons and holes located in BiVO₄, SnO₂, and CoO_x give absorption peaks at different wave-numbers. Hence, by observing the time-dependent absorption spectra, we could observe the individual electron- and hole-transfer processes from one material to the other materials. We obtained explicit evidence that electrons and holes excited in the BiVO₄ effectively transfer to the SnO₂ layer and CoO_x particles, respectively. As a result, recombination was suppressed and 2.4 and 3.6 times larger amounts of charge carriers survived at 5 μ s on BiVO₄/SnO₂ and CoO_x/BiVO₄/SnO₂, respectively. The electron transfer to an SnO₂ layer and hole transfer to CoO_x were accelerated even after a few picoseconds; hence, the long-range electric field force such as the band-bending effects is considered. The band-bending effects and charge transfer across the junction can individually cause charge separation. However, their synergistic effects work more effectively. As described above, the wide-band TAS unravels these complex behaviors of charge carriers at the heterojunctions. This knowledge would shed light on the design of superior heterojunction PEC systems.

■ ASSOCIATED CONTENT

Supporting Information

The Supporting Information is available free of charge at <https://pubs.acs.org/doi/10.1021/acsaem.9b02262>.

XRD, SEM, EDX, UV–vis, PL, PEC, and quantitative analysis.(PDF)

■ AUTHOR INFORMATION

Corresponding Author

*E-mail: yamakata@toyota-ti.ac.jp.

ORCID

Akira Yamakata: 0000-0003-3179-7588

Kosaku Kato: 0000-0002-9977-7439

Present Address

[§]Research Initiative for Supra-Materials (RISM), Shinshu University, 4-17-1 Wakasato, Nagano-shi, Nagano 380-8553, Japan.

Notes

The authors declare no competing financial interest.

■ ACKNOWLEDGMENTS

This work was supported by the Grant-in-Aid for Basic Research (B) (Grant Nos. 16H04188 and 19H02820), Scientific Research on Innovative Areas (Mixed Anion; Grant Nos. 17H05491 and 19H04708), the Strategic Research Infrastructure Project of MEXT, and Cooperative Research Program of Institute for Catalysis, Hokkaido University (Grant No. 17A1001). We thank to Prof. Hideki Kato of Tohoku University for supplying the BiVO₄ powder for the assignment of the transient absorption.

■ REFERENCES

- (1) Fujishima, A.; Honda, K. Electrochemical Photolysis of Water at a Semiconductor Electrode. *Nature* **1972**, *238*, 37–38.
- (2) Linsebigler, A. L.; Lu, G. Q.; Yates, J. T. Photocatalysis on TiO₂ Surfaces - Principles, Mechanisms, and Selected Results. *Chem. Rev.* **1995**, *95*, 735–758.
- (3) Hoertz, P. G.; Mallouk, T. E. Light-to-Chemical Energy Conversion in Lamellar Solids and Thin Films. *Inorg. Chem.* **2005**, *44*, 6828–6840.
- (4) Maeda, K.; Domen, K. New Non-Oxide Photocatalysts Designed for Overall Water Splitting under Visible Light. *J. Phys. Chem. C* **2007**, *111*, 7851–7861.
- (5) Kudo, A.; Miseki, Y. Heterogeneous Photocatalyst Materials for Water Splitting. *Chem. Soc. Rev.* **2009**, *38*, 253–278.
- (6) Inoue, Y. Photocatalytic Water Splitting by RuO₂-Loaded Metal Oxides and Nitrides with d(0)- And d(10)-Related Electronic Configurations. *Energy Environ. Sci.* **2009**, *2*, 364–386.
- (7) Qu, Y. Q.; Duan, X. F. Progress, challenge and perspective of heterogeneous photocatalysts. *Chem. Soc. Rev.* **2013**, *42*, 2568–2580.
- (8) Kudo, A.; Ueda, K.; Kato, H.; Mikami, I. Photocatalytic O₂ evolution under visible light irradiation on BiVO₄ in aqueous AgNO₃ solution. *Catal. Lett.* **1998**, *53*, 229–230.
- (9) Kudo, A.; Omori, K.; Kato, H. A Novel Aqueous Process for Preparation of Crystal Form-Controlled and Highly Crystalline BiVO₄ Powder from Layered Vanadates at Room Temperature and Its Photocatalytic and Photophysical Properties. *J. Am. Chem. Soc.* **1999**, *121*, 11459–11467.
- (10) Tan, H. L.; Wen, X.; Amal, R.; Ng, Y. H. BiVO₄ {010} and {110} Relative Exposure Extent: Governing Factor of Surface Charge Population and Photocatalytic Activity. *J. Phys. Chem. Lett.* **2016**, *7*, 1400–1405.
- (11) Li, R. G.; Han, H. X.; Zhang, F. X.; Wang, D. G.; Li, C. Highly efficient photocatalysts constructed by rational assembly of dual-cocatalysts separately on different facets of BiVO₄. *Energy Environ. Sci.* **2014**, *7*, 1369–1376.
- (12) Saito, R.; Miseki, Y.; Sayama, K. Highly efficient photoelectrochemical water splitting using a thin film photoanode of BiVO₄/SnO₂/WO₃ multi-composite in a carbonate electrolyte. *Chem. Commun.* **2012**, *48*, 3833–3835.

- (13) Liang, Y.; Tsubota, T.; Mooij, L. P. A.; van de Krol, R. Highly Improved Quantum Efficiencies for Thin Film BiVO₄ Photoanodes. *J. Phys. Chem. C* **2011**, *115*, 17594–17598.
- (14) Zhou, L.; Zhao, C.; Giri, B.; Allen, P.; Xu, X.; Joshi, H.; Fan, Y.; Titova, L. V.; Rao, P. M. High Light Absorption and Charge Separation Efficiency at Low Applied Voltage from Sb-Doped SnO₂/BiVO₄ Core/Shell Nanorod-Array Photoanodes. *Nano Lett.* **2016**, *16*, 3463–3474.
- (15) Zhang, L. M.; Ye, X. F.; Bolor, M.; Poletayev, A.; Melosh, N. A.; Chueh, W. C. Significantly enhanced photocurrent for water oxidation in monolithic Mo:BiVO₄/SnO₂/Si by thermally increasing the minority carrier diffusion length. *Energy Environ. Sci.* **2016**, *9*, 2044–2052.
- (16) Byun, S.; Kim, B.; Jeon, S.; Shin, B. Effects of a SnO₂ hole blocking layer in a BiVO₄-based photoanode on photoelectrocatalytic water oxidation. *J. Mater. Chem. A* **2017**, *5*, 6905–6913.
- (17) Pihosh, Y.; Turkevych, I.; Mawatari, K.; Uemura, J.; Kazoe, Y.; Kosar, S.; Makita, K.; Sugaya, T.; Matsui, T.; Fujita, D.; Tosa, M.; Kondo, M.; Kitamori, T. Photocatalytic generation of hydrogen by core-shell WO₃/BiVO₄ nanorods with ultimate water splitting efficiency. *Sci. Rep.* **2015**, *5*, 11141.
- (18) Louidice, A.; Cooper, J. K.; Hess, L. H.; Mattox, T. M.; Sharp, I. D.; Buonsanti, R. Assembly and Photocatalytic Dynamics of Heterostructured Nanocomposite Photoanodes from Multicomponent Colloidal Nanocrystals. *Nano Lett.* **2015**, *15*, 7347–7354.
- (19) Long, M.; Cai, W.; Cai, J.; Zhou, B.; Chai, X.; Wu, Y. Efficient Photocatalytic Degradation of Phenol over Co₃O₄/BiVO₄ Composite under Visible Light Irradiation. *J. Phys. Chem. B* **2006**, *110*, 20211–20216.
- (20) Trzesniewski, B. J.; Smith, W. A. Photocharged BiVO₄ photoanodes for improved solar water splitting. *J. Mater. Chem. A* **2016**, *4*, 2919–2926.
- (21) Zhang, Z. Q.; Bai, L. L.; Li, Z. J.; Qu, Y.; Jing, L. Q. Review of strategies for the fabrication of heterojunctional nanocomposites as efficient visible-light catalysts by modulating excited electrons with appropriate thermodynamic energy. *J. Mater. Chem. A* **2019**, *7*, 10879–10897.
- (22) Nguyen Van, C.; Do, T. H.; Chen, J. W.; Tzeng, W. Y.; Tsai, K. A.; Song, H. L.; Liu, H. J.; Lin, Y. C.; Chen, Y. C.; Wu, C. L.; Luo, C. W.; Chou, W. C.; Huang, R.; Hsu, Y. J.; Chu, Y. H. WO₃ mesocrystal-assisted photoelectrochemical activity of BiVO₄. *NPG Asia Mater.* **2017**, *9*, e357.
- (23) Zhang, X. L.; Wang, X.; Wang, D. F.; Ye, J. H. Conformal BiVO₄-Layer/WO₃-Nanoplate-Array Heterojunction Photoanode Modified with Cobalt Phosphate Cocatalyst for Significantly Enhanced Photoelectrochemical Performances. *ACS Appl. Mater. Interfaces* **2019**, *11*, 5623–5631.
- (24) Wang, D.; Li, R.; Zhu, J.; Shi, J.; Han, J.; Zong, X.; Li, C. Photocatalytic Water Oxidation on BiVO₄ with the Electrocatalyst as an Oxidation Cocatalyst: Essential Relations between Electrocatalyst and Photocatalyst. *J. Phys. Chem. C* **2012**, *116*, 5082–5089.
- (25) Wang, J.; Osterloh, F. E. Limiting factors for photochemical charge separation in BiVO₄/Co₃O₄, a highly active photocatalyst for water oxidation in sunlight. *J. Mater. Chem. A* **2014**, *2*, 9405–9411.
- (26) Zachaus, C.; Abdi, F. F.; Peter, L. M.; van de Krol, R. Photocurrent of BiVO₄ is limited by surface recombination, not surface catalysis. *Chem. Sci.* **2017**, *8*, 3712–3719.
- (27) Abdi, F. F.; van de Krol, R. Nature and Light Dependence of Bulk Recombination in Co-Pi-Catalyzed BiVO₄ Photoanodes. *J. Phys. Chem. C* **2012**, *116*, 9398–9404.
- (28) Bahnemann, D.; Henglein, A.; Lillie, J.; Spanhel, L. Flash-Photolysis Observation of The Absorption-Spectra of Trapped Positive Holes and Electrons in Colloidal TiO₂. *J. Phys. Chem.* **1984**, *88*, 709–711.
- (29) Yoshihara, T.; Katoh, R.; Furube, A.; Tamaki, Y.; Murai, M.; Hara, K.; Murata, S.; Arakawa, H.; Tachiya, M. Identification of Reactive Species in Photoexcited Nanocrystalline TiO₂ Films by Wide-wavelength-Range (400–2500 nm) Transient Absorption Spectroscopy. *J. Phys. Chem. B* **2004**, *108*, 3817–3823.
- (30) Schneider, J.; Bahnemann, D. Strong Transient Absorption of Trapped Holes in Anatase and Rutile TiO₂ at High Laser Intensities. *J. Phys. Chem. C* **2018**, *122*, 13979–13985.
- (31) Yamakata, A.; Vequizo, J. J. M.; Kawaguchi, M. Behavior and Energy State of Photogenerated Charge Carriers in Single-Crystalline and Polycrystalline Powder SrTiO₃ Studied by Time-Resolved Absorption Spectroscopy in the Visible to Mid-Infrared Region. *J. Phys. Chem. C* **2015**, *119*, 1880–1885.
- (32) Vequizo, J. J. M.; Matsunaga, H.; Ishiku, T.; Kamimura, S.; Ohno, T.; Yamakata, A. Trapping-Induced Enhancement of Photocatalytic Activity on Brookite TiO₂ Powders: Comparison with Anatase and Rutile TiO₂ Powders. *ACS Catal.* **2017**, *7*, 2644–2651.
- (33) Barroso, M.; Cowan, A. J.; Pendlebury, S. R.; Gratzel, M.; Klug, D. R.; Durrant, J. R. The Role of Cobalt Phosphate in Enhancing the Photocatalytic Activity of alpha-Fe₂O₃ toward Water Oxidation. *J. Am. Chem. Soc.* **2011**, *133*, 14868–14871.
- (34) Pendlebury, S. R.; Barroso, M.; Cowan, A. J.; Sivula, K.; Tang, J. W.; Gratzel, M.; Klug, D.; Durrant, J. R. Dynamics of photogenerated holes in nanocrystalline alpha-Fe₂O₃ electrodes for water oxidation probed by transient absorption spectroscopy. *Chem. Commun.* **2011**, *47*, 716–718.
- (35) Ravensbergen, J.; Abdi, F. F.; van Santen, J. H.; Frese, R. N.; Dam, B.; van de Krol, R.; Kennis, J. T. M. Unraveling the Carrier Dynamics of BiVO₄: A Femtosecond to Microsecond Transient Absorption Study. *J. Phys. Chem. C* **2014**, *118*, 27793–27800.
- (36) Ma, Y.; Pendlebury, S. R.; Reynal, A.; Le Formal, F.; Durrant, J. R. Dynamics of photogenerated holes in undoped BiVO₄ photoanodes for solar water oxidation. *Chem. Sci.* **2014**, *5*, 2964–2973.
- (37) Grigioni, I.; Stampelcoskie, K. G.; Selli, E.; Kamat, P. V. Dynamics of Photogenerated Charge Carriers in WO₃/BiVO₄ Heterojunction Photoanodes. *J. Phys. Chem. C* **2015**, *119*, 20792–20800.
- (38) Suzuki, Y.; Murthy, D. H. K.; Matsuzaki, H.; Furube, A.; Wang, Q.; Hisatomi, T.; Domen, K.; Seki, K. Rational Interpretation of Correlated Kinetics of Mobile and Trapped Charge Carriers: Analysis of Ultrafast Carrier Dynamics in BiVO₄. *J. Phys. Chem. C* **2017**, *121*, 19044–19052.
- (39) Aiga, N.; Jia, Q. X.; Watanabe, K.; Kudo, A.; Sugimoto, T.; Matsumoto, Y. Electron-Phonon Coupling Dynamics at Oxygen Evolution Sites of Visible-Light-Driven Photocatalyst: Bismuth Vanadate. *J. Phys. Chem. C* **2013**, *117*, 9881–9886.
- (40) Ma, Y. M.; Kafizas, A.; Pendlebury, S. R.; Le Formal, F.; Durrant, J. R. Photoinduced Absorption Spectroscopy of CoPi on BiVO₄: The Function of CoPi during Water Oxidation. *Adv. Funct. Mater.* **2016**, *26*, 4951–4960.
- (41) Pankove, J. I. *Optical Processes in Semiconductors*; Dover: New York, 1975.
- (42) Yamakata, A.; Ishibashi, T.; Onishi, H. Time-Resolved Infrared Absorption Spectroscopy of Photogenerated Electrons in Platinized TiO₂ Particles. *Chem. Phys. Lett.* **2001**, *333*, 271–277.
- (43) Yamakata, A.; Vequizo, J. J. M.; Matsunaga, H. Distinctive Behavior of Photogenerated Electrons and Holes in Anatase and Rutile TiO₂ Powders. *J. Phys. Chem. C* **2015**, *119*, 24538–24545.
- (44) Grigioni, I.; Abdellah, M.; Corti, A.; Dozzi, M. V.; Hammarstrom, L.; Selli, E. Photoinduced Charge-Transfer Dynamics in WO₃/BiVO₄ Photoanodes Probed through Midinfrared Transient Absorption Spectroscopy. *J. Am. Chem. Soc.* **2018**, *140*, 14042–14045.
- (45) Yamakata, A.; Yoshida, M.; Kubota, J.; Osawa, M.; Domen, K. Potential-Dependent Recombination Kinetics of Photogenerated Electrons in n- and p-Type GaN Photoelectrodes Studied by Time-Resolved IR Absorption Spectroscopy. *J. Am. Chem. Soc.* **2011**, *133*, 11351–11357.
- (46) Gamelin, D. R. Water Splitting Catalyst or Spectator? *Nat. Chem.* **2012**, *4*, 965–967.
- (47) Yamakata, A.; Kawaguchi, M.; Nishimura, N.; Minegishi, T.; Kubota, J.; Domen, K. Behavior and Energy States of Photogenerated Charge Carriers on Pt- or CoO_x-Loaded LaTiO₂N Photocatalysts: Time-Resolved Visible to Mid-Infrared Absorption Study. *J. Phys. Chem. C* **2014**, *118*, 23897–23906.

(48) Zhong, M.; Hisatomi, T.; Kuang, Y. B.; Zhao, J.; Liu, M.; Iwase, A.; Jia, Q. X.; Nishiyama, H.; Minegishi, T.; Nakabayashi, M.; Shibata, N.; Niishiro, R.; Katayama, C.; Shibano, H.; Katayama, M.; Kudo, A.; Yamada, T.; Domen, K. Surface Modification of CoO_x Loaded BiVO_4 Photoanodes with Ultrathin p-Type NiO Layers for Improved Solar Water Oxidation. *J. Am. Chem. Soc.* **2015**, *137*, 5053–5060.

(49) Miseki, Y.; Sayama, K. Highly efficient Fe(III) reduction and solar-energy accumulation over a BiVO_4 photocatalyst. *Chem. Commun.* **2018**, *54*, 2670–2673.

(50) Okuno, K.; Kato, H.; Vequizo, J. J. M.; Yamakata, A.; Kobayashi, H.; Kobayashi, M.; Kakihana, M. Expansion of the photoresponse window of a BiVO_4 photocatalyst by doping with chromium(VI). *RSC Adv.* **2018**, *8*, 38140–38145.

(51) Sakamoto, M.; Kawawaki, T.; Kimura, M.; Yoshinaga, T.; Vequizo, J. J. M.; Matsunaga, H.; Ranasinghe, C. S. K.; Yamakata, A.; Matsuzaki, H.; Furube, A.; Teranishi, T. Clear and transparent nanocrystals for infrared-responsive carrier transfer. *Nat. Commun.* **2019**, *10*, 406.

(52) Baek, J. H.; Kim, B. J.; Han, G. S.; Hwang, S. W.; Kim, D. R.; Cho, I. S.; Jung, H. S. $\text{BiVO}_4/\text{WO}_3/\text{SnO}_2$ Double-Heterojunction Photoanode with Enhanced Charge Separation and Visible-Transparency for Bias-Free Solar Water-Splitting with a Perovskite Solar Cell. *ACS Appl. Mater. Interfaces* **2017**, *9*, 1479–1487.

(53) Polo da Fonseca, C. N.; Depaoli, M. A.; Gorenstein, A. Electrochromism in cobalt oxide thin films grown by anodic electroprecipitation. *Sol. Energy Mater. Sol. Cells* **1994**, *33*, 73–81.

(54) Vequizo, J. J. M.; Hojamberdiev, M.; Teshima, K.; Yamakata, A. Role of CoO_x cocatalyst on Ta_3N_5 photocatalysts studied by transient visible to mid-infrared absorption spectroscopy. *J. Photochem. Photobiol., A* **2018**, *358*, 315–319.

(55) Hermans, Y.; Murcia-Lopez, S.; Klein, A.; van de Krol, R.; Andreu, T.; Morante, J. R.; Toupance, T.; Jaegermann, W. Analysis of the interfacial characteristics of BiVO_4 /metal oxide heterostructures and its implication on their junction properties. *Phys. Chem. Chem. Phys.* **2019**, *21*, 5086–5096.

(56) Abdi, F. F.; Savenije, T. J.; May, M. M.; Dam, B.; van de Krol, R. The Origin of Slow Carrier Transport in BiVO_4 Thin Film Photoanodes: A Time-Resolved Microwave Conductivity Study. *J. Phys. Chem. Lett.* **2013**, *4*, 2752–2757.

光触媒/光半導体を利用した 人工光合成

— 最先端科学から実装技術への発展を目指して —

監修 堂免 一成 瀬戸山 亨

光触媒/光半導体を利用した 人工光合成

— 最先端科学から実装技術への発展を目指して —

第3編 光半導体的アプローチ

第5章 光半導体による水分解の反応機構

時間分解分光測定を用いた光触媒のキャリアダイナミクス

豊田工業大学 山方 啓

第5章 光半導体による水分解の反応機構

時間分解分光測定を用いた光触媒のキャリアーダイナミクス



豊田工業大学 山方 啓

1. はじめに

エネルギー問題や環境問題を解決するために、太陽光を用いて水から水素を製造できる光触媒が注目されている。水を分解して製造した水素は燃焼時に、二酸化炭素を排出せず貯蔵や運搬が容易なため、次世代のエネルギー媒体として期待されている。しかし、この光触媒を工業的に利用化するためには、活性をさらに向上させる必要がある。光触媒反応は、半導体のバンドギャップを光で励起し、生成した電子と正孔がそれぞれ水を還元し、酸化させることで進行する。しかし、生成した大部分の電子と正孔は、再結合により水と反応する前に消滅してしまう。したがって、光触媒反応の効率を向上させるためには、再結合を抑制し、反応分子への電荷移動を促進させる必要がある。このためには、光触媒として用いる半導体粒子の中に生成した光励起電子と正孔の挙動をよく理解し、これをコントロールする必要がある。

光触媒を用いた水分解反応のメカニズムは、平たく言えば太陽電池を使って水を電気分解することと同じである。そして、その効率は光触媒の場合にも太陽電池の場合と同様に、用いる半導体材料の結晶性が良い方が高い。しかし、大きな違いは必要とする結晶のサイズにある。太陽電池の場合には数～数十センチメートルの大きな結晶が必要であるが、光触媒の場合には、それは数百ナノメートル～数マイクロメートルで良い。そして、粒子の表面に数ナノメートルの貴金属微粒子を担持すればこれらが“マイクロ太陽電池”として働き、粒子の表面で直接“水の電気分解”が起こる。小さな結晶は安価に製造することができ、さらに、使用する貴金属の量も大幅に減らせるので太陽電池よりも非常に安いコストで“水を電気分解”することができる。さらに、粉末は反応場となる表面積が大きいので反応物質をよりたくさん吸着させることができ、反応効率も高いという長所がある。

しかし、粉末の表面積が大きいということは、逆に表面欠陥の数も多くなる、という問題を含んでいる。表面にある原子は、バルク中にある原子に比べて、配位している原子の数が少ない不飽和な状態にある。そのため、エネルギー状態が高く、ステップやキンク、空孔などの欠陥が生じやすい。これらの欠陥は電子や正孔を捕捉し、より安定な状態に変わろうとする。その結果、捕捉された電子や正孔の移動度とそのエネルギー状態が低下し、再結合も促進されると考えられてきた。しかし、どのような欠陥がどのような影響を与えるのか、という問題はまだまだよくわかっていない。粉末の表面にはさまざまな結晶面が露出し、さまざまな構造の欠陥が形成されている。光触媒活性を低下させる欠陥もあれば、活性向上に役立つ欠陥もあるかもしれない。

そこで、筆者らは、水を完全分解できる光触媒として最も長い歴史を有する SrTiO_3 (チタン

酸ストロンチウム)¹⁾を用いて、粉末における光励起キャリアの挙動を調べた^{2) -4)}。SrTiO₃粉末を複数の試薬メーカーより購入し、欠陥が少ないと考えられるバルクの単結晶と比較した。さらに、粉末を熔融塩の中で高温加熱処理（フラックス処理）する効果を調べた。フラックス処理すると、再結晶化が促進され、表面欠陥が補修される。このフラックス処理が及ぼす粉末の構造変化と光触媒活性、光励起キャリアの挙動への影響について調べ、欠陥が及ぼす影響について検討した。

2. 光励起キャリアのエネルギー状態と減衰過程の観察

光励起キャリアの挙動を調べるためには、パルスレーザーを用いた時間分解分光測定が有効である。時間分光測定には、発光測定と吸光測定があり、発光測定では再結合時に発生する光を分析する。しかし、光触媒に応用する場合には注意が必要である。それは、間接遷移型の半導体材料の場合にはそもそも発光しないことに加えて、電子と正孔が完全に分離した場合や、反応によって電子あるいは正孔が消費されてしまった場合には、発光しなくなるからである。そのため、同じ実験結果を得ても解釈が分かれることがあるので注意が必要である。一方、吸収測定の場合には、直接遷移型か間接遷移型かに関係なく、電子や正孔を直接観察することができる。この光学過程を図1に示すが、伝導帯に励起された自由電子は、主に中赤外域に右肩上がりの構造のない吸収を与える⁵⁾。これは、伝導帯中における電子のバンド内遷移に帰属されている。一方、欠陥にトラップされた電子は、トラップ準位から伝導帯への遷移に帰属される吸収を可視から近赤外域に与える。したがって、吸収される光の波長から、トラップ準位の深さを見積もることができる。一方、正孔は価電子帯内のサブバンド間遷移、あるいは、価電子帯からトラップ正孔への電子遷移に帰属される吸収を可視から近赤外域に与える。したがって、可視から中赤外域の時間分解分光測定を行うことで自由電子やトラップ電子、正孔の動きを独立に調べることができる⁶⁾。

このような時間分解分光測定は、図2に示すような自作の装置を用いて行っている。粉末の光触媒は赤外光をよく透過するので、赤外域の測定は透過配置で行う。しかし、可視から近赤外域の光は散乱されるので、この領域では、拡散反射配置で行う。装置の時間分解能は、光検出器と信号増幅器の応答速度で決まり、可視から赤外域のいずれにおいても約1マイクロ秒程

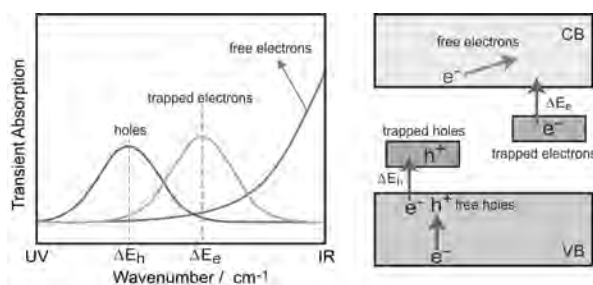


図1 光触媒を励起して生成する自由電子、トラップ電子、正孔による光吸収過程

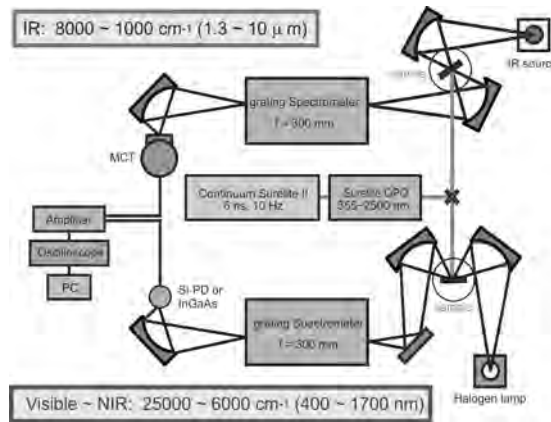


図2 可視から中赤外域まで測定可能なナノ秒時間分解分光装置

度である。また、これよりも速い現象については、フェムト秒レーザーを用いたポンププローブ法を用いることで測定することができる。これらの分光装置を組み合わせることで、フェムト秒から数秒の時間領域における過渡吸収測定を行うことができる。

3. 単結晶の光触媒材料における光励起キャリアの挙動

まず、欠陥が少ないことが期待される1枚の大きなSrTiO₃の単結晶(100面, 10×10×0.5 mm)に紫外光レーザーパルス(355 nm, 6 ns, 5 Hz)を照射し、透過配置で可視から中赤外域(400 nm~10 μm, 25,000~1,000 cm⁻¹)の過渡吸収スペクトルを測定した。結果を図3²⁾に示す。この図を見ると、25,000 cm⁻¹から2,500 cm⁻¹にかけて右肩上がりの単調な吸収が観察されることがわかる。赤外域にかけて強く観察されるこの単調な吸収は、図1で説明したように、伝導帯に励起された自由電子に帰属される。また、2,500 cm⁻¹ (0.2 eV) 付近に吸収ピークが観察されるが、これは伝導帯から約0.2 eV程度の浅い準位に捕捉された電子の寄与が含まれることを示唆している。ここで注目すべきことは、可視から近赤外域には他の吸収ピークは何も観察されないことである。この結果は、単結晶の場合、自由電子や浅いトラップ電子が大部分を占め、深くトラップされた電子や正孔は観察されないことを示している。

次に、伝導帯に励起された自由電子、あるいは浅いトラップ電子の減衰過程を2,500 cm⁻¹の吸収強度の減衰変化から調べた。その結果を図3の挿入図²⁾に示す。この図を見てわかるように、光励起電子は、光照射100 ns以内に完全に

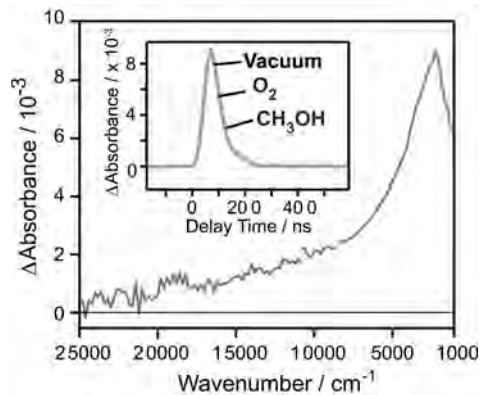


図3 SrTiO₃の単結晶に紫外レーザーパルス(355 nm, パルス幅6 ns)を照射して測定した過渡吸収スペクトル²⁾

消滅してしまう。そして、気相に酸素やメタノール蒸気を導入しても、減衰速度は全く変化しない。これは、単結晶の場合、光励起電子と正孔はいずれも気相に導入した分子と反応しないことを意味している。この原因の1つには、単結晶は表面積が小さいので反応分子の吸着量が少ないことが挙げられる。さらに、光励起キャリアの寿命が100 ns以内と短いので、光励起キャリアが反応分子と出会う前に再結合して消滅してしまう。つまり、単結晶の場合欠陥が少ないので大部分の光励起キャリアは深くトラップされていないが、しかし、寿命が短く、吸着分子の絶対量も少ないので分子と反応する確率が極めて小さいことがわかった。

4. 構造の異なる2種類の粉末光触媒材料における光励起キャリアの挙動

次に、単結晶より表面積が大きな粉末を用いて光励起キャリアの挙動を調べた。ここでは、製造元の異なる2種類のSrTiO₃粉末（Aldrich社：粒径100 nm，株高純度化学研究所：粒径1~2 μm）を用いてその違いを調べた。まず、Aldrich社の粉末を調べた結果を図4²⁾に示すが、スペクトルの形状が単結晶とは全く異なることがわかる。この粉末の場合にも単結晶で観察された自由電子、あるいは浅くトラップされた電子に帰属される吸収が4,000 cm⁻¹以下に観察されている。しかし、それよりも強くブロードな吸収が22,000 cm⁻¹と11,000 cm⁻¹付近に観測された。これらの2つの吸収は欠陥の少ない単結晶では観察されていないことから、前述のように、粒子の欠陥に深くトラップされた電子、あるいは正孔に帰属される。そして、大変興味深いことに、これらの吸収は光照射1 ms経過しても残存している。この結果は、粉末の場合、大部分の光励起キャリアは欠陥にトラップされているが、単結晶に比べて長い寿命を有していることを意味している。従来欠陥は再結合を促進すると考えられてきた。しかし、むしろ再結合を抑制していることがわかった。欠陥にキャリアがトラップされると、キャリアの移動度が低下し、電子と正孔が衝突する確率が低下する。その結果、再結合が遅くなったと解釈することができる。

問題はこれらの長い寿命を有する光励起キャリアが反応活性を有しているかどうかである。そこで、これらの光励起キャリアの反応活性を調べるために、気相に反応ガスを導入して減衰過程を調べた。2,500 cm⁻¹と11,000 cm⁻¹、20,000 cm⁻¹における減衰過程を調べた結果を図5²⁾に示す。まず、2,500 cm⁻¹の吸収強度の減衰過程をみると、酸素を導入すると特に0~3 μsにおける減衰速度が速くなっていることがわかる。これは、酸素分子がO₂+e⁻→O₂⁻のように光励起電子を反応消費することを意味している⁷⁾。一方、メタノールを導入すると0~1 msにおける減衰速度が遅くなった。これは表面に解離吸着したメタノールがCH₃O⁻(a)+h⁺

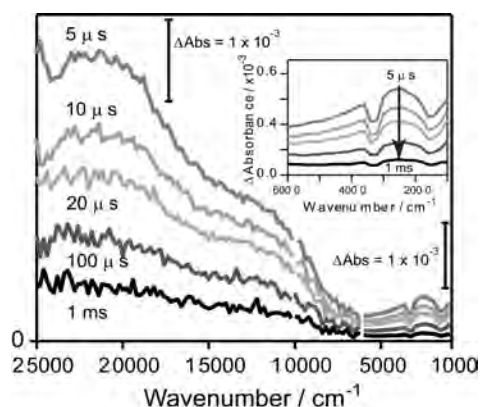
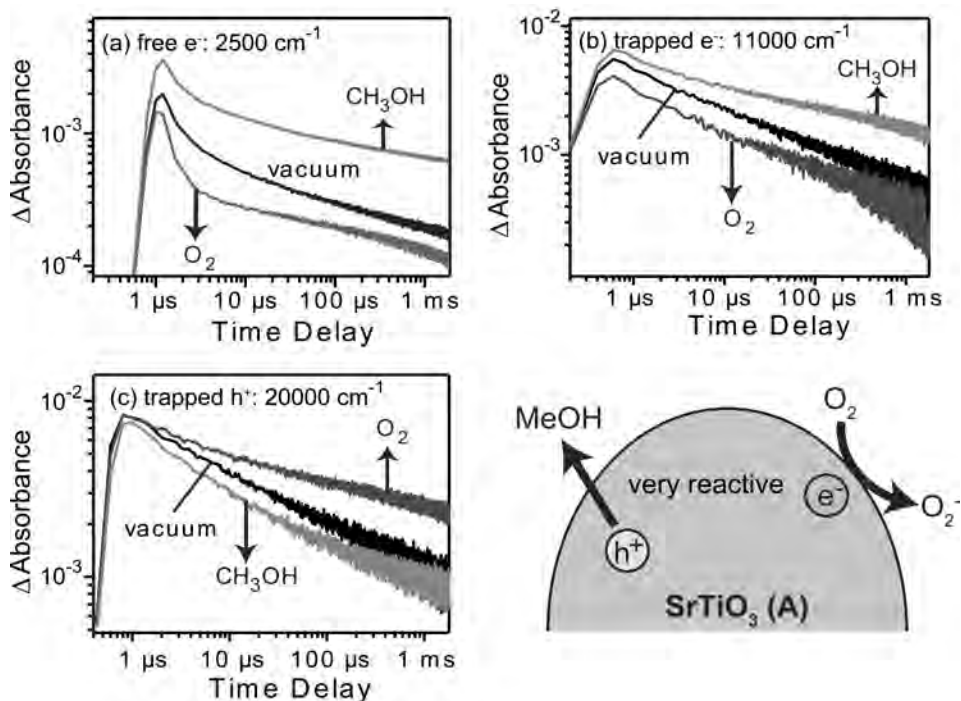


図4 Aldrich社のSrTiO₃の粉末に紫外レーザーパルス(355 nm, パルス幅6 ns)を照射して測定した過渡吸収スペクトル²⁾



真空中、酸素雰囲気下、メタノール蒸気を導入して、 $2,000\text{ cm}^{-1}$ 、 $11,000\text{ cm}^{-1}$ 、 $20,000\text{ cm}^{-1}$ における減衰過程を比較

図5 Aldrich社のSrTiO₃粉末に紫外レーザーパルス(355 nm, パルス幅6 ns)を照射して生成した自由電子, トラップ電子, 正孔の減衰過程²⁾

→CH₃O[•](a)のように正孔と反応するからである。正孔が消費されると電子は再結合できなくなるので電子の寿命は長くなる⁸⁾。したがって、これらの結果は、 $2,500\text{ cm}^{-1}$ の吸収は光励起電子の数を反映していることを示している。次に、 $11,000\text{ cm}^{-1}$ の吸収を見てみると、 $2,500\text{ cm}^{-1}$ の場合と同じように酸素の導入で減衰速度が速くなり、メタノールの導入で遅くなった。つまり、 $11,000\text{ cm}^{-1}$ の吸収強度も電子に帰属されることがわかる。一方、 $20,000\text{ cm}^{-1}$ の場合には、 $2,500\text{ cm}^{-1}$ や $11,000\text{ cm}^{-1}$ の場合とは異なり、減衰速度は酸素の導入で遅くなり、メタノールの導入で速くなった。この結果は、 $20,000\text{ cm}^{-1}$ の吸収強度は正孔の数を反映することを意味している。これらの結果は、粉末光触媒を励起して生成したキャリアは、その大部分が欠陥に捕捉されているが、電子も正孔もともに反応ガスとの反応性を維持していることがわかった。つまり、この粉末にある欠陥は再結合速度を遅くし、光触媒活性の向上に役立っていることがわかった。

粉末における光励起キャリアの挙動をより詳しく理解するために、他のメーカーのSrTiO₃粉末(株高純度化学研究所)についても同様な実験を試みた。同じ組成の粉末でも、製造メーカーが異なれば粉末の構造は異なることが期待される。そこで、まず(株高純度化学研究所)の粉末に紫外光レーザーパルスを照射して過渡吸収スペクトルを測定した(図6²⁾)。その結果、同じSrTiO₃の粉末であるにもかかわらず、スペクトルの形状が単結晶ともAldrich社のものとも全く異なることがわかる。最も大きな違いは、自由電子、あるいは浅くトラップされた電子に

帰属される $3,000\text{ cm}^{-1}$ 以下の吸収強度が非常に小さいことである。そして、 $11,000\text{ cm}^{-1}$ 付近の吸収が最も強く観察された。反応ガスを導入した際の、各波長における吸収強度の減衰過程を調べた結果が図7²⁾である。 $2,500\text{ cm}^{-1}$ と $20,000\text{ cm}^{-1}$ の吸収強度は、酸素とメタノールの導入によってAldrich社の粉末とそれぞれ同じような変化を示した。したがって、これらの吸収はそれぞれ電子と正孔に帰属される。しかし、反応活性は低く、酸素やメタノール蒸気を導入してもその変化量は小さい。一方、 $11,000\text{ cm}^{-1}$ の吸収は、Aldrich社の粉末とは異なり、酸素を導入すると増加し、メタノールを導入すると減少することから、電子ではなく正孔に帰属される。これらの結果は、同じ波長の吸収であるにもかかわらず、Aldrich社の粉末と(株)高純度化学研究所の粉末とは帰属が異なることを意味している。すなわち、同じ波長の吸収であっても、その帰属は粉末の特性によって異なることがわかった。

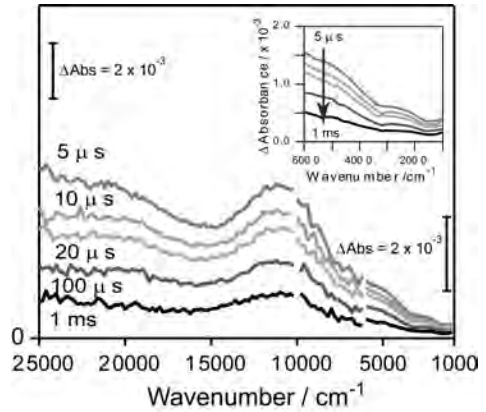
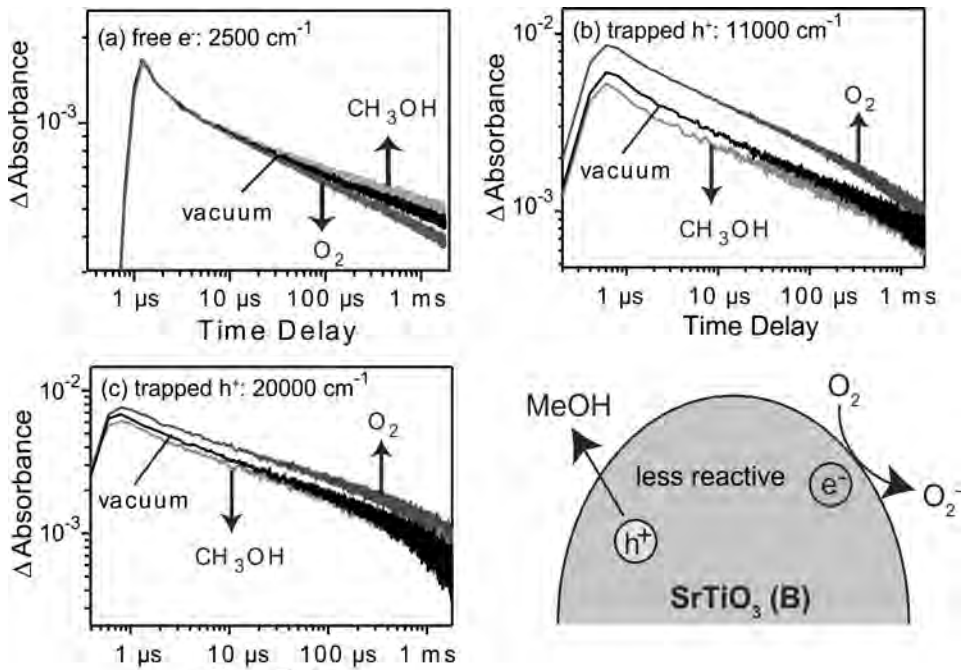


図6 (株)高純度化学研究所のSrTiO₃粉末に紫外レーザーパルス(355 nm, パルス幅6 ns)を照射して測定した過渡吸収スペクトル²⁾



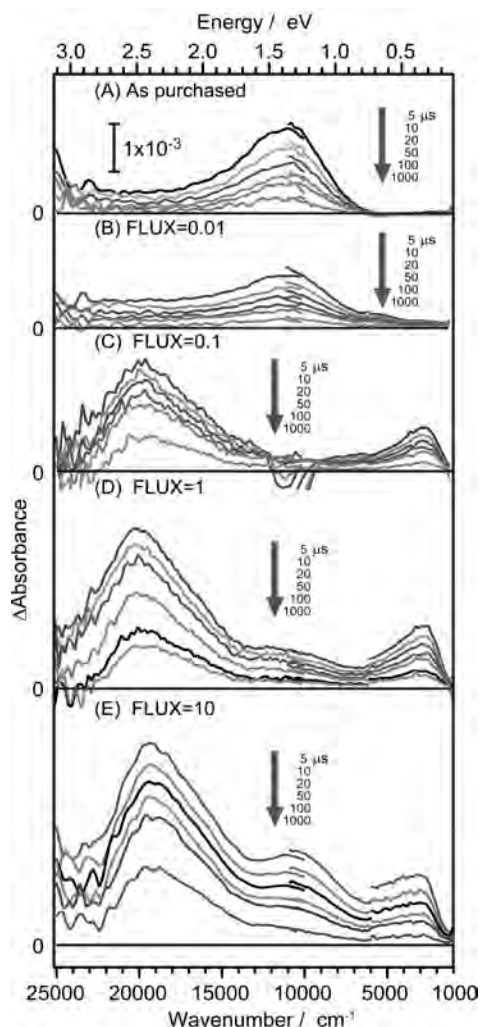
真空中、酸素雰囲気下、メタノール蒸気を導入して、 $2,000\text{ cm}^{-1}$ 、 $11,000\text{ cm}^{-1}$ 、 $20,000\text{ cm}^{-1}$ における減衰過程を比較。

図7 (株)高純度化学研究所のSrTiO₃粉末に紫外レーザーパルス(355 nm, パルス幅6 ns)を照射して生成した自由電子、トラップ電子、正孔の減衰過程²⁾

次に、これらの粉末の光触媒活性を比較するために、メタノール水溶液からの水素生成活性を調べた。その結果、Aldrich社 ($173 \mu\text{mol h}^{-1}$) の製品の方が(株)高純度化学研究所の製品 ($54 \mu\text{mol h}^{-1}$) より約3倍活性が高いことがわかった²⁾。この定常反応活性は、図5と図7を比較してわかるように、自由電子や浅くトラップされた電子の残存数が多い方が高い。深くトラップされた電子よりも、自由電子や浅くトラップされた電子の方が反応活性が高い。そして、このトラップの深さの違いは、欠陥構造の違いで決まると考えられる。つまり、同じ組成の粉末でも欠陥の構造は異なり、そこに捕捉される電子と正孔のエネルギー状態は異なることが推察される。したがって、粒子表面に存在する欠陥の構造を制御できれば、光触媒活性を向上させることができると考えられる。

5. SrTiO₃ 粉末の粒子の形態の違いによる影響

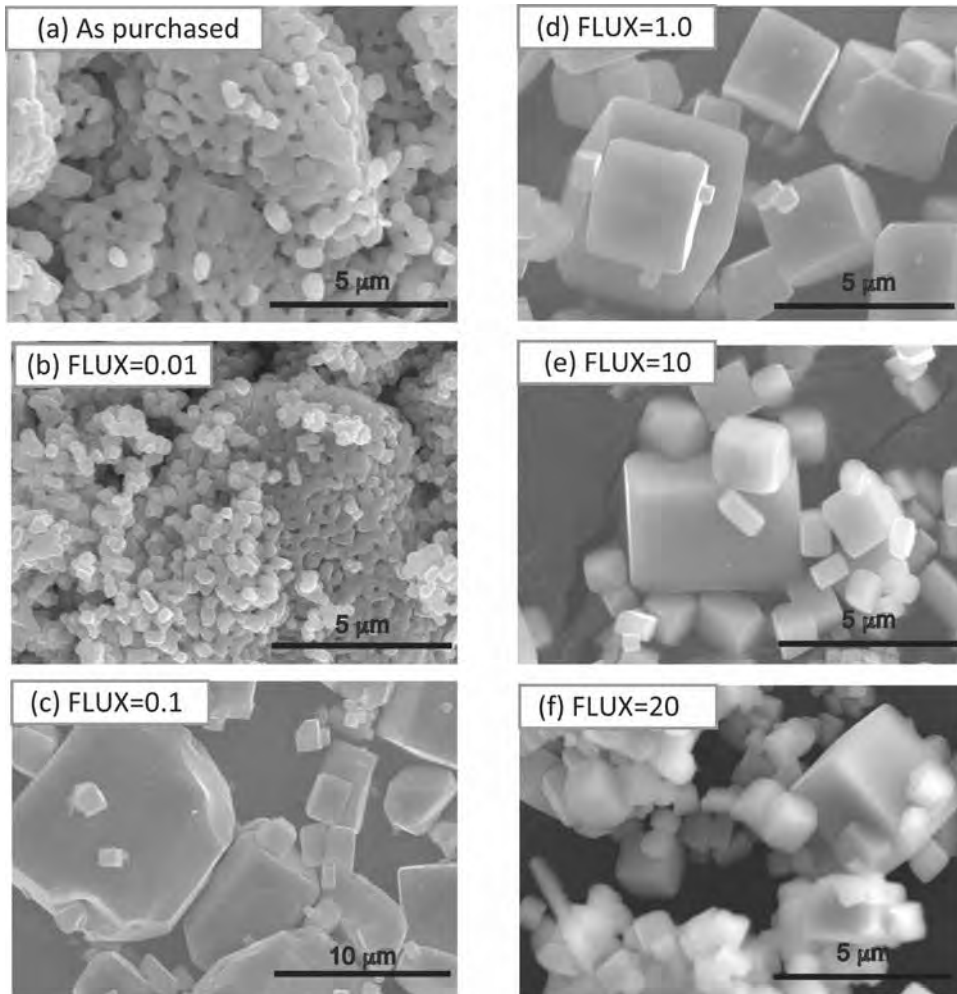
そこで、粒子の表面構造を制御して反応活性の変化を調べた。しかしその前にもう1社、別のメーカー(和光純薬工業(株))のSrTiO₃粉末を用いて過渡吸収スペクトルを測定した。時間分解分光測定の結果を図8(A)³⁾に示すが、吸収スペクトルの形状は、単結晶はおろか、Aldrich社とも(株)高純度化学研究所とも全く異なることがわかる。4,000 cm⁻¹以下の吸収と20,000 cm⁻¹付近の吸収がほとんど観察されず、11,000 cm⁻¹付近に強い吸収ピークが1本だけ現れるだけである。この吸収はメタノールの導入と酸素の導入に対してともに増加したので、トラップ電子とトラップ正孔の両方の寄与があることがわかった³⁾。この粉末の水分解に対する定常反応活性を調べた結果を表1に示すが、和光純薬工業(株)のSrTiO₃は水の分解に対してほとんど活性がない。これは、図8(A)を見てわかるように、大部分の電子は11,000 cm⁻¹に吸収を与える深い準位にトラップされており、4,000 cm⁻¹以下に吸収を与える反応活性が高い電子がほとんど残存しないことに起因する。この深い欠陥の由来について詳しく調べるために走査電子顕微鏡(SEM)を使って、粉末の構造を調べた(図9(a)³⁾)。小さな一次粒子が不規則に凝集した二次粒子が形成されている。そしてこのいびつな粒



FLUX=SrCl₂/SrTiO₃の比率を0.01~20まで変化
 図8 SrCl₂ 熔融塩でフラックス処理した市販のSrTiO₃の粉末に紫外レーザーパルス(355 nm, パルス幅6 ns)を照射して測定した過渡吸収スペクトル³⁾

表1 SrCl₂ 熔融塩でフラックス処理した和光純薬工業株の SrTiO₃ 粉末の水分解光触媒活性と組成比³⁾

FLUX (SrCl ₂ /STO)	Activity(mol/h)		FWHM of (110) peak	BET Surface area m ² g ⁻¹	[Sr]/[Ti]	2[Al]/([Sr]+[Ti])
	H ₂	O ₂			%	%
0	<1	<1	0.107	3.6	1.09	0.04
0.01	1	1	0.083	-	1.01	0.20
0.1	6	6	0.058	<0.3	1.02	0.19
1	40	21	0.061	0.5	1.00	0.18
5	470	240	0.064	0.8	-	-
10	450	240	0.066	0.9	0.98	0.31



FLUX=SrCl₂/SrTiO₃ の比率を 0.01~20 まで変化

図9 和光純薬工業株の SrTiO₃ 粉末を SrCl₂ 熔融塩中 (1,100℃) で 10 h 加熱処理して測定した走査電子顕微鏡写真³⁾

子の粒界や欠陥が光励起キャリアを深くトラップしていると考えられる。

金属酸化物の粉末は、溶融塩の中で加熱処理（フラックス処理）をすることで再結晶化させることができる^{9) 10)}。そこで、和光純薬工業(株)の粉末を SrCl_2 の溶融塩 ($1,100^\circ\text{C}$) の中で 10 h 加熱処理した。 SrCl_2 と SrTiO_3 の混合比 ($\text{FLUX} = \text{SrCl}_2/\text{SrTiO}_3$) を変えてフラックス処理した粉末の SEM 像を図9に示す。その結果、 $\text{FLUX} = 0.01$ のときに二次粒子がほぐれ始め、 FLUX を 1 以上に増やすと、きれいな立方体の結晶ができることがわかった。つまり、フラックス処理を行うことで結晶性が良く欠陥の少ない結晶を調製できることがわかった。

これらの粉末の水分分解活性を調べた結果が表1である。前述のようにフラックス処理を行わない市販の粉末は水分分解に対する活性がほとんどない。しかし、フラックス処理するに伴い、 $\text{FLUX} = 5$ まで活性が単調に向上することがわかった。

そこで、この活性向上のメカニズムを調べるために時間分解分光測定を行った。図8³⁾ に過渡吸収スペクトルを示す。その結果、フラックス処理すると、スペクトルの形状が劇的に変わることがわかる。 SrCl_2 を少量 ($\text{FLUX} = 0.01$) 混ぜて加熱すると、 $11,000\text{ cm}^{-1}$ の吸収強度が減少し、 $\text{FLUX} = 0.1$ まで増やすとこのピークは完全に消失する。そして、1つのピークがあたかも2つに分かれたかのように $20,000\text{ cm}^{-1}$ と $2,500\text{ cm}^{-1}$ に新しいピークが現れる。さらに $\text{FLUX} = 1$ まで増やすと、これらの2つの吸収強度がともに増加する。これらの吸収は、気相に酸素やメタノールを導入してその減衰速度を比較することで、それぞれ正孔と電子に帰属された³⁾。この帰属は、Aldrich 社や(株)高純度化学研究所の粉末と同じである。そして、スペクトルの形状変化と粒子の形状変化との関係を調べるために、図9の SEM 画像を再び確認すると、フラックス処理によりきれいな立方体状の結晶が形成し、凸凹だらけであった粉末の表面がフラットになっていることがわかる。つまり、フラックス処理により欠陥が低減するので自由電子の数が増えることがわかった。

次に、 FLUX を 1 から 10 まで増やすと、 $20,000\text{ cm}^{-1}$ と $2,500\text{ cm}^{-1}$ の吸収強度は若干増加するものの、一度消失した $11,000\text{ cm}^{-1}$ の吸収が再び現れ始めた。このとき、図9の SEM 画像を見ても粒子の形態に大きな変化は見られない。すなわち、粒子の形態変化とは異なる違いが現れていることがわかる。つまり、フラックス処理は2段階の変化を引き起こすことがわかる。この複雑な変化の原因は、粉末の組成を分析することで明らかにすることができた。元素分析の結果を表1に示すが、フラックス処理すると、 SrTiO_3 中に Al^{3+} がドーピングされる。 $\text{FLUX} = 0.01 \sim 1$ までは Al^{3+} の濃度は $0.18 \sim 0.20$ 程度であるが、 $\text{FLUX} = 10$ にすると 0.31 まで増加する。このフラックス処理には、 Al_2O_3 製のるつぼを使っており、 SrCl_2 の溶融塩で加熱すると、るつぼの表面が溶け出し、溶け出した Al^{3+} が SrTiO_3 にドーピングされることがわかった。 SrTiO_3 の Ti^{4+} を Ga^{3+} などへ、あるいは、 Sr^{2+} を Na^+ などの低原子価の元素と置換すると、光触媒活性が向上することが報告されている^{11) 12)}。したがって、 $\text{FLUX} = 10$ まで増加させたときの光触媒活性の向上は、欠陥の減少よりも、 Al^{3+} がドーピングされたことによる効果であると考えられる。事実、るつぼからの Al^{3+} の溶存効果はフラックスで腐食されにくい Y_2O_3 製のるつぼを使い、 Al^{3+} のドーピング量をコントロールすることで確認できた¹³⁾。一方、 Al^{3+} のドーピングによって $11,000\text{ cm}^{-1}$ 付近に再び新しいピークが出現したことは大変興味深い。この吸収が出現してから活性が劇的に向上したことから、この吸収を与える欠陥が活性向上に役立っていると考えられる。今のと

ころ、この欠陥がどのような構造を有しており、どのような性質を持っているのか不明である。しかし、これらの結果は、欠陥には活性向上に役立つ欠陥と活性を低下させるものがあり、これらの欠陥の構造を制御することで光触媒活性を向上させることができることを示している。

6. まとめ

本稿では、可視から中赤外域の過渡吸収スペクトルを測定することで、水を完全分解できる SrTiO₃ 粉末の欠陥における光励起キャリアの挙動を調べた結果について解説した。粉末は単結晶に比べて欠陥が多く、大部分の光励起キャリアは欠陥にトラップされていることを見出した。しかし、欠陥は必ずしも再結合を促進するわけではない。光励起キャリアの寿命は単結晶よりもむしろ粉末の方が長いことを明らかにした。また、欠陥に捕捉された光励起キャリアの反応活性は、欠陥の構造に依存し、準位がそれほど深くない場合には、高い反応活性を維持している。そして、定常反応活性は自由電子や浅いトラップ電子の残存量と良い相関があることがわかった。粒子の表面欠陥は、熔融塩を用いたフラックス処理で低減することができる。そして、フラックス処理を行うとトラップ準位の深さが浅くなることを見出した。つまり、粒子表面に存在する欠陥は光励起キャリアを捕捉するが、再結合速度を遅くする働きがあり、その構造をうまく制御することで定常反応活性を向上できることを見出した。

謝 辞

本稿で解説した研究内容は、堂免一成教授（東京大学）、酒多喜久教授（山口大学）および豊田工業大学、東京大学の研究員、学生との共同研究の成果である。また、本研究を行うにあたり JST（国立研究開発法人科学技術振興機構）さきがけ研究と文部科学省・科学研究費補助金（特別推進研究：23000009，基盤研究 B：23360360），文部科学省・私立大学戦略的研究基盤形成支援事業，日本板硝子財団（（公財）日本板硝子材料工学助成会）の支援を受けた。この場を借りて関係者に感謝する。

文 献

- 1) K. Domen, S. Naito, M. Soma, T. Onishi and K. Tamaru : *J. Chem. Soc.-Chem. Commun.*, 543 (1980).
- 2) A. Yamakata, J. J. M. Vequizo and M. Kawaguchi : *J. Phys. Chem. C*, **119**, 1880 (2015).
- 3) A. Yamakata, H. Yeilin, M. Kawaguchi, T. Hisatomi, J. Kubota, Y. Sakata and K. Domen : *J. Photochem. Photobiol. A-Chem.*, **313**, 168 (2015).
- 4) A. Yamakata, M. Kawaguchi, R. Murachi, M. Okawa and I. Kamiya : *J. Phys. Chem. C*, **120**, 7997 (2016).
- 5) J. I. Pankove : *Optical Processes in Semiconductors*. Dover, New York (1975).
- 6) A. Yamakata, M. Kawaguchi, N. Nishimura, T. Minegishi, J. Kubota and K. Domen : *J. Phys. Chem. C*, **118**, 23897 (2014).
- 7) A. Yamakata, T. Ishibashi and H. Onishi : *J. Phys. Chem. B*, **105**, 7258 (2001).
- 8) A. Yamakata, T. Ishibashi and H. Onishi : *J. Phys. Chem. B*, **106**, 9122 (2002).
- 9) Y. Miseki, K. Saito and A. Kudo : *Chem. Lett.*, **38**, 180 (2009).
- 10) H. Kato, M. Kobayashi, M. Hara and M. Kakihana : *Catal. Sci. Technol.*, **3**, 1733 (2013).
- 11) T. Takata and K. Domen : *J. Phys. Chem. C*, **113**, 19386 (2009).
- 12) Y. Sakata, Y. Miyoshi, T. Maeda, K. Ishikiriyama, Y. Yamazaki, H. Imamura, Y. Ham, T. Hisatomi, J. Kubota, A. Yamakata and K. Domen : *Applied Catalysis A : General*, **521**, 227 (2016).
- 13) Y. Ham, T. Hisatomi, Y. Goto, Y. Moriya, Y. Sakata, A. Yamakata, J. Kubota and K. Domen : *J. Mater. Chem. A*, **4**, 3027 (2016).



キャリア選択型太陽電池を用いた水素生成

豊田工業大学 半導体研究室

大下祥雄

Hydrogen generation by carrier selective contact solar cells

Yoshio Ohshita

Toyota Technological Institute, Tempaku, Nagoya, 468-8511, Japan

y_ohshita@toyota-ti.ac.jp

As a new alternative to the conventional p-n junction solar cell concept, dopant-free carrier-selective contacts (CSCs) solar cells are proposed to separate and collect photo generated free carriers in a cell structure. This high efficiency and low cost solar cells are one of the candidates to generate hydrogen molecules with the low cost enough for the future energy market. The water can be efficiently decomposed by the electrical power generated using the solar cells. One of the most promising electron-selective contact (ESC) materials is titanium oxides (TiO_2) and the electrons extracted by this contact will decompose the water. To realize the expected high performance, the band structure of this solar cell is determined by XPS analysis. Based on the obtained result, the moderate phosphorus is diffused into the Si substrate near the interface and the extraction of electrons performance is improved.

1. はじめに

化石エネルギーの将来における供給不安およびその使用に起因する地球温暖化などの環境汚染の問題を解決した脱炭素社会を実現することを目的として、再生可能エネルギーに関する研究が盛んに行われている。特に、太陽電池に関するデバイスおよび量産技術の進展が近年著しい。その結果、生産量が急激に拡大し、それに伴いモジュール価格が著しく低下している (<50 円/W)。世界的に見ると、国によっては最も安価な発電技術となっている。年間導入量は現在世界で 50GW 程度、累積では 500GW 程度に至っており、以前は遠い夢として語られていた 1 TW の電力が近い将来に太陽光発電で得ることが現実となる。太陽電池性能も年々向上しており、研究段階においてカネカ (株) により 26.33% が実現され、量産品においても 20% を超えてきている。

一方で、太陽光発電においては、夜間において発電できない、雨天には発電量が大幅に低下するなど、エネルギー供給源としての不安定性という本質的な課題を有している。電力全体に占める太陽光発電の占める割合の増加にともない、この問題がより大きくなってきている。この問題を解決することを目的として、揚水発電との組み合わせ、あるいはリチウム電池などの 2 次電池との組み合わせ技術、さらにはスマートグリッドと呼ばれる地域全体での電力制御技術などの開発が進められている。その一方で、将来の水素社会の実現に対して、太陽電池で発電した電気を用いて水を分解して水素として貯蔵し、必要に応じて燃料電池により貯蔵されている水素を用いて発電する試み

も進められている。一つの太陽電池により発生される電位差は、結晶シリコン太陽電池で 0.7V 程度、化合物半導体を用いたタンデム型で 3V 程度（三接合）である。結晶シリコンにおいても二つの太陽電池を直列にすれば、水の電気分解に必要な電位差が得られる。すなわち、太陽光発電における高い光-電気変換効率により、太陽電池を用いて高い効率での水素生成が期待できる。

2. 水素発生用デバイスとしての太陽電池

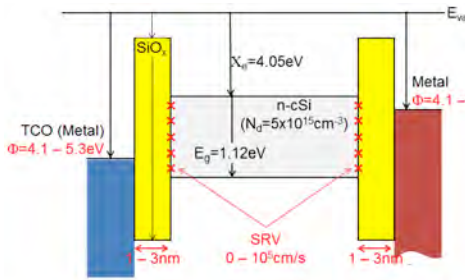


図 1 キャリア選択型太陽電池のデバイス構造

太陽電池を用いて水を分解することを考えるとき、その目的に適しているのがキャリア選択型太陽電池である。本太陽電池は、結晶シリコン太陽電池のさらなる高効率化ならびに低コスト化を目的として研究が精力的に進められているデバイスの一つである。本太陽電池の構造を図 1 に示す。通常の太陽電池は、光吸収により生成された電子と正孔を p n 接合により空間的に分離し、それらを外部に取り出すことにより電池としての動作をさせている。それに対して、本太陽電池においては、ダイオード構造を有していない。

本デバイスでは、結晶シリコンの両表面に薄い酸化膜などを形成する。本層は、結晶シリコン半導体表面における高品質なパッシベーション膜として働き、界面における低い少数キャリア再結合速度を実現し光照射時の電流量および電圧を向上させる。一方、本薄膜は、トンネル酸化膜としても働き、光吸収によりシリコン結晶中に生成された電子や正孔の効率的な取り出し層となる。その膜上には、電極材料を堆積する。電子を取り出すための電極としては、シリコンの伝導帯のエネルギーと同程度の仕事関数を有する材料を用いる。これにより、理想的には、光吸収により生成された電子に対してはエネルギー障壁がなく、電子を効率的に輸送することが可能となる。それに対して、正孔は界面におけるエネルギー障壁のため電極へは輸送されない。一方、正孔用には、シリコンの価電子帯と同程度の大きな仕事関数を有する材料を用いる。

本太陽電池を用いて効率的に水を分解するには、高い電圧と電流を実現することが必要である。そのためには、1) 少数キャリア寿命の長い良好なシリコンの結晶性、2) 再結合速度が低いパッシベーション特性、3) 良好なキャリア輸送特性が得られるバンド構造、などが得られる材料ならびにデバイス構造を実現することが求められる。これまでに、電子用ならびに正孔用材料の仕事関数が変換効率に与える影響をデバイスシミュレーションにより定量的に求め、高効率を得るために必要な電極の仕事関数を決定してきた。その結果をもとに、電子取り出し用材料としては酸化チタン、正孔取り出しには酸化モリブデンなどを選定し、それらの検討を進めている。光触媒においては、酸化チタン粒子に光が照射されると酸化チタン中に過剰キャリアが生成し、酸化チタン表面に到達した電子が触媒作用も含めて水素を発生する。同様に、酸化チタンを電極としたキャリア選択型太陽電池においては、シリコン半導体において光からキャリアが効率よく生成され（光電変換効率 25%あるいはそれ以上）、それらキャリアが酸化チタン層に輸送され電極（触媒）表面で水素を発生（全体効率 20%以上）することが期待される。水分解に必要な電圧は、本構造を基本として二つ以上の太陽電池が積層されたタンデム型により得ることが可能である。

3. キャリア選択型太陽電池の高性能化

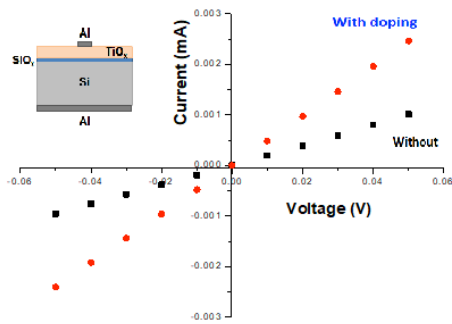


図2 キャリ輸送特性

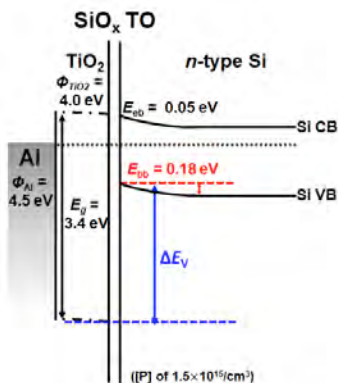


図3 電子用電極近傍のバンド構造

材料の制約などから、高い特性が得られる理想的なバンド構造を実現することは一般には困難である。その結果として、例えば、電極-半導体界面におけるキャリア輸送特性が悪くなる、すなわち、デバイス特性として直列抵抗が増加するなどの問題が生じる(図2)。この問題を解決するには、実デバイスにおけるバンド構造を実験的に求め、その上で特性向上を図ることが必要である。バンド構造の決定にはいくつかの方法があるが、我々は研究室レベルの光電子分光法(XPS)に加え、Spring-8の放射光を用いたHAXPES測定を行っている。

XPS測定により得られたバンド構造の一例を図3に示す。シリコン酸化膜近傍のシリコン結晶に、酸化チタンの仕事関数とシリコンのフェルミ準位との違いにより決定される表面ポテンシャルが電子輸送に対するエネルギー障壁として存在する。この表面ポテンシャルが直列抵抗増加の原因である。この問題を解決するため、界面近傍のシリコン結晶中に不純物をドーピングし、表面ポテンシャルの影響が及ぶ距離を短くすることにより界面でのキャリア輸送特性を改善した(図2)。

一方、電子用電極として検討している薄いシリコン酸化膜とアモルファス酸化チタンの構造においては、光照射によりパッシベーション特性が劣化する。この問題を解決し、水分解電極として耐性が高く長期使用に適した材料の探索も行っている。例えば、シリコン上の薄い絶縁膜としてアルミナを用い、その上に原子層エピタキシャル装置を用いて酸化チタンにタンタルを添加することにより特性が安定化するなどの結果が得られている。

4. まとめ

結晶シリコン太陽電池を用いて得られる電力のコストが近年急速に低下している。その結果、全発電量の中での太陽光発電の割合が急速に増加している。それに伴い、太陽光発電の不安定性の問題が従来以上にクローズアップされてきている。この問題を解決し、かつ、より効率的に再生エネルギーを利用する一つの方法として、太陽光発電により得られた余剰電力で水を分解し、そのエネルギーを水素の形に変換して貯蔵して、必要な時にそれを用いて発電するシステムの構築を検討している。ここでは、太陽電池を用いて水を直接分解するのに適したキャリア選択型太陽電池の開発状況を述べた。今後、本太陽電池の改良に加えて多接合タンDEM構造などの検討を進め、更なる高効率化ならびに高電圧化を目指す。

高活性電極触媒の開発に向けたナノ炭素材料の適用

豊田工業大学

○原正則, 吉村雅満

Application of modified nano-carbon materials to develop highly active catalysts

Masanori Hara*, Masamichi Yoshimura

Surface Science Laboratory, Toyota Technological Institute, Tempaku, Nagoya, 468-8511, Japan

haram@toyota-ti.ac.jp

To improve catalytic activity for oxygen evolution reaction (OER) by increasing the specific activity of catalysts, we develop novel alloy catalysts of iridium oxide with ruthenium oxide supported on modified nano-carbon materials, such as heteroatom (N or B) doped reduced graphene oxide (rGO), as the anode of the water electrolyzer. Structure, composition and electronic state of the synthesized catalyst was characterized by transmission electron microscopy, energy dispersed X-ray analysis, X-ray photoelectron spectroscopy. Electrochemical analysis for OER confirms high activity of the IrRuO_x alloy catalysts supported on N- or B-doped rGO compared to IrO₂ /rGO in acidic solution. The results suggest that the catalysts supported on modified nano-carbon materials are promising candidates for the anode of electrochemical hydrogen production system.

1. はじめに

近年、温暖化や石油枯渇といった環境・エネルギー問題の解決を目指し、新たなエネルギー供給源として太陽光や風力、水力などを利用した再生可能エネルギーが注目を集めており、これらのクリーンな電力を高効率で利用することが可能な電力供給システムの開発が進められている。しかしながら、再生可能エネルギーによる電力供給は気候や天候による時間変動が大きいため、電力貯蔵システムとの組み合わせが必要となっている¹⁾。余剰な再生可能エネルギーを利用して製造された水素²⁾を燃料として用いる電力貯蔵-発電システムは、低環境負荷な水素社会のエネルギー供給源として期待されており、低コスト・高効率な水素製造技術の確立が求められている。

水素の製造においては、現在、クリーンな製造法として水の電気分解反応を用いた水素生成の研究が進められており、エネルギー効率の向上やシステムの簡素化、低コスト化に加えて、長時間の耐久性および安定性の向上が求められている。Nafionなどのプロトン交換膜 (PEM) を用いた膜電極接合体

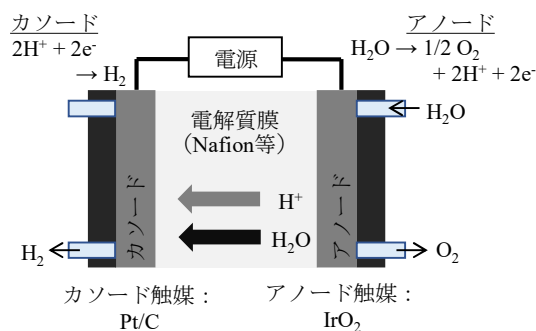


図1 固体高分子形水電解装置(PEWE)の模式図。

(MEA) 型の水電解システム (polymer electrolyte water electrolyzer (PEWE), 図 1) は, 高電流密度での作動性と電位変動に対する応答性の速さ, 構造の簡易さから, 次世代の水素製造システムとして期待されている¹⁾. しかし, 電極触媒に Pt や Ir などの貴金属触媒を使用するためにコストが高くであり, また触媒の耐久性も未だに不十分という課題がある. そのため, 高活性かつ高耐久性を有する電極触媒, 特に過電圧が大きく高電位で使用される酸素発生反応 (OER) 用のアノード触媒の開発が求められている^{2,3)}. 本研究グループでは, これまでにカーボンナノチューブ⁴⁾およびグラフェンとその誘導体⁵⁾などのナノ炭素材料を担体に用いた水電解反応用の IrO_2 触媒の合成と OER に対する触媒活性の評価を行い, ナノ炭素材料の担体上では IrO_2 触媒のナノ粒子化による比表面積の増加により触媒活性が大きく向上することを報告している.

本研究では, 異種元素 (窒素およびホウ素) をドーピングしたグラフェン (窒素ドーピング還元酸化グラフェン: N-rGO およびホウ素ドーピング還元酸化グラフェン: B-rGO) の担体への適用および IrO_2 触媒の RuO_2 触媒との合金化により, OER 活性を向上させた新規な IrO_2 ナノ粒子触媒 ($\text{IrO}_2/\text{N-rGO}$, $\text{IrO}_2/\text{B-rGO}$, $\text{IrRuO}_x/\text{N-rGO}$, および $\text{IrRuO}_x/\text{B-rGO}$) の開発について報告する.

2. 実験方法

本研究の触媒担体に用いる窒素およびホウ素ドーピンググラフェン (N-rGO および B-rGO, 図 2) は, 原料であるグラファイト (Sri Lankan natural graphite) の化学劈開処理 (改良 Hummers 法)⁶⁾ により作製した酸化グラフェン (GO) を, ドープ元素 (N および B) の原料となる尿素もしくは酸化ホウ素と混合し, 不活性雰囲気下で 800°C および 1000°C で加熱処理を行うことで合成した. IrO_2 もしくは IrRuO_x を担持した電極触媒は, H_2IrCl_6 錯体および RuCl_3 錯体と N-rGO もしくは B-rGO を混合した溶液を 150°C において 4 時間水熱合成を行うことにより, IrO_2 もしくは IrRuO_x ナノ粒子が N-rGO もしくは B-rGO 担体上に担持された水電解用アノード触媒 ($\text{IrO}_2/\text{N-rGO}$, $\text{IrO}_2/\text{B-rGO}$, $\text{IrRuO}_x/\text{N-rGO}$, および $\text{IrRuO}_x/\text{B-rGO}$) を合成した.

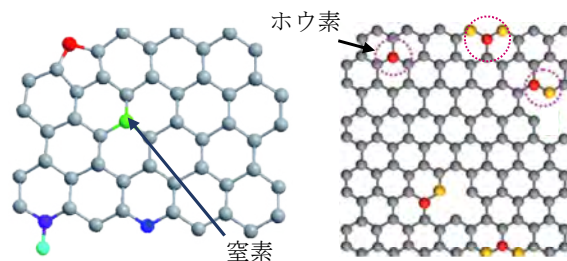


図2 (a) N-rGOおよび(b) B-rGOの構造モデル.

合成した電極触媒 ($\text{IrO}_2/\text{N-rGO}$, $\text{IrO}_2/\text{B-rGO}$, $\text{IrRuO}_x/\text{N-rGO}$, $\text{IrRuO}_x/\text{B-rGO}$) のキャラクターゼーションは, 透過電子顕微鏡 (TEM), X 線回折 (XRD), X 線光電子分光 (XPS), 走査電子顕微鏡 (SEM) およびエネルギー分散型 X 線分析 (EDX) により行った. 各触媒の OER 活性評価は, 0.5 M 硫酸水溶液中において回転ディスク電極 (RDE) を用いた電気化学測定 (サイクリックボルタンメトリー (CV) およびリニアスイープボルタンメトリー (LSV), 掃引速度: 5 mV s^{-1}) により行った.

3. 結果と考察

3-1. 異種元素ドーピンググラフェン上に担持した IrO_2 触媒の特性評価

水熱合成法により作製した $\text{IrO}_2/\text{N-rGO}$ および $\text{IrO}_2/\text{B-rGO}$ 触媒の TEM 像を図 3 に示す. TEM 像より, IrO_2 微粒子は均一に分散しており, 平均粒径は N-rGO 担体上では 1.3 nm , B-rGO 担体上では 1.7 nm であることが分かった. EDX 測定より, 異種元素のドーピング量は窒素で $9.6\text{ wt.}\%$, ホウ素

で 2.3 wt.% であり, IrO_2 担持量は $\text{IrO}_2/\text{N-rGO}$ で 10.1 wt.%, $\text{IrO}_2/\text{B-rGO}$ では 19.6 wt.% であった. また, XRD および XPS 測定より担体上に析出した触媒は rGO 担体に担持した場合と同様に IrO_2 であり, XPS 測定より Ir 4f のピ

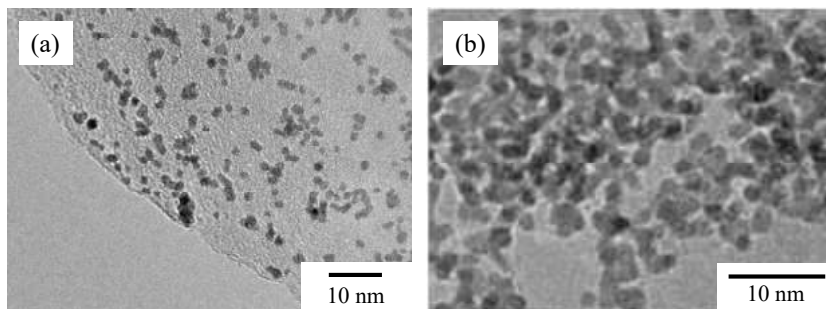


図3 (a) $\text{IrO}_2/\text{N-rGO}$, (b) $\text{IrO}_2/\text{B-rGO}$ 触媒のTEM像.

ークは IrO_2 粉末よりも 0.6 eV 程度, rGO 担体上の IrO_2 触媒より 0.3 eV 程度低束縛エネルギー側にシフトしていることが確認された. 異種元素をドーピングした rGO 担体上においても, IrO_2 触媒の担持に成功し, さらに担体の修飾により IrO_2 触媒の電子状態が変化したことが分かった. これは, 異種元素ドーピングしたグラフェン上では表面上の電荷分布が変化したため, 担体上の IrO_2 もこの影響を受けての電子状態が変化したためと考えられる.

次に, IrO_2 触媒の電子状態をさらに変化させるため, RuO_2 との合金化を行い, 異種元素ドーピング担体 (N-rGO および B-rGO) 上に IrRuO_x 触媒の担持を行った. 図 4 に $\text{IrRuO}_x/\text{N-rGO}$ および $\text{IrRuO}_x/\text{B-rGO}$ の TEM 像を示す. また, 比較として rGO 上に担持した $\text{IrRuO}_x/\text{rGO}$ の TEM 像も併せて示す. IrRuO_x ナノ粒子の平均粒径は rGO 上では 1.9 ± 0.8 nm, N-rGO 上では 1.7 ± 0.5 nm, B-rGO 上では 1.7 ± 0.3 nm であった. IrRuO_x 粒子が異種元素ドーピング担体に担持されている場合には, rGO に比べて触媒の粒子サイズが小さく, 粒子サイズ分布も狭い, 均一なナノ粒子が担体表面上に分散して担持されていることが分かる. 触媒粒子サイズの変化は, 異種元素がドーピングしたグラフェン上では, 担持された触媒粒子との相互作用が強くなり, rGO 上よりも強く結合するために合成時の触媒粒子の凝集が抑制されたためと考えられる.

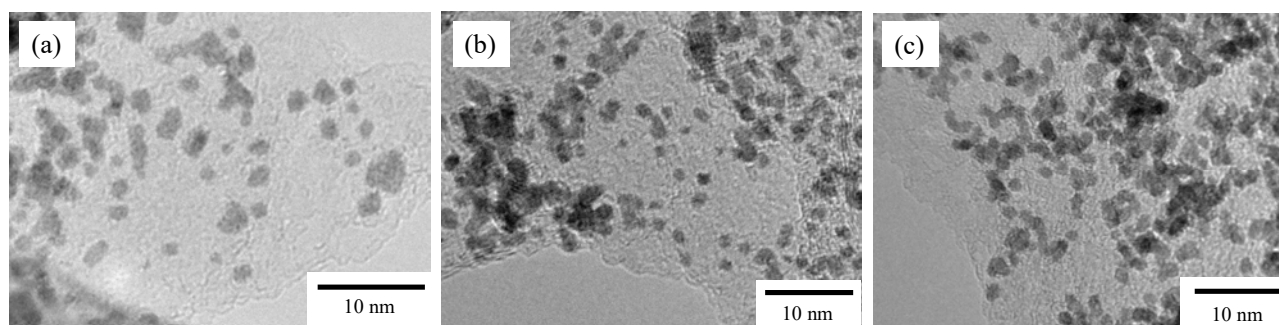


図4 (a) $\text{IrRuO}_x/\text{rGO}$, (b) $\text{IrRuO}_x/\text{N-rGO}$ および (c) $\text{IrRuO}_x/\text{B-rGO}$ のTEM像.

図 5 に $\text{IrRuO}_x/\text{N-rGO}$ および $\text{IrRuO}_x/\text{B-rGO}$ 触媒の XPS スペクトルを示す. ドーピング元素及び合金化した Ru が確認され, 目的とした触媒が合成できたことが分かる. XPS および EDX 測定より, 窒素およびホウ素のドーピング量は 7.6 wt.% および 3.8 wt.% であり, 触媒の IrRuO_x ($\text{Ir}:\text{Ru} = 1:1$) の担持量は N-rGO 上では 17.8 wt.%, B-rGO 上では 10.2 wt.% であった. また, rGO 上の XPS 測定より, Ir 4f のピーク位置 (図 6) は, IrRuO_x 触媒粒子の Ru の含有量が高いほど低束縛エネルギー側に移動することが分かった. 一方, IrO_2 の場合とは異なり, 異種元素ドーピング担体への担持による Ir 4f のピーク位置のシフトは小さく, 担体による電子状態の修飾に比べ合金化した Ru による効果の方が大きいことが示唆された.

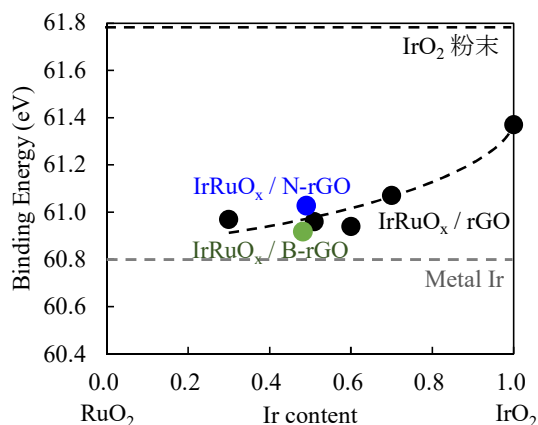
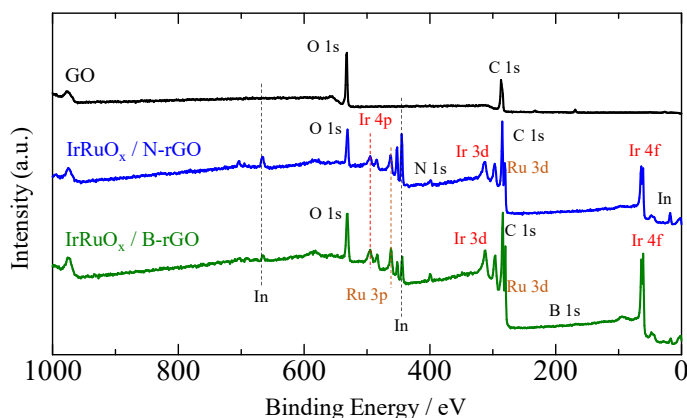


図5 IrRuO_x / N-rGOおよびIrRuO_x / B-rGOのXPSスペクトル. 図6 XPS測定より求めたIr 4f_{7/2} ピーク位置.

3-2. 異種元素ドーピンググラフェン上に担持した IrO₂ 触媒の OER 活性評価

図 7 に、0.5 M 硫酸溶液中における異種元素ドーピング rGO 担体および合金化ナノ粒子を用いた各種触媒上における、OER の電気化学測定 (LSV 測定) より求めた 1.55 V での OER 質量活性の比較を示す. 担体に異種元素をドーピングすることにより、IrO₂ の OER に対する触媒活性が IrO₂ / rGO に比べて N-rGO 担体上では 3.3 倍、B-rGO 担体上では 6 倍向上することが示された. 触媒の粒子サイズはほぼ同程度である

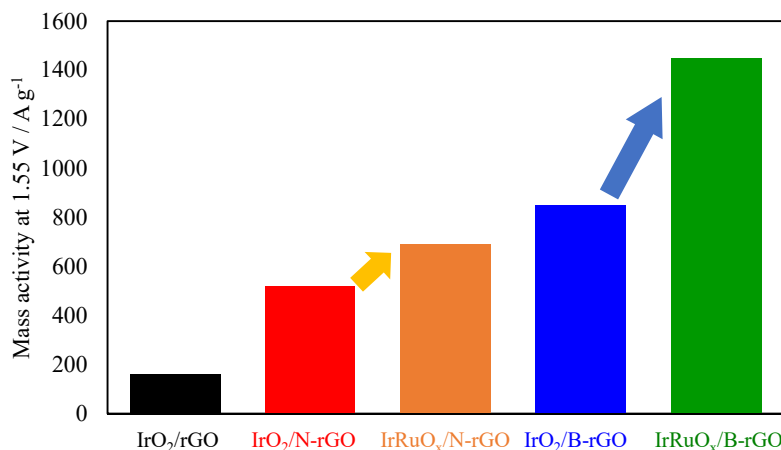


図7 N-rGOもしくはB-rGO担体上にIrO₂もしくはIrRuO_xナノ粒子を担持した触媒のOER活性.

ため、OER 活性の向上はナノ炭素担体の修飾による IrO₂ 触媒の電子状態変化によるものであり、OER の反応過程における水分子から触媒への電荷移動が起きやすくなったためと考えられる. さらに、IrO₂ 触媒を Ru と合金化した IrRuO_x / N-rGO および IrRuO_x / B-rGO 触媒では、OER 活性のさらなる向上が観察され、担体の修飾と触媒粒子の合金化の相乗効果により触媒の OER 活性を向上できることが示された. 今後、触媒粒子の表面構造制御やヘテロ接合構造体の担体への利用など、さらなる触媒のナノ構造の最適化により触媒の活性向上が見込めると期待される.

【参考文献】

- 1) M. Carmo, D. L. Fritz, J. Mergel, D. Stolten, Int. J. Hydrogen Energy, 38 (2013) 4901.
- 2) E. Antolini, ACS Catal., 4 (2014) 1426.
- 3) J. Cheng, H. Zhang, H. Ma, H. Zhong, Y. Zou, Electrochim. Acta, 55 (2010) 1855.
- 4) R. Badam, M. Hara, H.-H. Huang, M. Yoshimura, Int. J. Hydrogen. Energy, 43 (2018) 18095.
- 5) M. Hara, R. Badam, G. J. Wang, H.-H. Huang, M. Yoshimura, ECS Trans., 85 (2018) 27.
- 6) B. Garg, T. Bisht, Y. C. Ling, Molecules, 19 (2014) 14582.



Fabrication of reduced graphene oxide membranes for water desalination

Hsin-Hui Huang^a, Rakesh K. Joshi^{b,*}, K. Kanishka H. De Silva^a, Rajashekar Badam^a, Masamichi Yoshimura^a

^a Graduate School of Engineering, Toyota Technological Institute, Nagoya 468-8511, Japan

^b SMaRT Centre, School of Materials Science and Engineering, University of New South Wales, Sydney, NSW 2052, Australia



ARTICLE INFO

Keywords:

Membranes
Reduced graphene oxide
Graphene
Hydrothermal reduction

ABSTRACT

Reduced graphene oxide (rGO) has huge potential for membrane applications owing to its appropriate interlayer spacing (0.34–0.37 nm) that enables it to block salt ions as small as Na⁺ with high precision. However, fabrication of uniform rGO membranes is a great challenge because of the loss of its polar functional groups during preparation from graphene oxide (GO). Although there have been several studies on GO membranes and a few on rGO for water purification, very few attempts to understand the role of oxygen-containing functional groups in successful rGO membrane formation. The present work deals with the investigation of the key factors and functional groups that govern membrane formation. This work also utilizes the facile approach of synthesizing reduced GO by environmentally viable hydrothermal reduction. Further characterizations show that the hydroxyl and carboxyl groups are principally responsible for the formation of uniform rGO membranes. The rGO (treated at 160°C for 2 h) membrane with a small amount of unreduced GO presented shows the lowest Na⁺/Cl⁻ ion permeation with the highest membrane flux, which is suggested to be a potential candidate for water desalination.

1. Introduction

Membrane systems with controllable nano-sized pores or interlayer channels are of interest for separation processes such as water purification, water desalination, gas separation, and ion sieving [1–5]. The ideal membrane should be thin, stiff, and possess a large surface area to be able to function under high applied pressures and perform with a high selectivity. In this regard, carbon-based materials such as carbon nanotubes, graphene, graphene oxide (GO), and reduced graphene oxide (rGO) have been identified as promising candidates [3–9]. Among them, stacked graphene oxide has recently attracted attention due to its unique water pathway mechanism and ability to selectively prohibit the undesired ions or gases from passing through [7, 10–14]. Additionally, the preparation of GO is considered to be cost-effective in terms of the methodology and types of raw materials used (such as naturally abundant graphite) [15]. However, when GO membranes are placed in an aqueous solution, the spacing between the GO sheets increases up to 1.3 nm due to the effect of hydration. This increased spacing not only destabilizes the membranes but also reduces their selectivity, as the small hydrated ions (e.g., K⁺, Mg²⁺, Na⁺ and AsO₄³⁻) can pass through such enlarged channels [16]. To solve this issue, work has been done to narrow the interlayer spacing for ion

passage either by physical confinement [17] or chemical decoration [18]. Moreover, the negatively charged functional groups in GO cause it to disintegrate and deteriorate upon hydration due to electrostatic repulsion [15,19]. To improve their stability, it is necessary for GO sheets to be cross-linked with multivalent ions, organic crosslinkers [19,20], or by dopants [21]. On the other hand, rGO membranes with a smaller lattice parameter (~0.34 nm) and properties resembling graphene are an ideal candidate which can theoretically block out the salt ions based on size exclusion. However, fabricating uniform rGO membranes is challenging as they tend to agglomerate, aggregate, and crumple due to the reduced amount of oxygen functional groups. Additionally, rGO has less dispersibility, wettability, and mechanical and chemical stability compared to GO. Possible ways to restore these properties are to functionalize it again by decorating with N-(trimethoxysilylpropyl) ethylenediamine triacetic acid [22,23], coating with polydopamine [24], functionalizing by chitosan [25], using the pyridine-thermal strategy [26], etc. In addition to functionalization, laminated rGO membranes can be obtained by post-treatment of GO membranes. For instance, GO membranes were first prepared by filtering a GO dispersion followed by reduction using hydriodic acid [27,28] or thermal heating [29]. However, the abovementioned approaches might have drawbacks such as shrinkage, creating bubbles during the reduction of

* Corresponding author.

E-mail address: r.joshi@unsw.edu.au (R.K. Joshi).

<https://doi.org/10.1016/j.memsci.2018.10.085>

Received 23 July 2018; Received in revised form 26 October 2018; Accepted 30 October 2018

Available online 01 November 2018

0376-7388/ © 2018 Elsevier B.V. All rights reserved.

GO membranes and inhomogeneous composites, or widening of the d-spacing by the additives [30,31].

Among the plethora of reduction methods for GO that are available today, the hydrothermal approach is one of the most attractive [32,33]. This approach uses completely safe water as the sole chemical, involves a single step, and more importantly is an environmentally green reaction. Additionally, this simple experiment facilitates the tailoring of the number of functional groups by adjusting the temperature and time of the reaction. Here, we adopted the hydrothermal approach to synthesize rGO. The fabrication conditions were altered to study the changes in its structure and morphology and hence the capability to form laminated rGO membranes. To the best of our knowledge, the mechanisms involved in the fabrication of uniform rGO membranes remain unexplored until now. This work is intended to find the key factor which governs the formation of freestanding and scalable rGO sheets through a carefully controlled and designed experiment. With a better understanding of how the membranes are formed, this study is expected to not only widen their range of applications but also prolong the lifetime for use in industry.

2. Experimental

2.1. Preparation of graphene oxide and reduced graphene oxide

The starting material used for oxidation was natural graphite powder of 7 μm in particle size (RS Mines, Sri Lanka). GO was synthesized by a modified Hummers' method as reported [32] in which sulfuric acid and potassium permanganate were used as an intercalant and an oxidant, respectively. It was then followed by the use of water to exfoliate the GO sheets and the addition of hydrogen peroxide to stop the oxidation. The obtained suspension was then repeatedly washed by hydrochloric acid and water to remove the excessive salts. The resulting GO suspension was filtered and dried in a vacuum oven at a temperature of 60 $^{\circ}\text{C}$ for 24 h. Before the hydrothermal reduction, a stable dispersion of GO with a concentration of 1 mg/ml was prepared by dispersing dried GO in distilled water (green reductant) by sonication. It was then transferred into a Teflon-lined autoclave device (HU-50, San-Ai Kagaku Co., LTD.) and treated in an electric furnace (NHK-170AF, Nitto Kagaku Co., LTD.) under 160 $^{\circ}\text{C}$. The resulting product, rGO, was extracted at different hours from 0.5 h up to 8 h for time-dependence structural analysis.

2.2. Characterization

Surface morphology was examined by a field-emission scanning electron microscope (FE-SEM, Hitachi S-4700). A thin layer of uniform osmium (Meiwafofosis Co., LTD.) was deposited on the surface of the membranes to enhance the conductivity, hence avoiding the charging effect for SEM observation. The rGO samples were observed using an accelerating voltage of 5 kV. Interlayer spacing was determined by X-ray diffraction (XRD, Rigaku-Ultima IV X-ray diffractometer) with a step size of 0.02 $^{\circ}$ /min using a CuK α radiation ($\lambda = 0.154$ nm). Atomic force microscopy (AFM, Bruker MultiMode 8) was operated in the ScanAsyst mode using a silicon cantilever (Tap300-G). AFM sample was prepared by dispersing GO/rGO powders in water and followed by ultrasonication for 30 min. It was then spin-coated on the silicon substrate for observation. The chemical state of the samples was investigated by

an X-ray photoelectron spectroscopy (XPS, ULVAC-PHI PHI5000 Versa Probe II) with a source of AlK α 1486.6 eV. Fourier transformation infrared spectroscopy (FT-IR, Jasco, FT/IR-6200) was applied over the wave number range of 400–4000 cm^{-1} with pure KBr as the background. Transmission electron microscope (TEM, JEOL JEM-2100) operated at an accelerating voltage of 200 kV was used to study the microstructure and morphology of the samples. The TEM specimen was prepared by dispersing powders in ethanol followed by ultrasonication for 15 min. It was then dropped on the carbon coated copper grids for observations.

2.3. Permeation and water flow test

The concentration-driven permeation test was carried out by customized two-half L-shaped compartments. The holes on the plate and container are of 23 mm in diameter. The GO/rGO membranes along with the supporting microfilters such as polytetrafluoroethylene (PTFE) or polyvinylidene fluoride (PVDF) were attached on a polyethylene film contained a hole at the centre with a diameter of 25 mm. Two hundred millilitres of 0.1 mol NaCl and distilled water (DI water) were introduced into the feed and permeation parts at the same speed. The conductivity meter was placed in the permeate part to record the changes in ion conductivity. Water flow test was conducted using a vacuum filtration kit setup. The GO/rGO membranes were first made then followed by filling 20 ml of DI water to examine the time duration, at which it takes to allow all the DI water to pass through. This test was carried out under a constant vacuum by a dry vacuum pump (DA-15D, ULVAC KIKO, Inc.) with a pumping speed of 12 L/min and pressure of 6.65 kPa.

3. Results and discussion

The process to fabricate rGO membranes is illustrated in Fig. 1. Details of GO and rGO synthesis are described in the section of Experimental Procedures. To fabricate rGO membranes, the hydrothermally treated rGO dispersion was filtered using EMD Millipore Swinnex[™] filter holders along with supporting layers of polytetrafluoroethylene (PTFE) with the stated pore size of 0.2 μm . Reduced GO membranes with various thicknesses were prepared by varying the loading rGO volumes, and the thicknesses of the membranes were examined by scanning electron microscopy (SEM), as shown in Fig. 2. Membranes appear as layered and laminated structures. It was observed that there is an almost linear relationship between membrane thickness and the loading amount of rGO, indicating that the thickness of the rGO membrane can be precisely controlled. The freestanding rGO membrane has a diameter of 25 mm, the size being adjustable depending on the dimension of the filtering setup.

Interestingly, we found that the laminated rGO membranes can be formed only under certain circumstances. This is examined by performing hydrothermal reduction with time dependence to better understand the membrane formation mechanisms. The experiment shows that uniformly intact rGO membranes with a black appearance formed under reduction times of 0.5 h, 1 h and 2 h (insets in Fig. 3). In contrast, when treated for over 4 h, rGO sheets tend to agglomerate and form particles rather than films. The differences in membrane formability can be clearly visualized by atomic force microscopy (AFM). The rGO flakes (rGO 0.5 h, 1 h, and 2 h) appear flat, exfoliated and featureless on the Si substrate. In contrast, after reduction time of 4 h, 6 h, and 8 h,

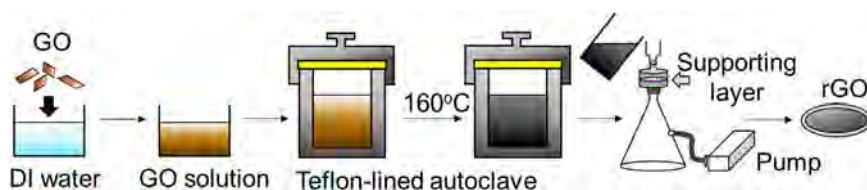


Fig. 1. Schematic representation of the fabrication procedure of rGO membranes.

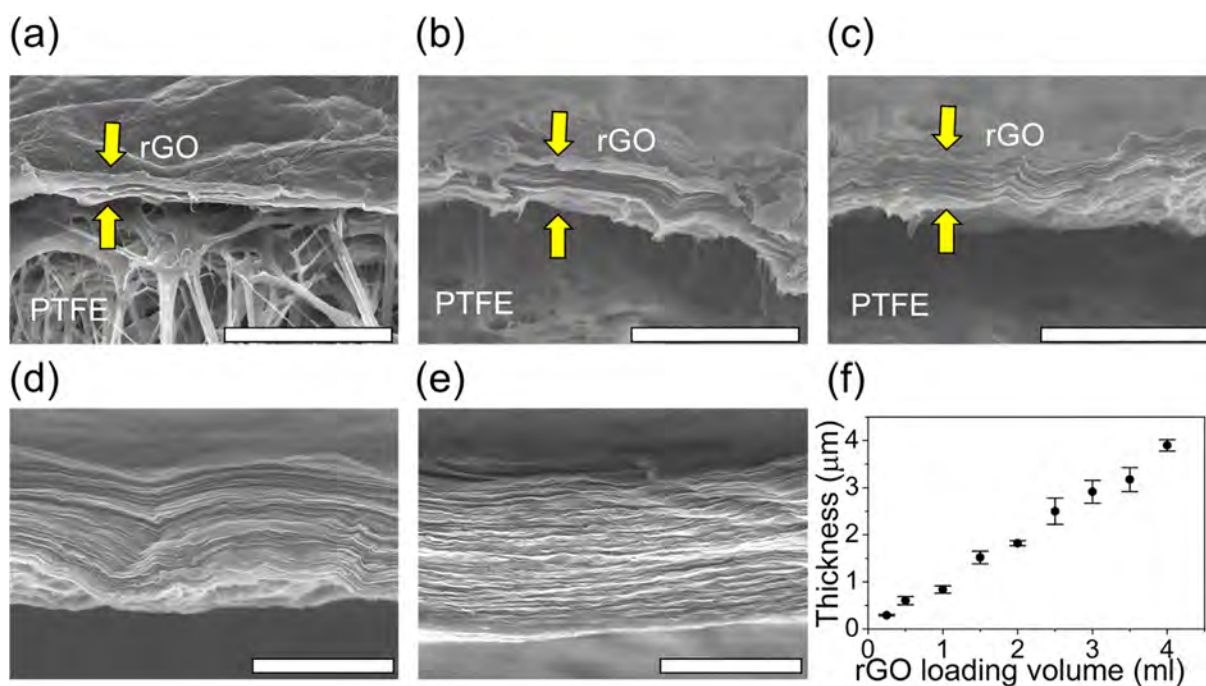


Fig. 2. Thickness examination of the rGO membranes. SEM cross-sectional images of rGO membranes with loading amount of (a) 1 ml, (b) 2 ml, (c) 3 ml, (d) 4 ml, and (e) 5 ml (scale bar is equal to 3 μm). (f) The variation of the membrane thickness as a function of rGO loading amount.

rGO sheets become corrugated with a large number of wrinkles. It suggests that surface morphology of the rGO sheets is crucial for achieving well-packed membrane.

Further, the differences between the two batches were examined by X-ray diffraction (XRD), as shown in Fig. 4(a). The uniform rGO membrane (including rGO 0.5, rGO 1 h and rGO 2 h samples) shows one peak of exfoliated rGO (interlayer spacings of 0.37–0.39 nm) and another peak of unreduced GO with lattice parameters in the range 0.78–0.84 nm. In other words, the uniform rGO membrane is in a state

of partial reduction of GO or the coexistence of GO and rGO phases. The interlayer spacing of each sample is listed in the Supporting information Table S1. Upon careful inspection on rGO 2 h sample, the partial reduction of the GO can be visualized by transmission electron microscopy (TEM) (Fig. 4(b)). In the region marked by the rectangular box, both reduced and unreduced layers were found, as schematically illustrated in Fig. 4(c). It is noted that the lattice parameters measured by XRD was averaging over a micrometre size region, while the lattice spacings shown by TEM was measured at a nanometre scale. According

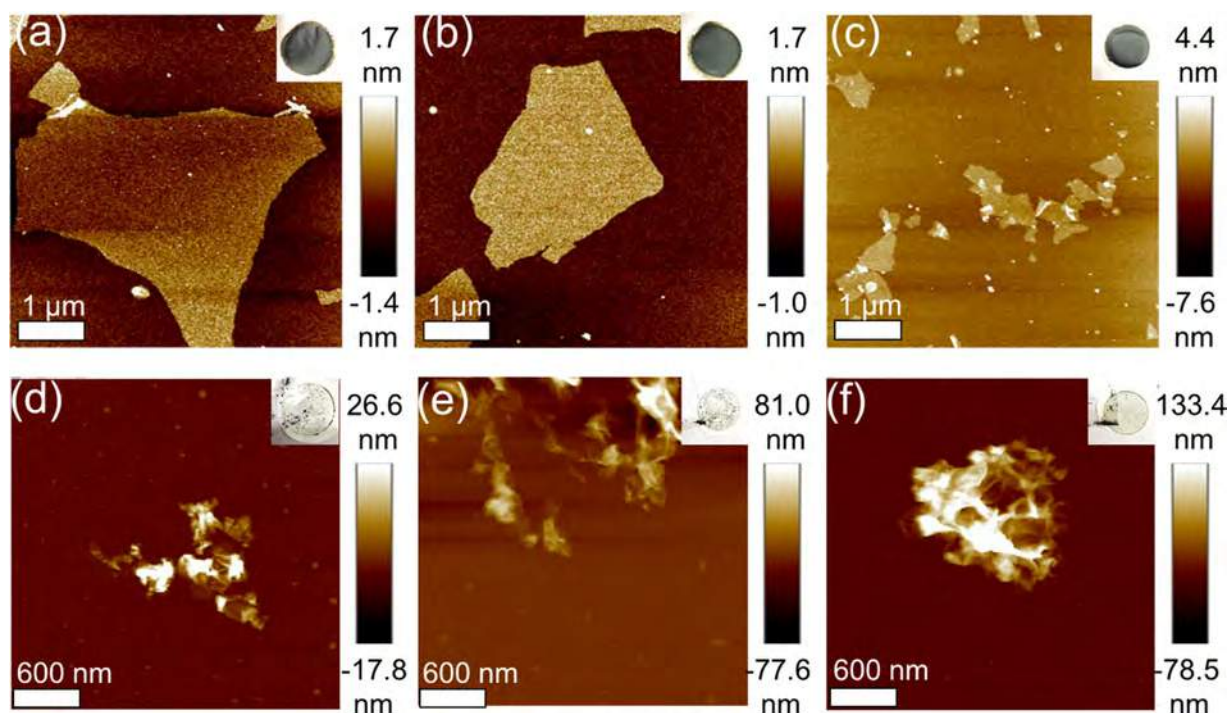


Fig. 3. Surface morphology of rGO sheets on Si substrate. AFM images of the rGO samples treated at (a) 0.5 h, (b) 1 h (c) 2 h, (d) 4 h, (e) 6 h, and (f) 8 h and the corresponding photographs showing the membrane formation behaviour after filtering.

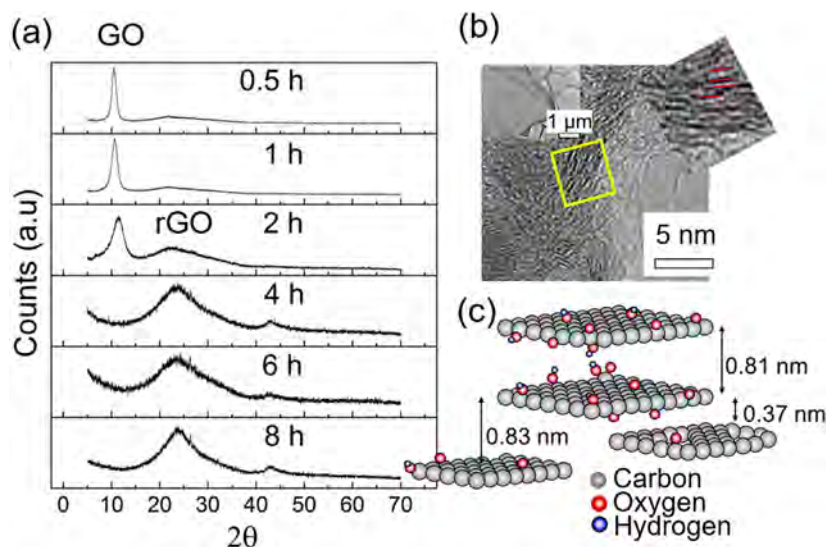


Fig. 4. Effect of structural change in the formation of rGO membrane. (a) The XRD patterns of rGO treated under different hydrothermal time. (b) Bright-field TEM image of 2 h rGO sample. The right-upper inset was taken from the yellow box showing the coexistence of rGO and GO phases, as schematically illustrated in (c).

to the widely accepted Lerf-Klinowski model, epoxide and hydroxyl groups are populated on the basal plane of the GO sheets, while carboxyl, carbonyl, and hydroxyl groups are attached at the edge of the sheets [34,35]. It is believed that the decrease in the interlayer spacing is related to oxygen functionalities on the basal plane (discussed later). It is noted that the partial reduction of GO might be caused by the difference in the stability, bond energy, kinetic energy of the oxygen functional groups. The broken rGO membrane (4–10 h) shows a broad peak with almost the same lattice spacing of approximately 0.37 nm. The GO peak has disappeared, indicating the complete reduction of the GO samples. To examine whether GO is key to forming membranes or not, we mixed GO dispersions with pure rGO, treated for 8 h, at different weight ratios. The resulting dispersions were dark brown with some aggregates after 1-h of sonication, as shown in Supporting information, Fig. S1. Surprisingly, it was found that the membranes can be formed in one piece, regardless of the GO to rGO weight ratio. This implies that the presence of GO (acts as a surfactant [36,37]) improves the dispersity of the rGO flakes and assists in forming a complete membrane, even by a small amount.

The degree of GO reduction, which is determined by the remaining oxygen content, was elucidated by X-ray photoelectron spectroscopy (XPS), as plotted in Fig. 5(a) along with the calculated lattice parameters. It shows that the oxygen content dramatically reduces to less than 20 at% after a 4 h-reduction. With the full or partial removal of oxygen functionalities, the wetting characteristics and hydrophilicity are expected to be reduced. As a result, the rGO sheets tend to cluster or agglomerate to form colloidal particles in order to lower their interfacial free energy or surface tension. Hence, it is suggested that the number of oxygen functional groups might have an impact on membrane formability. More specifically, the types of oxygen functional groups which govern the formation of membranes were revealed by a higher resolution scan of the C1s peak, as shown in Fig. 5(b). The double-peak structure of C1s gradually changes to a single-peak form with increasing reduction time, signifying the elimination of oxygen moieties. The C1s carbon spectra were deconvoluted into four peaks; C=C/C-C bonds at 284.6 eV, epoxide C-O and hydroxyl C-OH in 285.5–287.0 eV, carbonyl C=O bonds at 288.2 eV, and carboxyl O=C-OH at 289.3 eV. The fraction of each peak was plotted as a function of GO reduction time, as shown in Fig. 5(c). It was found that a dramatic decrease in the number of carboxyl groups after 4-h reduction, which suggests that the carboxyl groups might be responsible for fabricating uniform and intact rGO membranes. The difficulty in unambiguously

identifying the epoxy and hydroxyl groups by XPS has been addressed in the literature and is attributed to the overlap of the binding energy. Thus, it is wise to examine the chemical binding of the materials in parallel with other spectroscopies such as Fourier transformation infrared spectroscopy (FT-IR), as shown in Fig. 5(d). A broad peak in the wavenumber range 3600–2500 cm^{-1} corresponds to the OH stretching vibrations and physisorbed water molecules (peak position of each sample is given in Supporting information, Table S2). It can be seen that the OH peak has been significantly eliminated after 4 h reduction; however, the peaks related to the epoxide (C-O) groups in the range 1383 cm^{-1} still remain. Thus, we can speculate that the presence of hydroxyl and carboxyl groups are the key factors which govern the behaviour of membrane formation. Note that a weak peak at a wavelength of 3456 cm^{-1} in rGO 6 h might stem from the OH group in the ambient atmosphere or the adsorbed moisture in the sample.

The proposed mechanisms for membrane formation at the molecular level are illustrated schematically in Fig. 6. (1) In the presence of water (in the form of dispersion), it is known that hydrogen bonds form within the interlayer cavities between the functional groups such as hydroxyl and carboxyl groups on either side of the carbon sheets. This linkage strengthens the interfacial interaction between the neighbouring (in-plane) and adjacent (out-of-plane) sheets and hence, it holds the sheet firmly without deterioration even after drying. It has also been demonstrated previously that functional groups have a key role in the preparation of a stable, dispersive, soluble GO and/or rGO dispersion [38]. It is worth noting that hydroxyl/carboxyl groups play an important role in membrane formation (with certain amount). Moreover, upon reduction, the removal of oxygen functionalities decreases the interlayer spacing, resulting in a stronger π - π attraction between the adjacent sheets (not shown). (2) On the other hand, in the absence of hydroxyl groups or with few amount of oxygen functional groups (less than 10 at%), the rGO sheets formed aggregate due to the strong attractive force, which is a disadvantage in preparing uniform membranes. It is noted that the hydroxyl groups are located in both basal planes and edges of the sheets. Apart from the conclusion in this study, it should be noted that the membrane formability might be related to the dimension and size of the sheets, dispersibility, and colloidal stability, etc, which will be carried out in the future study.

Ion permeation across the blank filter paper, GO, rGO 0.5 h, rGO 1 h, and rGO 2 h membranes were evaluated by a homemade permeability apparatus (see the Supporting information Fig. S2). It is noted that the rGOs treated for more than 2 h were unable to make a uniform

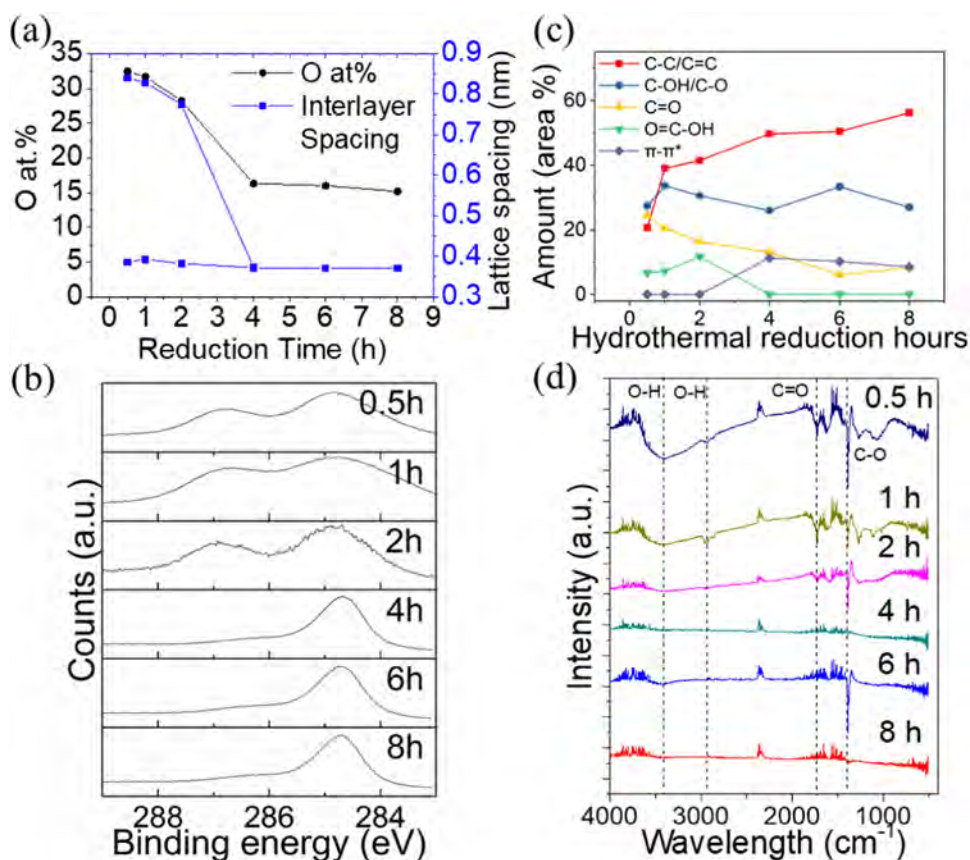


Fig. 5. Molecular insight into rGO membrane formation. (a) The change in lattice spacing and oxygen content of rGO samples with hydrothermal time. (b) The C1s spectra of the rGO samples. (c) The correlation between the fraction of individual oxygen functional groups and the reduction time. (d) FT-IR spectra of the rGO samples.

membrane, thus, only three samples were examined here. The membrane was sandwiched by two half-L-shaped compartments. The compartment facing the membrane was filled with the NaCl solution with a concentration of 0.1 mol/L (hereafter mentioned as the feed part), whereas the compartment facing the supporting layer (PVDF) was filled

with the DI water (hereafter mentioned as the permeate part). It is noted that GO/rGO membranes possess sufficient mechanical strength for the water desalination test and we used rGO membrane on top of the PVDF paper to extend their life time. The NaCl and DI water were introduced with the same speed to ensure that no external hydrostatic

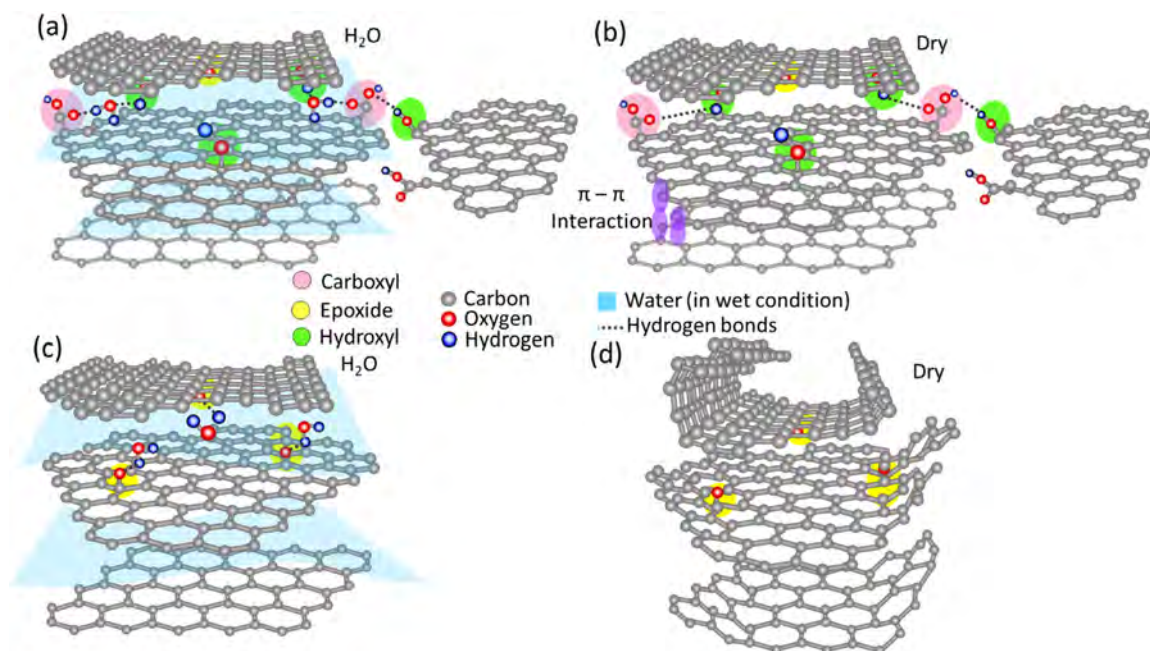


Fig. 6. Proposed mechanisms for membrane formation in wet and dry states for sample (a) with and (b) without hydroxyl/carboxyl groups. After drying, the membranes with (c) and without (d) hydroxyl/carboxyl groups give flat and aggregated morphologies, respectively.

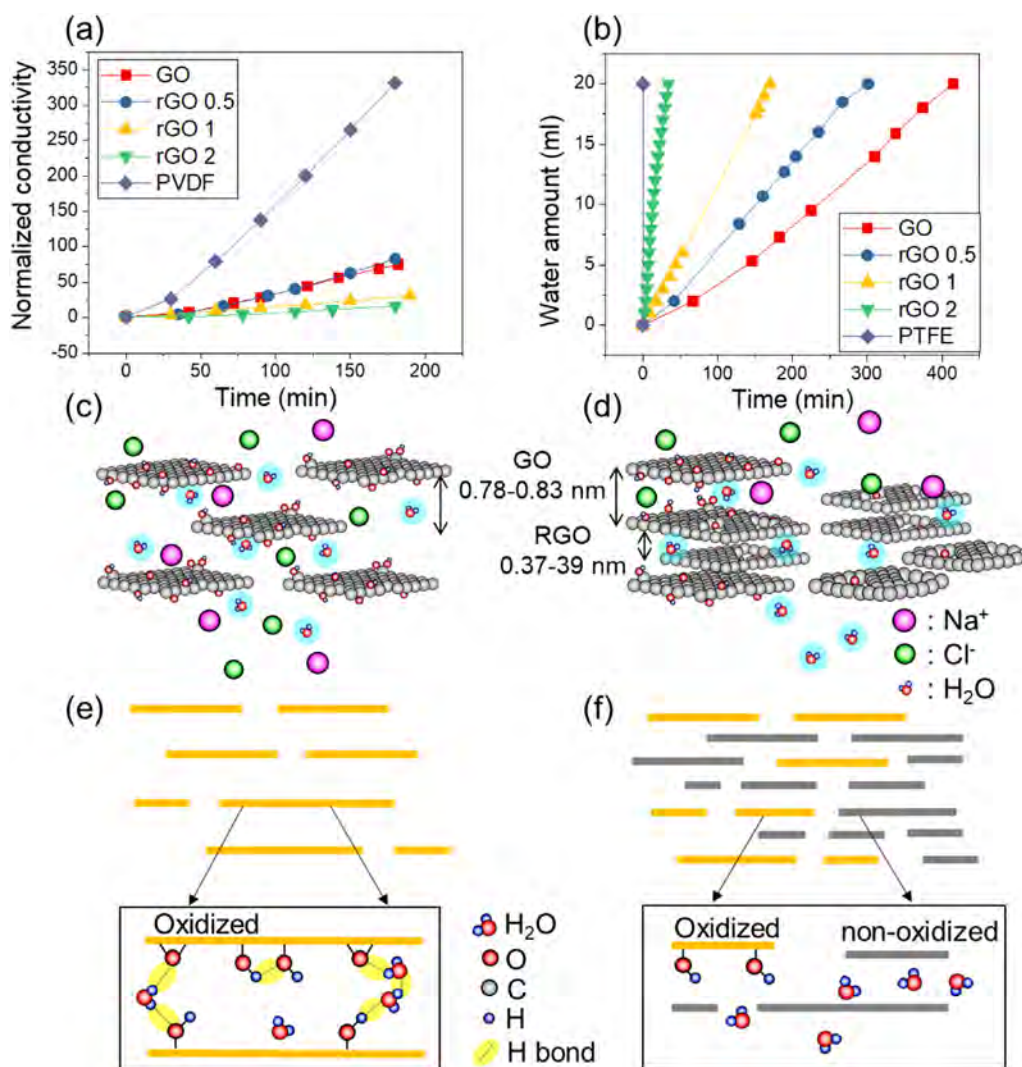


Fig. 7. (a) Permeation of Na⁺/Cl⁻ ions through the blank microfilter paper, GO, rGO 0.5 h, rGO 1 h, rGO 2 h membranes. (b) The plot of permeation flux versus time in GO/rGO membranes. The schematic illustration of the size exclusion on NaCl permeation through (c) GO membrane and (d) rGO 1 h/rGO 2 h membranes. The water transport behaviour through the (e) GO and (f) rGO 2 h membranes.

pressures were applied across the membrane. The permeation process was conducted under the mild magnetic stirring to eliminate the possible concentration gradients near the membrane. The conductivity meter was placed in the permeate part and the conductivity was detected at different time intervals. The changes in the conductivity, which reflects the amounts of ion transported through the membrane, were recorded and plotted in normalized values (by dividing by the initial conductivity of the permeate DI water), as shown in Fig. 7(a). Here, the driving force for ion transport is concentration difference. The permeation of Na⁺/Cl⁻ through the blank PVDF paper is the fastest due to the large in pore size (0.1 μm). The plots of GO/rGO membranes with the supporting PVDF paper are significantly different from the blank PVDF, implying that the ion transport behaviour is merely from the GO/rGO membranes. Moreover, it indicates that the GO/rGO membranes remain intact during or after the testing. Among all the GO/rGO membranes, GO and rGO 0.5 h membranes show relatively faster ion permeation, while the rGO 2 h membrane exhibits the slowest ion permeation. Based on structural examinations by XRD and TEM, the peak of GO, with a lattice parameter of approximately 0.8 nm, gradually diminishes with reduction time. Thus, with a short reduction time (i.e. rGO 0.5 h), the high amount of GO (large peak area in XRD pattern, see Supporting information Fig. S3) could allow more Na⁺/Cl⁻ ions to pass through based on the size exclusion (hydrated diameters of Na⁺

and Cl⁻ are 0.36 nm and 0.33 nm, respectively [14]. Moreover, it is worthy to mention that the interlayer channel in GO could be further expanded in aqueous medium on hydration, that is absorb water into the GO channel, proven by other researchers [39]. On the contrary, the rGO 1 h and rGO 2 h membranes experience relatively higher level of reduction, giving the smaller interlayer spacing to obstruct the Na⁺/Cl⁻ ions. Even though the GO has not been fully reduced, the interlayer spacing of GO might be split into two by the rGO sheet to give a higher ion sieving ability, as schematically shown in Fig. 7(c)(d).

The water transport behaviour was examined by a vacuum filtration setup and the results are shown in Fig. 7(b). As expected, with the introduction of the same amount of water under a constant vacuum, blank microfilter allows fast water transport compared to the GO/rGO membranes owing to its large in pore size. The GO/rGO membrane fluxes are listed in the descending order; rGO 2 h > rGO 1 h > rGO 0.5 h > GO, which is found to be inversely proportional to the oxygen contents of the materials. In terms of water transport behaviour in planar graphene nanochannels, the acceleration of water transport in rGO 2 h might be contributed to the presence of non-oxidized or reduced (hydrophobic) regions according to the XPS and FTIR results. This can be explained by the slip flow theory [40], as demonstrated in carbon nanotubes (CNTs) [41], where the flow enhancement is related to the slip length, hydrophobicity, smoothness, and diameter of the

nanotubes [42,43]. In CNTs, the flow enhancement increases with decrease in diameter of the CNT due to the decrease in activation energy and shear viscosity [44], which partially supports our water flow enhancement in rGO 2 h with relatively smaller interlayer spacing among all. In addition, the flow enhancement increases with hydrophobicity owing to the less interaction with water [43]. In water transport, involving solid-liquid interfacial interaction, the hydrogen-bond (H-bond) network plays an important role in determining the water transport properties. It has been shown that, when GO sheets immerse in liquid solution, H-bond is formed in between the functional groups attached to the same graphene sheets, between the functional groups attached to the adjacent graphene sheets, and between the water molecules (Fig. 7(e)). This hydrogen network might impede the water transport since they have a bond strength of 320 meV [45,46]. In our study, the rGO 2 h sample has lesser oxygen content (28.2 at%) compared to rGO 0.5 h (32.5 at%), giving more non-oxidized or reduced regions and less opportunity to build up hydrogen-bond network (Fig. 7(f)). Thus, it results in relatively higher water flux in rGO 2 h compared to rGO 0.5 h. Nevertheless, although slip flow theory supports our experiments, there is still some scope to improve the understanding. More experiments should be carried out to obtain deeper understanding for the fluid transport in 2D materials.

4. Conclusions

In summary, we have demonstrated a controllable process to prepare rGO membranes by an environmentally friendly hydrothermal approach. The mechanisms involved in fabricating a uniform membrane were elucidated through their dependence on the reduction time. At the molecular level, hydroxyl and carboxyl groups play a key role in the fabrication of rGO membranes. The rGO 2 h membrane with a small amount of unreduced GO presented shows the lowest Na^+/Cl^- ion permeation with the highest water flow rate, which is suggested to be a potential candidate for water desalination. We believe that the understanding of the formation of rGO membranes enables them to be used in a wide range of applications such as water purification and desalination, flexible electronics, thin-film devices and coatings.

Acknowledgements

The author would like to thank Ms Irem Efe from Sabanci University in Turkey for assisting in membrane thickness measurement. RKJ acknowledges the JSPS invitation Fellowship.

Conflicts of interest

There are no conflicts of interest to declare.

Appendix A. Supporting information

Supplementary data associated with this article can be found in the online version at doi:10.1016/j.memsci.2018.10.085

References

- [1] M.A. Shannon, P.W. Bohn, M. Elimelech, J.G. Georgiadis, B.J. Marinas, A.M. Mayes, Science and technology for water purification in the coming decades, *Nature* 452 (2008) 301–310.
- [2] Y. Yao, M. Li, X. Cao, P. Zhang, W. Zhang, J. Zheng, X. Zhang, L. Wang, A novel sulfonated reverse osmosis membrane for seawater desalination: experimental and molecular dynamics studies, *J. Membr. Sci.* 550 (2018) 470–479.
- [3] X. Du, Z. Zhang, K.H. Carlson, J. Lee, T. Tong, Membrane fouling and reusability in membrane distillation of shale oil and gas produced water: effects of membrane surface wettability, *J. Membr. Sci.* 567 (2018) 199–208.
- [4] L. Lin, T.M. Weigand, M.W. Farthing, P. Jutaporn, C.T. Miller, O. Coronell, Relative importance of geometrical and intrinsic water transport properties of active layers in the water permeability of polyamide thin-film composite membranes, *J. Membr. Sci.* 564 (2018) 935–944.
- [5] K.P. Lee, T.C. Arnot, D. Mattia, A review of reverse osmosis membrane materials for desalination—development to date and future potential, *J. Membr. Sci.* 370 (2011) 1–22.
- [6] A.K. Geim, Graphene: status and prospects, *Science* 324 (2009) 1530–1534.
- [7] Y. You, V. Sahajwalla, M. Yoshimura, R.K. Joshi, Graphene and graphene oxide for desalination, *Nanoscale* 8 (2016) 117–119.
- [8] D. Cohen-Tanugi, J.C. Grossman, Water desalination across nanoporous graphene, *Nano Lett.* 12 (2012) 3602–3608.
- [9] K. Guan, D. Zhao, M. Zhang, J. Shen, G. Zhou, G. Liu, W. Jin, 3D nanoporous crystals enabled 2D channel in graphene membrane with enhanced water purification performance, *J. Membr. Sci.* 542 (2017) 41–51.
- [10] J. Lyu, X. Wen, U. Kumar, Y. You, V. Chen, R.K. Joshi, Separation and purification using GO and r-GO membranes, *RCS Adv.* 8 (2018) 23130–23151.
- [11] B. Lian, Y. You, S. Alwarappan, V. Sahajwalla, S. Smith, G. Leslie, R.K. Joshi, Extraordinary water adsorption characteristics of graphene oxide, *Chem. Sci.* 9 (2018) 5106–5111.
- [12] Y. You, X. Jin, X. Wen, V. Sahajwalla, V. Chen, H. Bustamante, R.K. Joshi, Application of graphene oxide membranes for removal of natural organic matter from water, *Carbon* 129 (2018) 415–419.
- [13] R.R. Nair, H.A. Wu, P.N. Jayaram, I.V. Grigorieva, A.K. Geim, Unimpeded permeation of water through helium-leak-tight graphene-based membranes, *Science* 335 (2012) 442–444.
- [14] R.K. Joshi, S. Alwarappan, M. Yoshimura, V. Sahajwalla, Y. Nishina, Graphene oxide: the new membrane material, *Appl. Mater. Today* 1 (2015) 1–12.
- [15] B. Mi, Graphene oxide membranes for ionic and molecular sieving, *Science* 343 (2014) 740–742.
- [16] R.K. Joshi, P. Carbone, F.C. Wang, V.G. Kravets, Y. Su, I.V. Grigorieva, H.A. Wu, A.K. Geim, R.R. Nair, Precise and ultrafast molecular sieving through graphene oxide membranes, *Science* 343 (2014) 752–754.
- [17] J. Abraham, K.S. Vasu, C.D. Williams, K. Gopinadhan, Y. Su, C.T. Cheria, J. Dix, E. Prestat, S.J. Haigh, I.V. Grigorieva, P. Carbone, A.K. Geim, R.R. Nair, Tunable sieving of ions using graphene oxide membranes, *Nat. Nano* 12 (2017) 546–550.
- [18] W.-S. Hung, C.-H. Tsou, M. De Guzman, Q.-F. An, Y.-L. Liu, Y.-M. Zhang, C.-C. Hu, K.-R. Lee, J.-Y. Lai, Cross-linking with diamine monomers to prepare composite graphene oxide-framework membranes with varying d-spacing, *Chem. Mater.* 26 (2014) 2983–2990.
- [19] C.-N. Yeh, K. Raidongia, J. Shao, Q.-H. Yang, J. Huang, On the origin of the stability of graphene oxide membranes in water, *Nat. Chem.* 7 (2015) 166–170.
- [20] M. Hu, B. Mi, Enabling graphene oxide nanosheets as water separation membranes, *Environ. Sci. Technol.* 47 (2013) 3715–3723.
- [21] Y.-H. Xi, J.-Q. Hu, Z. Liu, R. Xie, X.-J. Ju, W. Wang, L.-Y. Chu, Graphene oxide membranes with strong stability in aqueous solutions and controllable lamellar spacing, *ACS Appl. Mater. Interfaces* 8 (2016) 15557–15566.
- [22] B. Lee, K. Li, H.S. Yoon, J. Yoon, Y. Mok, Y. Lee, H.H. Lee, Y.H. Kim, Membrane of functionalized reduced graphene oxide nanoplates with angstrom-level channels, *Sci. Rep.* 6 (2016) 28052.
- [23] S. Hou, S. Su, M.L. Kasner, P. Shah, K. Patel, C.J. Madarang, Formation of highly stable dispersions of silane-functionalized reduced graphene oxide, *Chem. Phys. Lett.* 501 (2010) 68–74.
- [24] E. Yang, C.-M. Kim, J.-h. Song, H. Ki, M.-H. Ham, I.S. Kim, Enhanced desalination performance of forward osmosis membranes based on reduced graphene oxide laminates coated with hydrophilic polydopamine, *Carbon* 117 (2017) 293–300.
- [25] W.-S. Hung, S.-M. Chang, R.L.G. Lecaros, Y.-L. Ji, Q.-F. An, C.-C. Hu, K.-R. Lee, J.-Y. Lai, Fabrication of hydrothermally reduced graphene oxide/chitosan composite membranes with a lamellar structure on methanol dehydration, *Carbon* 117 (2017) 112–119.
- [26] H. Wang, D. Zhang, T. Yan, X. Wen, L. Shi, J. Zhang, Graphene prepared via a novel pyridine-thermal strategy for capacitive deionization, *J. Mater. Chem.* 22 (2012) 23745–23748.
- [27] H. Liu, H. Wang, X. Zhang, Facile fabrication of freestanding ultrathin reduced graphene oxide membranes for water purification, *Adv. Mater.* 27 (2015) 249.
- [28] B. Tang, L. Zhang, R. Li, J. Wu, M.N. Hedhili, P. Wang, Are vacuum-filtrated reduced graphene oxide membranes symmetric? *Nanoscale* 8 (2016) 1108–1116.
- [29] A. Aher, Y. Cai, M. Majumder, D. Bhattacharyya, Synthesis of graphene oxide membranes and their behavior in water and isopropanol, *Carbon* 116 (2017) 145–153.
- [30] H. Kim, Y. Miura, C.W. Macosko, Graphene/polyurethane nanocomposites for improved gas barrier and electrical conductivity, *Chem. Mater.* 22 (2010) 3441.
- [31] R. Verdejo, M.M. Bernal, L.J. Romasanta, M.A. Lopez-Manchado, Graphene filled polymer nanocomposites, *J. Mater. Chem.* 21 (2011) 3301–3310.
- [32] H.-H. Huang, K.K.H. De Silva, G.R.A. Kumara, M. Yoshimura, Structural evolution of hydrothermally derived reduced graphene oxide, *Sci. Rep.* 8 (2018) 6849.
- [33] X. Mei, X. Meng, F. Wu, Hydrothermal method for the production of reduced graphene oxide, *Physica E* 68 (2015) 81–86.
- [34] A. Lerf, H. He, M. Forster, J. Klinowski, Structure of graphite oxide revisited, *J. Phys. Chem. B* 102 (1998) 4477–4482.
- [35] C.K. Chua, M. Pumera, Chemical reduction of graphene oxide: a synthetic chemistry viewpoint, *Chem. Soc. Rev.* 43 (2014) 291–312.
- [36] J. Kim, L.J. Cote, F. Kim, W. Yuan, K.R. Shull, J. Huang, Graphene oxide sheets at interfaces, *J. Am. Chem. Soc.* 132 (2010) 8180–8186.
- [37] J. Luo, L.J. Cote, V.C. Tung, A.T.L. Tan, P.E. Goins, J. Wu, J. Huang, Graphene oxide nanocolloids, *J. Am. Chem. Soc.* 132 (2010) 17667–17669.
- [38] P. Bansal, A.S. Panwar, D. Bahadur, Molecular-level insights into the stability of aqueous graphene oxide dispersions, *J. Phys. Chem. C* 121 (2017) 9847–9859.
- [39] S. Zheng, Q. Tu, J.J. Urban, S. Li, B. Mi, Swelling of graphene oxide membranes in aqueous solution: characterization of interlayer spacing and insight into water transport mechanisms, *ACS Nano* 11 (2017) 6440–6450.

- [40] Y. Han, Z. Xu, C. Gao, Ultrathin graphene nanofiltration membrane for water purification, *Adv. Funct. Mater.* 23 (2013) 3693–3700.
- [41] J.K. Holt, H.G. Park, Y. Wang, M. Stadermann, A.B. Artyukhin, C.P. Grigoropoulos, A. Noy, O. Bakajin, Fast mass transport through sub-2-nanometer carbon nanotubes, *Science* 312 (2006) 1034.
- [42] J.A. Thomas, A.J. McGaughey, Water flow in carbon nanotubes: transition to sub-continuum transport, *Phys. Rev. Lett.* 102 (2009) 184502.
- [43] S. Joseph, N. Aluru, Why are carbon nanotubes fast transporters of water? *Nano Lett.* 8 (2008) 452–458.
- [44] J.S. Babu, S.P. Sathian, The role of activation energy and reduced viscosity on the enhancement of water flow through carbon nanotubes, *J. Chem. Phys.* 134 (2011) 194509.
- [45] N. Wei, X. Peng, Z. Xu, Understanding water permeation in graphene oxide membranes, *ACS Appl. Mater. Interfaces* 6 (2014) 5877–5883.
- [46] N. Wei, X. Peng, Z. Xu, Breakdown of fast water transport in graphene oxides, *Phys. Rev. E* 89 (2014) 012113.



Review article

Chemical reduction of graphene oxide using green reductants

K.K.H. De Silva^a, H.-H. Huang^a, R.K. Joshi^{b,*}, M. Yoshimura^a^a Graduate School of Engineering, Toyota Technological Institute, 2-12-1 Hisakata, Tempaku, Nagoya 468-8511, Japan^b Centre for Sustainable Materials Research and Technology (SMaRT), School of Materials Science and Engineering, University of New South Wales, Sydney, NSW, 2052, Australia

ARTICLE INFO

Article history:

Received 19 February 2017

Received in revised form

13 April 2017

Accepted 15 April 2017

Available online 21 April 2017

Keywords:

Graphene oxide

Green reductants

Ascorbic acid

Contents

ABSTRACT

Graphene has exceptional physical, chemical, mechanical, thermal and optical properties which offer huge potential for applications in various sectors. Chemical oxidation of graphite to graphene oxide followed by the reduction process is the commonly used method for mass scale production of graphene or reduced graphene oxide (RGO). Among the large number of chemical reducing agents used to prepare RGO or graphene, the most efficient reductant is hydrazine. It is toxic in nature and harmful to the environment, thus it is in high demand to use green reductants for RGO synthesis. We understand that due to high demand of graphene/graphene oxide/reduced graphene oxide recently and which is expected to be more in future, green synthesis methods are extremely important. In this article, we have studied the synthesis methods, characterization and the possible mechanism for green reduction, especially by ascorbic acid. This article could possibly motivate the researcher worldwide to innovate new green methods for mass scale production of graphene based materials.

© 2017 Elsevier Ltd. All rights reserved.

Contents

1. Introduction	190
2. Need of green reducing agents	191
2.1. Organic acids	191
2.2. Plant extracts	192
2.3. Microorganisms	192
2.4. Sugars	193
2.5. Proteins and amino acids	193
2.6. Ascorbic acid above all green reducing agents	193
3. Reduced graphene oxide via ascorbic acid	194
3.1. Ascorbic acid/vitamin C	194
3.2. RGO synthesis via ascorbic acid	194
3.3. Characterization of RGO synthesized by ascorbic acid	195
3.4. Mechanism of action	197
4. Summary & outlook	197
References	198

1. Introduction

Graphene, as the first two-dimensional material to know, has become the celebrity in the nanomaterial world with the revolutionary discovery of graphene by Geim and co-workers [1]. Ever since the gold rush for graphene has enhanced. The reason being

* Corresponding author.

E-mail address: r.joshi@unsw.edu.au (R.K. Joshi).

that graphene has proven to have many outstanding properties applicable in diverse areas including electronic, light processing, energy related, sensors, and various biomedical applications [2]. Until now, many techniques have been introduced to synthesize graphene. Among all, the chemical reduction of graphene oxide (GO) is believed to be the most promising method with respect to large-scale productivity at a low cost in a short time. Why GO and its reduced product (here onwards referred to as RGO) are becoming popular among researchers? The answer being that both materials have confirmed to be applicable in many areas that pristine graphene cannot be directly applied in, such as water purification [3–6].

GO is not a naturally occurring compound. The mechanism of oxidation and the chemical structure of GO are still ambiguous due to its non-stoichiometric nature and strong hygroscopic property as it is rich in oxygen functionalities [7], [8]. The removal of these oxygen moieties is a vital topic that determines the properties of the ultimate product and to which extent RGO will resemble pristine graphene [9]. Therefore, finding a suitable reducing agent for this task is very important. The first known reducing agent, H_2S was introduced in 1934 [10] and there onwards, a large number of reductants have been used to reduce GO. Among these, hydrazine ($N_2H_4 \cdot H_2O$) is the best-known reductant in terms of giving RGO with improved electrical and structural properties resembling pristine graphene to a large extent [11]. However, hydrazine suffers from some problems which have encouraged researchers to find alternative reducing agents with qualities comparable to hydrazine. One such problem which has led to the introduction of the “green reduction” approach in this field is the toxic nature of hydrazine to the environment as well as to the living organisms [12]. The first known environmentally friendly reducing agent is ascorbic acid (2010), and it has verified to be the best alternative to toxic hydrazine and is being studied currently [13]. This review is mainly focused on the chemical reduction of GO by ascorbic acid which is a non-toxic, inexpensive organic acid Fig. 1.

2. Need of green reducing agents

When it comes to the term “green reduction”, it includes both chemical and non-chemical approaches. Chemical reduction of GO involves a reducing agent and sometimes a stabilizer. On the other hand, non-chemical reduction of GO, such as hydrothermal and solvothermal reduction [14], electrochemical reduction [15], UV and solar irradiation [16], supercritical fluids-based reduction [17] and photothermal reduction [18] is also being studied for years [12]. Nevertheless, chemical reduction has taken the priority over non-chemical reduction methods because of the high quality and productivity of acquired RGO and the ability to make stable dispersions essential for many applications [19,20].

Though hydrazine is an effective and efficient reductant for RGO synthesis, it suffers from a number of limitations. Hydrazine and its by-products are toxic to both the living organisms and the environment [21]. It is also unstable and could have detrimental effects and hence, care should be taken in handling such chemicals. Moreover, remediation of hazardous wastes generated may significantly increase the cost on industrial scale [22,23]. Also, if the final product contains residues of these hazardous chemicals, it may not be suitable for many applications particularly in biomedical applications and water remediation. To counteract above-mentioned problems, scientists have focused more on finding environmentally friendly reducing agents with the reducing power similar to or higher than hydrazine.

The thirst of finding such alternatives has introduced a number of green reductants within the last decade. They include organic acids, plant extracts, microorganisms, sugars, antioxidants, amino

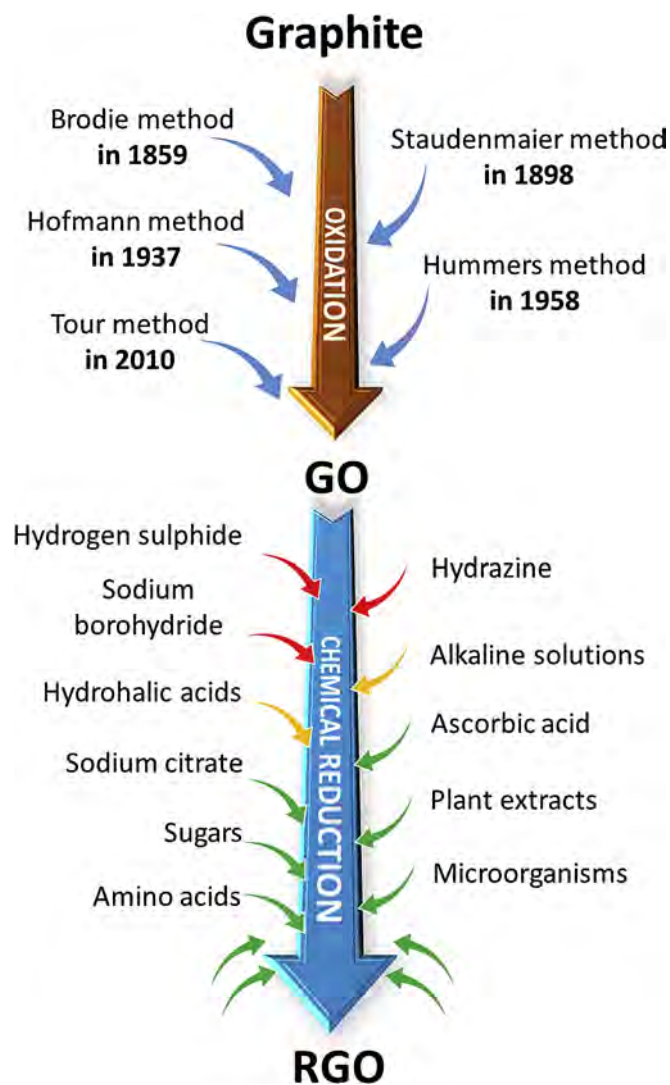


Fig. 1. Schematic representation of the major oxidation methods of graphite to graphene oxide and the chemical reduction of graphene oxide by some reductants. (A colour version of this figure can be viewed online.)

acids and proteins, etc. All these reductants are known as “green reducing agents” as they are non-toxic or environmentally friendly. However, as nothing is perfect, these reductants may also come with some limitations. Sometimes one agent may need a supporting agent to perform complete reduction or a stabilizer to prevent aggregation of RGO sheets, and the need of performing repeated centrifugation or filtration to remove excess reductant or its by-products. Therefore, the applicability of these green reductants is still under study for large-scale of RGO synthesis [24]. In one such environmentally friendly reduction method, Loryuenyong *et al.* have performed reduction of exfoliated GO solution in de-ionized water, in the absence of a reducing agent for 4 days at $95^\circ C$ [25]. Among all the green reducing agents mentioned above, ascorbic acid (AA), also known as Vitamin C, has attained a great interest in the field of RGO synthesis due to many reasons. The chemistry and the reducing behaviour of AA towards GO compared to other agents will be discussed in here.

2.1. Organic acids

The use of organic acids and/or their salts as reducing agents is

not a new topic. They have been used to synthesize metal nanoparticles [26]. Hence, their utilization in reducing GO is becoming popular, since almost all of them are environmentally friendly. AA is the first known green reductant for RGO synthesis and works based on it are becoming prominent compared to others due to many reasons, which will be discussed later. Followed by AA, few works based on sodium citrate (Na-citrate) have been reported [27,28]. Wan et al. have reported a scalable preparation of RGO (also called chemically converted graphene – CCG) films by vacuum-assisted self-assembly method with high strength reaching about 80 MPa using sodium-citrate as the reductant [27]. Samples have been cut into rectangular strips and the tensile strength has been measured by a homemade testing system (Fig. 2). Caffeic acid (CA) is another follower which has been used to synthesize RGO that can be applied in gas sensors and supercapacitors (Fig. 3) [29]. Not only that, Chong et al. have demonstrated that lemon juice is an efficient reductant for GO resulting in RGO with a conductance of 24.6 μS and C/O ratio of 8.2 [30]. Though these materials have shown to have potential to be used as a green reductant for GO, incessant involvement in the field is lacking in contrast to AA. In addition, recently, a binary reducing system of AA and Na-citrate has been reported in reducing GO [31].

2.2. Plant extracts

With the evolution of the phrase green reduction, many

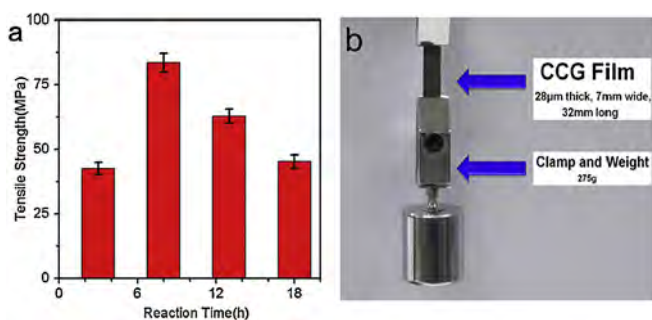


Fig. 2. (a) Tensile strength of CCG films prepared at different reaction times. (b) Digital photograph of a strip of graphene film supporting 275 g load (48 MPa). Adapted with permission from Ref. [27]. (A colour version of this figure can be viewed online.)

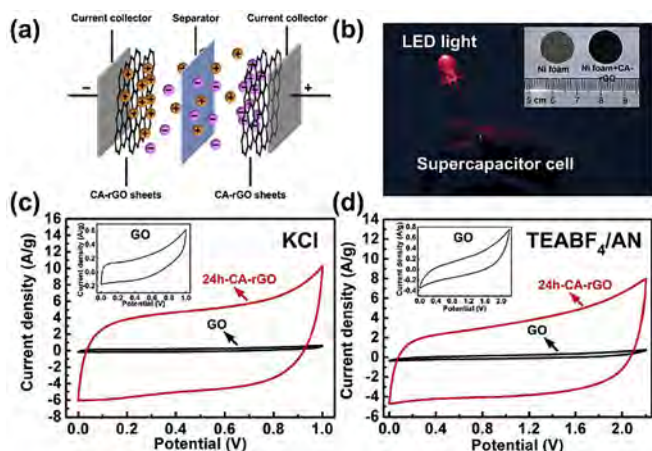


Fig. 3. (a) Schematic illustration of the RGO-based double-layer supercapacitor. (b) Digital photographs of an LED light powered by a supercapacitor cell. The inset shows a bare Ni foam before and after coating with 24 h-CA RGO sheets. CV curves of the supercapacitors using GO and 24 h-CA-RGO working electrodes in (c) 1 M KCl and (d) 1 M TEABF₄/AN electrolytes. Adapted with permission from Ref. [29]. (A colour version of this figure can be viewed online.)

researchers have focused on finding novel reducing agents. As a result, many reports on plant extracts have been published and still counting, including leaves, fruits and flowers. Mushroom extracts [32], green tea [22], *Salvadora persica* extract [33], carrot juice [34], Colocasia leaf and orange peel extracts [35], coconut water [36], pomegranate juice [37] and rose water [38] are few examples. The main objective of using these extracts in reducing GO is to make stable dispersions of biocompatible RGO sheets. Green polyphenols present in green tea has demonstrated its reducing power on GO and its applicability in bio-related materials [22]. Though it has a good reducing capacity for GO, the strong adsorption of polyphenol molecules on to RGO makes it less applicable for electronic applications. Tannic acid (TA), which is also an antioxidant mainly extracts from oak apple, is another candidate that can give stable RGO dispersions not only in aqueous media but also in organic solvents [39]. The mechanism for GO reduction [39] by TA is shown in Fig. 4. Almost all the plant extracts have large organic molecules as the reducing component that can interact with the RGO sheets resulting stable dispersions of RGO. However, for some applications like materials for conductive applications such kind of incorporation of molecules can be disadvantageous. Although these plant extracts are green and abundant in nature, making in the required form may need more time. Also, some of the plants are limited to one particular area or not ubiquitous and the majority does not show further adoption in RGO synthesis.

2.3. Microorganisms

Application of microbes such as bacteria and yeast in reducing GO has been practiced recently. *Escherichia coli* (*E. coli*) is a commonly known bacterium present in the human digestive tract and some strains of it can cause serious diseases. Akhavan et al. have performed the reduction of GO by *E. coli* in an anaerobic condition. It was found that the reduction is due to the metabolic activity of bacteria and the bacterially reduced GO can inhibit the proliferation of the surviving bacteria [40]. *Shewanella* is known to be a metal-reducing bacterium and it is ubiquitous. Salas et al. and Wang et al. have reduced GO by *Shewanella* under anaerobic [41] and aerobic environments [42] respectively. The metabolically generated electrons from *Shewanella* are transferred to an external electron acceptor either directly from the cell surface or using self-secreted electron mediators (extracellular electron transfer-EET). The mechanism of reduction of GO by the EET of *Shewanella* is given in Fig. 5. Yeast is also a cheap and abundant eukaryotic fungus

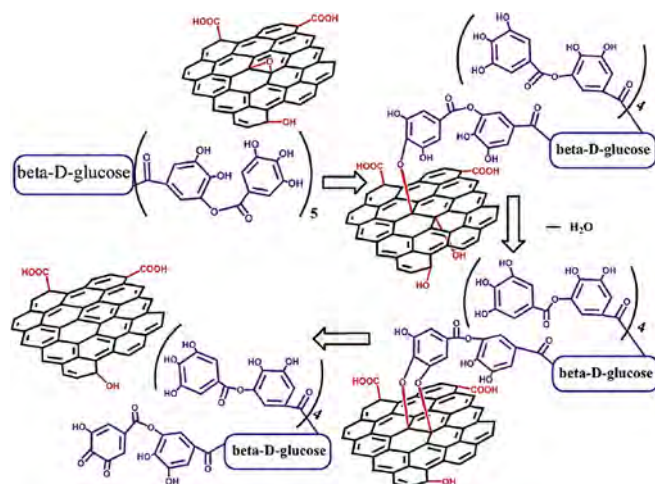


Fig. 4. Proposed mechanism of reduction of GO by TA. Adapted with permission from Ref. [39]. (A colour version of this figure can be viewed online.)

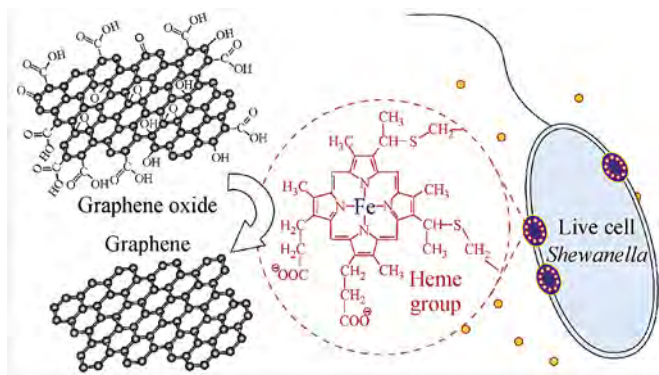


Fig. 5. Proposed mechanism of microbial reduction of graphene oxide. Orange dots, blue circles with white dots, and red dashed circle represent self-secreted electron mediators, multi-heme-containing outer-membrane *c*-type cytochromes, and the molecular structure of the heme group respectively. Adapted with permission from Ref. [42]. (A colour version of this figure can be viewed online.)

with the ability to reduce GO. It is believed that the enzyme nicotinamide adenine dinucleotide phosphate (NADPH) presents in yeast can readily reduce the epoxy ketones in GO and the bio-functionalization of NADPH on GO could give stable dispersions [21]. This report also shows that the RGO synthesized by yeast has an electrical conductivity of 43 S/m. Though these microbes give RGO with good qualities, the applicability of the reduced product is particularly limited to biomedical applications. Also the time of reduction may last for more than 3 days and care should be taken in handling cultures of microbes.

2.4. Sugars

Exploitation of common sugars and polysaccharides as green reductants for GO has also been reported. All these materials have the ability to act as a reducing agent as well as a capping/stabilizing agent thereby resulting in more stable RGO dispersions. Zhu et al. have shown the reducing ability of glucose, fructose and sucrose towards GO and its capability as good electrocatalysts towards catecholamines (dopamine, epinephrine and norepinephrine) (Fig. 6) [23]. Among which, glucose has shown the highest reducing ability toward GO. Glucose oxidized to aldonic acid in basic media and further converted into lactone which can form H-bonds with the residual oxygen functionalities present in RGO. Kim et al. have reported green synthesis of RGO and RGO-based gold nanocomposite by using dextran, which is most widely used biocompatible polysaccharide, as the reducing agent [43]. Dextran decorated RGO acts as a template for the direct synthesis of gold nanoparticles on its surface resulting hybrid structures. Moreover, RGO synthesized by dextran had an electrical conductivity of 1.1 S/m, which has increased to 10000 S/m after thermal treatment at 500 °C under Ar atmosphere due to the removal of dextran. A comparative study of three green reductants, namely AA, glucose

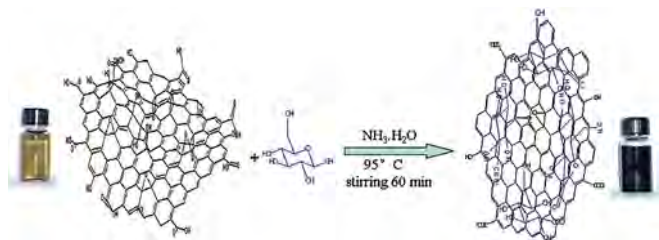


Fig. 6. Illustration of the reduction of GO by glucose. Adapted with permission from Ref. [23]. (A colour version of this figure can be viewed online.)

and tea polyphenol (TP), was done by Xu et al. [44]. Accordingly, RGO reduced by AA has given the highest electrical conductivity (9.8 S/cm) compared to glucose (3.53 S/cm) and TP (1.36 S/cm). On the other hand, they have proposed possible reduction mechanisms for these three agents. Both AA and TP reduce GO by S_N2 nucleophilic reaction, while the aldehyde group on the open chain structure of glucose gives its unique reducibility.

2.5. Proteins and amino acids

The first reported amino acid as a reducing agent for GO is L -cysteine [45]. RGO obtained after performing the reduction for 72 h at 26 °C, has shown an increment in the conductivity of about 10^6 times compared to GO. The thiol groups present in L -cysteine undergo redox reactions thereby involve in the reduction of GO. Bose et al. have carried out reduction using glycine under mild conditions and have obtained RGO with a carbon/oxygen atomic ratio as high as 11.24 [46]. The amine group of glycine undergoes covalent interaction with GO acting as a chemical functionalizer in addition of being a reductant. A protein-based environmentally friendly one-step reduction/decoration strategy was proposed by Liu et al. [47]. The protein they used is bovine serum albumin (BSA), which performs a dual function; it reduces GO into RGO and hence, provides a versatile platform to create graphene-based hybrid materials especially with pre-synthesized nanoparticles with different properties (Fig. 7). Both proteins and amino acids are biomaterials, which are very sensitive to reaction environment such as temperature and pH and can be denaturised above or below their optimum levels before performing the reduction. Hence, the reduction has to be performed under mild conditions that might cost more time for the reaction to be completed.

2.6. Ascorbic acid above all green reducing agents

Previous paragraphs introduced several reductants joined to the family of green reducing agents. Still, novel green reductants for RGO synthesis are being introduced but further practice of most of those is not much promising. On the contrary, the use of AA as the reducing agent for GO has been conducted in many cases, compared to others, and it is proven to be a powerful yet non-toxic reagent which can compete with hydrazine [48]. RGO synthesized by most of the green reductants, as listed previously, is mainly applicable for bio-medical applications, although it is advantageous in making stable dispersions of RGO [23,32]. In all due respect, AA-reduced GO has revealed to have a broad area of applications not only in bio-medical devices but also in electronic devices [49,50] which has made it an outstanding candidate for green reduction of GO and being the topic of this review. C/O ratio and the electrical

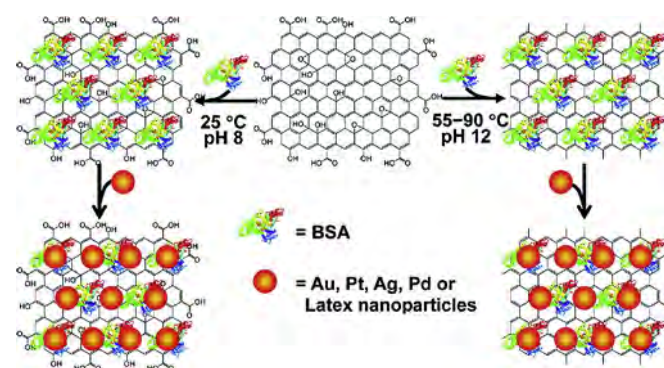


Fig. 7. Protein-based decoration and reduction of GO. Adapted with permission from Ref. [47]. (A colour version of this figure can be viewed online.)

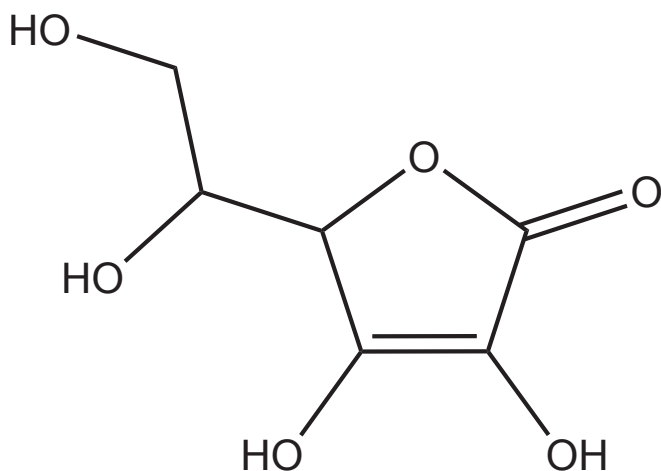


Fig. 8. Chemical structure of AA (C₆H₈O₆).

conductivity of RGO are two basic criteria used in determining the reducing ability of a particular reductant [19]. Table 1 summarises C/O ratio and conductivity of RGO results from few green reductants including their applicability. The table shows the details of a few green reductants and yet, compared to all other green reductants AA is at the top in terms of applicability (more applications will be discussed later). On the other hand, it is worthy to mention that the characteristics including C/O ratio and conductivity depend not only on the reduction conditions but also on the graphite precursor, the oxidation methodology and the resulting GO. Also, the experimental setup and approaches to measure the conductivity affect the results.

3. Reduced graphene oxide via ascorbic acid

3.1. Ascorbic acid/vitamin C

Ascorbic acid is a ubiquitous organic material with the chemical formula of (2R)-2-((1S)-1,2-dihydroxyethyl)-3,4-dihydroxy-2H-furan-5-one, and with a molecular weight of 176.12 g/mol [52] Fig. 8. It is known as an essential ingredient to our wellbeing as it has anti-oxidant, anti-diabetic, anti-tumour, anti-inflammatory properties. It is also used as a medication for preventing and treating

scurvy (antiscorbutic) and common cold, also in slowing aging, hardening of arteries, preventing clots in veins [53]. Synthetic AA is widely used as a food additive (E300) due to its anti-oxidant properties [54]. However, upon exposure to air/oxygen, it can get oxidized/degraded to its oxidized product [52]. Like many carbohydrates, due to the reactive functional groups present, AA can undergo many chemical reactions including methylation, acid-catalysed esterification and oxidation [54]. More interestingly, AA is a powerful reducing agent in aqueous solutions and as a result, it is now in use as a green reductant in RGO synthesis. Here onwards the application of AA in the reduction of GO will be discussed.

3.2. RGO synthesis via ascorbic acid

From the recent works done by researchers, AA has proven to be a remarkable green reducing agent for GO. There are many reasons to why this reagent is so important and so eminent in RGO synthesis. Apart from being an environmentally friendly and cheap reductant, it gives more stable RGO products in water than hydrazine [19]. This stability could be achieved by the oxidized forms of AA, namely guluronic acid or oxalic acid. These might form H-bonds with the residual oxygen functionalities and disrupt the π - π stacking between RGO sheets thereby preventing the agglomeration [13]. However, such stable suspensions of GO reduced by AA can also be prepared in common organic solvents, such as *N,N*-dimethylformamide (DMF) or *N*-methyl-2-pyrrolidone (NMP) [48] (Fig. 9). On the other hand, the reduction performed by AA is highly efficient and easily scalable, which is better for large-scale production [55]. Another advantage is that AA is only composed of carbon, hydrogen and oxygen, thus minimizes the risk of introducing heteroatoms to the reduced product [48].

The use of AA to reduce GO has been first demonstrated in the same time period by few research groups, separately. Zhang et al. [13] have performed the reduction of GO using AA in water at room temperature in the absence of any capping agent. They have shown the substantial removal of oxygen functionalities and restoration of electronic conjugation state of RGO. Parallel to that, Gao et al. have reduced GO under alkaline conditions in the presence of an amino acid as a stabilizer [56]. As another step forward, Fernandez-Merino et al. [48] have carried out a comparison of the performance of several reducing agents (hydrazine, sodium borohydride, pyrogallol in addition to AA) as well as by simply heating the suspensions

Table 1
Comparison of C/O ratio, conductivity and applicability of some green reductants with their reduction conditions.

Green reductant	Reduction conditions	C/O ratio of RGO	Conductivity S/m	Applications	Ref.
Na-citrate	30 mg of Na-citrate in 25 ml, 0.1 mg/ml GO reflux for 3 h	–	–	electrochemical sensing of biomolecules	[28]
	20 mg/ml of Na-citrate and 150 mg GO in 250 ml at 95 °C	4.7	30.6	Current collectors of supercapacitors and batteries	[27]
Caffeic acid	Different ratios of CA in 0.1 mg/ml GO at 95 °C/24 h	7.5	–	Electronic gas sensors and supercapacitors	[29]
Green tea	50 mg of GO in green tea solution refluxed at 90 °C in a nitrogen atmosphere	–	53	Bio-related applications	[22]
Pomegranate juice	40 ml pomegranate juice and 0.1 g GO stirred for 12, 18 and 24 h.	–	–	–	[37]
Rose water	10 ml rose water in 7 mg/ml GO autoclaved at 95 °C/5 h	–	–	Bio-related applications	[38]
Glucose	40 mg of glucose in 25 ml, 0.1 mg/ml GO at 95 °C/1 h	–	–	Electrocatalyst towards catecholamines, large-scale production of water-soluble graphene	[23]
Yeast	1.0 mg/ml glucose in 0.1 mg/ml GO at 95 °C/2 h	2.89	315	–	[44]
	200 mg of yeast and 100 mg GO in 200 ml at 35–40 °C/72 h	5.9	43	–	[21]
<i>Shewanella</i>	10 ml of <i>Shewanella</i> inoculate into a mixture of lactate and 2 mg GO and incubate at room temperature in dark	–	–	Bioremediation of bacteria	[41]
L-cysteine	0.2 g of L-cysteine in 20 ml of 0.5 mg/ml GO at 26 °C/72 h	–	0.124	–	[45]
Ascorbic acid (Vitamin C)	Different ratios of AA in 0.1 mg/ml GO at 95 °C	–	Up to 7700	–	[48]
	3 g AA in 3.0 mg/ml GO at 80 °C/1 h	–	1500	All-organic vapour sensor	[51]
	1.0 mg/ml AA in 0.1 mg/ml GO at 95 °C/2 h	5.15	980	Large range of applications	[44]

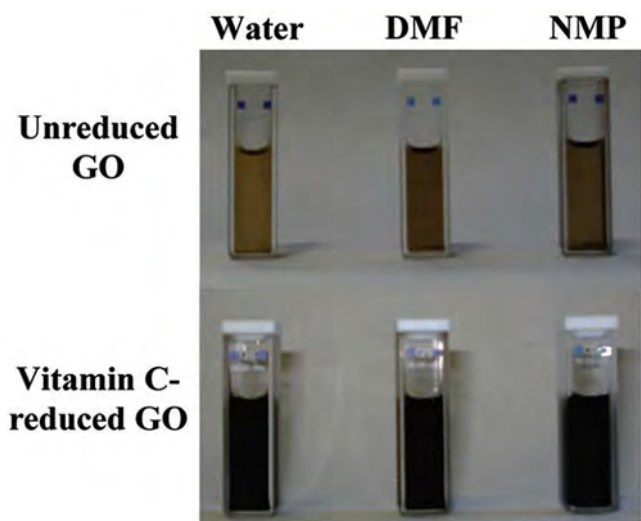


Fig. 9. Digital pictures of GO and RGO suspensions in different solvents. Adapted with permission from Ref. [48]. (A colour version of this figure can be viewed online.)

under alkaline conditions. They have shown that only AA can compete with hydrazine and it is a safe and effective reductant in the large-scale production of RGO. Later, the utilization of AA in the reduction of GO deeply subjected to study as a green reductant. There are few factors that determine the rate of GO reduction by AA: pH of the medium, concentration of GO and AA, reduction temperature and the power of stirring or sonication. Accordingly, high ultrasound power, high temperature, high pH value and large amount of AA increase the rate of reduction [50,57]. Alkaline conditions (particularly pH ~ 9–10) for the AA assisted reduction has been found to be more favourable over neutral conditions and gives more stable product [44]. It is believed that alkaline conditions promote the colloidal stability of GO sheets through electrostatic repulsion thereby preventing the agglomeration of resulting RGO sheets [44,48]. However, when synthesizing RGO hydrogels, acidic medium is more favoured over neutral or basic media [50,58]. On the other hand, though higher concentrations of AA increase the rate of reduction, there is a possibility of aggregation of RGO sheets because increasing amount of AA will remove more oxygen functionalities resulting more hydrophobic RGO [59]. As a solution for this, functionalization of GO prior to reduction has been studied to

obtain stable aqueous dispersions of RGO [59,60]. Table 2 summarises the reduction conditions employed by researchers in reducing GO by AA.

3.3. Characterization of RGO synthesized by ascorbic acid

The progress of reduction of GO by AA can be monitored by UV–Visible spectroscopic analysis. GO aqueous solution shows a λ_{\max} centred at ~230 nm (due to $\pi-\pi^*$ transition of aromatic C=C bonding) and a shoulder peak at ~300 nm (due to $n-\pi^*$ transition of C=O bonding) [28,66]. With the increase of reduction time, the peak at 230 nm red-shifts and the peak at 300 nm disappears gradually providing a hint that GO is reduced restoring the aromatic structure [13]. The maximum red-shift that can be obtained depends on the reductant used. Accordingly, when hydrazine and AA were presented as reductants, the absorption peak red-shifted up to a value of 268 nm upon reaction completion. However, the rate of completion depends on other factors like the concentration of the reductant and the temperature [48]. Similarly, in other studies done in the presence of AA, the maximum red-shift has been attained at different wavelengths (Table 3). AA has a broad absorption at less than 350 nm [57] and at pH 2.0 it has a λ_{\max} of 243 nm which undergoes a red-shift to 265 nm at pH 7.0 [54]. As a

Table 3
Summary of XRD, Raman, XPS and UV–vis results obtained for AA-reduced GO.

XRD d-spacing (nm)		Raman I_D/I_G		XPS C/O		UV–Vis RGO λ_{\max}	Ref.
GO	RGO	GO	RGO	GO	RGO		
0.111	0.37	N/A	N/A	N/A	N/A	264	[13]
N/A	N/A	N/A	N/A	2.3	12.5	268	[48]
0.839	0.3845	0.93	N/A	N/A	6.07	N/A	[55]
N/A	N/A	1.56	1.75	N/A	N/A	N/A	[56]
N/A	N/A	N/A	N/A	N/A	N/A	268	[57]
N/A	N/A	0.95	1.19	2.65	5.15	N/A	[44]
0.83	0.44	N/A	N/A	N/A	N/A	240	[59]
0.83	N/A	N/A	N/A	N/A	N/A	N/A	[60]
N/A	N/A	N/A	N/A	N/A	N/A	268	[61]
N/A	N/A	N/A	2.3	N/A	N/A	N/A	[63]
0.925	N/A	0.95	1.33	2.4	8.0	N/A	[64]
N/A	N/A	N/A	N/A	N/A	N/A	270	[70]
N/A	N/A	N/A	N/A	N/A	N/A	260	[62]
0.862	0.377	N/A	N/A	N/A	N/A	N/A	[50]
0.876	0.373	N/A	N/A	N/A	N/A	N/A	[65]
N/A	N/A	1.029	1.344	N/A	N/A	N/A	[49]

N/A = not applicable.

Table 2
Comparison of reduction conditions of GO via AA in different works.

Concentration of GO (mg/ml)	Concentration of AA (mg/ml)	Reduction temperature (°C)	Duration of reduction	pH of the medium	Special conditions	Ref.
0.1	5.0	80	24 h	Basic with NaOH	Amino acid stabilizer	[56]
0.1	1.0	RT	48 h	Neutral	N/A	[13]
0.1	0.3–2 mM	95	15–240 min	Basic with NH_3	N/A	[48]
1.0	20	RT	10 min, 2 and 6 days	Basic with NH_4OH	N/A	[61]
N/A	100 mM	60	30 min	Neutral	Excess H_2O_2	[62]
N/A	N/A	50	6 h	N/A	Functionalized GO	[60]
0.1	N/A	RT	24 h	N/A	Functionalized GO	[59]
N/A	10 (a drop per sample)	80	1 h	N/A	Single layered GO on Si substrate	[63]
0.1	4.0	25, 60	2, 6 h	Basic with NaOH	Ultrasonication	[57]
0.1	1.0	95	2 h	Basic with NH_3	N/A	[44]
N/A	N/A	95	1 h	Neutral	N/A	[64]
100 mM	2 mM	90	1–2 h	Basic with NH_3	N/A	[55]
3.0	3 g	80	1 h	Neutral	Triton-X100 stabilizer	[51]
4.0	Different ratios	25–80	1–3 h	Neutral to acidic	N/A	[50]
2.0	10.0	80	1 h	N/A	N/A	[65]
0.3	5.0	RT	48 h	N/A	TiO_2 composite	[49]

N/A = not applicable.

result, before performing UV–Vis analysis the removal of excess AA from the medium is necessary. One way of doing this to treat the reduced products with excess H_2O_2 to oxidize remaining AA by sonication and centrifuge to discard the supernatant [62] or by simply doing centrifugation only [57]. In another work, the reduced product taken at different time intervals were treated by HCl to precipitate GO and centrifuged to remove the supernatant. The solid obtained re-suspended in water *via* sonication and diluted for UV–Vis measurements [61].

RGO obtained by the reduction of GO *via* AA has also been characterized by a variety of microscopic and physical techniques including X-ray Diffraction (XRD), Raman spectroscopy, X-ray Photoelectron spectroscopy (XPS), Fourier Transform Infra-Red (FTIR) spectroscopy, Atomic Force Microscopy (AFM), Thermogravimetric analysis (TGA) *etc.* and the comparison of some of the obtained results are summarized in Table 3. Apart from all the above characterization methods the most direct way to observe the reduction is by visual observation, where the yellow-brownish GO turns into dark brown and finally to a black precipitate upon reduction [19]. XRD analysis gives the details of crystallinity, number of layers present and inter layer spacing (*d*-spacing). Raw graphite shows an intense sharp peak at $2\theta = \sim 26^\circ$ for the basal reflection (002) corresponding to a *d*-spacing of about 0.34 nm. The disappearance of this peak and the appearance of a peak in the range of $2\theta = \sim 9\text{--}11^\circ$ for the basal reflection (001) with a *d*-spacing of 0.8–1.0 nm confirms the oxidation of graphite into GO. This increase in *d*-spacing is due to the incorporation of oxygen functional groups on both sides of GO sheets. Further, upon reduction, the peak for GO upshifts and gives a broad peak centred at $2\theta = \sim 24^\circ$ and a *d*-spacing of about 0.37 nm. This is an indication of restoration of graphitic network in RGO by the removal of oxygen moieties (the values may change upon the reaction conditions) [13,24,32]. XRD data obtained by AA assisted reduction satisfies these criteria.

The formation of RGO can also be confirmed by XPS analysis in terms of C/O ratio and the appearance/disappearance of functional groups. Fig. 10 (Y) shows the fitted C1s spectra of GO and RGO

reduced by AA. It is obvious that the intensity of the peaks corresponding to functional groups has decreased, while the intensity of the peak located at 284.5 eV (assigned to sp^2 C) has increased after reduction [50]. Work done by comparing the reducing power of AA and hydrazine confirms that the decline of the high binding energy oxygen functionalities is much higher for GO reduced with AA than with hydrazine [48,55]. Also, no nitrogen attachment (no C–N peaks in XPS) is present in RGO obtained by AA [51]. According to TGA analysis, GO exhibits prominent weight loss compared to RGO due to the presence of large number of oxygen functional groups. However, the main weight loss for RGO takes place around 200 °C, which attributes to the decomposition of the most labile oxygen functionalities (CO, CO_2 and remaining water molecules) followed by a slow and steady weight loss above 300 °C that can be ascribed to the removal of more stable functional groups. It can be noticed that only AA matches the efficiency of hydrazine in the elimination of labile functional groups. But still, even these strong reductants are unable to remove most stable functional groups completely [32,48].

Raman spectroscopy is another tool to monitor properties of GO and RGO in terms of number of layers, quality of layers, doping level and confinement in graphene nanostructures by analysing the D, G and 2D bands. The G and 2D bands change in shape, position and relative intensity with number of graphene layers whereas the D band gives an indication about the degree of disorder [67]. Pristine graphite has a sharp prominent G band at $\sim 1580\text{ cm}^{-1}$ and a weak D band at $\sim 1350\text{ cm}^{-1}$ indicating a low degree of defects, probably at the edges of the sheets [68]. The G band of graphite blue-shifts upon oxidation to GO and at the same time, the intensity of the D band increases as a result of the formation of more sp^3 domains/defects. The I_D/I_G ratio (I = intensity) is used as a measurement of the disorder or restoration of the graphene structure [69]. According to Table 3, the ratio has increased after reduction suggesting that more sp^2 domains have formed during the reduction. AFM is used to determine the morphology, Z-height (thickness of a single layer) and the number

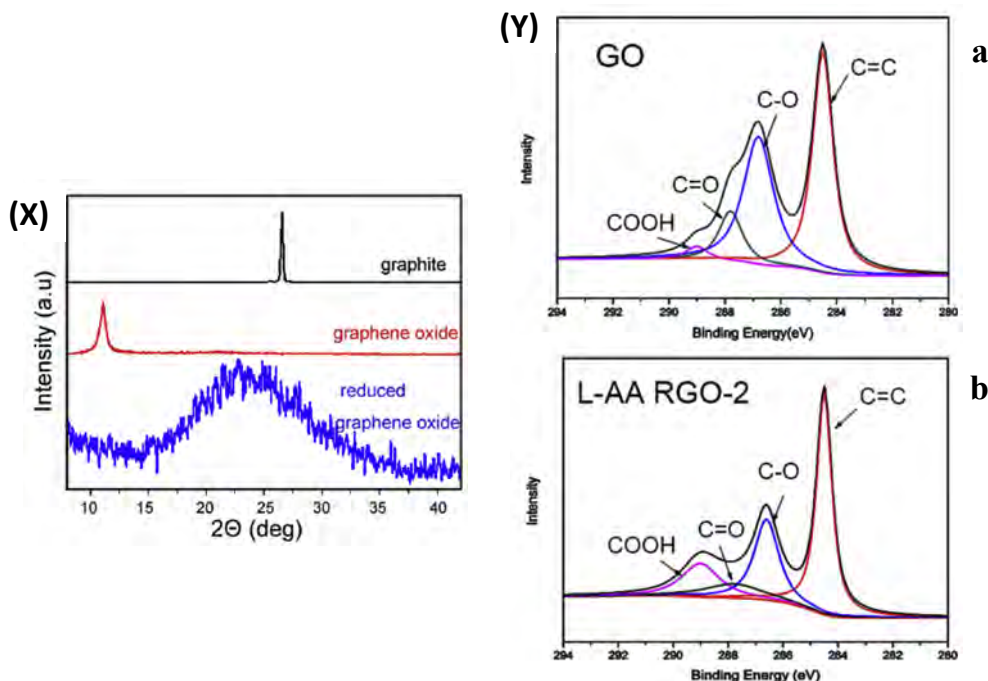


Fig. 10. (X) XRD patterns of graphite, GO and RGO synthesized by AA. Adapted with permission from Ref. [13], (Y) The C1s XPS spectra of GO (a) and RGO (b). Adapted with permission from Ref. [44]. (A colour version of this figure can be viewed online.)

of layers of the sample. During oxidation, the interlayer spacing of graphite increases due to the attachment of oxygen functionalities. Highly oxygenated GO can be exfoliated into monolayers, with a thickness of ~ 1 nm. Theoretically, in the case for RGO, the layer thickness should be lower than GO. However, only very few reports have shown a lower thickness for RGO by AFM measurements. According to Fig. 11, the AFM images show that RGO also has a thickness of ~ 1 nm indicating single layer character for both GO reduced by hydrazine and AA [48].

Above mentioned research works verify that AA is an outstanding alternative reductant to toxic hydrazine and other green reductants in terms of characteristic properties of RGO obtained and for large scale synthesis. Additionally, the physical properties such as electrical conductivity of AA-reduced GO has proven to be higher or similar to that obtained for hydrazine-reduced GO (Table 4). Dua et al. have used such AA-reduced RGO with good conductivity inkjet-printed on poly(ethylene terephthalate) (PET) to make organic vapour sensors [51], and Zhu et al. have shown Chitosan/AA-reduced GO modified electrode could be employed for simultaneous determination of dopamine and AA [62]. Also, Velasco-Soto et al. have proposed a method for controlling optical band gap of GO and RGO and have found that GO reduced by AA at pH 10 gives an optical band gap of 1.55 eV, which is particularly important in applications like solar cells [61]. All these results provide evidence where AA-RGO is suitable for diverse applications and AA is the best green reductant to date.

3.4. Mechanism of action

The mechanism for the chemical reduction of GO by AA and the

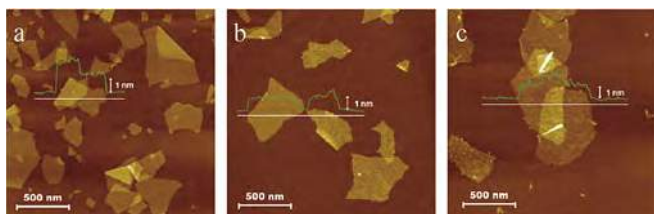


Fig. 11. AFM images of GO (a), hydrazine-reduced (b), AA-reduced (c) GO sheets deposited onto HOPG substrates. Adapted with permission from Ref. [48]. (A colour version of this figure can be viewed online.)

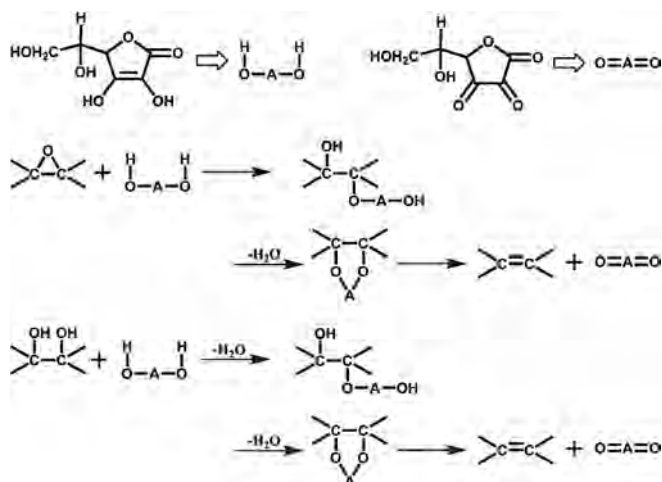


Fig. 12. Proposed reaction pathway for the chemical reduction of GO with AA. Adapted with permission from Ref. [56]. (A colour version of this figure can be viewed online.)

Table 4
Comparison of the electrical conductivity values obtained for AA-reduced GO.

Reduction condition	Electrical conductivity (S/m)	Ref.
0.1 mg/ml GO with 5.0 mg/ml AA at 80 °C for 24 h	14.1	[56]
0.1 mg/ml GO with 2 mM AA at 95 °C for 15 min	7700	[48]
0.1 mg/ml GO with 1.0 mg/ml AA at 95 °C for 2 h	980	[44]
3.0 mg/ml GO with 3 g AA at 80 °C for 1 h	1500	[51]
4.0 mg/ml GO with AA at 80 °C for 3 h	12.1	[50]

reason to why complete reduction is appeared to be impossible are still open questions, to which researchers are attentive on [48]. As mentioned earlier, AA can undergo many chemical reactions due to the presence of reactive functional groups. This section will discuss the possible reduction mechanism of GO by AA. During the reduction of GO, AA undergoes oxidation giving rise to few oxidative products. The formation of the first oxidative intermediate, dehydroascorbic acid (DHA), is reversible. At this stage, two protons will be released and these protons, which have high binding affinity to hydroxyl and epoxide groups, form water molecules [50]. DHA also exhibits reducing ability, especially in alkaline solutions, and irreversibly oxidized to guluronic acid and oxalic acid [44,54]. These products then form hydrogen bonds with residual oxygen functionalities present in GO, such as peripheral carboxylic groups. Additionally, alkaline condition may offer electrostatic repulsion between RGO sheets. As a result, π - π stacking among RGO sheets will be hindered and prevent the aggregation resulting in stable AA-RGO suspensions [13,44]. The reduction of GO can be represented as a two-step S_N2 nucleophilic reaction followed by one step of thermal elimination. AA acts as the nucleophile and attacks the reactive species, such as epoxide and hydroxyl groups on GO. As a result, water molecules are released and an intermediate is formed which undergoes a thermal elimination leading to the restoration of C=C bonds resulting RGO [56] (see Fig. 12). Additionally, Sui et al. have proposed a chemical reaction between GO and AA for the formation of RGO from nominal formulae of GO and RGO obtained by elemental analysis [50], where $C_{63}O_{55.8}H_{33.5}$ is GO, $C_6H_8O_6$ is AA, $C_6H_6O_6$ is DHA and $C_{63}O_{12.2}H_{10}$ is RGO. According to that, the amount of AA required to reduce GO is 3.33 times of GO by mass.

4. Summary & outlook

Among the research based on carbon nanomaterials, GO and RGO have gained great interest intersecting many areas like chemistry, physics, biomedicine, industrial related and nanotechnology. Synthesis of graphene or more precisely RGO by the reduction of GO is one of the fascinating topics because of the problems related to the fabrication of pristine graphene. As a result, there are many research works based on performing different reduction strategies on GO and among which chemical reduction is considered to be the most versatile method. Up to date, there is a large number of chemical reductants in the field of RGO synthesis, yet hydrazine is known to be the most powerful and efficient reductant in terms of giving RGO with good qualities. However, the toxic nature of hydrazine has furthered a new route to synthesize RGO, which is the green synthesis.

The use of green reductants over toxic harsh chemicals has recently become one of the enlightening topics in the graphene sector in this decade. This review has shown the use of green reductants in the chemical reduction of GO. All of them have proven to be environmentally friendly and the product obtained is highly dispersible and biocompatible, hence, are useful in one way or another. Amongst all the green reductants, ascorbic acid-AA (Vitamin C) has achieved the major interest as it has proven to be

an outstanding alternative in synthesizing RGO challenging the toxic yet powerful reductants like hydrazine. Here, the exploitation of AA as a reducing agent in RGO synthesis has been reviewed. AA is not a new compound to know. It is well-known as a medication as well as a food additive over many years. However, the utilization of AA as a reductant in RGO synthesis dates back to about six years. Researchers have synthesized RGO *via* AA under different conditions/parameters in order to find solutions for large-scale, cost-effective production of RGO with astonishing properties for a broad range of applications. Some of them have proposed the mechanism of RGO synthesis by AA. Nevertheless, further modelling and theoretical calculations would be necessary to give far-reaching overview in this respect.

Even still, AA has not proven to be responsible for complete removal of oxygen functionalities from GO, and also in some cases, formation of stable RGO dispersions is a problem without a stabilizer. On the other hand, the hygroscopic nature of AA is an obstacle to use it as a reductant. To achieve quality products by overcoming these limitations is a key task in the research field. More work and effort can assist in solving these problems resulting in new achievements based on RGO synthesis *via* AA to the graphene community. Moreover, the reduction of GO would be a green method if a green reductant is used. But still, the oxidation of graphite to synthesize GO needs harsh chemicals. Therefore, green synthesis of GO is another challenge to overcome.

References

- [1] K.S. Novoselov, A.K. Geim, S.V. Morozov, D. Jiang, Y. Zhang, S.V. Dubonos, et al., Electric field effect in atomically thin carbon films, *Science* 306 (5696) (2004) 666–669, <http://dx.doi.org/10.1126/science.1102896>.
- [2] S.C. Ray, S.C. Ray, Chapter 2 – application and uses of graphene oxide and reduced graphene oxide, in: *Appl. Graphene Graphene-Oxide Based Nanomater*, 2015, pp. 39–55, <http://dx.doi.org/10.1016/B978-0-323-37521-4.00002-9>.
- [3] R.K. Joshi, S. Alwarappan, M. Yoshimura, V. Sahajwalla, Y. Nishina, Graphene oxide: the new membrane material, *Appl. Mater. Today* 1 (1) (2015) 1–12, <http://dx.doi.org/10.1016/j.apmt.2015.06.002>.
- [4] Y. You, V. Sahajwalla, M. Yoshimura, R.K. Joshi, Graphene and graphene oxide for desalination, *Nanoscale* 8 (1) (2016) 117–119, <http://dx.doi.org/10.1039/C5NR06154G>.
- [5] J. Deng, Y. You, H. Bustamante, V. Sahajwalla, R.K. Joshi, Mechanism of water transport in graphene oxide laminates, *Chem. Sci.* 8 (3) (2017) 1701–1704, <http://dx.doi.org/10.1039/C6SC03909J>.
- [6] B. Lian, J. Deng, G. Leslie, H. Bustamante, V. Sahajwalla, Y. Nishina, R.K. Joshi, Surfactant modified graphene oxide laminates for filtration, *Carbon* 116 (2017) 240–245, <http://dx.doi.org/10.1016/j.carbon.2017.01.102>.
- [7] G. Shao, Y. Lu, F. Wu, C. Yang, F. Zeng, Q. Wu, Graphene oxide: the mechanisms of oxidation and exfoliation, *J. Mater. Sci.* 47 (10) (2012) 4400–4409, <http://dx.doi.org/10.1007/s10853-012-6294-5>.
- [8] A. Lerf, H. He, M. Forster, J. Klinowski, Structure of graphite oxide revisited, *J. Phys. Chem. B* 102 (23) (1998) 4477–4482, <http://dx.doi.org/10.1021/jp9731821>.
- [9] Y. Si, E.T. Samulski, Synthesis of water soluble graphene, *Nano Lett.* 8 (6) (2008) 1679–1682, <http://dx.doi.org/10.1021/nl080604h>.
- [10] U. Hofmann, A. Frenzel, The reduction of graphite oxide by hydrogen sulfide, *Kolloid.-Z* 68 (1934) 149–151, <http://dx.doi.org/10.1007/BF01451376>.
- [11] S. Stankovich, D.A. Dikin, R.D. Piner, K.A. Kohlhaas, A. Kleinhammes, Y. Jia, et al., Synthesis of graphene-based nanosheets via chemical reduction of exfoliated graphite oxide, *Carbon* 45 (7) (2007) 1558–1565, <http://dx.doi.org/10.1016/j.carbon.2007.02.034>.
- [12] J.I. Paredes, S. Villar-Rodil, M.J. Fernandez-Merino, L. Guardia, A. Martinez-Alonso, J.M.D. Tascón, Environmentally friendly approaches toward the mass production of processable graphene from graphite oxide, *J. Mater. Chem.* 21 (2011) 298–306, <http://dx.doi.org/10.1039/C0JM01717E>.
- [13] J. Zhang, H. Yang, G. Shen, P. Cheng, J. Zhang, S. Guo, Reduction of graphene oxide via L-ascorbic acid, *Chem. Commun.* 46 (7) (2010) 1112–1114, <http://dx.doi.org/10.1039/b917705a>.
- [14] Y. Zhou, Q. Bao, L.A.L. Tang, Y. Zhong, K.P. Loh, Hydrothermal dehydration for the “green” reduction of exfoliated graphene oxide to graphene and demonstration of tunable optical limiting properties, *Chem. Mater.* 21 (13) (2009) 2950–2956, <http://dx.doi.org/10.1021/cm9006603>.
- [15] X. Zhang, D. Zhang, Y. Chen, X. Sun, Y. Ma, Electrochemical reduction of graphene oxide films: preparation, characterization and their electrochemical properties, *Chin. Sci. Bull.* 57 (2012) 3045–3050, <http://dx.doi.org/10.1007/s11434-012-5256-2>.
- [16] N.N. Nyangiwe, M. Khenfouch, F.T. Thema, K. Nukwa, L. Kotsedi, M. Maaza, Free-green synthesis and dynamics of reduced graphene sheets via sun light irradiation, *Graphene* 4 (3) (2015) 54–61, <http://dx.doi.org/10.4236/graphene.2015.43006>.
- [17] C.Y. Kong, W.L. Song, M.J. Meziani, K.N. Tackett, L. Cao, A.J. Farr, et al., Supercritical fluid conversion of graphene oxides, *J. Supercrit. Fluids* 61 (2012) 206–211, <http://dx.doi.org/10.1016/j.supflu.2011.09.008>.
- [18] M.-H. Yeh, L.-Y. Lin, L.-Y. Chang, Y.-A. Leu, W.-Y. Cheng, J.-J. Lin, et al., Dye-sensitized solar cells with reduced graphene oxide as the counter electrode prepared by a green photothermal reduction process, *ChemPhysChem* 15 (6) (2014) 1175–1181, <http://dx.doi.org/10.1002/cphc.201301128>.
- [19] S. Pei, H.M. Cheng, The reduction of graphene oxide, *Carbon* 50 (9) (2012) 3210–3228, <http://dx.doi.org/10.1016/j.carbon.2011.11.010>.
- [20] L. Huang, Y. Huang, J. Liang, X. Wan, Y. Chen, Graphene-based conducting inks for direct inkjet printing of flexible conductive patterns and their applications in electric circuits and chemical sensors, *Nano Res.* 4 (7) (2011) 675–684, <http://dx.doi.org/10.1007/s12274-011-0123-z>.
- [21] P. Khanra, T. Kuila, N.H. Kim, S.H. Bae, D. Sheng Yu, J.H. Lee, Simultaneous bio-functionalization and reduction of graphene oxide by baker’s yeast, *Chem. Eng. J.* 183 (2012) 526–533, <http://dx.doi.org/10.1016/j.cej.2011.12.075>.
- [22] Y. Wang, Z.X. Shi, J. Yin, Facile synthesis of soluble graphene via a green reduction of graphene oxide in tea solution and its biocomposites, *ACS Appl. Mater. Interfaces* 3 (4) (2011) 1127–1133, <http://dx.doi.org/10.1021/am101261g>.
- [23] C. Zhu, S. Guo, Y. Fang, S. Dong, Reducing sugar: new functional molecules for the green synthesis of graphene nanosheets, *ACS Nano* 4 (4) (2010) 2429–2437, <http://dx.doi.org/10.1021/nn1002387>.
- [24] M.T.H. Aunkor, I.M. Mahbulul, R. Saidur, H.S.C. Metselaar, The green reduction of graphene oxide, *RSC Adv.* 6 (2016) 27807–27828, <http://dx.doi.org/10.1039/C6RA03189G>.
- [25] V. Loryuonyong, K. Totepvimarn, P. Eimburanaprat, W. Boonchompoo, A. Buasri, Preparation and characterization of reduced graphene oxide sheets via water-based exfoliation and reduction methods, *Adv. Mater. Sci. Eng.* 2013 (2013) 1–5, <http://dx.doi.org/10.1155/2013/923403>.
- [26] K.S. Merza, H.D. Al-Attabi, Z.M. Abbas, H.A. Yusr, Comparative study on methods for preparation of gold nanoparticles, *Green Sustain. Chem.* 2 (2012) 26–28, <http://dx.doi.org/10.4236/gsc.2012.21005>.
- [27] W. Wan, Z. Zhao, H. Hu, Y. Gogotsi, J. Qiu, Highly controllable and green reduction of graphene oxide to flexible graphene film with high strength, *Mater. Res. Bull.* 48 (11) (2013) 4797–4803, <http://dx.doi.org/10.1016/j.materresbull.2013.08.031>.
- [28] Z. Zhang, H. Chen, C. King, M. Guo, F. Xu, X. Wang, et al., Sodium citrate: a universal reducing agent for reduction/decoration of graphene oxide with Au nanoparticles, *Nano Res.* 4 (6) (2011) 599–611, <http://dx.doi.org/10.1007/s12274-011-0116-y>.
- [29] Z. Bo, X. Shuai, S. Mao, H. Yang, J. Qian, J. Chen, et al., Green preparation of reduced graphene oxide for sensing and energy storage applications, *Sci. Rep.* 4 (2014) 4684, <http://dx.doi.org/10.1038/srep04684>.
- [30] S.W. Chong, C.W. Lai, S.B. Abdul Hamid, Green preparation of reduced graphene oxide using a natural reducing agent, *Ceram. Int.* 41 (8) (2015) 9505–9513, <http://dx.doi.org/10.1016/j.ceramint.2015.04.008>.
- [31] J. Tian, H. Zhang, Preparation and characterization of reduced graphene oxide using ascorbic acid and sodium citrate as binary reductant, *Fuller. Nanotub. Carbon Nanostruct.* 25 (1) (2017) 17–22, <http://dx.doi.org/10.1080/1536383X.2016.1247052>.
- [32] K. Muthoosamy, R. Geetha Bai, I.B. Abubakar, S.M. Sudheer, H.N. Lim, H.S. Loh, et al., Exceedingly biocompatible and thin-layered reduced graphene oxide nanosheets using an eco-friendly mushroom extract strategy, *Int. J. Nanomed.* 10 (1) (2015) 1505–1519, <http://dx.doi.org/10.2147/IJN.S75213>.
- [33] M. Khan, A.H. Al-Marrji, M. Khan, M.R. Shaikh, N. Mohri, S.F. Adil, et al., Green approach for the effective reduction of graphene oxide using *Salvadora persica* L. Root (Miswak) extract, *Nanoscale Res. Lett.* 10 (2015) 281, <http://dx.doi.org/10.1186/s11671-015-0987-z>.
- [34] T. Kuila, S. Bose, P. Khanra, A.K. Mishra, N.H. Kim, J.H. Lee, A green approach for the reduction of graphene oxide by wild carrot root, *Carbon* 50 (3) (2012) 914–921, <http://dx.doi.org/10.1016/j.carbon.2011.09.053>.
- [35] S. Thakur, N. Karak, Green reduction of graphene oxide by aqueous phytoextracts, *Carbon* 50 (14) (2012) 5331–5339, <http://dx.doi.org/10.1016/j.carbon.2012.07.023>.
- [36] B. Kartick, S.K. Srivastava, I. Srivastava, Green synthesis of graphene, *J. Nanosci. Nanotechnol.* 13 (6) (2013) 4320–4324, <http://dx.doi.org/10.1166/jnn.2013.7461>.
- [37] F. Tavakoli, M. Salavati-Niasari, A. Badii, F. Mohandes, Green synthesis and characterization of graphene nanosheets, *Mater. Res. Bull.* 63 (1) (2015) 51–57, <http://dx.doi.org/10.1080/1536383X.2016.1247052>.
- [38] B. Haghghi, M.A. Tabrizi, Green-synthesis of reduced graphene oxide nanosheets using rose water and a survey on their characteristics and applications, *RCS Adv.* 3 (32) (2013) 13365–13371, <http://dx.doi.org/10.1039/C3RA40856F>.
- [39] Y. Lei, Z. Tang, R. Liao, B. Guo, Hydrolysable tannin as environmentally friendly reducer and stabilizer for graphene oxide, *Green Chem.* 13 (7) (2011) 1655–1656, <http://dx.doi.org/10.1039/c1gc15081b>.
- [40] O. Akhavan, E. Ghaderi, *Escherichia coli* bacteria reduce graphene oxide to bactericidal graphene in a self-limiting manner, *Carbon* 50 (5) (2012) 1853–1860, <http://dx.doi.org/10.1016/j.carbon.2011.12.035>.
- [41] E.C. Salas, Z. Sun, A. Lu, J.M. Tour, Reduction of graphene oxide via bacterial


- respiration, *ACS Nano* 4 (8) (2010) 4852–4856.
- [42] G. Wang, F. Qian, C.W. Saltikov, Y. Jiao, Y. Li, Microbial reduction of graphene oxide by *Shewanella*, *Nano Res.* 4 (6) (2011) 563–570, <http://dx.doi.org/10.1007/s12274-011-0112-2>.
- [43] Y.-K. Kim, M.-H. Kim, D.-H. Min, Biocompatible reduced graphene oxide prepared by using dextran as a multifunctional reducing agent, *Chem. Commun.* 47 (11) (2011) 3195–3197, <http://dx.doi.org/10.1039/c0cc05005a>.
- [44] C. Xu, X. Shi, A. Ji, L. Shi, C. Zhou, Y. Cui, Fabrication and characteristics of reduced graphene oxide produced with different green reductants, *PLoS One* 10 (2015) 1–15, <http://dx.doi.org/10.1371/journal.pone.0144842>.
- [45] D. Chen, L. Li, L. Guo, An environment-friendly preparation of reduced graphene oxide nanosheets via amino acid, *Nanotechnology* 22 (2011) 325601, <http://dx.doi.org/10.1088/0957-4484/22/32/325601>.
- [46] S. Bose, T. Kuila, A.K. Mishra, N.H. Kim, J.H. Lee, Dual role of glycine as a chemical functionalizer and a reducing agent in the preparation of graphene: an environmentally friendly method, *J. Mater. Chem.* 22 (19) (2012) 9696–9703, <http://dx.doi.org/10.1039/c2jm00011c>.
- [47] J. Liu, S. Fu, B. Yuan, Y. Li, Z. Deng, Toward a universal “adhesive nanosheet” for the assembly of multiple nanoparticles based on a protein-induced reduction/ decoration of graphene oxide, *J. Am. Chem. Soc.* 132 (21) (2010) 7279–7281, <http://dx.doi.org/10.1021/ja100938r>.
- [48] M.J. Fernández-Merino, L. Guardia, J.I. Paredes, S. Villar-Rodil, P. Solís-Fernández, A. Martínez-Alonso, et al., Vitamin C is an ideal substitute for hydrazine in the reduction of graphene oxide suspensions, *J. Phys. Chem. C* 114 (14) (2010) 6426–6432, <http://dx.doi.org/10.1021/jp100603h>.
- [49] H. Ding, S. Zhang, J.-T. Chen, X.-P. Hu, Z.-F. Du, Y.-X. Qiu, et al., Reduction of graphene oxide at room temperature with vitamin C for RGO–TiO₂ photoanodes in dye-sensitized solar cell, *Thin Solid Films* 584 (2015) 29–36, <http://dx.doi.org/10.1016/j.tsf.2015.02.038>.
- [50] Z. Sui, X. Zhang, Y. Lei, Y. Luo, Easy and green synthesis of reduced graphite oxide-based hydrogels, *Carbon* 49 (13) (2011) 4314–4321, <http://dx.doi.org/10.1016/j.carbon.2011.06.006>.
- [51] V. Dua, S.P. Surwade, S. Ammu, S.R. Agnihotra, S. Jain, K.E. Roberts, S. Park, R.S. Ruoff, S.K. Manohar, All-organic vapor sensor using inkjet-printed reduced graphene oxide, *Angew. Chem. Int. Ed.* 49 (12) (2010) 2154–2157, <http://dx.doi.org/10.1002/anie.200905089>.
- [52] D. Fadhel, Spectrophotometric determination of ascorbic acid in aqueous solutions, *J. Nucl. Org.* 15 (3) (2012) 88–94.
- [53] V. Hima, S. Rubesh Kumar, N. Duganath, N. Devanna, Quantization of ascorbic acid in ayurvedic amla capsule by various analytical techniques, *Der Pharm. Chem.* 5 (3) (2013) 8–17.
- [54] D.A. Davies, Michael B. Austin, John Partidge, Vitamin C: its chemistry and biochemistry, *R. Soc. Chem.* (1991) 38–41.
- [55] M. Fathy, A. Gomaa, F.A. Taher, M.M. El-Fass, A.E.H.B. Kashyout, Optimizing the preparation parameters of GO and rGO for large-scale production, *J. Mater. Sci.* 51 (12) (2016) 5664–5675, <http://dx.doi.org/10.1007/s10853-016-9869-8>.
- [56] J. Gao, F. Liu, Y. Liu, N. Ma, Z. Wang, X. Zhang, Environment-friendly method to produce graphene that employs vitamin C and amino acid, *Chem. Mater.* 22 (7) (2010) 2213–2218, <http://dx.doi.org/10.1021/cm902635j>.
- [57] A. Abulizi, K. Okitsu, J.J. Zhu, Ultrasound assisted reduction of graphene oxide to graphene in l-ascorbic acid aqueous solutions: kinetics and effects of various factors on the rate of graphene formation, *Ultrason. Sonochem.* 21 (3) (2014) 1174–1181, <http://dx.doi.org/10.1016/j.ultsonch.2013.10.019>.
- [58] J.M. Chem, Green synthesis of carbon nanotube–graphene hybrid aerogels and their use as versatile agents for water purification, *J. Mater. Chem.* 22 (2012) 8767–8771, <http://dx.doi.org/10.1039/c2jm0005e>.
- [59] A. Pruna, D. Pullini, D. Busquets, Influence of synthesis conditions on properties of green-reduced graphene oxide, *J. Nanopart. Res.* 15 (2013) 1605, <http://dx.doi.org/10.1007/s11051-013-1605-6>.
- [60] A. Pruna, D. Pullini, D. Busquets, Green-reduction of covalently functionalized graphene oxide with varying stoichiometry, *Int. J. Chem. Mol. Nucl. Mat. Metall. Eng.* 7 (2013) 444–447.
- [61] M.A. Velasco-Soto, S.A. Pérez-García, J. Alvarez-Quintana, Y. Cao, L. Nyborg, L. Licea-Jiménez, Selective band gap manipulation of graphene oxide by its reduction with mild reagents, *Carbon* 93 (2015) 967–973, <http://dx.doi.org/10.1016/j.carbon.2015.06.013>.
- [62] X. Zhu, Q. Liu, X. Zhu, C. Li, M. Xu, Y. Liang, Reduction of graphene oxide via ascorbic acid and its application for simultaneous detection of dopamine and ascorbic acid, *Int. J. Electrochem. Sci.* 7 (2012) 5172–5184.
- [63] S. Eigler, S. Grimm, M. Enzelberger-Heim, P. Müller, A. Hirsch, Graphene oxide: efficiency of reducing agents, *Chem. Commun.* 49 (67) (2013) 7391–7393, <http://dx.doi.org/10.1039/C3CC43612H>.
- [64] S. Abdolhosseinzadeh, H. Asgharzadeh, H. Seop Kim, Fast and fully-scalable synthesis of reduced graphene oxide, *Sci. Rep.* 5 (2015) 10160, <http://dx.doi.org/10.1038/srep10160>.
- [65] J. Li, J. Li, L. Li, M. Yu, H. Ma, B. Zhang, Flexible graphene fibers prepared by chemical reduction-induced self-assembly, *J. Mater. Chem. A* 2 (18) (2014) 6359–6362, <http://dx.doi.org/10.1039/c4ta00431k>.
- [66] N.M. Huang, H.N. Lim, C.H. Chia, M.A. Yarmo, M.R. Muhamad, Simple room-temperature preparation of high-yield large-area graphene oxide, *Int. J. Nanomed.* 6 (2011) 3443–3448, <http://dx.doi.org/10.2147/IJN.S26812>.
- [67] S. Reich, C. Thomsen, Raman spectroscopy of graphite, *Philos. Trans. R. Soc. A Math. Phys. Eng. Sci.* 362 (2004) 2271–2288, <http://dx.doi.org/10.1098/rsta.2004.1454>.
- [68] S.T. Mitchell, N. Frese, A. Golzhauser, A. Browsers, K. Sattler, Ultralight carbon nanofoam from naphthalene-mediated hydrothermal sucrose carbonization, *Carbon* 95 (2015) 434–441, <http://dx.doi.org/10.1016/j.carbon.2015.08.001>.
- [69] M. Iliut, C. Leordean, V. Canpean, C.-M. Teodorescu, S. Astilean, A new green, ascorbic acid-assisted method for versatile synthesis of Au-graphene hybrids as efficient surface-enhanced Raman scattering platforms, *J. Mater. Chem. C* 1 (26) (2013) 4094–4104, <http://dx.doi.org/10.1039/C3TC30177J>.
- [70] E. Andrijanto, S. Shoelarta, G. Subiyanto, S. Rifki, Facile synthesis of graphene from graphite using ascorbic acid as reducing agent, *AIP Conf. Proc.* 1725 (2016) 020003, <http://dx.doi.org/10.1063/1.4945457>.

SCIENTIFIC REPORTS



OPEN

Structural Evolution of Hydrothermally Derived Reduced Graphene Oxide

Hsin-Hui Huang¹ , K. Kanishka H. De Silva¹, G. R. A. Kumara² & Masamichi Yoshimura¹

Hydrothermal reduction is a promising approach for graphene oxide (GO) reduction since it is environmentally friendly, simple, and cost effective. We present a detailed study of structural changes occurring in graphene oxide during the reduction process. The correlations between the interlayer spacing, chemical states, work functions, surface morphology, level of disorders, the number of layers, and processing time are elucidated. The results reveal that GO flakes remain in the early stage of the reduction process and that they are fully reduced after a 4-h hydrothermal treatment. With an increase in the reduction time, the resulting product, *i.e.*, reduced graphene oxide, has a low oxygen content, small interlayer spacing, and crumbled and wrinkled structures. We are convinced that these properties can be tuned to a desired level for various applications.

Graphene, a two-dimensional monolayer of carbon atoms in a hexagonal lattice with an sp^2 bonding hybridization, has come to the forefront in the field of materials science and nanotechnology since the early 2000s in view of its outstanding electrical and thermal properties combined with excellent mechanical strength^{1–3}. These superior properties lead to graphene making a significant impact on the field of materials science and nanotechnology, with graphene now being considered to replace other materials used in existing applications. To date, the most common methods used to fabricate graphene are micromechanical exfoliation, chemical vapour deposition, and chemical oxidation and reduction of graphite^{3–5}. However, each of these methods has certain problems and limitations, *e.g.*, in terms of yields, defect contents, costs, steps, or production time⁶. Chemical oxidation and reduction of exfoliated graphite is the best solution among all the other methods due to the relative ease of creating sufficient quantities of products at a desired quality level. However, the chemical reduction involves the use of hazardous reducing agents, such as hydrazine or sulfonate, and its residues might have a significant effect on the structures and properties of the final products. On the other hand, hydrothermal reduction is a simple, fast, and environmentally friendly route which involves water only. The experimental setup is rather cost effective and easy and it only requires an autoclave with a Teflon-lined container along with a furnace. It has been reported that a closed system with certain temperature and internal pressure promotes the restoration of the aromatic structure which is favourable for minimizing the defects⁷. Moreover, it has a good scalability and suits industrial large-scale production.

Hydrothermal process was first introduced in the late nineteenth century, and it was mainly used in the production of synthetic minerals^{8,9}. Since then, many studies have been performed across a wide range of the field, and the attention on the process is still growing. For instance, a graphene/silicon composite can be hydrothermally pruced for use as an anode in lithium ion batteries. A hydrothermally fabricated molybdenum disulphide (MoS_2)/graphene composite shows a good onset potential in the hydrogen evolution reaction, giving one of the best performances among MoS_2 -based catalysts^{10,11}. Reduced graphene oxide (rGO) decorated with titanium dioxide synthesized via a hydrothermal approach exhibits improved photocatalytic properties and would, therefore, be a promising material for future photovoltaic applications¹². Additionally, composites of graphene and V_2O_5 have been developed for enhanced electrochemical energy storage¹³. Recently, a new form of self-assembled hydrogel rGO developed through a hydrothermal route has received a great deal of attention owing to the high mechanical strength (storage modulus of 450–490 kPa) of 1–3 orders of magnitude higher than conventional self-assembled hydrogels¹⁴, high compressive strength of 6 orders higher than conventional graphite products¹⁵, and an electrical conductivity as high as $5 \times 10^{-3} S/cm$ ¹⁴. Moreover, a three-dimensional $Ni_xCo_{1-x}S_2$ particle/

¹Graduate School of Engineering, Toyota Technological Institute, Nagoya, 468-8511, Japan. ²National Institute of Fundamental Studies, Kandy, 20000, Sri Lanka. Correspondence and requests for materials should be addressed to M.Y. (email: yoshi@toyota-ti.ac.jp)

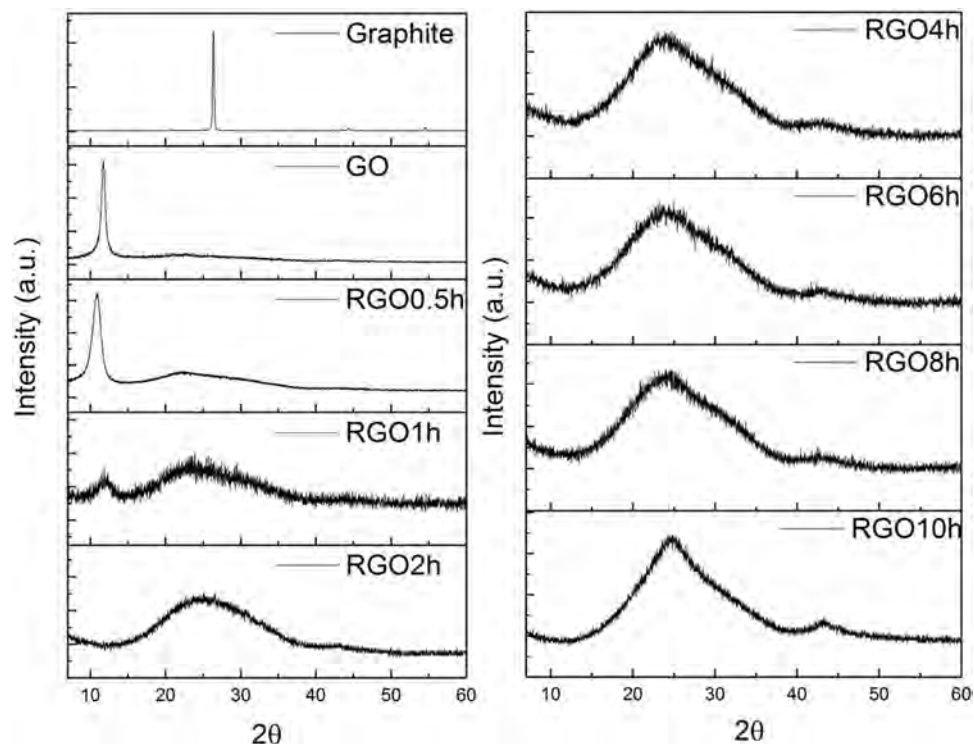


Figure 1. XRD patterns of graphite, GO, and rGO samples treated at different hours.

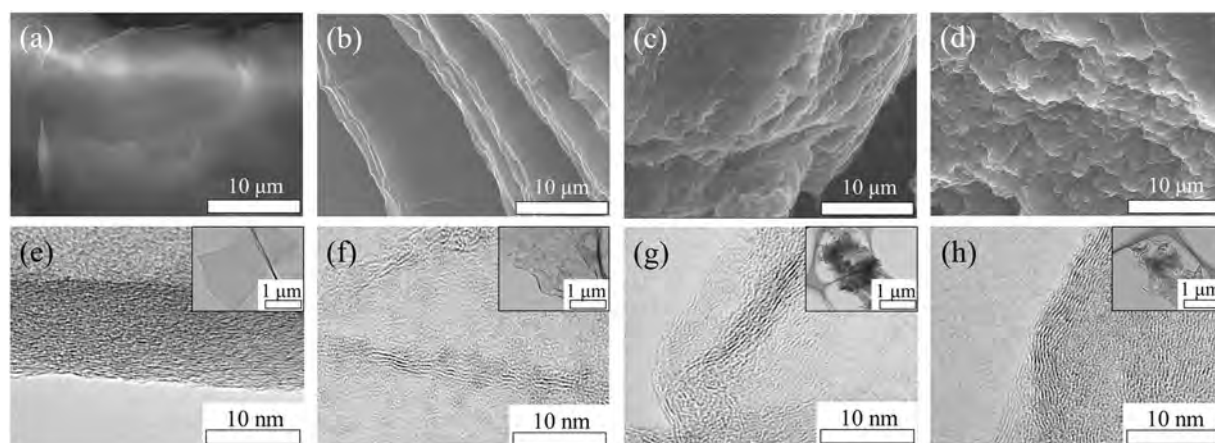


Figure 2. SEM images of (a) GO, and its deoxygenated samples treated under (b) 1 h, (c) 4 h and (d) 10 h. The corresponding TEM images are shown in (e–h), respectively. The insets of TEM images showing the sheets in low magnification.

graphene composite hydrogel was shown to have an interconnected porous network with pore sizes in the range of several micrometres giving high performance as the active material in supercapacitors¹⁶.

While hydrothermal treatment is a unique synthetic approach to graphene oxide reduction and even though it has been used for years, it is faced with the challenges of firmly understanding the deoxygenation activity, preparing graphene with high quality and dispersibility, and precisely controlling the structure and morphology. Moreover, the structures and properties of the resulting products might vary depending on the control parameters used in the reduction process. Thus, it is necessary to clarify the reduction mechanisms and structural changes throughout the process, since the structure is strongly related to the final properties and hence the performance of the devices. Here, we present a detailed study on the structural, morphological, and electrical changes during the reduction process from the initial 30 min up to 10 h at 200 °C; hereafter, we refer to the individual samples as rGO 0.5 h, 1 h, 2 h, 4 h, 8 h, and 10 h. The gradual changes in the morphology and dramatic drop in the inter-layer spacing were elucidated using X-ray diffraction (XRD), scanning electron microscopy (SEM), atomic force

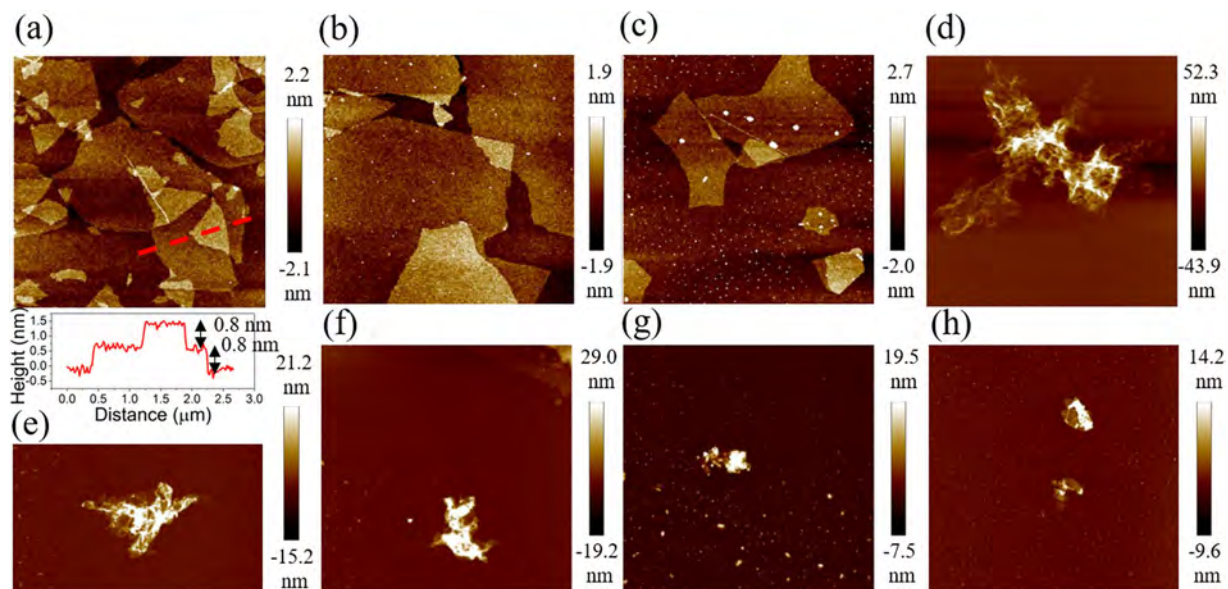


Figure 3. AFM images of the rGO samples treated at (a) GO, rGO (b) 30 min, (c) 1 h, (d) 2 h, (e) 4 h, (f) 6 h, (g) 8 h, (h) 10 h.

microscopy (AFM), and transmission electron microscopy (TEM). The degree of oxidation and reduction and the defects such as vacancies were confirmed using Raman spectroscopy and X-ray photoelectron spectroscopy (XPS). The electrical properties of the reduced graphene oxide at different stages were revealed through investigation of the strong correlation between oxygen content and contact potential difference/work function. We provide an insight into the structural evolution during graphene oxide reduction through a controllable hydrothermal route. We greatly believe that the resulting products can be tailored, according to their specific properties and structures, for desired applications.

Results and Discussion

The structural change in the GO flakes was first revealed by XRD analysis, as shown in Fig. 1. In raw graphite, an intense crystalline peak was found at $2\theta = 26.4^\circ$ (lattice spacing of 0.34 nm), which corresponds to the (002) diffraction peak of graphite¹⁷. After oxidation, the peak shifts to a lower angle at $2\theta = 10.9^\circ$ with a lattice spacing of 0.81 nm, indicating the success in oxidation. As reported earlier, an increase in interlayer spacing is mainly attributed to the intercalation with water and the presence of oxygen functionalities such as epoxide and hydroxyl groups which populate on the basal plane of the carbon sheet^{18–21}. Notably, the sharp and distinct peak is attributed to the preserved and ordered stacking along the c-axis. After 30-min hydrothermal treatment, the intensity of the distinct peak in GO reduces and the peak becomes broader due to the partial breakdown of the long-range order of the GO. Moreover, the peak position has slightly shifted towards a higher angle ($2\theta = 11.1^\circ$) showing the decrease in the lattice spacing (0.80 nm). Meanwhile, a relatively weak and broad shoulder was observed at $2\theta = 22.8^\circ$, yielding an interlayer separation of 0.39 nm. This indicates that the reduction has taken place within 30 mins. After a 1-h hydrothermal reduction, the broad and diffuse peak becomes dominant. The interlayer spacing was calculated to be the (002) graphite peak of 0.35 nm. However, a weak GO peak still can be observed ($2\theta = 11.9^\circ$, $d = 0.75$ nm), denoting the coexistence of rGO and GO or incompleteness of GO reduction. After 2 h reduction, the GO peak was undetectable and left a broad rGO peak on the spectrum with a d-spacing of 0.35 nm. The rGO peak position remains almost the same up to a reduction time of 10 h (details are shown in the Supporting Information Table S1). Intriguingly, in sample rGO 10 h, the intensity of the rGO peak increases corresponding to restacking or overlapping of rGO sheets²².

The surface morphology of GO, and hydrothermally reduced GO were analysed by SEM, TEM and AFM. Before hydrothermal treatment, the GO sample (Fig. 2(a)) shows a laminated structure. A monolayer or a few-layer GO could be achieved after dispersing in water, in which the thickness of a single layer was measured to be 0.8–0.9 nm, as observed by TEM and AFM (Figs 2(e) and 3(a)). The charging effect seen in the image has arisen due to the non-conductive nature of GO resulted from the defects and oxygen functionalities. Further, SEM and TEM images of the rGO 1 h, 4 h and 10 h are shown in Fig. 2(b–d) and (f–h) (SEM and TEM images of rest of the rGO samples can be found in the Supplementary Informations S1–S3). SEM image of rGO 1 h shows that the sheets still possess the layered structure. However, the TEM image of rGO 1 h sample indicates the coexistence of GO (layered structure) and rGO (disordered structure). Meanwhile, the number of layers reduces to less than 10 (Fig. 2(f)) showing the breakdown of the long-range-order stacking, which is consistent with XRD observation. With the increase in reduction time, the layered nature becomes disordered, crumpled and smaller. This behaviour can be visualized in the AFM topographic image in Fig. 3. It shows that the rGO flakes are flat, similar to the GO flakes, when they are treated for less than or equal to 1 h. According to the XRD results, a small GO peak appears in rGO 1 h sample but vanishes when reduction time increases to 2 h. It implies that the rGO

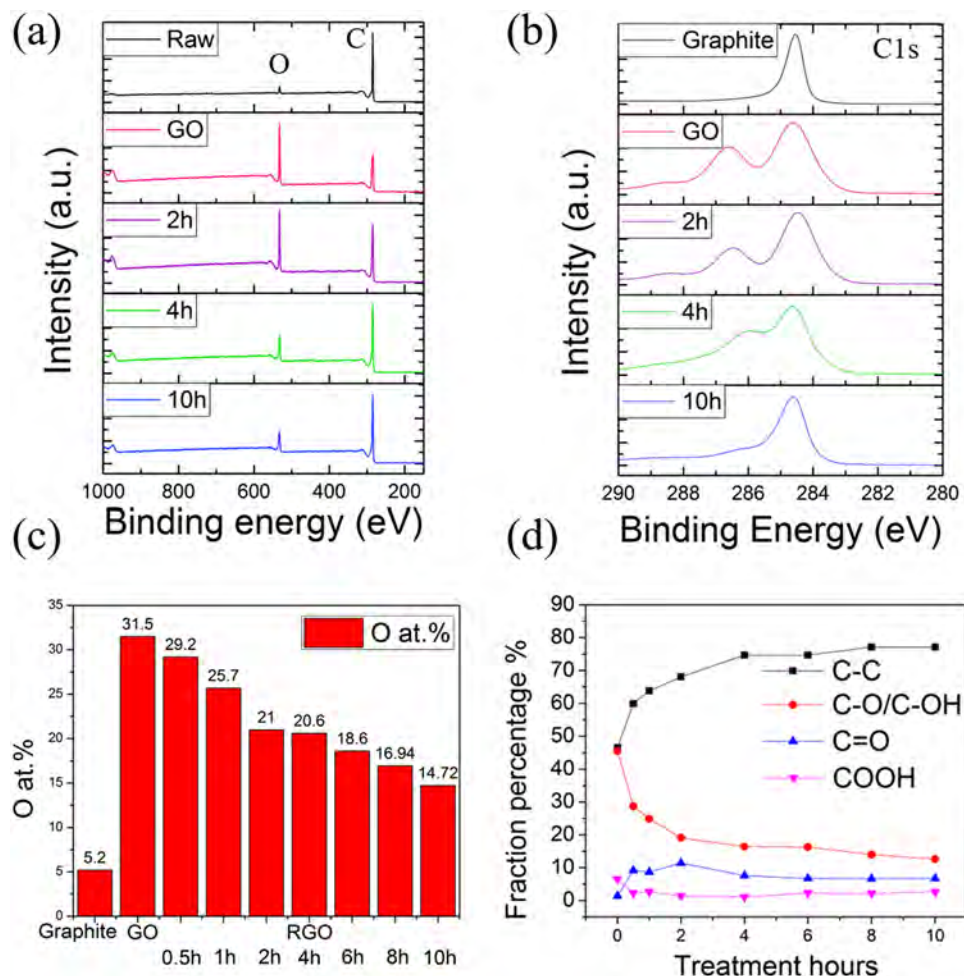


Figure 4. (a) XPS full spectra of raw graphite, GO, rGO 2 h, 4 h, and 10 h samples and (b) the corresponding high resolution C1s spectra. (c) Oxygen content as a function of reduction time. (d) Change in fraction percentage of the individual oxygen function group with reduction time.

0.5 h and 1 h samples might still preserve the nature of GO giving the applicability to make a uniform thin film or membrane for related applications. In contrast, rGO 2–10 h samples show many wrinkles. The possible explanation is; in GO dispersion, the presence of negatively charged oxygen functionalities provides static repulsive force stabilizing the exfoliated sheets. Thus, when they are dropped onto the substrate, monolayer GO sheets lie flat on the substrate. On the contrary, when GO sheets are reduced, they become regionally hydrophobic due to the removal of the oxygen functionalities, as confirmed by XRD and X-ray photoelectron spectroscopy results (discuss later). After dropping onto the substrate, the locally hydrophobic rGO sheets will tend to aggregate to reduce the free energy, leading to the formation of wrinkled and folded morphology. Moreover, the edge-to-edge attraction interactions due to the hydrogen bonding between the remaining oxygen functionality might result in the aggregation of rGO sheets.

In order to probe the chemical structure, we performed XPS on raw graphite, GO, and the series of rGO samples; the full-scan spectra, higher resolution C1s spectra, atomic percentage of oxygen, and fraction percentage of each oxygen functionality are shown in Fig. 4(a–d), respectively (full analyses of all the specimens can be found in the Supporting Information Figure S4). Initially, pristine graphite contains a small amount of oxygen of 5.2 at% (from the atmosphere or trapped in the Earth's crust) which yields a high carbon to oxygen (C/O) ratio of 16.9. After oxidation, a well-defined double peak with a small tail towards higher binding energy was found in the high resolution C1s spectrum, which is a signature of a considerable degree of oxidation. It is also demonstrated by a significant increase in oxygen contents to 31.5 at%. It is noted that the C peak in sample GO showed a clear shift towards higher binding energy, reflecting significant surface charging caused by the electrically insulating oxygen functional groups. Here, it has been shifted back for ease of analysis. The C1s spectrum of GO was deconvoluted into four major components, including C-C/C=C (284.6 eV), epoxide C-O/hydroxyl C-OH (286.1–287.1 eV), carbonyl C=O (288.2 eV), and carboxyl COOH (289.3 eV) groups. Due to the similar binding energies, it is challenging to precisely determine a separate quantification of epoxide and hydroxyl groups, and therefore, their XPS peaks are discussed together.

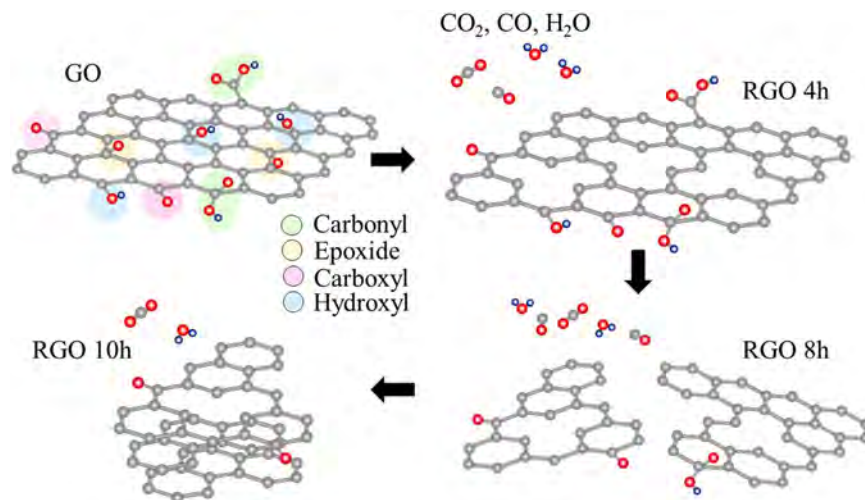


Figure 5. Schematic illustration of GO reduction with time dependence.

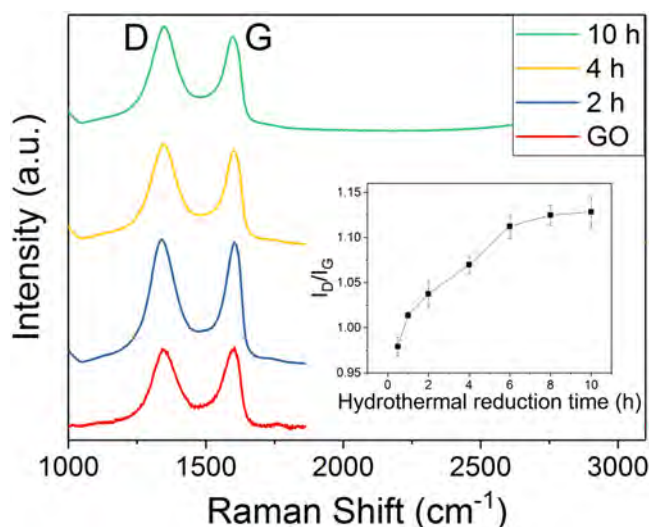


Figure 6. Raman spectra of graphene oxide, rGO 2 h, 4 h, and 10 h samples. (b) Insert shows the intensity ratio of D band over G band for GO and rGO treated at different hours.

Upon 0.5 h reduction (Figure S4), the double peak is present but there is a small decrease in the oxygen-related peak. The fraction of the epoxide/hydroxyl groups drops from 46% to approximately 34%. Based on the XRD analysis, the intensity of the GO peak is greatly reduced and, meanwhile, a small broad peak corresponding to rGO appears indicating that the GO has been partially reduced and converted to rGO. This suggests that the reduction of GO took place in such a short period of time due to the removal of thermally unstable epoxy groups²³. After 2 h, the fractional percentage of C-O/C-OH bonds was further reduced but not fully eliminated. According to the density functional theory calculations reported by Kim *et al.*²⁴ and Gao *et al.*²⁵, the hydroxyl group attached to the edge of the sheets and the lattice vacancies is more stable. Therefore, the peak which is contributed to C-O/C-OH groups still can be seen. Interestingly, the rGO 2 h sample has a lattice parameter corresponding to that of graphite/graphene with a relatively small oxygen content, giving it an enhanced hydrophilicity (contact angle is approximately 58.6°), as shown in the Supporting Information Figure S5.

Upon further hydrothermal reduction, several changes were observed. The intensity of the C1s gradually increases while the intensity of the O1s peak drops with increasing reduction time, as shown in Fig. 4(a) and (c). It is noted that the C-C bond is stable during the treatment, whereas the C bonded to oxygen-carrying functionalities decreases which results in an increase in the C-C (sp² and sp³) component contents. The oxygen content reaches the lowest value of 14.7 at% for sample rGO 10 h; at this point, the C-O/C-OH fractional content also decreases to its minimum value. This suggests that the C-OH bond is the major residual oxygen functional group which is the key metric to determine the level of reduction. Additionally, when the C-OH and C-O groups are removed, they break/cut off the rGO sheets into small pieces; as a consequence, the sheets will agglomerate to

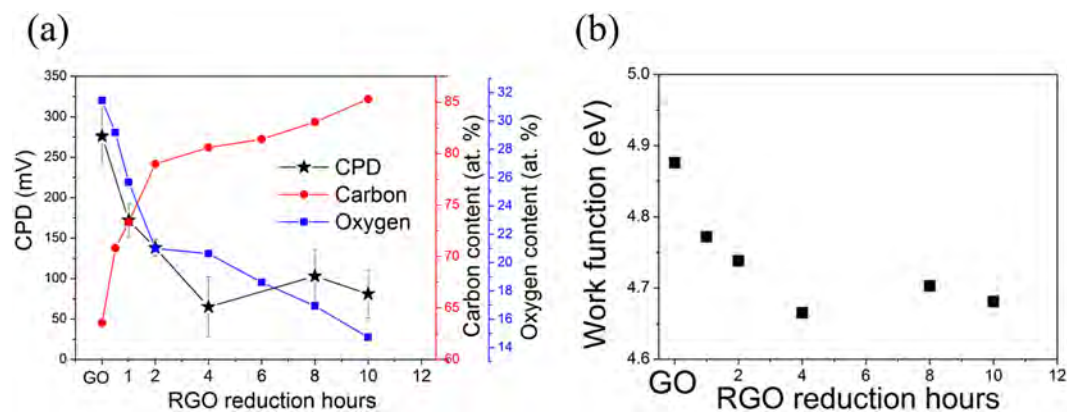


Figure 7. (a) The changes in CPD, carbon and oxygen content of rGO samples with its associated time dependence. (b) The work function of rGO samples as a function of reduction time.

reduce the surface energy and re-stacking could occur, as shown previously and illustrated in Fig. 5. The success in GO reduction and the evidence of aggregation in the 10 h sample are further demonstrated by ultraviolet (UV)-visible spectroscopy (Supporting Information Figure S6). Ma *et al.* have reported similar observations: the large sheets ($>2\mu\text{m}$) are almost absent after hydrothermal treatment and that the size of the rGO is dependent on the hydrothermal treatment temperature²⁶. In brief, this implies that deoxygenation could be regulated by the hydrothermal reduction time. It is worth noting that only C and O peaks were observed in the spectra for all the samples, indicating that no other undesired compounds were formed due to the use of water as a reductant.

Raman spectroscopy offers further insights to the structural changes in rGO (Fig. 6). The main features of the GO and its derivatives have D, G, and 2D peaks. The G peak at around $1580\text{--}1600\text{ cm}^{-1}$ is due to the bond stretching of sp^2 carbons in rings and chains, while the D peak at approximately $1330\text{--}1340\text{ cm}^{-1}$ originates from the breathing modes of the six-membered rings that are activated by defects²⁷. The change in the intensity ratio of D and G bands (I_D/I_G) with time-dependent GO reduction is plotted in the inset of Fig. 6. It shows a slight yet gradual increment of the I_D/I_G ratio with the increase in reduction time. In the early stage of reduction, the I_D/I_G ratio slightly increases which refers to the increase in edge of the sheets when sp^2 domains are torn apart by the removal of the oxygen functionalities²⁸. With further reduction, deoxygenation continues as demonstrated in XPS results, which might remove some of the carbons from the graphitic structure and leave pores and defects. Hence, it results in a deteriorated structure, giving an increase in the I_D/I_G ratio. However, one should be noted that a solid conclusion is tough to make in the interpretation of Raman spectra for GO and its derivatives. This is due to the manifold defects within the carbon lattice which makes almost no change in the Raman spectra as compared to the pristine graphene or single-layer or few-layer GO and rGO²⁹. The Raman spectra of all the samples are shown in the Supporting Information Figure S8.

The electronic properties of materials can be probed through the work function (WF), which can be derived from the contact potential difference (CPD) measured using Kelvin probe force microscopy (KPFM). Basically, the KPFM image maps the variation of the surface potential on the sample. By using a substrate with a known work function, the work function of the sheet can be calculated from the measured CPD difference (ΔV_{CPD}) between the substrate and sheet, as shown in the following equation, $\Delta V_{\text{CPD}} = 1/e (\Phi_{\text{substrate}} - \Phi_{\text{film}})$, where Φ denotes the work function³⁰. The measured V_{CPD} of GO and rGO samples were plotted along with carbon and oxygen content in Fig. 7(a). Initially, GO has the highest V_{CPD} which might be attributed to the large amount of chemisorbed oxygen on the graphene surface. During the GO reduction process, the CPD value decreases gradually with time. It is seen that the profile of oxygen content is similar to that of the CPD curve, while the carbon content shows the opposite trend. As reported earlier, the work function of a material is dependent on the chemical potential (such as oxidation state and defect sites) and surface dipoles^{31–33}. In GO, the oxygen atoms, such as hydroxyl and epoxide, are bonded with carbon on either side of the basal planes with specific dipole moments. The strength of the dipole moment can be altered by modifying the overall oxygen content during reduction; thus, it is expected to lead to changes in CPD/work function. Even though here we show that a similar trend of work function and oxygen content were observed, which implies a clear correlation between the two, oxygen content might be merely one of multiple parameters including temperature, thickness, specific oxygen functionalities, *etc.* that contributes to the work function. More specifically, a theoretical study with molecular dynamics and density functional theory calculations has reported that each oxygen-containing functional group has different impact on the work function³⁴. Nevertheless, at this stage, we considered only the correspondence of total oxygen atomic percentage with CPD changes.

The calculated work functions of all the samples are plotted in Fig. 7(b). It has been shown that the electronic properties can be enhanced by deoxygenation of GO. Care must be taken because the measured CPD is not simply due to the WF of the sheets but also due to the more complicated interplays between the electrical properties of the GO or rGO, underlying substrates, surface properties like atom absorption, the type of tip, *etc.*³⁵. Therefore, the measured WF should be considered as the work function of the aggregate systems. Here, we mainly compared the trend and the changes in WF/CPD for series rGO samples under the same measurement conditions, such

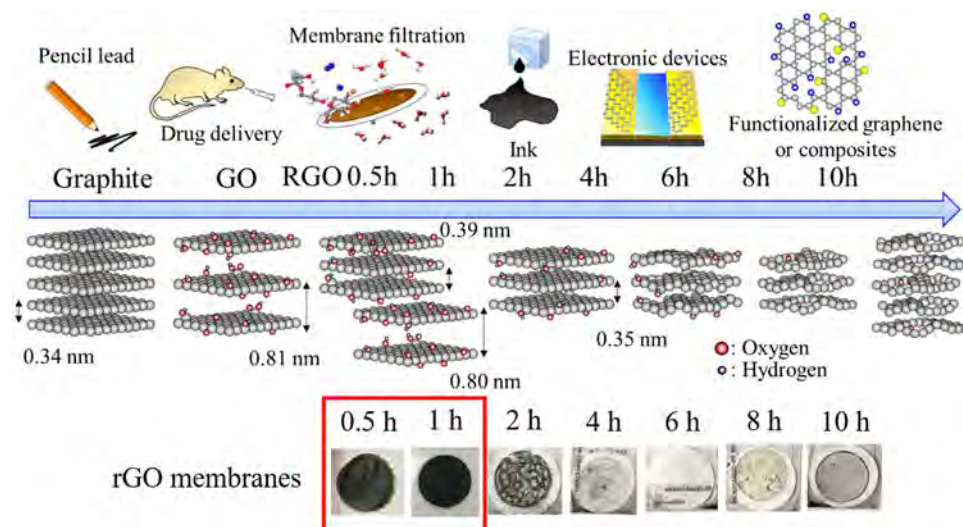


Figure 8. Schematic illustration of overall structural evolution of hydrothermally reduced GO and its potential applications. Lower part: the photographs of rGO membranes formed at different time intervals.

as, the use of the same tip and substrate. A more systematic study focused on, among other things, the effects of interfacial dipoles and substrates will be the subject of a future investigation.

Overall, the structural evolution from raw graphite to oxidized graphite to reduced graphene oxide along with its associated time dependence is summarized in the schematic in Fig. 8. Understanding the structural and microstructural changes during the reduction process offers valuable information in terms of its applications, since the structure of the material is strongly related to its physical, electronic, and mechanical properties, and hence the performance in applications. In this work, we observed that GO and rGO coexist in sample rGO 0.5 h and 1 h preserving the lattice spacing of graphite and high hydrophilicity similar to GO phases. The rGO membrane can be formed under this condition (see Fig. 8), which can be utilized in the field of water desalination and purification where the interlayer spacing is a key factor for ion molecular sieving^{36,37}. Additionally, it could possibly be applied to ink production since it possesses high dispersity due to the presence of oxygen functional groups and acceptable electronic properties. Samples rGO 2 h to rGO 8 h have better electronic properties due to the removal of the oxygen functional groups. The damaged and porous rGO 10 h sample provides the sites for polymerization or metal oxide decoration/doping. In conclusion, we can design or tune the structure of the materials by controlling or modifying the parameters in the hydrothermal reduction process to satisfy the requirements for future or current devices. A few potential or existing applications is schematically illustrated in Fig. 8.

Methods

Synthesis of graphite oxide. GO was synthesized by modified Hummers' method⁵. 1 g of graphite powders with average particle size of 7 μm (Sri Lanka natural graphite, RS Mines) was used as a starting material. Oxidation of graphite was achieved by treating with concentrated sulfuric acid and potassium permanganate, followed by adding the hydrogen peroxide. Lastly, the graphite oxide dispersion was washed with 1 M hydrochloric acid solution and distilled water with the assistance of centrifuge to remove the excessive soluble ions until it reaches neutral pH value. Note that the lower deposited gel-like dark-brown product was collected and dried in vacuum for hydrothermal reduction.

Fabrication of reduced graphite oxide. A liquidous dispersion of GO was prepared by adding the dried GO flakes into the distilled (DI) water (1 mg/ml). It was then transferred to a Teflon-lined autoclave (HU-50, San-Ai Kagaku Co., LTD.), and heated in an electric furnace under 200 $^{\circ}\text{C}$ (NHK-170AF, Nitto Kagaku Co., LTD.). Samples were extracted from the furnace at different hours, 0.5 h, 1 h, 2 h, 4 h, 6 h, 8 h, and 10 h. The resulting product appeared in black and hereafter we named the individual samples as rGO 0.5 h, 1 h, 2 h, 4 h, 8 h, and 10 h. The rGO 0.5 h and 1 h were found to have high dispersity as the dispersion have no aggregates, while the black precipitates were found sinking at the bottom of the container for the rest of the samples. The suspensions were then vacuum filtered and dried at room temperature for further characterization.

Characterization. Atomic force microscopy (AFM, Bruker MultiMode 8) and field-emission scanning electron microscopy (FE-SEM, Hitachi S-4700) were used for structural and morphological analysis. GO sample was observed using an accelerating voltage of 5 kV to eliminate the charging effect, while the rGO samples were viewed at an accelerating voltage of 15 kV. Interlayer spacing was determined by X-ray diffraction (XRD, Rigaku-Ultima IV X-ray diffractometer) with a step size of 0.02 $^{\circ}$ /min using a CuK α 1 radiation ($\lambda = 0.154 \text{ nm}$). The elemental composition analysis was performed by X-ray photoelectron spectroscopy (XPS, ULVAC-PHI PHI5000 Versa Probe II) with a source of AlK α 1486.6 eV. Transmission electron microscopy (TEM, JEOL JEM-2100) operated at an accelerating voltage of 200 kV was used to study the microstructure and morphology of the samples. The TEM specimen was prepared by dispersing powders in ethanol and followed by ultrasonication for

15 mins. It was then dropped on the carbon film-coated copper grids for observation. Few-layered GO and rGO samples were used for Raman measurements. The GO or rGO dispersions were first dropped on a Si substrate with a layer of 300 nm-thick SiO₂ followed by spin coating. Raman spectroscopy was conducted (Renishaw - InVia Raman Spectroscopy) using a 532-nm laser. It is noted that each sample was measured for more than 10 points and Raman spectra were taken in the central areas of the flakes. Electronic property was examined by a frequency-modulated Kelvin probe force microscopy (FM-KPFM) (MultiMode 8, Bruker) in a peakforce tapping mode. A platinum-coated silicon cantilever (Olympus, OMCL-AC240TM-R3) was used. UV-visible spectra were collected using a V-650 spectrophotometer (Jasco) in the wavelength range of 200–500 nm with a resolution of 2.0 nm. Noted that all the dispersions were prepared at the same concentration, however, rGO 10h sample could not be dissolved completely due to the high hydrophobicity in nature.

References

- Geim, A. K. & Novoselov, K. S. The rise of graphene. *Nat. Mater.* **6**, 183–191 (2007).
- Geim, A. K. Graphene: Status and prospects. *Science* **324**, 1530–1534 (2009).
- Novoselov, K. S. *et al.* Electric field effect in atomically thin carbon films. *Science* **306**, 666–669 (2004).
- Rabenu, A. Epitaxial graphene: How silicon leaves the scene. *Nat. Mater.* **8**, 171–172 (2009).
- Abdolhosseinzadeh, S., Asgharzadeh, H. & Kim, H. S. Fast and fully-scalable synthesis of reduced graphene oxide. *Sci. Rep.* **5**, 10160 (2005).
- Banhart, F., Kotakoski, J. & Krasheninnikov, A. V. Structural defects in graphene. *ACS Nano* **5**, 26–41 (2011).
- Zhou, Y., Bao, Q., Tang, L. A. L., Zhong, Y. & Loh, K. P. Hydrothermal dehydration for the “green” reduction of exfoliated graphene oxide to graphene and demonstration of tunable optical limiting properties. *Chem. Mater.* **21**, 2950–2956 (2009).
- Morey, G. W. & Niggli, P. The hydrothermal formation of silicates, a review. *J. Am. Chem. Soc.* **35**, 1086–1130 (1913).
- Rabenu, A. The role of hydrothermal synthesis in preparative chemistry. *Angew. Chem. Int. Ed.* **24**, 1026–1040 (1985).
- Youn, D. H. *et al.* Fabrication of graphene-based electrode in less than a minute through hybrid microwave annealing. *Sci. Rep.* **4**, 5492 (2014).
- Yu, Z., Ye, J., Chen, W., Xu, S. & Huang, F. Fabrication of few-layer molybdenum disulfide/reduced graphene oxide hybrids with enhanced lithium storage performance through a supramolecule-mediated hydrothermal route. *Carbon* **114**, 125–133 (2017).
- Shen, J. *et al.* One step hydrothermal synthesis of TiO₂-reduced graphene oxide sheets. *J. Mater. Chem.* **21**, 3415–3421 (2011).
- Lee, M. *et al.* One-step hydrothermal synthesis of graphene decorated V₂O₅ nanobelts for enhanced electrochemical energy storage. *Sci. Rep.* **5**, 8151 (2015).
- Xu, Y., Sheng, K., Li, C. & Shi, G. Self-assembled graphene hydrogel via a one-step hydrothermal process. *ACS Nano* **4**, 4324–4330 (2010).
- Bi, H. *et al.* Low Temperature casting of graphene with high compressive strength. *Adv. Mater.* **24**, 5124–5129 (2012).
- Li, G. & Xu, C. Hydrothermal synthesis of 3D Ni_xCo_{1-x}S₂ particles/graphene composite hydrogels for high performance supercapacitors. *Carbon* **90**, 44–52 (2015).
- Trucano, P. & Chen, R. Structure of graphite by neutron diffraction. *Nature* **258**, 136–137 (1975).
- Krishnamoorthy, K., Veerapandian, M., Yun, K. & Kim, S. J. The chemical and structural analysis of graphene oxide with different degrees of oxidation. *Carbon* **53**, 38–49 (2013).
- He, H., Riedl, T., Lerf, A. & Klinowski, J. Solid-state NMR Studies of the structure of graphite oxide. *J. Phys. Chem.* **100**, 19954–19958 (1996).
- Lerf, A., He, H., Forster, M. & Klinowski, J. Structure of graphite oxide revisited. *J. Phys. Chem. B* **102**, 4477–4482 (1998).
- Chua, C. K. & Pumera, M. Chemical reduction of graphene oxide: a synthetic chemistry viewpoint. *Chem. Soc. Rev.* **43**, 291–312 (2014).
- Wong, C., Lai, C., Lee, K. & Hamid, S. Advanced chemical reduction of reduced graphene oxide and its photocatalytic activity in degrading reactive black 5. *Materials* **8**, 5363 (2015).
- Mungse, H.P., Sharma, O.P., Sugimura, H. & Khatri, O.P. Hydrothermal deoxygenation of graphene oxide in sub- and supercritical water. *RSC Advances* **4**, 22589–22595 (2014).
- Kim, M. C., Hwang, G. S. & Ruoff, R. S. Epoxide reduction with hydrazine on graphene: A first principles study. *J. Chem. Phys.* **131**, 064704 (2009).
- Gao, X., Jang, J. & Nagase, S. Hydrazine and thermal reduction of graphene oxide: reaction mechanisms, product structures, and reaction design. *J. Phys. Chem. C* **114**, 832–842 (2010).
- Ma, C., Chen, Z., Fang, M. & Lu, H. Controlled synthesis of graphene sheets with tunable sizes by hydrothermal cutting. *J. Nanopart. Res.* **14**, 996 (2012).
- Lucchese, M. M. *et al.* Quantifying ion-induced defects and Raman relaxation length in graphene. *Carbon* **48**, 1592–1597 (2010).
- Tuinstra, F. & Koenig, J. L. Raman spectrum of graphite. *J. Chem. Phys.* **53**, 1126–1130 (1970).
- Dimiev, A. M. & Eigler, S. Characterization techniques. In *Graphene oxide: fundamentals and applications* 85 (John Wiley & Sons, Ltd, 2016).
- Sadewasser, S. & Glatzel, T. Kelvin probe force microscopy: measuring and compensating electrostatic forces 7–24 (Springer-Verlag Berlin Heidelberg, 2011).
- Wells, R. L. & Fort, T. Interaction of oxygen with clean aluminum surfaces by measurement of work function changes. *Surf. Sci.* **33**, 172–178 (1972).
- Mishra, M., Joshi, R. K., Ojha, S., Kanjilal, D. & Mohanty, T. Role of oxygen in the work function modification at various stages of chemically synthesized graphene. *J. Phys. Chem. C* **117**, 19746–19750 (2013).
- Huber, E. E. & Kirk, C. T. Work function changes due to the chemisorption of water and oxygen on aluminum. *Surf. Sci.* **5**, 447–465 (1966).
- Kumar, P. V., Bernardi, M. & Grossman, J. C. The impact of functionalization on the stability, work function, and photoluminescence of reduced graphene oxide. *ACS Nano* **7**, 1638–1645 (2013).
- Amy, F., Chan, C. & Kahn, A. Polarization at the gold/pentacene interface. *Org. Electron.* **6**, 85–91 (2005).
- Joshi, R. K. *et al.* Precise and Ultrafast Molecular Sieving Through Graphene Oxide Membranes. *Science* **343**(6172), 752–754 (2014).
- Nair, R. R., Wu, H. A., Jayaram, P. N., Grigorieva, I. V. & Geim, A. K. Unimpeded permeation of water through helium-leak-tight graphene-based membranes. *Science* **335**, 442–444 (2012).

Author Contributions

M.Y. led the research study. H.-H.H. prepared the manuscript and characterized the samples. K.K.H.D.S. measured the adsorption property of the sample. G.R.A.K. assisted on synthesis of the GO and rGO. All authors discussed the results and commented on the manuscript.

Additional Information

Supplementary information accompanies this paper at <https://doi.org/10.1038/s41598-018-25194-1>.

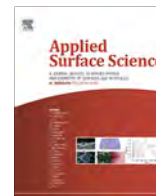
Competing Interests: The authors declare no competing interests.

Publisher's note: Springer Nature remains neutral with regard to jurisdictional claims in published maps and institutional affiliations.



Open Access This article is licensed under a Creative Commons Attribution 4.0 International License, which permits use, sharing, adaptation, distribution and reproduction in any medium or format, as long as you give appropriate credit to the original author(s) and the source, provide a link to the Creative Commons license, and indicate if changes were made. The images or other third party material in this article are included in the article's Creative Commons license, unless indicated otherwise in a credit line to the material. If material is not included in the article's Creative Commons license and your intended use is not permitted by statutory regulation or exceeds the permitted use, you will need to obtain permission directly from the copyright holder. To view a copy of this license, visit <http://creativecommons.org/licenses/by/4.0/>.

© The Author(s) 2018



Full Length Article

Progress of reduction of graphene oxide by ascorbic acid

K. Kanishka H. De Silva*, Hsin-Hui Huang, Masamichi Yoshimura

Surface Science Laboratory, Toyota Technological Institute, Nagoya 468-8511, Japan



ARTICLE INFO

Article history:

Received 6 September 2017

Revised 26 March 2018

Accepted 31 March 2018

Available online 1 April 2018

Keywords:

Natural graphite

Graphene oxide

Reduced graphene oxide

Ascorbic acid

ABSTRACT

Graphene oxide (GO) and reduced graphene oxide (RGO) are in greater demand in many research fields. As a result, the synthesis of these materials on a large scale in a cost-effective manner is more concerned for numerous applications. In the present work, GO was synthesized by oxidizing natural graphite and reduced by ascorbic acid (AA), which is a green reductant. The reduced products obtained at different time periods were in detail characterized by UV–Visible spectroscopy, X-ray diffraction (XRD), X-ray photoelectron spectroscopy (XPS), attenuated total reflectance Fourier transform infrared (ATR–FT–IR) spectroscopy, Raman spectroscopy, thermogravimetric analysis (TGA), atomic force microscopy (AFM) and scanning electron microscopy (SEM). Results showed that the oxidation of graphite has given highly oxidized GO with a 9.30 Å interlayer space and about 33% of oxygen atomic percentage. Until 50 min of the reduction, both GO and RGO coexist. The reduction rate is fast within the first 30 min. In addition, the suitability of natural graphite over synthetic graphite for the synthesis of GO is shown. The findings of this work pave the way to select GO and RGO for applications of interest in a cheap, green and efficient manner.

© 2018 Elsevier B.V. All rights reserved.

1. Introduction

It has been over 150 years since the British Chemist B.C. Brodie discovered a highly oxidized form of natural graphite, named “graphon” [1] which is currently known as “graphite oxide” or “graphene oxide”. However, it has been re-emerged as a material of interest after the groundbreaking discovery of graphene and its diverse methods of synthesis [2]. Later on, many researchers have performed various methods to synthesize graphite oxide from either natural or synthetic graphite. The term GO is interchangeably used to abbreviate both graphite oxide and graphene oxide. Graphite oxide can be considered as a highly oxidized form of graphite with a higher inter-layer spacing due to the presence of a large number of oxygen functionalities. On the other hand, graphene oxide is the exfoliated form of graphite oxide, consisting of one, two or few layers [3]. The GO is a non-stoichiometric macro-molecule having controlled physical and chemical properties depending on the synthetic variables such as graphite precursor, type of the oxidant and the dose, stirring or sonication strength, oxidation temperature and duration [4,5]. The most acceptable structural model proposed for GO is Lerf-Klinowski model in which, basal planes of GO are decorated by hydroxyl

and epoxide groups, whereas the edges are mainly occupied by carboxyl and carbonyl groups in a random manner resulting in mixed sp^2 - sp^3 carbon containing sheets [6,7]. Up to date, many methods have been developed to synthesize GO among which Hummers’ method [8] and its modified approaches are well known. However, most of these methods have used synthetic graphite or pre-oxidized and purified of graphite [9,10]. Use of natural graphite over synthetic graphite possesses both advantages and disadvantages. Synthetic graphite can be produced in purest grades compared to natural graphite yet, the process of making synthetic graphite is costly and much energy consuming [9]. Nevertheless, it is worthy to mention that natural graphite in Sri Lanka is famous for being highly crystalline and pure in the range of 95–99% of carbon [11,12]. As a result, Sri Lankan natural graphite can be used as the graphite source to synthesize GO without any purification step in a cost-effective manner [13].

Apart from being electrically insulating, GO itself has remarkable properties such as high chemical reactivity and hydrophilicity due to more sp^3 domains accompanied by high oxygen content, and hence GO is widely applied as an outstanding material in many fields including industrial and medicinal [14,15]. However, the application of GO to produce graphene in large scale is the fieriest area in the carbon-based research field. Reduction of GO involves not only the removal of oxygen functionalities and other atomic-scale lattice defects but also the recovery or repair of the conjugated graphitic network [16,17]. Currently, numerous methods

* Corresponding author.

E-mail addresses: sd16501@toyota-ti.ac.jp (K. Kanishka H. De Silva), h.h.huang@toyota-ti.ac.jp (H.-H. Huang), yoshi@toyota-ti.ac.jp (M. Yoshimura).

have been developed to prepare graphene from GO having various properties which in turn affects the final performance of the material [18]. Among all, chemical reduction of GO to synthesize graphene (or more precisely RGO) is known to be a relatively simple, cheap and rapid path which gives high yields of product along with controllable properties. The RGO also has many applications, such as in sensors [19], electrode materials [20], catalysis [21] and water remediation [22,23] where in some cases pristine graphene is not applicable directly.

Finding a suitable reducing agent that can be used to synthesize RGO resembling pristine graphene to a larger extent in terms of physical and chemical properties is of great importance. Stankovich et al. have reduced GO with several reductants and their study found that hydrazine hydrate ($\text{N}_2\text{H}_4 \cdot \text{H}_2\text{O}$) is the best in producing thin RGO sheets with good electrical conductivity [24]. Since then, the use of hydrazine as the reducing agent for RGO synthesis has been extended. However, due to the toxic nature of hydrazine to the environment as well as to the living organisms, the “green reduction” approach was introduced to the field [25]. During the last decade, a number of such alternatives such as organic acids [26–28], plant extracts [14,29,30], amino acids [31], microorganisms [32,33], sugars [34], antioxidants [35], etc. have been originated. Among all these, the first known environmentally friendly reducing agent for GO has been recognized as ascorbic acid (AA), which is confirmed to be the best alternative to toxic hydrazine and currently being studied [26]. Hitherto many works based on AA assisted reduction has been performed, and proven that AA is an outstanding alternative reductant to hydrazine in terms of characteristic properties of RGO obtained and for large-scale synthesis for many applications. Additionally, the physical properties such as electrical conductivity of AA-reduced GO has confirmed to be higher or similar to that obtained from hydrazine-reduced GO [36]. On the other hand, some previous studies have shown that GO reduced by AA is suitable for various applications including sensors [19], dye-sensitized solar cells [37], and flexible graphene fibers [38]. Removal of oxygen functional groups by AA is relatively easy as a small amount of AA could perform the reduction in a short time resulting in a product with high C/O ratio as 12 [39]. In some applications, the presence of these functionalities is advantageous and hence, the control of the degree of reduction would be a key point in this regard [40].

In the present work, we aimed to provide a comprehensive analysis of properties of RGO reduced by AA for a limited period of time. The graphite source used in this study is natural graphite from Sri Lanka, hark back the pioneer work done by Brodie who has used Sri Lankan natural graphite inventing GO [1]. However, in this work, oxidation was performed by modified Hummers' method and the reduction was performed using AA.

2. Experimental

2.1. Materials

Natural graphite ($\sim 125 \mu\text{m}$) from Bogala mines - Sri Lanka, sulphuric acid (H_2SO_4 - 98%) from Wako, potassium permanganate (KMnO_4 - 99%) from Nacalai tesque, hydrogen peroxide (H_2O_2 - 34%), NH_3 solution (28%) and hydrochloric acid (HCl - 36%) from Chameleon reagent, ascorbic acid ($\text{C}_6\text{H}_8\text{O}_6$) from Iwaki chemicals and Synthetic graphite ($>20 \mu\text{m}$) from Sigma Aldrich.

2.2. Synthesis of graphene oxide and reduced graphene oxide

Graphene oxide was synthesized by a modified version of Hummers' method reported elsewhere with few variations [41]. A suspension of GO (0.1 mg/ml) was prepared by sonicating dried GO in

distilled water. To its 100 ml, 100 mg of ascorbic acid was added. The pH of the medium was adjusted to ~ 10 by adding NH_3 solution to promote colloidal stability through the electrostatic repulsion [39]. The mixture was allowed to stir at 65°C and samples were withdrawn at 10 minutes' intervals until 1 h (here onwards denoted as RGO1, RGO2, RGO3, RGO4, RGO5, and RGO6). The resulting suspensions were filtered through cellulose acetate membrane filter papers with a pore size of $0.20 \mu\text{m}$, washed with copious of distilled water and dried at 50°C in a vacuum oven. In addition, GO was synthesized by synthetic graphite following the same procedure and the details of characterization are shown in the [supplementary document](#).

2.3. Material characterization

The crystalline properties were determined by an X-ray diffractometer (XRD - Rigaku-Ultima IV X-ray Diffractometer) operated at 40 kV and 200 mA with $\text{Cu-K}\alpha 1$ radiation at a step size of 0.02° and a step time of 1.0 s from 5° to 90° (for graphite 50 mA current was used due to the higher crystallinity). The progress of reduction as a function of time was monitored via ultraviolet-visible (UV-vis) absorption spectra using a UV-vis spectrometer (Jasco, V-650). Surface composition of the samples was determined by X-ray photoelectron spectroscopy (XPS, ULVAC-PHI 5000) with a monochromatic $\text{Al-K}\alpha$ X-ray source and the functional group analysis was done by attenuated total reflectance Fourier transform infra-red spectroscopy (ATR-FT-IR, Jasco, FT/IR-6200). The morphological characterization was done by atomic force microscopy (AFM - Bruker Nanoscope Multimode 8) and scanning electron microscopy (SEM - Hitachi SU-3500). To monitor the structural changes such as the degree of defects, Raman spectroscopy was conducted (Renishaw - InVia Raman Spectroscopy) using a 532 nm laser. Thermogravimetric analysis (TGA) was done under air flow at a heating rate of $5^\circ\text{C}/\text{min}$ (for graphite $10^\circ\text{C}/\text{min}$), using Pt crucibles (Shimadzu TA-60WS/DTG-60H). All the samples were vacuum dried before subjecting to characterization.

3. Results and discussion

The progress of reduction was monitored by UV-vis spectroscopy. The typical maximum absorption peak (λ_{max}) ascribed to GO was observed at 230 nm, due to π - π^* transitions from $\text{C}=\text{C}$ double bonds, which is typical for GO. In addition to that, a shoulder peak at 300 nm, which is associated with n - π^* transitions from $\text{C}=\text{O}$ was obtained [42] (see Fig. 1A). With the increase of reduction time, the red-shift of the λ_{max} peak and the disappearance of the shoulder peak was observed, which indicates the restoration of double bond conjugation in RGO sheets and the simultaneous removal of oxygen functionalities respectively [26]. Fig. 1B shows the peak shift with the increase of reduction time. The rate of red-shifting of the peak is high until about 30 min of reduction and slow forth giving a maximum absorption at 263 nm for RGO6. AA itself has a λ_{max} value of 266 nm in aqueous media [43] and hence, the removal of excess AA before UV-vis measurements is vital. Therefore, each sample, before UV-vis measurements, was washed with excess distilled water. The results clearly show a gradual shifting of the peak from 230 nm to 263 nm with time.

Fig. 2 shows XRD patterns for raw graphite, GO and RGO synthesized at different times. The intense graphitic peak positioned at 26.6° with an interlayer spacing of 3.35 \AA has blue-shifted to 9.50° upon oxidation resulting in an interlayer spacing of 9.30 \AA due to the intercalation of oxygen functional groups (such as epoxy and hydroxyl), especially on the basal planes of either side of the GO sheets. This peak is not sharp as the main peak in graphite,

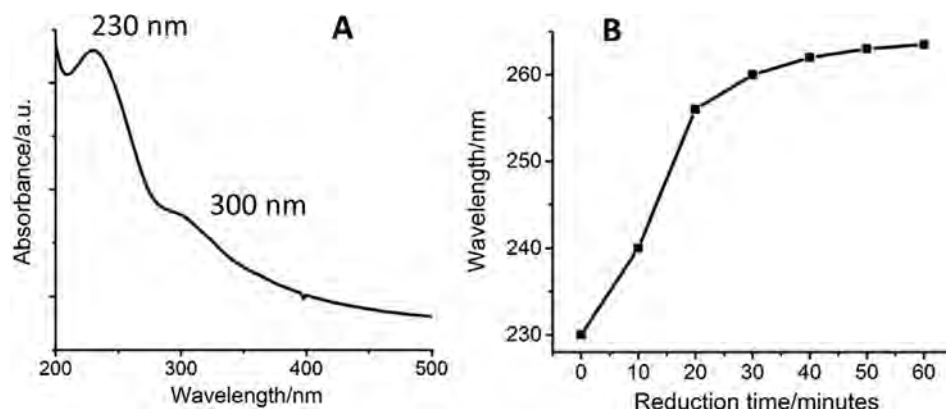


Fig. 1. UV-vis spectrum of GO (A) and C=C peak shifting of RGO synthesized at different times (B).

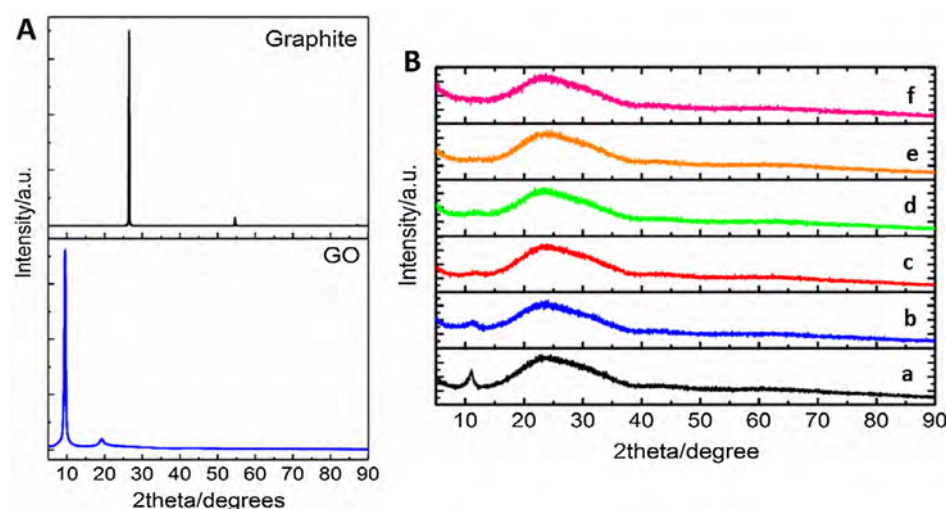


Fig. 2. XRD patterns of graphite and GO (A) and RGO synthesized at different times (B), RGO1-6 (a-f).

caused by the deterioration of the crystal structure. The position of the GO peak mainly depends on the degree of oxidation of graphite. Higher inter-layer spacing for GO indicates higher order of oxidation and exfoliation [41]. With increase time of reduction, the up-shifting of the GO peak simultaneously giving a broad peak centering at about 25.0° can be observed clearly due to the removal of the oxygen functionalities and the consequent restoration of the C=C bonds (Table 1). From RGO1-RGO4, both GO and RGO peaks coexist resulting in mixtures of GO and RGO with different interlayer spacing and finally giving an average value of 3.58 \AA for the broad RGO peak. A possible reason for this peak broadening could be the lack of long-range order of RGO sheets and the presence of residual oxygen functionalities.

SEM images in Fig. 3 show the morphological changes of graphite, GO and RGO that have been taken place during the oxidation and reduction processes, which further clarified the results obtained by XRD. Graphite (Fig. 3A and B) shows well developed

layered structure with sharp edges. On the other hand, GO (Fig. 3C and D) shows re-stacked exfoliated sheets with wavy edges. The stacking nature of GO has occurred after drying [52]. This layered nature present in GO has been disappeared with the increase in time of reduction (Fig. 3E and F). It can also be observed that the sheets have torn resulting in veil-like sheets with scrolling edges but well-exfoliated morphology and more porous nature [14]. The reduction accompanied by vigorous stirring may have caused the increase in porous nature in RGO with time. The broad peak for RGO obtained in XRD is as a result of the disordered sacking of RGO sheets as can be seen in the SEM images.

Changes of functional groups in GO and RGOs were studied by FT-IR and XPS. Fig. S4 shows the ATR-FT-IR spectra of GO and RGO. According to FT-IR spectra, GO shows a broad peak centered at 3400 cm^{-1} attributed to O-H vibration in hydrogen bonded hydroxyl groups and adsorbed water molecules, a peak at 2925 cm^{-1} assigned to asymmetric vibrations of $-\text{CH}_2$ groups, a peak

Table 1
Peak assignment for graphite, GO and RGO.

Sample	Graphite	GO	RGO1	RGO2	RGO3	RGO4	RGO5	RGO6
$2\theta/^\circ$	26.56	9.50	10.97	11.52	11.72	13.30	24.86	24.86
$d/\text{\AA}$	3.35	9.30	8.06	7.68	7.55	6.70	3.58	3.58
			3.73	3.68	3.58	3.58		

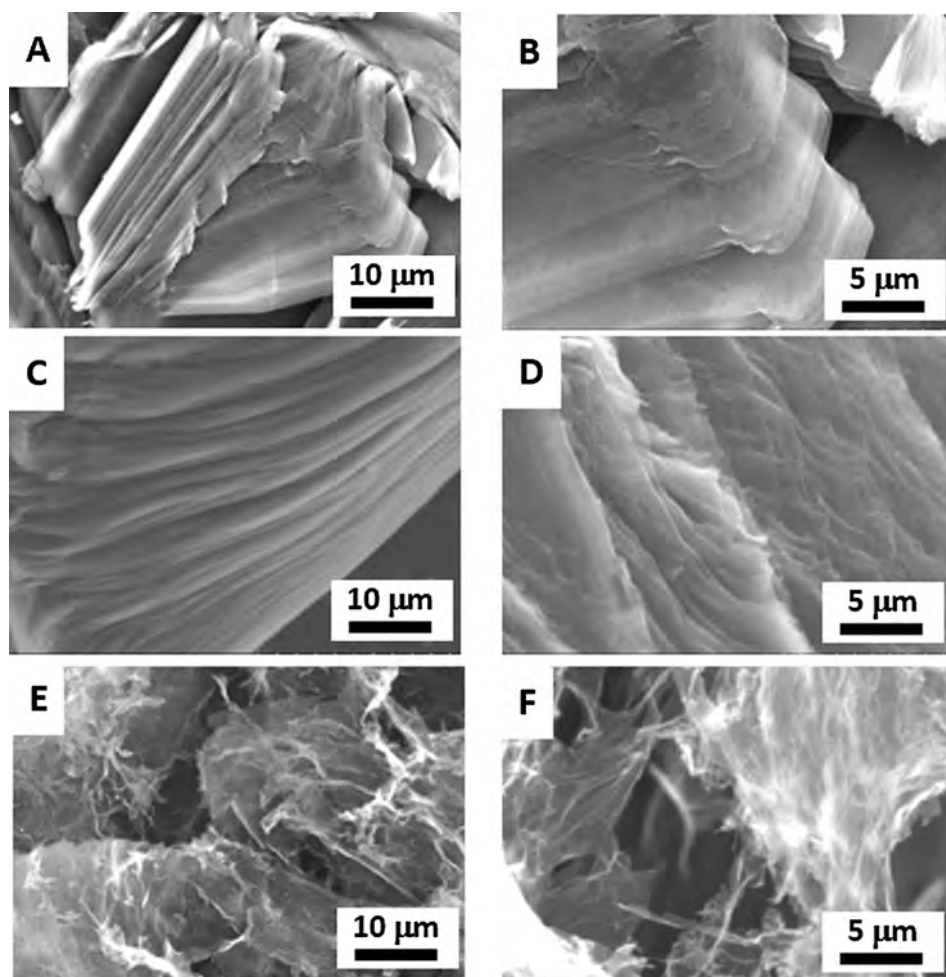


Fig. 3. SEM images of graphite (A, B), GO (C, D) and RGO6 (E, F).

for C=O stretching at 1718 cm^{-1} , two peaks at 1200 cm^{-1} and 1050 cm^{-1} for C–O stretching, an O–H deformation peak at 1400 cm^{-1} , and at 1632 cm^{-1} a peak assigned for C=C stretching. After 30 min of reduction (RGO3), the intensity of most of the oxygen functionalities has been diminished, but still traces of C=O groups could be observed. However, in RGO4 and RGO6 intensity of these peaks was observed to be further declined. This variation of oxygen functional groups was further analyzed by XPS. The oxygen content of samples is expressed as carbon to oxygen ratio (C/O) by analyzing XPS survey spectra. Natural graphite shows 98.3% of carbon and 1.7% of oxygen atomic percentage and no other elements could be detected. Upon oxidation of graphite, the atomic percentage of oxygen has increased up to 33% indicating a higher degree of oxidation of natural graphite flakes (Table 2). On the other hand, with the reduction, the atomic percentage of oxygen has gradually decreased resulting a value of 17.5% after 60-min of reduction which signifies that most of the oxygen functionalities have been removed, (Fig. S4 in supplementary) In order to determine how these oxygen functional groups would change during

reduction, deconvolution of the C1s core level spectra of GO and RGO samples was carried out (see Fig. 4). The GO shows four major peaks centered at 284.6, 286.5, 288.5 and 290 eV corresponding to sp^2/sp^3 carbon (C=C and C–C), C–O bond in epoxy/alkoxy/hydroxyl groups, carbonyl (C=O) and carboxyl (O–C=O) groups respectively [41,44]. The highest intensity shown by the C–O bonds attributes to epoxy and hydroxyl groups compared to other functional groups signifying that GO is mainly occupied by epoxy and hydroxyl groups upon oxidation, which are the dominant functionalities on the basal planes of GO sheets [14]. However, the intensity of C=O and COOH groups that are largely located at the sheet edges is much lower. Chemical reduction protocols, which are usually carried out from room temperature to moderate temperatures, do not eliminate the edge functionalities [45]. On the other hand, it has been shown by Gao et al. by using density functional theory (DFT) calculations that the hydroxyl and epoxy groups located at interior of aromatic domains of GO sheets are less stable than those located at the edges or defected domains and easily dissociate even at room temperature [46].

Table 2
C/O ratio variation of graphite, GO and RGO.

Sample ID		Graphite	GO	RGO1	RGO2	RGO3	RGO4	RGO5	RGO6
Atomic%	C1s	98.3	77.1	74.6	75.2	77.4	78.8	79.9	82.5
	O1s	1.7	32.9	25.4	24.8	22.6	21.2	20.1	17.5
C/O ratio		57.8	2.0	2.9	3.0	3.4	3.7	4.0	4.7

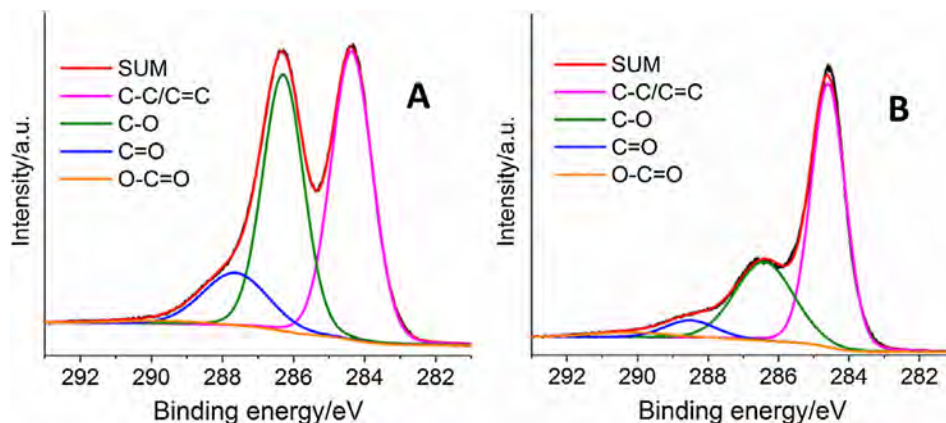


Fig. 4. XPS spectra of GO (A) and RGO after 60 min (B).

Fig. 5 shows the types of oxygen functionalities present in GO and RGO after reduction by AA. With the reduction, the intensity of the peaks responsible for oxygen functionalities in GO has been decreased (especially epoxy and hydroxyl groups). On the other hand, the intensity of the peak for C=C bond has increased in agreement with the results obtained from XRD, where the inter-layer space has declined due to the removal of oxygen functionalities and the restoration has been taken place. However, as represented in Fig. 6 the variation of these groups with reduction does not show a gradual variation. The peak at 284.6 eV is attributed to both C–C and C=C bonds. The fluctuation of these peaks could be due to the change in the individual component during the reduction. The first drop in the peak area% of C–O groups in RGO1 maybe due to the elimination of less stable hydroxyl and epoxy groups by AA which has carried out at a moderate temperature. The change in the peak area% is not gradual but decreased. Reduction of epoxy groups by AA, which is a ring opening reaction, results in C–OH moieties at an intermediate stage of the reduction mechanism and as mentioned earlier, these groups if present at the interior domains will be eliminated easily. Also, at 10 min reduction the peak area% of C=O group shows somewhat drastic drop and has decreased slowly at almost the same value.

Raman spectroscopy is a versatile tool for the structural characterization of carbon materials [47]. Graphite has a prominent peak at 1578 cm^{-1} (G-band) corresponding to sp^2 carbon domains, a

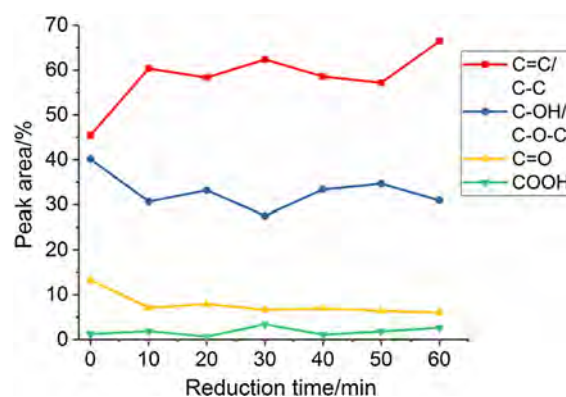


Fig. 6. Change in area percentage of functionalities of RGO with reduction time.

weak peak at 1345 cm^{-1} (D-band) corresponding to sp^3 carbons, structural defects or edge planes and another peak at 2713 cm^{-1} (G'-peak with two components) [48]. In GO, the G band has up-shifted to 1585 cm^{-1} and the D band has intensified due to the formation of oxygen functionalities, which corresponds to defect sites created in graphite during oxidation (see Fig. 7A). In addition to that, a flat G' region can be observed. The intensity ratio of D and

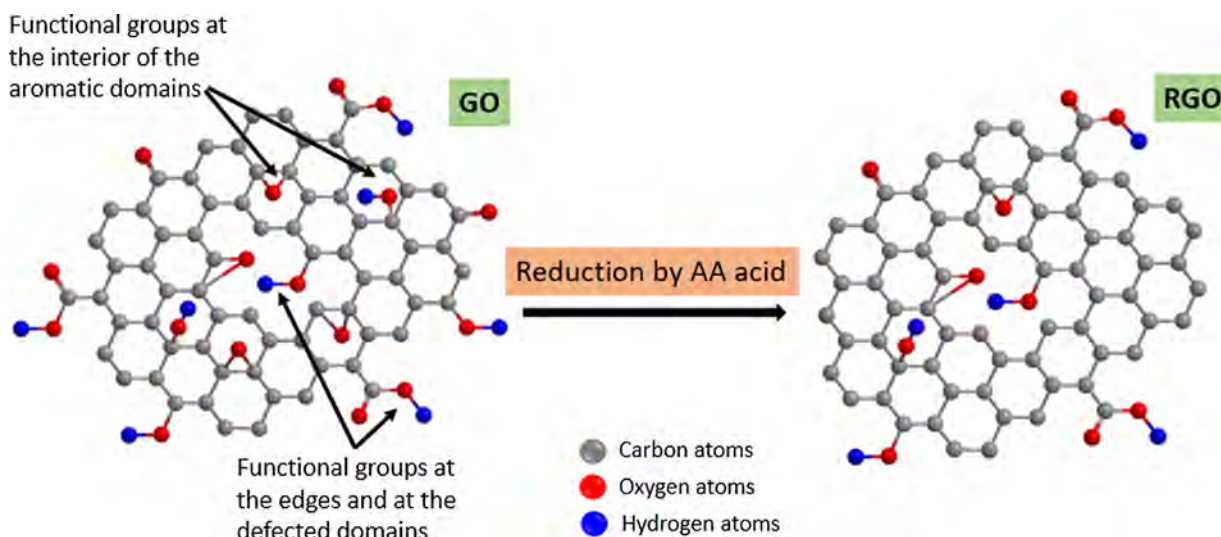


Fig. 5. Schematic representation of the oxygen functionalities presents in GO and RGO.

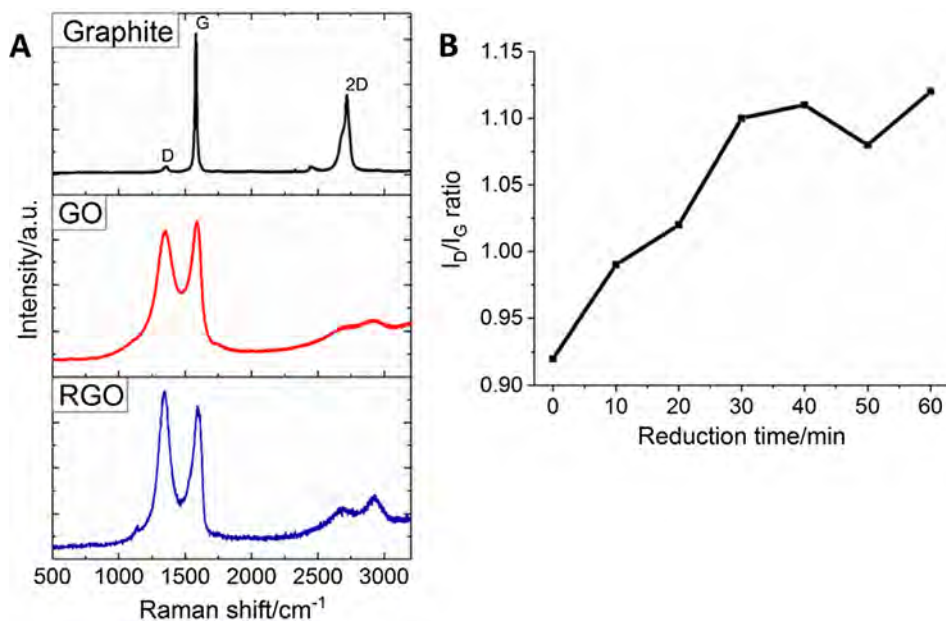


Fig. 7. Raman spectra of graphite, GO and RGO6 (A) and the variation of I_D/I_G ratio with the reduction time (B).

G bands (I_D/I_G) is an estimation of the level of disorder in the graphitic structure. This ratio has increased from 0.92 (for GO) to 1.12 (for RGO6) upon reduction and the peaks have become sharper. It could be due to the formation of smaller sized sp^2 domains/RGO in larger quantities or the increased fraction of graphene edges [49]. However, the D peak is sharper in RGO6 compared to GO as a result of the removal of amorphous moieties during reduction. Also, in RGO6, at the G' region, a less intense additional peak observed at around 2925 cm^{-1} which is denoted as the D+G mode. This is a

defect activated band and will present only when there are sufficient defects [50]. Fig. 7B shows the variation of the Raman I_D/I_G ratio with the increase in time of reduction. Except for the slight drop in the ratio in RGO5, overall the value has increased with the increase in time of reduction. As shown in TGA plots in Fig. 8, graphite is stable up to $650\text{ }^\circ\text{C}$. On the other hand, GO shows a stepwise weight loss. First is about 10% of loss below $100\text{ }^\circ\text{C}$ attributed to the removal of adsorbed water. The most significant weight loss has occurred at about $200\text{ }^\circ\text{C}$ due to the decomposition

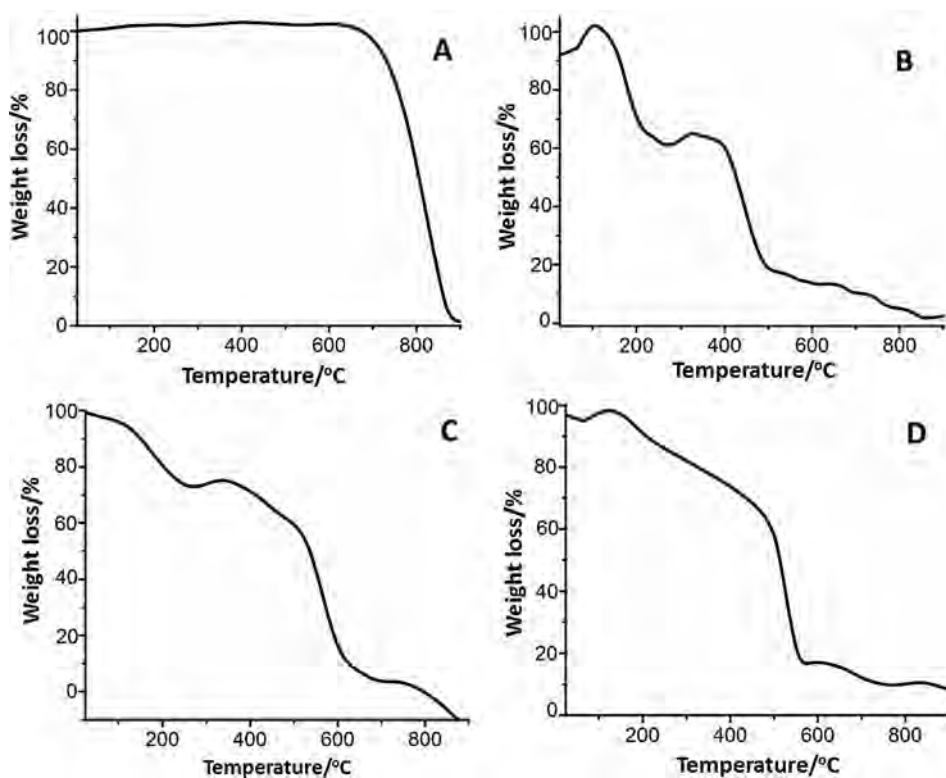


Fig. 8. TGA plots of graphite (A), GO (B), RGO at 40 min (C) and RGO at 60 min (D).

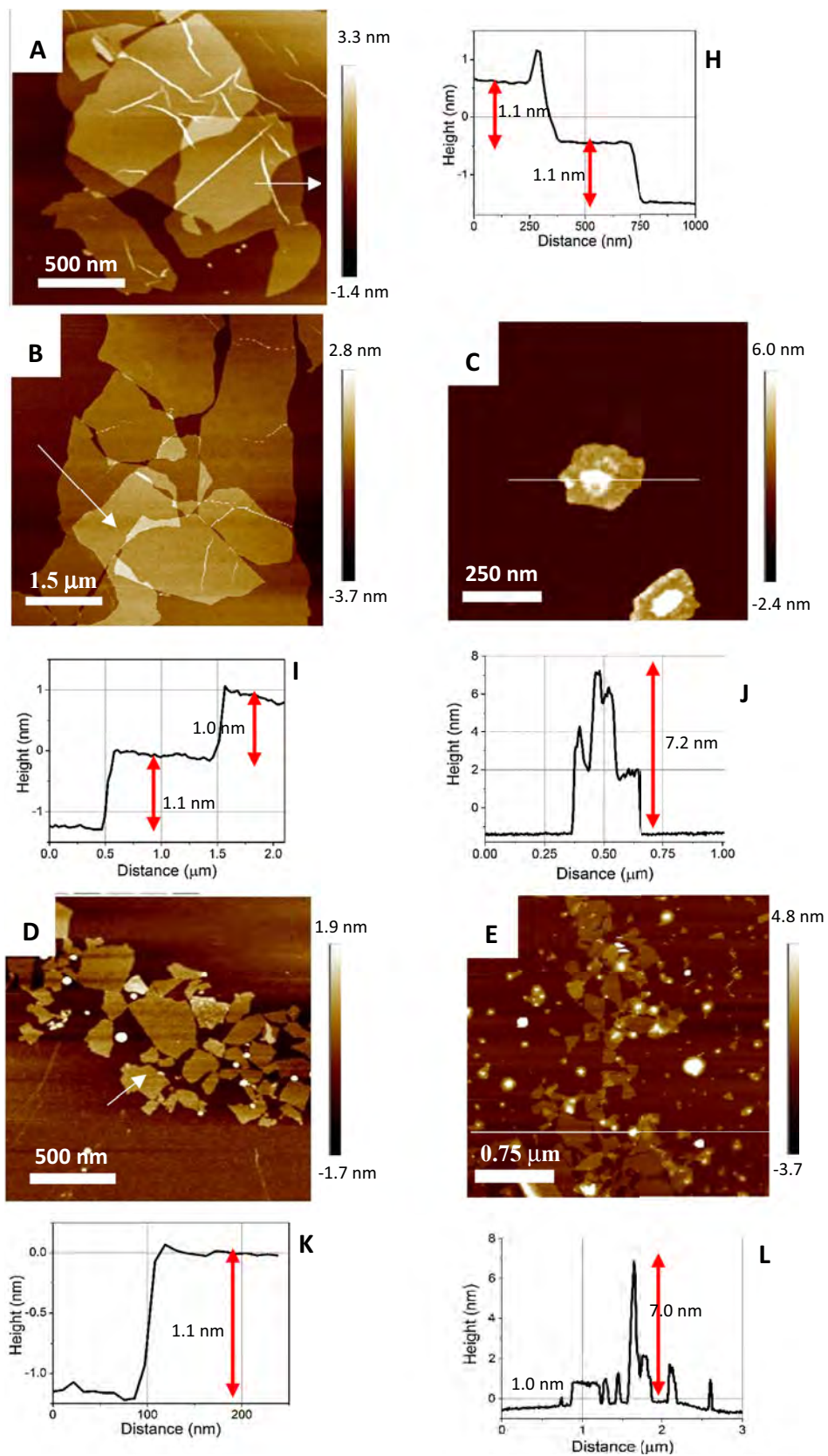


Fig. 9. AFM images of GO (A), RGO1 (B, C), RGO4 (D, E) and RGO6 (F, G) and their corresponding height profiles (H–N).

of the most labile oxygen functional groups. Another drop can be observed at around 500 °C for the decomposition of stable oxygen functionalities and finally a steady drop above 500 °C attributed to

the decomposition of the carbon skeleton in GO. In the plot of RGO4 (Fig. 8C), same step-wise weight loss as in GO can be observed but the steepness of the steps has been declined due to

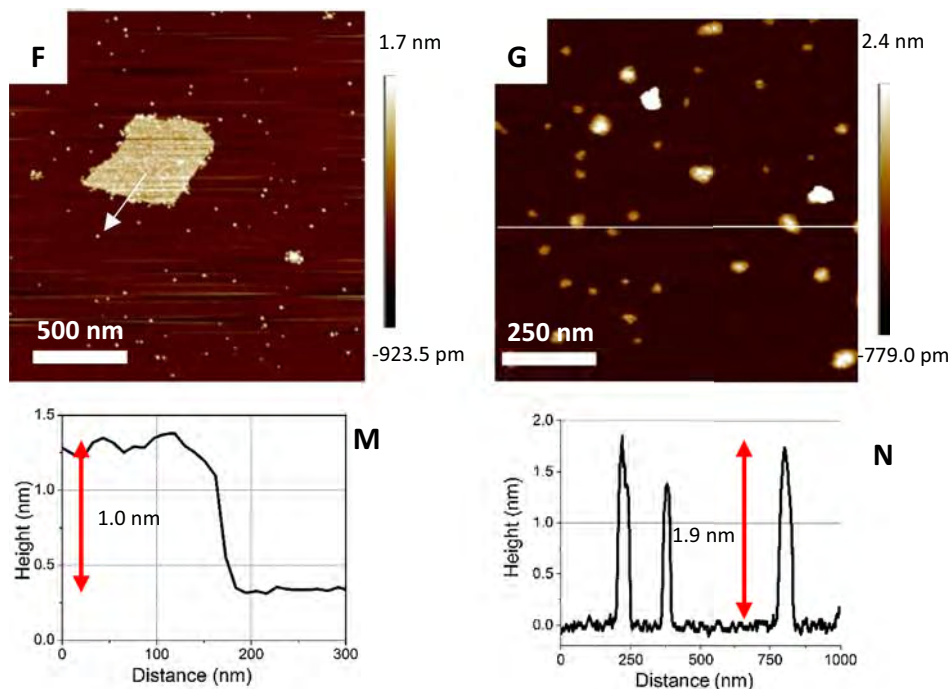


Fig. 9 (continued)

the prior removal of oxygen functionalities during the chemical reduction, especially the less stable hydroxyl and epoxy groups as shown in the XPS results. The plot for RGO6 (Fig. 8D) confirms the results obtained from XPS indicating the presence of residual oxygen functionalities.

AFM is typically used to characterize the sheet thickness and surface topography of GO and RGO. Fig. 9 shows the change in topography and thickness during reduction of GO measured by peak-force tapping mode. For AFM analysis, the samples were prepared by dispersing dry GO and RGOs in water by sonication. Large amount of oxygen functionalities formed during the oxidation make hydrogen bonds with water permitting easy dispersibility of GO and give highly exfoliated GO sheets. In contrast, the dispersibility of RGO becomes difficult with the increase in time of reduction due to the removal of oxygen functional groups. As a result, longer times of sonication is necessary. The GO and RGO suspensions were drop-casted on a freshly cleaved mica and air dried before taking measurements. The thickness of a single layer of GO is about 1 nm (Fig. 9A), which is consistent with the data reported in the literature [26]. Also, the flakes show a wide range of lateral size distribution (3–10 μm) with smooth surfaces with some wrinkles. These wrinkles or folding may have been formed upon drying of GO on the substrate after deposition [51]. With the increase in reduction time, GO sheets have been torn apart and small crumpled structures could be observed. In the AFM image of RGO1, sheets with smooth surfaces resembling GO with a thickness of ~ 1 nm, and a few crumpled RGO structures with a large height of ~ 7 nm and a smaller lateral size (~ 250 nm) were observed (Fig. 9C). The latter structures are crumpled RGO sheets, appearing as bright spots due to the large height. Even though the majority of the basal plane functionalities has been eliminated (the first drastic drop of the oxygen content in GO seen in XPS results), the remaining edge functionalities can make physical interactions such as hydrogen bonding, among each other resulting in aggregated structures. AFM images of RGO4 show (Fig. 9D and E) that both GO and RGO sheets and small crumpled RGO structures coexist in this partially reduced product. Though the GO and RGO sheets have the same height of ~ 1 nm, the topography shows a dif-

ference; GO sheets are smoother whereas the RGO sheets look rough. This rough nature may have arisen as a result of the removal of functional groups present on the basal plane. After 60 min of reduction, complete absence of GO like sheets but sheets with a rough topography can be observed. However, the thickness of a single RGO sheet is also about 1 nm, though theoretically, it should be lower than that. In addition to that, many small crumpled structures were observed with a height of ~ 2 nm (Fig. 9G). The smaller sheet size for RGO may be caused during the reduction process and also due to the sonication treatment carried out in order to disperse RGO in water for AFM analysis.

4. Conclusion

The progress of reduction of GO by ascorbic acid was performed by controlling the reduction time for 1 h. GO was synthesized by natural graphite, without any purification or pre-oxidation step, following a recently proposed method with few modifications. Reduction of GO was done by ascorbic acid, which is the first known and the most efficient green reductant to date. Results showed that graphite has been successfully oxidized to highly oxygenated and exfoliated GO sheets. Reduction of GO was monitored in 10 minutes' intervals up to 1 h to study how the structural and morphological changes would take place. Though XRD results display a complete removal of the GO peak by 50 min, other characterization techniques indicated the presence of residual oxygen functionalities. XPS results show that the decline of oxygen atomic percentage is mainly due to the removal of hydroxyl and epoxy groups located at the basal planes of GO sheets and to a small extent due to edge carbonyl groups. AFM characterization indicated that at the intermediate stages of reduction, both GO and RGO coexist in the material as confirmed by XRD results (peaks for both GO and RGO coexist from RGO1–RGO4). This tunable layer spacing and oxygen functionalities would determine the point of application of RGO reduced at different degrees such as in water purification. Also, the degree of oxidation of high purity grade Sri Lankan natural graphite and synthetic graphite was determined.

As a whole, this work has opened a much cheaper and scalable way of synthesizing graphene oxide with good qualities from natural graphite along with a green and controllable way of synthesizing reduced graphene oxide from ascorbic acid.

Acknowledgement

Many thanks goes to Dr. G. R. A. Kumara (National Institute of Fundamental Studies, Sri Lanka) for supplying natural graphite samples.

Appendix A. Supplementary material

Supplementary data associated with this article can be found, in the online version, at <https://doi.org/10.1016/j.apsusc.2018.03.243>.

References

- [1] B.C. Brodie, On the atomic weight of graphite, *Philos. Trans. R. Soc. London*. 149 (1859) 249–259.
- [2] K.S. Novoselov, A.K. Geim, S.V. Morozov, D. Jiang, Y. Zhang, S.V. Dubonos, I.V. Grigorieva, A.A. Firsov, Electric field effect in atomically thin carbon films, *Science* 306 (2004) 666–669.
- [3] C.K. Chua, M. Pumera, Chemical reduction of graphene oxide: a synthetic chemistry viewpoint, *Chem. Soc. Rev.* 43 (2014) 291–312.
- [4] W. Gao, The chemistry of graphene oxide, in: *Graphene oxide reduct. Recipes, Spectrosc. Appl.* (2015) 61–95.
- [5] J.H. Kang, T. Kim, J. Choi, J. Park, Y.S. Kim, M.S. Chang, H. Jung, K.T. Park, S.J. Yang, C.R. Park, Hidden second oxidation step of hummers method, *Chem. Mater.* 28 (2016) 756–764.
- [6] P. Sun, Y. Wang, H. Liu, K. Wang, D. Wu, Z. Xu, H. Zhu, Structure evolution of graphene oxide during thermally driven phase transformation: is the oxygen content really preserved?, *PLoS One* 9 (2014) 1–8.
- [7] A. Lerf, H. He, M. Forster, J. Klinowski, Structure of graphite oxide revisited, *J. Phys. Chem. B*. 102 (1998) 4477–4482.
- [8] W.S. Hummers, R.E. Offeman, Preparation of graphitic oxide, *J. Am. Chem. Soc.* 80 (1958) 1339.
- [9] C. Botas, P. Álvarez, C. Blanco, R. Santamaría, M. Granda, P. Ares, F. Rodríguez-Reinoso, R. Menéndez, The effect of the parent graphite on the structure of graphene oxide, *Carbon N. Y.* 50 (2012) 275–282.
- [10] C. Xu, X. Shi, A. Ji, L. Shi, C. Zhou, Y. Cui, Fabrication and characteristics of reduced graphene oxide produced with different green reductants, *PLoS One*. 10 (2015) 1–15.
- [11] H.P.T.S. Hewathilake, N.W.B. Balasooriya, H.M.T.G.A. Pitawala, H.W.M.A.C. Wijayasinghe, Use of crystal morphologies to unravel the origin of vein graphite in Sri Lanka, *J. Geol. Soc. Sri Lanka* 17 (2015) 65–73.
- [12] N.P. Wijayananda, The Graphite Industry in Sri Lanka, Natural Resources Energy & Science Authority, Sri Lanka, 1987.
- [13] R.M.N.M. Rathnayake, H.W.M.A.C. Wijayasinghe, H.M.T.G.A. Pitawala, M. Yoshimura, H.H. Huang, Synthesis of graphene oxide and reduced graphene oxide by needle plate natural vein graphite, *Appl. Surf. Sci.* 393 (2017) 309–315.
- [14] K. Muthoosamy, R. Geetha Bai, I.B. Abubakar, S.M. Sudheer, H.N. Lim, H.S. Loh, N.M. Huang, C.H. Chia, S. Manickam, Exceedingly biocompatible and thin-layered reduced graphene oxide nanosheets using an eco-friendly mushroom extract strategy, *Int. J. Nanomed.* 10 (2015) 1505–1519.
- [15] S.C. Ray, S.C. Ray, Chapter 2 – Application and Uses of Graphene Oxide and Reduced Graphene Oxide, in: *Appl. Graphene Graphene-Oxide Based Nanomater*, 2015, pp. 39–55.
- [16] S. Eigler, M. Enzelberger-Heim, S. Grimm, P. Hofmann, W. Kroener, A. Geworski, C. Dotzer, M. Röckert, J. Xiao, C. Papp, O. Lytken, H.P. Steinrück, P. Müller, A. Hirsch, Wet chemical synthesis of graphene, *Adv. Mater.* 25 (2013) 3583–3587.
- [17] V. López, R.S. Sundaram, C. Gómez-Navarro, D. Olea, M. Burghard, J. Gómez-Herrero, F. Zamora, K. Kern, Chemical vapor deposition repair of graphene oxide: A route to highly-conductive graphene monolayers, *Adv. Mater.* 21 (2009) 4683–4686.
- [18] S. Pei, H.M. Cheng, The reduction of graphene oxide, *Carbon N. Y.* 50 (2012) 3210–3228.
- [19] V. Dua, S.P. Surwade, S. Ammu, S.R. Agnihotra, S. Jain, K.E. Roberts, S. Park, R.S. Ruoff, S.K. Manohar, All-organic vapor sensor using inkjet-printed reduced graphene oxide, *Angew. Chem. - Int. Ed.* 49 (2010) 2154–2157.
- [20] M.-H. Yeh, L.-Y. Lin, L.-Y. Chang, Y.-A. Leu, W.-Y. Cheng, J.-J. Lin, K.-C. Ho, Dye-sensitized solar cells with reduced graphene oxide as the counter electrode prepared by a green photothermal reduction process, *Chemphyschem.* 15 (2014) 1175–1181.
- [21] B. Garg, T. Bisht, Y.C. Ling, Graphene-based nanomaterials as heterogeneous acid catalysts: a comprehensive perspective, *Molecules* 19 (2014) 14582–14614.
- [22] T.H. Tight, Unimpeded permeation of water, *Science* 335 (2012) 442–444.
- [23] R.K. Joshi, S. Alwarappan, M. Yoshimura, V. Sahajwalla, Y. Nishina, Graphene oxide: the new membrane material, *Appl. Mater. Today* 1 (2015) 1–12.
- [24] S. Stankovich, D.A. Dikin, R.D. Piner, K.A. Kohlhaas, A. Kleinhammes, Y. Jia, Y. Wu, S.B.T. Nguyen, R.S. Ruoff, Synthesis of graphene-based nanosheets via chemical reduction of exfoliated graphite oxide, *Carbon* 45 (2007) 1558–1565.
- [25] J.I. Paredes, S. Villar-Rodil, M.J. Fernández-Merino, L. Guardia, a Martínez-Alonso, J.M.D. Tascon, Environmentally friendly approaches toward the mass production of processable graphene from graphite oxide, *J. Mater. Chem.* 21 (2011) 298–306.
- [26] J. Zhang, H. Yang, G. Shen, P. Cheng, J. Zhang, S. Guo, Reduction of graphene oxide via L-ascorbic acid, *Chem. Commun.* 46 (2010) 1112–1114.
- [27] W. Wan, Z. Zhao, H. Hu, Y. Gogotsi, J. Qiu, Highly controllable and green reduction of graphene oxide to flexible graphene film with high strength, *Mater. Res. Bull.* 48 (2013) 4797–4803.
- [28] Z. Bo, X. Shuai, S. Mao, H. Yang, J. Qian, J. Chen, J. Yan, K. Cen, Green preparation of reduced graphene oxide for sensing and energy storage applications, *Sci. Rep.* 4 (2014) 4684.
- [29] Y. Wang, Z.X. Shi, J. Yin, Facile synthesis of soluble graphene via a green reduction of graphene oxide in tea solution and its biocomposites, *ACS Appl. Mater. Interfaces.* 3 (2011) 1127–1133.
- [30] S. Thakur, N. Karak, Green reduction of graphene oxide by aqueous phytoextracts, *Carbon* 50 (2012) 5331–5339.
- [31] D. Chen, L. Li, L. Guo, An environment-friendly preparation of reduced graphene oxide nanosheets via amino acid, *Nanotechnology* 22 (2011) 325601.
- [32] G. Wang, F. Qian, C.W. Saltikov, Y. Jiao, Y. Li, Microbial reduction of graphene oxide by *Shewanella*, *Nano Res.* 4 (2011) 563–570.
- [33] P. Khanra, T. Kuila, N.H. Kim, S.H. Bae, D. Sheng Yu, J.H. Lee, Simultaneous bio-functionalization and reduction of graphene oxide by baker's yeast, *Chem. Eng. J.* 183 (2012) 526–533.
- [34] C. Zhu, S. Guo, Y. Fang, S. Dong, Reducing sugar: new functional molecules for the green synthesis of graphene nanosheets, *ACS Nano.* 4 (2010) 2429–2437.
- [35] A. Esfandiari, O. Akhavan, A. Irajizad, Melatonin as a powerful bio-antioxidant for reduction of graphene oxide, *J. Mater. Chem.* 21 (2011) 10907.
- [36] K.K.H. De Silva, H.-H. Huang, R.K. Joshi, M. Yoshimura, Chemical reduction of graphene oxide using green reductants, *Carbon N. Y.* 119 (2017) 190–199.
- [37] H. Ding, S. Zhang, J.-T. Chen, X.-P. Hu, Z.-F. Du, Y.-X. Qiu, D.-L. Zhao, Reduction of graphene oxide at room temperature with vitamin C for RGO-TiO₂ photoanodes in dye-sensitized solar cell, *Thin Solid Films* 584 (2015) 29–36.
- [38] J. Li, J. Li, L. Li, M. Yu, H. Ma, B. Zhang, Flexible graphene fibers prepared by chemical reduction-induced self-assembly, *J. Mater. Chem. A*. 2 (2014) 6359–6362.
- [39] M.J. Fernández-Merino, L. Guardia, J.I. Paredes, S. Villar-Rodil, P. Solís-Fernández, A. Martínez-Alonso, J.M.D. Tascón, Vitamin C is an ideal substitute for hydrazine in the reduction of graphene oxide suspensions, *J. Phys. Chem. C*. 114 (2010) 6426–6432.
- [40] L.A. Dobrzański, P.M. Vel Prokopowicz, K. Lukaszewicz, A. Drygała, M. Szindler, Graphene oxide film as semi-transparent counter electrode for dye-sensitized solar cell, *J. Achiev. Mater. Manuf. Eng.* 73 (2016) 13–20.
- [41] S. Abdolhosseinzadeh, H. Asgharzadeh, H. Seop Kim, Fast and fully-scalable synthesis of reduced graphene oxide, *Sci. Rep.* 5 (2015) 10160.
- [42] A. Abulizi, K. Okitsu, J.J. Zhu, Ultrasound assisted reduction of graphene oxide to graphene in l-ascorbic acid aqueous solutions: kinetics and effects of various factors on the rate of graphene formation, *Ultrason. Sonochem.* 21 (2014) 1174–1181.
- [43] M.B. Davies, J. Austin, D.A. Partridge, Vitamin C : Its Chemistry and Biochemistry, Royal Society of Chemistry, London, 1991.
- [44] Z. Sui, X. Zhang, Y. Lei, Y. Luo, Easy and green synthesis of reduced graphite oxide-based hydrogels, *Carbon* 49 (2011) 4314–4321.
- [45] R. Rozada, J.I. Paredes, M.J. Lopez, S. Villar-Rodil, I. Cabria, J.A. Alonso, A. Martínez-Alonso, J.M.D. Tascon, From graphene oxide to pristine graphene: revealing the inner working of the full structural restoration, *Nanoscale* 7 (2015) 2374–2390.
- [46] X. Gao, J. Jang, S. Nagase, Hydrazine and thermal reduction of graphene oxide: reduction mechanisms, product structures, and reaction design, *J. Phys. Chem.* 114 (2010) 832–842.
- [47] A.C. Ferrari, J. Robertson, Raman spectroscopy of amorphous, nanostructured, diamond-like carbon, and nanodiamond, *Philos. Trans. A. Math. Phys. Eng. Sci.* 362 (2004) 2477–2512.
- [48] A.C. Ferrari, J.C. Meyer, V. Scardaci, C. Casiraghi, M. Lazzeri, F. Mauri, S. Piscanec, D. Jiang, K.S. Novoselov, S. Roth, A.K. Geim, Raman spectrum of graphene and graphene layers, *Phys. Rev. Lett.* 97 (2006) 187401.
- [49] M. Fathy, A. Goma, F.A. Taher, M.M. El-Fass, A.E.H.B. Kashyout, Optimizing the preparation parameters of GO and rGO for large-scale production, *J. Mater. Sci.* 51 (2016) 5664–5675.
- [50] A. Kaniyoor, S. Ramaprabhu, A Raman spectroscopic investigation of graphite oxide derived graphene, *AlP Adv.* 2 (2012) 032183.
- [51] D.K. Pandey, T. Fung, G. Prakash, R. Piner, Y.P. Chen, R. Reifengerber, Surface science folding and cracking of graphene oxide sheets upon deposition, *Surf. Sci.* 605 (2011) 1669–1675.
- [52] M.A. Velasco-Soto, S.A. Pérez-García, J. Alvarez-Quintana, Y. Cao, L. Nyborg, L. Licea-Jiménez, Selective band gap manipulation of graphene oxide by its reduction with mild reagents, *Carbon* 93 (2015) 967–973.

SCIENTIFIC REPORTS



OPEN

Chemical Stability of Graphene Coated Silver Substrates for Surface-Enhanced Raman Scattering

Seiya Suzuki & Masamichi Yoshimura

Surface enhanced Raman spectroscopy (SERS) is a novel method to sense molecular and lattice vibrations at a high sensitivity. Although nanostructured silver surface provides intense SERS signals, the silver surface is unstable under acidic environment and heated environment. Graphene, a single atomic carbon layer, has a prominent stability for chemical agents, and its honeycomb lattice completely prevents the penetration of small molecules. Here, we fabricated a SERS substrate by combining nanostructured silver surface and single-crystal monolayer graphene (G-SERS), and focused on its chemical stability. The G-SERS substrate showed SERS even in concentrated hydrochloric acid (35–37%) and heated air up to 400 °C, which is hardly obtainable by normal silver SERS substrates. The chemically stable G-SERS substrate possesses a practical and feasible application, and its high chemical stability provides a new type of SERS technique such as molecular detections at high temperatures or in extreme acidic conditions.

Surface-enhanced Raman spectroscopy (SERS) is a novel method to sense molecular and lattice vibrations^{1–3}. The origin of the intense Raman signals in SERS is enhancement of local electromagnetic fields via the localized surface plasmon resonance effect⁴ in nanostructured metal surface or metal colloids. The main contribution of SERS enhancement is electromagnetic (EM) enhancement up to 10¹⁰ times^{5–7}, and another minor contribution is chemical enhancement including the resonance Raman effect, the charge-transfer effect, and the adsorption effect⁸. Coinage metals such as silver, gold, and copper, are the most common elements for SERS due to its large SERS enhancement and well-known fabrication methods. Gold and copper have interband absorption in the visible wavelength range, which decreases the maximum SERS intensity⁹. On the other hand, interband absorption of silver is located in the ultraviolet wavelength range, which leads the largest SERS intensity for visible light among these metals^{9,10}.

Despite the superior enhancement, silver is difficult to use in acid or heated environment with oxidative gas because of dissolution or oxidation of silver. Graphene, a single atomic carbon layer, has a prominent stability for chemical agents, and its honeycomb lattice completely prevents the penetration of small molecules like hydrogen and water¹¹. Therefore, graphene can be useful for a prominent protecting layer of nanostructured silver surfaces for SERS. Besides, graphene has only 2.3% absorption from near infrared to visible range¹², minimizing the loss of SERS signals from silver.

Composites of nanostructured silver and graphene for SERS have been widely reported using various types of graphene materials such as graphene oxide^{13,14}, reduced graphene oxide^{15–17}, mechanically exfoliated graphene from bulk graphite^{18,19}, and graphene grown by chemical vapor deposition (CVD)^{19–22}. Although there are a lot of works on SERS using graphene, there are no reports to focus on the effectiveness of graphene as a protective layer for the plasmonic metal surfaces. Here we studied the chemical stability of graphene in the SERS substrate, consisting of silver nanostructures and single-crystal monolayer graphene^{23,24}. Since the SERS for physisorbed molecules on graphene/plasmonic metal has been referred to as graphene-mediated SERS (G-SERS)¹⁹, we call our developed SERS substrate G-SERS substrate. It is found that the G-SERS substrate showed SERS even in concentrated hydrochloric acid (35–37%) and in heated air up to 400 °C, which is unattainable by the bare silver SERS substrates. The enhancements of Raman signals were observed not only for the protective graphene but

Graduate School of Engineering, Toyota Technological Institute, 2-12-1 Hisakata, Tempaku, Nagoya, 468-8511, Japan. Correspondence and requests for materials should be addressed to S.S. (email: seiya09417@gmail.com)

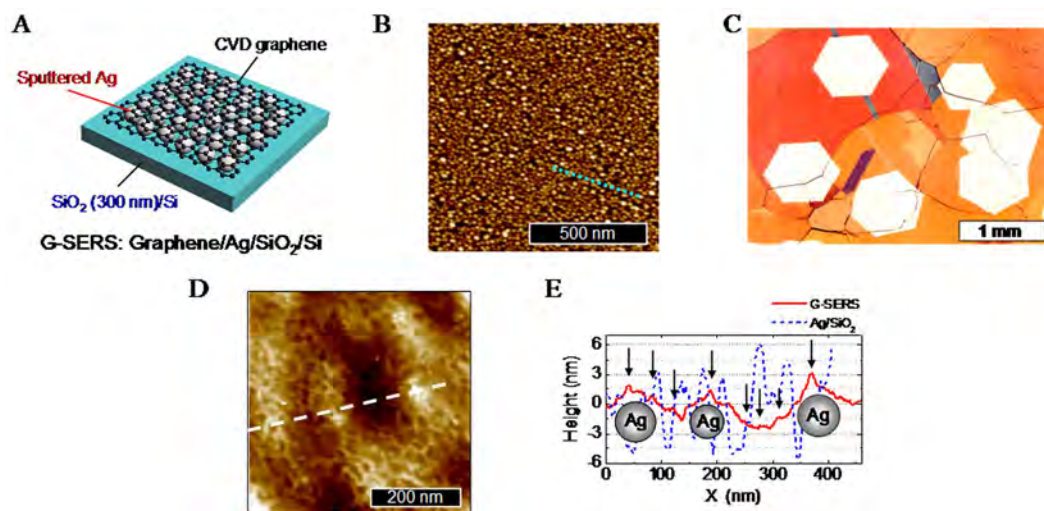


Figure 1. Structure and morphology. (A) Schematic illustration of the G-SERS. (B) AFM image of sputtered silver on SiO₂/Si. The deposited thickness of silver (measured by quartz oscillator) was ~ 2 nm. (C) CVD graphene grown on Cu. (D) AFM image of the G-SERS surface. (E) AFM line profiles along the broken lines in (B) and (D).

also rhodamine 6G (R6G) molecules adsorbed on the graphene, indicating G-SERS can be used for the molecular sensing. Unstable peaks due to nonuniform molecular adsorption, structural change of molecules induced by laser, and metal-molecular interaction are usually observed on the bare silver SERS substrate but G-SERS substrate does not show such behavior which enables us to measure stable and reliable Raman spectra. The high chemical stability of G-SERS can be utilized for new types of SERS techniques such as molecular detections at high temperatures or in extreme acidic conditions.

Results and Discussion

Figure 1A shows a schematic illustration of the G-SERS substrate. The structure of the G-SERS substrate can be described as graphene/Ag/SiO₂/Si, where the graphene as a protective layer was prepared by CVD and transfer process, and the silver as plasmonic metal was deposited by sputtering. Figure 1B is an atomic force microscope (AFM) image of the as-deposited silver on a SiO₂/Si. The sputtering resulted in the formation of nanoparticles with the average height of 6.4 ± 0.7 nm which is considered as the average diameter of the nanoparticles. Figure 1C is an optical microscope image of CVD graphenes on Cu after oxidation at ~ 200 °C for visualizing graphene. The hexagonal structure corresponds to a single crystal domain of graphene^{25,26}, and the size of the domains was approximately 1 mm in diameter. The present CVD graphene is monolayer which is confirmed by Raman spectrum shown in Fig. 2A (discussed later). Figure 1D shows an AFM image of the G-SERS surface. Figure 1E shows AFM line profiles along the broken lines in Fig. 1B and D. In the AFM line profile of the G-SERS (Fig. 1E), we can see large protrusions (3–5 nm) and small protrusions (a few sub-nanometers), as are pointed by arrows. The large protrusions come from the web structure as seen in Fig. 1D, and would be wrinkles of the CVD graphene. The large protrusions are caused by underlying silver particles since the height has similar order to that of the Ag nanoparticles on SiO₂ (Fig. 1E). The slight decrease of the protrusions in height and density were observed after transfer of graphene (Fig. 1E), indicating bridging of graphene on Ag nanoparticles and aggregation of Ag nanoparticles during the transfer process. Thus, the graphene has a wavy structure along with silver surface. In this configuration, the distance between graphene and silver becomes short, leading to strong enhancement for adsorbed molecules on the graphene²⁷.

Figure 2A shows Raman spectra of Ag/SiO₂/Si (upper), graphene/SiO₂/Si (middle), and G-SERS substrate (lower). To compare peak intensities, all spectra were taken at the same conditions (laser power: 24 μ W, exposure time: 1 s). The number located above each spectrum shows the magnification for the intensity scale. The spectrum of Ag/SiO₂ shows various intense peaks indicating SERS, although these peaks are not reproducible in peak position, width, and intensity (Fig. S1). These non-reproducible peaks are due to carbonaceous impurities adsorbed on silver surface. The carbonaceous impurities initially come from gas molecules from the ambience where the sample was exposed (i.e. in the sputtering chamber²⁸ and the Raman measurement chamber (air)). The structure of the adsorbed carbonaceous species can be changed by laser heating^{29,30}, which is called photocarbonization^{19,29}. The photocarbonization can be seen in Fig. 1SA, and possible peak origins in the Fig. 1SA are summarized in Table S1.

The Raman spectrum of the G-SERS shows G', G, and negligible small D peaks at around 2680, 1590, and 1345 cm^{-1} , respectively. The larger intensities of G' than G, and small D peak (G/D peak intensity ratio is ~ 20 , see Fig. S2 and Table S2) indicate a monolayer graphene with high crystallinity^{31–33}. The G' and G peaks are also observed in the graphene/SiO₂ but the intensities are very low compared to the G-SERS substrate. Contrary to Ag/SiO₂/Si, the spectrum of G-SERS shows steady peaks whereby more stable and reliable SERS can be achieved.

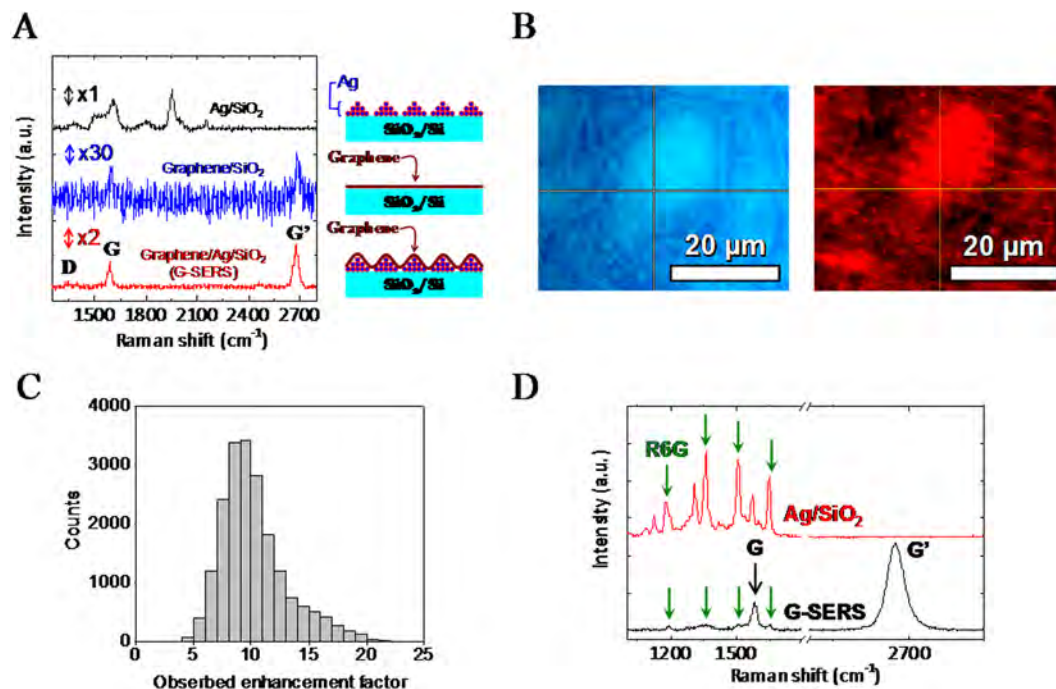


Figure 2. Enhancement of Raman peaks by G-SERS substrate. (A) Raman spectra of Ag/SiO₂/Si (black), graphene/SiO₂/Si (blue), and graphene/Ag/SiO₂/Si (red). The number located above each spectrum shows magnifications for the intensity scale. Schematic illustrations for each sample are also shown. (B) Optical microscope image (left) and G' peak intensity map (right) of G-SERS. (C) Histogram of the observed enhancement factor of G' peak intensity. (D) Raman spectra of R6G/G-SERS (black) and R6G/Ag/SiO₂/Si (red).

Figure 2B shows an optical microscope image (left) and the G' peak intensity map (right) of G-SERS. There is a spatial variation in G' peak intensity, probably due to the variation of microscopic surface structure as shown in the AFM image (Fig. 1D). Figure 2C is the histogram of the observed enhancement factor of G' peak, which is extracted from the mapping data (Fig. 2B). The enhancement was observed over the entire surface of G-SERS, and the maximum and average enhancement factors were ~ 24.7 and 10.2 ± 0.6 . Figure S6C shows the average Raman spectra of Ag/SiO₂/Si, graphene/SiO₂/Si, and G-SERS. The enhancement of the G' peak was obviously observed in the average spectra, ensuring that SERS enhancement occurs on the entire surface of G-SERS. Figure 2D shows Raman spectra of R6G/G-SERS and R6G/Ag/SiO₂/Si in air. The R6G specimen was prepared by dropping and drying 30 μl of R6G/DI solution (10 nM) on each substrate. Prominent Raman peaks of R6G at 1180, 1361, 1507, and 1647 cm⁻¹ for R6G/Ag/SiO₂ and 1195, 1361, 1506, and 1652 cm⁻¹ for R6G/G-SERS are observed, in agreement with previous reports^{34–36}. Slight peak shifts in the R6G peaks for the G-SERS substrate would be due to the different charge transfer effect between R6G and silver or graphene. The peaks located at 1584 and 2673 cm⁻¹ are G and G' peak, respectively. The other peaks in R6G/Ag/SiO₂ cannot be assigned, but would be from carbonaceous impurities as mentioned above. In contrast, there are no additional peaks in G-SERS, indicating that G-SERS can be suitable for molecular sensing.

The enhancement mechanism for molecules on G-SERS has been already discussed in a previous work¹⁹. Xu *et al.* revealed that monolayer graphene shell on Au nanospherical dimer enhances the localized electromagnetic fields rather than decrease¹⁹. The enhancement mechanism would be same also in our G-SERS since the structure of G-SERS is basically same. The relatively small enhancement for R6G on the G-SERS would be due to structural change of Ag nanoparticles during the process of graphene transfer (Fig. 2B,D, and E).

To examine chemical stability, the G-SERS substrate was immersed in hydrochloric acid (HCl) with continuously taking Raman spectra. Figure 3A and B show the time-resolved surface-enhanced Raman spectra of Ag/SiO₂/Si and G-SERS at 60s interval, respectively. The concentration of the HCl was 1×10^{-5} M. The SERS peaks in Ag/SiO₂/Si were disappeared at 60s, but were recovered at 120 s, and then finally completely disappeared at 240s. To understand this behavior, the immersed Ag/SiO₂/Si surface was observed by AFM, where the size of the silver nanoparticles became larger (Fig. S3C). The size change of the silver particles would be due to silver chloride formation by reaction between HCl and silver nanoparticles³⁷, which can also be confirmed by X-ray photoelectron spectroscopy (Fig. S4). The chemical reaction caused the variation in SERS intensities and finally lost enhancement ability of the silver nanoparticles. On the other hand, all SERS peaks in G-SERS were stable after immersing in HCl (Fig. 3B).

Figure 3C shows normalized intensities at 1600 cm⁻¹ in Ag/SiO₂/Si and of G' peak in G-SERS with respect to time after immersing in HCl. The intensity of G' peak initially decreases by 40%, and then keep constant, while the peak intensity of 1600 cm⁻¹ in Ag/SiO₂/Si is completely disappeared. Since the average enhancement factor is ~ 10 (Fig. 2C), the G' peak was still enhanced nevertheless the decrease by HCl. The decrease in G' peak would be due to the change of doping level in graphene by HCl³⁸. These results indicate that graphene in the G-SERS

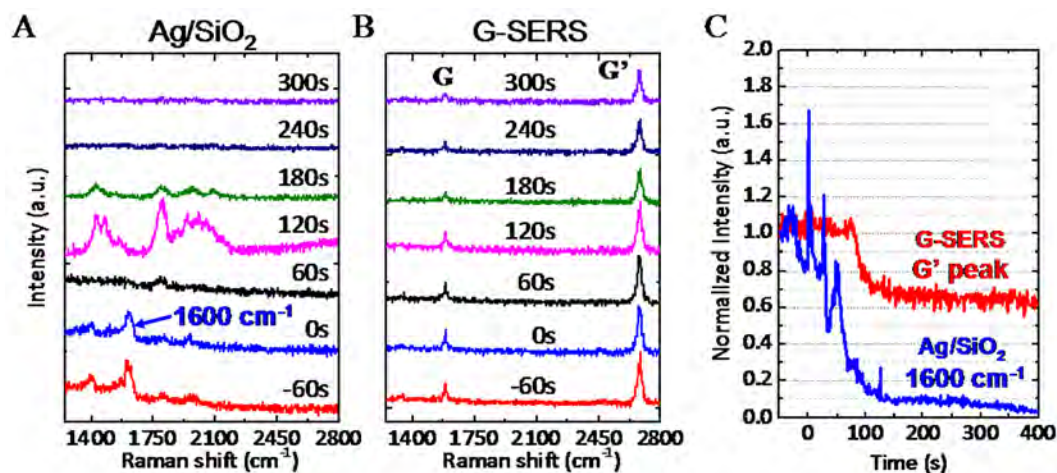


Figure 3. *In situ* HCl test of G-SERS. Time-resolved surface-enhanced Raman spectra of (A) Ag/SiO₂/Si and (B) G-SERS at 60 s interval in diluted HCl solution. The concentration of the HCl was 1×10^{-5} M. (C) Normalized intensities at 1600 cm^{-1} (blue) in (A) Ag/SiO₂/Si and of G' peak (red) in (B) G-SERS with respect to time after immersing in HCl.

substrate works as a protective layer which prevents the chemical reaction between silver and HCl. It is also noted that the G-SERS substrate shows SERS after immersing in concentrated HCl (35–37%), indicating its high chemical stability.

To show a potential of G-SERS for practical applications, we focused on the chemical reaction which requires HCl. Normal Ag SERS substrate cannot be used in such chemical reactions, although monitoring chemical reaction is one of the SERS application³⁹. As a demonstration for the G-SERS, we measured tertiary butyl chloride (TBC) which was synthesized by tertiary butyl alcohol (TBA) and HCl.

Figure S5 shows Raman spectra of TBA and TBC on G-SERS and SiO₂/Si substrate. For TBA, a Raman peak at 749.7 cm^{-1} was observed, corresponding to C-C-O (C₃C-O) symmetric stretching mode⁴⁰ in the molecule. The peak intensity of C-C-O stretching was 2.4 times higher on G-SERS than that on SiO₂/Si. For TBC, the peak position of C-C-O was shifted to 745.8 cm^{-1} , which corresponds to C-Cl stretching mode⁴¹ in the molecule. The peak intensity of C-Cl stretching was 1.8 times higher on G-SERS than that on SiO₂/Si. The observed enhancement factors are relatively small, which would be due to weak adsorption of TBA and TBC onto the graphene.

Since the peak shift from C-C-O to C-Cl stretching was clearly observed by G-SERS, G-SERS has enough potential to monitor such chemical reaction. For the practical application for monitoring chemical reactions by G-SERS, its enhancement ability has to be improved, for example, by designing the structure of nanoparticles³⁹.

Subsequently, thermal durability of G-SERS was examined. Figure 4A and B show *in situ* Raman spectra of G-SERS and Ag/SiO₂/Si at elevated temperatures in air, respectively. These spectra are taken under the same conditions (laser power: $24 \mu\text{W}$, exposure time: 5s), and are shown on the same intensity scale. The G-SERS sample shows several large peaks around the G peak at lower than 250°C (Fig. 4A). The peaks would be from residual polymethyl methacrylate (PMMA) which was used as a supporting layer for the transfer process of graphene. These PMMA peaks were greatly enhanced at 100, 200, and 250°C , and were disappeared at 300°C . The disappearance of the peaks would be explained by the complete removal of PMMA residue by oxidation. In the case of Ag/SiO₂/Si, the SERS was observed until 140°C , and then disappeared at 160°C . The temperature of 160°C is much lower than that the SERS was disappeared in G-SERS. We measured Ag/SiO₂/Si by X-ray photoelectron spectroscopy (XPS) before and after heating at 200°C for 15 min (Table S5), and found that the silver was oxidized after the heating. Thus, heating around 200°C causes oxidation of silver nanoparticles, resulting in the loss of SERS in Ag/SiO₂/Si. In the G-SERS, graphene is valid as a protective layer for preventing oxidation of silver, resulting in SERS at high temperatures. In addition, G-SERS has uniform spatial distribution in SERS intensity for the mild temperature range ($100\text{--}140^\circ\text{C}$) as shown in Fig. S11, which is an advantage for SERS applications.

To validate the protective function of graphene for long heating duration time, we measured Raman spectroscopy of benzoic acid (BA) dissolved in isopropyl alcohol (IPA) on Ag/SiO₂/Si and G-SERS. To give clear difference for the long time stability in SERS, Ag/SiO₂/Si and G-SERS were heated at 150°C in air up to 63 hours (h).

Figure S8B shows the dependence of the peak intensity of BA at $\sim 1000 \text{ cm}^{-1}$ on heating duration time. The intensity of BA on Ag/SiO₂/Si was drastically decreased in the first 1 h, and kept nearly constant until 30 h, and completely disappeared after 63 h. The intensity of BA on G-SERS was fluctuated for the first 2 h, and reached maximum at 30 h, and decreased to be nearly half of the initial count (~ 1000) but existing. To examine the reason of the intensity changes in Fig. S8B, we have performed XPS and AFM. XPS analysis revealed that oxidation of Ag particles nearly completed within 1 h, and it does not proceed significantly from 1 to 63 h (Fig. S8C) in Ag/SiO₂/Si. AFM analysis revealed that the aggregation of Ag particles proceeds gradually by belonging the heating duration time. The speed of aggregation of Ag particles is slower in G-SERS than Ag/SiO₂/Si (Fig. S9), which provides long time stability in SERS for G-SERS substrates.

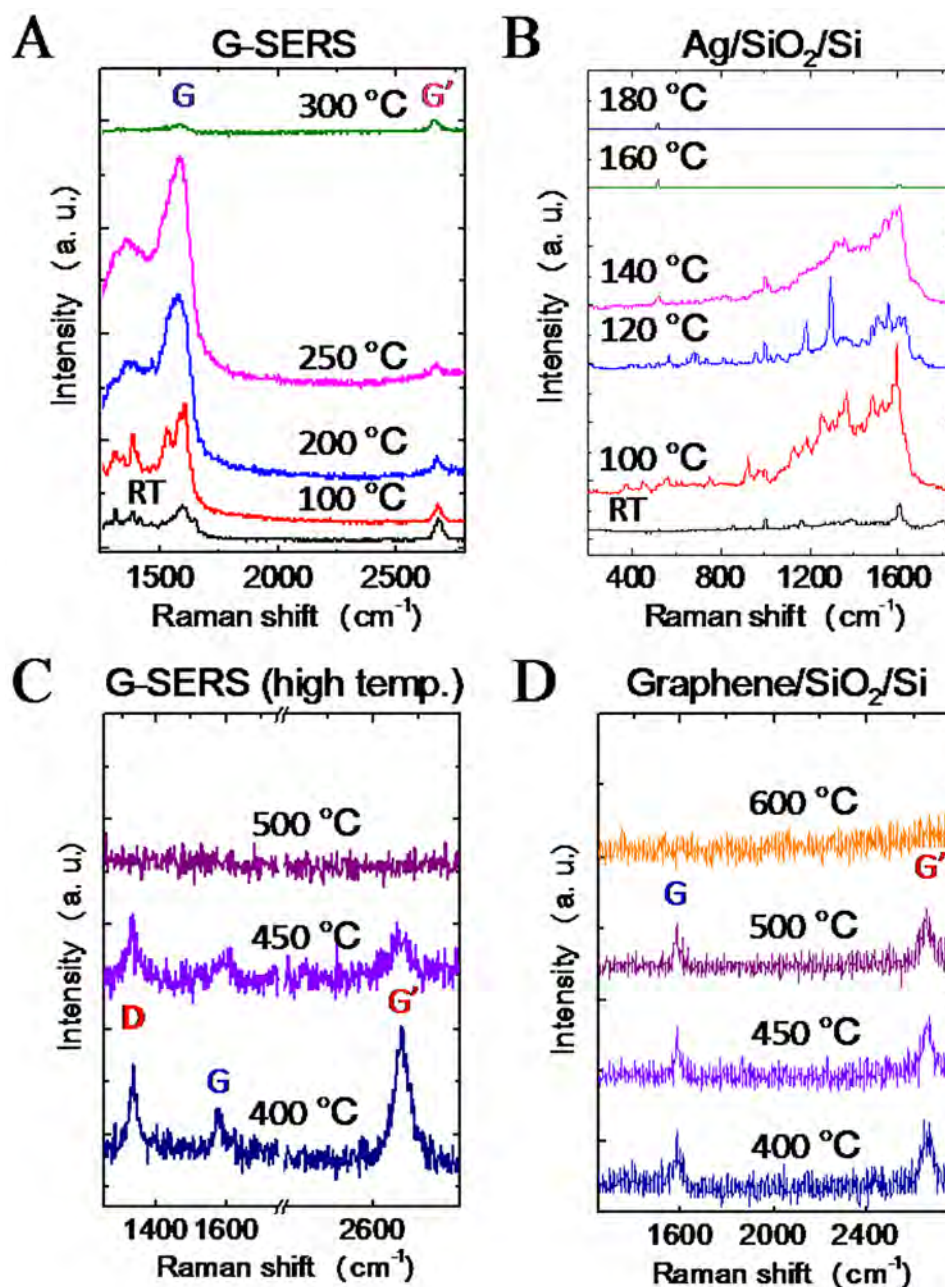


Figure 4. Thermal stability of G-SERS substrate. *In situ* Raman spectra of (A) G-SERS and (B) Ag/SiO₂/Si for low temperature heating (<300 °C) in air. *In situ* Raman spectra of (C) G-SERS and (D) graphene/SiO₂/Si for high temperature heating (>400 °C) in air.

Figure 4C and D show *in situ* Raman spectra of G-SERS for higher temperatures (>400 °C) and graphene/SiO₂/Si at each temperature in air, respectively. In the G-SERS substrate (Fig. 4C), the D peak was appeared at 400 °C and the peak intensities of D, G, and G' peaks were decreased at 450 °C, and eventually all peaks were disappeared at 500 °C, indicating the loss of graphene. In the graphene/SiO₂/Si (Fig. 4D), G and G' peaks were observed until 500 °C but disappeared at 600 °C. To understand the loss of graphene at lower temperature in G-SERS, we compared the G' peak positions and temperature as shown in Fig. S7. The G' peak positions were monotonically decreased both for G-SERS and graphene/SiO₂/Si, while the G' peaks in G-SERS show lower position at almost all temperature. The redshift of G' peak indicates that graphene is stretched by heating^{42–44}. The larger redshifts in G-SERS than graphene/SiO₂/Si indicate that the graphene in G-SERS is initially stretched by following the structure of Ag particles (Fig. 1D). Since the stretched graphene is more reactive for oxygen radicals than the flat graphene⁴⁵, the initial stretch would result in loss of graphene at lower temperatures. It is also noted that the G' peak at 400 °C in G-SERS (Fig. 4C) has ~2.8 times larger peak intensity than that in normal graphene, indicating that the enhancement still occurs at 400 °C. This result shows that the present G-SERS substrate can be useful for high temperature SERS applications.

Conclusions

In conclusion, a chemically stable G-SERS substrate was successfully fabricated by using single crystal monolayer CVD graphene. We revealed that the G-SERS substrate has high tolerance with HCl and high temperature oxidation up to 400 °C. The maximum and average observed enhancement factors of G' peaks were ~ 24.7 and 10.2 ± 0.6 , and the enhancement was observed over the entire surface. The enhancement factor can be further increased by adjusting the preparation process of silver nanoparticles. The fabrication method of the G-SERS substrate including CVD graphene is a scalable process. Thus, the chemically stable G-SERS substrate has a practical and feasible application and its high chemical stability can provide new type of SERS technique such as molecular detections at high temperatures or in extreme acidic conditions.

Methods

Silver nanoparticles were deposited by dc magnetron sputtering (Quorum Technologies, Q300T D) at room temperature with a silver target of 99.99% purity in argon atmosphere. The deposition pressure and rate were 1 Pa and ~ 1.3 Å/s. The deposited thickness (assuming uniform film structure) was measured by a quartz oscillator in the sputtering chamber to control the particle size of silver. The deposited thickness was used to control the particles size. The deposited thickness of silver ranging from 2 to 6 nm shows similar order enhancements in Raman signals for 532 nm wavelength.

Graphene was grown by a custom-made atmospheric pressure chemical vapor deposition (CVD) system^{23,24}. The purities of H₂ and Ar gasses are 99.99999% (7N), and 99.9999% (6N), respectively. The chamber pressure has been kept to be near atmospheric pressure (0.123–0.128 MPa) during the CVD process. 100 μm-thick commercial Cu foils (Nilaco, #113321) with the size of ~ 2 cm \times 10 cm were used as catalytic substrates for the growth. The grown graphene was transferred onto arbitrary target substrate with a conventional method, which uses a spin-coated polymethyl methacrylate (PMMA) support layer, ammonium peroxodisulfate for etchant of Cu, and the mixture of acetone, isopropyl alcohol, and methyl isobutyl ketone for removal of PMMA^{46,47}.

Surface morphologies of samples were microscopically observed using an atomic force microscope (AFM, Bruker, Multimode) in the peak force tapping mode and an optical microscope (Keyence, Digital Microscope VHX-5000). Surface elemental analyses were performed by XPS (ULVAC-PHI, PHI 5000 VersaProbe II) under a base pressure of $\sim 6 \times 10^{-8}$ Pa and a monochromatized AlK α (1486.6 eV) X-ray source. Raman spectra were recorded with a Raman microscope (Renishaw, InVia) at a wavelength of 532 nm in the backscattering geometry. *In situ* heating experiments were carried out in the temperature controllable stage (Linkam, THMS 600).

References

- Fleischmann, M., Hendra, P. J. & McQuillan, A. J. Raman spectra of pyridine adsorbed at a silver electrode. *Chem. Phys. Lett.* **26**, 163–166 (1974).
- Jeanmaire, D. L. & Van Duyne, R. P. Surface Raman spectroelectrochemistry: Part I. Heterocyclic, aromatic, and aliphatic amines adsorbed on the anodized silver electrode. *J. Electroanal. Chem. Interfacial Electrochem.* **84**, 1–20 (1977).
- Albrecht, M. G. & Creighton, J. A. Anomalously Intense Raman-Spectra of Pyridine at a Silver Electrode. *J. Am. Chem. Soc.* **99**, 5215–5217 (1977).
- Moskovits, M. Surface roughness and the enhanced intensity of Raman scattering by molecules adsorbed on metals. *J. Chem. Phys.* **69**, 4159–4161 (1978).
- Johansson, P., Xu, H. X. & Kall, M. Surface-enhanced Raman scattering and fluorescence near metal nanoparticles. *Phys. Rev. B* **72**, 035427 (2005).
- Inoue, M. & Ohtaka, K. Surface enhanced Raman scattering by metal spheres. I. Cluster effect. *J. Phys. Soc. Jpn.* **52**, 3853–3864 (1983).
- Yamamoto, Y. S. & Itoh, T. Why and how do the shapes of surface-enhanced Raman scattering spectra change? Recent progress from mechanistic studies. *J. Raman Spectrosc.* **47**, 78–88 (2016).
- Jensen, L., Aikens, C. M. & Schatz, G. C. Electronic structure methods for studying surface-enhanced Raman scattering. *Chem. Soc. Rev.* **37**, 1061–1073 (2008).
- West, P. R. *et al.* Searching for better plasmonic materials. *Laser Photon. Rev.* **4**, 795–808 (2010).
- See, K. C., Spicer, J. B., Brupbacher, J., Zhang, D. & Vargo, T. G. Modeling Interband Transitions in Silver Nanoparticle–Fluoropolymer Composites. *J. Phys. Chem. B* **109**, 2693–2698 (2005).
- O'Hern, S. C. *et al.* Selective ionic transport through tunable subnanometer pores in single-layer graphene membranes. *Nano Lett.* **14**, 1234–1241 (2014).
- Nair, R. R. *et al.* Fine structure constant defines visual transparency of graphene. *Science* **320**, 1308–1308 (2008).
- Xu, C. & Wang, X. Fabrication of Flexible Metal-Nanoparticle Films Using Graphene Oxide Sheets as Substrates. *Small* **5**, 2212–2217 (2009).
- Zhang, Z. *et al.* A facile one-pot method to high-quality Ag-graphene composite nanosheets for efficient surface-enhanced Raman scattering. *Chem. Commun.* **47**, 6440–6442 (2011).
- Sun, S. & Wu, P. Competitive surface-enhanced Raman scattering effects in noble metal nanoparticle-decorated graphene sheets. *Phys. Chem. Chem. Phys.* **13**, 21116–21120 (2011).
- Lu, G. *et al.* Surface enhanced Raman scattering of Ag or Au nanoparticle-decorated reduced graphene oxide for detection of aromatic molecules. *Chem. Sci.* **2**, 1817–1821 (2011).
- Ouyang, Y. & Chen, L. Surface-enhanced Raman scattering studies of few-layer graphene on silver substrate with 514 nm excitation. *J. Mol. Struct.* **992**, 48–51 (2011).
- Lee, J., Novoselov, K. S. & Shin, H. S. Interaction between metal and graphene: dependence on the layer number of graphene. *ACS Nano* **5**, 608–612 (2010).
- Xu, W. *et al.* Surface enhanced Raman spectroscopy on a flat graphene surface. *Proc. Natl. Acad. Sci. USA* **109**, 9281–9286 (2012).
- Liu, C.-Y. *et al.* Plasmonic coupling of silver nanoparticles covered by hydrogen-terminated graphene for surface-enhanced Raman spectroscopy. *Opt. Express* **19**, 17092–17098 (2011).
- Dai, Z. *et al.* Monolayer graphene on nanostructured Ag for enhancement of surface-enhanced Raman scattering stable platform. *Nanotechnology* **26**, 125603 (2015).
- Dai, Z.-G. *et al.* Plasmon-driven reaction controlled by the number of graphene layers and localized surface plasmon distribution during optical excitation. *Light: Science and Applications* **4**, e342 (2015).
- Suzuki, S., Kiyosumi, K., Nagamori, T., Tanaka, K. & Yoshimura, M. Low Density Growth of Graphene by Air Introduction in Atmospheric Pressure Chemical Vapor Deposition. *e-J. Surf. Sci. Nanotechnol.* **13**, 404–409 (2015).

24. Suzuki, S., Nagamori, T., Matsuoka, Y. & Yoshimura, M. Threefold atmospheric-pressure annealing for suppressing graphene nucleation on copper in chemical vapor deposition. *Jpn. J. Appl. Phys.* **53**, 095101 (2014).
25. Vlasiuk, I. *et al.* Role of hydrogen in chemical vapor deposition growth of large single-crystal graphene. *ACS Nano* **5**, 6069–6076 (2011).
26. Yan, Z. *et al.* Toward the synthesis of wafer-scale single-crystal graphene on copper foils. *ACS Nano* **6**, 9110–9117 (2012).
27. Xu, W. *et al.* Graphene-Veiled Gold Substrate for Surface-Enhanced Raman Spectroscopy. *Adv. Mater.* **25**, 928–933 (2013).
28. Büchel, D. *et al.* Sputtered silver oxide layers for surface-enhanced Raman spectroscopy. *Appl. Phys. Lett.* **79**, 620–622 (2001).
29. Zhang, N., Tong, L. & Zhang, J. Graphene-based enhanced Raman scattering toward analytical applications. *Chem. Mater.* **28**, 6426–6435 (2016).
30. Cooney, R. P., Mahoney, M. R. & Howard, M. W. Intense Raman spectra of surface carbon and hydrocarbons on silver electrodes. *Chem. Phys. Lett.* **76**, 448–452 (1980).
31. Malard, L., Pimenta, M., Dresselhaus, G. & Dresselhaus, M. Raman spectroscopy in graphene. *Phys. Rep.* **473**, 51–87 (2009).
32. Ferrari, A. C. & Robertson, J. Raman spectroscopy of amorphous, nanostructured, diamond-like carbon, and nanodiamond. *Phil. Trans. R. Soc. A* **362**, 2477–2512 (2004).
33. Ferrari, A. *et al.* Raman spectrum of graphene and graphene layers. *Phys. Rev. Lett.* **97**, 187401 (2006).
34. Nie, S. & Emory, S. R. Probing Single Molecules and Single Nanoparticles by Surface-Enhanced Raman Scattering. *Science* **275**, 1102–1106 (1997).
35. Michaels, A. M., Nirmal, M. & Brus, L. Surface enhanced Raman spectroscopy of individual rhodamine 6G molecules on large Ag nanocrystals. *J. Am. Chem. Soc.* **121**, 9932–9939 (1999).
36. Dieringer, J. A. *et al.* Surface-enhanced Raman excitation spectroscopy of a single rhodamine 6G molecule. *J. Am. Chem. Soc.* **131**, 849–854 (2009).
37. Li, L. & Zhu, Y.-J. High chemical reactivity of silver nanoparticles toward hydrochloric acid. *J. Colloid Interface Sci.* **303**, 415–418 (2006).
38. Das, A. *et al.* Monitoring dopants by Raman scattering in an electrochemically top-gated graphene transistor. *Nat. Nanotechnol.* **3**, 210–215 (2008).
39. Xie, W., Walkenfort, B. & Schlücker, S. Label-free SERS monitoring of chemical reactions catalyzed by small gold nanoparticles using 3D plasmonic superstructures. *J. Am. Chem. Soc.* **135**, 1657–1660 (2012).
40. Kipkemboi, P. K., Kiprono, P. C. & Sanga, J. J. Vibrational spectra of t-butyl alcohol, t-butylamine and t-butyl alcohol + t-butylamine binary liquid mixtures. *Bull. Chem. Soc. Ethiop.* **17** (2003).
41. Lin-Vien, D., Colthup, N. B., Fateley, W. G. & Grasselli, J. G. *The handbook of infrared and Raman characteristic frequencies of organic molecules.* (Elsevier, 1991).
42. Wang, W., Peng, Q., Dai, Y., Qian, Z. & Liu, S. Temperature dependence of Raman spectra of graphene on copper foil substrate. *J. Mater. Sci. Mater. Electron.* **27**, 3888–3893 (2016).
43. Calizo, I., Balandin, A., Bao, W., Miao, F. & Lau, C. Temperature dependence of the Raman spectra of graphene and graphene multilayers. *Nano Lett.* **7**, 2645–2649 (2007).
44. Mohiuddin, T. *et al.* Uniaxial strain in graphene by Raman spectroscopy: G peak splitting, Grüneisen parameters, and sample orientation. *Phys. Rev. B* **79**, 205433 (2009).
45. Tao, H. H., Moser, J., Alzina, F., Wang, Q. & Sotomayor-Torres, C. M. The Morphology of Graphene Sheets Treated in an Ozone Generator. *J. Phys. Chem. C* **115**, 18257–18260 (2011).
46. Reina, A. *et al.* Large area, few-layer graphene films on arbitrary substrates by chemical vapor deposition. *Nano Lett.* **9**, 30–35 (2009).
47. Jeong, H. J. *et al.* Improved transfer of chemical-vapor-deposited graphene through modification of intermolecular interactions and solubility of poly(methylmethacrylate) layers. *Carbon* **66**, 612–618 (2014).

Acknowledgements

This work was supported in part by the Grant-in-Aid for Young Scientist (Start-up) (No. 15H06723), and Strategic Research Foundation Grant-aided Project for Private Universities from the Ministry of Education, Culture, Sport, Science, and Technology, Japan (MEXT).

Author Contributions

S.S. designed and performed experiments and wrote the manuscript. S.S. compiled and analyzed all the results with due discussion with M.Y.

Additional Information

Supplementary information accompanies this paper at <https://doi.org/10.1038/s41598-017-14782-2>.

Competing Interests: The authors declare that they have no competing interests.

Publisher's note: Springer Nature remains neutral with regard to jurisdictional claims in published maps and institutional affiliations.



Open Access This article is licensed under a Creative Commons Attribution 4.0 International License, which permits use, sharing, adaptation, distribution and reproduction in any medium or format, as long as you give appropriate credit to the original author(s) and the source, provide a link to the Creative Commons license, and indicate if changes were made. The images or other third party material in this article are included in the article's Creative Commons license, unless indicated otherwise in a credit line to the material. If material is not included in the article's Creative Commons license and your intended use is not permitted by statutory regulation or exceeds the permitted use, you will need to obtain permission directly from the copyright holder. To view a copy of this license, visit <http://creativecommons.org/licenses/by/4.0/>.

© The Author(s) 2017

**FABRICATION AND EVALUATION OF NANOCARBON SUPPORTED
IRIDIUM OXIDE CATALYSTS FOR WATER ELECTROLYSIS**

M. Hara^{*}, R. Badam, K. de Silva, H. Huang and M. Yoshimura

*Graduate School of Engineering, Toyota Technological Institute, 2-12-1 Hisakata, Tempaku,
Nagoya 468-8511, Japan*

**haram@toyota-ti.ac.jp*

In recent years, progressing toward sustainable societies has become important topic to overcome environmental issues, such as global warming and depletion of fossil fuels. In terms of effective utilization of renewable energies, conversion of renewable energies to hydrogen via water electrolysis for energy storage has attracted attention. However, for the practical application of water electrolysis systems, activity, durability, and cost of catalysts are insufficient due to high over-potential and low kinetics of electrode reactions, especially, oxygen evolution reaction (OER) on the anode. In this study, we focus on improvement of specific surface area, surface area per weight, of anode catalysts. As the anode catalysts, we use iridium oxide (IrO₂) catalysts, which is one of the most active anode catalysts for OER. Novel catalysts of the IrO₂ nanoparticle supported on nano-carbon (NC) materials, such as graphene and carbon nanotube (CNT), with high durability and conductivity were prepared. The IrO₂ supported on reduced graphene oxide (rGO) or CNT catalysts was synthesized by the hydrothermal method. For the synthesis, mixture of H₂IrCl₆ complex and graphene oxide (GO) or oxidized CNT dispersed in ethanol/water mixture solution was heated at 80 °C for 6 h in a flask and at 150 °C for 4 h in a hydrothermal autoclave. The IrO₂/rGO and IrO₂/CNT catalysts were characterized by XRD, TEM, EDX, XPS and electrochemical methods, LSV and RDE. The OER activity of the IrO₂/graphene and IrO₂/CNT catalysts was examined in sulfuric acid solution. TEM observation of the IrO₂/rGO and IrO₂/CNT catalysts shows that the IrO₂ nanoparticles with an average particle size in the range 1.5-1.7 nm were uniformly dispersed on both the rGO and CNT substrates surface. The loading amount of the IrO₂ nanoparticles on rGO and CNT, 28 and 4 wt%, was estimated respecting from XPS and EDX results. Electrochemical measurement reveals that the IrO₂/rGO and IrO₂/CNT catalysts have high activity for OER. Onset potential of OER is ca. 1.43 V and mass activity at 1.60 V is ca. 380 A g⁻¹ for both IrO₂/rGO and IrO₂/CNT catalysts. The overvoltage of the IrO₂/NC catalysts is 70 mV lower than that of conventional IrO₂ powder catalysts. In addition, both IrO₂/rGO and IrO₂/CNT catalysts showed high durability, 20% and 9% reduction in the current density, respectively, for 1000 potential cycling between 1.2-1.65 V. High activity and durability of the IrO₂/NC catalysts indicate that the IrO₂/NC is a promising candidate of anode for polymer electrolyte water electrolyzer.

Acknowledgements:

This work was supported by JSPS KAKENHI Grant number 17K05969.

Keywords: Carbon nanotube, Graphene, Iridium oxide, Oxygen evolution reaction, Water electrolysis

Synthesis and Evaluation of Iridium Oxide Nanoparticle Catalysts Supported on Nitrogen-Doped Reduced Graphene Oxides

Masanori Hara, Rajashekar Badam, Guan Jhong Wang, Hsin-Hui Huang
and Masamichi Yoshimura

Graduate School of Engineering, Toyota Technological Institute,
2-12-1 Hisakata, Tenpaku, Nagoya 468-8511, Japan

We synthesized IrO₂ nanoparticle catalyst supported on nitrogen-doped graphene aerogel (IrO₂/N-rGO). Electron donation from nitrogen-doped graphene to the IrO₂ nanoparticles is expected to improve activity of oxygen evolution reaction (OER). To prepare nitrogen-doped graphene aerogel (N-rGO) and to decorate IrO₂ nanoparticles on N-rGO, combination of modified Hummers' method and hydrothermal method was employed. Successful fabrication of IrO₂/N-rGO was confirmed by transmission electron microscopy (TEM) and X-ray photoelectron spectroscopy (XPS) and its catalytic activity was evaluated by electrochemical methods. TEM image of IrO₂/N-rGO shows that the IrO₂ nanoparticles with an average particle size of 1.2 nm are uniformly dispersed on the N-rGO surface. The XPS results revealed the presence of nitrogen and IrO₂ in the N-rGO aerogel substrate. The IrO₂/N-rGO catalyst also shows high activity for OER. Our results suggest IrO₂/N-rGO is a promising candidate as anode for water electrolysis system.

Introduction

In recent years, progress toward sustainable societies with renewable energies has been a critical issue to overcome environmental and social problems, for example, global warming and depletion of fossil fuels. To utilize effectively renewable energies such as solar and wind energy, conversion of renewable energies to hydrogen via water electrolysis is one of the most attractive approaches for energy storage (1-3). One of the candidate systems for water electrolysis is polymer electrolyte water electrolyzer (PEWE), which is assembled from polymer electrolyte, iridium oxide as anode and Pt/C cathode (4,5). The advantages of a PEWE system are clean production of hydrogen, higher product amount of hydrogen per unit cell, fast response to current and voltage fluctuation and simple structure. Therefore, PEWE is expected as a promising future system for the hydrogen production. However, for the practical application of water electrolysis systems, its activity, durability and cost of catalysts are insufficient due to high over-potential and low kinetics of electrode reactions, especially, oxygen evolution reaction (OER) at the anode (4,6,7).

As anode catalyst, iridium oxide (IrO₂) particles have been used because of its high activity and durability for OER (8-12). However, iridium is one of the platinum group metals and reducing loading amount of iridium is required to reduce catalyst cost. To improve the activity of IrO₂ catalyst, preparation of ultrafine nanoparticles dispersed on a

stable substrate has been explored. Carbon materials and conductive metal oxide such as titanium sub-oxides were examined to support IrO_2 nanoparticle catalysts (13-15). They reported that the dispersion of IrO_2 provides higher catalytic activity. Recently, Denis *et al.* reported a synthesis procedure of IrO_2 nanoparticle catalysts supported on reduced graphene oxide (rGO) as a high surface area and conductive substrate (15), as shown in figure 1. Recently, we also have successfully synthesized novel catalysts, IrO_2 nanoparticle catalysts supported on nanocarbon materials with improved specific surface area of anode catalysts for PEWE (16).

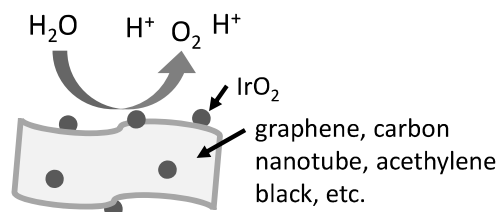


Figure 1. Schematic model of oxygen evolution reaction on IrO_2 /nanocarbon.

On the other hand, tailoring the electronic state of iridium oxide by electron donation from support materials is another approach for further improvement of the catalytic activity. It has been known that physical, chemical and electronic properties of a carbon material substrates were modified by doping heteroatoms, such as nitrogen, boron, sulfur, or phosphorus (17-19). In addition, high surface area and three dimensional electronic conductivities by the support will also enhance the activity of the catalyst. For oxygen reduction reaction, improving the performance of electrocatalysts by heteroatoms doping into the carbon support was reported (21-23). Pt and Pt-alloy supported on nitrogen-functionalized carbon showed improved particle dispersion and size distribution along with the durability due to enhancement of binding between the nanoparticles and the supports (24,25). However, precise contributions of various N-functionalities, as shown in figure 2(a), are still under investigation. Furthermore, the heteroatom-doped support materials have rarely been examined for water electrolysis catalyst. From this perspective, we use graphene with heteroatoms as a substrate of the catalyst for water electrolysis to enhance electro-catalytic activities.

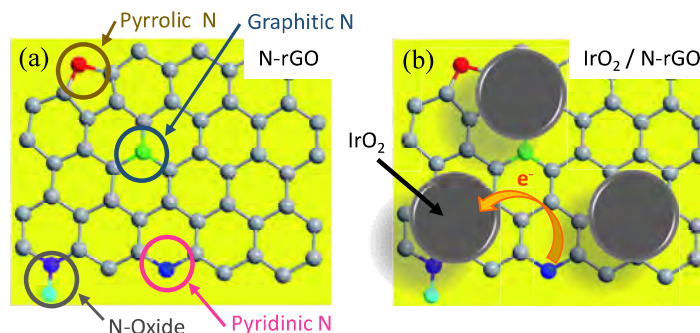


Figure 2. Schematic model of (a) nitrogen doped graphene and (b) IrO_2 /N-rGO.

In this study, we focus on the modification of nitrogen-doped reduced graphene oxide aerogel (N-rGO) substrate with IrO_2 nanoparticles (figure 2(b)). The graphene aerogel possesses three dimensional (3D) porous network structure with high surface area

and sufficient interstitial space to accommodate water for electrolysis (26). Further, the effect of substrate on the electronic state and catalytic OER activity of the material is investigated by transmission electron microscopy, X-ray photoelectron spectroscopy, scanning electron microscopy equipped with energy dispersed X-ray analysis, and electrochemical methods in sulfuric acid solution using rotating disk electrode system.

Experimental

Novel catalyst with IrO₂ nanoparticles supported on nitrogen-doped reduced graphene oxide aerogel was prepared by hydrothermal synthesis. Graphene oxide (GO) was prepared by modified Hummers' method (27-29). In brief, mixture of natural graphite powder, concentrated sulfuric acid (Wako Pure Chemical Industries Ltd.) and potassium permanganate (Nacalai Tesque Inc.) were stirred and ultrasonicated to oxidize the graphite flakes and exfoliate the graphene layers. Then, deionized water and hydrogen peroxide (Kishida Chemical Co.) were added to quench the reaction and the mixture was centrifuged. The prepared GO was mixed with urea (Kishida Chemical Co.) in ethanol and water mixture solution. The GO dispersed urea containing solution was ultrasonicated for 60 min, then the solution was hydrothermally treated at 180 °C for 12 h in an autoclave to synthesize N-rGO aerogel. To deposit IrO₂ on N-rGO, the mixture of H₂IrCl₆ complex (Wako Pure Chemical Industries Ltd.) and N-rGO dispersed in ethanol/water mixture solution was stirred at 80 °C for 6 h in a flask to attach iridium oxide colloid to N-rGO and heated at 150 °C for 4 h in a hydrothermal autoclave to form IrO₂ nanoparticles on the N-rGO aerogel substrate (15). The resulting material was filtered, washed and dried in vacuum oven at 120 °C for 4 h.

The morphology of the IrO₂ nanoparticles deposited on the N-rGO aerogel support was measured by transmission electron microscopy (TEM, TEM-2100, JEOL, operated at 200 kV). The loading amount of the IrO₂ catalyst on N-rGO was estimated by scanning electron microscopy (SEM, SU3500, Hitachi High Technologies Co., operated at 10 kV) equipped with an energy dispersive X-ray spectrometry (EDX, EMAX Evolution X-Max, Horiba Ltd.). Surface elemental and electron states were analyzed by X-ray photoelectron spectroscopy (XPS, PHI5000 Versa Probe II, ULVAC-PHI) with Al-Mg anode.

To prepare working electrodes, a similar method of our previous works was used (16,30). Briefly, catalyst ink containing IrO₂/N-rGO, IPA and Nafion was prepared by ultrasonicated the mixture solution. To form a thin film containing IrO₂/N-rGO, an appropriate amount of the ink was drop-casted on glassy carbon (GC, 5 mm in diameter) disk electrode as substrate of rotating disk electrode (RDE). The catalyst coated electrode was dried in vacuum oven at 60 °C. The OER catalytic activity of the synthesized IrO₂/N-rGO catalyst was measured by linear sweep voltammetry (LSV) with RDE equipment (RRDE-3A, BAS Inc.) at room temperature. The hydrodynamic voltammograms in the potential region from 1.20 to 1.65 V vs. reversible hydrogen electrode (RHE) were recorded by a potentiostat (HSV-110, Hokuto Denko Co.) at the scan rate of 5 mV s⁻¹ and rotation rate of 1600 rpm in 0.5 M H₂SO₄ (Kanto Chemical Co.) under nitrogen saturated condition. A platinum wire and Ag/AgCl electrode in 3 M KCl solution were used as a counter electrode and reference electrode, respectively, for the electrochemical measurement. Before the electrochemical measurement, the electrolyte solution was purged with nitrogen gas for 30 min.

Results and Discussion

Figure 3 shows TEM image of the synthesized IrO₂/N-rGO catalysts. The deposited IrO₂ nanoparticles on the N-rGO aerogel substrate were observed as spherical dark spots with an average particle size of 1.2 nm. The TEM image shows the IrO₂ nanoparticles are uniformly dispersed on the surface of the N-rGO substrate. Elemental analysis by SEM-EDX revealed that the IrO₂/N-rGO catalyst contains 9 and 7 wt% of Ir and N, respectively. The average particle size of the IrO₂ nanoparticles was smaller than that of IrO₂ supported on rGO, 1.7 nm, in a previous paper (15) because of lower loading amount and nitrogen doping on the reduce graphene oxide substrate. Our results suggest that fine dispersion of the deposited nanoparticles was promoted on the nitrogen-doped carbon materials.

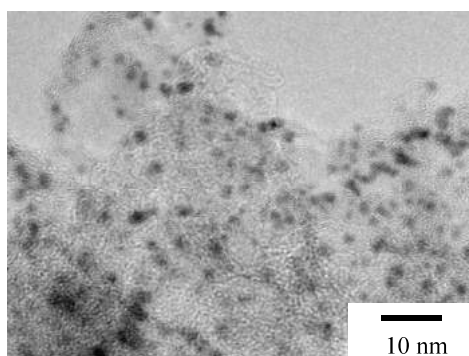


Figure 3. TEM image of IrO₂/N-rGO.

Figure 4 shows survey spectra of XPS investigation on GO, N-rGO, and IrO₂/N-rGO. In the XPS spectra, O 1s and C 1s peaks were observed on GO, whereas N 1s and Ir 4f peaks were found for N-rGO and IrO₂/N-rGO. The XPS data reveal nitrogen doping on GO by hydrothermal treatment of GO with urea. The intensity of O 1s was decreased due to reduction of GO during the hydrothermal reaction. The Ir 4f peak exhibits the deposition of IrO₂ on the N-rGO aerogel substrate after the hydrothermal reaction between H₂IrCl₆ and N-rGO. The loading amount of nitrogen and iridium estimated from each peak intensity was consistent with the results of SEM-EDX analysis in our group.

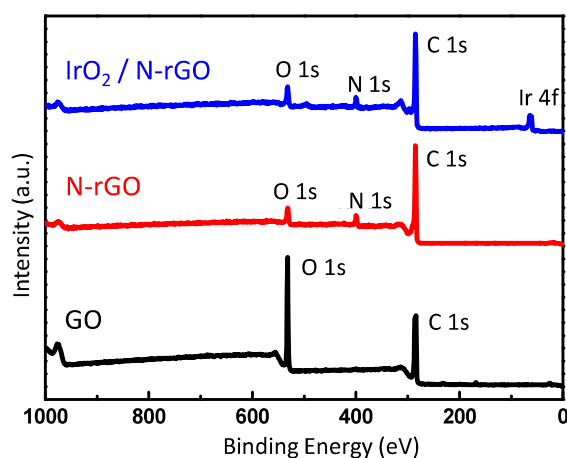


Figure 4. XPS survey spectra of GO, N-rGO, and IrO₂/N-rGO.

Chemical binding states and relative amount of various nitrogen species present in the aerogel substrate before and after IrO₂ decoration were analyzed by deconvolution of N 1s XPS spectra. Figure 5 shows deconvolution N 1s spectra of N-rGO and the IrO₂/N-rGO catalyst. Deconvolution of the N 1s spectra revealed that both N-rGO and IrO₂/N-rGO contains three different types of nitrogen entities, namely pyridinic, pyrrolic, and graphitic type. The peaks of pyridinic N, pyrrolic N, and graphitic N were located at 398.3, 399.6, and 401.3 eV, respectively (22,31). On the other hand, N-oxide peak was not observed, because synthesis of N-rGO and IrO₂/N-rGO was done under reduced condition. For IrO₂/N-rGO, the position of each peak is a similar as that of N-rGO and peak shift is less than 0.1 eV for all nitrogen types after hydrothermal reaction. The position of the N 1s peaks is also similar as that of IrO₂ deposited nitrogen-doped carbon nanotube prepared by hydrothermal method (32).

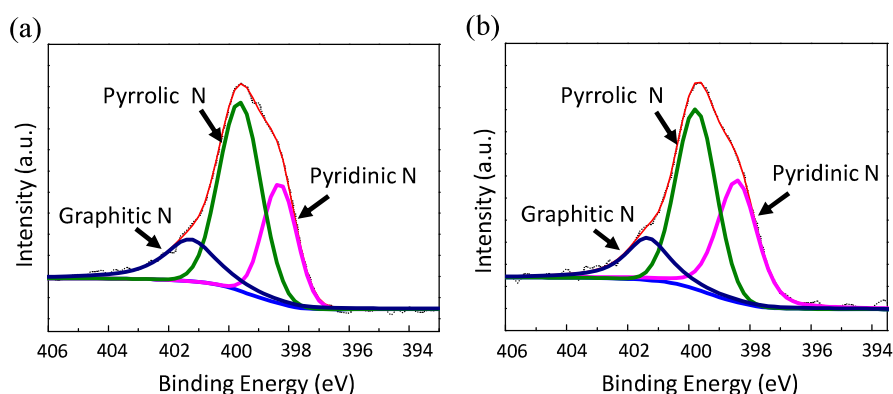


Figure 5. Deconvolution spectra of XPS N 1s peak of (a) N-rGO and (b) IrO₂/N-rGO.

In regard to nitrogen component, the previous reports for ORR demonstrated that the pyridinic N and graphitic N are electrocatalytically active sites (22,23). However, the effects for water electrolysis on IrO₂ is remained to be elucidated and we will discuss it in future work. Table 1 shows the relative content of various nitrogen components on N-rGO and IrO₂/N-rGO. For both of N-rGO and IrO₂/N-rGO, nitrogen functional structure mainly possesses the pyrrolic N group. Amount of catalytically active pyridinic and graphitic types of nitrogen was found to be nearly 50 at% in both N-rGO and IrO₂/N-rGO samples. However, the pyridinic type was found to be increased after deposition of the IrO₂ nanoparticles. The structural change of nitrogen functional group toward pyridinic N was proceeded during hydrothermal reaction, suggesting that pyridinic N group is more stable than other groups. A re-formation process of these nitrogen containing groups will be discussed in future works.

TABLE 1. Atomic percentage of various types of nitrogen species in both the samples.

	pyridinic N	pyrrolic N	graphitic N	N-oxide
N-rGO	27.0	52.5	20.5	0
IrO ₂ /N-rGO	36.3	46.9	16.8	0

Figure 6 shows deconvolution of core level Ir 4f spectra of the IrO₂/N-rGO, it consists of Ir 4f 5/2 and 7/2 peaks with three satellite peaks, shown as two solid lines and three dotted lines in figure 6, respectively (11,33). The XPS spectrum reveals that the deposited Ir is of Ir^{IV} oxidation state with rutile phase and it does not contain any metallic

Ir^0 or other oxidation state of Ir. The result confirms that the precursor Ir complex was completely transformed into metal oxide, IrO_2 , without any other metallic or hydrated forms. Furthermore, the binding energy of the Ir 4f peak was shifted to 0.8 eV lower energy state compared to that for unsupported IrO_2 , which is generally 61.9 eV (33). The peak shift reveals that the electron cloud shift from N-rGO aerogel to IrO_2 which is intrinsically electronegative in nature. This modulation of electronic state as well as interaction strengthen anchoring between deposited metal oxide and substrate. The strong interaction improves transport of electrons between the metal oxide and the substrate, enhancing the activity for OER and durability of the catalyst.

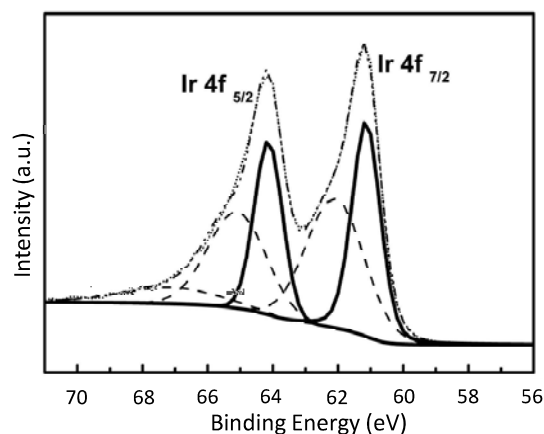


Figure 6. Deconvolution of XPS Ir 4f peak spectra of $\text{IrO}_2/\text{N-rGO}$.

Linear sweep voltammetry of the $\text{IrO}_2/\text{N-rGO}$ catalyst coated glassy carbon electrode was performed using RDE in nitrogen saturated 0.5 M H_2SO_4 to evaluate the electrocatalytic activity for OER. Figure 7 shows linear sweep voltammogram of the $\text{IrO}_2/\text{N-rGO}$ catalyst. Electrochemical measurement reveals high activity of the $\text{IrO}_2/\text{N-rGO}$ catalyst for OER. Onset potential of OER is ca. 1.43 V and its mass activity at 1.60 V is ca. 1000 A g^{-1} . The overvoltage of the $\text{IrO}_2/\text{N-rGO}$ catalysts is 70 mV lower than that of conventional IrO_2 powder or IrO_2 -graphene catalysts (12,15).

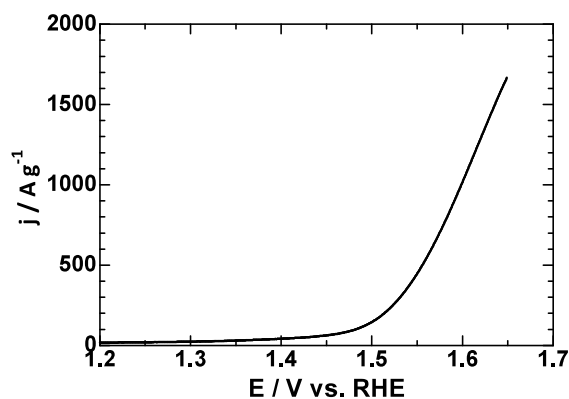


Figure 7. Linear sweep voltammogram of the $\text{IrO}_2/\text{N-rGO}$ catalyst in 0.5 M H_2SO_4 solution. Scan rate: 5 mV s^{-1} .

Modifying N-rGO with the fine nanoparticles will increase surface area of the IrO₂ catalyst, which improves its catalytic activity for OER. In addition, the N-rGO aerogel substrate could improve the electronic conductivity of the IrO₂ which is intrinsically semi-conductor in nature and enhances the electrocatalytic activity. Furthermore, the XPS results suggest a strong anchoring of the IrO₂ nanoparticle catalysts with that of the N-rGO aerogel substrate, which is expressed by modulation of the electronic structure of IrO₂ leading to easy mass transfer during the OER. Synergetic effect of morphological and electrical improvement of the IrO₂ catalyst might cause notable enhancement of its catalytic activity for OER (15). High activity of the IrO₂/N-rGO catalyst indicates that the IrO₂/N-rGO catalyst is a promising candidate of anode material for PEWE.

Conclusions

In this study, we synthesized a novel 3D electrocatalyst, IrO₂/N-rGO, in the form of aerogel to improve catalytic activity for OER. As the support materials for the catalyst, the nitrogen-doped graphene aerogel was hydrothermally prepared from graphene oxide, which was produced from graphite by modified Hummers' method. Finally, we obtained the IrO₂/N-rGO catalyst with 9 wt% of Ir by hydrothermal method. The prepared catalyst was characterized by TEM, XPS, and SEM-EDX and the successful synthesis of the IrO₂/N-rGO catalyst was confirmed. The IrO₂ nanoparticles are uniformly distributed on the N-rGO surface and the average particle size is ~1.2 nm. The analysis of the oxidation state of Ir reveals that the IrO₂ catalyst have Ir^{IV} oxidation state without any metallic Ir⁰ or other oxidation states. The electrochemical activity for OER of IrO₂/N-rGO was examined in 0.5 M H₂SO₄ solution. The IrO₂/N-rGO catalyst showed prospective OER performance, high catalytic activity and low onset potential. The high surface area and presence of the heteroatoms on the N-rGO substrates facilitate uniform dispersion of fine IrO₂ nanoparticles over the surface of N-rGO aerogel. The improved performance of the catalyst proposes that the IrO₂/N-rGO catalyst will be a promising candidate as OER catalyst for future water electrolysis system.

Acknowledgments

This work was supported by Japan Society for the Promotion of Science (JSPS) KAKENHI Grant number 17K05969 and Strategic Research Foundation Grant-aided Project for Private Universities from the Ministry of Education, Culture, Sport, Science, and Technology, Japan (MEXT).

References

1. T. R. Cook, D. K. Dogutan, S. Y. Reece, Y. Surendranath, T. S. Teets, and D. G. Nocera, *Chem. Rev.*, **110**, 6474 (2010).
2. J. Lee, B. Jeong, and J. D. Ocon, *Current Appl. Phys.*, **13**, 309 (2013).
3. M. Paidar, V. Fateev, and K. Bouzek, *Electrochim. Acta*, **209**, 737 (2016).
4. E. Antolini, *ACS Catal.*, **4**, 1426 (2014).
5. N.-T. Suen, S.-F. Hung, Q. Quan, N. Zhang, Y.-J. Xu, and H. M. Chen, *Chem. Soc. Rev.*, **46**, 337 (2017).

6. M. Carmo, D. L. Fritz, J. Mergel, and D. Stolten, *Int. J. Hydrogen Energy*, **38**, 4901 (2013).
7. J. Herranz, J. Durst, E. Fabbri, A. Patru, X. Cheng, A. A. Permyakova, and T. J. Schmidt, *Nano Energy*, **29**, 4 (2016).
8. T. Reier, M. Oezaslan, and P. Strasser, *ACS Catal.*, **2**, 1765 (2012).
9. A. Minguzzi, C. Locatelli, O. Lugaresi, E. Achilli, G. Cappelletti, M. Scavini, M. Coduri, P. Masala, B. Sacchi, A. Vertova, P. Ghigna, and S. Rondinini, *ACS Catal.*, **5**, 5104 (2015).
10. T. D. Nguyen, G. G. Scherer, and Z. J. Xu, *Electrocatalysis*, **7**, 420 (2016).
11. W. Sun, J.-Y. L., X.-Qing Gong, W.-Q. Zaman, L.-M. Cao, and J. Yang, *Sci. Reports*, **6**, 38429 (2016).
12. D. F. Abbott, D. Lebedev, K. Waltar, M. Povia, M. Nachttegaal, E. Fabbri, C. Copéret, and T. J. Schmidt, *Chem. Mater.*, **28**, 6591 (2016).
13. S. Siracusano, V. Baglio, C. D. Urso, V. Antonucci, and A. S. Aricò, *Electrochim Acta*, **54**, 6292 (2009).
14. V. K. Puthiyapura, S. Pasupathi, H. Su, X. Liu, B. Pollet, and K. Scott, *Int. J. Hydrogen Energy*, **39** 1905 (2014).
15. F.-D. Kong, S. Zhang, G.-P. Yin, J. Liu, and Z.-Q. Xu, *Int. J. Hydrogen Energy*, **38**, 9217 (2013).
16. R. Badam, M. Hara, H.-H. Huang, and M. Yoshimura, to be submitted.
17. Y. K. Zhou, K. Neyerlin, T. S. Olson, S. Pylypenko, J. Bult, H. N. Dinh, T. Gennett, Z. P. Shao, and R. O'Hayre, *Energy Environ. Sci.*, **3**, 1437 (2010).
18. H. Wang, T. Maiyalagan, and X. Wang, *ACS Catal.*, **2**, 781 (2012).
19. F. Razmjooei, K. P. Singh, D.-S. Yang, W. Cui, Y. H. Jang, and J.-S. Yu, *ACS Catal.*, **7**, 2381 (2017).
20. Z.-S. Wu, S. Yang, Y. Sun, K. Parvez, X. Feng, and K. Müllen, *J. Am. Chem. Soc.*, **134**, 9082 (2012).
21. Z. B. Lei, M. Y. Zhao, L. Q. Dang, L. Z. An, M. Lu, A. Y. Lo, N. Y. Yu, and S. B. Liu, *J. Mater. Chem.*, **19**, 5985 (2009).
22. S. Pylypenko, A. Queen, T. S. Olson, A. Dameron, K. O'Neill, K. C. Neyerlin, B. Pivovar, H. N. Dinh, D. S. Ginley, T. Gennett, and R. O'Hayre, *J. Phys. Chem. C*, **115**, 13667 (2011).
23. W. He, P. Xue, H. Du, L. Xu, M. Pang, X. Gao, J. Yu, Z. Zhang, T. Huang, *Int. J. Hydrogen Energy*, **42**, 4123 (2017).
24. X. G. Li, S. Park, and B. N. Popov, *J. Power Sources*, **195**, 445 (2010).
25. C. Jackson, G. T. Smith, D. W. Inwood, A. S. Leach, P. S. Whalley, M. Callisti, T. Polcar, A. E. Russell, P. Levecque and D. Kramer, *Nature Commun.*, **8**, 15802 (2016).
26. J. Zhang, C. Li, Z. Peng, Y. Liu, J. Zhang, Z. Liu, and D. Li, *Sci. Reports*, **7**, 4886 (2017).
27. B. Garg, T. Bisht, and Y.-C. Ling, *Molecules*, **19**, 14582 (2014).
28. W. S. Hummers and R. E. Offeman, *J. Am. Chem. Soc.*, **80**, 1339 (1958).
29. K. K. H. De Silva, H.-H. Huang, R. K. Joshi, and M. Yoshimura, *Carbon*, **119**, 190 (2017).
30. R. Badam, R. Vedarajan, and N. Matsumi, *Chem. Comm.*, **51**, 9841 (2015).
31. C. Xu, Y. Su, D. Liu and X. He, *Phys. Chem. Chem. Phys.*, **17**, 25440 (2015).
32. Y. Zhang, X. Li, M. Zhang, S. Liao, P. Dong, J. Xiao, Y. Zhang and X. Zeng, *Ceram. Int.*, **43**, 14082 (2017).

33. V. Pfeifer, T. E. Jones, J. J. V. Vélez,ac C. Massué, M. T. Greiner, R. Arrigo, D. Teschner, F. Girgsdies, M. Scherzer, J. Allan, M. Hashagen, G. Weinberg, S. Piccinin, M. Hävecker, A. Knop-Gericke, and R. Schlöglac, *Phys. Chem. Chem. Phys.*, **18**, 2292 (2016).

Available online at www.sciencedirect.com

ScienceDirect

journal homepage: www.elsevier.com/locate/he

Synthesis and electrochemical analysis of novel IrO₂ nanoparticle catalysts supported on carbon nanotube for oxygen evolution reaction

Rajashekar Badam, Masanori Hara*, Hsin-Hui Huang, Masamichi Yoshimura

Toyota Technological Institute, 2-12-1 Hisakata, Tempaku, 468-8511 Nagoya, Japan

ARTICLE INFO

Article history:

Received 24 April 2018

Received in revised form

23 June 2018

Accepted 7 August 2018

Available online 29 August 2018

Keywords:

Water electrolysis

Oxygen evolution reaction

Iridium oxide

Carbon nanotube

ABSTRACT

In this paper, we report synthesis of novel nanoparticle catalyst of iridium oxide supported on carbon nanotube (IrO₂/CNT) and characterization of activity and durability for oxygen evolution reaction (OER). The IrO₂/CNT catalyst was prepared from iridium complex and COOH-CNT by hydrothermal method. The synthesized IrO₂/CNT catalysts were characterized by transmission electron microscopy, x-ray diffraction, Raman microscopy, Fourier transfer-infrared spectroscopy, x-ray photoelectron spectroscopy, thermogravimetric analysis and electrochemical methods. The average particle size of the IrO₂ particles on CNT is 1.7 nm and the loading amount of IrO₂ is 4 wt%. The XPS measurement reveals that Ir complex was completely converted to iridium oxide through hydrothermal treatment. The IrO₂/CNT catalyst showed sufficient performance for OER activity and durability in sulfuric acid solution. Our results indicate that IrO₂/CNT is one of the prospective candidate catalysts for water electrolyzer.

© 2018 Hydrogen Energy Publications LLC. Published by Elsevier Ltd. All rights reserved.

Introduction

Recent years, the development of sustainable societies with renewable energies has become important topic to overcome environmental issues, such as global warming and depletion of fossil fuels. In order to utilize effectively the renewable energies possessing the nature of volatile output power, such as wind-powered electricity and solar cells, conversion of the surplus energies to hydrogen via water electrolysis has attracted attention as a candidate of energy storage systems [1–4]. Polymer electrolyte water electrolyzer (PEWE), which is composed of polymer electrolyte, Pt/C cathode, and iridium oxide as anode, is one of the water electrolysis systems [5,6].

The PEWE system is one of the cleanest way to produce hydrogen, and its advantages are operation at high current density, which represents production of higher amount hydrogen per cell size, fast response to electricity fluctuation, and simple structure similar to PEFC. Thus PEWE is expected as a next generation hydrogen production system. However, in water electrolysis systems, activity, durability, and cost of catalysts are insufficient for practical application due to high over-potential and low kinetics of electrode reactions, especially, oxygen evolution reaction (OER) at the anode [5,7,8].

At the anode of the PEWE cell, oxygen and proton are produced by splitting water. Oxide of Iridium, which is one of the Pt group metals, has been used as electro-catalysts for OER because Iridium oxide shows second best activity amongst

* Corresponding author.

E-mail address: haram@toyota-ti.ac.jp (M. Hara).

<https://doi.org/10.1016/j.ijhydene.2018.08.034>

0360-3199/© 2018 Hydrogen Energy Publications LLC. Published by Elsevier Ltd. All rights reserved.

metal oxide catalysts [9–18], whereas RuO₂, most active catalysts, has poor durability [19–21]. The phenomena for water splitting, such as reaction pathway and catalytic activity, on metals or metal oxides, including IrO₂, are theoretically discussed by many research groups [21–27]. They reported that binding or adsorption free energy of oxygen species, HOO*, O*, HO*, as well as oxygen vacancy on surface are important factors for OER [25–27]. As electrode for OER or water electrolyzer, in general, iridium dioxide (IrO₂) powder catalyst without support have been used as anode [11,12,15–18], and the diameter of traditional IrO₂ powder catalysts is 5–30 nm. Therefore, a loading amount of IrO₂ is high and specific surface area, surface area per weight, is low. Mass activity, activity per weight, is an important index for precious metal catalysts and estimated by multiply specific surface area by specific activity, activity per surface area. Whereas the IrO₂ powder catalyst has high durability, mass activity of the catalyst is low due to low specific surface area. To commercialize the PEWE cell, improving mass activity and reducing the loading amount of iridium are important topics. Many researchers demonstrated improvement of catalytic activity by alloying the IrO₂ catalysts [28–38]. Other approach to improve mass activity is increment of specific surface area of OER catalysts by employing nanoparticle catalyst. In theory, specific surface area is depended on particle size of a catalyst, therefore stable and conductive materials are employed as support materials of nanoparticle catalysts to increase the surface area and suppress agglomeration of the catalyst nanoparticles. Carbon black, graphene, and conductive oxide were examined as support materials for IrO₂ catalysts [39–46]. It is well known that carbon materials have high surface area and high conductivity, and is one of the most standard support materials for electrodes. However, a carbon black is unstable at the potential region where oxygen evolution reaction takes place, and carbon supported IrO₂ catalyst was tested as cathode catalyst for hydrogen evolution reaction (HER) [39]. Nano carbon materials such as carbon nanotube (CNT) possess higher durability because of its high crystallinity, high chemical and mechanical stability [47–49]. The strategy of our research is utilization of nanocarbon as supporting materials to control the size of IrO₂ nanoparticles. The nanocarbon supports will improve specific surface area of the IrO₂ nanoparticles and increase electron conductivity of the catalysts, as used for electrodes of LiO₂ battery [50], supercapacitor [51], and direct methanol fuel cell [52].

Recently, CNTs have been used as a substrate of electrocatalyst, for example cathode catalysts for oxygen reduction reaction of polymer electrolyte fuel cell, empirically and theoretically [52–59]. The Pt nanoparticles deposited CNT catalysts showed high activity and durability for oxygen reduction reaction, because CNT has high chemical stability and conductivity [53–55]. However, it is difficult to deposit high loading amount of size controlled-catalysts on a CNT substrate due to lower number of defect sites where catalyst particles nucleate. For water electrolysis, CNT has not been employed as a substrate materials because it is difficult to modify CNT with highly dispersed IrO₂ nanoparticles. In addition, stability of the CNT support and catalyst particles on CNT is not clarified under a reaction potential where oxygen evolution is performed. The clarification of degradation

mechanism is also important topic for development of the catalysts for OER.

In this study, we have prepared novel nanoparticle catalysts of IrO₂ supported on multi-walled carbon nanotube (MWCNT) by hydrothermal method. The MWCNT substrate is modified with carboxyl groups as nucleation site for IrO₂ deposition and the oxidized MWCNT is reduced during hydrothermal reaction. The IrO₂/CNT catalyst is characterized as a novel anode catalyst for water electrolysis and performance of OER activity is evaluated.

Materials and methods

Synthesis of the catalyst

The IrO₂/CNT catalyst was synthesized by hydrothermal method. Commercial MWCNT (MTR Ltd.) with diameter of 10–20 nm was used as substrate for IrO₂. Firstly, CNT was functionalized with COOH functional group to improve the nucleation sites and to enhance metal oxide-substrate interaction [60]. For this CNT was ultra-sonicated in 3:1 (vol/vol) mixture of concentrated sulfuric acid and nitric acid solution at room temperature for 90 min. Then, required amount of H₂IrCl₆·nH₂O complex (Wako Pure chemical Industries, Ltd.) and oxidized CNT (CNT-COOH) were dispersed in 9:1 (vol/vol) ethanol/water mixture solution. The mixture was heated at 80 °C for 6 h with constant stirring and then hydrothermally treated at 150 °C in a hydrothermal autoclave for 4 h [61]. The resulting material was filtered and washed with 9:1 (vol/vol) ethanol/water mixture solution. Further, the sample was dried up in vacuum oven at 120 °C for 4 h. Commercial IrO₂ powder catalyst was purchased from Alfa Aesar and commercial Ir metal powder was purchased from Sigma-Aldrich Co. All commercial catalysts were used for measurements as received.

Characterization of catalyst

The crystal structure of the synthesized IrO₂/CNT catalyst was characterized by X-ray diffraction (XRD, Ultima4, Rigaku Co.) with Cu K α radiation (0.15405 nm). The morphology and distribution of IrO₂ nanoparticles deposited on the CNT supports were analyzed by transmission electron microscopy (TEM, JEM-2100, JEOL), operated at 120 kV. The loading amount of IrO₂ on CNT was estimated by scanning electron microscopy (SEM, SU3500, Hitachi High Technologies Co.) with an energy dispersive X-ray spectrometry (EDX, EMAX Evolution X-Max, Horiba). X-ray photoelectron spectroscopy (XPS, PHI5000 Versa Probe II, ULVAC-PHI) with Al K α radiation (1486.6 eV) was utilized for the analysis of surface elementals and their electron states. The structure of the support CNT was investigated by a Raman microscope (InVia Raman Microscope, Renishaw plc.) using a 532 nm excitation laser. A 1800-line mm⁻¹ grating, a Peltier-cooled CCD camera, and 50 × magnification objective were utilized for Raman microscopy. The infrared spectroscopic measurements were conducted by a fourier transfer infrared (FTIR) spectrometer (FT/IR6200, JASCO Co.) equipped with an MCT detector. The spectral resolution was set at 2 cm⁻¹. All the measurements

were conducted with unpolarized infrared radiation. The loading amount of IrO₂ nanoparticles decorated on the CNT substrates was confirmed by a thermogravimetric (TG) measurement (DTG-60H, Shimadzu Co.) in air. Aluminum powder was used as a reference material for weight balance. The temperature of sample was increased at a rate of 2 °C/min and the sample was heated till 700 °C.

Electrochemical measurement

The preparation method for working electrodes was similar to that of our previous works [61]. Briefly, IrO₂/CNT catalyst ink was prepared using a mixture of isopropyl alcohol, water and Nafion. An appropriate amount of the ink was taken and drop casted on the glassy carbon (GC, 5 mm in diameter) disk electrode as substrate of rotating disk electrode (RDE) to form a thin film containing 15 µg of Ir (0.076 mg_{Ir} cm⁻²). As-prepared electrode was dried in vacuum oven at 60 °C for 30 min. The OER catalytic activity of the IrO₂/CNT catalysts was measured by linear sweep voltammetry (LSV) with RDE equipment in 0.1 M H₂SO₄ (Kanto Chemical Co.) solution at room temperature. The hydrodynamic voltammograms were recorded by sweeping the potential from 1.20 to 1.65 V vs. reversible hydrogen electrode (RHE) at scan rate of 5 mV s⁻¹ and rotation rates of 1600 rpm in nitrogen saturated 0.1 M H₂SO₄. Cycle characteristic and durability of the catalysts were evaluated by cyclic voltammetry (CV) and chronopotentiometry. The CV measurement was performed between 1.20 and 1.65 V vs. RHE for 2500 cycles at a scan rate of 50 mV s⁻¹ and rotation rate of 1600 rpm. On the other hand, chronopotentiometry was carried out at a current density of 10 mA cm⁻² for 3 h. For the electrochemical measurement, a platinum wire and Ag/AgCl electrode in 3 M KCl solution were used as a counter electrode and reference electrode, respectively. A potentiostat (HSV-110, Hokuto Denko Co.) was utilized for the LSV and CV measurements. The RDE measurement was performed by RRDE-3A instrument (BAS Inc.). Before the LSV and CV measurement, the electrolyte solution was purged with nitrogen gas for 30 min.

Results and discussion

Fig. 1 shows TEM micrograph of the IrO₂ nanoparticles decorated on the CNT catalysts. Fig. 1(a) shows the IrO₂ nanoparticles deposited on the surface of MWCNTs with different diameters of tubes. The deposited IrO₂ nanoparticles were observed as spherical dark spots. Fig. 1(b) shows that the nanoparticles of IrO₂ are homogeneously dispersed all over surface layer of the CNT substrate. A histogram of the IrO₂ nanoparticles size distribution is shown in Fig. 1(c). An average size of the IrO₂ nanoparticles is 1.7 ± 0.3 nm. Specific surface area estimated from the diameter of IrO₂ nanoparticles is 303 m²/g. On the other hand, particle size of commercial IrO₂ powder or Ir metal powder without support substrate, shown in Figure S1 and S2, respectively, is one to two orders of magnitude larger than that of the IrO₂ nanoparticles on CNT. Because specific surface area is proportional to the reciprocal diameter of particles, the commercial IrO₂ and Ir metal powders are suggested to have one to two orders

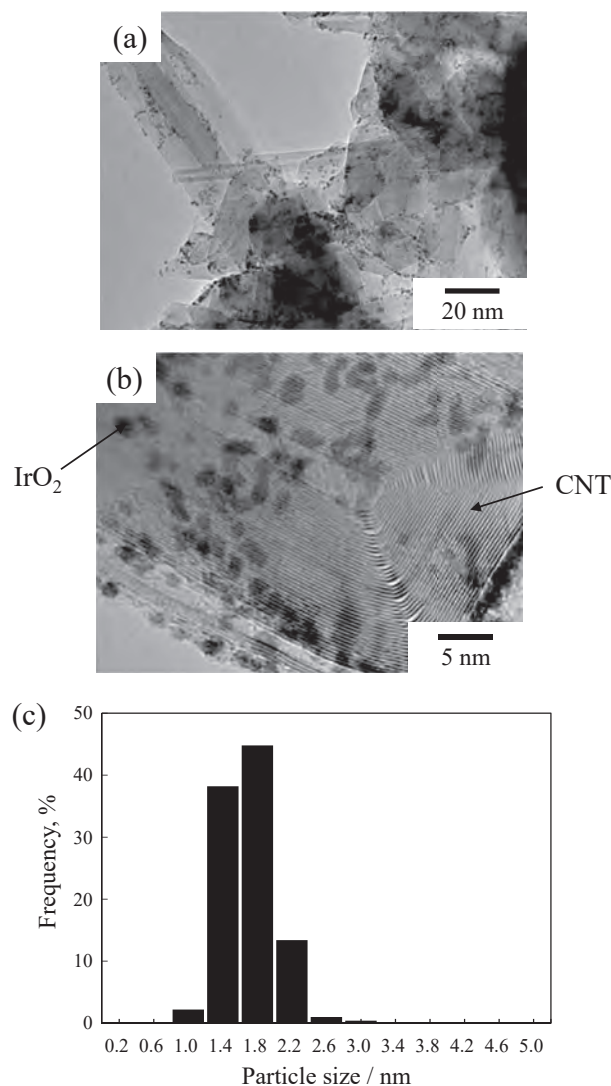


Fig. 1 – (a) The large scale and (b) magnified TEM micrographs of IrO₂/CNT showing the multi-layered nature of CNT and IrO₂ nanoparticles decorated on CNT. (c) The particle size distribution histogram of IrO₂ nanoparticles on CNT supports.

of magnitude lower specific surface area than the IrO₂ nanoparticles. Fig. 2(a) shows high-resolution TEM image of the IrO₂/CNT catalyst. Lattice fringes of IrO₂ nanoparticle and CNT layer were observed. The intensity profiles across the IrO₂ and CNT, plotted in Fig. 2(b), are analyzed to estimate lattice spacings of IrO₂ and CNT. The average lattice spacings of IrO₂ nanoparticle and CNT are 0.220 ± 0.010 and 0.333 ± 0.019 nm, respectively. The lattice spacing of IrO₂ corresponds to the (020) plane of the IrO₂ rutile structure [62]. In contrast, the average lattice spacings of commercial IrO₂ and Ir metal powders observed in high-resolution TEM images, Figure S1 and S2, are 0.304 ± 0.021 and 0.345 ± 0.024 nm, respectively, which correspond to the (110) plane of IrO₂ rutile and the (100) plane of the Ir face centered cubic structure. The TEM result indicates that the catalysts with uniform distribution of the IrO₂ nanoparticles on CNT was successfully synthesized by hydrothermal method. In addition, the loading amount of Ir

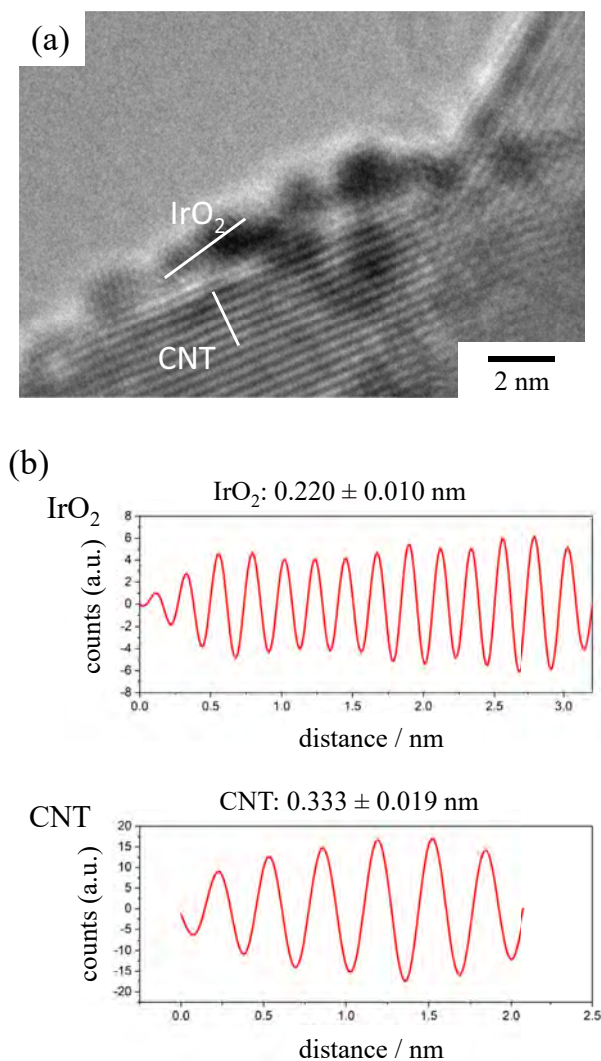


Fig. 2 – (a) High-resolution TEM micrographs of IrO₂/CNT showing lattice spacing of IrO₂ and CNT. (b) Cross section analysis of lattice spacing of IrO₂ and multi-wall CNT. Analyzed positions are indicated by white line in high-resolution TEM image.

estimated by using SEM-EDX was determined to be 4 wt% on the CNT substrate.

Fig. 3(a) shows XRD patterns of the catalyst and support materials to analyze the crystal structure of MWCNT during the synthesis. The 2θ peak at 26.1° , 42.3° , 53.6° and 77.5° are corresponding to the diffraction of CNT, (002), (101), (100) and (110) reflection, respectively [55,63]. No major peak shift was observed on the XRD patterns of pristine, oxidized, and IrO₂ supported CNT, suggesting that any crystallinity change of the CNT substrate was hardly occurred during the synthesis. Fig. 3(b) shows enlarged XRD patterns of CNT, COOH-CNT, and IrO₂/CNT. A small broad peak around 40° resulted from a diffraction of nanoparticles was observed only on IrO₂/CNT and the peak was overlapped with the diffraction peak of CNT (101) at 42.3° . The broad peak around 40° can be ascribed to (020) plane of IrO₂ rutile crystal, which is also shown on XRD

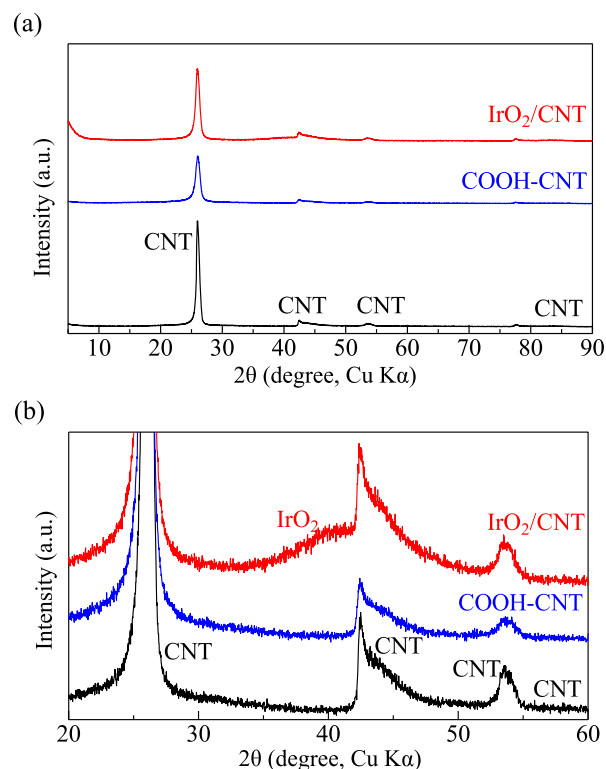


Fig. 3 – (a) The XRD patterns of CNT (black line), oxidized CNT (blue line), and IrO₂/CNT (red line) catalyst and (b) extended XRD patterns. (For interpretation of the references to color/colour in this figure legend, the reader is referred to the Web version of this article.)

pattern of the commercial IrO₂ powder in Figure S3(a). In addition, the appearance of peak for the (020) plane is consistent with the result of lattice space analysis in high resolution TEM image, as shown in Fig. 2. However, the Ir metal powders also have (111) peak around 41° , as shown in

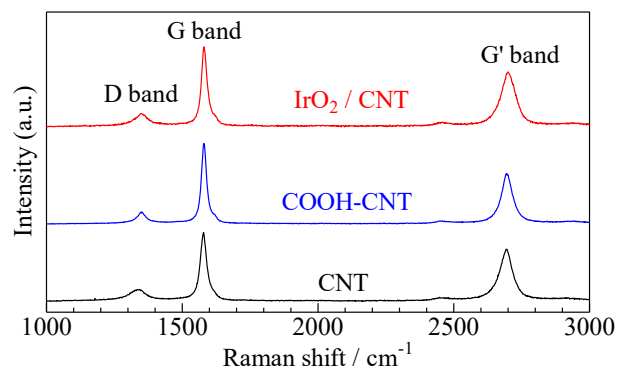


Fig. 4 – Raman spectra, using a 532 nm excitation laser, of CNT (black line), oxidized CNT (blue line), and IrO₂/CNT (red line) showing characteristic D, G and G' bands of CNT. (For interpretation of the references to color/colour in this figure legend, the reader is referred to the Web version of this article.)

Figure S3(b). The nanoparticles generally have broad peaks on XRD pattern and identification of peak around 40° has ambiguity.

Fig. 4 shows Raman spectra of CNT, COOH-CNT, and IrO₂/CNT. No change in the peak position and intensity suggests that either acid functionalization or the IrO₂ decoration hardly changed the crystallinity of CNT through the synthesis. The results are consistent with the XRD results, as shown in Fig. 2.

To identify the type of functional group formed on the acid treated CNT, FTIR spectra of pristine, oxidized and IrO₂ supported CNT were obtained, as shown in Fig. 5. A peak around 3400 cm^{-1} corresponding to COOH functional group [63,64], as denoted by a red arrow on the spectrum of oxidized CNT, was appeared in the spectrum of acid treated CNT. However, this peak was disappeared for IrO₂/CNT. The FTIR measurement indicates COOH functional groups were formed on the wall of CNT upon acid treatment to CNTs and COOH functional groups were completely reduced after hydrothermal synthesis process.

Fig. 6(a) shows XPS spectra of CNT and the catalyst, survey XPS spectra of the pristine CNT, the oxidized CNT, and the IrO₂ supported CNT materials. To analyze chemical state of IrO₂ nanoparticles in detail, deconvolution spectrum of the Ir 4f peak of the IrO₂/CNT catalyst are shown in Fig. 6(b). In the survey spectra, the pristine CNT contains only C 1s peak, whereas O 1s peak appears after the oxidation of CNT because of the modification of CNT with COOH functional groups. After hydrothermal procedure, Ir 4f peak with corresponding binding energies for IrO₂ nanoparticles is observed. On XPS survey spectrum of the commercial IrO₂ powder, as shown in Figure S4(a), we observed peaks of Ir element, O 1s peak, as well as Cl 2p as an impurity of the IrO₂ powder. On the other hand, no impurity was detected on the IrO₂/CNT catalyst. Iridium loading amount of IrO₂/CNT is 4 wt%, which is estimated from the intensity of Ir 4f peak. The Ir loading amount

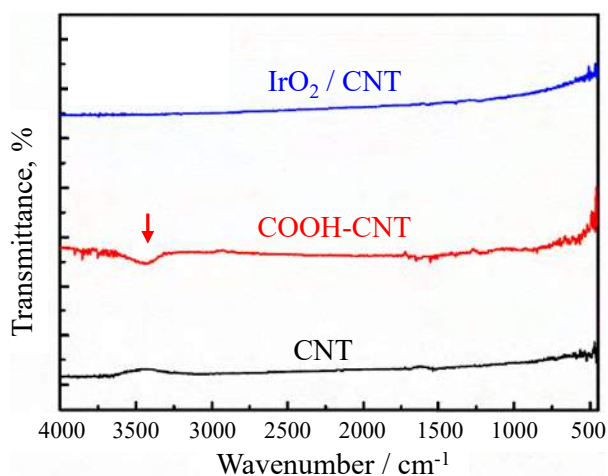


Fig. 5 – FT-IR spectra of CNT (black line), oxidized CNT (red line), and IrO₂/CNT (blue line) reveals the presence of COOH groups in COOH-CNT and not in CNT and IrO₂/CNT. Red arrow at 3400 cm^{-1} corresponds to COOH functional group on CNT. (For interpretation of the references to color/colour in this figure legend, the reader is referred to the Web version of this article.)

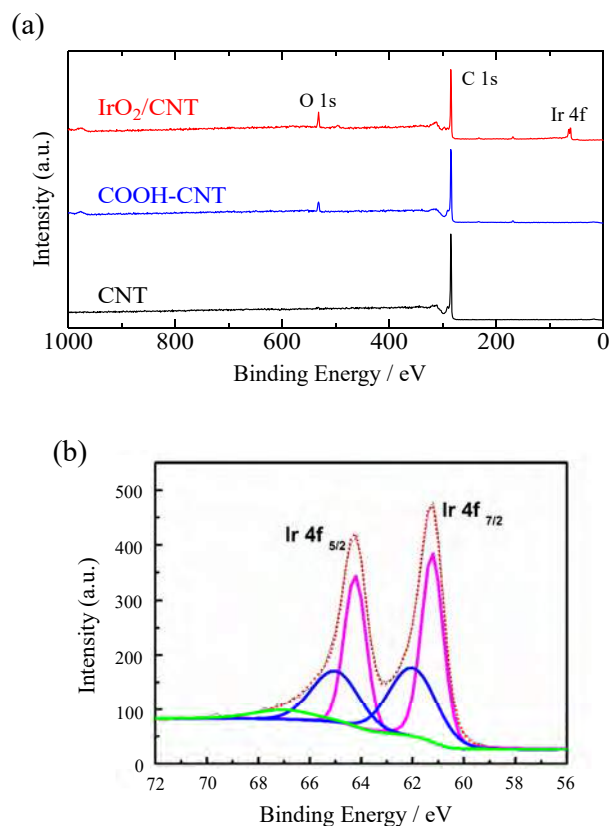


Fig. 6 – (a) XPS spectra of CNT (black line), oxidized CNT (blue line), and IrO₂/CNT (red line). (b) Expanded Ir 4f peak of XPS spectrum (red dotted line) and deconvolution of Ir 4f peak (fit envelope: black dotted line) for IrO₂/CNT. Ir 4f_{7/2} and 4f_{5/2} peaks on the spectrum are deconvoluted to two main peaks (pink line) and three satellite peaks (blue and green line). (For interpretation of the references to color/colour in this figure legend, the reader is referred to the Web version of this article.)

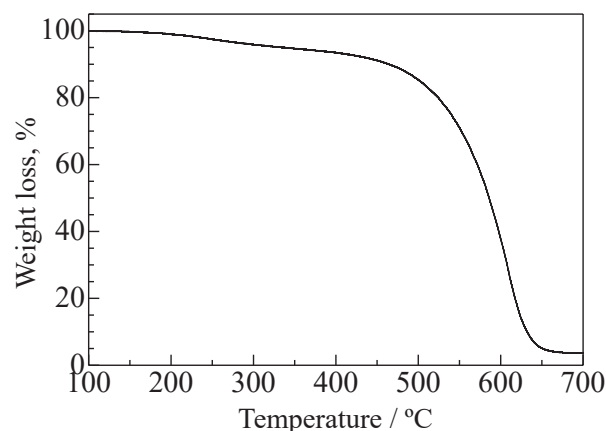


Fig. 7 – Thermogravimetric analysis of the IrO₂/CNT catalyst from 100 to 750 °C in air. Temperature increasing rate: 2 °C/min.

obtained from Fig. 6(a) is consistent with that by SEM-EDX analysis (3.8 wt%). In addition, we confirmed loading amount of IrO₂ on CNT by thermogravimetric analysis, as shown in Fig. 7. The loading amount of Ir measured by TG, 3.4 wt%, is also consistent with XPS and SEM-EDX analysis. Fig. 6(b) shows the deconvolution spectrum of the Ir 4f peak on the IrO₂/CNT catalyst. The deconvoluted spectrum consists of Ir 4f_{5/2} and 4f_{7/2} peaks at 64.2 and 61.3 eV, respectively, with three satellite peaks at 67.2, 65.1, and 62.1 eV, respectively, and bended background base line [65]. To compare electronic state of Ir in the deposited nanoparticles and commercial IrO₂ or Ir metal particle, XPS Ir 4f peak of the both particles are shown in Figure S4(b) and 4(c), respectively. The spectrum in Fig. 6(b) shows that Ir element with Ir 4f peaks at 64.2 and 61.3 eV is in the form of Ir^{IV} oxidation state on IrO₂/CNT, without any traces of Ir⁰, which possess binding energy of 63.8 and 60.8 eV as shown in Figure S4(c), or other oxidation states, 65.4 and 62.4 eV for Ir^{III} [65]. The XPS results imply that the Ir precursor complex is completely transformed into IrO₂ without the hydrated form [65,66]. These deconvolution results also confirm that the IrO₂ particles decorated on CNT have rutile structure [65]. It is noteworthy here that the binding energy of Ir 4f was shifted by 0.6–0.7 eV compared to unsupported IrO₂, as shown in Figure S4(b), where peak positions of Ir 4f_{5/2} and 4f_{7/2} are 64.8 and 61.8 eV, respectively [65]. We suggest that IrO₂ is more electronegative than CNT and electron cloud is shifted towards IrO₂ from the peak shift of Ir 4f. This electronic interaction is generally called as strong metal substrate interaction, and the interaction is one of the key factors determining the electrocatalytic activity as well as the durability of the catalyst [67].

To evaluate the electrocatalytic OER activity of IrO₂/CNT, linear sweep voltammetry was performed in 0.1 M H₂SO₄. Fig. 8(a) and (b) show LSV and Tafel plot of the IrO₂/CNT catalyst. In addition, CV of double-layer capacity region is shown in Figure S6, where no specific peak was observed expect for charging capacity of CNT substrate and the IrO₂ nanoparticles surface. The current density of IrO₂/CNT was found to be ~42 mA cm⁻² at 1.65 V vs RHE, which is nearly 40 times compared to the IrO₂ powder catalyst [18]. The onset potential is found to be around 1.42 V, which value is 80 mV less compared to the IrO₂-graphene catalyst [40]. In Fig. 8(b), the Tafel slope is around 60 mV dec⁻¹, which is consistent with that of IrO₂ powder catalyst [9,10,18]. Recently, Audichon et al. reported IrO₂@RuO₂ core-shell nanoparticles show ~6 mA cm⁻² at 250 mV of overpotential in H₂SO₄ [43]. The IrO₂/CNT catalyst shows nearly 1.16 times higher current density at 250 mV of overpotential, while the loading weight of the catalyst metals, such as Ir or Ir + Ru, on the working electrode is nearly 5 times lesser than that of a previous result. We also compare the catalytic activity of IrO₂/CNT with recently reported high activity catalysts decorated on various conducting substrates in Table 1 [44–46]. Two important and conventionally used parameters for electrocatalysts are the mass activity at a given overpotential, here 250 mV (potential 1.48 V), and the overpotential required to achieve a specific current density, here 10 mA/cm² in geometrical area. Table 1 shows that the IrO₂/CNT catalyst has nearly 9–20 times higher mass activity at 1.48 V compared to various recent reports on IrO₂ based materials and exhibits less overpotential

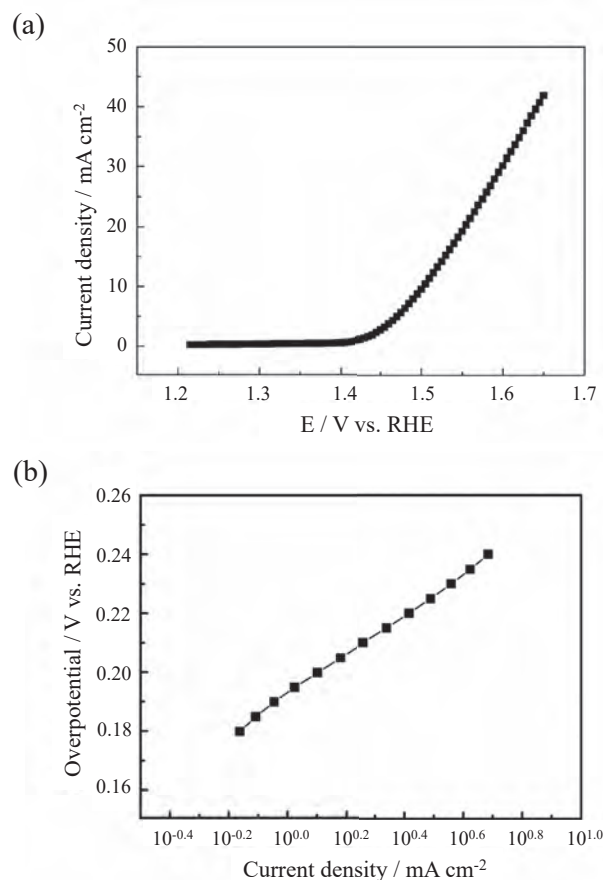


Fig. 8 – (a) Linear sweep voltammogram of the IrO₂/CNT catalyst in 0.1 M H₂SO₄. Scan rate: 5 mV s⁻¹. Loading amount of Ir: 76 μg cm⁻². (b) Tafel plot of OER on the IrO₂/CNT catalyst estimated from LSV curve.

for achieving 10 mA/cm², around 12 and 50 mV lesser than that on nanoporous IrO₂ and IrO₂/Pt, respectively. While Ir metal content is as small as ~4 wt% in the material, the IrO₂/CNT catalyst with both high activity and low overpotential indicates the potential of commercial viability. The IrO₂ catalyst has semiconducting electronic properties, therefore improving the electronic conductivity will enhance the electrocatalytic activity by reducing the overpotential. It is also well known that the specific surface area of the catalysts plays a major role in its catalytic activity. The LSV curve of the commercial IrO₂ powder with large average particle size is shown in Figure S5. The current density on the commercial IrO₂ is around 40 times smaller than that on IrO₂/CNT because of its small specific surface area, regardless Ir metal loading amount on the GC electrode is 1.7 times higher than that of IrO₂/CNT. Both the above strategies are established by decorating ultra-small IrO₂ nanoparticles uniformly on conducting substrate like CNT. In addition, the XPS results reveals that the electronic structure of IrO₂ is also modulated by strong anchoring with CNT to ease the electron transport on the IrO₂ electrode surface during OER.

Further, the durability of the IrO₂/CNT was investigated by the accelerated degradation test (ADT) by potential cycling and chronopotentiometry. In ADT experiment, working

Table 1 – List of OER activity of IrO₂ catalysts reported in recent papers. Mass activity is obtained at 1.48 V (at 250 mV of overpotential) and the value of overpotential is measured at 10 mA/cm².

Catalyst	Loading (mg/cm ²)	Electrolyte	Mass activity (A/g)	Overpotential at 10 mA/cm ²	Reference
IrO ₂ /CNT	0.076 (Ir)	0.1 H ₂ SO ₄	88	270	This work
Pt/IrO ₂	0.3 (Ir)	0.5 H ₂ SO ₄	5	330	[44]
IrO ₂	0.38 (IrO ₂)	0.5 H ₂ SO ₄	9.6	282	[45]
IrOx-Ir	0.13 (IrOx-Ir)	0.5 H ₂ SO ₄	8	–	[44]
Ir/Ti4O7	0.033 (Ir)	0.5 H ₂ SO ₄	4.2	–	[46]

electrode with the IrO₂/CNT catalyst was subjected to 2500 cycles between 1.30 and 1.65 V at the scan rate of 50 mV s⁻¹. The LSV measurement was performed before and after the potential cycling to observe the difference in the performance. Fig. 9(a) shows the LSV results before and after 1000 and 2500 potential cycles. The voltammograms reveal that the IrO₂/CNT catalyst showed promising durability and sustained nearly 80% of initial current density even after 2500 potential cycles. Our results suggest that the IrO₂/CNT catalyst has high durability in the potential region between 1.20 and 1.65 V vs. RHE. Durability of the catalyst was also studied by

chronopotentiometry as shown in Fig. 9(b). The potential was monitored at 10 mA cm⁻², and found to be very stable over a period of 3 h. In this study, we examined our sample only 3 h by chronopotentiometry as a primary durability test. In our future work, we will extend examination period, especially in actual water electrolyzer with our catalyst. Fig. 10 shows large scale and magnified TEM images of the IrO₂/CNT catalyst after the durability test of 2500 potential cycles. For IrO₂ powder catalyst, degradation of the catalyst was proceeded by agglomeration and increase of particle size of the IrO₂

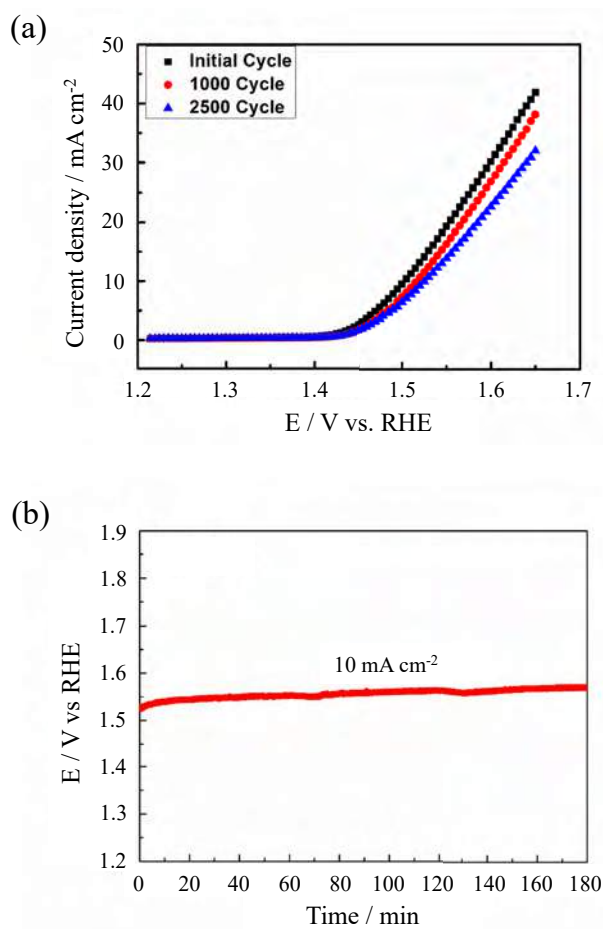


Fig. 9 – (a) Current density change of linear sweep voltammogram on the IrO₂/CNT catalyst during durability test. (b) Chronopotentiometry measurement of IrO₂/CNT at 10 mA cm⁻².

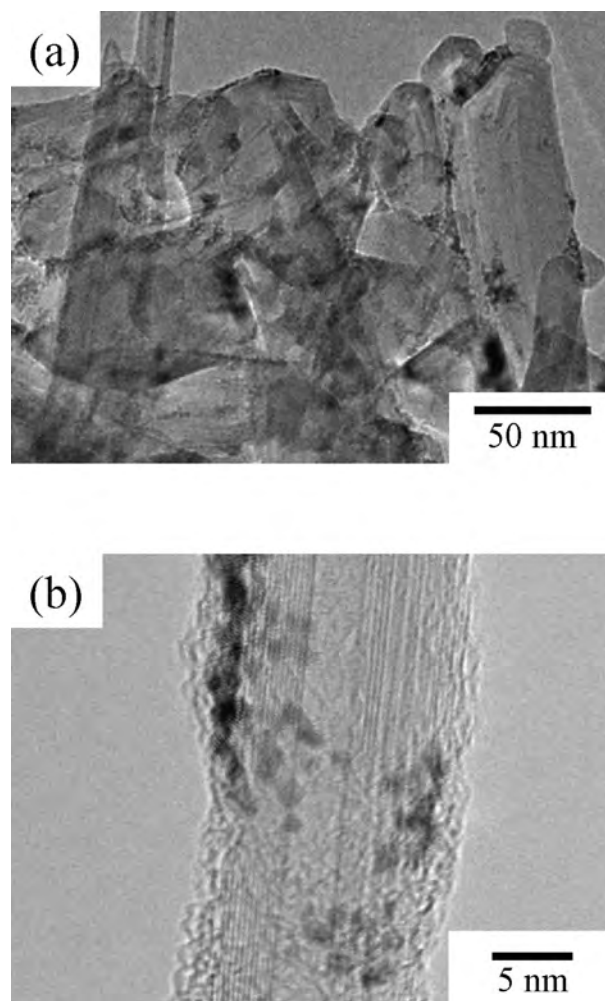


Fig. 10 – (a) A large scale and (b) magnified TEM micrograph of IrO₂/CNT after the durability test showing the corrosion of carbon along the walls of CNT.

particles [68]. In Fig. 10, the agglomeration of IrO₂ nanoparticles was observed in large scale TEM image, Fig. 10(a), as well as magnified TEM image, Fig. 10(b). The image suggested that of IrO₂ nanoparticles firstly agglomerated after durability test, whereas the particle size was maintained. The results suggested that degradation of catalytic activity for OER is initiated by the migration of catalyst particles on a support material surface and agglomeration of particles. On the IrO₂/CNT catalyst, high durability for OER is due to the strong interaction between IrO₂ nanoparticles and CNT, which is appeared as the negative shift of Ir 4f peak on the XPS spectrum. In the future, further increment of interaction between catalyst particles and substrates will be required to suppress the catalyst degradation completely.

With the activity and durability results, the IrO₂/CNT catalyst stands as an active as well as very durable material. Here, it is worthwhile that we reaffirm the results of XPS measurement, especially Ir 4f peak. The high durability can be ascribed to the strong metal substrate interaction, in other words strong anchoring between the nanoparticles and the CNT substrate. This strong anchoring will not allow the easy displacement of nanoparticles to agglomerate and thereby reduction of the specific surface area. In this paper, we firstly synthesized the IrO₂/CNT catalyst and performed introductory characterization of the catalyst with discussion of origin of its high activity. However, optimization of particles size or loading amount of the IrO₂ nanoparticles is incomplete. In our future work, we will optimize particle morphology as well as electronic state to improve catalytic activity and we plan to examine OER activity in both acidic and alkaline medium. Our results imply that the IrO₂/CNT catalyst also have high activity for OER in alkaline solution because of its high specific surface area.

Conclusions

The IrO₂/CNT nano electro-catalyst for OER was prepared by simple and facile hydrothermal method. The pre-oxidized COOH-CNT was used as the substrate to decorate IrO₂ nanoparticles. The COOH functional groups were employed as nucleation sites to improve the specific surface area of IrO₂ without altering the crystallinity of CNT. The unchanged crystallinity of CNT before and after IrO₂ decoration revealed that CNT retained the electronic conductivity all through the process. The XPS measurement revealed the formation of the strong electronic interaction between the nanoparticles and CNT. Further electrochemical studies of the IrO₂ nanoparticles supported on the CNT substrate prepared by hydrothermal method exhibit considerably high OER activity along with high durability. All the above observations reveal that increasing specific surface area of IrO₂ is due to its small particle size by involvement of electronically conducting CNT as substrate. We suggest that improving the anchoring interaction between substrate and nanoparticles are the factors responsible for the high OER activity and durability in acidic conditions. These results show that IrO₂/CNT is a promising OER catalyst and will find applications as anode in PEWE.

Acknowledgements

This work was supported by JSPS KAKENHI Grant number 17K05969 and Strategic Research Foundation Grant-aided Project for Private Universities from the Ministry of Education, Culture, Sport, Science, and Technology, Japan (MEXT).

Appendix A. Supplementary data

Supplementary data related to this article can be found at <https://doi.org/10.1016/j.ijhydene.2018.08.034>.

REFERENCES

- [1] Cook TR, Dogutan DK, Reece SY, Surendranath Y, Teets TS, Nocera DG. Solar energy supply and storage for the legacy and nonlegacy worlds. *Chem Rev* 2010;110:6474–502.
- [2] Lee J, Jeong B, Ocon JD. Oxygen electrocatalysis in chemical energy conversion and storage technologies. *Curr Appl Phys* 2013;13:309–21.
- [3] Paidar M, Fateev V, Bouzek K. Membrane electrolysis—history, current status and perspective. *Electrochim Acta* 2016;209:737–56.
- [4] McCrory CCL, Jung S, Ferrer IM, Chatman SM, Peters JC, Jaramillo TF. Benchmarking hydrogen evolving reaction and oxygen evolving reaction electrocatalysts for solar water splitting devices. *J Am Chem Soc* 2015;137:4347–57.
- [5] Antolini E. Iridium as catalyst and cocatalyst for oxygen evolution/reduction in acidic polymer electrolyte membrane electrolyzers and fuel cells. *ACS Catal* 2014;4:1426–40.
- [6] Suen NT, Hung SF, Quan Q, Zhang N, Xu YJ, Chen HM. Electrocatalysis for the oxygen evolution reaction: recent development and future perspectives. *Chem Soc Rev* 2017;46:337–65.
- [7] Carmo M, Fritz DL, Mergel J, Stolten D. A comprehensive review on PEM water electrolysis. *Int J Hydrogen Energy* 2013;38:4901–34.
- [8] Herranz J, Durst J, Fabbri E, Patru A, Cheng X, Permyakova AA, et al. Interfacial effects on the catalysis of the hydrogen evolution, oxygen evolution and CO₂-reduction reactions for (co-)electrolyzer development. *Nanomater Energy* 2016;29:4–28.
- [9] Marshall AT, Haverkamp RG. Nanoparticles of IrO₂ or Sb–SnO₂ increase the performance of iridium oxide DSA electrodes. *J Mater Sci* 2012;47:1135–41.
- [10] Reier T, Oezaslan M, Strasser P. Electrocatalytic Oxygen Evolution Reaction (OER) on Ru, Ir, and Pt catalysts: a comparative study of nanoparticles and bulk materials. *ACS Catal* 2012;2:1765–72.
- [11] Pavlovic Z, Ranjan C, Gao Q, van Gastel M, Schlögl R. Probing the structure of a water-oxidizing anodic iridium oxide catalyst using Raman Spectroscopy. *ACS Catal* 2016;6:8098–105.
- [12] Nguyen TD, Scherer GG, Xu ZJ. A facile synthesis of size-controllable IrO₂ and RuO₂ nanoparticles for the oxygen evolution reaction. *Electrocatalysis* 2016;7:420–7.
- [13] Ahmed J, Mao Y. Ultrafine iridium oxide nanorods synthesized by molten salt method toward electrocatalytic oxygen and hydrogen evolution reactions. *Electrochim Acta* 2016;212:686–93.

- [14] Sun1 W, Liu JY, Gong XQ, Zaman WQ, Cao LM, Yang J. OER activity manipulated by IrO_6 coordination geometry: an insight from pyrochlore iridates. *Sci Rep* 2016;6:38429.
- [15] Lee BS, Ahn SH, Park HY, Choi I, Yoo SJ, Kim HJ, et al. Development of electrodeposited IrO_2 electrodes as anodes in polymer electrolyte membrane water electrolysis. *Appl Catal B Environ* 2015;179:285–91.
- [16] Papaderakis A, Tsiplakides D, Balomenou S, Sotiropoulos S. Electrochemical impedance studies of IrO_2 catalysts for oxygen evolution. *J Electroanal Chem* 2015;757:216–24.
- [17] Minguzzi A, Locatelli C, Lugaresi O, Achilli E, Cappelletti G, Scavini M, et al. Easy accommodation of different oxidation states in iridium oxide nanoparticles with different hydration degree as water oxidation electrocatalysts. *ACS Catal* 2015;5:5104–15.
- [18] Abbott DF, Lebedev D, Waltar K, Povia M, Nachtegaal M, Fabbri E, et al. Iridium oxide for the oxygen evolution reaction: correlation between particle size, morphology, and the surface hydroxo layer from operando XAS. *Chem Mater* 2016;28:6591–604.
- [19] Trasatti S. Electrocatalysis in the anodic evolution of oxygen and chlorine. *Electrochim Acta* 1984;29:1503–12.
- [20] Matsumoto Y, Sato E. Electrocatalytic properties of transition metal oxides for oxygen evolution reaction. *Mater Chem Phys* 1986;14:397–426.
- [21] Lee J, Shah SAS, Yoo PJ, Lim B. Hydrated RuO_2 nanoparticles as highly active electrocatalysts for hydrogen evolution reaction. *Chem Phys Lett* 2017;673:89–92.
- [22] Rossmeisl J, Qu Z-W, Zhu H, Kroes G-J, Nørskov JK. Electrolysis of water on oxide surfaces. *J Electroanal Chem* 2007;607:83–9.
- [23] Song Y, Yang J, Gong X-Q. Prediction of $\text{Ir}_{0.5}\text{M}_{0.5}\text{O}_2$ ($\text{M} = \text{Cr}, \text{Ru}$ or Pb) mixed oxides as active catalysts for oxygen evolution reaction from first-principles calculations. *Top Catal* 2015;58:675–81.
- [24] Zhang X, Bieberle-Hütter A. Modeling and simulations in photoelectrochemical water oxidation: from single level to multiscale modeling. *ChemSusChem* 2016;9:1223–42.
- [25] Zhang X, Klaver P, van Santen R, van de Sanden MCM, Bieberle-Hütter A. Oxygen evolution at hematite surfaces: the impact of structure and oxygen vacancies on lowering the overpotential. *J Phys Chem C* 2016;120:18201–8.
- [26] Valdés A, Brillet J, Grätzel M, Gudmundsdóttir H, Hansen HA, Jónsson H, et al. Solar hydrogen production with semiconductor metal oxides: new directions in experiment and theory. *Phys Chem Chem Phys* 2012;14:49–70.
- [27] Gauthier JA, Dickens CF, Chen LD, Doyle AD, Nørskov JK. Solvation effects for oxygen evolution reaction catalysis on $\text{IrO}_2(110)$. *J Phys Chem C* 2017;121:11455–63.
- [28] Seitz LC, Dickens CF, Nishio K, Hikita Y, Montoya J, Doyle A, et al. A highly active and stable $\text{IrO}_x/\text{SrIrO}_3$ catalyst for the oxygen evolution reaction. *Science* 2017;353:1011–4.
- [29] Lebedev D, Povia M, Waltar K, Abdala PM, Castelli IE, Fabbri E, et al. Highly active and stable iridium pyrochlores for oxygen evolution reaction. *Chem Mater* 2017;29:5182–91.
- [30] González-Huerta RG, Ramos-Sánchez G, Balbuena PB. Oxygen evolution in Co-doped RuO_2 and IrO_2 : experimental and theoretical insights to diminish electrolysis overpotential. *J Power Sources* 2014;268:69–76.
- [31] Kadakia KS, Jampani PH, Velikokhatnyi OI, Datta MK, Park SK, Hong DH, et al. Nanostructured F doped IrO_2 electrocatalyst powders for PEM based water electrolysis. *J Power Sources* 2014;269:855–65.
- [32] Cheng J, Zhang H, Chen G, Zhang Y. Study of $\text{Ir}_x\text{Ru}_{1-x}\text{O}_2$ oxides as anodic electrocatalysts for solid polymer electrolyte water electrolysis. *Electrochim Acta* 2009;54:6250–6.
- [33] Diaz-Morales O, Raaijman S, Kortlever R, Kooyman PJ, Wezendonk T, Gascon J, et al. Iridium-based double perovskites for efficient water oxidation in acid media. *Nature Commun* 2016;7:12363.
- [34] Papaderakis A, Pliatsikas N, Prochaska C, Vourlias G, Patsalas P, Tsiplakides D, et al. Oxygen evolution at IrO_2 Shell–Ir–Ni core electrodes prepared by galvanic replacement. *J Phys Chem C* 2016;120:19995–20005.
- [35] Patel P, Chung SJ, Park SK, Poston JA, Manivannan A, Kumta PN. Study of fluorine doped $(\text{Nb},\text{Ir})\text{O}_2$ solid solution electro-catalyst powders for proton exchange membrane based oxygen evolution reaction. *Mater Sci Eng B* 2016;212:101–8.
- [36] Siracusanova S, van Dijk N, Payne-Johnson E, Baglio V, Aricò AS. Nanosized IrO_x and IrRuO_x electrocatalysts for the O_2 evolution reaction in PEM water electrolyzers. *Appl Catal B Environ* 2015;164:488–95.
- [37] Kadakia K, Datta MK, Velikokhatnyi OI, Jampani P, Park SK, Saha P, et al. Novel $(\text{Ir},\text{Sn},\text{Nb})\text{O}_2$ anode electrocatalysts with reduced noble metal content for PEM based water electrolysis. *Int J Hydrogen Energy* 2012;37:3001–13.
- [38] Ghadge SD, Patel PP, Datta MK, Velikokhatnyi OI, Kuruba R, Shanthi PM, et al. Fluorine substituted $(\text{Mn},\text{Ir})\text{O}_2\cdot\text{F}$ high performance solid solution oxygen evolution reaction electro-catalysts for PEM water electrolysis. *RSC Adv* 2017;7:17311–24.
- [39] Cheng J, Zhang H, Ma H, Zhong H, Zou Y. Study of carbon-supported IrO_2 and RuO_2 for use in the hydrogen evolution reaction in a solid polymer electrolyte electrolyzer. *Electrochim Acta* 2010;55:1855–61.
- [40] Kong FD, Zhang S, Yin GP, Liu J, Xu ZQ. IrO_2 -graphene hybrid as an active oxygen evolution catalyst for water electrolysis. *Int J Hydrogen Energy* 2013;38:9217–22.
- [41] Siracusanova S, Baglio V, Urso CD, Antonucci V, Aricò AS. Preparation and characterization of titanium suboxides as conductive supports of IrO_2 electrocatalysts for application in SPE electrolyzers. *Electrochim Acta* 2009;54:6292–9.
- [42] Puthiyapura VK, Pasupathi S, Su H, Liu X, Pollet B, Scott K. Investigation of supported IrO_2 as electrocatalyst for the oxygen evolution reaction in proton exchange membrane water electrolyser. *Int J Hydrogen Energy* 2014;39:1905–13.
- [43] Audichon T, Napporn TW, Canaff C, Morais C, Comminges C, Kokoh KB. IrO_2 coated on RuO_2 as efficient and stable electroactive nanocatalysts for electrochemical water splitting. *J Phys Chem C* 2016;120:2562–73.
- [44] da Silva GC, Fernandes MR, Ticianelli EA. Activity and stability of Pt/IrO_2 bifunctional materials as catalysts for the oxygen evolution/reduction reactions. *ACS Catal* 2018;8:2081–92.
- [45] Li G, Li S, Xiao M, Ge J, Liu C, Xing W. Nanoporous IrO_2 catalyst with enhanced activity and durability for water oxidation owing to its micro/mesoporous structure. *Nanoscale* 2017;9:9291–8.
- [46] Lettenmeier P, Wang L, Golla-Schindler U, Gazdzicki P, Cañas NA, Handl M, et al. Nanosized IrO_x -Ir catalyst with relevant activity for anodes of proton exchange membrane electrolysis produced by a cost-effective procedure. *Angew Chem Int Ed* 2016;55:742–6.
- [47] Tomanek D, Enbody RJ. Science and application of nanotubes. New York: Kluwer Academic/Plenum Publishers; 2000.
- [48] Reddy ALM, Gowda SR, Shaijumon MM, Ajayan PM. Hybrid nanostructures for energy storage applications. *Adv Mater* 2012;24:5045–64.
- [49] Zhang Q, Huang JQ, Qian WZ, Zhang YY, Wei F. The road for nanomaterials industry: a review of carbon nanotube production, post-treatment, and bulk applications for composites and energy storage. *Small* 2013;9:1237–65.
- [50] Zhang Y, Li X, Zhang M, Liao S, Dong P, Xiao J, et al. IrO_2 nanoparticles highly dispersed on nitrogen-doped carbon

- nanotubes as an efficient cathode catalyst for high-performance Li-O₂ batteries. *Ceram Int* 2017;43:14082–9.
- [51] Shih YT, Lee KY, Huang YS. Characterization of iridium dioxide–carbon nanotube nanocomposites grown onto graphene for supercapacitor. *J Alloy Compd* 2015;619:131–7.
- [52] Wang H, Zheng J, Peng F, Yu H. Pt/IrO₂/CNT anode catalyst with high performance for direct methanol fuel cells. *Catal Commun* 2013;33:34–7.
- [53] Fujigaya T, Nakashima N. Fuel cell electrocatalyst using polybenzimidazole-modified carbon nanotubes as support materials. *Adv Mater* 2013;25:1666–81.
- [54] Guo L, Jiang WJ, Zhang Y, Hu JS, Wei ZD, Wan LJ. Embedding Pt nanocrystals in N-Doped porous carbon/carbon nanotubes toward highly stable electrocatalysts for the oxygen reduction reaction. *ACS Catal* 2015;5:2903–9.
- [55] Bharti A, Cheruvally G, Muliankeezhu S. Microwave assisted, facile synthesis of Pt/CNT catalyst for proton exchange membrane fuel cell application. *Int J Energy Res* 2017;42:11622–31.
- [56] Akbari E, Buntat Z. Benefits of using carbon nanotubes in fuel cells: a review. *Int J Energy Res* 2017;41:92–102.
- [57] Huang TZ, Fang HY, Mao S, Yu JM, Qi L. In-situ synthesized TiC@CNT as high-performance catalysts for oxygen reduction reaction. *Carbon* 2017;126:566–73.
- [58] Li Y, Lu X, Li Y, Zhang X. Oxygen evolution reaction in nanoconfined carbon nanotubes. *Phys E Low-dimens Syst Nanostruct* 2018;99:1–5.
- [59] Deng D, Yu L, Chen X, Wang G, Jin L, Pan X, et al. Iron encapsulated within pod-like carbon nanotubes for oxygen reduction reaction. *Angew Chem Int Ed* 2013;52:371–5.
- [60] Badam R, Vedarajan R, Matsumi N. Platinum decorated functionalized defective acetylene black; a promising cathode material for the oxygen reduction reaction. *Chem Commun* 2015;51:9841–4.
- [61] Hara M, Badam R, Wang GJ, Huang HH, Yoshimura M. Synthesis and evaluation of iridium oxide nanoparticle catalysts supported on nitrogen-doped reduced graphene oxides. *ECS Trans* 2018;85:27–35.
- [62] Bolzan AA, Fong C, Kennedy BJ, Howard CJ. Structural studies of rutile-type metal dioxides. *Acta Crystallogr* 1997;B53:373–80.
- [63] Baykal A, Senel M, Unal B, Karaoğlu E, Sözeri H, Toprak MS. Acid functionalized multiwall carbon nanotube/magnetite (MWCNT)-COOH/Fe₃O₄ hybrid: synthesis, characterization and conductivity evaluation. *J Inorg Organomet Polym* 2013;23:726–35.
- [64] Lin-Vien D, Colthup NB, Fateley WG, Grasselli JG. The handbook of infrared and Raman characteristic frequencies of organic molecules. San Diego: Academic Press Inc; 1991.
- [65] Pfeifer V, Jones TE, Vélezac JJV, Massué C, Greiner MT, Arrigo R, et al. The electronic structure of iridium oxide electrodes active in water splitting. *Phys Chem Chem Phys* 2016;18:2292–6.
- [66] Papaderakis A, Pliatsikas N, Prochaska C, Vourlias G, Patsalas P, Tsiplakides D, et al. Oxygen evolution at IrO₂ Shell–Ir–Ni core electrodes prepared by galvanic replacement. *J Phys Chem C* 2016;120:19995–20005.
- [67] Jackson C, Smith GT, Inwood DW, Leach AS, Whalley PS, Callisti M, et al. Electronic metal-support interaction enhanced oxygen reduction activity and stability of boron carbide supported platinum. *Nature Commun* 2017;8:15802.
- [68] Rakousky C, Reimer U, Wippermann K, Carmo M, Lueke W, Stolten D. An analysis of degradation phenomena in polymer electrolyte membrane water electrolysis. *J Power Sources* 2016;326:120–8.

PAPER

Growth of vertically-aligned carbon nanotubes on graphite for electric double-layer capacitors

To cite this article: Daisuke Yoneda *et al* 2019 *Mater. Res. Express* **6** 086322

View the [article online](#) for updates and enhancements.



IOP ebooksTM

Bringing you innovative digital publishing with leading voices to create your essential collection of books in STEM research.

Start exploring the collection - download the first chapter of every title for free.



PAPER

Growth of vertically-aligned carbon nanotubes on graphite for electric double-layer capacitors

RECEIVED
21 February 2019REVISED
15 May 2019ACCEPTED FOR PUBLICATION
22 May 2019PUBLISHED
31 May 2019Daisuke Yoneda, Seiya Suzuki , Satoshi Hiramoto, Yuki Matsuoka, Masanori Hara and Masamichi Yoshimura

Graduate School of Engineering, Toyota Technological Institute, 2-12-1 Hisakata, Tempaku, Nagoya 468-8511, Japan

E-mail: yoshi@toyota-ti.ac.jp**Keywords:** vertically aligned carbon nanotubes, chemical vapor deposition, carbon nanotubes/graphite electrode, electric double layer capacitor, plasma etching of graphite**Abstract**

Recently, electric double-layer capacitors (EDLCs) have attracted great attention as an energy storage device with high input-output power density. In this study, we synthesized carbon nanotubes (CNTs)/graphite with high surface area as a novel electrode component for EDLC. CNTs were grown on a defective graphite surface by alcohol catalytic chemical vapor deposition for the first time. We found that oxidative plasma treatment time for graphite surface attributes to selective growth of laterally-aligned (LA) or vertically-aligned (VA) CNTs. Electrochemical analysis reveals VACNTs/graphite possesses the highest electrostatic capacity of 1.5 mF cm^{-2} among pristine graphite, LACNTs/graphite, and VACNTs/graphite. We suggest that increase of specific surface area with CNTs results in the increase of electrostatic capacity for the EDLC electrode. The results indicate that VACNTs/graphite electrodes are expected to improve the performance of EDLCs.

1. Introduction

Recent years, many efforts have been made to utilize renewable energy for stable electric power sources such as solar cell and wind power. However, the output electric power of renewable energy fluctuates dependent on natural environment such as weather conditions. For practical and efficient application of renewable energy, the renewable power generation system is required to combine with an energy storage system with high capacity and fast response against the fluctuation of supplied electric power. Electric double-layer capacitors (EDLCs), in which electric charge is accumulated at the electrode surfaces, is one of the candidates of energy storages because EDLCs have significantly high electron charge-discharge rate and long-life periods. Conductive materials with high-surface-area, e.g. carbon materials [1–4], are desirable for the electrodes of EDLCs since the capacity is proportional to the surface area.

Activated carbon is the most major electrode material for commercial EDLCs because of the advantages of high-surface-area, relatively low cost, and well-established electrode production technologies [5]. The structure of activated carbon is porous with various pore sizes which are categorized by micropores (<2 nm), mesopores (2–50 nm), and macropores (>50 nm), according to IUPAC nomenclature [6]. In contrast to micropores and macropores, mesopores are important since the number of mesopores effectively increase the capacitance of activated carbon-based EDLCs [7, 8]. However, controlling pore sizes of activated carbon is difficult [7, 9]. In addition, drawbacks of activated carbon such as insufficient chemical stability and low electrical conductivity [7, 10] limit the performance of EDLC. Thus, new materials are strongly needed to improve EDLC electrodes.

Carbon nanotube (CNT) is a promising candidate for EDLC electrodes owing to high aspect ratio [11], large specific surface area [12, 13], and high electrical conductivity [14]. CNTs have already been widely used as the active electrodes in EDLCs (or supercapacitors) [13, 15–17]. Vertically-aligned CNTs (VACNTs) grown by chemical vapor deposition (CVD) have advantages for EDLC electrodes in terms of well-defined tube-spacing, which provides a more electrolyte-accessible surface morphology than the electrode comprising randomly entangled CNTs [9, 10]. The superiority of VACNTs for EDLCs has widely been demonstrated [18–24]. For

applying VACNTs as electrodes, direct growth of VACNTs on a current collector has advantages to reduce the contact resistance between them.

The growth of VACNTs on conductive materials for EDLCs and supercapacitors has been reported on aluminum [25, 26], tantalum [22], carbon fabric [27], carbon fiber [28], and functionalized graphene nanosheets [29]. Notably, carbon materials have potential for significant reduce of the contact resistance in VACNTs-EDLC by forming carbon-carbon covalent bonds. However, the aforementioned carbon materials [27–29] lack chemical stability. Thus, a chemically stable carbon material is highly demanded as a current collector for VACNTs-EDLC.

Bulk graphite is one of the prominent materials for such current collector since it is highly conductive and chemically stable. In the present report, we studied the growth of CNTs on highly oriented pyrolytic graphite (HOPG) using alcohol catalytic (AC) CVD. It is found that oxidative plasma etching of HOPG surface allows growing CNTs on the surface. Insufficient plasma etching results in the lack or less of CNTs growth because of the aggregation of catalyst particles. Prolonging plasma etching time increased surface roughness of HOPG, and VACNTs were successfully grown on a HOPG. We also demonstrate that the synthesized VACNTs/HOPG works as an electrode for EDLC. VACNTs/graphite possesses the higher electrostatic capacity of 1.5 mF cm^{-2} than pristine graphite, or LACNTs/graphite.

2. Experimental

2.1. Synthesis of CNTs/HOPG electrodes

Mechanically cleaved HOPGs with the size of 5×5 and $10 \times 10 \text{ mm}^2$ were used as substrates for structural characterization and electrochemical evaluation, respectively, and were exposed to oxidative plasma (soft plasma etching device SEDE-GE, Meiwafofos Co., Ltd). The plasma treatment of the HOPG was carried for $0.5 \sim 5$ min at 3 mA under 8 Pa air as a source of oxidative gas. After the plasma treatment, cobalt (Co) or iron (Fe) with the thickness of ~ 2 nm was deposited on the HOPG under 1×10^{-4} Pa using an arc plasma deposition system (ZB05-7058, Ulvac). Subsequently, CNTs were grown on the HOPG by ACCVD using ethanol vapor as carbon feedstock (99.5% purity, Wako Pure Chemical Industries). During CVD processes, the flow rate of the ethanol vapor was kept at 200 sccm under the total pressures of 10 and 1 kPa for Co and Fe deposited substrates, respectively. The CNT growth was held at $650 \text{ }^\circ\text{C}$ – $700 \text{ }^\circ\text{C}$ for 10 min.

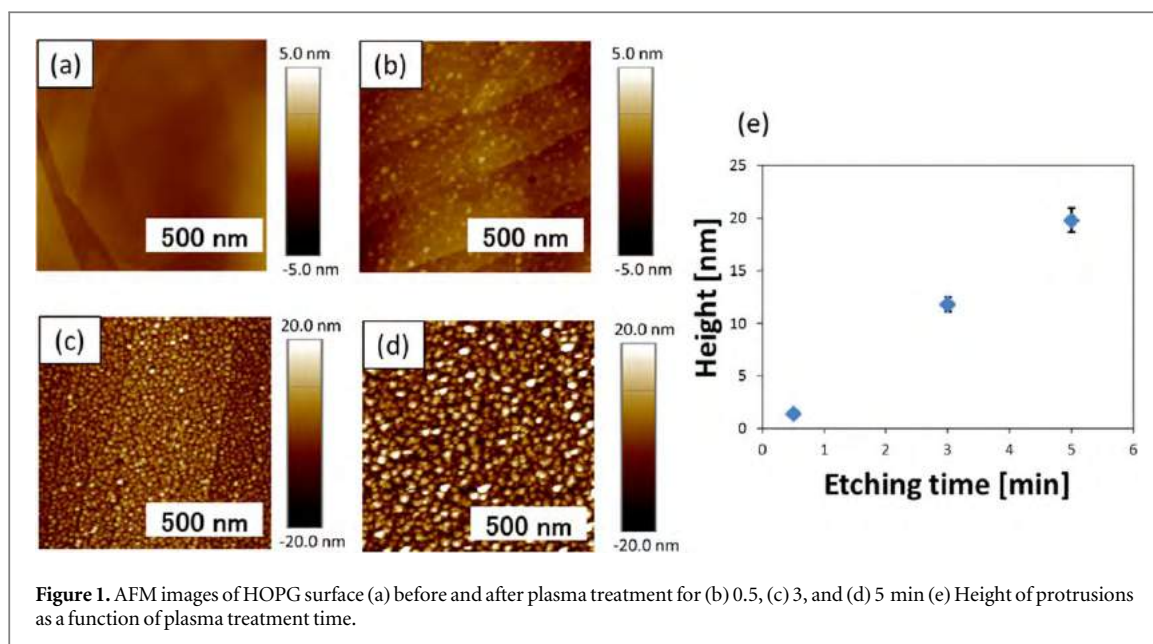
2.2. Structural characterizations

Surface morphology of the HOPG after the plasma treatment was observed by atomic force microscopy (AFM: Multimode, Bruker Co.). The synthesized CNTs/HOPG before and after electrochemical evaluation were observed by scanning electron microscopy (SEM: S-4700, Hitachi), operated at 20 kV. The structure of the CNTs was characterized by Raman spectroscopy (InVia, Renishaw plc.). A 532 nm excitation laser focused with a $50\times$ objective lens and a 1800 lines/mm grating were utilized for Raman spectroscopy. Elemental analysis of HOPG surface was performed by x-ray photoelectron spectroscopy (XPS: PHI 5000 VersaProbe II, ULVAC PHI) under a base pressure of $\sim 6 \times 10^{-8}$ Pa and a monochromatized Al $K\alpha$ (1486.6 eV) x-ray source.

2.3. Electrochemical evaluation

Electrochemical properties of the synthesized CNTs/HOPG electrodes were investigated by cyclic voltammetry (CV), constant current charge-discharge measurement (CDC), and electrochemical impedance measurement (EIS) using an electrochemical workstation (HZ-7000, Hokuto Denko Corp.) in a 3-electrode electrochemical cell for a plate electrode in 1 M H_2SO_4 (Kanto Chemical Co.) solution at room temperature. The cyclic voltammograms were recorded by potential sweeping between 0.0 and 1.0 V versus reversible hydrogen electrode (RHE) at a scan rate of 50 mV s^{-1} in nitrogen saturated 1 M H_2SO_4 . The charge-discharge performance was tested at constant current density from 2 to $100 \mu\text{A cm}^{-2}$ in a potential region between 0.5 and 1.0 V. The EIS plot was obtained at open circuit potential (ca. 0.4 V) and frequency scan from 100 kHz to 1 Hz with the potential modulation of 10 mV. For these measurements, Ag/AgCl electrode in 3 M KCl solution and a Pt wire were used as a reference electrode (RE) and counter electrode (CE), respectively. The H_2SO_4 electrolyte solution was purged with nitrogen gas for 15 min before the electrochemical measurements.

To analyze performance of the CNTs/HOPG electrodes in an actual EDLC cell, electrostatic capacity of the synthesized CNTs/HOPG electrodes was evaluated by chronoamperometric method with a double electrode cell. The EDLC cell was composed two HOPG or CNTs/HOPG electrodes as working and counter electrodes, Au current correctors, and filter paper soaked in 1 M H_2SO_4 solution (FUJIFILM Wako Pure Chemical Co.) as an electrolyte membrane. A potential was applied to the EDLC cell by a potentiostat (HSV-110, Hokuto Denko Co.). The applied voltage and the time duration of chronoamperometric measurement were 1.0 V and 3 s,



respectively, and the measurement was repeated 10 times at room temperature. After chronoamperometric measurements, the morphology change of the electrodes was investigated by SEM.

3. Results and discussion

Figures 1(a)–(d) show AFM images of surface morphology of HOPG before and after plasma treatments. While as-cleaved HOPG have a flat surface (figure 1(a)), protrusions with ~ 1.4 nm in height were observed after the plasma treatment for 0.5 min (figure 1(b)). The sizes of the protrusions increased to ~ 11.8 and ~ 19.8 nm in height after the treatment for 3 and 5 min, respectively, while the densities were ~ 600 and $\sim 250/\mu\text{m}^2$. Figure 1(e) shows the average height of the protrusions as a function of the plasma treatment time. We found that the size of the protrusions proportionately increased with increasing plasma treatment time.

In order to know the effects of plasma treatment on HOPG, we examined the HOPG surfaces before and after plasma treatment by XPS. Figures 2(a)–(d) show C1s XPS spectra of HOPGs before and after plasma treatment with different processing time. In the XPS spectra of plasma treated HOPGs, additional peaks were appeared with the major C1s peak (figures 2(b)–(d)). The major C1s peak at ca. 284.8 eV is originated from sp^2 carbon, and the others at around 286, 288, 289, and 291 eV are hydroxyl (C–OH), carbonyl (C=O), carboxyl group (O–C=O), and π - π^* satellite, respectively. These functional groups are defects induced by the plasma treatment. Table 1 summarizes the relative peak area ratios of sp^2 carbon, C–OH, C=O, O–C=O, and π - π^* satellite normalized by the peak area of sp^2 carbon with different plasma treatment time. The ratio of C=O increased with increasing plasma treatment time. The protrusions found in the AFM images (figures 1(b)–(d)) would be related to oxidative defects of carbon.

Figure 3(a) shows Raman spectra of HOPG before and after plasma treatments, where G and D peaks originating from graphitic structure and its defects [30–32] were observed around 1580 and 1360 cm^{-1} in the spectra, respectively. The absence of D peak in the spectrum of HOPG indicates high quality in crystallinity. Figure 3(b) shows the dependence of the intensity ratio of G divided by D peak (G/D), corresponding to crystallinity of graphitic materials [30–32], on plasma treatment time. The G/D of HOPG was drastically decreased to 2 by the plasma treatment for the initial 1 min indicating that defects are induced in its graphitic structure. Further plasma treatment does not largely change the G/D of HOPG indicating that the amount of defects was nearly constant.

Figures 4(a)–(d) show the top-view SEM images of Co deposited HOPG specimens after ACCVD with different plasma treatment time. Figure 4(e) is the magnified SEM image of figure 4(a). Figure 4(f) is the cross-sectional SEM image of figure 4(d). As shown in figure 4(a), CNTs were not grown on the HOPG without plasma treatment, and the particles with $25 \sim 80$ nm in diameter (figure 4(e)) were observed on the surface. The particles would be thermally aggregated Co catalysts for ACCVD. Prolonging the plasma treatment time of HOPG, the density of CNTs was increased as seen in figures 4(b)–(d). The densities of CNTs counted from the corresponding SEM images were 1.5×10^{10} (figure 4(c)) and $6.3 \times 10^{10}\text{ cm}^{-2}$ (figure 4(d)) on the HOPG with the plasma treatment for 3 and 5 min, respectively. The CNTs on the former and the latter HOPG were laterally

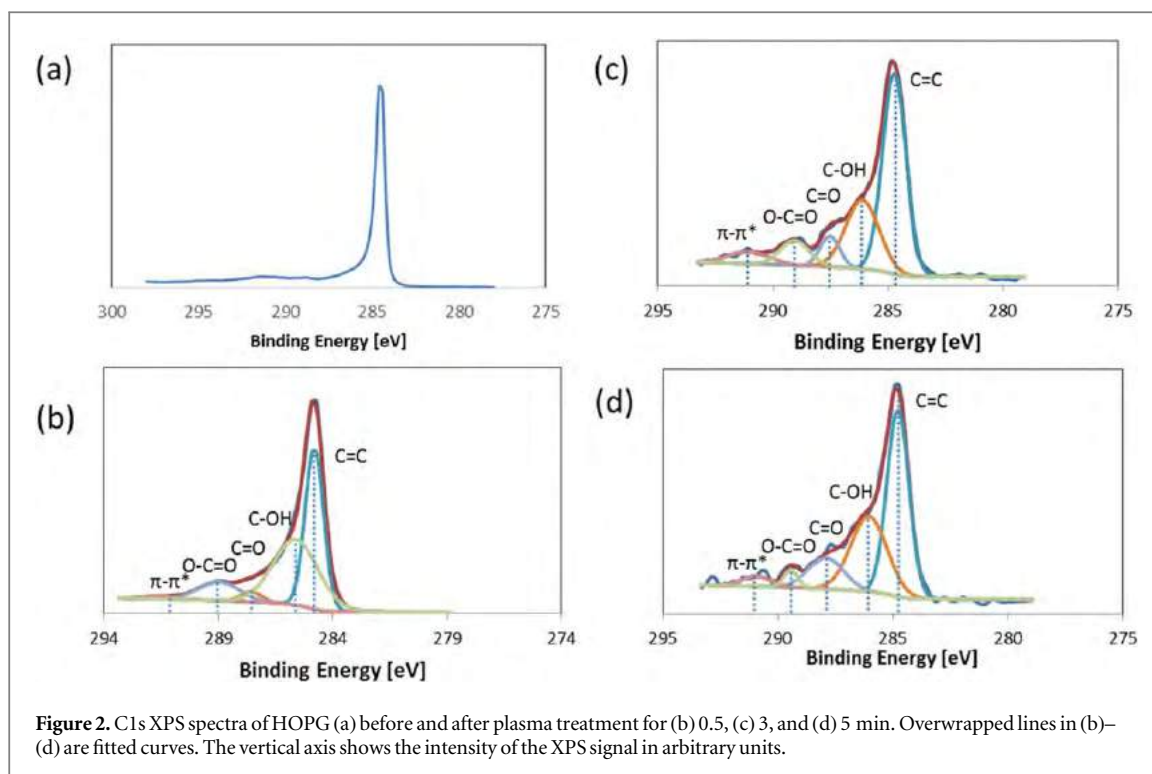
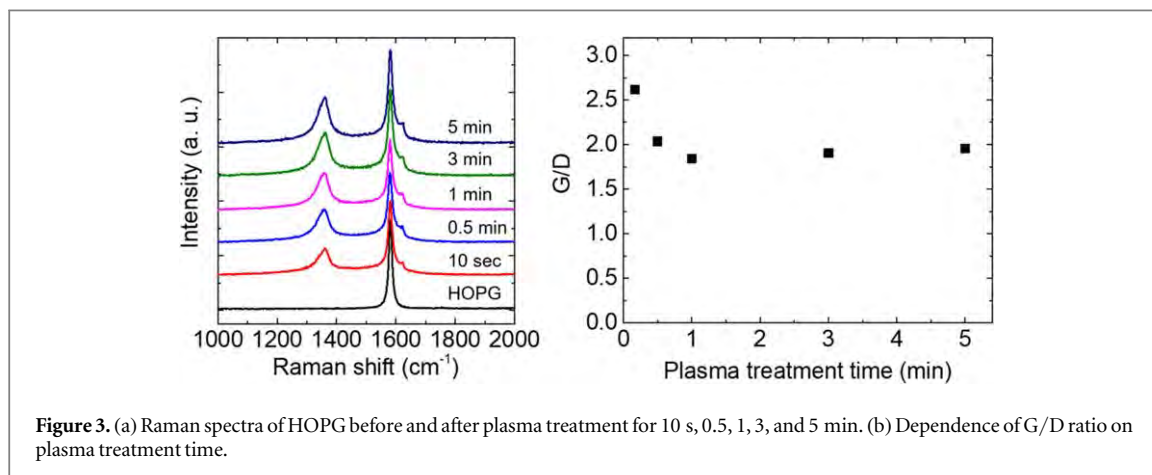


Table 1. Normalized peak areas of the fitted curves in figures 2(b)–(d). The peaks are corresponding to sp^2 carbon (sp^2 C), hydroxyl (C–OH), carbonyl (C=O), carboxyl (O–C=O) groups, and π - π^* satellite. All peak areas were divided by the peak area of the sp^2 C in each spectrum for the normalization.

Normalized peak area	0.5 min	3 min	5 min
sp^2 carbon	1	1	1
C–OH	0.40	0.49	0.40
C=O	0.060	0.12	0.16
O–C=O	0.11	0.095	0.097
π - π^*	0.014	0.047	0.054



aligned (LA) and VACNTs, respectively. The length of the VACNTs, which were observed by cross-sectional SEM (figure 4(f)), was $\sim 1 \mu\text{m}$. These results indicate that plasma treatment of HOPG causes the structural changes of the surface, leading different growth conditions for CNTs. The densely grown CNTs in figures 4(c) and (d) would be the result of suppression of thermal aggregation of Co particles on the plasma treated HOPG

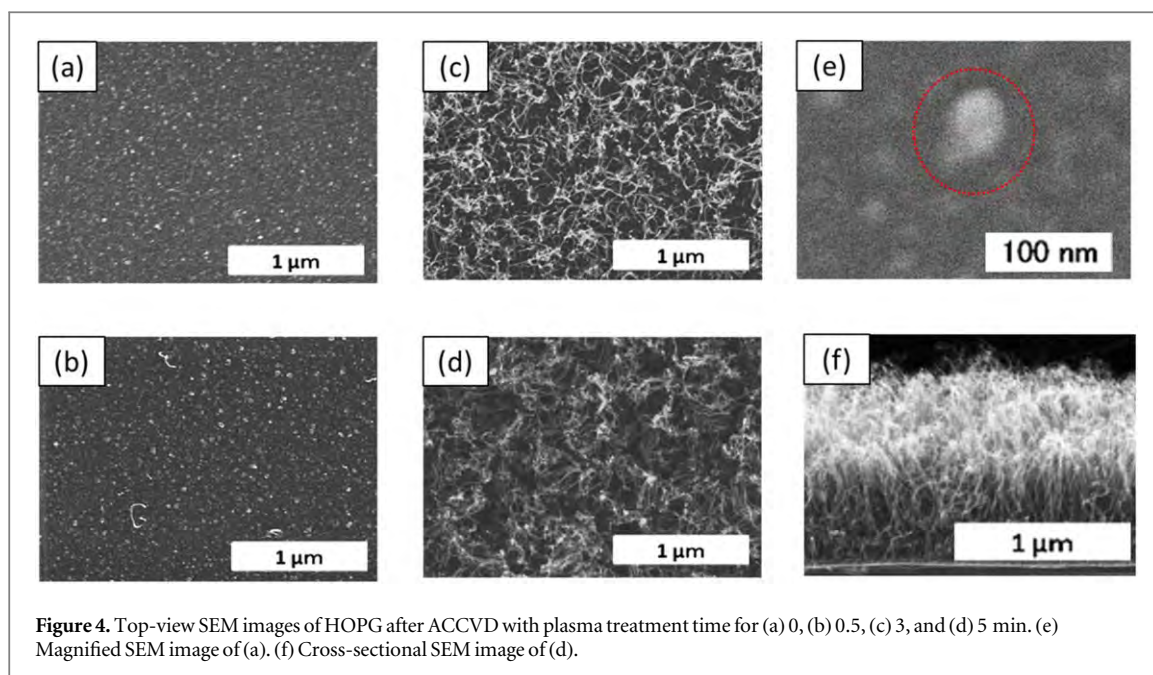


Figure 4. Top-view SEM images of HOPG after ACCVD with plasma treatment time for (a) 0, (b) 0.5, (c) 3, and (d) 5 min. (e) Magnified SEM image of (a). (f) Cross-sectional SEM image of (d).

surface. It is worthy to note that CNTs growth on Fe deposited HOPG specimens shows the same trend of that on the Co deposited HOPG.

Since the density of VACNTs is typically $10^{10} \sim 10^{11} \text{ cm}^{-2}$ [33–35], the density of the latter CNTs (figure 4(d)) reasonably explains the formation of VACNTs. On the other hand, the density of both the LACNTs ($1.5 \times 10^{10} \text{ cm}^{-2}$) and the VACNTs ($6.3 \times 10^{10} \text{ cm}^{-2}$) are different from that of the protrusions ($6 \times 10^{10} \text{ cm}^{-2}$ and $2.5 \times 10^{10} \text{ cm}^{-2}$), indicating the protrusion is not likely to be the nucleation site of CNTs. To discuss the nucleation site and the alignment difference of grown CNTs, surface chemical information of the plasma treated HOPG has to be taken into account.

Previous research groups reported that in CNT growth, suppressing aggregation of catalyst nanoparticles during CVD is crucial [36]. For instance, alumina surface suppresses diffusion and aggregation of catalyst nanoparticles, and a high density of nanoparticles forms VACNTs [36]. In the present CNT growth on HOPG, C=O bonding on surface described above would stick with Co nanoparticles and suppress their aggregation, leading growth of CNTs.

Since the plasma treated HOPG surface for 3 and 5 min showed similar G/D ratio (figure 3(b)) but the different surface C=O amount (table 1), the interaction between C=O bonding and Co nanoparticles would also attribute to the morphology difference of LA or VA of CNTs. On the other hand, surface roughness also affects CNT growth in terms of their alignment and density [37]. As seen in AFM images of HOPG surface (figures 1(a)–(d)), the plasma treatments changes surface roughness. Thus, a possible explanation for the selective growth of LACNTs or VACNTs is due to the difference in both or either of the surface roughness and amount of C=O bonding on HOPG surface.

Figures 5(a) and (b) show Raman spectra of the LACNTs and the VACNTs, where G and D peaks were observed around 1590 and 1350 cm^{-1} , respectively. Four peaks of radial breathing mode (RBM) were observed only in the spectrum for LACNTs (figure 5(b)), indicating the existence of single-walled CNTs (SWNTs). From the peak positions of the four RBM peaks ($187.9, 218.8, 236.1, 272.5 \text{ cm}^{-1}$), the diameters of SWNTs are assigned to $1.21, 1.04, 0.96,$ and 0.83 nm by using the equation of $\omega_{\text{RBM}} = 227/d_t$ [38, 39], where ω_{RBM} and d_t are peak position of RBM and diameter of SWNT, respectively. On the other hand, the absence of RBM peaks for the spectrum of VACNTs suggests that VACNTs consists of multi-walled nanotubes. The G/D for LACNTs and VACNTs were ~ 3.3 and ~ 1.1 , respectively. Because the LACNTs layer has thinner thickness and lower density, the intensities of G and D peaks of the HOPG are involved in the G/D for LACNTs, resulting in the higher value than that of VACNTs.

The synthesized electrodes were characterized by several electrochemical methods, CV, CDC, and EIS to evaluate their performance as EDLC electrodes. Figure 6 shows the cyclic voltammogram of LACNTs/HOPG, VACNTs/HOPG with $0.5 \mu\text{m}$ thick CNT forest, and pristine HOPG electrodes obtained in $1 \text{ M H}_2\text{SO}_4$ solution. All CV curves of these electrodes have no specific peaks in the potential region between 0.0 and 1.0 V , while double layer charging current of the CV curves depended on the synthesis condition of the electrodes because of the different surface area of each electrode. The reduction current represented around 0.0 V on the CV curves, especially for CNTs/HOPG electrodes, corresponds to the hydrogen evolution reaction on the edge site or defect

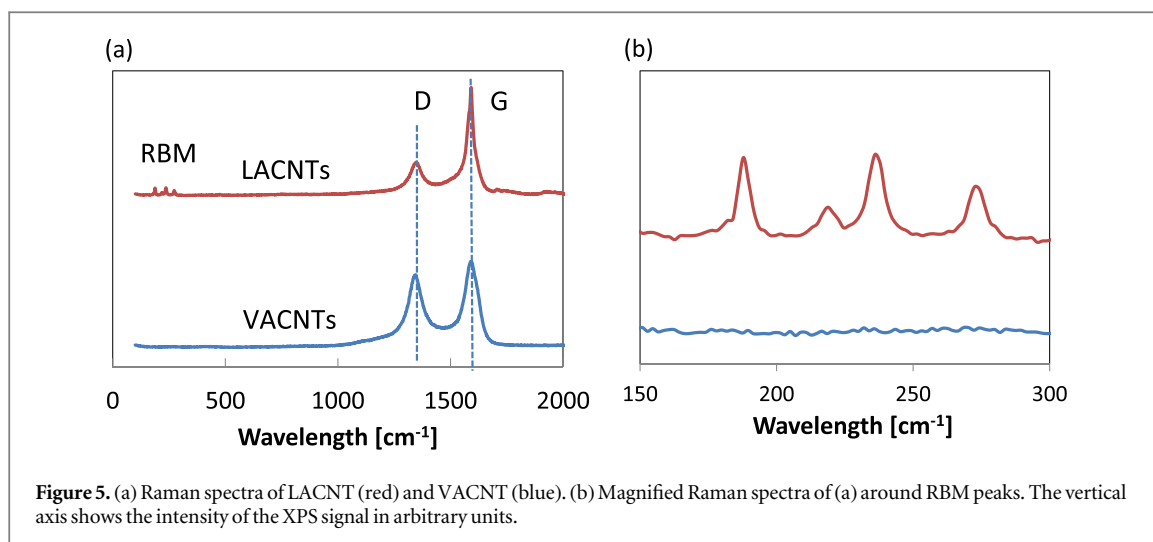


Figure 5. (a) Raman spectra of LACNT (red) and VACNT (blue). (b) Magnified Raman spectra of (a) around RBM peaks. The vertical axis shows the intensity of the XPS signal in arbitrary units.

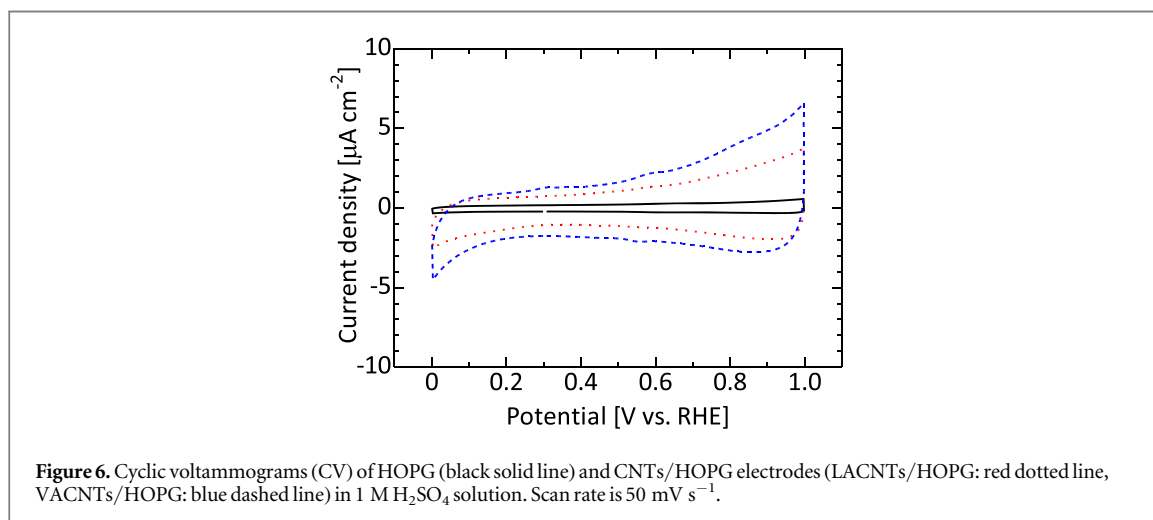
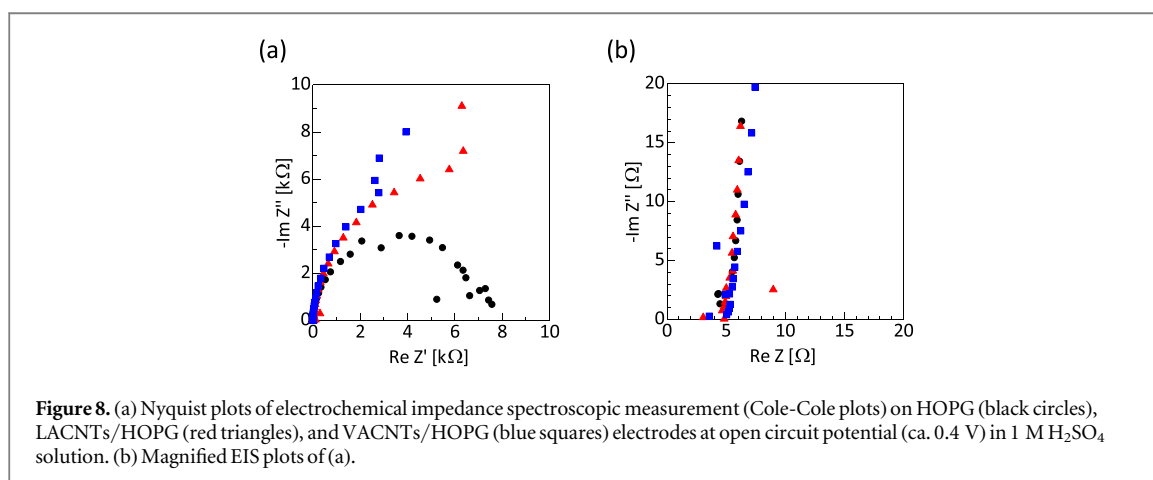
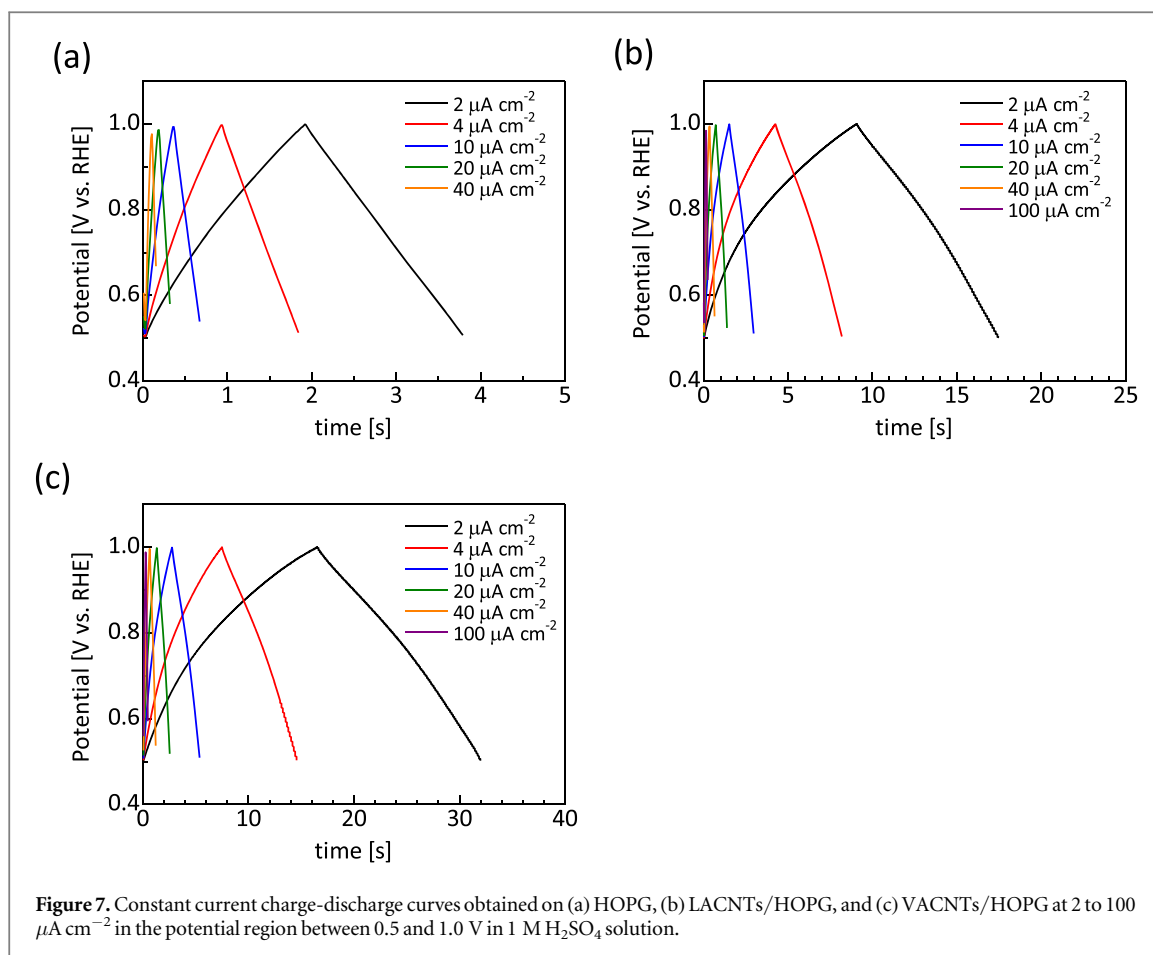


Figure 6. Cyclic voltammograms (CV) of HOPG (black solid line) and CNTs/HOPG electrodes (LACNTs/HOPG: red dotted line, VACNTs/HOPG: blue dashed line) in 1 $\text{M H}_2\text{SO}_4$ solution. Scan rate is 50 mV s^{-1} .

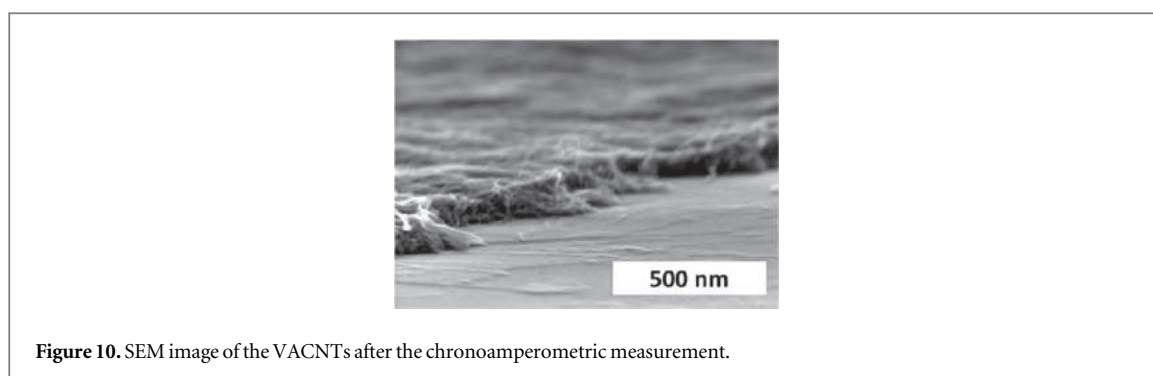
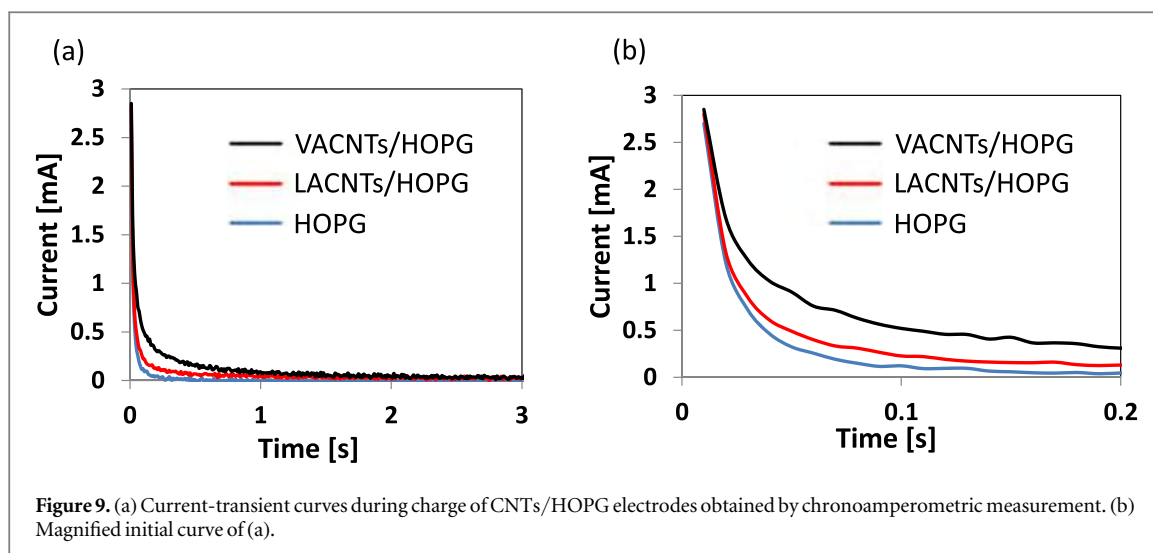
site of the plasma treated or CNTs modified HOPG surface. The oxidation current around 1.0 V is due to the onset of oxidation of carbon material surface containing functional groups or defect site as well as adsorption of hydroxide ions on the defective surface. The shape of the CV curves reveals that no additional reaction was performed in the potential region of the CV measurement except double layer charging reaction. It is also well known that current density of double layer charging is proportional to the surface area of an electrode. The present results suggest that the CNTs/HOPG electrodes have higher surface area than pristine HOPG.

Figure 7 shows the constant current charge-discharge curves between 0.5 and 1.0 V on the HOPG and CNTs/HOPG electrodes in 1 $\text{M H}_2\text{SO}_4$ solution. Electrode potential was increased or decreased in proportion to the current applying period of charging or discharging, respectively. The linear potential rising and declining on the pristine HOPG is consistent with its CV shape as shown above. The linear CDC lines suggest that the capacity on the HOPG electrode is due to ideal double layer charging on the electrode surface. On the other hands, the curved CDC lines on the CNTs/HOPG electrodes reflect the current density change of double layer region on both electrodes because of electrode surface oxidation or adsorption of hydroxide ions on defective or amorphous carbon materials surface, as described above. The estimated electric charge capacity of the HOPG, and LACNTs/HOPG electrodes were 3.8, and $18.1 \mu\text{C cm}^{-2}$, respectively, during potential transition from 0.5 to 1.0 V and vice versa. The electric charge and discharge capacity of the VACNTs/HOPG electrode were 33.2 and $30.7 \mu\text{C cm}^{-2}$, respectively, because of the irreversible oxidation current on the VACNTs/HOPG electrode. The CDC curves, or charging period, indicates the CNTs/HOPG electrodes have higher capacity as EDLC electrodes due to its high surface area.

Figure 8 shows Nyquist plots of electrochemical impedance measurement, Cole-Cole plots, on the HOPG and CNTs/HOPG electrodes. The plots for all the sample have hemispherical shape derived from electron transfer reaction of double-layer capacity charging on an electrode-electrolyte interface. The plots are represented by a standard equivalent circuit model, comprising constant phase element of double-layer



capacitance, solution resistance, electron transfer resistance, and Warburg impedance as reported in previous report [40]. The intercept value of the X axis, which is related to solution resistance, is ca. 4.8Ω due to high concentration of H_2SO_4 solution. The value of the electron transfer resistance estimated from the diameter of the hemisphere is ca. $6 \text{ k}\Omega$ on the HOPG surface. We assume that the high resistance is due to low density of defects sites or reaction sites for electron transfer reaction, such as redox reaction of functional groups on the surface. In addition, impedance of ion diffusion around the electrode was observed on the CNTs/HOPG electrodes in low frequency region. We assumed that the CNTs modified surfaces have larger roughness and higher capacitance, so the EIS plots express an effect of ion diffusion to transfer ions from bulk electrolyte to adsorption sites. The EIS results suggests that the reaction on the HOPG and CNTs/HOPG surface is general charging-discharging reaction of the double-layer capacity on the electrode surface without any additional reaction, which is consistent with the CV and CDC measurements.



For further evaluation of the synthesized CNTs/HOPG performance as electrodes of an actual double-electrode EDCL cell, an electrostatic capacity of CNTs/HOPG was measured by the chronoamperometric method. Figure 9 shows current-transient curves during charge of CNTs/HOPG electrodes obtained by chronoamperometric measurement. The current density on both LACNTs/HOPG and VACNTs/HOPG electrodes is higher than that on a pristine HOPG electrode. The capacities estimated from the current-transient curves obtained on the pristine HOPG, LACNTs/HOPG, and VACNTs/HOPG electrodes are 0.2, 0.8, and 1.5 mF cm^{-2} , respectively. Increase of current density and capacity by CNT growth is due to increase of specific surface area, leading to increase of the adsorption amount of sulfuric anion. The capacity of the present VACNTs/HOPG is larger than the capacities per unit area and CNT length of VACNTs/TiN (0.47 mF cm^{-2} per 1 μm CNT) [40] or VACNTs/Al (0.65 mF cm^{-2} per 1 μm CNT) [41]. In the present study, the average diameter of the VACNTs is 10 nm, which is smaller than that of the previous paper, 20 nm (VACNTs/TiN) [40]. The cross-sectional SEM image of VACNTs (figure 4) indicates CNTs are densely grown. We conclude that the highly dense CNTs provide high surface area as active surface for EDLC, resulting in the high capacity.

To know how much surface area of the VACNTs/HOPG is active for EDLC, we estimated the surface area from the size and the density of CNTs which is extracted from SEM images. From the estimation, we realized that the estimated capacity of the VACNTs/HOPG is two times higher than the actual capacity obtained by the chronoamperometric measurement. To clarify the variance of the capacity, we observed the surface morphology of the VACNTs/HOPG after the chronoamperometric measurement by SEM. Figure 10 shows the SEM image of the VACNTs/HOPG electrode after the electrostatic capacity measurement. The SEM image reveals the VACNTs/HOPG electrode is deformed to sheet-like structure with 100 nm in height. We assumed the morphology change reduces the active surface area and capacity of the VACNTs/HOPG electrode. In addition, hydrophobicity of CNT surface will contribute to decrease the active surface area, because sulfuric acid solution is repelled on the surface of the compressed CNTs layer and cannot fully percolate into the CNTs layer. Thus, further improvements in modifying repellency and stiffening of the CNTs will increase the capacity of VACNTs/HOPG electrodes for EDLCs. It is noted that the present evaluation of electrochemical analysis is preliminary and we will perform further investigation such as cyclic voltammetry, charge-discharge study, and electrochemical impedance spectroscopy to evaluate the performance in detail.

4. Conclusion

In this study, we synthesized and demonstrated a novel EDLC electrode by growing CNTs on HOPG by ACCVD. The key technique for the direct growth of CNTs on HOPG is the oxidative plasma treatment which induces defects on HOPG surface such as hydroxyl, carbonyl, and carboxyl groups. LACNTs and VACNTs are selectively grown on HOPG depending on the surface morphology controlled by plasma treatment time. Electrochemical analysis reveals VACNTs/HOPG possesses higher electrostatic capacity of 1.5 mF cm^{-2} than pristine graphite or LACNTs/HOPG. Although the improvement of the capacity by CNT growth is due to increase of specific surface area, inactive surface is still remained on the VACNTs/HOPG electrode. Further improvement of stiffening and hydrophilicity functionalization of the CNTs will leads to higher capacity of VACNTs/HOPG electrodes for EDLCs.

Acknowledgments

Strategic Research Foundation Grant-aided Project for Private Universities from the Ministry of Education, Culture, Sport, Science, and Technology, Japan (MEXT).

Author contributions

M Y designed the research. D Y performed almost all experiments, analyzed data, and wrote the first draft in Japanese. S S and M H co-wrote the manuscript. S S wrote the 'Experimental' and 'Results and Discussion' for CNT growth, and the 'Introduction' with significant modification from the first draft. M H wrote the 'Experimental' and 'Results and Discussion' for electrochemical evaluation. M H designed, performed, and analyzed experiments for electrochemical evaluation. S H and Y M prepared CNTs/HOPG for additional electrochemical evaluation (CV, CDC, and EIS). All author discussed the experimental results.

Competing financial interest

There are no competing financial interests.

ORCID iDs

Seiya Suzuki  <https://orcid.org/0000-0003-2445-7462>

References

- [1] Obreja V V 2008 On the performance of supercapacitors with electrodes based on carbon nanotubes and carbon activated material—a review *Physica E* **40** 2596–605
- [2] Inagaki M, Konno H and Tanaike O 2010 Carbon materials for electrochemical capacitors *J. Power Sources* **195** 7880–903
- [3] Li X and Wei B 2013 Supercapacitors based on nanostructured carbon *Nano Energy* **2** 159–73
- [4] González A, Goikolea E, Barrena J A and Mysyk R 2016 Review on supercapacitors: technologies and materials *Renew. Sustain. Energy Rev.* **58** 1189–206
- [5] Dai L, Chang D W, Baek J B and Lu W 2012 Carbon nanomaterials for advanced energy conversion and storage *Small* **8** 1130–66
- [6] Rouquerol J, Avnir D, Fairbridge C, Everett D, Haynes J, Pernicone N, Ramsay J, Sing K and Unger K 1994 Recommendations for the characterization of porous solids (technical report) *Pure Appl. Chem.* **66** 1739–58
- [7] Frackowiak E and Beguin F 2001 Carbon materials for the electrochemical storage of energy in capacitors *Carbon* **39** 937–50
- [8] Rufford T E, Hulicova-Jurcakova D, Zhu Z and Lu G Q 2009 Empirical analysis of the contributions of mesopores and micropores to the double-layer capacitance of carbons *J. Phys. Chem. C* **113** 19335–43
- [9] Qu D and Shi H 1998 Studies of activated carbons used in double-layer capacitors *J. Power Sources* **74** 99–107
- [10] Chen T and Dai L 2013 Carbon nanomaterials for high-performance supercapacitors *Mater. Today* **16** 272–80
- [11] Iijima S 1991 Helical microtubules of graphitic carbon *Nature* **354** 56
- [12] Cinke M, Li J, Chen B, Cassell A, Delzeit L, Han J and Meyyappan M 2002 Pore structure of raw and purified HiPco single-walled carbon nanotubes *Chem. Phys. Lett.* **365** 69–74
- [13] Niu C, Sichel E K, Hoch R, Moy D and Tennent H 1997 High power electrochemical capacitors based on carbon nanotube electrodes *Appl. Phys. Lett.* **70** 1480–2
- [14] Ebbesen T, Lezec H, Hiura H, Bennett J, Ghaemi H and Thio T 1996 Electrical conductivity of individual carbon nanotubes *Nature* **382** 54
- [15] An K H, Kim W S, Park Y S, Moon J M, Bae D J, Lim S C, Lee Y S and Lee Y H 2001 Electrochemical properties of high-power supercapacitors using single-walled carbon nanotube electrodes *Adv. Funct. Mater.* **11** 387–92
- [16] Frackowiak E, Jurewicz K, Delpeux S and Beguin F 2001 Nanotubular materials for supercapacitors *J. Power Sources* **97** 822–5
- [17] Kaempgen M, Chan C K, Ma J, Cui Y and Gruner G 2009 Printable thin film supercapacitors using single-walled carbon nanotubes *Nano Lett.* **9** 1872–6

- [18] Du C, Yeh J and Pan N 2005 High power density supercapacitors using locally aligned carbon nanotube electrodes *Nanotechnology* **16** 350
- [19] Lu W, Qu L, Henry K and Dai L 2009 High performance electrochemical capacitors from aligned carbon nanotube electrodes and ionic liquid electrolytes *J. Power Sources* **189** 1270–7
- [20] Futaba D N, Hata K, Yamada T, Hiraoka T, Hayamizu Y, Kakudate Y, Tanaike O, Hatori H, Yumura M and Iijima S 2006 Shape-engineerable and highly densely packed single-walled carbon nanotubes and their application as super-capacitor electrodes *Nat. Mater.* **5** 987
- [21] Zhang H, Cao G and Yang Y 2007 Using a cut–paste method to prepare a carbon nanotube fur electrode *Nanotechnology* **18** 195607
- [22] Zhang H, Cao G, Wang Z, Yang Y, Shi Z and Gu Z 2008 Growth of manganese oxide nanoflowers on vertically-aligned carbon nanotube arrays for high-rate electrochemical capacitive energy storage *Nano Lett.* **8** 2664–8
- [23] Chen Q-L, Xue K-H, Shen W, Tao F-F, Yin S-Y and Xu W 2004 Fabrication and electrochemical properties of carbon nanotube array electrode for supercapacitors *Electrochim. Acta* **49** 4157–61
- [24] Zhang H, Cao G, Yang Y and Gu Z 2008 Comparison between electrochemical properties of aligned carbon nanotube array and entangled carbon nanotube electrodes *J. Electrochem. Soc.* **155** K19–22
- [25] Arcila-Velez M R, Zhu J, Childress A, Karakaya M, Podila R, Rao A M and Roberts M E 2014 Roll-to-roll synthesis of vertically aligned carbon nanotube electrodes for electrical double layer capacitors *Nano Energy* **8** 9–16
- [26] Reit R, Nguyen J and Ready W J 2013 Growth time performance dependence of vertically aligned carbon nanotube supercapacitors grown on aluminum substrates *Electrochim. Acta* **91** 96–100
- [27] Lv P, Zhang P, Li F, Li Y, Feng Y and Feng W 2012 Vertically aligned carbon nanotubes grown on carbon fabric with high rate capability for super-capacitors *Synth. Met.* **162** 1090–6
- [28] Qiu Y, Li G, Hou Y, Pan Z, Li H, Li W, Liu M, Ye F, Yang X and Zhang Y 2015 Vertically aligned carbon nanotubes on carbon nanofibers: a hierarchical three-dimensional carbon nanostructure for high-energy flexible supercapacitors *Chem. Mater.* **27** 1194–200
- [29] Kumar R, Singh R K, Dubey P K, Singh D P, Yadav R M and Tiwari R S 2015 Freestanding 3D graphene–nickel encapsulated nitrogen-rich aligned bamboo like carbon nanotubes for high-performance supercapacitors with robust cycle stability *Advanced Materials Interfaces* **2** 1500191
- [30] Ferrari A, Meyer J, Scardaci V, Casiraghi C, Lazzeri M, Mauri F, Piscanec S, Jiang D, Novoselov K and Roth S 2006 Raman spectrum of graphene and graphene layers *Phys. Rev. Lett.* **97** 187401
- [31] Ferrari A C and Robertson J 2004 Raman spectroscopy of amorphous, nanostructured, diamond-like carbon, and nanodiamond *Phil. Trans. R. Soc. A* **362** 2477–512
- [32] Malard L, Pimenta M, Dresselhaus G and Dresselhaus M 2009 Raman spectroscopy in graphene *Phys. Rep.* **473** 51–87
- [33] Bedewy M, Meshot E R, Reinker M J and Hart A J 2011 Population growth dynamics of carbon nanotubes *ACS Nano* **5** 8974–89
- [34] Bedewy M, Meshot E R, Guo H, Verploegen E A, Lu W and Hart A J 2009 Collective mechanism for the evolution and self-termination of vertically aligned carbon nanotube growth *J. Phys. Chem. C* **113** 20576–82
- [35] Esconjauregui S, Xie R, Guo Y, Pfaendler S M-L, Fouquet M, Gillen R, Cepek C, Castellarin-Cudia C, Eslava S and Robertson J 2013 Electrical conduction of carbon nanotube forests through sub-nanometric films of alumina *Appl. Phys. Lett.* **102** 113109
- [36] Kaneko A, Yamada K, Kumahara R, Kato H and Homma Y 2012 Comparative study of catalytic activity of iron and cobalt for growing carbon nanotubes on alumina and silicon oxide *J. Phys. Chem. C* **116** 26060–5
- [37] Atthipalli G, Wang H and Gray J L 2013 Catalyst-assisted vertical growth of carbon nanotubes on Inconel coated commercial copper foil substrates versus sputtered copper films *Appl. Surf. Sci.* **273** 515–9
- [38] Araujo P T, Maciel I, Pesce P, Pimenta M, Doorn S, Qian H, Hartschuh A, Steiner M, Grigorian L and Hata K 2008 Nature of the constant factor in the relation between radial breathing mode frequency and tube diameter for single-wall carbon nanotubes *Phys. Rev. B* **77** 241403
- [39] Araujo P, Pesce P, Dresselhaus M, Sato K, Saito R and Jorio A 2010 Resonance Raman spectroscopy of the radial breathing modes in carbon nanotubes *Physica E* **42** 1251–61
- [40] Kao E, Yang C, Warren R, Kozinda A and Lin L 2016 ALD titanium nitride on vertically aligned carbon nanotube forests for electrochemical supercapacitors *Sens. Actuators, A* **240** 160–6
- [41] Dogru I B, Durukan M B, Turel O and Unalan H E 2016 Flexible supercapacitor electrodes with vertically aligned carbon nanotubes grown on aluminum foils *Progress in Natural Science: Materials International* **26** 232–6

Part 3

III. 研究報告

4. 熱的プロセスによるバイオマスからの水素製造と安全利用技術

武野 計二 (熱エネルギー工学研究室)

5. 新規な金属クラスターの発生法と触媒機能

本山 幸弘 (触媒有機化学研究室)

6. 放射光 X 線および中性子回折技術に基づく合成高分子の結晶構造解析 :

田代 孝二 (田代孝二特任教授研究室)

熱的プロセスによるバイオマスからの水素製造と安全利用技術

豊田工業大学
○武野計二

Hydrogen production from biomass by thermal process and safety technology of utilization

Keiji Takeno

Toyota Technological Institute, Tempaku, Nagoya, 468-8511, Japan

takeno@toyota-ti.ac.jp

The utilization of hydrogen for energy use is attractive since the exhaust gas is H₂O alone and will spread widely, when renewable energies and CO₂ reduction technologies are combined with the hydrogen-oxygen energy chain. For the purpose, the gasification technology for biomass has been developed. In this report, the overview of hydrogen energy chain and gasification technology is introduced and the influence of CO₂ in the devolatilization process on the gasification reaction is reported. Furthermore, the ignition and flame stabilization when the high-pressurized hydrogen would be released as a hypothetical accident is elucidated. The mechanism of flame stabilized behind the Mach disk was clarified on the basis of the experimental data and numerical simulation.

1. 水素エネルギーチェーン

クリーンエネルギーの切り札として水素社会の到来が言われ続けているが、水素は化石燃料とは異なり変換過程を経て得られる二次エネルギーであり、利用促進には製造、輸送、貯蔵、消費の全てのプロセスにおけるトータルとしてコストメリットが必要となる。水素は、気体では単位体積当たりの発熱量がメタンの約 1/3、プロパンの約 1/8 と小さく、また液体では沸点は約 20K と低いため、特に輸送と貯蔵の面で避け難いコストインパクトが生じる[1].

太陽光が地球に供給する全エネルギーのうち、再生可能エネルギーとして現状利用できている比率は 0.01%程度と試算されているが、利用が困難な最たる理由はエネルギー密度の低さにある[2]. 例えば、太陽光エネルギーがかなり凝縮した産物である木材や草などのバイオマスは、電力用エネルギーとして経済的に成り立つには半径 200km 以内からの収集が必要条件とされる[3]. ここで、風車やバイオマスなど再生可能エネルギーの大規模導入、エネルギー貯蔵、

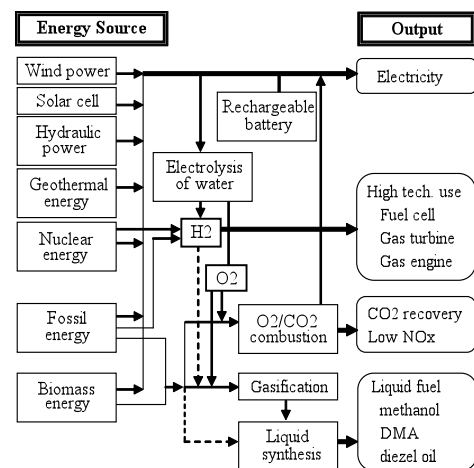


図1 水素を核としたエネルギーチェーン

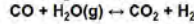
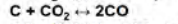
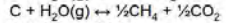
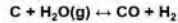
およびCO₂排出削減・固定化まで広げて考えると、図1に示す通り、水電解にて水素を製造する場合の副産物である酸素が、エネルギーチェーンの中で極めて重要な役割を演じることがわかる。すなわち、酸素は化石燃料やバイオマスのガス化生成ガスからアルコールやBDFなど液体燃料を合成するプロセスで不可欠であり、排ガスからのCO₂回収の容易性を狙ったCO₂/O₂燃焼にも活用できる。また、バイオマスは示性式でCH₂Oと概略表記されるが、そのガス化生成ガスから液体燃料を合成するには水素原子が炭素原子との比率として不足するので、水を水素源として添加するのが通常である。ここで水の代わりに水素ガスを用いると、熱収率が格段に増加する[4, 5]。このように、酸素や水素の効用によって再生エネルギーの導入や液体としてのエネルギー貯蔵に無駄が無くなり、水素社会の実現も現実的になるものと考えられる。

Gasification reactions in an updraft gasifier

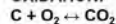
DRYING:
fuel → H₂O + dry fuel

PYROLYSIS:
fuel → tars + gases + carbon

GASIFICATION:



OXIDATION:



Thermoneutral reaction for carbon:

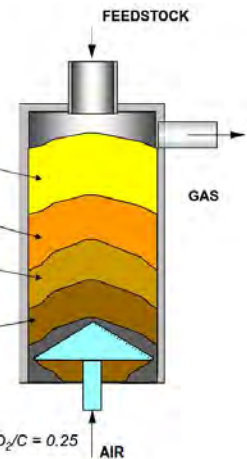
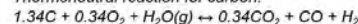


図2 ガス化炉内の主要反応

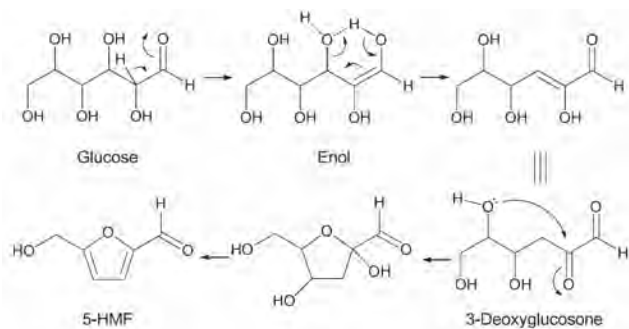


図3 グルコースの熱分解過程

2. 熱的プロセスによる水素製造

2.1 全体プロセス

図2は、固体燃料をCO+H₂に変換する上向き流通型ガス化炉の概要である。主要なガス化反応は大きな吸熱反応なので、一部の燃料を燃焼（発熱反応）させ、ガス化炉全体のエネルギーをバランスさせており、この方式は部分酸化ガス化と呼ばれている。

2.2 熱分解過程

図2に示すPyrolysisは、熱のみで分解する反応を示しており、揮発分、タール（2環以上の芳香族炭化水素と定義）、およびチャー（炭素が主体）が生成する。図3には熱分解によってセルロース構造が分解する過程の研究結果を示す[6]。また図4より、550℃の雰囲気では約1s以内に熱分解が完了すること、チャーの生成比率は燃料によって異なり石炭では50~60wt%と大きいのにに対しバイオマスでは10~20wt%と小さいことがわかる。しかし、その残った10~20wt%のチャー

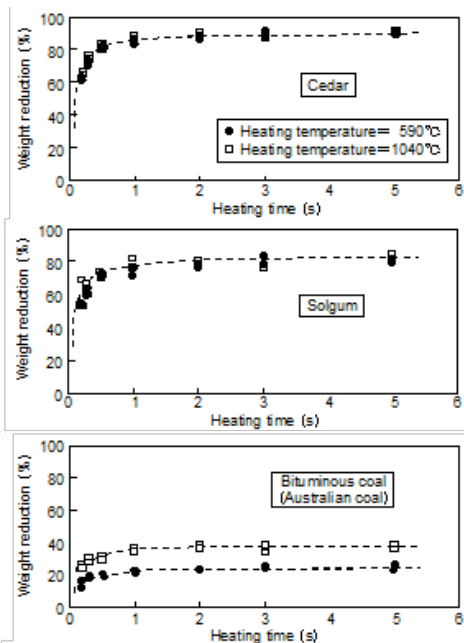
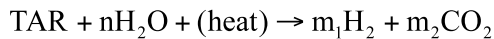


図4 固体燃料の熱分解速度

の反応速度は次項に示す通り熱分解速度の 1/5 程度しかなく、未燃の燃料はこのチャーの未反応分に相当する。

タールは沸点が 200°C 程度以上なので、これが分解できずに排出されると後流機器に付着するなどの不具合の原因となる。そのため、タールの分解反応が調べられているが、ガス化炉の後流に存在する雰囲気組成では (図 2)、以下の総括反応で示される水添分解が主体となること、またこの反応を 1s オーダーで進ませる温度や水蒸気分圧条件が示されている [7]。



2.3 チャーのガス化過程

チャーのガス化は、CO₂ や H₂O 等のガス化剤が炭素骨格の活性部位に吸着と脱離を繰り返しながら反応が進行することがわかっている (Langmuir の吸着等温式)。流通管型反応装置を用いて、チャーのガス化速度を計測した結果を図 5 に示す。図 5 は、固体粒子に多数の通路 (ポア) が生じ、その側面で固気界面反応が進行するとの以下の式で表されるランダムポアモデルを用いて実験データを解析した結果である [4, 5]。

$$S = S_0(1 - X)\sqrt{1 - \psi \ln(1 - X)}$$

ここで、S は単位体積 (空隙を含む) 当りの細孔表面積を、X は反応率を、 Ψ はチャーの種類で決まる構造パラメータを表す。

図 5 より、バイオマスから作製されたチャーは、石炭由来のチャーより反応速度は 5 倍程度速いこと、また温度依存性は同等であることがわかる。また、石炭ガス化炉はガス化部分は平均 1300°C 程度と高く設定し、且つチャーのリサイクルを施しているが、バイオマスガス化では 900~1000°C 程度の温度でもワンパスでのガス化が可能であることがわかる。

2.4 共存ガスの影響

前項までの反応速度の計測および解析は、バイオマスの加熱や H₂O との反応など、共存ガスの影響が考慮されていないが、図 2 に示すように、特に部分酸化ガス化炉では燃焼によって生じた CO₂ が常に高濃度で共存している。そこで、バイオマスの熱分解を CO₂ の存在下で行わせ、生成したチ

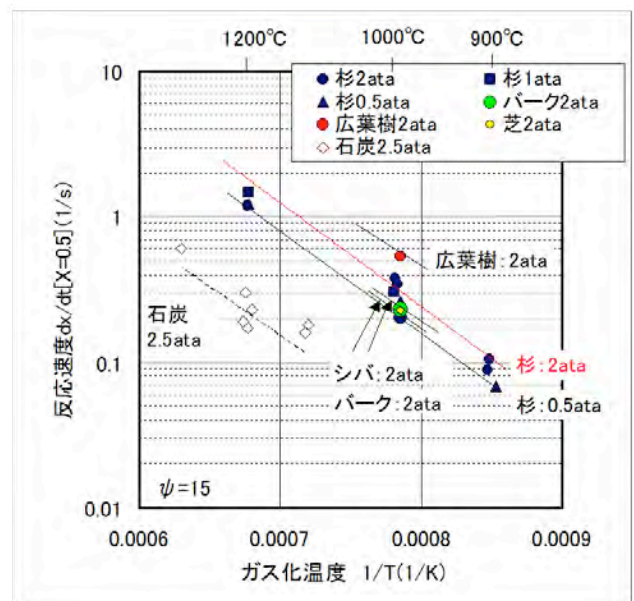


図 5 各種チャーの H₂O ガス化反応速度

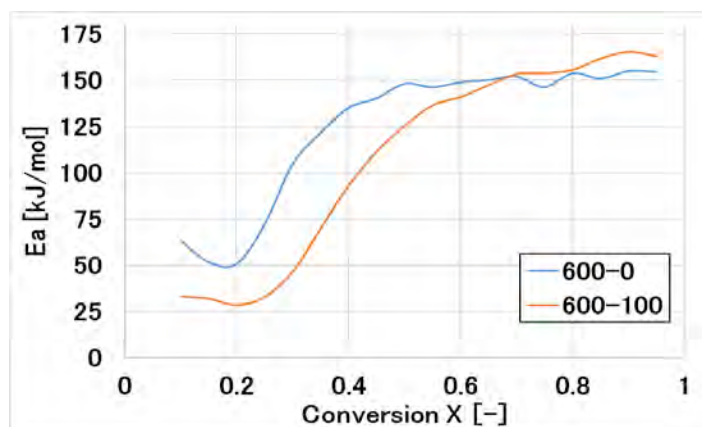


図 6 600°C 雰囲気での作製チャーの CO₂ ガス化反応における活性化エネルギー (共存ガスの影響)

チャーの性状を調べると共に、そのチャーのガス化反応性を調べた[8, 9].

CO₂ 濃度 100%および 0%の 2 種の条件で乾留させてチャーを作製し、それぞれのチャーのガス化反応を計測した. 図 6 は構築した CO₂ ガス化反応速度式の活性化エネルギーを比較したものである. 図より, CO₂ 濃度 100%雰囲気で作製したチャーは, 転換率が 0.5 以下と低いガス化初期の段階における活性化エネルギーが小さく, ガス化初期かつ低温雰囲気からガス化反応が進行し易い性質を有することがわかる. これは, 乾留段階から CO₂ 濃度が高い部分酸化型ガス化炉が, 全体のガス化反応の進行に対して, 間接加熱型より有利であることを示唆している. なお, 乾留時の CO₂ 共存の有無によって, 作製されたチャーの CHO 比に違いは見られなかった. またラマンスペクトルによるチャーの炭素構造解析においても, 有意な差は見られなかった. よって, ガス化反応への影響は, CO₂ によるカルボキシル基などの側鎖の脱離反応の促進, および脱離位置における活性炭素の生成によるものと推定される.

3. 水素の大規模利用

前述の通り水素は単位体積当たりの発熱量が低いので, 燃料電池自動車用では走行距離をガソリン車並みとするために 90MPa 程度の高圧搭載が進められている. このように高圧になると, 貯蔵や輸送技術が重要になる. また, インフラとして市街地に水素スタンドが必要になるので, 高圧水素に対するリスクアセスメントが進められている[3, 10]. そのための基礎資料として, 水素の噴出・拡散[11, 12], 着火・保炎[13, 14], 着火時の爆発規模や火炎スケール[15]などが調べられてきた. ここでは, 高圧水素の漏洩(噴出)時における着火(保炎)の基礎現象について述べる.

3.1 高圧水素噴出火炎の流体力学的構造

水素火炎内には, 可視光を吸収する化学種が存在しないため無色透明である. そのため, 噴出事象時にも着火しているか否か判明できず, 火傷を被る危険性がある.

図 7 に噴出直後の火炎基部の代表的なシュリーレン写真を示す. 高圧気体が噴出した場合, 噴出軸と垂直方向には樽型の衝撃波面(barrel shock)が, 噴出軸方向には円盤状の衝撃波面(Mach disk)が形成される. そして, Mach disk の後方に着火点が存在することがわかる. これは Mach disk の背後で流速が大きく減少する領域が形成され, 火炎が安定化したものと考えられる.

3.2 着火点における化学反応および数値計算

流体力学解析に H₂/O₂ 素反応をカップリングさせ, 火炎基部の着火現象を解析した結果を図 8 に示す (d=1mm, P=40MPa). ここで, 素反応セットとしては着火と消炎が高精度で解析できるとされている 19 段モデルを使用し[16], 乱流計算とは EDC (Eddy Dissipation Concept) モデルによりカップリングした. EDC モデルでは, 乱流計算はいわゆる RANS で解き, 格子以下の乱流微細構造につ

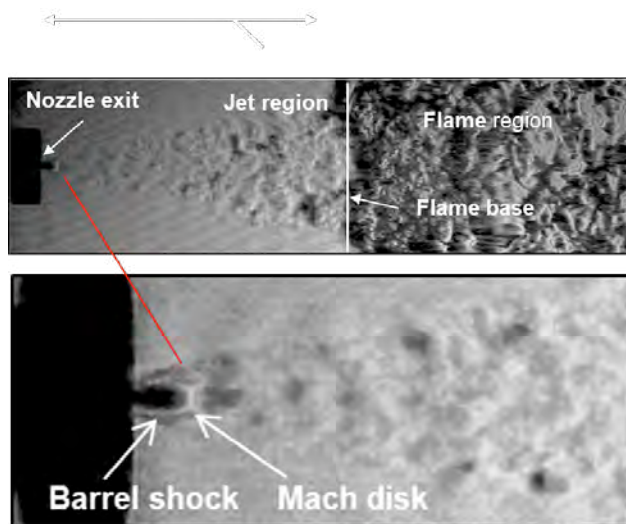


図 7 ノズル出口に生じる衝撃波および火炎 (ノズル直径:d=0.5mm, 圧力:P=11MPa)

いては、流体の特性時間だけ反応が進行するとしたモデルである。図8より、ショック面の背後で着火し全温 (total temperature) が上昇していること、活性基である OH, H, O ラジカルの濃度分布は温度分布とほぼ一致するが、水素燃焼反応の開始反応 (initiation) で生成されると言われる H₂O₂ ラジカルは、火炎の内側 (水素側) に高濃度で存在することがわかる。そして、 $H_2+O_2 \rightarrow H_2O_2+H$ の反応で生成する H ラジカル濃度の最大域は、OH や O ラジカルよりも火炎内側 (中心軸側) に存在する。また、ショック面の背後において barrel shock と Mach disk の交点付近から噴流の中心へと、酸素が拡散して侵入する様子が見られるが、その酸素と水素の混合物が外郭の火炎から熱を受け、H₂O₂ ラジカルが生成しているものと考えられる。マッハ数 10 以上の水素噴流に安定に保炎できる機構は、ショック面背後における流速の低下と、この領域への酸素の拡散によるものと考えられる。

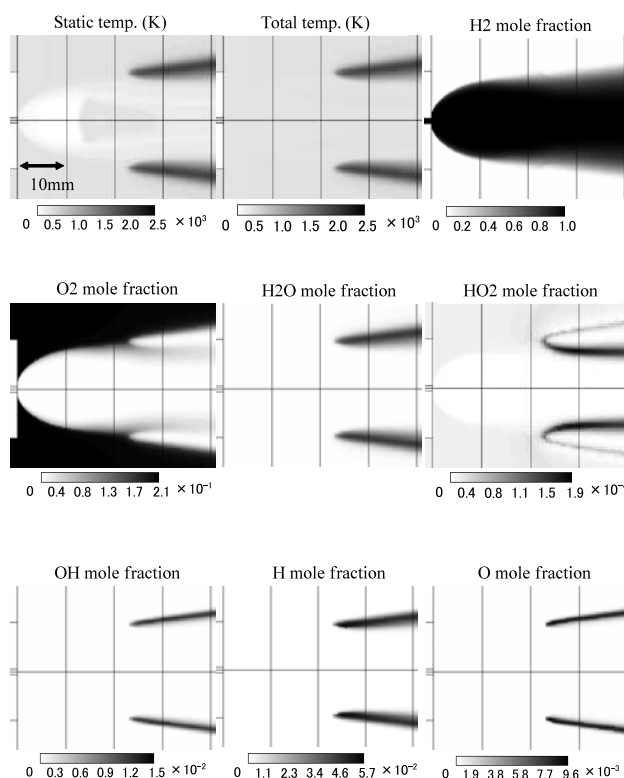


図8 ノズル出口近傍の温度および化学種分布 (ノズル直径: $d=1\text{mm}$, 圧力: $P=40\text{MPa}$)

参考文献

1. 水素エネルギー読本, 1,2 章, オーム社 (2007).
2. 石井弘実, 武野計二, バイオマスの噴流床部分酸化ガス化・液体燃料合成一貫システムの開発, *Journal of the Japanese Institute of Energy*, 84, 420-425 (2007).
3. 菊川重紀, 水素インフラに関する安全技術開発, NEDO 燃料電池・水素技術開発成果報告会要旨集 (2004).
4. Matsumoto, K., Takeno, K., and Ichinose, T., Gasification reaction kinetics on biomass char obtained as a by-product of gasification in an entrained-flow gasifier with steam and oxygen at 900-1000C, *Fuel*, 88, 519-527 (2009).
5. Matsumoto, K., Takeno, K., and Ichinose, T., Ogi, Tomoko, Nakanishi, Masakazu, Behavior of Alkali Metals As the Carbonate Compounds in the Biomass Char Obtained As a Byproduct of Gasification with Steam and Oxygen at 900-1000 C, *Energy and Fuel*, 24, 1980-1986 (2010).
6. 河本晴雄, セルロースの熱分解反応と分子機構, *木材学会誌*, 61, 1, 1-24 (2015).
7. 武野計二, 一ノ瀬利光, 福田憲弘, バイオマスの熱分解特性およびガス化反応シミュレーション, *日本機械学会論文集(B編)* 72,715, 778-783 (2007).
8. Gao, S., Zhao, J., Wang, Z., Wang, J., Effect of CO₂ on pyrolysis behaviors of lignite, *Journal of Fuel*

Chemistry and Technology, 41, 3, 257-264 (2013).

9. Yang, M., et al., *Journal of Renewable and Sustainable Energy*, 10(1), 13108 (2018).
10. 三石洋之, 水素安全利用等基盤技術開発－車両関連機器に関する研究開発－, NEDO 燃料電池・水素技術開発成果報告会要旨集 (2004).
11. Kouchi, A., Okabayashi, K., Takeno, K. and Chitose, K. Dispersion tests on concentration and its fluctuation for 40MPa pressurized hydrogen. *Proceeding of International Conference on Hydrogen Safety*, Sep. 8-10, 2007, Pisa, Italy.
12. Takeno, K., Okabayashi, K., Kouchi, A., Misaka, N. and Hashiguchi, K. Concentration Fluctuation and Ignition Characteristics during Atmospheric Diffusion of Hydrogen Spouted from high Pressure Storage. *International Journal of Hydrogen Energy*, 42(22), 15426-15434 (2017)..
13. 武野計二, 岡林一木, 橋口和明, 野口文子, 千歳敬子, 40MPa 高圧水素ガスの噴出火炎に関する実験的研究, *環境管理*, 41, 10, 33-40 (2005).
14. Yamamoto, S., Sakatsume, R. and Takeno, K. Blow-off process of highly under-expanded hydrogen non-premixed jet flame. *International Journal of Hydrogen Energy*, 43(10), 5199-5205 (2018).
15. Takeno, K., Okabayashi, K., Kouchi, A., Nonaka, T., Hashiguchi, K. and Chitose, K. Dispersion and explosion field tests for 40MPa pressurized hydrogen. *International Journal of Hydrogen Energy*, 32, 2144-2153 (2007).
16. Hishida, M. and Hayashi, K., *Proceeding of Eighteenth International Symposium on Space Technology and Science*, Kagoshima, 673-678 (1992).

Available online at www.sciencedirect.com

ScienceDirect

journal homepage: www.elsevier.com/locate/he

Blow-off process of highly under-expanded hydrogen non-premixed jet flame



Shohei Yamamoto ^a, Ryo Sakatsume ^b, Keiji Takeno ^{b,*}

^a Department of Mechanical Systems Engineering, Tokyo University of Agriculture and Technology, 2-24-16 Naka-cho, Koganei-city, Tokyo 184-8588, Japan

^b Department of Advanced Science and Technology, Toyota Technological Institute, 2-12-1 Hisakata, Tenpaku-ku, Nagoya 468-8511, Japan

ARTICLE INFO

Article history:

Received 7 August 2017

Received in revised form

29 November 2017

Accepted 21 January 2018

Available online 15 February 2018

Keywords:

Under-expanded jet

Blow-off

Turbulence

Non-premixed flame

Notional nozzle

ABSTRACT

Relationships between flame lift-off heights and reservoir pressure were experimentally investigated in order to clarify blow-off process of hydrogen non-premixed jet flames with a highly under-expanded jet structure. In this study, straight nozzles with diameters of 0.34, 0.53, 0.75 and 1.12 mm were used with maximum reservoir pressure for spouting hydrogen of 13.2 MPa. Experimental results are shown that lift-off heights in stable under-expanded jet flames do not vary significantly and are independent of the reservoir pressure in the range of studied pressure. However, the lifted heights are affected by the nozzle diameters and become smaller as the nozzle diameters increase. From experimental results, the condition for the blow-off process of under-expanded subsonic jet flames was proposed. It was concluded that the under-expanded jet flame could be blown off when the maximum waistline position, where radial distance from the jet axis to an elliptic stoichiometric contour reaches its maximum comes closer to the nozzle exit than the edge of the jet flame base.

© 2018 Hydrogen Energy Publications LLC. Published by Elsevier Ltd. All rights reserved.

Introduction

Storing gaseous hydrogen in high pressure vessels under high pressure is the most common way to make it available as an energy carrier because of its low volumetric energy density. The hydrogen pressure for vehicular fuel cell applications can reach 70 MPa. At such a high pressure, if a hydrogen release from the vessel ignited, a non-premixed jet flame with the structure of a highly under-expanded jet would be formed.

The characteristics of an under-expanded hydrogen jet flame have been investigated by many researchers [1–9], and the results could be used for establishing safety evaluation

criteria. Straight nozzles were used in experiments with diameters ranging from 0.32 to 10.0 mm. All experiments were performed by Takeno et al. under a maximum reservoir pressure of 40 MPa for spouting hydrogen [4–9]. The conditions at the nozzle (diameter and reservoir pressure) required for stable under-expanded hydrogen jet flames were explained in Refs. [4,6] and an empirical equation for the length of the under-expanded hydrogen jet flame was provided. The formula is expressed as a function of the nozzle diameter and the reservoir pressure [4,5]. As for researches for the length of hydrogen jet flames, Molkov et al. have reviewed in their literature [7]. It was also reported that an ignited flame propagates at over 600 m/s in the hydrogen jet immediately

* Corresponding author.

E-mail address: takeno@toyota-ti.ac.jp (K. Takeno).

<https://doi.org/10.1016/j.ijhydene.2018.01.116>

0360-3199/© 2018 Hydrogen Energy Publications LLC. Published by Elsevier Ltd. All rights reserved.

after hydrogen release [8–10]. However, the stability and blow-off mechanism of the jet flame formed after ignition were not mentioned.

An increase of pressure in the reservoir results in blow-off for the stable subsonic non-premixed jet flames. Studies on blow-off velocities for various fuels have been performed [11–13], and the blow-off phenomena was also suggested [14,15]. Experimental investigation of blow-off stability for non-premixed jet flames in various fuels was done by Kalghatgi [11]. Correlations for the blow-off velocity were proposed based on the reported experimental results [11,12]. Wu et al. suggested the condition for the blow-off process in a turbulent non-premixed jet flames based on the theoretical and experimental investigation of fuel distribution concentration in jets [15].

Birch et al. showed conditions required for stable under-expanded natural gas jet flames [16]. The straight nozzles with diameters from 5.5 to 38.1 mm were used for their experiments, and the maximum reservoir pressure was 10 MPa. They suggested that the blow-off pressure can be predicted from extrapolating blow-off velocities measured in subsonic jets by applying a notional nozzle concept where it was assumed that jets appeared as if they originate from notional nozzles [17]. They also reported that the blow-off in under-expanded jet flames occurs when the storage pressure decreases [18]. However, the blow-off process of under-expanded jet flames is unclear.

In the present paper, the blow-off pressure is predicted and is compared with the experimentally obtained blow-off pressure based on the notional nozzle concept [19–22] and the subsonic jet flame blow-off condition proposed by Wu et al. [15]. The condition for the blow-off process of under-expanded jet flames is proposed.

Experimental setup and conditions

Fig. 1 shows the schematic diagram of the experimental setup and the optical system used in this study. The highly under-expanded jet was formed by blow-down of hydrogen from a high pressure cylinder through a straight nozzle with a round outlet. The jet was ignited by a non-premixed natural gas jet flame, which was located at the position of 70 mm downstream in the jet axis direction. The ignition source was removed after the ignition of hydrogen jet was confirmed. The release of hydrogen from the high pressure cylinder was manually controlled by a needle valve, and pressure in the passage was measured by a pressure transducer (TP-AR, TEAC) at 520 mm upstream of the nozzle exit. The measured maximum pressure was almost constant (deviations were within 0.20 MPa) when the needle valve was fully opened. Output signals from the pressure transducer was amplified by an amplifier (DAS-406B, Minebea) and recorded by a data acquisition unit (GL-7000, GRAPHTEC). Data sampling frequency was set at 10 kHz. The pressure data was acquired synchronously with schlieren imaging. Diameters d of straight nozzles used in this study and the values of the maximum reservoir pressure p_{max} measured in experiments are listed at Table 1.

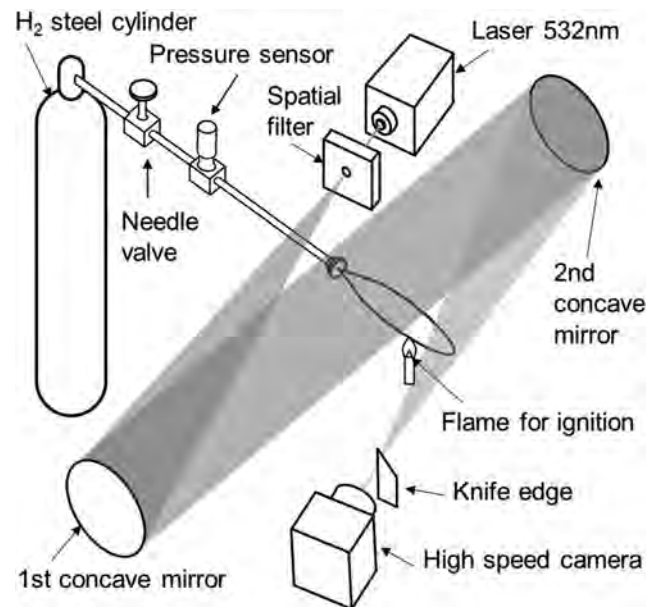


Fig. 1 – Schematic diagram of experimental set up.

Table 1 – Experimental conditions of nozzle diameters d and maximum reservoir pressure p_{max} .

d [mm]	Maximum reservoir pressure p_{max} [MPa]
0.34	12.6
	13.2
0.53	9.5
	13.1
0.75	3.6
	5.5
1.12	0.7
	2.2

In this study, lift-off heights in highly under-expanded hydrogen jet flames were measured from schlieren images. A schlieren optical system was consisted of a laser (wave length: 532 nm, maximum output: 50 mW, G50-B, KATO KOKEN), a spatial filter, two concave mirrors (diameter: 150 mm, focus length: 1500 mm) and a knife edge. Schlieren images were recorded by a high speed camera (UX100, Photon) at 1000 fps frame rate and 12.9 μ s exposure time.

Experimental results and discussion

Variations in lift-off height and mach disk position

Fig. 2 shows schlieren images obtained in the single experiment under the condition of $d = 0.53$ mm and $p_{max} = 13.1$ MPa. The values of pressure in these images denote the measured reservoir pressure p_1 at photographing time, and the variation in p_1 was caused by continuously closing the needle valve. A Mach disk approaches gradually the nozzle exit as p_1 decreases. As shown in Fig. 3, the measured L_{MD} (distance along the nozzle axis direction from the nozzle exit to the Mach disk) coincides well with L_{MD} predicted by an empirical equation $L_{MD}/d = 0.62 \eta_0^{0.51}$

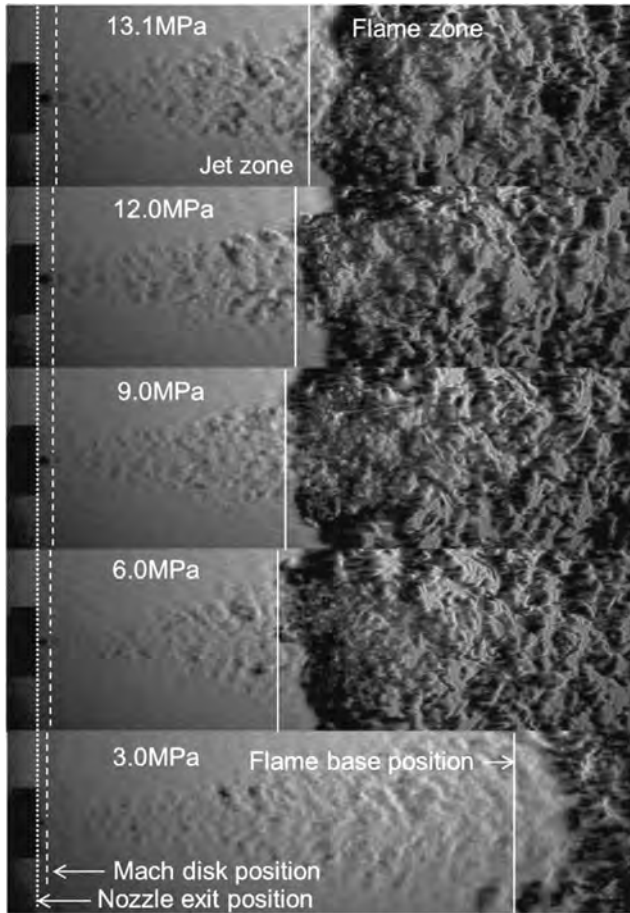


Fig. 2 – Schlieren image of under-expanded non-premixed jet flame ($d = 0.53$ mm, $p_{max} = 13.1$ MPa).

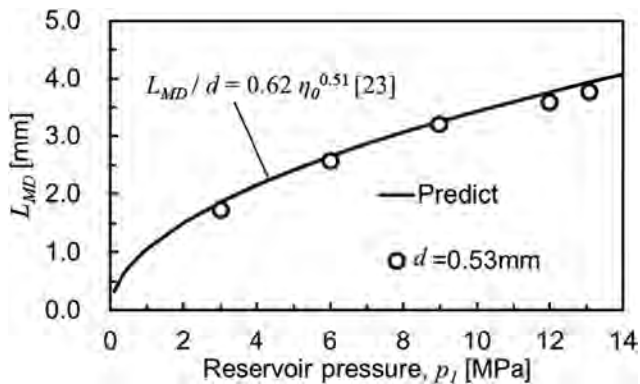


Fig. 3 – Comparison between measured and predicted distance along the jet axis from the nozzle exit to the Mach disk.

($\eta_0 = p_1/p_{amb}$, p_{amb} : atmospheric pressure), which is provided by Franquet et al. [23]. Lift-off heights in these depicted jet flames over the range from $p_1 = 6.0$ – 13.1 MPa are almost constant. However, the lifted height at $p_1 = 3.0$ MPa becomes sufficiently larger than that at any other pressures.

Fig. 4(b) shows the relationship between p_1 and H_{fb} (distance along the nozzle to the jet flame base position) in cases of $d = 0.53$ mm ($p_{max} = 9.5$ or 13.1 MPa). Flame base height H_{fb}

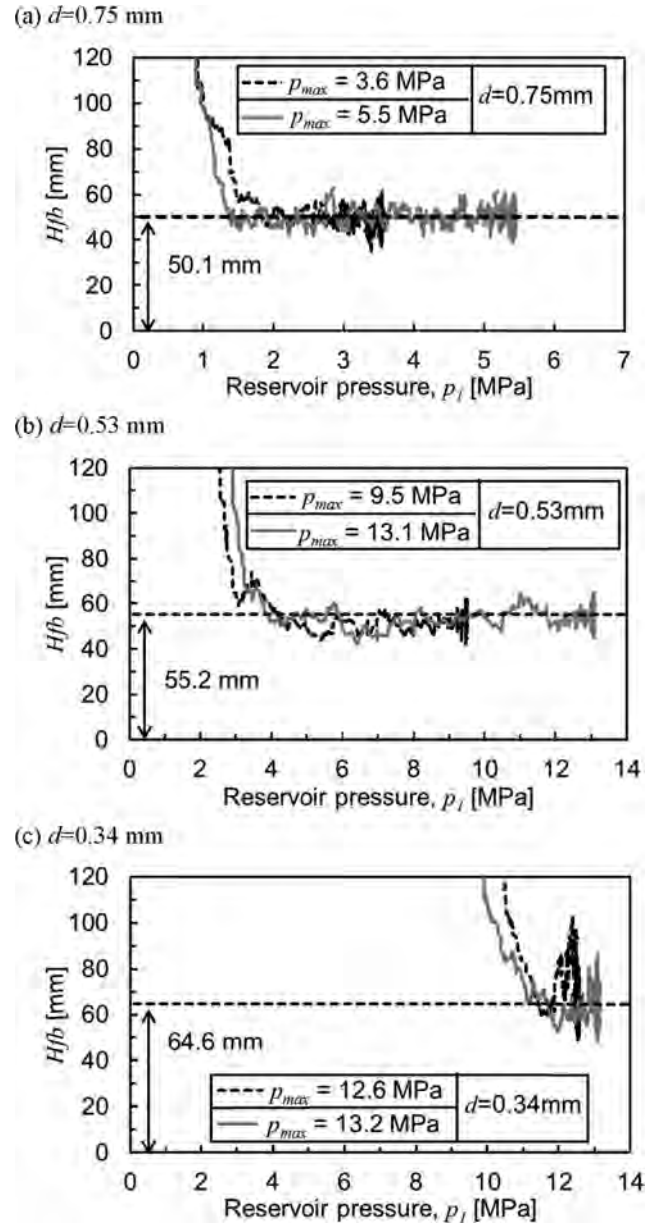


Fig. 4 – Relationship between the measured reservoir pressure p_1 and H_{fb} with $d = 0.34$, 0.53 , and 0.75 mm (H_{fb} : distance along the nozzle axis direction from the nozzle exit to the flame base position).

at $p_1 = 4.0$ MPa or higher is almost constant regardless of p_{max} , and the jet flame base position starts to move downstream when p_1 becomes less than 4.0 MPa. Almost constant H_{fb} is kept at $H_{fb} = 55.2$ mm.

Fig. 4(a) and (c) show cases of $d = 0.75$ mm ($p_{max} = 3.6$ or 5.5 MPa) and 0.34 mm ($p_{max} = 12.6$ or 13.2 MPa) respectively. Flame base height H_{fb} for $d = 0.75$ mm is equal to 50.1 mm, and p_1 at which the jet flame base starts to recede is about 1.5 MPa irrespective of p_{max} as shown in Fig. 4(a). On the other hand, $H_{fb} = 64.6$ mm as shown in Fig. 4(c) when $d = 0.34$ mm. The fluctuation in the jet flame base position is larger than other two cases of $d = 0.53$ and 0.75 mm. The value of p_1 which leads the flame base into the regression is about 12.6 MPa.

Relationships between jet flame blow-off pressures and nozzle diameters which were presented by Takeno et al. [4,6] are shown in Fig. 5. Blank circle symbols denote conditions (the reservoir pressure and the nozzle diameter) required for stable jet flames, and X symbols denote conditions under which the jet flame is blown off. Aforementioned reservoir pressure to lead the jet flame base into the regression is also plotted in this figure. The regression pressure is located nearly on the line which represents conditions separating the blow-off and stabilization of jet flames. This means that the regression pressure is almost the same as the blow-off pressure presented in the literature. Moreover, conditions required for a notional nozzle diameter $dn = 2.06$ mm are indicated by a dotted line. The notional nozzle diameter dn was calculated using the method proposed by Molkov et al. [22]. The model is based on the concept of Birch et al. [17] but the effect of the non-ideal behaviour of the high-pressurized hydrogen is additionally taken into account through Abel-Nobel equation for isentropically expanded gas. The pressure and velocity at the notional nozzle are atmospheric and the sound speed of hydrogen respectively. A temperature at the pseudo nozzle is calculated from conservation equations of mass, total energy and the Abel-Nobel equation. Notional nozzle dn is determined uniquely from the reservoir pressure and the nozzle diameter if target gas is decided as follows [22]. Density in the reservoir from the Abel-Nobel equation of state is calculated:

$$\rho_1 = p_1 / (bp_1 + R_{H_2}T_1), \quad (1)$$

where b is a constant ($=7.69 \text{ m}^3/\text{kg}$), R_{H_2} is a gas constant for hydrogen ($=4124 \text{ J}/(\text{kg K})$) and a subscript 1 means “reservoir”. Density ρ_2 at the nozzle exit is determined by solving an isentropic expansion equation:

$$\left(\frac{\rho_1}{(1 - b\rho_1)} \right)^\gamma = \left(\frac{\rho_2}{(1 - b\rho_2)} \right)^\gamma \left[1 + \frac{(\gamma - 1)}{2(1 - b\rho_2)^2} \right]^{\frac{\gamma}{1-\gamma}} \quad (2)$$

Temperature T_2 at the nozzle exit is obtained from the following equation:

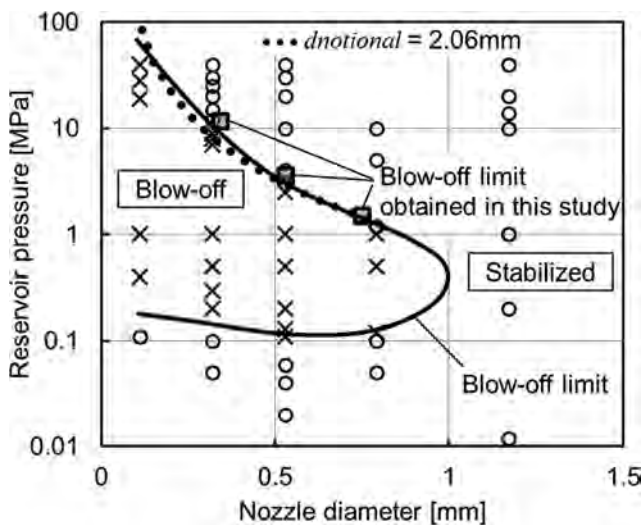


Fig. 5 – Relationships between pressure for blowing off of jet flames and nozzle diameters.

$$T_1/T_2 = 1 + (\gamma - 1) / 2(1 - b\rho_2)^2, \quad (3)$$

where γ is the ratio of specific heats ($=1.405$), and then pressure p_2 at the nozzle exit can be calculated from the Abel-Nobel equation of state. Flow is choked at the nozzle exit and hydrogen velocity V_2 is determined using the following equation for the sound speed:

$$V_2^2 = \gamma R_{H_2} T_2 / (1 - b\rho_2)^2. \quad (4)$$

Temperature T_3 at the notional nozzle can be calculated from the following energy conservation equation:

$$c_p T_2 + V_2^2/2 = c_p T_3 + V_3^2/2, \quad (5)$$

where c_p is a specific heat at constant pressure. The hydrogen velocity V_3 at the notional nozzle is assumed to be equal to the local sound speed:

$$V_3^2 = \gamma R_{H_2} T_3. \quad (6)$$

From above two equations, the temperature T_3 is expressed as

$$T_3 = \frac{2T_2}{\gamma + 1} + \frac{\gamma - 1}{\gamma + 1} \frac{p_2}{\rho_2(1 - b\rho_2)R_{H_2}} \quad (7)$$

Finally, from the conservation equation of mass the notional nozzle diameter dn can be calculated:

$$dn = d(\rho_2 V_2 / \rho_3 V_3)^{0.5}, \quad (8)$$

where ρ_3 is hydrogen density which is calculated with the assumption that pressure p_3 at the notional nozzle is equal to the ambient pressure.

The dotted line coincides well with the line of the blow-off limit conditions when the nozzle diameter d is less than about 0.8 mm. Thus, the structure of highly under-expanded jets injected at the blow-off pressure can be modelled by a jet spouted through the notional nozzle with a certain single diameter.

Blow-off process of highly under-expanded jet flames

Fig. 6(a) shows the schematic diagram of the blow-off process for turbulent non-premixed jet flames proposed by Wu et al. [15]. The maximum waistline position is defined as a position where distance in radial direction perpendicular to nozzle axis reaches maximum on the elliptic stoichiometric contour in jets. The position is the dividing point separating stable and unstable region of subsonic turbulent non-premixed jet flames in the blow-off. H_w is the distance from nozzle exit to the intersection of two lines which are the nozzle axis and a perpendicular line from the maximum waistline position to the nozzle axis. Then, the stable and unstable conditions of turbulent non-premixed jet flames are shown as follows. $H_{fb} \leq H_w$ is the condition for the stable lifted jet flame. In this case, the flame base exists in the stable region in Fig. 6(a). The jet flame base position starts pulsating when H_{fb} becomes larger than H_w because of the increase in the flow velocity of gas released out of the nozzle exit (the jet flame base exists in the pulsating region in Fig. 6(a)). Moreover, if the jet flame base

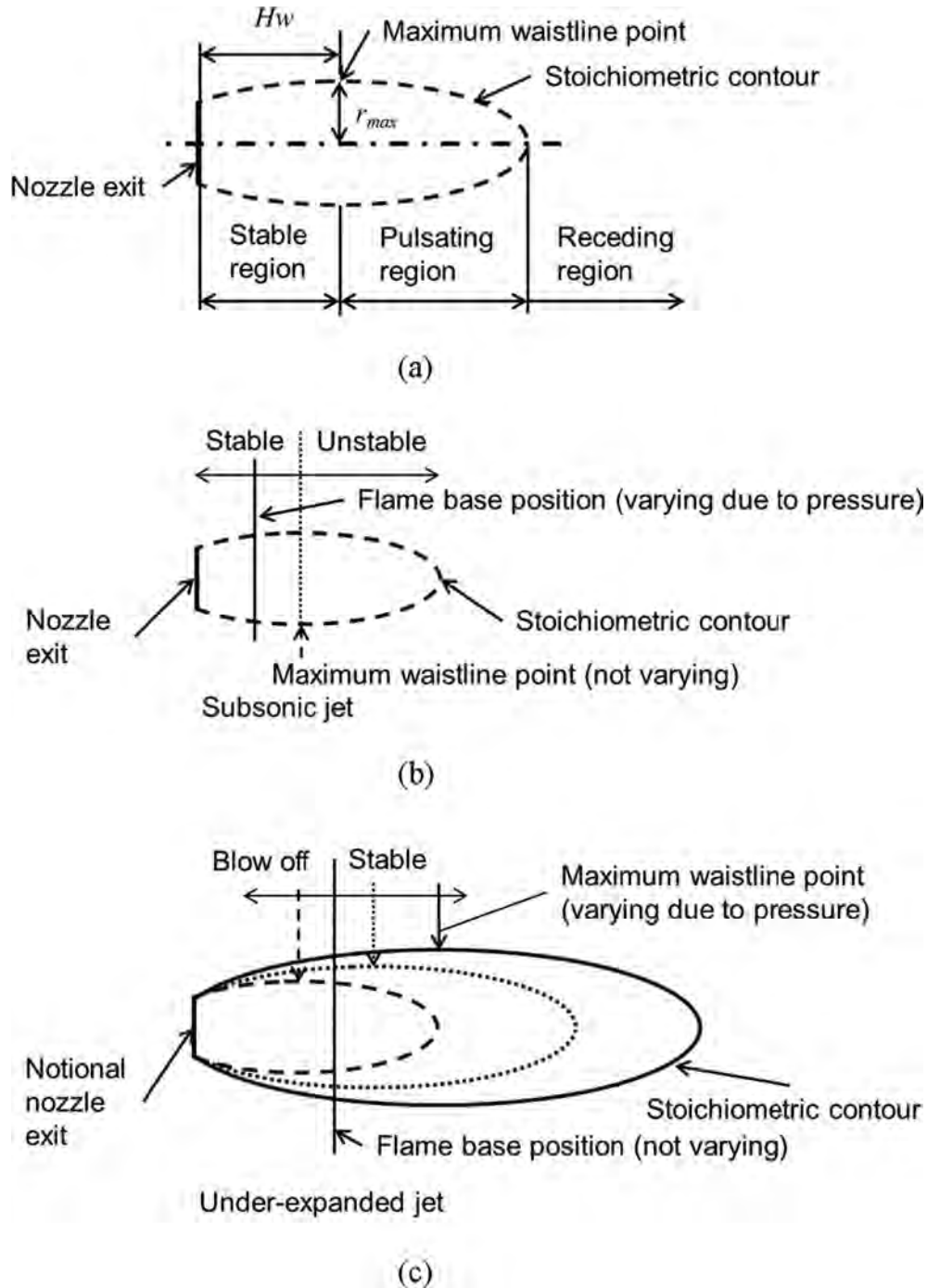


Fig. 6 – Schematics showing flame stability and blow-off process of subsonic and under-expanded jet flames. (a) Change in flame stability due to the flame base position [14]. (b) Schematic of blow-off process of subsonic jet flames. (c) Schematic of blow-off process of under-expanded jet flames.

is pushed further downstream and exceeds the tip of the elliptic stoichiometric contour, the flame base position recedes downstream continuously and finally the jet flame is blown off. The value of H_w can be theoretically predicted using the model proposed by Birch et al. [24] and is experimentally verified by Wu et al. [15]. They reported that although the model overpredicted H_w (Relative deviation of shown data was almost 16%), the predicted data agreed fairly well with the measured one [15]. In the model, H_w is

calculated from three parameters, injected gas density at the nozzle exit, ambient gas density and the diameter of the nozzle exit regardless of the flow velocity at the nozzle exit as follows [15]. A normalized axial profile of mass fraction in a jet can be expressed as

$$\bar{\theta}_c / \bar{\theta}_e = k_1 d_{eff} / (z + a_1), \quad d_{eff} = d(\rho_e / \rho_\infty)^{0.5}, \quad (9)$$

where $\bar{\theta}$, ρ , z , and d_{eff} are the fuel mass fraction, density, distance in an axial direction from the nozzle exit and effective

diameter respectively. And k_1 and a_1 are 4.0 and $-5.8d$ respectively. Subscripts e and ∞ denote conditions at the nozzle exit and in an ambient atmosphere. A normalized radial profile of mass fraction in the jet is also described as

$$\bar{\theta}/\bar{\theta}_c = e^{\{-D(r/z)^2\}}, \quad (10)$$

where D is found to be 73.6, r is distance in a radial direction from the jet axis. Substituting Eq. (9) into Eq. (10) and $\bar{\theta}_s$ (stoichiometric mass fraction) into $\bar{\theta}$, the stoichiometric elliptic contour can be obtained and is shown as

$$r^2 + \frac{z^2}{73.6} \ln \frac{\bar{\theta}_s(z - 5.8d)}{4\bar{\theta}_e d_{eff}} = 0. \quad (11)$$

The maximum waistline position of the contour can be expressed by setting $dr/dz = 0$:

$$2 \ln \left[\frac{\bar{\theta}_s}{4\bar{\theta}_e d_{eff}} z - \frac{5.8d\bar{\theta}_s}{4\bar{\theta}_e d_{eff}} \right] = -\frac{z}{z - 5.8d}. \quad (12)$$

The value of H_w can be calculated by solving Eq. (12) for z .

As mentioned above, H_w of a subsonic jet is determined uniquely from the diameter at the nozzle exit and doesn't vary with the nozzle exit velocity (i.e. the reservoir pressure) if it's assumed that densities of injected and ambient gas are constants. However, the situation is markedly different when considering highly under-expanded jets. Maximum waistline position of the under-expanded jet H_w can be varied with the reservoir pressure because the notional nozzle diameter depends on the actual nozzle diameter and the reservoir pressure. The relationships between reservoir pressure and H_w of the under-expanded jets are shown in Fig. 7. The value of H_w in the under-expanded jet was calculated by setting d in Eq. (12) to dn . Experimentally obtained flame base heights H_{fb} are also shown in the figure. Pressure at points of intersection of H_w and H_{fb} lines are 11.4 MPa, 3.4 MPa and 1.4 MPa for $d = 0.34$ mm, 0.53 mm and 0.75 mm respectively as shown in Fig. 7. These are almost the same as the regression pressure previously described. Hence, the condition required for the stable under-expanded jet flame is also thought to be $H_{fb} \leq H_w$.

Consequently, $H_{fb} > H_w$ can be the blow-off condition regardless of whether jet flames have the structure of the under-expanded jet or not. However, the blow-off process of

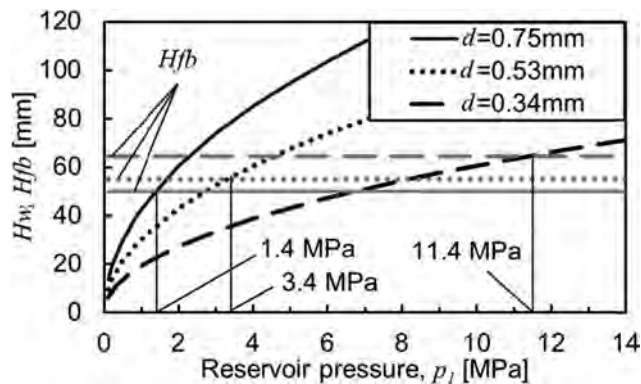


Fig. 7 – Prediction of the reservoir pressure required for stable under-expanded jet flames.

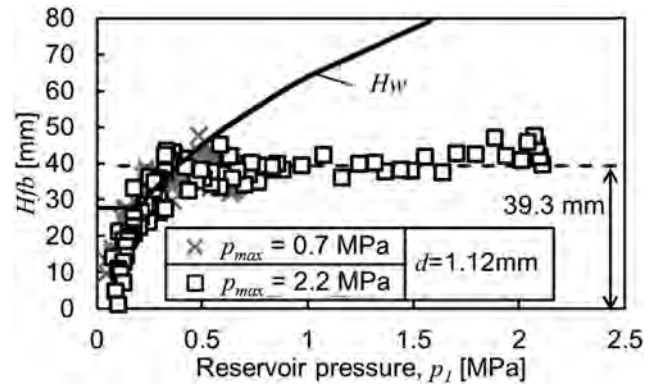


Fig. 8 – Relationship between measured H_{fb} and predicted H_w ($d = 1.12$ mm) in the case that jet flames are always stable irrespective of reservoir pressure.

the under-expanded jet flame is thought to be different from that of the subsonic jet flame. Fig. 6(b) shows the stoichiometric contour, the maximum waistline position and the jet flame base position for the stable subsonic jet flame. The maximum waistline position in the subsonic jet is invariable (i.e. $H_w = \text{constant}$) if the nozzle diameter is constant. The flame base position is variable when varying the flow velocity at the nozzle exit as shown in literature [11,25]. Therefore, $H_{fb} > H_w$ (blow-off condition) can be achieved only by increasing the nozzle exit velocity. On the other hand, a schematic of the blow-off process for the under-expanded jet flame is shown in Fig. 6(c). The flame base position of the stable under-expanded jet flame is nearly invariable irrespective of the reservoir pressure as indicated in results of this study (i.e. $H_{fb} = \text{constant}$). The maximum waistline position is variable because of varying the notional nozzle diameter with the reservoir pressure. Therefore, $H_{fb} > H_w$ can be achieved only by decreasing the reservoir pressure. This is the blow-off process of the under-expanded jet flame. Although this blow-off process is observed when reducing the reservoir pressure, the blow-off due to reduction in the reservoir pressure may never occur if the injection nozzle diameter is large enough as shown in Fig. 5.

Fig. 8 shows experimentally measured H_{fb} , the reservoir pressure and theoretically estimated H_w for the nozzle diameter of 1.12 mm. Hydrogen jet through this nozzle diameter sustains stable jet flames irrespective of the reservoir pressure. Therefore, $H_{fb} \leq H_w$ (stable condition) is sufficiently satisfied over the entire reservoir pressure range as shown in this figure.

Concluding remarks

The relationship between the highly under-expanded jet flame base position and the reservoir pressure was investigated under the condition continuously decreasing the reservoir pressure in order to clarify the blow-off process of the jet flames. The obtained results are as follows.

The measured distance along the nozzle axis direction from the nozzle exit to the jet flame base position H_{fb} of the stable highly under-expanded jet flame is almost constant.

However, H_{fb} depends on the nozzle exit diameter, and the larger nozzle exit diameter can have smaller H_{fb} .

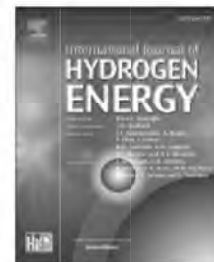
To predict the blow-off pressure for under-expanded jet flames, the blow-off condition was proposed. Then, the predicted blow-off pressure was in good agreement with the measured pressure which the jet flame base starts to move downstream. It is concluded that the condition required for the stable under-expanded jet flame is $H_{fb} \leq H_w$. On the other hand, the blow-off of the under-expanded jet flame occurs when H_w becomes smaller than H_{fb} because of decreasing the reservoir pressure. When the jets released through the nozzle hole with larger than a certain diameter sustains stable flames irrespective of the reservoir pressure, $H_{fb} \leq H_w$ (stable condition) has been sufficiently satisfied over the entire reservoir pressure range in this study.

REFERENCES

- [1] Annushkin YM, Sverdlov ED. Stability of submerged flames in subsonic and underexpanded supersonic gas-fuel streams. *Combust Explos Shock Waves* 1979;14(5):597–605.
- [2] Yoon Y, Donbar JM, Driscoll JF. Blow-out stability limits of a hydrogen jet flame in a supersonic heated coflowing air stream. *Combust Sci Technol* 1994;97(1–3):137–56.
- [3] Wu Y, Lu Y, Al-Rahbia IS, Kalghatgi GT. Prediction of the liftoff, blowout and blowoff stability limits of pure hydrogen and hydrogen/hydrocarbon mixture jet flames. *Int J Hydrogen Energy* 2009;34(14):5940–5.
- [4] Takeno K. Characteristics and safety for open-jet flame of high-pressurized hydrogen. *J Combust Soc Japan* (in Japanese) 2010;52(160):121–9.
- [5] Takeno K, Okabayashi K, Hashiguchi K, Noguchi F, Chitose K. Experimental Study on open jet diffusion flame of 40MPa high-pressure hydrogen. *Environ Manag* 2005;41:33–40.
- [6] Takeno K, Hashiguchi K, Okabayashi K, Chitose K, Kushiyaama M, Noguchi F. Experimental study on open jet diffusion flame and unconfined explosion for leaked high-pressurized hydrogen. *J Japan Soc Saf Eng* 2005;44:398–406.
- [7] Molkov V, Saffers J-B. Hydrogen jet flames. *Int J Hydrogen Energy* 2013;38(19):8141–58.
- [8] Takeno K, Okabayashi K, Ichinose T, Kouchi A, Nonaka T, Hashiguchi K, et al. Phenomena of dispersion and explosion of high pressurized hydrogen. In: *International conference on hydrogen safety*; Sep. 8-10, 2005. Pisa, Italy.
- [9] Takeno K, Okabayashi K, Kouchi A, Nonaka T, Hashiguchi K, Chitose K. Dispersion and explosion field tests for 40MPa pressurized hydrogen. *Int J Hydrogen Energy* 2007;32:2144–53.
- [10] Kouchi A, Okabayashi K, Takeno K, Chitose K. Dispersion tests on concentration and its fluctuation for 40MPa pressurized hydrogen. In: *Proceeding of international conference on hydrogen safety*; Sep. 8-10, 2005. Pisa, Italy.
- [11] Kalghatgi GT. Blow-out stability of gaseous jet diffusion flames. Part I: in still air. *Combust Sci Technol* 1981;26(5):233–9.
- [12] Broadwell JE, Dahm WJA, Mungal MG. Blowout of turbulent diffusion flames. 20th Symposium (International) on Combustion20(1); 1985. p. 303–10.
- [13] Pitts WM. Assessment of theories for the behavior and blowout of lifted turbulent jet diffusion flames. 22nd Symposium (International) on Combustion22(1); 1989. p. 809–16.
- [14] Schefer RC, Goix PJ. Mechanism of flame stabilization in turbulent lifted-jet flames. *Combust Flame* 1998;112:559–74.
- [15] Wu CY, Chao YC, Cheng TS, Li YH, Lee KY, Yuan T. The blowout mechanism of turbulent jet diffusion flames. *Combust Flame* 2006;145(3):481–94.
- [16] Birch AD, Brown DR, Cook DK, Hargrave GK. Flame stability in underexpanded natural gas jets. *Combust Sci Technol* 1988;58:267–80.
- [17] Birch AD, Hughes DJ, Swaffield F. Velocity decay of high pressure jets. *Combust Sci Technol* 1987;52:161–71.
- [18] Birch AD, Hargrave GK. Lift-off heights in underexpanded natural gas jet flames. 22nd Symposium (International) on Combustion22(1); 1989. p. 825–31.
- [19] Birch AD, Brown DR, Dodson MG, Swaffield F. The structure and concentration decay of high pressure jets of natural gas. *Combust Sci Technol* 1984;35(5–6):249–61.
- [20] Ewan BCR, Moodie K. Structure and velocity measurements in underexpanded jets. *Combust Sci Technol* 1986;45(5–6):275–88.
- [21] Schefer RW, Houff WG, Williams TC, Bourne B, Colton J. Characterization of high-pressure, underexpanded hydrogen-jet flames. *Int J Hydrogen Energy* 2007;32(12):2081–93.
- [22] Molkov V, Makarov D, Bragin M. Physics and modelling of under-expanded jets and hydrogen dispersion in atmosphere. In: *Physics of extreme state of matter*; 2009. p. 143–5.
- [23] Franquet E, Perrier V, Gibout S, Bruel P. Free underexpanded jets in a quiescent medium: a review. *Prog Aero Sci* 2015;77:25–53.
- [24] Birch AD, Brown DR, Dodson MG, Thomas JR. The turbulent concentration field of a methane jet. *J Fluid Mech* 1978;88(3):431–49.
- [25] Kalghatgi GT. Lift-off heights and visible lengths of vertical turbulent jet diffusion flames in still air. *Combust Sci Technol* 1984;41(1):17–29.

Available online at www.sciencedirect.com

ScienceDirect

journal homepage: www.elsevier.com/locate/hydro

Non-steady characteristics of dispersion and ignitability for high-pressurized hydrogen jet

K. Okabayashi ^{a,*}, K. Tagashira ^a, K. Kawazoe ^a, K. Takeno ^b,
M. Asahara ^c, A.K. Hayashi ^d, M. Komori ^e

^a Mitsubishi Heavy Industries, Ltd., Research and Innovation Center, 5-717-1 Fukahori, Nagasaki 851-0392, Japan

^b Toyota Technological Institute, Graduate School of Engineering, 2-12-1 Hisakata, Tempaku-ku, Nagoya 468-8511, Japan

^c Gifu University, Faculty of Engineering, 1-1 Yanagido, Gifu 501-1193, Japan

^d Aoyama Gakuin University, Graduate School of Science and Engineering, 5-10-1 Fuchinobe, Chuo-ku, Sagami-hara-shi, Kanagawa 252-5258, Japan

^e Japan Petroleum Energy Center, Sumitomo Fudosan Shiba-Koen Tower, 11-1, Shibakoen 2-Chome, Minato-Ku, Tokyo 105-0011, Japan

ARTICLE INFO

Article history:

Received 15 January 2018

Received in revised form

5 May 2018

Accepted 7 May 2018

Available online 1 June 2018

Keywords:

Hydrogen jet

Dispersion

Ignitability

High-pressure

Concentration fluctuation

Non-steady characteristics

ABSTRACT

Hydrogen gas concentrations and jet velocities were measured downstream by a high response speed flame ionization detector and PIV (Particle Image Velocimetry) in order to investigate the characteristics of dispersion and ignitability for 40–82 MPa high-pressurized hydrogen jet discharged from a nozzle with 0.2 mm diameter. The light emitted from both OH radical and water vapor species yielded from hydrogen combustion, ignited by an electric spark, were recorded by two high speed cameras. From the results, the empirical formula concerning the relationships for time-averaged concentrations, concentration fluctuations and ignition probability were obtained to suggest that they would be independent of hydrogen discharge pressure.

© 2018 Hydrogen Energy Publications LLC. Published by Elsevier Ltd. All rights reserved.

Introduction

Recently, hydrogen energy has been in focus as a clean energy in the future. There is a great expectation for fuel cell vehicles as one of utilizations of hydrogen energy. Therefore, to

promote the introduction of fuel cell vehicles, the safe installation of hydrogen stations at urban areas is an urgent task. To do this, the relaxation of regulation for safety is necessary. In the present regulation, the distance between the dispenser of the station and public boundary is kept in more

* Corresponding author.

E-mail addresses: kazuki_okabayashi@mhi.co.jp (K. Okabayashi), takeno@toyota-ti.ac.jp (K. Takeno), asahara@gifu-u.ac.jp (M. Asahara), hayashi@me.aoyama.ac.jp (A.K. Hayashi), ma-komori@pecj.or.jp (M. Komori).
<https://doi.org/10.1016/j.ijhydene.2018.05.047>

0360-3199/© 2018 Hydrogen Energy Publications LLC. Published by Elsevier Ltd. All rights reserved.

than a distance which is 1/4 lower flammable limit concentration distance (i.e. 1/4 LFL distance). For example, for a 82 MPa filling station, the 1/4 LFL distance is about 8 m and is too long to install the station at urban area that doesn't have room, particularly in Japan.

It is not clarified whether the 1/4 LFL distance has any degree of risk or safety margin. Therefore, in order to examine the possibility to reduce the 1/4 LFL distance in a safe way, we investigate the characteristics of dispersion and ignitability on 40–82 MPa high-pressurized hydrogen jet from a pinhole of 0.2 mm diameter, where a leak from an aperture of piping joints etc. at a hydrogen station is thought as a typical accident case [1].

Although similar experimental researches [2–5] have been performed during the last ten years, many studies have not been made under high pressures where real gas effect appears. Kouchi et al. [2] and Takeno et al. [3] investigated the relation between concentration and ignitability of the choked hydrogen jet at the pressures of 40 MPa and 20 MPa with and without an obstacle in their jet. The characteristics of the upstream discharged hydrogen jet without choke was investigated by Schefer et al. [4] at the planar section along the jet axis. Ruggles et al. [5] studied the characteristics of a choked jet discharged from 1.5 mm diameter with a 10:1 pressure ratio and demonstrated that the similarity law as the scalar field of no-choked jet could be applied to the choked jet by using an appropriate effective source exit diameter (equivalent diameter).

The purpose of this paper is to clarify that the dispersion and ignition characteristics of the hydrogen jet under very high pressures of 40–82 MPa and to discuss the effect of different pressure on their characteristics.

Experimental set-up

High-pressurized hydrogen jet was discharged horizontally from a pinhole of 0.2 mm diameter in the large enclosed space of the Hy-SEF facility, JARI (Japan Automobile Research Institute).

Two kinds of the experiment for the hydrogen jet; dispersion and ignition, were carried out. First of all, concentration and velocity on vertical plane including jet axis were measured downward by FID (Flame Ionization Detector) and PIV (Particle Image Velocimetry) system. They are called the dispersion experiment.

Secondly, the gas on the jet axis was ignited by the electric spark and then the optical radiation emitted from both OH radical and water vapor (H₂O) species yielded from the ignited gas were recorded by two high speed cameras. The concentration of hydrogen was directly measured by Raman scattering system to record OH profiles by a high speed camera [6]. The shadowgraph image was also taken around the spark ignition point to visualize the ignited flame structure and to record by another high speed camera. These measurements were made simultaneously.

The schematic diagram of the measurement system for the ignition experiment is shown in Fig. 1.

Dispersion experiment

In the dispersion experiment, the hydrogen gas containing a small amount of methane as the tracer was spouted into air.

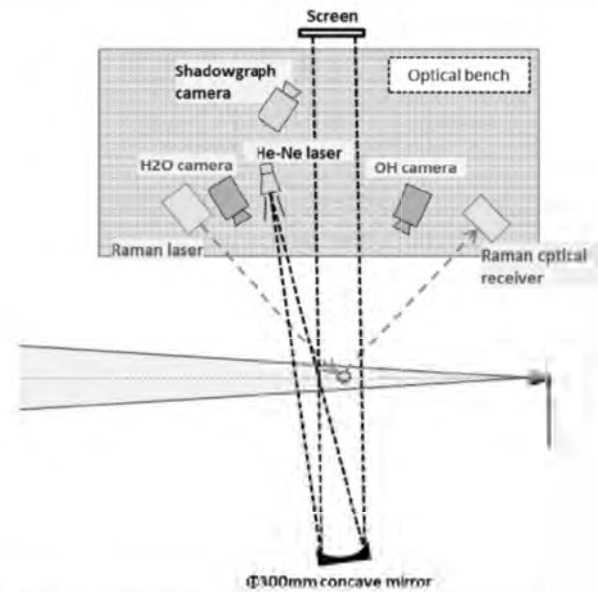


Fig. 1 – Outline of experiment measurement.

The concentration of methane in the jet was measured by the high-response speed flame ionization detector HFR500 (Combustion Ltd.), where the gas in the jet is sampled through a syringe of 0.25 mm inner diameter at the sampling rate of 200 Hz and then the concentration of hydrogen is obtained from the concentration of methane, as follows.

$$C_{H_2} = C_{CH_4} / C_0 \quad (1)$$

where C_0 is the concentration of methane at the exit of pinhole and C_{CH_4} the concentration of methane measured by FID and C_{H_2} concentration of hydrogen.

The velocities on the four vertical planes along the jet axis, the centers of which located at 0.5 m, 1.0 m, 1.5 m and 2.0 m from the nozzle (pinhole) exit, were measured by the two dimensional PIV system with a double pulse laser. The image of the area that is about 300 mm downstream and about 260 mm high, where the center of the area coincides with that of the above-mentioned vertical plane, was taken at 15 Hz. The seeding of dioctyl sebacate (DOS) was fed immediately after the exit of the pinhole.

The dispersion experiment was carried out for 60 MPa and 82 MPa hydrogen jet. But PIV measurements were not made for 60 MPa hydrogen jet because the flow field of 60 MPa would be able to be estimated by the similarity with 82 MPa.

Ignition experiment

The ignition experiment was carried out only for 82 MPa hydrogen jet. The electric spark with 3.5 mm distance between two electrodes was installed on the jet axis and ignited the spouted hydrogen jet, which was 100% concentration of hydrogen without methane. The electric spark with 30 mJ was generated at 10 Hz during the discharge of hydrogen. But the spark occurred sometimes irregularly and occasionally because the generation of the spark depended on the state of flow between electrodes. The concentration of hydrogen at the ignited point was simultaneously measured by Raman scattering

method (measured with 416.6 nm wavelength) to be compared with the FID's results, so that we could check whether the difference in measurement method influences the measured concentration or not. Also, the optical radiations from both OH radical and water vapor (H_2O) species ignited by the electric spark and emitted from hydrogen jet were detected and recorded at 500 fps by two high speed cameras to measure their concentrations. The two high speed cameras of FASTCAM SA-X2 (Photron Ltd.) and PHANTOM V2551 (Nobby Tech. Ltd.) were used for OH radical and H_2O , respectively. The emitted light from OH radical was amplified by the image intensifier C10880-03 (Hamamatsu Photonics) and then recorded through the band pass filter (299–318 nm), where the incident light into the camera for OH radical was blocked during the spark because the image intensifier could be damaged by a high-intensity spark. The emitted light from H_2O was recorded through the long pass filter (cut wave length 830 nm) during the measurement. Furthermore, the visualization of flame ignited by the spark was recorded by the shadowgraph imaging system using a He-Ne laser with 632.8 nm wavelength to avoid the interference with Raman scattering lights and emitted lights from OH radical and H_2O .

In the ignition experiment, four kinds of measurements such as concentrations of hydrogen, OH radical, water vapor and the visualization of flame were performed simultaneously. The outline of the experiment is shown in Fig. 1.

The spark generation was judged by the H_2O images captured through a camera, except that the image of OH radical wasn't recorded while the 10 Hz spark was used.

The ignition experiment was carried out only for 82 MPa hydrogen jets when the location of the spark was moved every 0.1 m from 0.4 m to 2.0 m downstream from the pinhole exit.

40 MPa hydrogen jet experiment

40 MPa hydrogen jet experiments [2] similar to the 82 MPa dispersion and ignition experiments were also carried out in

order to discuss the effect of different pressure from 82 MPa on the ignitability of hydrogen jet. Since the 40 MPa experiment was carried out at outside, unlike the 82 MPa experiment, their results were influenced somewhat by the wind and were performed at low wind conditions (almost calm). In the 40 MPa experiment, the hydrogen concentration and the velocity of the jet were measured by FID and PIV system in the similar way as the 82 MPa experiment, respectively. The images of OH radical was also taken and recorded by the high speed camera of FASTCAM-APX (Photron Ltd.) with the band pass filter (303–323 nm) through an image intensifier. The major differences of the 40 MPa experimental condition from 82 MPa experiment were that the electric spark energy is 120 mJ and the distance between electrodes is 1.5 mm. The effect of the above-mentioned differences on the experimental results seems negligible comparing with a changeable outdoor wind.

Experimental results

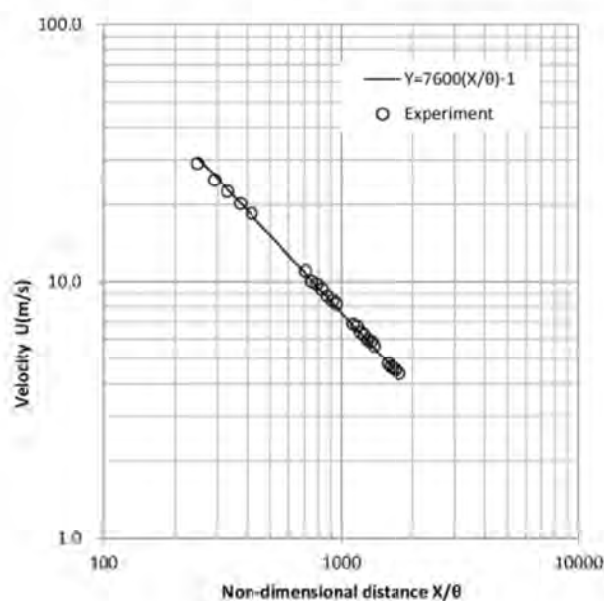
Velocity measurement results

The streamwise velocity U in the spouted jet of 82 MPa was measured by the PIV system at the 4 representative locations along the jet axis. From these results, the velocity U and its half width b_u were analyzed as shown in Fig. 2(a) and (b), then the velocity U on the jet axis can be expressed by Equation (2) using the after-mentioned equivalent diameter θ . The half width b_u is expressed as a function of the distance X from the exit by Equation (3).

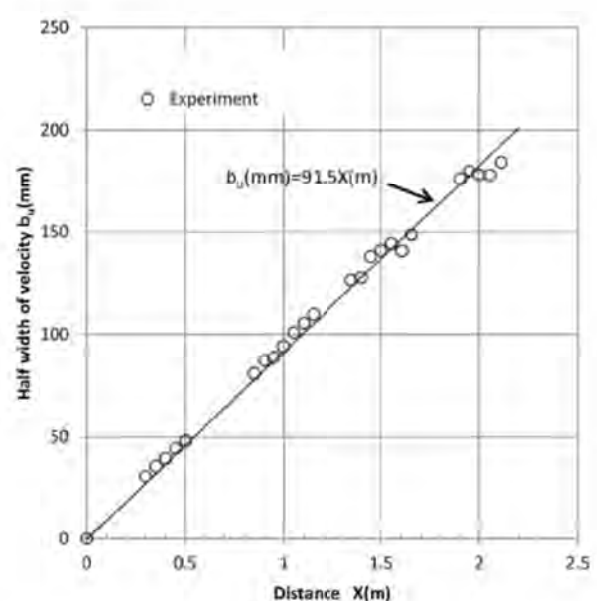
$$U = 7600/(X/\theta) \quad (2)$$

$$b_u = 0.091X \quad (3)$$

$$\theta = D \cdot (\rho_e/\rho_a)^{0.5} \quad (4)$$



(a) Streamwise velocity



(b) Half width of streamwise velocity

Fig. 2 – Results by PIV measurement.

where D is the diameter of a pinhole (the exit of the jet), ρ_e density of hydrogen at the exit and ρ_a density of air. The ρ_e is the density at the choke condition which is obtained under an isentropic change of ideal gas. It should be noted that the ρ_e for real gas is preferred in Equation (4).

These expressions are consistent with the previous studies at choke conditions [5,7] and no choke conditions [8]. Particularly, the expression of the half width b_c is in common whether the choking occurs or not.

Concentration measurement results

In this section, the results of hydrogen concentration measured by FID in the dispersion experiment are summarized. The time dependent concentration data were analyzed using the following statistic quantities: the time averaged concentration C , the half width of the concentration b_c , the intensity of concentration fluctuations σ_c/C , the occurrence probability of concentration P and the spectrum of concentration S . The time averaged concentration C and the occurrence probability of concentration P were also compared with the data from Raman scattering measurement in the ignition experiment to check whether the difference in the concentration measuring method influences the experimental results.

The concentration distribution along the jet axis is shown in Fig. 3. The concentrations of 82 MPa, 60 MPa and 40 MPa measured by FID and 82 MPa by Raman scattering method are shown in Fig. 3. All data are almost in agreement except for the data in the nearfield by Raman. In the near jet exit,

hydrogen is ignited due to the existence of flammable mixture where hydrogen concentration measured by Raman decreases than the one by FID. Moreover, there is a possibility that the measuring point is slightly out of alignment on the jet axis in the near jet exit.

From the results, it is concluded that the difference in the measuring methods of concentration doesn't influence the experimental results and hydrogen concentration measured by FID is appropriate.

The distance X from the exit of the jet in the horizontal axis in Fig. 3 is non-dimensional by the equivalent diameter θ defined by Equation (4).

It is found in Fig. 3 that the concentration downstream along the jet axis decreases in inverse proportion to the distance similarly to the previous studies [5,7–11]. In this study, the concentration profile along the jet axis was expressed by the following Equation (5).

$$C = 4300 \cdot (X/\theta)^{-1} \quad (5)$$

The results imply that the region downstream along the jet axis up to the LFL distance, i.e. the distance downstream the exit of the jet to decrease to LFL concentration (4%), is influenced by momentum more strongly than by buoyancy.

The half width b_c of concentration is obtained from both vertical and horizontal profiles of concentration as shown in Fig. 4. It is found by approximating the experimental data of a Gaussian distribution using the method of least squares. It contains relatively large errors because the sufficient amount of data were not obtained. Particularly, b_c with a parenthesis notation in Fig. 4 is non-credible because of the approximation by only three measuring points. Except for the data of three points approximation, the half width b_c could be expressed by the following Equation (6). It is almost the same results as the previous studies for both a compressible jet with choke conditions [5] and an incompressible jet without choke conditions [8,12].

$$b_c = (0.10 \sim 0.11)X \quad (6)$$

The intensities of concentration fluctuations at 82 MPa and 60 MPa are shown in Fig. 5. The distance from the jet exit is normalized by the equivalent diameter θ defined by Equation (4). The vertical axis σ_c/C is expressed by Equation (7). The intensity of concentration fluctuations, σ_c/C , is almost constant downstream the jet which is similar to the previous studies [5].

$$\sigma_c/C = 0.20 \sim 0.25, \quad (7)$$

where σ_c is a standard deviation of concentration fluctuations.

We also examined two characteristics of concentration fluctuation in addition to the standard deviation. One is the occurrence probability distribution of concentration along the jet axis, P_c , and another is the power spectrum of concentration, $f \cdot S/\sigma_c^2$.

The occurrence probability distributions measured at $X = 0.6$ m and 2.0 m on the 82 MPa jet axis are shown in Fig. 6. The probability distribution functions P 's approximated by Log-normal and Gaussian distributions, which are expressed by Equations (8) and (9), respectively, were also indicated in Fig. 6. The values C and σ_c/C in Equations (8) and (9) were obtained directly from the stochastic analysis of

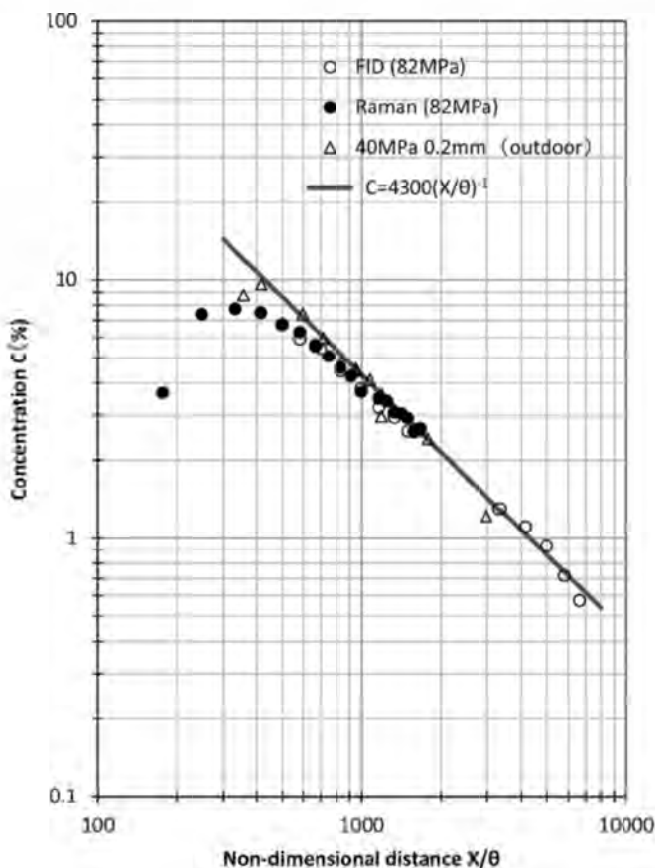


Fig. 3 – Concentration distribution along jet axis.

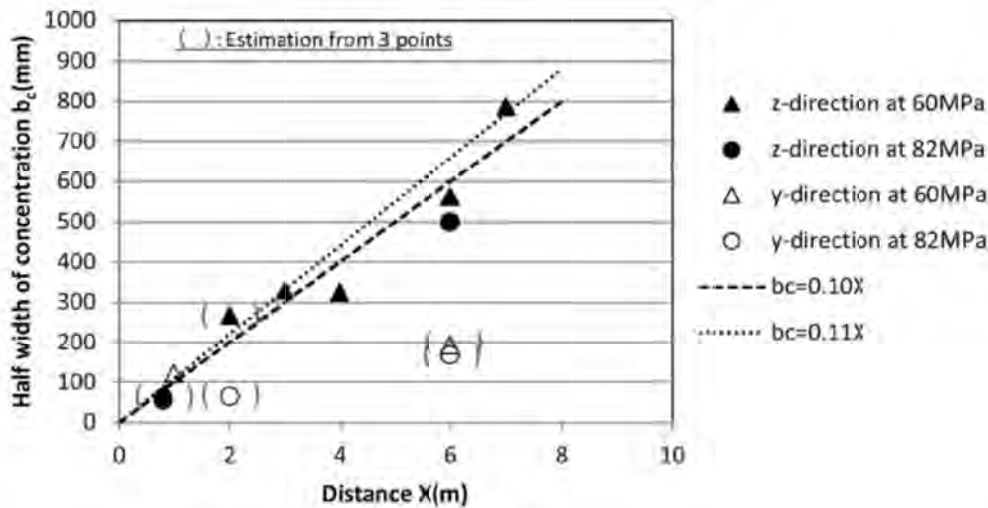


Fig. 4 – Half width of concentration.

concentration data measured in the experiment. It was found that Gaussian distribution fits experimental data better than Lognormal distribution because of the measurement on the jet axis. In the past studies for passive plume [13,14], it was examined whether various probability distribution functions would fit the stochastic characteristics of concentration fluctuations measured in the field or laboratory experiments. As a result, it was pointed out that the probability distribution of concentration was non-Gaussian distribution [13]. But in the present study, the Gaussian distribution fits the measurement results the same as the previous studies [2–4]. This cause is probably that the measurement is not conducted for a passive plume, but done for a very strong jet and on its jet axis

$$P(c) = \frac{1}{\sqrt{2\pi}\sigma_c} \text{Exp}\left(-\frac{(\ln c - m)^2}{2\sigma^2}\right) \text{ for Log - normal distribution} \tag{8}$$

$$\sigma^2 = \ln\left((\sigma_c/C)^2 + 1\right), \quad m = \ln\left(C / \sqrt{1 + (\sigma_c/C)^2}\right)$$

$$P(c) = \frac{1}{\sqrt{2\pi}\sigma_c} \text{Exp}\left(-\frac{(c - C)^2}{2\sigma_c^2}\right) \text{ for Gaussian distribution} \tag{9}$$

where C is the averaged concentration, c the instantaneous concentration and σ_c/C the intensity of concentration

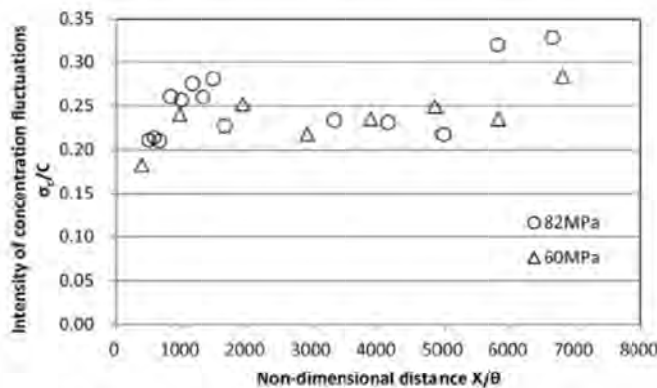


Fig. 5 – Intensity of concentration fluctuation.

fluctuations. The values C and σ_c/C are also obtained from Equations (5) and (7), respectively.

In addition, the occurrence probability of flammable concentration P_c (4–75%) along the jet axis is summarized in Fig. 7. The relation between the flammable concentration probability P_c and the non-dimensional distance X/θ shown in Fig. 7 can be also obtained by Equations (8) or (9) because Equations (8) and (9) are in a good agreement with the experiment data.

Another characteristics is the power spectra of concentration at 82 MPa and 60 MPa as shown in Fig. 8, where the power spectrum S is normalized by the frequency f and the standard deviation of concentration σ_c . In addition, the power spectrum of 40 MPa obtained from the experiment by Kouchi et al. [2] is also shown in Fig. 8. The frequency f is also normalized by the

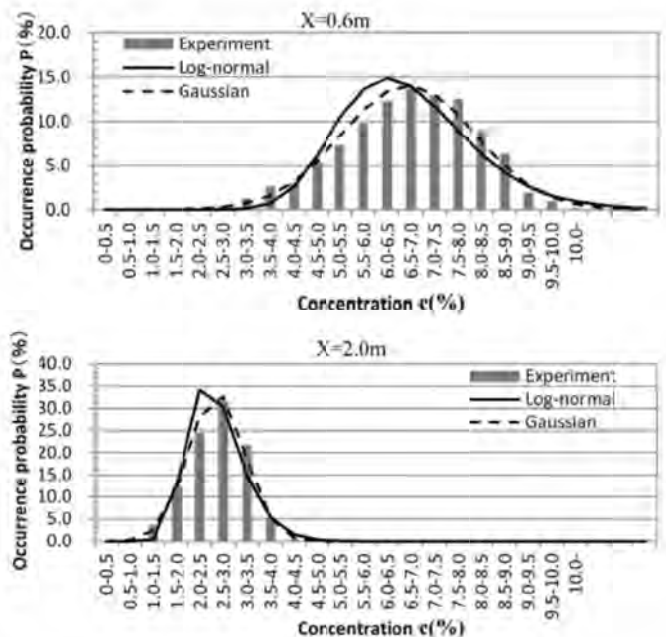


Fig. 6 – Occurrence probability distribution of concentration on jet axis at 82 MPa.

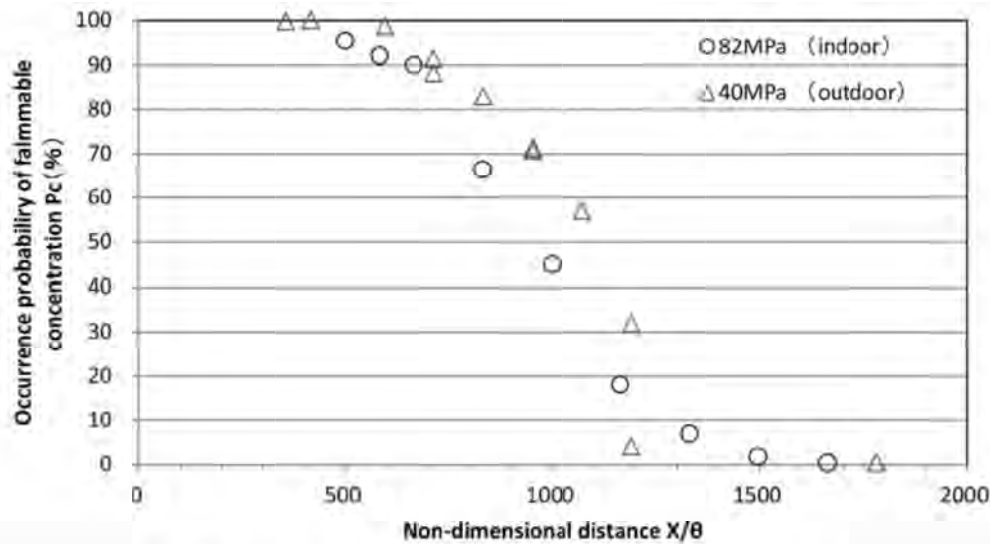


Fig. 7 – Occurrence probability of flammable concentration.

streamwise flow speed U on the jet axis and the half width of concentration b_c is in the similar way as Hanna [15]. The flow speed U and the half width of concentration b_c are obtained by Equations (2) and (6), respectively. Fig. 8 is indicated in non-dimensional notation in addition to the overbar. The non-dimensional spectra of 82 MPa, 60 MPa and 40 MPa are in a good agreement each other. It is considered this is why the self-preserving jet is satisfied up to the LFL distance. It is noted the representative speed U of 60 MPa in Equation (10) is obtained from the above-mentioned Equation (2) because of no measurement of velocity in the 60 MPa experiment. It is assumed Equation (2) is satisfied even at 60 MPa.

The spectrum distributions of 82 MPa, 60 MPa and 40 MPa could be approximated by Equation (10) proposed by Pasquill and Bulter [16] and then Equation (10) is indicated by a solid line in Fig. 8.

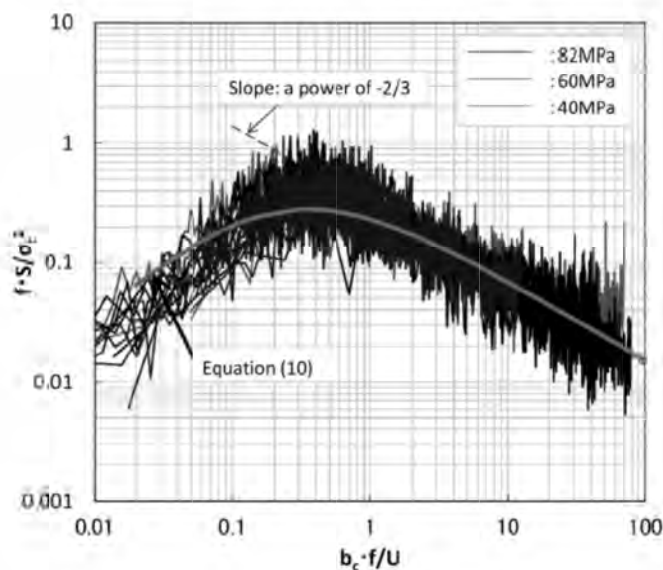


Fig. 8 – Spectrum of concentration at 82 MPa, 60 MPa and 40 MPa.

$$\bar{S} = \frac{A \bar{f} / \bar{f}_m}{\left(1 + 1.5 \bar{f} / \bar{f}_m\right)^{5/3}} \quad \left(A = 1.3, \bar{f}_m = 0.35\right) \quad (10)$$

$$\bar{S} = f \cdot S / \sigma_c^2, \quad \bar{f} = f \cdot b_c / U,$$

where \bar{S} , \bar{f} and \bar{f}_m are non-dimensional quantities of a spectrum, a frequency and a frequency of spectrum peak, respectively. In addition, the values of A and \bar{f}_m are determined to fit the spectrum distribution measured in this experiment.

This means the property of concentration fluctuations does not change depending on pressures and locations along the jet axis by some adequate scaling.

Ignition probability

In the ignition experiment, three high speed cameras were used for the imaging of the lights emitted from OH radical, H₂O and shadowgraph of the flame, respectively. The example of the recorded images is shown in Fig. 9. There were the sparks generated irregularly apart from 10 Hz. Therefore, the condition of the spark generation was judged by whether the spark was captured by the high speed camera for H₂O. From this examination, the number of the total ignition was obtained.

The ignition experiment was carried out during 20–30 s for each measurement. Therefore, the number of total ignition are about 200–300 under one experimental condition because the most sparks were generated at the interval of 0.1 s (10 Hz). The ignition probability P_i is defined by the following Equation (11):

$$P_i = N_i / N_s, \quad (11)$$

where N_i is the total number of ignited trials and N_s the total number of spark generations in a measurement, and then

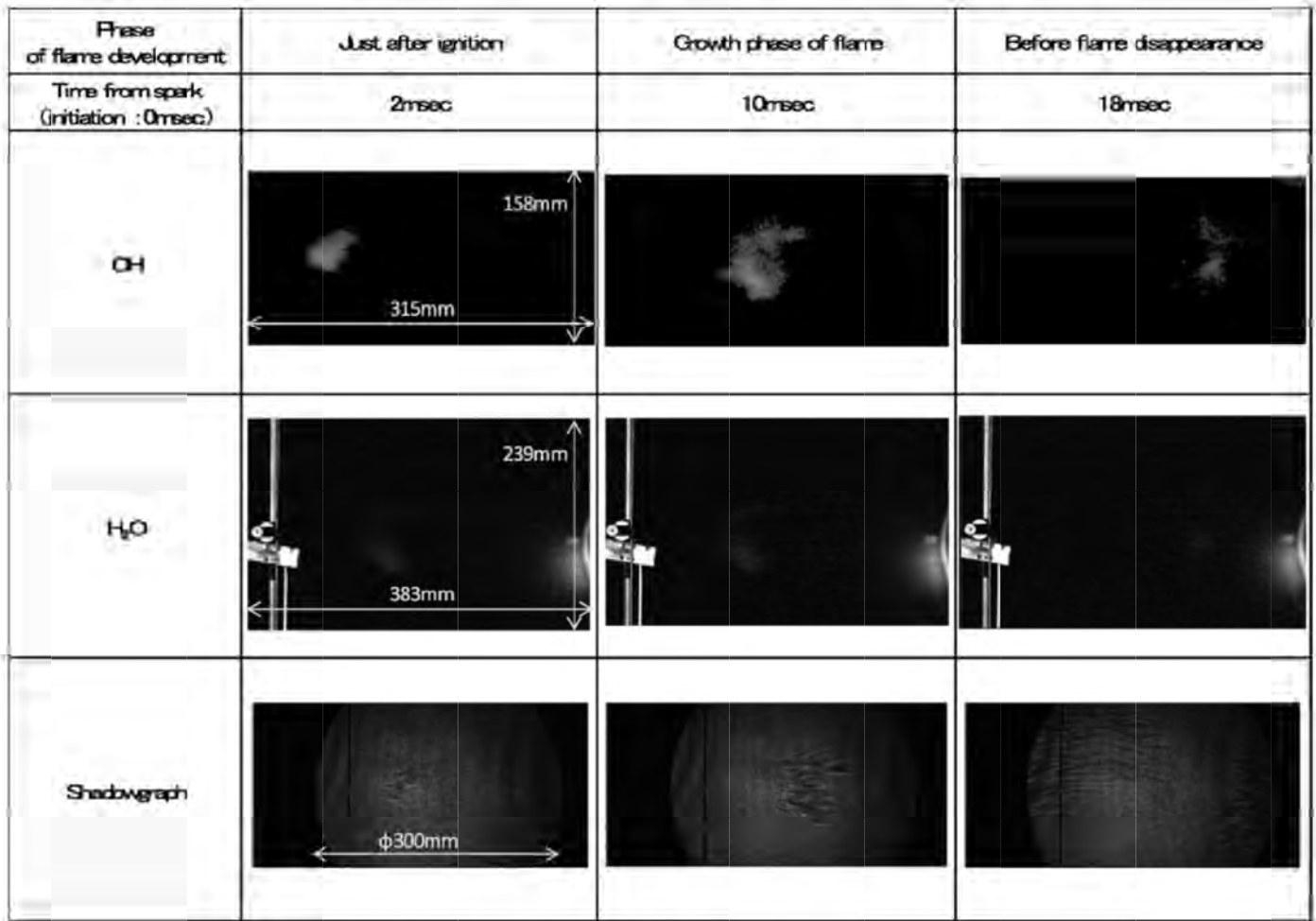


Fig. 9 – Example of recorded images at 600 mm from the exit of jet to ignition point.

ignitions were determined by whether the light emitted from OH radical was detected.

The ignition probability P_f against the distance from the exit of the jet is shown in Fig. 10. It is found that the ignition

probabilities of 82 MPa and 40 MPa decreases in the similar way each other as the location of the spark moves away from the exit of the jet. This could be expected by the similarity of concentration, concentration fluctuations and occurrence

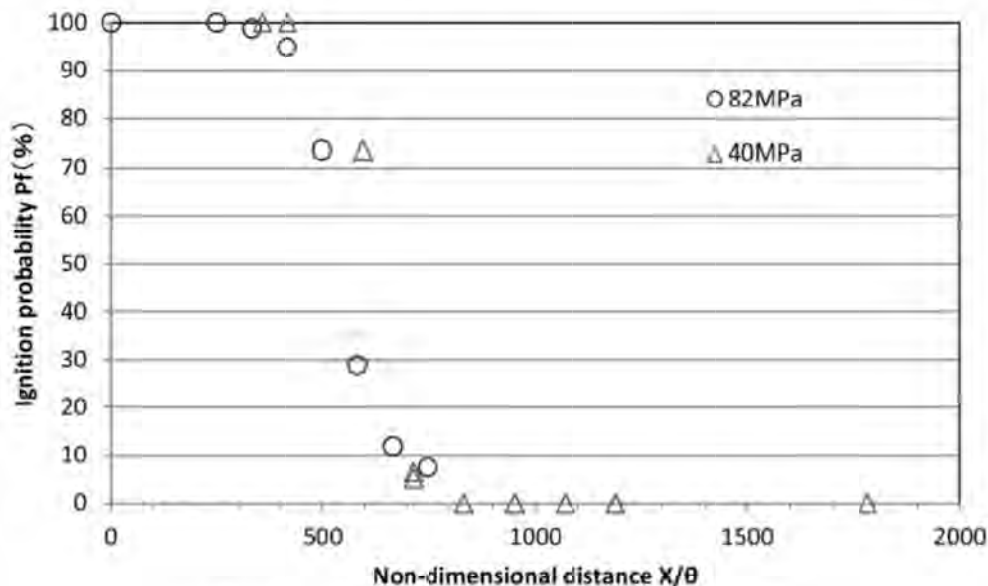


Fig. 10 – Ignition probability along the jet axis.

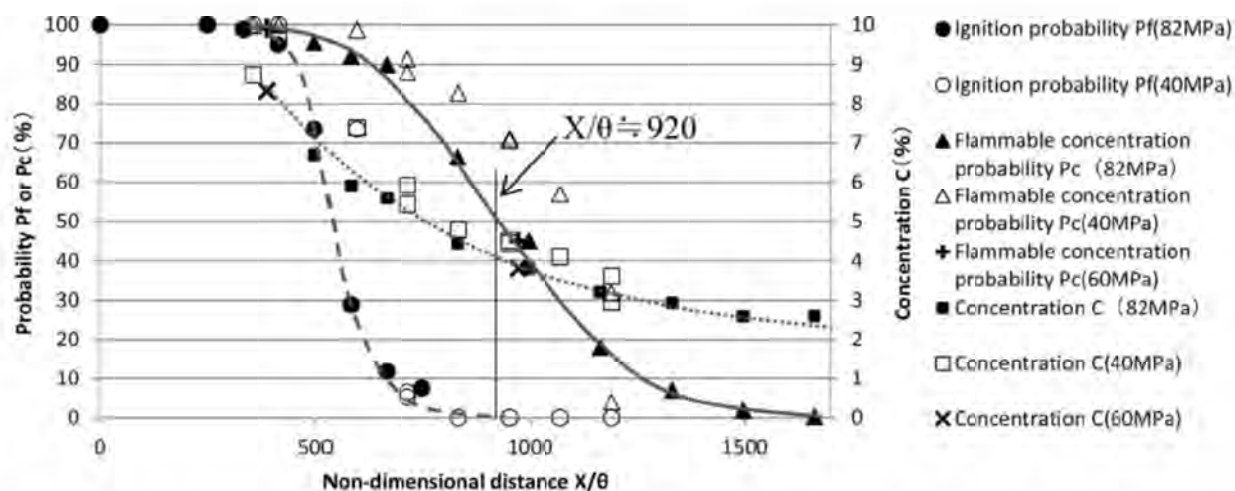


Fig. 11 – Relationship between Concentration, Ignition and Flammable concentration probabilities.

probability of flammable concentration with respect to X/θ , as shown in Figs. 3, 5 and 7 (i.e. Equation (8) or (9)), respectively. Moreover, it would be also attributed to the self-similarity of the power spectrum of concentration fluctuation as shown in Fig. 8.

Relationship between ignition and concentration fluctuations

The relation among concentration C , occurrence probability P_c of flammable concentration and ignition probability P_f for 82 MPa is shown in Fig. 11. In order to study the effect of the different pressures, the concentrations of 60 MPa and 40 MPa and the occurrence probability of flammable concentration of 40 MPa are shown as the experimental data in Fig. 11.

When it is considered that the experiment of 40 MPa has the errors due to the outdoor experiment, we may understand all data indicated in Fig. 11 will not depend on the discharge pressure. From Fig. 11, it was found that the averaged concentration C and the occurrence probability of flammable concentration P_c were about 4% and 50%, respectively at the location of $X/\theta \approx 920$ where the ignition probability P_f is zero. In order to discuss the hydrogen safety, the boundary where ignition probability P_f is zero is a very important factor.

According to the previous study of the hydrogen jet with low exit velocity by Schefer et al. [4], which is in incompressible flow region, their results showed that C and P_c are about 4% and 30%, respectively. It is considered that the difference of P_c from the present study is probably caused by the difference between incompressible jet and compressible jet. It means compressible jet is ignited harder than incompressible one because the velocity in the compressible jet is faster and the jet is stronger than that of incompressible jet.

Conclusion

We studied the non-steady behavior of the high-pressurized hydrogen jet with 40–82 MPa discharge pressure in detail and then discussed the similarity of flow and dispersion of

high-pressurized hydrogen jets to clarify the characteristics of ignitability, normalizing by the representative scales.

Through the above discussion, we tried to obtain the boundary at $P_f = 0$ for any high-pressurized hydrogen jet discharged from a diameter of 0.2 mm. As results, the boundary where ignition probability P_f is zero would be estimated as follows.

- 1) From the relation between the concentration C and the distance X expressed by Equation (5), we determine the concentration $C(X)$ at the distance X along the hydrogen jet axis, which is in the jet region without the influence of buoyancy.
- 2) From the value of the intensity of concentration fluctuation σ_c/C indicated by Equation (7), the standard deviation of concentration fluctuation σ_c is obtained.
- 3) From the occurrence probability density function $P(C)$ of concentration C expressed by Equations (8) or (9), the occurrence probability of flammable concentration P_c is estimated.
- 4) By repeating the above procedures from 1) to 3), we can obtain the relationship of the concentration C and the flammable concentration probability P_c against the distance X like Fig. 11.
- 5) We find out the distance X (the boundary at $P_f = 0$) where C and P_c are 4% and 50%, respectively. If the distance X at $C = 4\%$ and that at $P_c = 50\%$ are not same, the larger distance may be better to choose for safety.

We expect the effect of the exit diameter of the hydrogen jet will be also investigated in the future.

Acknowledgement

This research was supported by the New Energy and Industrial Technology Development Organization (NEDO) in Japan, under the fund of Research and Development of Technology for Hydrogen Utilization. The authors are thankful for the

supports of NEDC, and then gratefully acknowledge valuable advice and discussions to the members of the working committee, which is set up to technologically promote this research.

REFERENCES

- [1] The high pressure gas safety institute of Japan, Report of the Review Committee for 70 MPa Hydrogen Station Technical Standards. February 2012. p. 56 [Accessed 24 April 2018], http://www.meti.go.jp/meti_lib/report/2012fy/EO02008.pdf.
- [2] Kouchi A, Okabayashi K, Takeno K, Chitose K. Proceedings of the Second International Conference on Hydrogen Safety. September 2007. p. 11–3. San Sebastian (Spain).
- [3] Takeno K, Okabayashi K, Kouchi A, Misaka N, Hashiguchi K. Concentration fluctuation and ignition characteristics during atmospheric diffusion of hydrogen spouted from high pressure storage. *Int J Hydrogen Energy* 2017;42:15426–34.
- [4] Schefer RW, Evans GH, Zhang J, Ruggles AJ, Greif R. Ignitability limits for combustion of unintended hydrogen release: experimental and theoretical results. *Int J Hydrogen Energy* 2011;36(3):2426–35.
- [5] Ruggles AJ, Ekoto IW. Ignitability and mixing of underexpanded hydrogen jets. *Int J Hydrogen Energy* 2012;37(22):17549–60.
- [6] Asahi I, Ninomiya H, Sugimoto S. Remote sensing of hydrogen concentration by low power laser. *IEEJ Trans Electron Inf Syst* 2010;130(7):1145–50.
- [7] Okabayashi K, Tagashira K, Takeno K, Asahara M, Hayashi AK, Komori M. Non-steady characteristics of dispersion and ignitability for high-pressurized hydrogen jet. In: 54th Symposium (Japanese) on Combustion, Sendai. Japan: Sendai International Center; November 2016. p. 23–5.
- [8] Ishigaki H, Murakami M. The properties of a round turbulent buoyant jet. Technical Report of National Aerospace Laboratory, TR-826; 1984.
- [9] Okabayashi K, Nonaka T, Sakata N, Takeno K, Hirashima H, Chitose K. Characteristics of dispersion for leakage of high-pressurized hydrogen gas. *J Jpn Soc Saf Eng* 2005;44(6):391–7.
- [10] Ruggles AJ, Ekoto IW. Experimental investigation of nozzle aspect ratio effects on underexpanded hydrogen jet release characteristics. *Int J Hydrogen Energy* 2014;39(35):20331–8.
- [11] Okabayashi K, Uchino T, Tagashira K, Asahara M, Hayashi AK, Komori M. Characteristics of dispersion and ignitability for 82MPa high-pressurized hydrogen jet discharged from a pinhole. In: Proceedings of the 2016 year's Autumn Meeting of Japan Explosive Society, 10–11 November, 2016. p. 119–22. Nagasaki (Japan).
- [12] Sato K. Behavior of a jet discharged at high pressure. *J Jpn Soc Saf Eng* 1984;23(2):88–92.
- [13] Yee E, Wilson DJ, Zelt BW. Probability distributions of concentration fluctuations of a weakly diffusive passive plume in a turbulent boundary layer. *Bound Layer Meteorol* 1993;64:321–54.
- [14] Hanna SR. The exponential probability density function and concentration fluctuations in smoke plume. *Bound Layer Meteorol* 1984;29:361–75.
- [15] Hanna SR, Insley EM. Time series analyses of concentration and wind fluctuations. *Bound Layer Meteorol* 1989;47:131–47.
- [16] Pasquill F. Atmospheric diffusion. 2nd ed. Ellis Horwood Ltd; 1974. p. 61.

Effect of Hydrothermal Carbonization Conditions on the Physicochemical Properties and Gasification Reactivity of Energy Grass

Nasim Qadi,^{*,†} Keiji Takeno,[†] Alexander Mosqueda,[‡] Makoto Kobayashi,[§] Yukihiro Motoyama,[†] and Kunio Yoshikawa[‡]

[†]Department of Advanced Science and Technology, Toyota Technological Institute, 2-12-1 Hisakata Tenpaku, Nagoya 468-8511, Japan

[‡]Department of Environmental Science and Technology, Tokyo Institute of Technology, G5-8, 4259 Nagatsuta-cho, Midori-ku, Yokohama 226-8502, Japan

[§]Institute of Livestock and Grassland Science, National Agriculture and Food Research Organization (NARO-ILGS), Senbonmatsu 768 Nasu-Shiobara, Tochigi 329-2793, Japan

ABSTRACT: In this study, *Erianthus arundinaceus* energy grass was examined by conducting hydrothermal carbonization (HTC) using a laboratory-scale autoclave in the temperature range of (180–240 °C) and the retention time of (0–120 min). The parent material and hydrochars were investigated in terms of mass yield, proximate and elemental analyses, the higher heating value (HHV), X-ray diffraction, Fourier transform infrared, and X-ray fluorescence (XRF) analyses. Furthermore, CO₂ gasification was conducted on the pyrolysis char prepared from the parent material and the hydrochars using thermogravimetric analysis. It was found that increasing the HTC temperature and residence time caused the mass yield to decrease and the HHV to increase. Hydrochar crystallinity increased with HTC temperature up to 210 °C as a result of the deformation of the amorphous components, while under 240 °C, the crystallinity declined from its peak at 210 °C due to the commencing of cellulose degradation. The XRF analysis showed that the alkali index was increased due to increasing temperature and residence time. Gasification reactivity of the pyrolyzed hydrochar prepared at 180 °C was enhanced due to longer residence time (120 min), while those from very short residence time (0 min) showed a weaker reactivity than the parent material. Changing the HTC temperature showed minimal effect on the reactivity. At higher HTC temperature (240 °C), the catalytic activity was restricted by the highly ordered structure. This was not the case at 180 °C and long residence time of 120 min, where the reactivity was mainly controlled by the increased minerals.

1. INTRODUCTION

Upgrading raw biomass to energy-densified solid fuel is an important step toward more efficient thermochemical processing as in gasification. Pretreatment of biomass can be accomplished by several technologies such as dry torrefaction and hydrothermal carbonization (HTC), which also is referred as wet torrefaction. In the past few years, considerable attention has been paid to HTC as a prominent alternative for upgrading biomass and producing a more stable coal-like material known as hydrochar.

HTC is a process of heating biomass together with water in the temperature range of 180–250 °C in a pressure vessel with a residence time varying between a few minutes and few hours.¹ Under these conditions, as the reaction proceeds, the biomass is transformed into a char via a combination of reactions such as hydrolysis, dehydration, decarbonylation, decarboxylation, polymerization, recondensation, etc.² Compared to other pretreatment methods like dry torrefaction, HTC avoids the costly and energy-intensive drying process, where the ionized water acts as a reactant or even a catalyst.^{2,3} The produced hydrochar contains 41–90% of the mass and 80–85% of the fuel value of the original biomass.^{4,5} Hydrochar possesses higher fuel properties than raw biomass, such as higher heating value, higher carbon content, higher energy

density, and lower oxygen contents and will result in lowering greenhouse gas emissions in solid-fuel applications.^{6,7} HTC facilitates the mechanical dewatering of the produced hydrochar, which reduces the energy requirement for thermal drying.⁸ Also, the grindability and the hydrophobicity of hydrochar are enhanced to a greater extent than the raw biomass or even pyrochar from dry torrefaction.^{9,10} In this context, HTC would be a better pretreatment choice in terms of logistics.

Previous studies have confirmed that not only do the operating parameters (such as peak temperature and retention time) influence the hydrochar quality but also the feedstock type greatly affects the properties of hydrochar.¹¹ A wide range of biomass types have been explored under different HTC conditions to understand the nature of HTC and its effects on the hydrochar yield and quality, including woody biomass,¹² industrial paper and pulp sludge,¹³ biomass waste,¹⁴ forestry energy crop (willow),¹⁵ grass,¹⁶ and algae.¹⁷ Despite the importance and popularity of energy grass crops, the studies that examined the energy grass by HTC are still mainly limited

Received: April 1, 2019

Revised: June 3, 2019

Published: June 19, 2019



Table 1. Proximate Analysis, Ultimate Analysis, HHV, and Mass and Energy Yields of Eri and Hydrochars

sample	Eri	HC180-30	HC210-30	HC240-30	HC180-0	HC180-120
Proximate Analysis (wt %, Dry Basis)						
volatile matter	91.42	89.69	85.38	72.10	90.90	88.00
fixed carbon	5.43	7.03	10.75	23.60	6.29	8.50
ash	3.15	3.28	3.87	4.30	2.77	3.50
Ultimate Analysis (% Dry-Ash Free Basis)						
carbon	47.07	51.71	56.32	61.51	49.37	53.71
hydrogen	6.3	6.34	6.36	5.90	6.55	6.28
nitrogen	0.75	0.96	1.01	1.16	0.84	1.07
oxygen	45.88	40.99	36.30	31.43	43.23	38.94
Other Characteristics (Dry-Ash Free Basis)						
O/C (molar ratio)	0.73	0.59	0.48	0.38	0.66	0.54
H/C (molar ratio)	1.60	1.47	1.36	1.15	1.59	1.40
HHV (MJ kg ⁻¹)	16.92	19.41	21.87	23.82	18.54	20.36
HHV improvement (%)	0.00	6.79	20.27	31.00	2.00	11.99
mass yield (wt %)	1.00	78.98	69.26	61.08	95.40	72.90
energy yield (%)	100	90.59	89.48	85.95	98.37	87.70

Table 2. Major Inorganic Constituents (wt %) in the Raw Eri Grass and Hydrochars

sample	Eri	HC180-30	HC210-30	HC240-30	HC180-0	HC180-120
SiO ₂	1.19	1.30	1.55	1.60	0.99	1.34
K ₂ O	0.95	0.97	1.13	1.22	0.91	1.08
SO ₃	0.35	0.27	0.35	0.43	0.26	0.32
P ₂ O ₃	0.25	0.23	0.32	0.31	0.23	0.23
CaO	0.17	0.17	0.19	0.24	0.14	0.19
MgO	0.13	0.14	0.17	0.23	0.13	0.16
Al ₂ O ₃	0.07	0.10	0.11	0.13	0.07	0.09
Na ₂ O	0.05	0.06	0.02	0.10	0.04	0.06
Fe ₂ O ₃	0.02	0.02	0.02	0.03	0.01	0.02
MnO	0.01	0.01	0.01	0.01	0.01	0.01
alkali index (AI)	3.3	3.2	3.5	4.5	3.2	3.7

on miscanthus,^{9,18–21} and less commonly switchgrass,^{21,22} and prairie cord grass.²³ Meanwhile, the main focus of these studies was the hydrochar characterization under different HTC conditions with respect to their fuel properties¹⁸ or surface properties.¹⁹ However, studies that link HTC pretreatment with the gasification application are still limited, and so more fundamental research is needed. In this study, *Eriarthus arundinaceus* (Eri) energy grass is introduced with the goal to explore the effects of HTC conditions on the gasification reactivity of hydrochar.

Eri is a perennial energy grass species native to southern and southeastern Asian countries. The annual dry matter yield is estimated to be about 40–60 ton ha⁻¹,^{24,25} and this yield is huge compared to those of other energy grass crops, e.g., 12–40 ton ha⁻¹ for miscanthus spp. and 7–35 ton ha⁻¹ for switchgrass,²⁴ which can be considered as a promising energy grass crop. However, Eri still retains the same drawbacks of other biomass feedstocks such as high moisture content, low bulk density, high volatile and oxygen content, and low calorific value, and its tenacious and fibrous nature creates challenges to store the biomass for long hours to transport and convert efficiently into fuels and other products.^{26,27} Therefore, conducting HTC can overcome these challenges, and provide solid fuel with upgraded chemical and physical characteristics that can be considered a better fit for the gasification technology.

Despite the limited studies that integrate hydrochar with gasification, we could only find few studies that investigated

the gasification of hydrochar with respect to syngas quality and gasification reactivity. However, most studies performed the steam gasification,^{28,29} or the air gasification.³⁰ The findings of these studies were promising in terms of the quality of syngas produced, and a higher gasification reactivity was achieved. Very limited recent studies dealt with the gasification of hydrochar under CO₂ atmosphere. Based on thermogravimetric analysis, Lin et al.³¹ reported that HTC as a pretreatment has improved the CO₂ gasification of municipal solid waste (MSW) and promoted a higher reactivity. Ulbirsch et al.³² reported that char reactivity of spent grains decreased with the increase of both residence time and temperature due to the formation of fixed carbon in the hydrochar. Gunarathne et al.³³ conducted the updraft pilot-scale gasifier experiment of the hydrochar produced from spent grains from a brewery and reported the improved syngas quality of hydrochar, also ash slagging was noticed. Based on the available literature, none of these studies talked about energy grass or whether the available information applies to the hydrochar from energy grass. However, biomass type with different chemical composition will respond to HTC differently. Therefore, this study is devoted to tackle the effect of HTC conditions (temperature and time) on properties, structure, and alkali index, and to understand its influence on the gasification reactivity of the newly modified species of *E. arundinaceus* energy grass that has never been studied before in similar context.

2. MATERIALS AND METHODS

2.1. Biomass Feedstock Characterization Methods. Breeding lines of *E. arundinaceus* energy grass were harvested in March 2015 and supplied by the Institute of Livestock and Grassland Science, National Agriculture and Food Research Organization (NARO-ILGS). Raw grass was chopped using electrical blender, where around 80% of the resulted sample has particle size less than 1 mm. The original moisture content of the raw Eri grass is 4.4% (as-received basis). The proximate analysis was carried out using the thermogravimetric analyzer (DTG-50, Shimadzu Inc.). The elemental analysis was performed using a Vario Micro Cube Elemental Analyzer (Elementary, Germany). The proximate and ultimate analyses are given in Table 1. The parent material and the produced hydrochar are denoted as follows: raw *E. arundinaceus* (Eri), where the hydrochar are labeled as HCXX-YY, where XX and YY represented temperature and residence time in minutes, respectively.

The mineral composition of the ash was measured by X-ray fluorescence (XRF, energy-dispersive X-ray fluorescence spectrometer, BRUKER AXS) and is given in Table 2. The carbon crystalline structures of chars were tested by X-ray diffraction (XRD, Rigaku RINT-TTR III, Japan). The chars were scanned in a step scan mode (0.02/step) over the angular range of 10–70° using 200 mA and 40 kV Cu K α radiation. The functional groups were determined by Fourier transform infrared (FTIR) spectra (Shimadzu IRAffinity-1, Japan). The spectrum of dried samples recorded a wavenumber that ranges from 400 to 4000 cm⁻¹.

2.2. Hydrothermal Carbonization (HTC). HTC experiments were conducted using a commercially available batch-type autoclave reactor (MMJ-500, Japan). The facility consists of a reactor equipped with an automatic stirrer, a controllable electrical heater, and a condenser. The detailed configurations of the facility can be found elsewhere.³⁴ The reactor was closed, purged with argon, and heated to the target temperatures with a PID-controlled electrical heater. Reactor pressure was observed from a pressure gauge and was approximately equal to the saturated vapor pressure of water at the respective reactor temperatures. After an isothermal holding for the specific period of time, the reactor was cooled with the help of a fan and the gases were vented to a fume hood. Reactor solid and liquid phases were separated by vacuum filtration through a Whatman 1.6 μ m filter paper. In this study, hydrochar from Eri energy grass was prepared under two different set of conditions. The first one is by conducting HTC at temperatures of 180, 210, and 240 °C and constant residence time of 30 min. The second is HTC at 180 °C with a residence time of 0, 30, and 120 min. The water-to-biomass ratio was kept constant at 5:1.

2.3. Pyrolysis Char Preparation Experiments. Figure 1 shows the schematic diagram of the infrared gold image furnace (IGIF) used

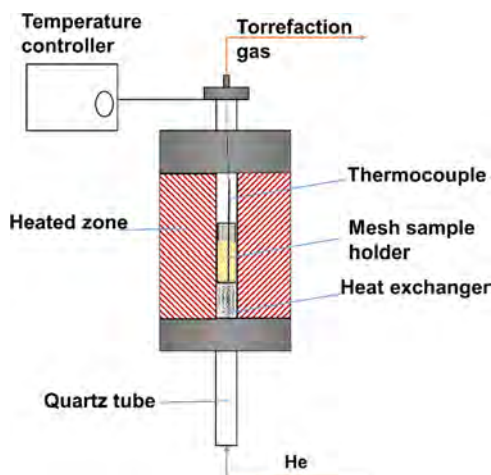


Figure 1. A schematic diagram of the infrared gold image furnace (IGIF).

for char preparation at 800 °C from both Eri grass and hydrochars. IGIF is equipped with ellipsoidal reflector to enable high-speed heating to high temperatures. The heated zone dimensions are ($\Phi = 30$ mm, $L = 140$ mm), and a quartz-type tube was inserted through the furnace body. The temperature was detected by a thermocouple (K-type) in contact with the biomass bed and controlled by temperature controller. In all experiments, around 3–4 g of sample was loaded in a cylindrical mesh-type sample holder (SUS 310 S, 45 mesh) with dimensions of ($\Phi = 20$ mm, $L = 120$ mm). Before starting the heating and to ensure air-free atmosphere inside the reactor, the reactor was purged with helium for 30 min with a flow rate of 400 mL min⁻¹ and heated at the heating ramp of 10 °C min⁻¹. After reaching the target temperature of 800 °C, the samples were kept under the same helium flow rate for 30 min before starting the cooling down to room temperature. Finally, the samples were taken and stored in a desiccator.

2.4. Char Gasification Experiment. A group of isothermal gasification experiments were conducted in the temperature range of 780–850 °C (temperatures' steady state error around ± 3 °C) using a thermogravimetric analyzer (DTG-50, Shimadzu Inc.). In this experiment, the pyrolysis char samples prepared at 800 °C were crushed and sieved using a mesh size of 100 μ m. The char samples were heated to the target temperature under the helium flow rate of 150 mL min⁻¹. After reaching the target temperature, the chars were kept under pure helium for 10 min to ensure most of the volatile contents are released. The final char sample weight was kept around 5.5 mg before replacing helium CO₂ at 150 mL min⁻¹. Each experiment was conducted at least twice, and the results showed a very good repeatability of the replicate experimental measurements; the average data were adopted for further calculations and modeling.

2.5. Data Analysis Methods. The mass and energy yields of HTC are expressed according to eqs 1 and 2. The higher heating value (HHV) is calculated according to the Dulong–Berthelot formula as in eq 3.³⁵

$$\text{mass yield (\%)} = \frac{\text{hydrochar weight}}{\text{Eri feedstock weight}} \times 100 \quad (1)$$

$$\text{energy yield (\%)} = \frac{\text{HHV of hydrochar}}{\text{HHV of Eri}} \times \text{mass yield} \quad (2)$$

$$\begin{aligned} \text{HHV} = & 0.3414 \times C + 1.4445 \times (H - (N + O - 1)/8) \\ & + 0.093 \times S \end{aligned} \quad (3)$$

Crystallinity index (CI) was calculated according to eq 4. It represents the ratio of the difference between maximum diffraction intensity at 2θ of 22.7° (I_{max}) and the amorphous diffraction intensity at 2θ of 18° (I_{am}) to the maximum diffraction intensity, which reflects the relative amount of crystalline cellulose in the total biomass.³⁶

$$\text{CI (\%)} = \left(\frac{I_{\text{max}} - I_{\text{am}}}{I_{\text{max}}} \right) \times 100 \quad (4)$$

The alkali index (AI), which was proposed by Sakawa et al.,³⁷ is used to quantify the catalytic abilities of the inherited minerals. The alkali index is defined as in eq 5

$$\text{alkali index (AI)} = \text{ash} \cdot \frac{\text{Fe}_2\text{O}_3 + \text{CaO} + \text{MgO} + \text{Na}_2\text{O} + \text{K}_2\text{O}}{\text{SiO}_2 + \text{Al}_2\text{O}_3} \quad (5)$$

where ash represents the ash content in the sample.

The gasification conversion ratio (X) and gasification reaction rate (r) are calculated according to eqs 6 and 7, respectively.

$$X = \frac{m_0 - m_t}{m_0 - m_f} \quad (6)$$

where m_0 , m_t , and m_f represent the initial sample weight, the instantaneous weight, and the final weight, respectively.

$$r = \frac{dX}{dt} \quad (7)$$

3. RESULTS AND DISCUSSION

3.1. Fuel Properties and Yield. The proximate analysis, ultimate analysis, and HHV of the parent material and the derived hydrochars are presented in Table 1. It can be seen that the volatile matter fraction decreased and the fixed carbon increased with the increase of temperature, while the effect of residence time is less significant. The ash content exhibited an obvious increase due to both temperature and residence time. However, HTC helps to remove loose minerals (dirt) collected during harvesting,³⁸ and the additional acidity produced during HTC may solubilize and remove organics.³⁹ Possible explanation of the increased ash content in the hydrochar samples is that a major part of inorganics exists in the more stable components of biomass as cellulose and lignin that is difficult to dissolve during HTC at lower reaction temperature. Moreover, the decomposition of cellulose increases the porosity of the hydrochar.⁴⁰ This porosity may permit the inorganics to be absorbed inside the porous structure. Table 2 shows the inorganic constituents of the ash of Eri and hydrochars. It can be seen that the concentrations of most metals were slightly changed. This behavior suggests the internal structural transformation in the solid body of the samples during HTC rather than extensive removal of the volatile contents and inorganics.

The results of mass yields, energy yields, and HHV are shown in Table 1, the hydrochar yield gradually decreased with the increase of operating temperature and residence time. In the studied temperatures range of 180–240 °C, the reduction of mass yield could be explained as a result of hemicellulose, extractives, and partially cellulose degradation. Nevertheless, lignin hardly degrades at temperature lower than 260 °C.^{21,41,42} Here, the results of mass yield of Eri are almost comparable to those of the miscanthus energy grass reported in other studies.^{18,21} Furthermore, HHV increased with the increase of operating temperature. The improvement on HHV ranged from 6.8, 20.23, and 31% for the residence time of 30 min and temperatures of 180, 210, and 240 °C, respectively. However, the improvement of HHV was insignificant for a very short residence time as the HC180-0 sample (around 2%), while the sample treated under longer residence time of 120 min exhibited a 12% increase in HHV. The changes and rearrangements of the hydrochar chemical composition during HTC were responsible for the reduction in mass yields and the increase of HHV. On the other hand, the energy yield of the derived hydrochar was relatively high (86–91%), and the reduction of energy yield with increase of HTC severity was milder than the reduction of mass yield, indicating that the energy per unit mass was enhanced by the HTC process.

A good indicator of the carbonization process during HTC is given in the Van Krevelen diagram shown in Figure 2. In this method, the changes of atomic ratios of O/C and H/C are used to indicate the degree of coalification and offers a clear insight into the chemical transformations through the reaction pathways of decarboxylation, dehydration, and demethanation during the carbonization process.⁴³ From the ultimate analysis shown in Table 1, a gradual reduction in O content coupled with a gradual increase in C content can be observed with the increase of HTC severity conditions; for example, the O content in Eri decreased from 45.9 to 31.4% for HC240-30

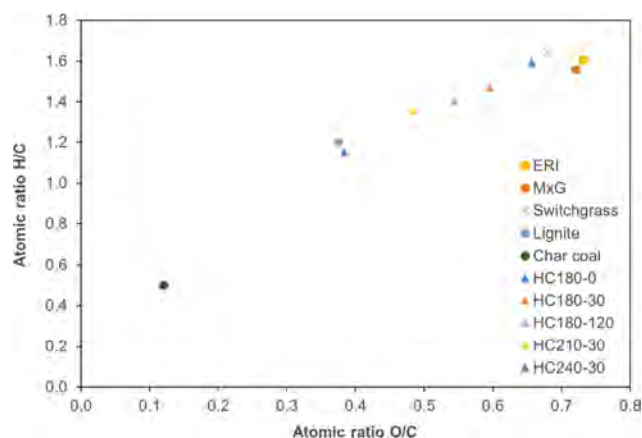


Figure 2. Van krevelen graph of Eri grass and hydrochars.

hydrochar, while the C content in Eri increased from 47 to 61.5% for HC240-30. In this regard, although the effect of the residence time was less influential than the effect of increasing operating temperature, still differences can be easily observed on the Van Krevelen diagram. It can be seen from Figure 2 that the dominant reaction pathways are the dehydration and decarboxylation paths, which are similar to those of HTC of other lingocellulosic biomasses reported in the literature.^{14,44,45} Moreover, by increasing the HTC severity conditions, the produced hydrochar approached somewhere closer to the region of lignite, which ensures the merits of HTC in terms of energy densification.

3.2. Structural Characterization. 3.2.1. XRD Analysis.

Figure 3 shows the XRD diffractograms of the untreated Eri

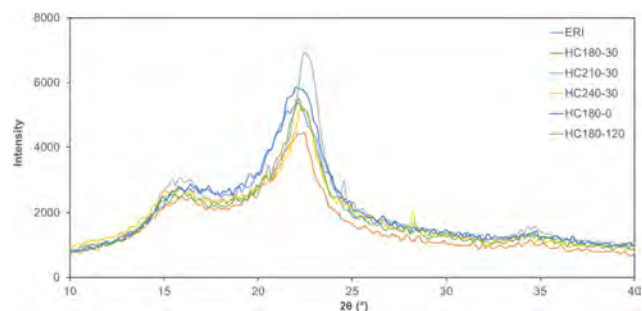


Figure 3. XRD patterns of Eri and the produced hydrochar at different HTC conditions.

and the produced hydrochar. The untreated sample has a broader diffraction pattern, which indicates the presence of both amorphous and crystalline components. All of the samples exhibited diffraction peaks around 2θ values of 18, 22, and 35°. According to Hashaiekh et al.,¹⁵ these peaks represent the crystalline cellulose peaks. It is clear that the hydrochar showed sharper peaks than the untreated sample. However, the strongest peak was noticed for HC210-30, followed by that for HC240-30 sample, this behavior indicates that within the temperatures range less than 240 °C, the amorphous components that mainly come from the hemicellulose had been almost entirely degraded and the microcrystalline structure was preserved. Raising the temperature up to 240 °C resulted in the deformation of parts of the cellulose structure. The dissolution of the cellulose at such a low temperature is explained by the fact that not all of the cellulose

is crystalline, and part of it is amorphous.¹⁵ It was also reported that certain smaller least-ordered cellulose crystallites could have been degraded during the HTC process because they are reactive, but the bulky and impeccable cellulose crystallites will persist unaltered.⁴⁶

To quantify trends of crystallinity, the crystallinity index (CI) was calculated. The CI exhibited values of 54.1, 55.9, 54.4, 61.1, 66.7, and 57.4% for Eri, HC180-0, HC180-30, HC180-120, HC210-30, and HC240-30 samples, respectively. These values support the explanation mentioned above; here, the HC210-30 sample showed the highest CI value due to the removal of amorphous hemicellulose, similar phenomenon was reported in previous studies for argan nut shell, sugarcane bagasse, and wood.^{47–49} The elevated temperature of the HC240-30 sample caused the CI values to drop to 57.4% due to the commencement of cellulose dissolution; a previous study has reported similar phenomenon for lawn grass.¹⁶ On the other hand, longer residence time during the HTC process produces hydrochar with improved crystallinity as in the case of HC180-120, which exhibited the CI value of 61.1%.

3.2.2. FTIR Spectra. The Fourier transform infrared (FTIR) spectroscopy of untreated grass and the produced hydrochars are presented in Figure 4. The FTIR spectra of the

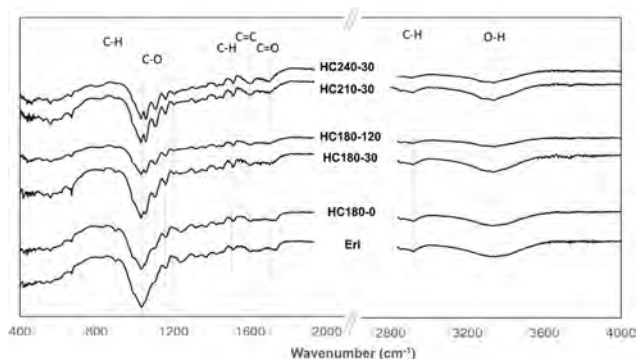


Figure 4. FTIR spectra of Eri and hydrochar samples.

raw and the hydrochars samples show some differences in intensity values that correspond to the functional groups, indicating the effects of HTC experimental parameters (temperature and residence time) on the chemical structure evolution of the produced hydrochar. For this purpose, the transmittance (%) in the wavenumber range of 400–4000 cm^{-1} were compared for all of the studied samples. The wide band 3000–3700 cm^{-1} was associated with the O–H vibration in the hydroxyl and carboxyl groups. The peak intensity exhibited reduction with the increase of temperature and residence time as a result of deoxygenation and dehydration during HTC.⁵⁰ The band around 2915 cm^{-1} is attributed to the aliphatic C–H stretching vibration and deforming vibration. The absorbance peak around 1700 cm^{-1} is associated with C=O, and increased with the increase of HTC temperature, indicating that the chemical components of Eri grass start to degrade and simultaneously undergo the reaction of polymerization.¹⁶ However, the relatively small peak around 1735 cm^{-1} disappeared after HTC processing as a result of the deformation of C=O in the hemicellulose, similar behavior was reported in other studies.^{14,21,51} The increased peak intensity at 1600 cm^{-1} is due to the aromatic C=C vibration, which reveals the occurrence of aromatization process during HTC and is consistent with the elemental

analysis in Table 1. Here, increasing the HTC temperature showed stronger peaks than the increasing of the residence time. The decreasing intensity of bands at 1515 and 1606 cm^{-1} is attributed to the C–H deformation of cellulose and hemicellulose and partial decomposition of lignin. The wide band at 1035 to 1200 cm^{-1} , which split into several bands, corresponds to the deformation of the C–O bonds of the cellulose, hemicellulose, and aromatic chars.⁵² Increasing of both temperature and residence time weakened the band at 900 cm^{-1} , probably due to the degradation of the cellulose and hemicellulose and partial decomposition of lignin. Interestingly, the longer residence time up to 120 min during the HTC process showed significant effects on the chemical structure and the functional groups, no less the impact of increasing the temperature of the HTC process. Finally, Eri grass and the produced hydrochar showed similar FTIR spectra to other lingo-cellulosic feedstocks pretreated by the HTC process.^{14,44,53}

3.3. Char Gasification Reactivity. As discussed earlier, hydrochar has a higher carbon content when compared to the parent material; thus, the hydrochar can provide greater proportion of syngas when it is gasified. However, gasification performance is affected by several factors such as char reactivity, gasifying agent, and temperature. The HTC process can permanently alter the reactivity characteristics of chars and may provide an improved gasification performance. Therefore, this section discussed the char gasification reactivity under CO_2 atmosphere. Pyrolyzed char at 800 °C was prepared from the parent material as well as the hydrochar samples. Here, the letter P was added to the sample's name to refer to the pyrolyzed char at 800 °C.

Figure 5 illustrates char conversion profiles during CO_2 gasification at 780 and 850 °C. It can be seen that gasification at higher temperature of 850 °C prompted the conversion

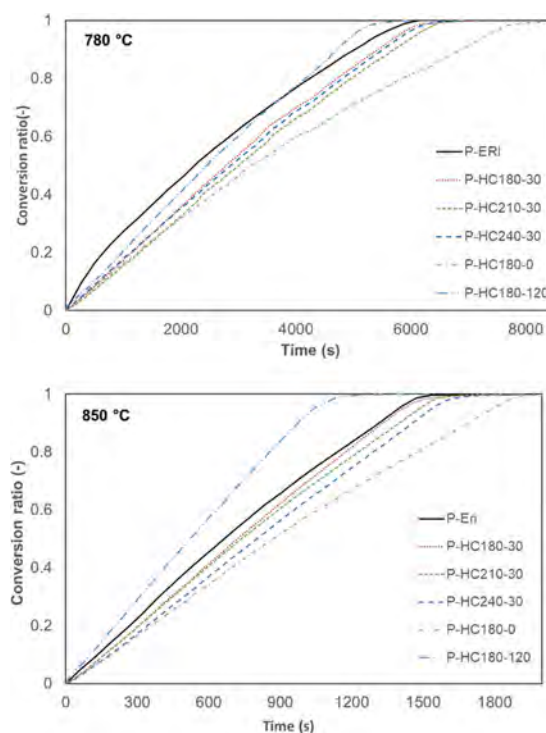


Figure 5. Carbon conversion during CO_2 gasification of the pyrolysis char prepared from Eri grass and hydrochar samples.

speed of P-HC180-120 char to surpass that of the parent material. It seems that the char prepared from hydrochar favored high gasification temperatures. However, changing the HTC temperature from 180 to 240 °C reduced the conversion speed of the pyrolyzed hydrochar to lesser extent than that of the parent material. Moreover, there was no big difference in the conversion speeds of chars prepared at different HTC temperatures as P-HC180-30, P-HC210-30, and P-HC240-30. It was probably due to the increased structure ordering of these char samples. The decreased H/C and O/C ratios indicate the lowering of reaction sites and the increased structure ordering due to the increased temperature.⁵⁴

On the other hand, the pyrolyzed hydrochars prepared at different residence times during the HTC process exhibited remarkable gasification conversion speed at either gasification temperature. Interestingly, a longer residence time during HTC resulted in char with the highest conversion speed among all of the samples tested. The P-HC180-120 sample possess the longest residence time and the best gasification performance. However, the P-HC180-0 sample, which is treated at 180 °C and 0 min residence time during HTC, showed the slowest conversion speed among all of the studied samples, indicating the great effects of residence time on the hydrochar gasification performance.

For a more detailed picture of the gasification performance, Figure 6 demonstrates the instantaneous reactivity curves at

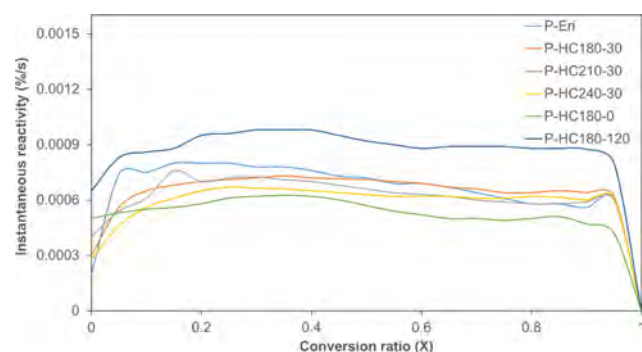


Figure 6. Instantaneous reactivity at 850 °C of the pyrolysis char prepared from Eri grass and the hydrochar samples.

850 °C. To avoid the influence of any specific phenomenon at the beginning or at the end of the reaction, the reactivity profiles are compared in the region of $X = 0.05\text{--}0.9$. In this region, up to conversion values of $X = 0.8$, the char reactivity was in the order P-HC180-120 > P-Eri > P-HC180-30 > P-HC210-30 > P-HC240-30 > P-HC180-0. It is clear that the differences in reactivity were higher at the beginning and become smaller as the reaction progressed. Reactivity profiles of P-HC180-30, P-HC210-30, and P-HC240-30 were slightly different from each other, while compared to P-Eri profile, they exhibited lower reactivity except at high conversion values when they showed opposite trend and became slightly higher than P-Eri. This behavior could be explained as a result of the enrichment of ash in the remaining char, which may produce higher catalytic effect.

Differences in reactivity among the examined samples could be attributed to the combined effects of differences in inorganic constituents and carbon structure. It is likely that the optimum balance of these two factors resulted in the reactivity behavior shown in Figure 6. Here, as shown in Table

1, the ash was increased with increasing HTC temperature and residence time denoting more inorganic matter preserved in the hydrochar samples. The inherent minerals, especially alkali and alkaline metals, have influential catalytic effects on gasification reactivity, where Si and Al play an inhibiting role.⁵⁵ The alkali index (AI), which was proposed by Sakawa et al.,³⁷ is used to quantify the catalytic abilities of the inherited minerals, accounting for the catalytic and inhibiting effects. The results of XRF analysis and the calculated values of alkali index are presented in Table 2. Alkali index values were increased with the increase of temperature and residence time during the HTC process. It can be seen that HC240-30 char has the highest alkali index value of 4.5, followed by HC180-120 with the AI value of 3.7. Thus, the pyrolyzed char reactivity was consistent with the alkali index values except for those of the samples that underwent treatment at higher HTC temperature as HC240-30, which means that other physicochemical properties of hydrochars are greatly different. The carbon crystalline structure plays a vital role in determining the gasification reactivity. Here, although HC180-120 char exhibited the CI value of 61.1%, which is relatively higher than that of most samples, the reactivity of its pyrolyzed char was the highest, which means that the gasification reactivity is not directly related to the crystalline structure. It should be ascribed to the fact that in comparison to the basal plane carbon atoms, the edge carbon atoms are chemically unstable and the gasification mainly occurs on the active sites located at these edges of carbon crystallites.⁵⁶ The reduction in reactivity of P-HC240-30 could be attributed to the more stable carbon structures formed within the body of hydrochar and preserved during the subsequent carbonization during pyrolysis.^{32,57} In addition, referring to the FTIR spectra, the peak intensity of the band 1600 cm^{-1} of the samples prepared at higher HTC temperatures as HC240-30 was greater than that of HC180-120 sample. This behavior indicates that the degree of aromatization goes to a higher extent with HTC temperature. According to Zhao et al.,⁵⁸ the postcarbonization during pyrolysis would induce progressive aromatization in the carbon skeleton, which may explain further thermal stability of the pyrolysis char and so lower reactivity.

Moreover, longer residence time as in HC180-120 could provide enough time for the rearrangements of the chemical structure and allow more metals to be absorbed inside the porous structure of the newly formed hydrochar, which may contribute to the improved reactivity of the pyrolyzed char. In addition, the reduction of mass yield, which indicates that the degradation of biomass components cellulose, hemicellulose, and extractives will leave the remaining hydrochar with higher porosity.²¹ With regard to the low reactivity of the P-HC180-0 sample, the inorganic matter availability of HC180-0 expressed with alkali index was not the only contributor to the char reactivity. Here, the alkali index was similar to that of sample HC180-30, which exhibited an obviously higher reactivity. Similarly, the residence time was not sufficient to absorb more minerals inside the porous structure and to degrade enough biomass components that may contribute to increase char porosity as can be indicated by the high mass yield shown in Table 1. Finally, Lin et al.³¹ mentioned that the elevation of the reaction time during HTC of MSW resulted in the reduction in carbon conversion efficiency and reactivity, which contradicted the results of this study. This may confirm the important role of the feedstock type on the characteristics of the obtained hydrochar.

It could be concluded that the influence of the HTC process on the chemical composition and structure of the hydrochar is likely to have follow-on effects in the performance of char gasification. The improved reactivity was mainly due to the increased catalytic activity in the hydrochar sample. However, increasing the HTC temperature was found to be responsible for char deactivation during gasification process, as it increased the carbon structure ordering. The residence time during the HTC process played an important role, as it may provide the opportunity for more inorganics to be absorbed inside the pores.

4. CONCLUSIONS

The HTC parameters (temperature and residence time) caused the mass yield to decrease and the HHV to increase. The crystallinity of the hydrochar increased with increasing temperature to the level around 210 °C as a result of deformation of the amorphous components of the hydrochar, while increasing the temperature to a level of 240 °C caused the crystallinity to deteriorate from its peak at 210 °C due to partial cellulose degradation. XRF analysis showed that the alkali index was increased due to increase of temperature and residence time. Eri grass and the produced hydrochar showed FTIR spectra similar to those of other lignocellulosic feedstocks pretreated by HTC. Gasification reactivity of hydrochar is enhanced due to longer residence time at 180 °C, while very short residence time caused the reactivity to be weaker than that of the parent material. Changing the HTC temperature showed minimal effect on the reactivity. The higher HTC temperature of 240 °C limited the role of catalytic AAEM from dominating gasification reactivity, as more stable structure that attained at higher HTC temperature become more influential. This was not the case at 180 °C and long residence time of 120 min, where the reactivity was mainly controlled by the increased catalytic activity. This study demonstrated that the integration of HTC with gasification has promising potential on reactivity enhancements of energy grass.

■ AUTHOR INFORMATION

Corresponding Author

*E-mail: nmnqadi@gmail.com.

ORCID

Nasim Qadi: 0000-0003-3124-836X

Notes

The authors declare no competing financial interest.

■ REFERENCES

- (1) Erlach, B.; Harder, B.; Tsatsaronis, G. Combined Hydrothermal Carbonization and Gasification of Biomass with Carbon Capture. *Energy* **2012**, *45*, 329–338.
- (2) Román, S.; Libra, J.; Berge, N.; Sabio, E.; Ro, K.; Li, L.; Ledesma, B.; Alvarez, A.; Bae, S. Hydrothermal Carbonization: Modeling, Final Properties Design and Applications: A Review. *Energies* **2018**, *11*, 216.
- (3) Jin, F.; Wang, Y.; Zeng, X.; Shen, Z.; Yao, G. Water under High Temperature and Pressure Conditions and Its Applications to Develop Green Technologies for Biomass Conversion. In *Application of Hydrothermal Reactions to Biomass Conversion*; Springer, 2014; pp 3–28.
- (4) Kobayashi, N.; Okada, N.; Hirakawa, A.; Sato, T.; Kobayashi, J.; Hatano, S.; Itaya, Y.; Mori, S. Characteristics of Solid Residues Obtained from Hot-Compressed-Water Treatment of Woody Biomass. *Ind. Eng. Chem. Res.* **2009**, *48*, 373–379.

- (5) Yan, W.; Acharjee, T. C.; Coronella, C. J.; Vasquez, V. R. Thermal Pretreatment of Lignocellulosic Biomass. *Environ. Prog. Sustainable Energy* **2009**, *28*, 435–440.

- (6) Islam, M. A.; Kabir, G.; Asif, M.; Hameed, B. H. Combustion Kinetics of Hydrochar Produced from Hydrothermal Carbonisation of Karanj (*Pongamia Pinnata*) Fruit Hulls via Thermogravimetric Analysis. *Bioresour. Technol.* **2015**, *194*, 14–20.

- (7) Kang, S.; Li, X.; Fan, J.; Chang, J. Characterization of Hydrochars Produced by Hydrothermal Carbonization of Lignin, Cellulose, D-Xylose, and Wood Meal. *Ind. Eng. Chem. Res.* **2012**, *51*, 9023–9031.

- (8) Erlach, B. Biomass Upgrading Technologies for Carbon-Neutral and Carbon-Negative Electricity Generation, PhD. Dissertation, Technische Universität, Berlin, Germany, 2014. DOI: [10.14279/depositon-4224](https://doi.org/10.14279/depositon-4224).

- (9) Kambo, H. S.; Dutta, A. Comparative Evaluation of Torrefaction and Hydrothermal Carbonization of Lignocellulosic Biomass for the Production of Solid Biofuel. *Energy Convers. Manag.* **2015**, *105*, 746–755.

- (10) Yan, W.; Perez, S.; Sheng, K. Upgrading Fuel Quality of Moso Bamboo via Low Temperature Thermochemical Treatments: Dry Torrefaction and Hydrothermal Carbonization. *Fuel* **2017**, *196*, 473–480.

- (11) Diakité, M.; Paul, A.; Jäger, C.; Pielert, J.; Mumme, J. Chemical and Morphological Changes in Hydrochars Derived from Microcrystalline Cellulose and Investigated by Chromatographic, Spectroscopic and Adsorption Techniques. *Bioresour. Technol.* **2013**, *150*, 98–105.

- (12) Bai, L.; Kudo, S.; Norinaga, K.; Wang, Y.; Hayashi, J. Kinetics and Mechanism of Steam Gasification of Char from Hydrothermally Treated Woody Biomass. *Energy Fuels* **2014**, *28*, 7133–7139.

- (13) Mäkelä, M.; Benavente, V.; Fullana, A. Hydrothermal Carbonization of Industrial Mixed Sludge from a Pulp and Paper Mill. *Bioresour. Technol.* **2016**, *200*, 444–450.

- (14) Cai, J.; Li, B.; Chen, C.; Wang, J.; Zhao, M.; Zhang, K. Hydrothermal Carbonization of Tobacco Stalk for Fuel Application. *Bioresour. Technol.* **2016**, *220*, 305–311.

- (15) Hashaikeh, R.; Fang, Z.; Butler, I. S.; Hawari, J.; Kozinski, J. A. Hydrothermal Dissolution of Willow in Hot Compressed Water as a Model for Biomass Conversion. *Fuel* **2007**, *86*, 1614–1622.

- (16) Guo, S.; Dong, X.; Liu, K.; Yu, H.; Zhu, C. Chemical, Energetic, and Structural Characteristics of Hydrothermal Carbonization Solid Products for Lawn Grass. *BioResources* **2015**, *10*, 4613–4625.

- (17) Park, K. Y.; Lee, K.; Kim, D. Characterized Hydrochar of Algal Biomass for Producing Solid Fuel through Hydrothermal Carbonization. *Bioresour. Technol.* **2018**, *258*, 119–124.

- (18) Wnukowski, M.; Owczarek, P.; Niedźwiecki, Ł. Wet Torrefaction of Miscanthus—Characterization of Hydrochars in View of Handling, Storage and Combustion Properties. *J. Ecol. Eng.* **2015**, *16*, 161–167.

- (19) Budai, A.; Wang, L.; Gronli, M.; Strand, L. T.; Antal, M. J., Jr; Abiven, S.; Dieguez-Alonso, A.; Anca-Couce, A.; Rasse, D. P. Surface Properties and Chemical Composition of Corn cob and Miscanthus Biochars: Effects of Production Temperature and Method. *J. Agric. Food Chem.* **2014**, *62*, 3791–3799.

- (20) Wilk, M.; Magdziarz, A. Hydrothermal Carbonization, Torrefaction and Slow Pyrolysis of Miscanthus Giganteus. *Energy* **2017**, *140*, 1292–1304.

- (21) Reza, M. T.; Lynam, J. G.; Uddin, M. H.; Coronella, C. J. Hydrothermal Carbonization: Fate of Inorganics. *Biomass Bioenergy* **2013**, *49*, 86–94.

- (22) Ramsurn, H.; Kumar, S.; Gupta, R. B. Enhancement of Biochar Gasification in Alkali Hydrothermal Medium by Passivation of Inorganic Components Using Ca (OH) 2. *Energy Fuels* **2011**, *25*, 2389–2398.

- (23) Cybulska, I.; Lei, H.; Julson, J. Hydrothermal Pretreatment and Enzymatic Hydrolysis of Prairie Cord Grass. *Energy Fuels* **2010**, *24*, 718–727.

- (24) Hattori, T.; Shiotsu, F.; Doi, T.; Morita, S. Suppression of Tillering in *Erianthus ravennae* (L.) Beauv. Due to Drought Stress at Establishment. *Plant Prod. Sci.* **2010**, *13*, 252–255.
- (25) Mislevy, P.; Martin, F. G.; Adjei, M. B.; Miller, J. D. Harvest Management Effects on Quantity and Quality of *Erianthus* Plant Morphological Components. *Biomass Bioenergy* **1997**, *13*, 51–58.
- (26) van der Stelt, M. J. C.; Gerhauser, H.; Kiel, J. H. A.; Ptasinski, K. J. Biomass Upgrading by Torrefaction for the Production of Biofuels: A Review. *Biomass Bioenergy* **2011**, *35*, 3748–3762.
- (27) Tumuluru, J. S.; Sokhansanj, S.; Hess, J. R.; Wright, C. T.; Boardman, R. D. A Review on Biomass Torrefaction Process and Product Properties for Energy Applications. *Ind. Biotechnol.* **2011**, *7*, 384–401.
- (28) Moon, J.; Mun, T.-Y.; Yang, W.; Lee, U.; Hwang, J.; Jang, E.; Choi, C. Effects of Hydrothermal Treatment of Sewage Sludge on Pyrolysis and Steam Gasification. *Energy Convers. Manag.* **2015**, *103*, 401–407.
- (29) Gai, C.; Guo, Y.; Liu, T.; Peng, N.; Liu, Z. Hydrogen-Rich Gas Production by Steam Gasification of Hydrochar Derived from Sewage Sludge. *Int. J. Hydrogen Energy* **2016**, *41*, 3363–3372.
- (30) Tremel, A.; Stemann, J.; Herrmann, M.; Erlach, B.; Spliethoff, H. Entrained Flow Gasification of Biocoal from Hydrothermal Carbonization. *Fuel* **2012**, *102*, 396–403.
- (31) Lin, Y.; Ma, X.; Peng, X.; Yu, Z.; Fang, S.; Lin, Y.; Fan, Y. Combustion, Pyrolysis and Char CO₂-Gasification Characteristics of Hydrothermal Carbonization Solid Fuel from Municipal Solid Wastes. *Fuel* **2016**, *181*, 905–915.
- (32) Ulbrich, M.; Preßl, D.; Fendt, S.; Gaderer, M.; Spliethoff, H. Impact of HTC Reaction Conditions on the Hydrochar Properties and CO₂ Gasification Properties of Spent Grains. *Fuel Process. Technol.* **2017**, *167*, 663–669.
- (33) Gunarathne, D. S.; Mueller, A.; Fleck, S.; Kolb, T.; Chmielewski, J. K.; Yang, W.; Blasiak, W. Gasification Characteristics of Hydrothermal Carbonized Biomass in an Updraft Pilot-Scale Gasifier. *Energy Fuels* **2014**, *28*, 1992–2002.
- (34) Nakhshinev, B.; Gonzales, H. B.; Yoshikawa, K. Hydrothermal Treatment of Date Palm Lignocellulose Residue for Organic Fertilizer Conversion: Effect on Cell Wall and Aerobic Degradation Rate. *Compost Sci. Util.* **2012**, *20*, 245–253.
- (35) Channiwala, S. A.; Parikh, P. P. A Unified Correlation for Estimating HHV of Solid, Liquid and Gaseous Fuels. *Fuel* **2002**, *81*, 1051–1063.
- (36) Li, G.-Y.; Huang, L.-H.; Hse, C.-Y.; Qin, T.-F. Chemical Compositions, Infrared Spectroscopy, and X-Ray Diffractometry Study on Brown-Rotted Woods. *Carbohydr. Polym.* **2011**, *85*, 560–564.
- (37) Sakawa, M.; Sakurai, Y.; Hara, Y. Influence of Coal Characteristics on CO₂ Gasification. *Fuel* **1982**, *61*, 717–720.
- (38) Chen, S.-F.; Mowery, R. A.; Scarlata, C. J.; Chambliss, C. K. Compositional Analysis of Water-Soluble Materials in Corn Stover. *J. Agric. Food Chem.* **2007**, *55*, 5912–5918.
- (39) Lynam, J. G.; Coronella, C. J.; Yan, W.; Reza, M. T.; Vasquez, V. R. Acetic Acid and Lithium Chloride Effects on Hydrothermal Carbonization of Lignocellulosic Biomass. *Bioresour. Technol.* **2011**, *102*, 6192–6199.
- (40) Funke, A.; Ziegler, F. Hydrothermal Carbonization of Biomass: A Summary and Discussion of Chemical Mechanisms for Process Engineering. *Biofuels, Bioprod. Biorefin.* **2010**, *4*, 160–177.
- (41) Peterson, A. A.; Vogel, F.; Lachance, R. P.; Fröling, M.; Antal, M. J., Jr.; Tester, J. W. Thermochemical Biofuel Production in Hydrothermal Media: A Review of Sub- and Supercritical Water Technologies. *Energy Environ. Sci.* **2008**, *1*, 32–65.
- (42) Zhang, B.; Huang, H.-J.; Ramaswamy, S. Reaction Kinetics of the Hydrothermal Treatment of Lignin. In *Biotechnology for Fuels and Chemicals*; Springer, 2007; pp 487–499.
- (43) Van Krevelen, D. W. Graphical-Statistical Method for the Study of Structure and Reaction Processes of Coal. *Fuel* **1950**, *29*, 269–284.
- (44) Sevilla, M.; Maciá-Agulló, J. A.; Fuertes, A. B. Hydrothermal Carbonization of Biomass as a Route for the Sequestration of CO₂: Chemical and Structural Properties of the Carbonized Products. *Biomass Bioenergy* **2011**, *35*, 3152–3159.
- (45) Sevilla, M.; Fuertes, A. B.; Mokaya, R. High Density Hydrogen Storage in Superactivated Carbons from Hydrothermally Carbonized Renewable Organic Materials. *Energy Environ. Sci.* **2011**, *4*, 1400–1410.
- (46) Xiao, L.-P.; Sun, Z.-J.; Shi, Z.-J.; Xu, F.; Sun, R.-C. Impact of Hot Compressed Water Pretreatment on the Structural Changes of Woody Biomass for Bioethanol Production. *BioResources* **2011**, *6*, 1576–1598.
- (47) Zbair, M.; Bottlinger, M.; Ainassaari, K.; Ojala, S.; Stein, O.; Keiski, R. L.; Bensitel, M.; Brahmi, R. Hydrothermal Carbonization of Argan Nut Shell: Functional Mesoporous Carbon with Excellent Performance in the Adsorption of Bisphenol A and Diuron. *Waste Biomass Valorization* **2018**, 1–20.
- (48) Chen, W.; Yu, H.; Liu, Y.; Chen, P.; Zhang, M.; Hai, Y. Individualization of Cellulose Nanofibers from Wood Using High-Intensity Ultrasonication Combined with Chemical Pretreatments. *Carbohydr. Polym.* **2011**, *83*, 1804–1811.
- (49) Kumar, A.; Negi, Y. S.; Choudhary, V.; Bhardwaj, N. K. Characterization of Cellulose Nanocrystals Produced by Acid-Hydrolysis from Sugarcane Bagasse as Agro-Waste. *J. Mater. Phys. Chem.* **2014**, *2*, 1–8.
- (50) Fan, F.; Zheng, Y.; Huang, Y.; Lu, Y.; Wang, Z.; Chen, B.; Zheng, Z. Preparation and Characterization of Biochars from Waste *Camellia Oleifera* Shells by Different Thermochemical Processes. *Energy Fuels* **2017**, *31*, 8146–8151.
- (51) Xiao, L.-P.; Shi, Z.-J.; Xu, F.; Sun, R.-C. Hydrothermal Carbonization of Lignocellulosic Biomass. *Bioresour. Technol.* **2012**, *118*, 619–623.
- (52) Liu, Z.; Quek, A.; Hoekman, S. K.; Balasubramanian, R. Production of Solid Biochar Fuel from Waste Biomass by Hydrothermal Carbonization. *Fuel* **2013**, *103*, 943–949.
- (53) Reza, M. T.; Charles, J.; Bishnu, P.; Glenn, C.; et al. Hydrothermal Carbonization (HTC) and Pelletization of Two Arid Land Plants Bagasse for Energy Densification. *ACS Sustainable Chem. Eng.* **2016**, *4*, 1106–1114.
- (54) Lu, L.; Kong, C.; Sahajwalla, V.; Harris, D. Char Structural Ordering during Pyrolysis and Combustion and Its Influence on Char Reactivity. *Fuel* **2002**, *81*, 1215–1225.
- (55) Miura, K.; Hashimoto, K.; Silveston, P. L. Factors Affecting the Reactivity of Coal Chars during Gasification, and Indices Representing Reactivity. *Fuel* **1989**, *68*, 1461–1475.
- (56) Xu, X. F.; Cui, H.; Gu, Y. D.; Chen, S. Y.; Wu, D. Influence of Charring Conditions of Coal Chars on Their Gasification Reactivity by Air. *J. Fuel Chem. Technol.* **1996**, *24*, 404–410.
- (57) Funke, A. Hydrothermal Carbonization of Biomass - Reaction Mechanisms and Heat of Reaction, 2012. DOI: [10.14279/depositonce-3303](https://doi.org/10.14279/depositonce-3303).
- (58) Zhao, M.; Li, B.; Cai, J.-X.; Liu, C.; McAdam, K. G.; Zhang, K. Thermal & Chemical Analyses of Hydrothermally Derived Carbon Materials from Corn Starch. *Fuel Process. Technol.* **2016**, *153*, 43–49.

SUSTAINABLE ENERGY

Influence of torrefaction after densification on the fuel characteristics and the inherited gasification kinetics of *Erianthus arundinaceus* energy grass

Nasim Qadi¹  | Makoto Kobayashi² | Keiji Takeno¹

¹Department of advanced Science and Technology, Toyota Technological Institute, Nagoya, Japan

²Institute of Livestock and Grassland Science, National Agriculture and Food Research Organization (NARO-ILGS), Nasushiobara, Tochigi, Japan

Correspondence

Nasim Qadi, Department of advanced Science and Technology, Toyota Technological Institute, Nagoya, 468-8511, Japan.
Email: nmqadi@gmail.com

Abstract

In this study, a mixture of breeding lines of *Erianthus arundinaceus* energy grass was pretreated prior to gasification. Although biomass torrefaction and subsequent pelletizing of torrefied biomass (TOP process) have been studied in details, the torrefaction of pellets (TAP process) still in its infancy. Therefore, samples prepared by TAP, torrefaction-only and pelletizing-only were compared in terms of fuel characteristics and gasification kinetics. Results showed that the mass yield decreased with increasing torrefaction temperature, whereas the higher heating value (HHV) continued to increase with temperature, which can be seen in the evolution of O/C and H/C atomic ratios. Tradeoff between mass yield and HHV points to 250°C as the optimum torrefaction temperature, as mass yield above 76% could be achieved. TAP process was superior not only in terms of producing fuel with higher energy density, but also the gasification reactivity was higher than that of torrefied-only or densified-only samples, suggesting TAP is promising to be employed within the gasification process. Yet, conducting TAP under higher torrefaction temperatures may weaken the reactivity due to the more release of potassium during pyrolysis. Lastly, gasification kinetics data revealed that the pretreated samples exhibited slightly higher activation energy.

KEYWORDS

energy grass, gasification kinetics, reactivity, TAP process

1 | INTRODUCTION

The major part of energy demand is met by fossil fuels that are non-renewable, increase greenhouse gas (GHG) emissions and make many countries heavily dependent on import.¹ Biomass is considered as one of the most promising solid fuels, because it is renewable, sustainable, and environmentally neutral fuel. Lingocellulosic energy crops are more attractive than the traditional waste biomass, especially crops with high biomass yield and disease resistance that can be grown on marginal land.²

Erianthus arundinaceus is a warm-season, perennial species native to Japan and other southern and southeastern Asian countries. It is characterized by its tall stalk (2–4 m), dense cluster, and high tolerance

to environmental stresses probably due to their large and deep root systems.² The annual dry matter yield is estimated about 40–60 ton/ha^{3,4} and this yield is huge compared to other energy grass crops, for example, 12–40 ton/ha in miscanthus spp. and 7–35 ton/ha in switchgrass.³ The high biomass yield and low inorganic contents makes it a promising energy grass crop. However, *E arundinaceus* grass like any other biomass feedstock has high moisture content, low bulk density, high volatile and oxygen content, low calorific value and its tenacious and fibrous nature create challenges to store the biomass for long hours, to transport and convert efficiently into fuels and other products.^{5,6}

Converting low-value biomass into a higher-value syngas can be achieved by gasification. However, pretreatment of biomass, either

thermally, or mechanically, is needed to upgrade virgin biomass into more efficient solid fuel for gasification. Recently, torrefaction technology has attracted more attention to upgrade biomass and make it useable in gasification or combustion.⁷ Torrefaction is a mild thermochemical process that has been widely studied aiming to mitigate biomass drawbacks, performed in oxygen-free atmosphere in the temperatures range of 200–300°C for several minutes or few hours.^{8,9} The torrefied biomass is hydrophobic, that is, it practically does not reabsorb moisture during storage and remains stable for long storage times.¹⁰ Moreover, torrefaction helps to produce fuel with higher energy density, better grindability, and more uniform properties.⁵ However, the bulk density of the torrefied biomass is low, even lower than the raw biomass itself, which makes the transportation and handling economically challenging.¹¹ Consequently, integrating torrefaction with densification process such as pelletizing can solve challenges in storing and transporting biomass and facilitate a feasible use of the torrefied biomass as bioenergy commodity.¹² In this context, the first pathway involves torrefaction followed by pelletizing process (TOP process).¹³ In this process, using a binding agent is necessary due to the weakening of bonding forces between biomass particles and the loss of natural bonding characteristics of lignin after torrefaction.¹⁴ Here, pelletizing power consumption is increased due to the reduced water content and the brittle nature of the torrefied biomass while the grinding power consumption is decreased when it is used as pulverized solid fuel.¹⁵ In the second pathway, pelletizing is followed by torrefaction (TAP process).¹² In this process, pelletizing of raw material is possible without adding binding agents, the torrefied pellets stay intact and could facilitate handling, feeding, and safe torrefaction operation.¹⁶ Moreover, the pelletizing power consumption is decreased and the grinding power consumption is increased.¹⁵

Biomass reactivity is influenced by pretreatment conditions. In TOP process, due to the fragile and abrasive particle structure, biomass may lose porous structure and surface area due to the mechanical compression and interlocking of particles with surrounding ones, which in turn impose resistance to mass transfer.¹⁷ It is understandable that the char particles from TOP process become more densified and so the reactivity of densified particles may decrease due to the differences in the heating conditions on the surface and the internal zones.¹⁸ Consequently, char produced by TAP process help to mitigate this effect on reactivity. On the other hand, char reactivity is influenced by the concentration of the inherited catalytic elements (such as Na, K, Fe, and Ca), where torrefaction may influence the release of these elements during pyrolysis and gasification.¹⁹ The binder material could produce a vital catalytic role during gasification. Moreover, some other works, especially under fast heating conditions, have reported that the char reactivity could be affected by the interaction between cellulose and lignin components, which may induce synergistic effects.^{20,21} Also, torrefaction greatly reduce the biomass reactivity when it is conducted under high heating rate, therefore, conducting torrefaction under low heating rates conditions will mitigate reactivity reduction, and this is in agreement with Fisher et al.,²² almost all particles from low heating rate chars keep the fibrous structure of the initial biomass with minimal effect on reactivity.

From the kinetics perspective, it was reported that the torrefaction temperature has significant effects on kinetics data.²³ Among the reactions occurring inside gasifiers, CO₂-char gasification represents the rate determination step. Therefore, it is important to study the CO₂-char gasification.²⁴ However, studying char gasification kinetics could be vulnerable to mass transfer limitations. Thus, under confined experimental conditions on TGA scale, the mass transfer limitations could be eliminated provided that a few milligrams of biomass char of particle size less than 0.5–1.0 mm were used,²⁵ and under a high enough flow rate of reactant gas.²⁶ Despite the fact that research about char gasification kinetics is widely available in literature as of great importance on gasifier design and efficiency,²⁷ few efforts have been made to investigate kinetics of torrefied biomass. For example, gasification kinetics of torrefied forest residue was reported by Tran et al.²⁸ and the kinetics of the torrefied wood investigated by Wang et al.²⁹ Moreover, there is lack in knowledge of the gasification kinetics of the torrefied pellets. Especially, the pyrolysis char from torrefied pellets might have different properties, which may affect the gasification performance.

Recently, there were conflicting claims about the impact of torrefaction on the gasification reactivity of various biomass feedstocks. However, the gasification reactivity of the torrefied biomass was predominantly lower than the reactivity of the parent biomass material and a few cases showed opposite direction, Zhang et al.⁸ summarized all these data. In particular, several energy grass species have been explored in similar context. Xue et al.³⁰ studied the impact of torrefaction on properties of miscanthus × giganteus (MxG) grass relevant to gasification and concluded that torrefaction conditions of 250°C and 30 min residence time will produce char with higher reactivity and the torrefied material favors high gasification temperatures. Sarkar et al.¹ reported that the combined torrefaction and densification of switchgrass resulted in higher gasification efficiency. Nevertheless, most of earlier studies focus on the torrefaction of coarse material prior to densification (TOP process) as Temmerman et al.³¹ noted. To our knowledge, studies about gasification kinetics of the torrefied pellets produced by TAP process, especially from grass feedstock, still missing in literature.

Therefore, the first goal of this study is to compare the effects of sole densification or torrefaction with the combined torrefaction and densification (TAP process) on the fuel characteristics and gasification kinetics of *E arundinaceus*. The second goal is to establish systematic study focusing on the solid fuel production prepared by torrefaction of the newly modified species of *E arundinaceus* that has never been studied before in similar context.

2 | MATERIALS AND METHODS

2.1 | Biomass feedstock

Breeding lines of *E arundinaceus* were harvested in March 2015 and a mixture of them was pelletized. Both of the raw *E arundinaceus* and *E arundinaceus* pellets were supplied by the Institute of Livestock and Grassland Science, National Agriculture and Food Research Organization (NARO-ILGS). The compressed pellets were prepared under the room

temperature conditions without using binder material. Before that, the raw biomass was subjected to sun drying and the moisture content was kept in the range 10–15%. The density of the produced pellets was 700 kg/m³. Raw *E arundinaceus* was chopped using electrical blender, where around 80% of the resulted sample has particle size less than 1 mm. Figure 1 is a photograph for raw *E arundinaceus* and *E arundinaceus* pellets samples. The proximate analysis was carried out using thermogravimetric analyzer (DTG-50, Shimadzu Inc.). The method of proximate analysis can be found elsewhere.³² The elemental analysis was performed using a Vario Micro Cube Elemental Analyzer (Elementary, Germany). The mineral composition of the ash was performed using scanning electron microscopy (SEM) combined with energy dispersive X-ray (EDX). The analysis was performed using a high resolution analytical field emission SEM (SU6600, Hitachi) and X-max, large area EDS silicon drift detector, (Oxford instruments). The proximate and ultimate analyses are given in Table 1 for raw *E arundinaceus* (ERI), torrefied *E arundinaceus* at 200°C (Torr200), torrefied *E arundinaceus* at 250°C (Torr250), torrefied *E arundinaceus* at 300°C (Torr300), *E arundinaceus* pellet (Pellet), torrefied *E arundinaceus* pellet at 200°C (TP200), torrefied *E arundinaceus* pellet at 250°C (TP250) and torrefied *E arundinaceus* pellet at 300°C (TP300) samples.

2.2 | Torrefaction and pyrolysis experiments

Figure 2 shows the schematic diagram of the infrared gold image furnace (IGIF) used for torrefaction and char preparation at 800°C experiments. IGIF is equipped with ellipsoidal reflector to enable high-speed heating to high temperatures. The heated zone dimensions are ($\varnothing = 30$ mm, L = 140 mm), and a quartz-type tube was inserted through the furnace body. The temperature was detected by a thermocouple (K-type) in contact with the biomass bed and controlled by temperature controller. In all raw *E arundinaceus* torrefaction experiments, around 3–4 g sample was loaded in a cylindrical mesh-type sample holder (SUS 310 S, 45 mesh) with dimensions of ($\varnothing = 20$ mm, L = 120 mm), while the sample weight of pellets torrefaction experiment was around 10 g. Before start heating up and in order to ensure air-free atmosphere inside the reactor, the reactor was purged with helium for 30 min with flow rate of 400 mL/min. Low heating rate was used to eliminate any heat transfer limitations that may appear due to the particle size

differences between raw and pellets samples. Therefore, heating ramp of 10°C/min was used in all torrefaction experiments. After reaching the target temperature of (200, 250, and 300) °C, samples were kept for 30 min before start cooling down to the room temperature under the same helium flow rate. Finally, samples were taken and stored in a desiccator.

2.3 | Char gasification experiment

A group of isothermal gasification experiments under CO₂ atmosphere was conducted in the temperature range of 780–845°C (temperatures steady state error around $\pm 3^\circ\text{C}$) using a thermogravimetric analyzer (DTG-50, Shimadzu Inc.). In this experiment, the pyrolysis char samples that were prepared at 800°C, were then crushed and sieved using a mesh size of 100 μm . Char samples were heated to the target temperature under helium flow rate of 150 mL/min. After reaching the target temperature, chars were kept under pure helium for 10 min in order to ensure most of volatile contents are released. The final char sample weight was kept around 5.5 mg before replacing helium with 150 mL/min of CO₂. Each experiment was conducted at least twice and the results showed a very good repeatability of the replicate experimental measurements, the average data were adopted for further calculations and modeling.

2.4 | Data analysis methods

The mass and energy yields of torrefaction are expressed on the basis of the organic part presence in the biomass, which means on dry and ash-free basis (daf) as given by Bergman et al.¹³ The higher heating value is calculated according to the Dulong-berthelot formula as mentioned elsewhere.³³ The gasification conversion ratio (X), gasification reaction rate (r) are calculated according to Equations (1) and (2), respectively.

$$X = \frac{m_0 - m_t}{m_0 - m_f} \quad (1)$$

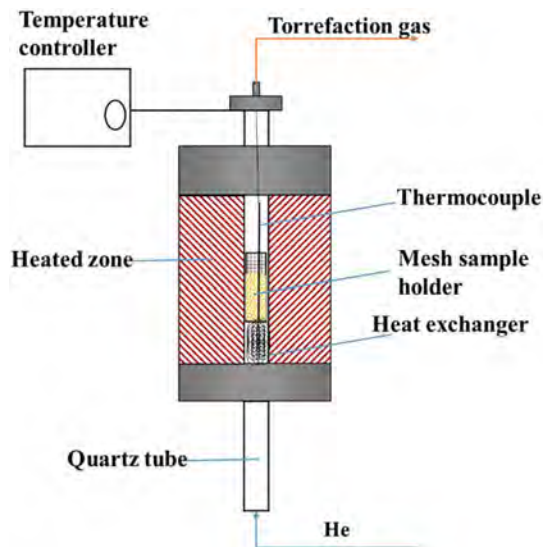
Where m_0 , m_t , and m_f represents initial sample weight, instantaneous weight and the final weight, respectively.



FIGURE 1 A photograph of *Erianthus arundinaceus* grass and *E arundinaceus* pellets [Colour figure can be viewed at wileyonlinelibrary.com]

TABLE 1 Proximate and ultimate analyses, molar ratios of (O/C) and (H/C), higher heating value, mass and energy yields for all studied samples

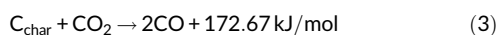
Sample	ERI	Torr200	Torr250	Torr300	Pellet	TP200	TP250	TP300
Proximate analysis (wt% dry basis)								
Volatile matter	91.1	91.08	88.42	65.5	90.57	90.38	77.5	63.5
Fixed carbon	5.4	5.84	7.34	27.63	6.27	6.05	18.1	30.5
Ash	3.5	3.08	4.23	6.87	3.17	3.57	4.4	6
Ultimate analysis (dry-ash-free basis)								
Carbon	47.07	49.79	51.8	66.04	47.71	49.01	53.65	60.94
Hydrogen	6.3	6.2	6.17	5.45	6.29	6.25	5.95	5.54
Nitrogen	0.75	0.74	0.85	1.36	0.71	0.74	0.92	1.12
Oxygen	45.88	43.27	41.18	27.15	45.29	43.99	39.49	32.39
Sulfur	Nd	Nd	Nd	Nd	Nd	Nd	Nd	Nd
Other characteristics (dry-ash-free basis)								
O/C (molar ratio)	0.73	0.65	0.6	0.31	0.71	0.67	0.55	0.4
H/C (molar ratio)	1.6	1.49	1.43	0.99	1.58	1.53	1.33	1.09
HHV (MJ/kg)	16.92	18.18	19.2	25.45	17.25	17.87	19.79	22.94
Mass yield (wt%)	100	87	76	42	100	95	79	57
Energy yield (wt%)	100	93	86	63	100	99	90	76

**FIGURE 2** A schematic diagram of the infrared gold image furnace (IGIF) [Colour figure can be viewed at wileyonlinelibrary.com]

$$r = \frac{dX}{dt} \quad (2)$$

2.5 | Kinetics analysis

Char- CO_2 gasification is a single reaction process, described by the so called Boudouard reaction (Equation [3]), where the fundamental kinetic formula is represented by the change in the apparent reaction rate as shown in Equation (4)



$$\frac{dX}{dt} = k(T, P_{\text{CO}_2})f(X) \quad (4)$$

k , T , and P_{CO_2} represents the reaction rate constant, temperature in kelvin and CO_2 partial pressure, where the function $f(X)$ has a structural meaning and will be explained later in this section.

On the assumption that CO_2 partial pressure remains constant during the gasification process, the reaction rate constant (k) can be represented according to Arrhenius equation as in Equation (5).

$$k = A \exp(-E/RT) \quad (5)$$

A , R , and E are the pre-exponential factor, the universal gas constant (8.314 J/mol k) and the activation energy, respectively.

The structural function $f(X)$ depends on the mass conversion ratio throughout the gasification reaction. In this regard, several models have been proposed in order to describe weight conversion behavior closely. In this study, the following models were tested by applying their linearized solutions: the volumetric model (VM), the shrink core model (SCM) and the random pore model (RPM).

The VM assumes homogenous reaction throughout the volume of the reactant particle³⁴ and is given by Equation (6) as:

$$\frac{dX}{dt} = k_{\text{VM}}(1-X) \quad (6)$$

SCM assumes that the non-reacting core is at the center and the reaction basically takes place on the particle surface and gradually penetrates inside the particle³⁴ and is given by Equation (7) as:

$$\frac{dX}{dt} = k_{SCM}(1-X)^{\frac{2}{3}} \quad (7)$$

RPM proposed by Bahtia and Perlmutter, and assumes that the surface area increases due to the coalescence and overlapping of the pores,³⁵ and is given as in Equation (8) as:

$$\frac{dX}{dt} = k_{RPM}(1-X)\sqrt{1-\Psi \ln(1-X)} \quad (8)$$

The structural parameter (Ψ) has a physical meaning and describes the structural changes during the gasification process,³⁶ and it can be calculated according to Equation (9) as:

$$\Psi = 2/(2\ln(1-X_{MAX}) + 1) \quad (9)$$

X_{MAX} represents the mass conversion ratio when the reactivity reaches its peak.

3 | RESULTS AND DISCUSSION

3.1 | Pretreatments effects on the fuel properties of *E arundinaceus* energy grass

Table 1 shows the proximate analysis, ultimate analysis, and HHV results of the torrefied samples along with their raw sources. Compared to $M \times G$ energy grass,³⁰ *E arundinaceus* has relatively similar fuel characteristics. Since measurements were carried out on oven dry basis, the effect on moisture contents is not explained in this study. However, it is well-known that thermal treatment by torrefaction helps to drive out water content and hydroxyl (OH) groups from biomass.¹ A notable volatile matter reduction was noticed at 250°C, where the pelleted samples exhibited higher reduction than the non-pelleted samples due to the densification process that assist the release of volatile matter. Significant reduction in the volatile matter was noticed when severe torrefaction temperature was applied at 300°C, and this behavior was noticed for both pelleted and non-pelleted samples. In general, the biomass components, cellulose, hemicellulose and lignin, start to degrade at different temperatures. Hemicellulose is the most reactive part of biomass and is

subjected to limited devolatilisation and carbonization below 250°C; cellulose decomposes at 305–375°C; and lignin gradually decomposes over the temperature range of 250–500°C.^{37,38} Therefore, the decomposition of hemicellulose and some short chain lignin polymers are responsible of the devolatilisation in the studied temperature range, which leads to release gaseous products such as H₂O, CO, CO₂, and CH₄.³⁸ On the other hand, both fixed carbon and ash contents increased as torrefaction temperature increased, and it is more prominent at higher torrefaction temperature as of 300°C which may be attributed to the notable reduction of volatile matter (concentration effect).

The SEM–EDX analyses of ash from raw and pretreated samples are presented in Table 2. The concentration of each element was calculated relative to the fuel mass. Elements that characterized by their catalytic role as K, Mg, and Ca have increased when torrefaction temperature increased as a result of relatively low temperatures during torrefaction.³⁹ It should be further mentioned that chlorine has increased when torrefaction temperature increased. Yet, TAP process has restricted the chlorine growing in the fuel sample when torrefaction temperature was increased. For example, the chlorine content in TP300 sample was 10 times lower than in Torr300. Other similar studies have demonstrated that the chlorine content, which is known by its limitations on biomass fuel applicability, has dropped following the torrefaction pretreatment.³⁰ It is reported that chlorine reacts with potassium to form KCl, which could lead to deposit formation in the flue gas channel upon subsequent cooling of the flue gas.⁴⁰

Figure 3 is Van Krevelen diagram. It is clear that the raw *E arundinaceus* is comparable with other energy grass crops such as $M \times G$.³⁰ However, higher torrefaction temperatures help to shift the atomic ratios O/C and H/C closer to lignite region that usually used for heat and power generation. The HHV was increased when a higher torrefaction temperature was applied. This behavior is attributed to the reduction in both atomic ratios of H/C and O/C as shown in Table 1. The differences in HHV could have resulted from the differences in carbon contents, where HHV increased with the increase of carbon content. The consistent increase in HHV with torrefaction temperatures was also reported by Uemura et al.⁴¹ and Poudel et al.⁴²

Mass yield is a useful measure of the torrefaction process efficiency. It was reported that a linear trend between the mass reduction and peak

TABLE 2 SEM–EDX results of the ash elemental composition per gram sample

Element	Elemental content, mg element/g sample							
	ERI	Torr200	Torr250	Torr300	Pellet	TP200	TP250	TP300
K	5.99	7.39	10.03	16.83	5.17	6.21	7.79	10.26
Si	7.25	4.77	6.77	10.72	6.56	7.35	8.23	12.42
Mg	1.37	0.95	1.18	2.06	1.27	1.50	2.11	2.34
Ca	1.54	1.08	1.40	2.75	1.49	1.61	1.72	2.64
P	0.60	0.68	0.97	1.79	0.67	0.64	0.88	1.02
S	0.95	1.05	1.02	1.65	0.79	1.14	1.32	1.62
Fe	0.46	0.09	0.13	0.00	0.19	0.18	0.18	0.78
Cl	0.14	1.32	1.82	2.47	0.16	0.25	0.13	0.24

Abbreviation: EDX, energy dispersive X-ray; SEM, scanning electron microscopy.

temperature in torrefaction temperature up to 300°C.⁴³ The highest efficiency of torrefaction can be achieved if the biomass exhibited about 20–30% mass reduction, and if the process is designed in such a way that all torrefaction gas is recovered for drying and torrefaction purpose.⁵ As just explained, drying and partial biomass decomposition are responsible for this mass reduction. Mass yield results are shown in Table 1, where mass yield decreased steadily when temperature increased. Low and mild torrefaction at 200 and 250°C show mass yield more than 70%, whereas severe torrefaction at 300°C resulted in less than 50% mass yield for samples prepared from non-pelleted *E. arundinaceus*. It is clear that the mass yield of samples prepared from pellets were always higher non-pelleted samples at the same pretreatment temperature. The energy yield decreased when temperature increased. However, the reduction in energy yield was moderate compared to the mass yield at higher torrefaction temperature (300°C), which means that the energy per unit

mass was enhanced by torrefaction. A reasonable energy yield can be achieved through the torrefaction of pellets instead of torrefaction of non-pelleted samples. For example, the energy yield at 300°C of Torr300 and TP300 samples were 63 and 76%, respectively.

3.2 | Gasification reactivity

Isothermal char-CO₂ gasification experiments were carried out using TGA. The effects of torrefaction, pelletizing and TAP process on the inherited reactivity characteristics were investigated. Figure 4 shows mass conversion ratio profiles versus time at 780 and 845°C, respectively. Despite samples showed different conversion speed, the curves shapes were almost similar, suggesting the global gasification mechanism was not affected by the torrefaction process.²² It is clear that the increase in gasification temperature from 780 to 845°C resulted in faster

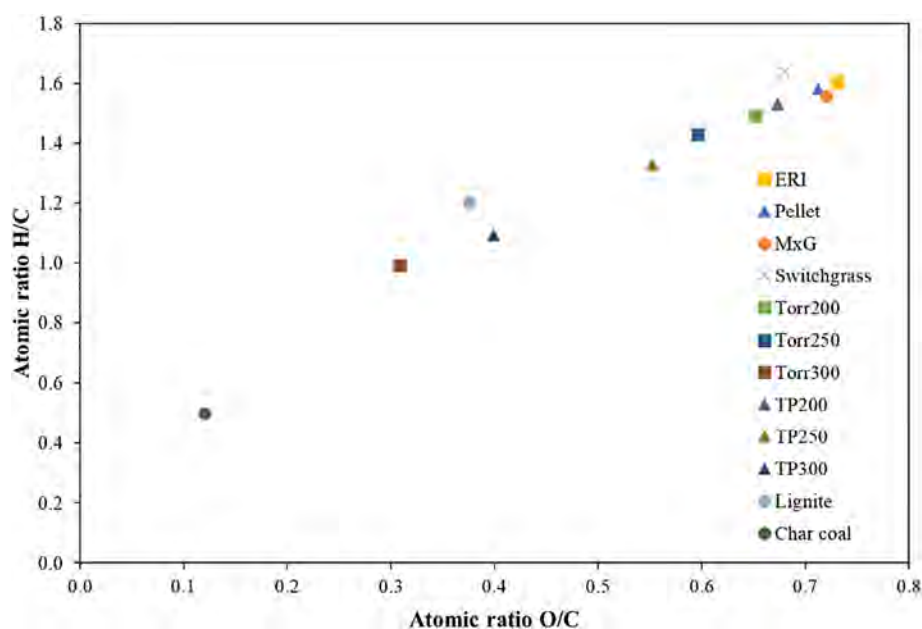


FIGURE 3 Van krevelen diagram of *Erianthus arundinaceus* compared to other energy grass samples, pretreated samples, lignite, and char coal [Colour figure can be viewed at wileyonlinelibrary.com]

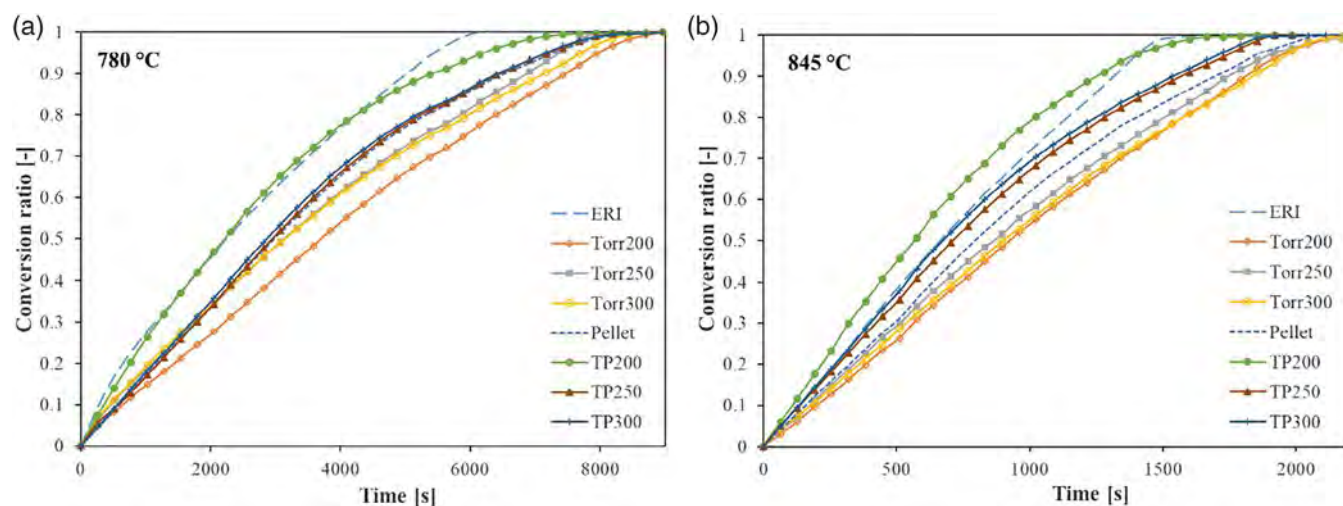


FIGURE 4 CO₂ gasification conversion profiles at 780 and 845°C of ERI, Torr200, Torr250, Torr300, pellet, TP200, TP250, and TP300 samples [Colour figure can be viewed at wileyonlinelibrary.com]

char conversion and higher reaction rate, since higher temperatures enhanced the molecules reactivity and increased the active sites for char-CO₂ gasification, which enhanced the reactivity and improved the reaction rate.⁴⁴ The torrefied pellets showed faster conversion than the non-pelleted samples at any gasification temperatures. The conversion speed of the torrefied pellets at higher gasification temperature of 845°C improved even more than that of the raw *E arundinaceus* as of TP200.

Figure 5 shows the instantaneous reactivity at 845°C of raw *E arundinaceus* compared to that of pelleted samples (Figure 5a) and to the non-pelleted samples (Figure 5b). It can be seen that at the very beginning, most samples exhibited reaction rate profiles start from high values that may appear as a result of uncompleted devolatilisation process, as rates of the solid devolatilisation is much faster than the CO₂-char gasification,⁴⁵ especially, the char conversion is more complicated than solid devolatilisation as it is a heterogeneous process where the surface is the location of the chemical reactions.⁴⁶ The reactivity was in the order TP200 > ERI > TP250, TP300 > Pellet > Torr200, Torr250, Torr300. Hence, torrefied pellets samples exhibited higher reactivity than the torrefied-only samples. This behavior could be explained as: during torrefaction process, biomass undergo changes in chemical structure, inorganic constituents, and porosity, which would be affected the gasification reactivity.³⁰ However, the ash content in the pyrolysis char was almost similar for all samples, around 12–14%, as shown in (Table S1). Hu et al.⁴⁷ has reported that despite the ash content was stable in the pyrolysis chars, the compositions was different especially when severe torrefaction conditions were applied, particularly the content of potassium exhibited reduction when torrefaction temperature increased which reduced the char gasification reactivity. Hence, low torrefaction temperature produces char with higher reactivity as in the case of TP200 char. On the other hand, the volatile content in the pyrolysis char from non-pelleted samples was 10 to 15% higher than that in char from pellets samples as shown in (Table S1). These results indicated the role of pelletizing process that may help extractives to migrate to the particles surface and so facilitate further removal of volatile and tar cracking. Unlike torrefaction-only pretreatment that may result in less volatile removal

and tar cracking during pyrolysis, resulting in reduction of pore volume and surface area and so reducing the char gasification reactivity.^{48,49}

However, it should be noted that other factors could contribute to the apparent differences in the reactivity. Reactivity can be affected by the char obtained by the secondary reaction, which is partly responsible for the loss of reactivity.⁵⁰ During torrefaction process the possibility of secondary char formation from tar is high, as the efficiency of tar sweeping away in the used reactor is lower than the TGA as a bigger amount of sample is used, and this may contribute to the inconsistency of reactivity values between the studied samples, especially for the torrefied-only samples.²⁹ On the other hand, pellet making process helps to remove tar, which decreases the light volatiles that may be converted into secondary char during torrefaction process, and this may explain the lower effect of secondary char in the pellet samples.⁵¹

3.3 | Gasification kinetics

The next step in this study is to investigate the influence of pretreatments on the inherited gasification kinetics. For this purpose, CO₂-char gasification experiments were conducted. The family of models that elucidated earlier was applied. The linearized solution of VM, SCM, and RPM were selected to fit the experimental data in order to calculate reaction kinetics parameters. Here, under the applied experimental conditions, mass transfer limitation is not likely to influence the reaction progress under chemically-controlled regime the size of char particles was minimized to a size less than 100 μm, and this in accordance with that the internal mass resistance could be neglected when particles size less than 0.5–1.0 mm.²⁵ Moreover, the concentration of the reactant gas was high enough to exclude the influence of mass transfer limitations.²⁶ Here, the data indicating carbon conversion ratio from X = 0 to X = 0.8 was used. The reason behind this is that at high conversion ratio, due to the collapsing of actual pore structure characteristics, the ash layer dominates the process completion.⁵² The accuracy of models fitting was assessed by calculating the coefficient of determination (R²). The linearized solution of SCM, RPM, and VM are shown in Figures 6, S1 and S2, respectively. It is

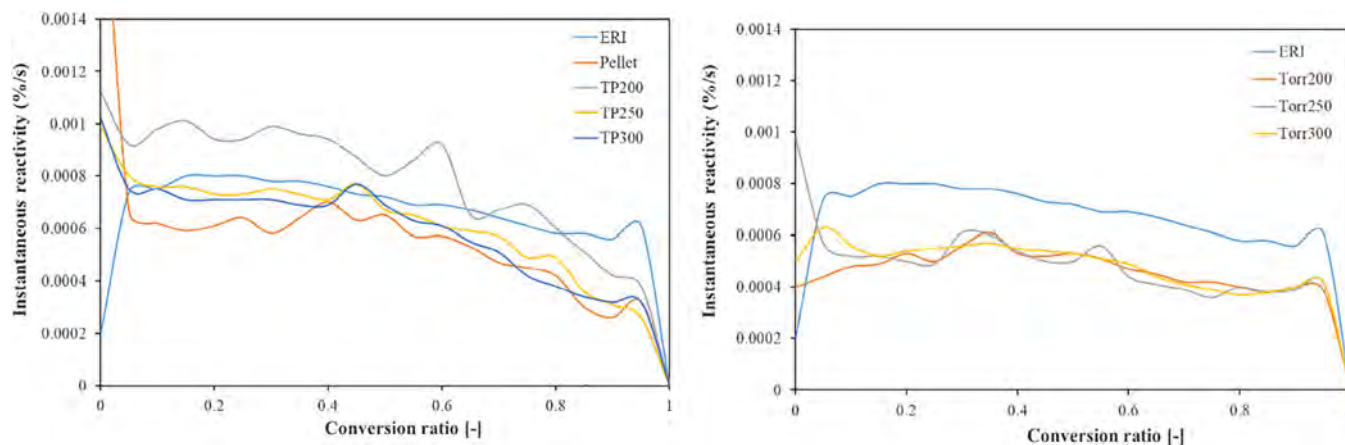


FIGURE 5 Instantaneous reactivity versus conversion at 845°C of (a) *Erianthus arundinaceus*, pellets and torrefied pellets (TP200, TP250, and TP300), (b) *E arundinaceus* and torrefied raw *E arundinaceus* (Torr200, Torr250, and Torr300) [Colour figure can be viewed at wileyonlinelibrary.com]

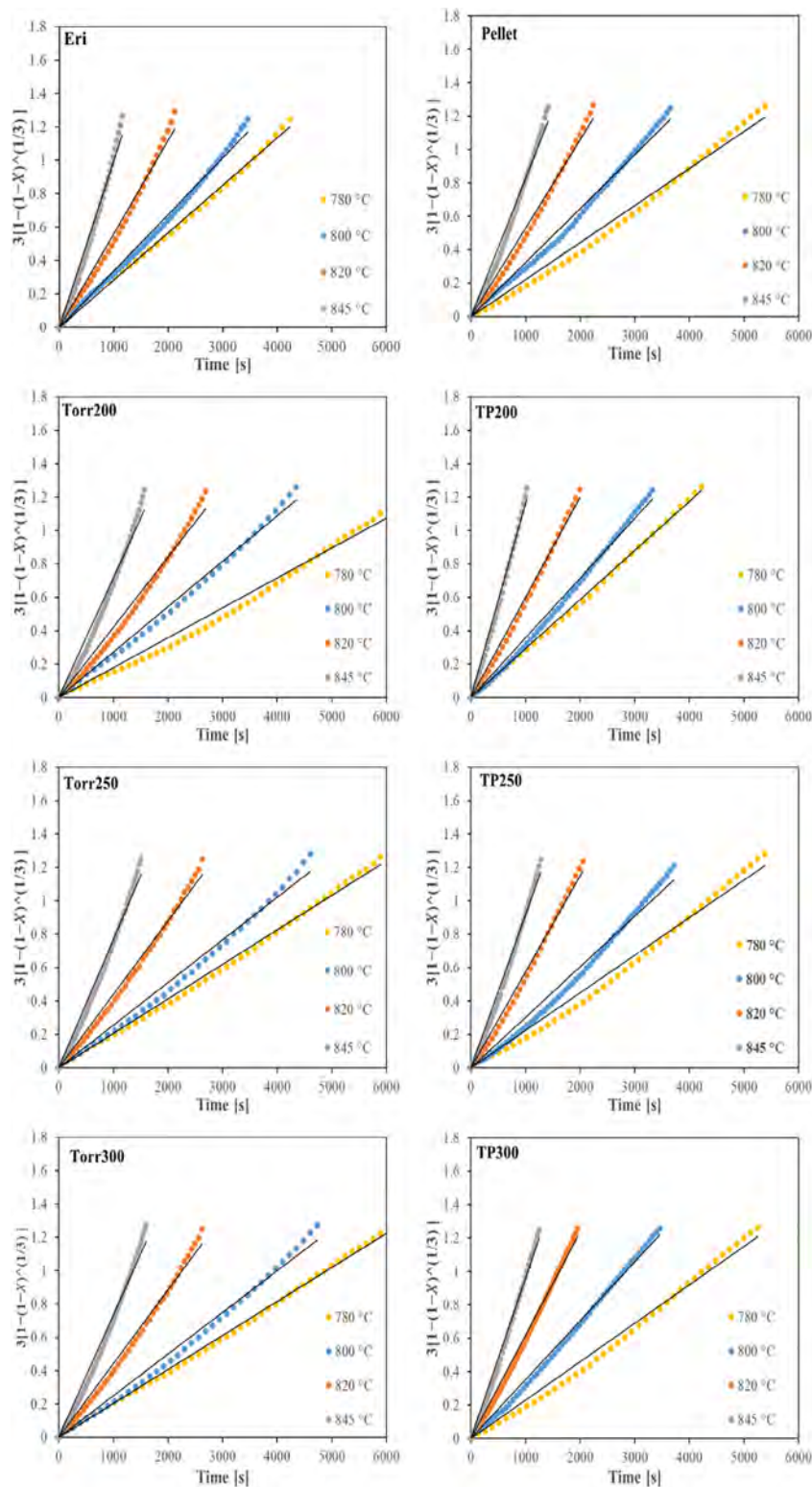


FIGURE 6 SCM linearized solution fitted to the experimental data of *Erianthus arundinaceus* (ERI), Torr200, Torr250, Torr300, pellet, TP200, TP250, and TP300 samples. SCM, shrink core model [Colour figure can be viewed at wileyonlinelibrary.com]

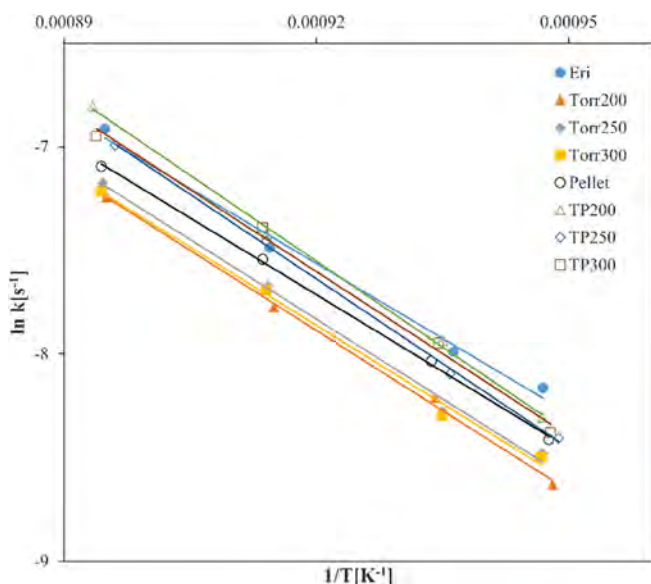
revealed that the VM showed the poorest fitting quality among the studied models. Yet, the fitting quality of SCM and RPM is comparable. Tables 3, S2, and S3 present reaction rate constant (k) and the coefficient of determinations (R^2) values for SCM, VM, and RPM, respectively. The structural parameter (Ψ) was calculated according to Equation (9) and assumed to be constant at different gasification temperatures, therefore, Ψ (Ave.) is calculated by taking the average of Ψ

at all studied temperatures. However, Ψ parameter is a function of the initial char structure and the pore structure development.³⁵ It is clear that for all samples the differences among Ψ parameter values are insignificant which may refer to similar char structure regardless of the pretreatment being applied.

Despite this, calculating the maximum reaction rate is still problematic. Indeed, some researchers reported about the nonexistence of

TABLE 3 The extracted kinetic data from the shrink core model

Sample	Temperature (°C)							
	780		800		820		845	
	Model parameters							
	k	R ²	k	R ²	k	R ²	k	R ²
ERI	0.00028	0.9966	0.00034	0.9956	0.00056	0.9909	0.00099	0.9852
Torr200	0.00018	0.9858	0.00027	0.9941	0.00042	0.9848	0.00071	0.9795
Torr250	0.00021	0.9965	0.00025	0.9868	0.00047	0.9924	0.00077	0.9855
Torr300	0.00020	0.9957	0.00025	0.9899	0.00046	0.9911	0.00073	0.9858
Pellet	0.00022	0.9864	0.00032	0.9806	0.00053	0.9787	0.00083	0.9695
TP200	0.00025	0.9944	0.00036	0.9920	0.00060	0.9932	0.00111	0.9925
TP250	0.00022	0.9851	0.00030	0.9828	0.00058	0.9898	0.00092	0.9891
TP300	0.00023	0.9883	0.00035	0.9939	0.00062	0.9935	0.00096	0.9910

**FIGURE 7** Arrhenius graphs based on the kinetics data obtained from the shrink core model for *Erianthus arundinaceus* (ERI), Torr200, Torr250, Torr300, pellet, TP200, TP250, and TP300 samples [Colour figure can be viewed at [wileyonlinelibrary.com](https://onlinelibrary.wiley.com)]

the maximum reaction rate and it is just a consequence of dispersion of the gases in the reaction chamber when reacting gases being changed, especially for highly reactive char, and nothing related to char reactivity.⁵³ In our study, we have experienced this behavior when a high gasification temperature was used, particularly above 820°C, which is completely compatible with the findings of Gomez et al.⁵³ Consequently, despite RPM fitting gives slightly higher R² values than SCM, values of the reaction rate constant (k) from SCM were utilized to calculate Arrhenius parameters as SCM is simple model and nothing of concern about maximum reaction rate.

Figure 7 illustrates Arrhenius plots for all samples. The relationship between the natural logarithm of the reaction rate constant (ln k) and the absolute temperature's reciprocal (1/T) was calculated for each sample in the studied temperature range. As seen in Figure 7, no

TABLE 4 The extracted kinetics parameters from Arrhenius plot based on SCM data

Sample	E [kJ/mol]	A [s ⁻¹]	R ²
ERI	200.33	2,200,071	0.9909
Torr200	213.78	7,060,313	0.9978
Torr250	212.86	6,729,423	0.9947
Torr300	208.99	4,260,939	0.9945
Pellet	205.21	3,249,462	0.9991
TP200	229.43	55,728,375	0.9981
TP250	225.96	34,865,209	0.9989
TP300	219.24	17,158,427	0.9944

Abbreviation: SCM, shrink core model.

noticeable change in the slopes of the Arrhenius relations was observed, proving that increasing temperature does not shift the reaction from chemically controlled regime to diffusion controlled regime. The activation energy (E) and the frequency factor (A) were calculated by finding the slopes and the intersections values, respectively. Table 4 presents both Arrhenius parameters for all samples. Results showed that the activation energy values reported in this study (200–230 kJ/mol) fall in the range of the typical biomass char values (80.3–261 kJ/mol).⁴⁵ The activation energy of raw *E arundinaceus* is the lowest value. Torrefied-only samples have slightly higher activation energy values. In addition, the torrefied pellet samples demonstrated higher activation energy values than the raw pellet sample, which assure the effect of torrefaction on the activation energy which is slightly increased. Previous works showed similar trend.^{29,54}

4 | CONCLUSION

Torrefaction was performed for raw *E arundinaceus* and its pellets. Fuel characteristics before and after pretreatments were compared. In addition, CO₂ gasification kinetics study was carried out in order to identify pretreatments impacts on the inherited kinetics characteristics. Results

showed that a mass yield higher than 70% could be achieved when torrefaction temperatures around 250°C. Severe torrefaction at 300°C resulted in more than 50% mass reduction, which is economically infeasible. The higher the torrefaction temperatures, the higher the HHV can be achieved. Samples prepared by TAP process were superior to torrefied only samples in different aspects. Torrefied pellets exhibited slightly higher HHV than the torrefied-only sample within the mild torrefaction temperatures. Reactivity of the torrefied pellets was comparable with that of the raw *E arundinaceus* sample, even slightly higher at higher gasification temperatures, unlike the reactivity of torrefied-only samples, which goes to a lower extent. The retention of unwanted chlorine in the fuel sample was less prominent in the torrefied pellets. Kinetics parameters were derived for char gasification using different models. Values of coefficient of determination of RPM and SCM were almost similar, which enabled us to calculate Arrhenius parameters from simpler model as SCM and to avoid RPM that may involve calculation uncertainty resulted from the maximum reaction rate calculation. Finally, the activation energy of torrefied samples was slightly higher than the raw sample and values fall in the range 200–229 KJ/mol.

ORCID

Nasim Qadi  <https://orcid.org/0000-0001-6327-3338>

REFERENCES

- Sarkar M, Kumar A, Tumuluru JS, Patil KN, Bellmer DD. Gasification performance of switchgrass pretreated with torrefaction and densification. *Appl Energy*. 2014;127:194-201.
- Hu Y, Zhang L, Hu J, et al. Assessments of *Erianthus arundinaceus* as a potential energy crop for bioethanol and biomethane production. *Bioresources*. 2017;12:8786-8802.
- Hattori T, Shiotsu F, Doi T, Morita S. Suppression of Tillering in *Erianthus ravennae* (L.) Beauv. Due to Drought Stress at Establishment. *Plant Product Sci*. 2010;13:252-255.
- Mislevy P, Martin FG, Adjei MB, Miller JD. Harvest management effects on quantity and quality of *Erianthus* plant morphological components. *Biomass Bioenergy*. 1997;13:51-58.
- van der Stelt MJC, Gerhauser H, Kiel JHA, Ptasiński KJ. Biomass upgrading by torrefaction for the production of biofuels: a review. *Biomass Bioenergy*. 2011;35:3748-3762.
- Shankar Tumuluru J, Sokhansanj S, Hess JR, Wright CT, Boardman RD. A review on biomass torrefaction process and product properties for energy applications. *Ind Biotechnol*. 2011;7:384-401.
- Guan Y, Ma Y, Zhang K, et al. Co-pyrolysis behaviors of energy grass and lignite. *Energy Convers Manag*. 2015;93:132-140.
- Zhang Y, Geng P, Liu R. Synergistic combination of biomass torrefaction and co-gasification: reactivity studies. *Bioresour Technol*. 2017;245:225-233.
- Fanphanich M, Mani S. Impact of torrefaction on the grindability and fuel characteristics of forest biomass. *Bioresour Technol*. 2011;102:1246-1253.
- Chen W-H, Kuo P-C. Torrefaction and co-torrefaction characterization of hemicellulose, cellulose and lignin as well as torrefaction of some basic constituents in biomass. *Energy*. 2011;36:803-811.
- Kai J, Ramesh A, Talbro S, et al. Changes of chemical and mechanical behavior of torrefied wheat straw. *Biomass Bioenergy*. 2012;40:63-70.
- Kumar L, Koukoulas AA, Mani S, Satyavolu J. Integrating Torrefaction in the wood pellet industry: a critical review. *Energy Fuel*. 2016;31:37-54.
- Bergman PCA. Combined torrefaction and pelletization: The TOP process. Report ECN-C-05-073, ECN. 2005.
- Stelte W, Nielsen NPK, Hansen HO, Dahl J, Shang L, Sanadi AR. Reprint of: pelletizing properties of torrefied wheat straw. *Biomass Bioenergy*. 2013;53:105-112.
- Mišljenović N, Bach Q-V, Tran K-Q, Salas-Bringas C, Skreiberg Ø. Torrefaction influence on pelletability and pellet quality of Norwegian forest residues. *Energy Fuel*. 2014;28:2554-2561.
- Ghiasi B, Kumar L, Furubayashi T, et al. Densified biocoal from woodchips: is it better to do torrefaction before or after densification? *Appl Energy*. 2014;134:133-142.
- Hu Q, Shao J, Yang H, Yao D, Wang X, Chen H. Effects of binders on the properties of bio-char pellets. *Appl Energy*. 2015;157:508-516.
- Erlich C, Björnbohm E, Bolado D, Giner M, Fransson TH. Pyrolysis and gasification of pellets from sugar cane bagasse and wood. *Fuel*. 2006;85:1535-1540.
- Guo P, Saw WL, van Eyk PJ, et al. Gasification reactivity and physico-chemical properties of the chars from raw and Torrefied wood, grape Marc, and macroalgae. *Energy Fuel*. 2017;31:2246-2259.
- George A, Morgan TJ, Kandiyoti R. Pyrolytic reactions of lignin within naturally occurring plant matrices: challenges in biomass pyrolysis modeling due to synergistic effects. *Energy Fuel*. 2014;28:6918-6927.
- Volpe R, Zabaniotou AA, Skoulou V. Synergistic effects between lignin and cellulose during pyrolysis of agricultural waste. *Energy Fuel*. 2018;32:8420-8430.
- Fisher EM, Dupont C, Darvell LI, et al. Combustion and gasification characteristics of chars from raw and torrefied biomass. *Bioresour Technol*. 2012;119:157-165.
- Bach Q-V, Trinh TN, Tran K-Q, Thi NBD. Pyrolysis characteristics and kinetics of biomass torrefied in various atmospheres. *Energy Convers Manag*. 2017;141:72-78.
- Umeki K, Moilanen A, Gómez-Barea A, Kontinen J. A model of biomass char gasification describing the change in catalytic activity of ash. *Chem Eng J*. 2012;207-208:616-624.
- Irfan MF, Usman MR, Kusakabe K. Coal gasification in CO₂ atmosphere and its kinetics since 1948: a brief review. *Energy*. 2011;36:12-40.
- Jess A, Andresen A-K. Influence of mass transfer on thermogravimetric analysis of combustion and gasification reactivity of coke. *Fuel*. 2010;89:1541-1548.
- Dupont C, Nocquet T, Da Costa JA, Verne-Tournon C. Kinetic modeling of steam gasification of various woody biomass chars: influence of inorganic elements. *Bioresour Technol*. 2011;102:9743-9748.
- Tran K-Q, Bui H-H, Luengnaruemitchai A, Wang L, Skreiberg Ø. Isothermal and non-isothermal kinetic study on CO₂ gasification of torrefied forest residues. *Biomass Bioenergy*. 2016;91:175-185.
- Wang L, Várhegyi G, Skreiberg Ø. CO₂ gasification of torrefied wood: a kinetic study. *Energy Fuel*. 2014;28:7582-7590.
- Xue G, Kwapinska M, Kwapinski W, Czajka KM, Kennedy J, Leahy JJ. Impact of torrefaction on properties of *Miscanthus × giganteus* relevant to gasification. *Fuel*. 2014;121:189-197.
- Temmerman M, Jensen PD, Hébert J. Von Rittinger theory adapted to wood chip and pellet milling, in a laboratory scale hammermill. *Biomass Bioenergy*. 2013;56:70-81.
- Qadi MNM, Hidayat A, Takahashi F, Yoshikawa K. Co-gasification kinetics of coal char and algae char under CO₂ atmosphere. *Biofuels*. 2017;8:281-289.
- Channiwala SA, Parikh PP. A unified correlation for estimating HHV of solid, liquid and gaseous fuels. *Fuel*. 2002;81:1051-1063.
- Molina A, Mondragón F. Reactivity of coal gasification with steam and CO₂. *Fuel*. 1998;77:1831-1839.
- Bhatia SK, Perlmutter DD. A random pore model for fluid-solid reactions: I. isothermal, kinetic control. *AIChE J*. 1980;26:379-386.

36. Feroso J, Stevanov C, Moghtaderi B, et al. High-pressure gasification reactivity of biomass chars produced at different temperatures. *J Anal Appl Pyrolysis*. 2009;85:287-293.
37. Pentananunt R, Rahman ANMM, Bhattacharya SC. Upgrading of biomass by means of torrefaction. *Energy*. 1990;15:1175-1179.
38. Bergman PCA, Boersma AR, Zwart RWR, Kiel JHA. Torrefaction for biomass co-firing in existing coal-fired power stations. Rep. No. ECN-C-05-013. 2005.
39. Olsson JG, Jäglid U, Pettersson JBC, Hald P. Alkali metal emission during pyrolysis of biomass. *Energy Fuel*. 1997;11:779-784.
40. Zevenhoven-Onderwater M, Backman R, Skrifvars B-J, Hupa M. The ash chemistry in fluidised bed gasification of biomass fuels. Part I: predicting the chemistry of melting ashes and ash-bed material interaction. *Fuel*. 2001;80:1489-1502.
41. Uemura Y, Omar W, Othman NA, Yusup S, Tsutsui T. Torrefaction of oil palm EFB in the presence of oxygen. *Fuel*. 2013;103:156-160.
42. Poudel J, Oh S. Effect of torrefaction on the properties of corn stalk to enhance solid fuel qualities. *Energies*. 2014;7:5586-5600.
43. Volpe R, Messineo A, Millan M, Volpe M, Kandiyoti R. Assessment of olive wastes as energy source: pyrolysis, torrefaction and the key role of H loss in thermal breakdown. *Energy*. 2015;82:119-127.
44. Emami Taba L, Irfan MF, Wan Daud WAM, Chakrabarti MH. The effect of temperature on various parameters in coal, biomass and CO-gasification: a review. *Renew Sust Energ Rev*. 2012;16:5584-5596.
45. Di Blasi C. Combustion and gasification rates of lignocellulosic chars. *Prog Energy Combust Sci*. 2009;35:121-140.
46. Klose W, Wölki M. On the intrinsic reaction rate of biomass char gasification with carbon dioxide and steam. *Fuel*. 2005;84:885-892.
47. Hu Q, Yang H, Xu H, et al. Thermal behavior and reaction kinetics analysis of pyrolysis and subsequent in-situ gasification of torrefied biomass pellets. *Energy Convers Manag*. 2018;161:205-214.
48. Chen H, Chen X, Qin Y, Wei J, Liu H. Effect of torrefaction on the properties of rice straw high temperature pyrolysis char: pore structure, aromaticity and gasification activity. *Bioresour Technol*. 2017;228:241-249.
49. Li M-F, Chen L-X, Li X, et al. Evaluation of the structure and fuel properties of lignocelluloses through carbon dioxide torrefaction. *Energy Convers Manag*. 2016;119:463-472.
50. Volpe R, Menendez JMB, Reina TR, Messineo A, Millan M. Evolution of chars during slow pyrolysis of citrus waste. *Fuel Process Technol*. 2017;158:255-263.
51. Sarohia GS, Ghuman HS, James AK, Thring RW, Plourde GL. Characterization of tar from wood pellet production. *Int J Chem*. 2014;6.
52. Feroso J, Arias B, Pevida C, Plaza MG, Rubiera F, Pis JJ. Kinetic models comparison for steam gasification of different nature fuel chars. *J Therm Anal Calorim*. 2008;91:779-786.
53. Gomez A, Silbermann R, Mahinpey N. A comprehensive experimental procedure for CO₂ coal gasification: is there really a maximum reaction rate? *Appl Energy*. 2014;124:73-81.
54. Rollinson AN, Williams O. Experiments on torrefied wood pellet: study by gasification and characterization for waste biomass to energy applications. *R Soc Open Sci*. 2016;3:150578.

How to cite this article: Qadi N, Kobayashi M, Takeno K. Influence of torrefaction after densification on the fuel characteristics and the inherited gasification kinetics of *Erianthus arundinaceus* energy grass. *Environ Prog Sustainable Energy*. 2019;e13266. <https://doi.org/10.1002/ep.13266>

Available online at www.sciencedirect.com

ScienceDirect

journal homepage: www.elsevier.com/locate/he

Effect of shock structure on stabilization and blow-off of hydrogen jet flames

Keiji Takeno^{1,*}, Shohei Yamamoto², Ryo Sakatsume¹, Shiori Hirakawa¹, Hiroki Takeda¹, Volodymyr Shentsov^c, Dmitriy Makarov^c, Vladimir Molkov^c

¹ Department of Advanced Science and Technology, Toyota Technological Institute, 2-12-1 Hisakata, Tenpaku-ku, Nagoya 468-8511, Japan

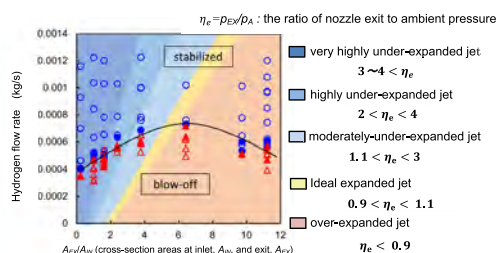
² Department of Mechanical Systems Engineering, Tokyo University of Agriculture and Technology, 2-24-16 Naka-cho, Koganei-city, Tokyo 184-8588, Japan

^c HySAFER Centre, Ulster University, Shore Road, Newtownabbey, BT37 0QB, UK

HIGHLIGHTS

- Hydrogen release tests at pressures up to 13 MPa were conducted.
- Three types of nozzle were used: convergent, straight and divergent.
- Relationship between shock structure and blow-off characteristics was examined.
- Jet flame with multiple diamond shock structure require higher mass flow rate.
- Blow-off is controlled by position of stoichiometric contour and flame base.

GRAPHICAL ABSTRACT



ARTICLE INFO

Article history:

Received 13 November 2019

Received in revised form

27 December 2019

Accepted 26 January 2020

Available online 27 February 2020

Keywords:

Blow-off

Lift-off

ABSTRACT

Under-expanded hydrogen jet has characteristic shock structure immediately downstream of the nozzle exit. The shock structure depends on the ratio p_{EX}/p_A , i.e. the ratio of nozzle exit to ambient pressure, and the distributions of velocity and concentration in an under-expanded hydrogen jet depend on characteristics of the shock structure. Therefore, the shock structure should affect the blow-off behaviour of under-expanded hydrogen jet flame. Since this issue has not been investigated in detail, this study aims to close this knowledge gap. The effect of changes in shock structure on lift-off length and blow-off conditions for non-premixed turbulent hydrogen free jet flame has been experimentally investigated. The shock structure was varied by using three types of nozzles: convergent, straight and divergent nozzles. Inlet diameters of nozzles change from 0.31 to 1.04 mm and

* Corresponding author.

E-mail address: takeno@toyota-ti.ac.jp (K. Takeno).

<https://doi.org/10.1016/j.ijhydene.2020.01.217>

0360-3199/© 2020 Hydrogen Energy Publications LLC. Published by Elsevier Ltd. All rights reserved.

Non-premixed turbulent flame
 Under-expanded jet
 Convergent and divergent nozzles
 Shock structure

outlet diameters from 0.34 to 1.7 mm. The static pressure and the ratio of cross-section area at the nozzle inlet to that at the outlet were varying parameters in this study. Hydrogen was horizontally spouted through a nozzle to atmosphere. The maximum static pressure in a nozzle was 13.2 MPa. The experiments revealed that when the hydrogen jet had sequential shock cell structures, which occurred in the range of p_{EX}/p_A smaller than 2.45, a higher mass flow rate of hydrogen was needed for the stabilization of a jet flame than that for p_{EX}/p_A larger than 2.45 and that when closed to the ideal expansion ($p_{EX}/p_A = 1$), the mass flow rate for stable flame became maximum. In addition, it was observed that the lift-off length of stable flames followed with sequential shock cell structures were almost the same when the minimum cross-section area of used nozzles was constant. However, when hydrogen jet had a shock structure with single Mach disk, the lift-off lengths and the minimum mass flow rate required for the stable jet flame were decreasing with the decrease of the cross-sectional area ratio of the nozzle exit to inlet.

© 2020 Hydrogen Energy Publications LLC. Published by Elsevier Ltd. All rights reserved.

Introduction

Use of hydrogen from renewable sources is a pathway to achieve low carbon society targets, because only water could be exhausted when hydrogen is used as an energy carrier [1]. Therefore, the effective use of hydrogen would be indispensable for building the sustainable society [2,3]. Generally, hydrogen is stored under high pressure because under atmospheric pressure it has low volumetric energy density. The pressure in composite vessels is very high and can reach 90 MPa for fuel cell vehicles. If hydrogen is released under such high pressure and ignited, a non-premixed turbulent flame of under-expanded jet can be established. The studies on under-expanded jet flames were performed to establish safety evaluation criteria [4–12]. Takeno et al. carried out experiments under unprecedentedly high static pressure of 80 MPa and revealed that the static pressure required for stable jet flames changes with nozzle diameter, and the jet flame length was expressed as a function of nozzle diameter and static pressure [7–12]. The authors have experimentally examined the relationship between the static pressure and the blow-off conditions and explained the blow-off phenomenon for hydrogen non-premixed turbulent flame originating from under-expanded jet for the case of single Mach disk [13]. However, the experiments in above-mentioned studies were performed using only straight nozzles of constant diameter. Non-premixed hydrogen flames in jets spouted through tapered nozzles whose cross-section area increases or decreases have not been investigated up to now.

The shocks structure generated near the nozzle exit was investigated experimentally and numerically [14–17]. According to review by Franquet et al. [18], the changes in the shocks structure are governed by the ratio p_0/p_A , where p_0 is the static pressure, and p_A is the atmospheric pressure, or by the ratio p_{EX}/p_A , where p_{EX} is the pressure at the nozzle exit, and can be classified as follows. Moderately under-expanded jets, which have oblique shock waves from a lip of the nozzle exit toward the nozzle axis and its reflected shock waves, are generated in the pressure range $1.1 \leq p_{EX}/p_A \leq 3$. Under-expanded jets in the range $2 \leq p_{EX}/p_A \leq 4$ consist of a

barrel shock starting at the nozzle lip and Mach disk. At pressure ratios $4 \leq p_{EX}/p_A$, jets have single Mach disk and they are called highly under-expanded jets. The change in shocks structure due to change of p_{EX}/p_A ratio is thought to give different distribution of spouted gas concentration and velocity field. Thus, the shocks structure could affect the lift-off length and the conditions required for stable non-premixed jet flames.

In the present paper, lift-off lengths and blow-off conditions for expanded hydrogen jet flames were experimentally investigated, and distributions of velocities and hydrogen concentration in unignited hydrogen jets were numerically examined. The variation of the shock structure downstream of the nozzle exit was provided by change of pressure in the stagnation point and the exit from the nozzle. The pressure at the nozzle exit was changed by using divergent or convergent nozzles whose cross-section area linearly increased or decreased in the nozzle axis direction. The relationship between conditions for the sustained jet flame and the shock structure is discussed, and a qualitative model of blow-off for expanded hydrogen jet flame is proposed.

Experimental setup and conditions

Fig. 1 shows a schematic of an experimental setup and an optical measurement system. High-pressurized hydrogen jet was released horizontally by blowdown from a reservoir with maximum pressure of 13.2 MPa. Spouted hydrogen jets were ignited by a pilot natural gas non-premixed flame set at 700 mm downstream of the nozzle exit. This flame was removed after the jet flame was stabilized. The spouting pressure was adjusted by the valve and measured by a piezoelectric pressure sensor (TP-AR, TEAC) installed between valve and nozzle and the pressure data was collected by 10 kHz digital recorder. Since the maximum hydrogen velocity inside hydrogen piping from valve to nozzle was less than several centimetres per second, the measured static pressure was estimated to coincide with the stagnation pressure in the chamber of nozzle.

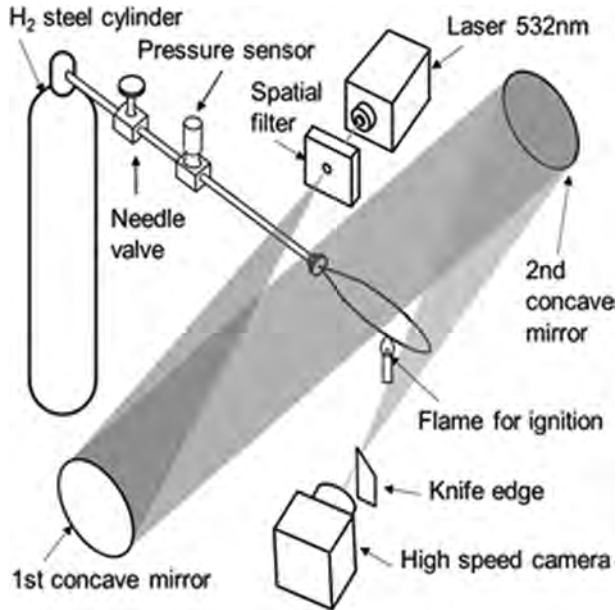


Fig. 1 – Schematic diagram of experimental set up.

Table 1 shows the identification and parameters of three types of nozzle, i.e. measured diameters at the nozzle inlet, d_{IN} , and exit, d_{EX} , cross-section areas at inlet, A_{IN} , and exit, A_{EX} , as well as their ratio A_{EX}/A_{IN} . Three straight, six divergent and

one convergent nozzle were used in this study, and their cross-section drawings are shown in Fig. 2. For the divergent and convergent nozzles, the minimum diameter of nozzle throat d_{thr} was almost the same about 0.5 mm to provide the same hydrogen flow rate.

Light source of the optical system for taking schlieren images was Nd:YVO₄ laser (G50-B, kato koken) with a wave length of 532 nm, a maximum output of 50 mW. A parallel beam of the light for the schlieren imaging was prepared using two concave mirrors with its diameter of 150 mm and focal length of 1500 mm (CM series, kato koken). Laser beam of 0.5 mm diameter was expanded through the spatial filter located at the focal point of first concave mirror. A knife edge was installed at the focal point of second concave mirror, and cut the focal point in perpendicular to the hydrogen flow direction. Schlieren images were taken by a high-speed camera (UX100, Photron) at 2000 fps and exposure time of 12.5 μ s through camera lens (focal length = 200 mm, Nikon).

Experimental results and discussion

Fig. 3 shows a typical schlieren images of hydrogen turbulent non-premixed jet flames obtained in this study at the static pressure of around 8 MPa with different cross-section area ratio, A_{EX}/A_{IN} , and the three kinds of nozzle. Hydrogen mass flow rate, m , was practically the same in the range of

Table 1 – Types and dimensions of used nozzles.

Nozzle type	Abbreviation	INLET		EXIT		A_{EX}/A_{IN}
		d_{IN} [mm]	A_{IN} [mm ²]	d_{EX} [mm]	A_{EX} [mm ²]	
Straight	d0.3	0.31	0.08	0.34	0.09	1.20
	d0.5	0.51	0.20	0.53	0.22	1.09
	d0.7	0.73	0.41	0.75	0.44	1.06
Divergent	d0.5–0.65	0.52	0.21	0.66	0.34	1.62
	d0.5–0.80	0.53	0.22	0.81	0.52	2.40
	d0.5–1.00	0.52	0.21	1.01	0.79	3.78
	d0.5–1.30	0.52	0.21	1.32	1.36	6.44
	d0.5–1.60	0.52	0.22	1.64	2.10	9.73
	d0.5–1.65	0.51	0.20	1.70	2.28	11.2
Convergent	d1.00–0.5	1.04	0.85	0.50	0.19	0.23

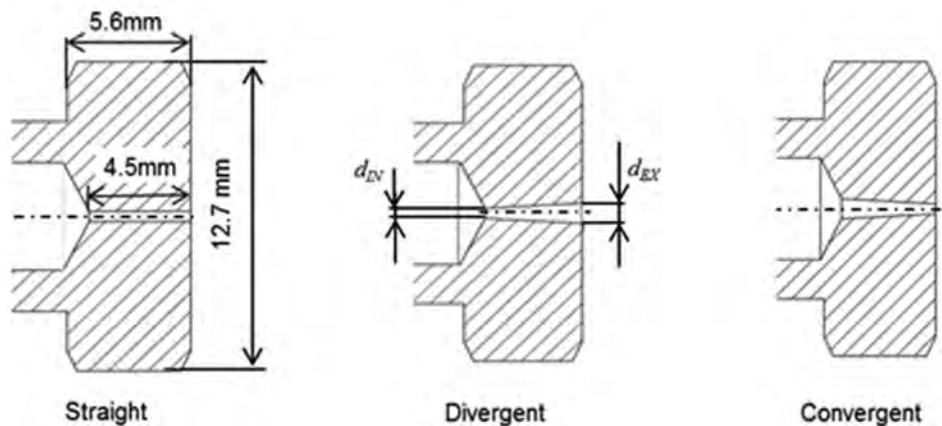


Fig. 2 – Cross-section drawings of three types of nozzles.

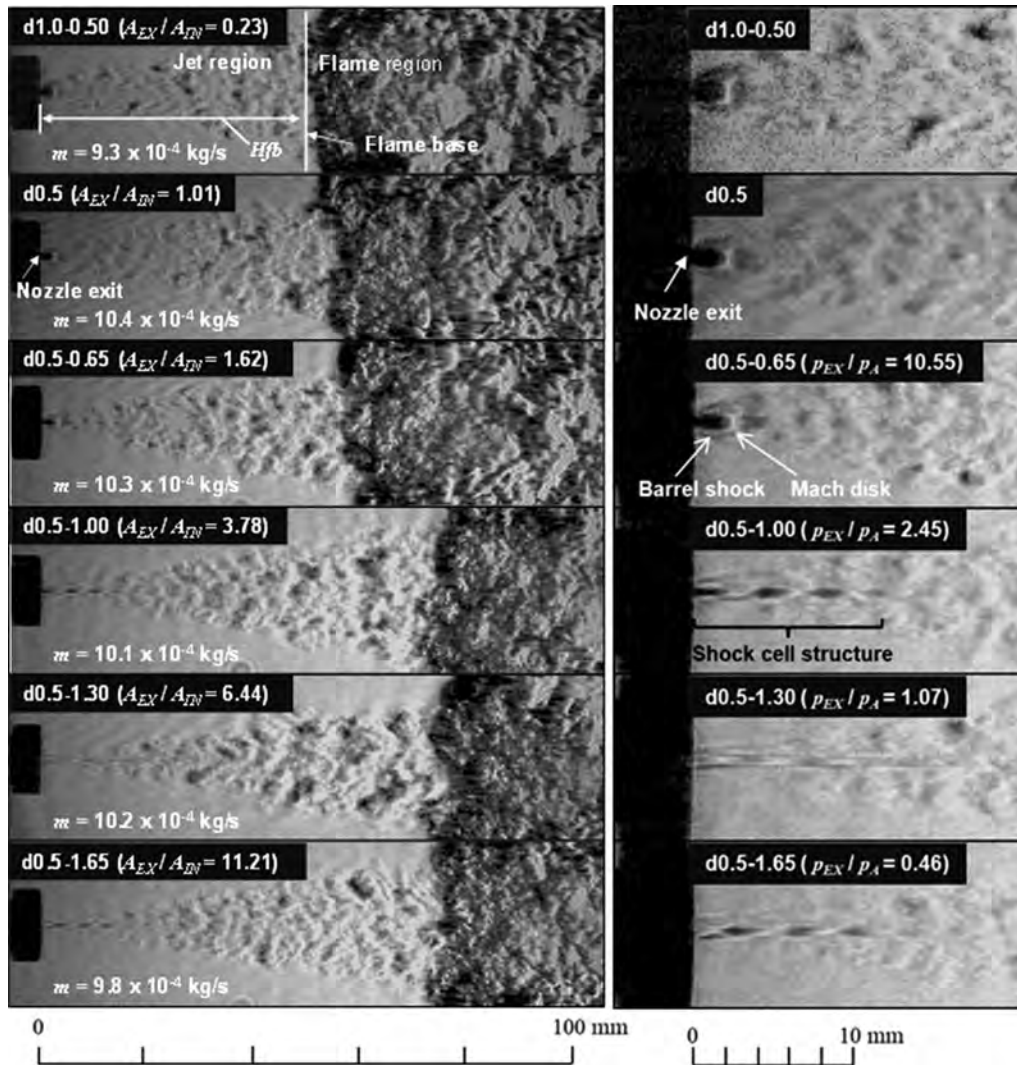


Fig. 3 – Schlieren images of turbulent non-premixed jet flames with different ratio of the exit cross-section area of nozzle to the inlet cross-section area, A_{EX}/A_{IN} , with the hydrogen mass flow rates kept almost constant. The right figures are the enlarged schlieren images focused on the shock structures near the nozzle exit.

0.93–1.03 g/s, which was calculated from the static pressures and cross-section areas, A_{EX} and A_{IN} , assuming isentropic expansion. The lift-off length H_{fb} was defined as the length from the nozzle exit to the time-averaged position of the flame base. For ratios $A_{EX}/A_{IN} < 3.78$, the value of H_{fb} increased with the increase of A_{EX}/A_{IN} . However, for $A_{EX}/A_{IN} \geq 3.78$, the values of H_{fb} were almost constant regardless of A_{EX}/A_{IN} .

In order to clearly show the shock wave structure, enlarged images near the nozzle exit were shown in Fig. 3 (right column), where pressure ratio, p_{EX}/p_A , which is the ratio of nozzle exit pressure, p_{EX} , to the ambient pressure, p_A , are also shown. A shock wave structure consisting of a barrel shock and single Mach disk was observed for ratios $A_{EX}/A_{IN} \leq 1.62$. For ratios $A_{EX}/A_{IN} > 1$ the nozzle exit pressure p_{EX} decreases as A_{EX}/A_{IN} increases, and a series of shocks (diamond structure) can be seen in images for $A_{EX}/A_{IN} \geq 3.78$. The value of p_{EX}/p_A was almost unity as shown in the image for $A_{EX}/A_{IN} = 6.44$ (d0.5–1.30), and an over-expanded jet can be seen in the image

for $p_{EX}/p_A < 1$ (d0.5–1.65). The observed variation of shock structure with A_{EX}/A_{IN} and p_{EX}/p_A agrees quantitatively with conclusions of previous study [18].

Fig. 4 shows the relationship between H_{fb} and A_{EX}/A_{IN} for stable jet flames when using the minimum diameter of nozzle throat, d_{thr} , in the narrow range 0.51–0.53 mm, so that the relationship between hydrogen mass flow rate and static pressure was determined regardless of the nozzle throat type. Hydrogen mass flow rate was in the range $0.40 \leq \dot{m} \leq 1.48$ g/s depending on the static pressure of hydrogen, and resulted in the scatter of H_{fb} in Fig. 4. For ratios $A_{EX}/A_{IN} > 3.78$, the values of H_{fb} for the same A_{EX}/A_{IN} were almost constant regardless of the mass flow rate, and the values of H_{fb} for $A_{EX}/A_{IN} < 3.78$ tended to decrease with the decrease in A_{EX}/A_{IN} . When $A_{EX}/A_{IN} \sim 3.78$, jet flames were stable in the range of $0.69 \leq \dot{m} \leq 1.48$ g/s (equivalent to $1.67 \leq p_{EX}/p_A \leq 3.59$), accompanied with sequential shock cell structures shown in Fig. 3. Such jet is shown in the image of d0.5–1.00 and is classified as the highly under-expanded jet which occurs in

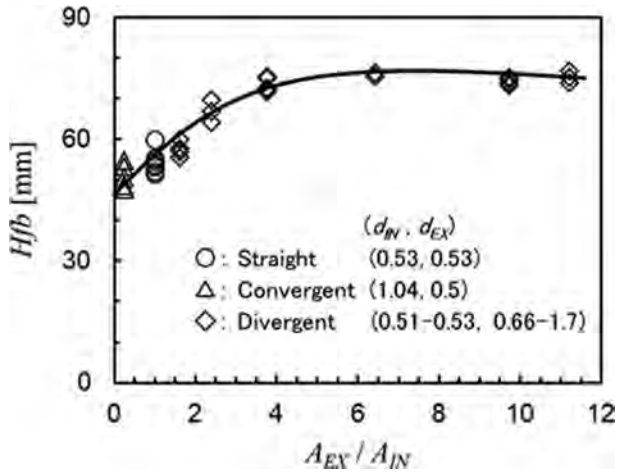


Fig. 4 – Dependence of lift-off length H_{fb} on A_{EX}/A_{IN} .

the range of $2 \leq p_{EX}/p_A \leq 4$ [18]. For $A_{EX}/A_{IN} \geq 3.78$ the value of H_{fb} was almost constant independent of A_{EX}/A_{IN} . This result shows that the value of H_{fb} for all three types of observed in experiments jets (highly under-expanded jet, expanded jet and over-expanded jet), which occur at pressure ratio $p_{EX}/p_A \leq 2.45$, can be expected to be constant. In addition, for pressure ratio $p_{EX}/p_A > 2.45$, the value of H_{fb} in highly under-expanded jets accompanied with a barrel shock and single Mach disk can be expected to decrease with the increase of p_{EX}/p_A because the decrease in A_{EX}/A_{IN} causes the increase in p_{EX}/p_A . Accordingly, the lift-off length H_{fb} depends on the kind of shock structure just downstream the nozzle exit.

Fig. 5 shows the conditions for existence of stable hydrogen jet flame and flame blow-off. It is presented in the coordinates “mass flow rate” and “ratio A_{EX}/A_{IN} ” for nozzles $0.51 \leq d_{thr} \leq 0.53$ mm. This figure shows that a minimum mass flow rate for the stable jet flame exists, and that the minimum value increases with the increase of A_{EX}/A_{IN} and reaches extreme at $5 \leq A_{EX}/A_{IN} \leq 7$, where the flow is close to the ideal expansion ($p_{EX}/p_A \sim 1$). For region $A_{EX}/A_{IN} \lesssim 4$, which is classified as the region of highly under-expanded jets, the minimum mass

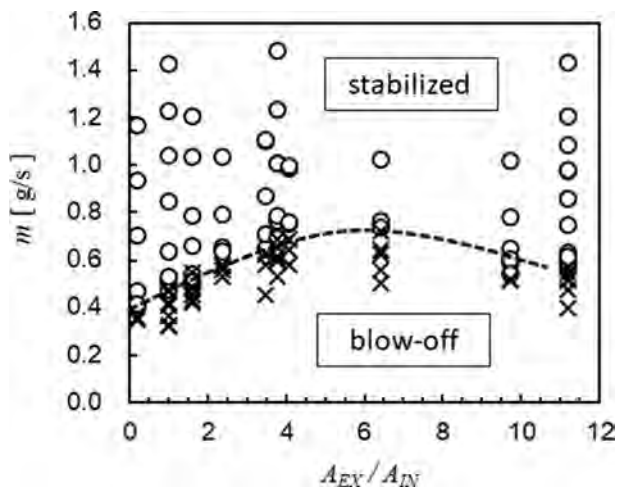


Fig. 5 – Conditions for hydrogen flame stabilization (○), and blow-off (×).

flow rate for stable flame decreased as the value of A_{EX}/A_{IN} decreased. For $A_{EX}/A_{IN} \geq 7$, where the jet is over-expanded, the shock wave just out of the nozzle exit is a compression wave as shown in Fig. 3, and the minimum mass flow rate decreases as A_{EX}/A_{IN} increases.

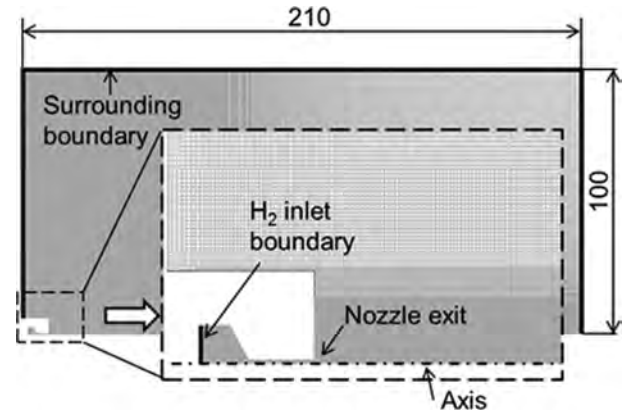


Fig. 6 – Computational domain and enlarged image near the nozzle exit.

Table 2 – Nozzle dimensions in numerical simulations.

Nozzle type	d_{IN} [mm]	d_{EX} [mm]	A_{EX}/A_{IN}
Straight	0.50	0.50	1.00
Divergent	0.50	0.65	1.69
	0.50	0.80	2.56
	0.50	1.00	4.00
	0.50	1.16	5.38
	0.50	1.30	6.76
	0.50	1.50	9.00
0.50	1.65	10.9	
Convergent	1.00	0.50	0.25

Table 3 – Boundary conditions of simulations.

	H2 inlet	Surrounding
Temperature [K]	300	300
Absolute pressure [MPa]	3 to 10	0.1
Composition (Mass fraction)	1H ₂	0.23 O ₂ 0.77 N ₂

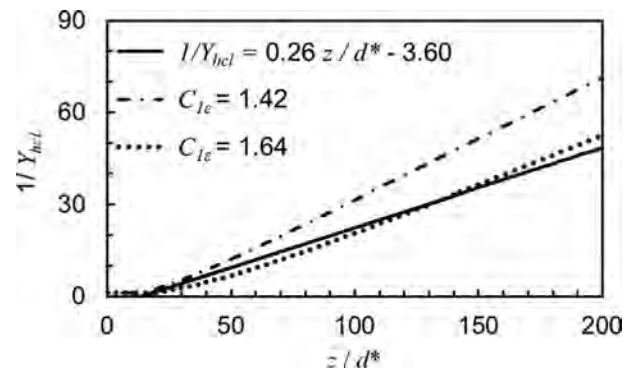


Fig. 7 – Change in the reciprocal of H₂ mass fraction Y_{hcl} along the non-dimensional jet axis with changing RNG $k-\epsilon$ turbulence model coefficient $C_{1\epsilon}$.

Numerical study

Model details

The effects of shock structure on velocity and hydrogen concentrations distributions were numerically studied by carrying out steady state simulations in two-dimensional axisymmetric formulation. The computational domain and

enlarged image in the vicinity of nozzle outlet are shown in Fig. 6. Simulated nozzle dimensions are given in Table 2. The sizes of simulated nozzles were determined corresponding to the experimental conditions with maximum deviation within 0.01 mm. The computational domain width was 210 mm and height 100 mm. The grids had square shape, and the mesh size near the nozzle axis was set finer. The minimum grid dimension was 30 μm , and the number of control volumes in a

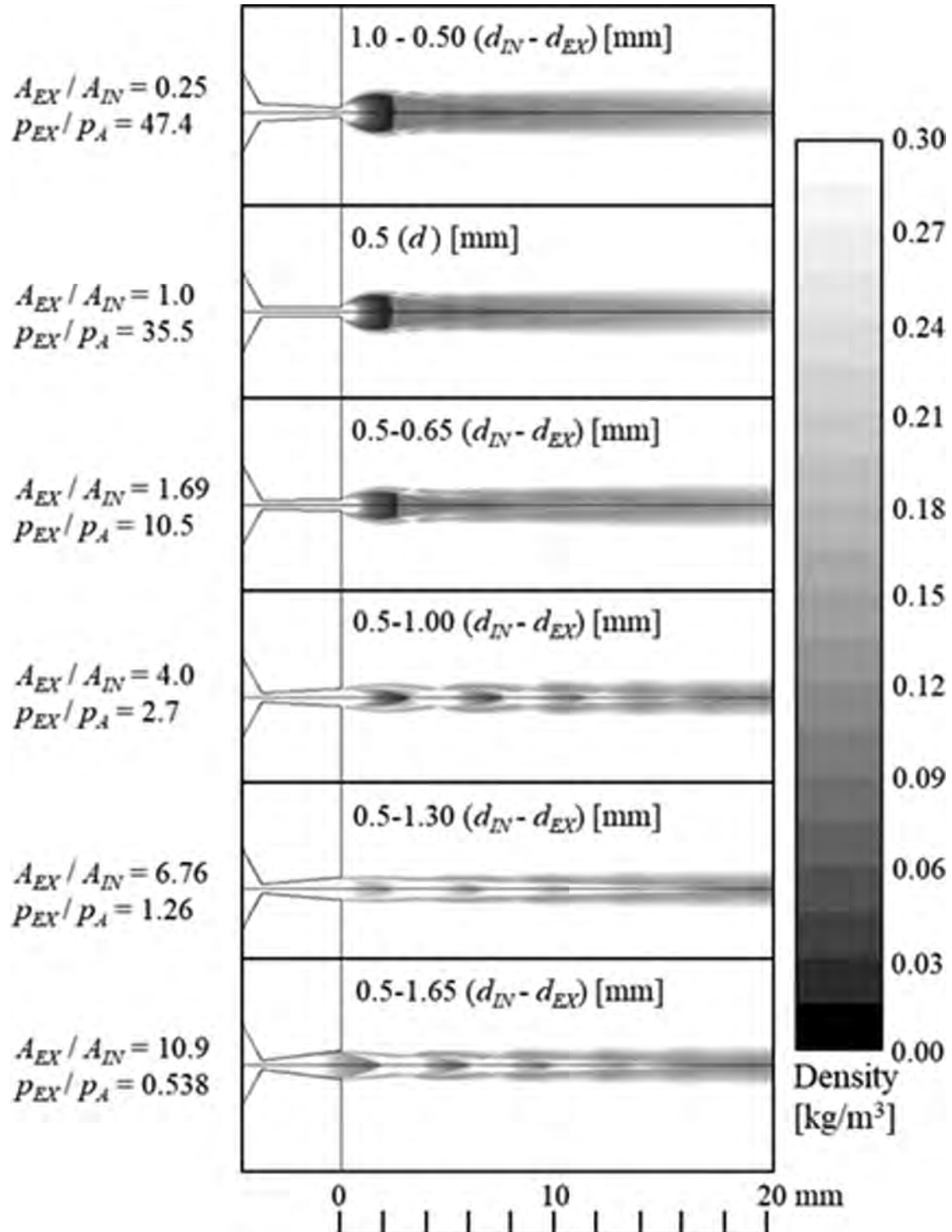


Fig. 8 – Simulation results of density contour near the nozzle exit, with the static pressure and mass flow rate set at 8 MPa and 0.98 g/s, respectively.

grid was about 25,000. The grid convergence value of 30 μm could be determined by the following procedure that the mesh sizes were repeatedly decreased half and half, and then the simulated results were compared with those with the previous mesh sizes. Boundary conditions in the simulation are shown in Table 3.

Governing equations of mass, momentum, energy and chemical species transport equations were solved using ANSYS Fluent 16.2 as computational engine. The RNG $k-\epsilon$ model [19] was used as a turbulent model, where the model constant $C_{1\epsilon}$ was changed from default value 1.42 to 1.64. The value of 1.64 was selected so that the simulated hydrogen mass fraction distribution along the nozzle axis could be corresponded with the distribution estimated by the empirical equation by Li et al. [20]. In Fig. 7, Y_{HCl} is the hydrogen mass fraction, z is the distance from nozzle exit along nozzle axis, and d^* is defined as $d_{\text{EX}} (\rho_{\text{EX}}/\rho_{\infty})^{0.5}$, where ρ_{EX} is gas density at nozzle exit, ρ_{∞} is surrounding gas density. The value of ρ_{EX} was calculated using the under-expanded jet theory [21]. As shown in Fig. 7, the empirical relationship between hydrogen mass fraction and non-dimensional distance could be well reproduced when value 1.64 is used to the model constant $C_{1\epsilon}$.

Calculated results

Typical results of density distributions for the static pressure in nozzle of 8 MPa ($m = 0.98 \text{ g/s}$) are shown in Fig. 8. The single Mach disk exists for $0.25 \leq A_{\text{EX}}/A_{\text{IN}} \leq 1.69$, and densities along the nozzle axis were changed rapidly adjacent to the nozzle exit. The distance L_{MD} from the nozzle exit to the Mach disk for the straight nozzle of $d_{\text{IN}} = d_{\text{EX}} = 0.5 \text{ mm}$ is 2.82 mm. This is just by 0.9 mm longer than value calculated with the empirical equation, $L_{\text{MD}}/d_{\text{EX}} = 0.62 (p_{\text{EX}}/p_A)^{0.51}$ [18]. Densities along nozzle axis for $A_{\text{EX}}/A_{\text{IN}} \geq 4$ repeated increasing and decreasing downstream creating so-called diamond shock structures. Fig. 9 shows the scalar of velocity vector along the nozzle axis for different ratios $A_{\text{EX}}/A_{\text{IN}}$. Jets for $A_{\text{EX}}/A_{\text{IN}} \leq 1.69$ have one Mach disk at position 2.80–2.85 mm downstream of the nozzle exit, where the scalar of velocity rapidly decreased to approximately 500 m/s. Then, the velocity gradually increased and had a peak of 1200–1700 m/s. On the other hand, jets for $A_{\text{EX}}/A_{\text{IN}} \geq 4$ have multiple shock diamond structures and maintain its higher velocity of 2000–2500 m/s for over $z = 20 \text{ mm}$, and then the velocity monotonically decreases downstream.

Blow-off model for high-pressurized hydrogen jet flames

In the previous study for very highly under-expanded hydrogen jet with straight nozzle, the blow-off limit could be arranged only with the flow rate of spouted hydrogen, regardless of the static pressure in nozzle or the throat diameter of nozzle [7,8,13]. On the other hand, it is shown in Fig. 5 that the required minimum hydrogen flow rate for the flame stabilization depends upon $A_{\text{EX}}/A_{\text{IN}}$ or the structure of shock downstream of nozzle exit. An attempt would be made to interpret it by considering the distributions of velocity and concentration.

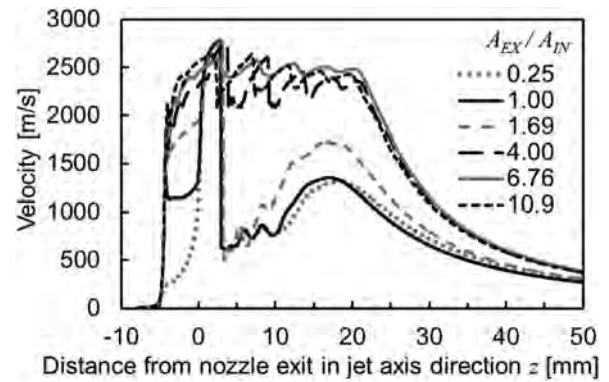


Fig. 9 – Simulation results of velocity distribution along the jet axis, where the calculation conditions correspond to those of Fig. 8.

Fig. 10 shows the value of v_{phi1} , which is the velocity at an intersection point between the stoichiometric contour of hydrogen concentration in the jet and line at $z = 70 \text{ mm}$ perpendicular to the nozzle axis. The value $z = 70 \text{ mm}$ means the distance H_{fb} from the nozzle exit to the flame base for $A_{\text{EX}}/A_{\text{IN}} \geq 4$ as shown in Fig. 3. The value of v_{phi1} increases as $A_{\text{EX}}/A_{\text{IN}}$

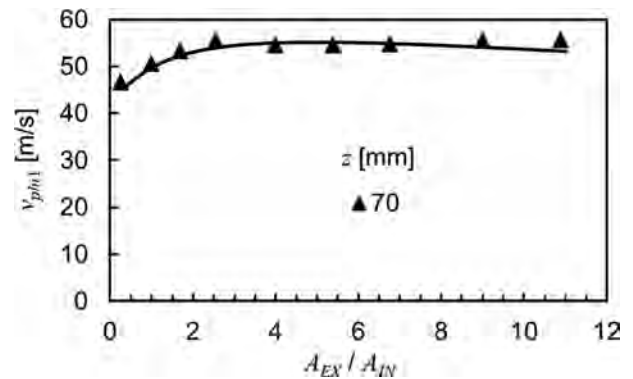


Fig. 10 – Simulation results of velocity v_{phi1} at the intersection point between the stoichiometric contour and $z = 70 \text{ mm}$ line perpendicular to the jet axis.

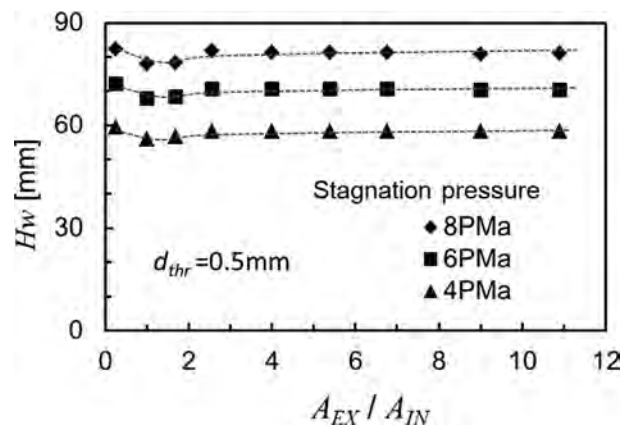


Fig. 11 – Relationship between H_w and $A_{\text{EX}}/A_{\text{IN}}$ with the variation of static pressure in nozzle, where the.

A_{IN} increases and becomes almost constant at $A_{EX}/A_{IN} \geq 4$. The variation of Hfb for $A_{EX}/A_{IN} \leq 4$ could be explained when considering flame base position as the one where flow velocity is equal to flame propagation velocity [22], and in the assumption that the stable flame base position lies at the stoichiometric contour [4]. In other words, the velocities on the stoichiometric contour for $A_{EX}/A_{IN} \leq 4$ were obviously lower than those for $A_{EX}/A_{IN} \geq 4$ at the same position ($z = 70$ mm) in z -direction. Therefore, the flow velocity for $A_{EX}/A_{IN} \leq 4$ could be balanced with the turbulent burning velocity farther upstream than cases with $A_{EX}/A_{IN} \geq 4$. Consequently, as shown in Figs. 3 and 4, the value of Hfb for $A_{EX}/A_{IN} \leq 4$ could be smaller.

The criterion required for stable non-premixed flames in subsonic jets was formulated as $Hw > Hfb$ [23], where Hw is the distance from the nozzle exit to the intersection of two lines, one being the jet axis and another being perpendicular line from the jet axis to the maximum radial location of the stoichiometric contour. The value of Hw could be estimated from an actual nozzle diameter, spouted and ambient gas densities by using the equations proposed by Birch et al. [24] and was validated in the literature [23]. It was reported that characteristics of under-expanded jets could be predicted using the

notional nozzle theory proposed by Molkov et al. [25,26]. The values of Hw calculated by the notional nozzle diameter are shown in Fig. 11 [13]. This figure demonstrates that the values of Hw depends little on A_{EX}/A_{IN} but depend on the static pressure, and that Hw can be determined by hydrogen flow rate regardless of nozzle types or shock structures. As the static pressure in nozzle increases, the hydrogen flow rate and Hw increase.

For the nozzles with the same d_{thr} , when the static pressure or mass flow rate is the same, the values of Hw change little regardless of the type of shock structure, while the value of Hfb having the structure of Mach disk is clearly smaller than Hfb' whose shock structure is sequential shock cell type, as shown in Figs. 3 and 4, because the value of velocity v_{phi1} in Fig. 10 increases as the increase of A_{EX}/A_{IN} and becomes constant for $A_{EX}/A_{IN} \geq 4$. This means that the velocity and concentration fields are not linearly linked each other, due to the variations of shock structure. The cases where the flame is stabilized and stable regardless of a type of shock structure seem to have the relationship of $Hw > Hfb' > Hfb$ shown in Fig. 12(a). If the static pressure or mass flow rate gradually decreases, Hw decreases while both of Hfb and Hfb' don't change essentially as shown in Fig. 4. In this case, the

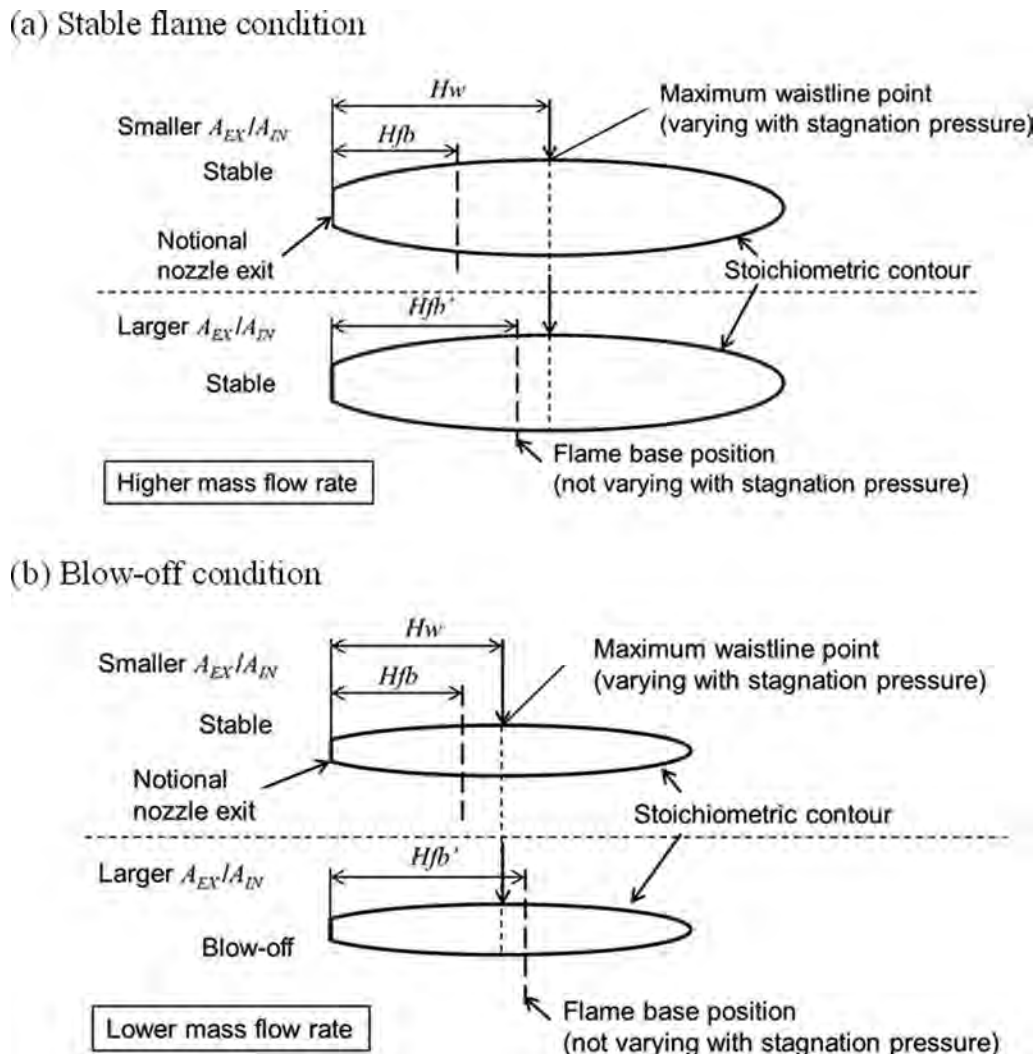


Fig. 12 – Schematic illustrations on the relationship between Hfb and Hw and qualitative model for blow-off or stable flame.

relationship of $Hfb' > Hw > Hfb$ shown in Fig. 12(b) can hold, and the flame with sequential shock cells will blow-off, while the flame with one Mach disk will be still stabilized. If the static pressure or mass flow rate decreases further, the relationship of $Hfb' > Hfb > Hw$ is realized and the flame will blow-off regardless of a type of shock structure. This shows qualitatively that minimum static pressure or mass flow rate required for stable flames in the high-pressurized hydrogen jet with sequential shock cell structures should be higher, as shown in Fig. 5.

Conclusions

The change of cross-section area ratio A_{EX}/A_{IN} changes the shock structure downstream the nozzle exit even the static pressure in the nozzle is kept the same, where the ratio p_{EX}/p_A , i.e. the ratio of nozzle exit to ambient pressure changes in conjunction. The flame lift-off length Hfb and the blow-off condition of the turbulent non-premixed flame for high-pressure hydrogen jets are experimentally examined, with $A_{EX}/A_{IN} = 0.23$ –11.2 (minimum throat diameter is constant at 0.5 mm) and hydrogen flow rate = 0.3–1.48 g/s being parameters.

It is shown that when ratio A_{EX}/A_{IN} is the same, Hfb for stable flames slightly depends on the static pressure. For $A_{EX}/A_{IN} < 3.78$ ($p_{EX}/p_A > 2.45$), a single barrel shock and Mach disk could be observed at the nozzle exit, and Hfb increases with the increase of A_{EX}/A_{IN} . On the other hand, for $A_{EX}/A_{IN} \geq 3.78$ ($p_{EX}/p_A \leq 2.45$), the sequential shock cell (diamond) structures is observed and Hfb was almost constant regardless of A_{EX}/A_{IN} , and a higher mass flow rate of hydrogen was needed for the stabilization of jet flames. Moreover, when the flow in the nozzle was close to ideal expansion ($A_{EX}/A_{IN} = 6$ –7, $p_{EX}/p_A = 0.9$ –1.1), the mass flow rate for existence of stable flame became maximum.

The numerical simulation at static pressure of 8 MPa demonstrated that hydrogen jets with $A_{EX}/A_{IN} \geq 4$ have the sequential shock cell (diamond) structure, and the velocity at the intersection point between the stoichiometric contour and the line perpendicular to the nozzle axis at 70 mm downstream from the nozzle exit is almost the same. Hydrogen jets with $A_{EX}/A_{IN} \leq 4$ have single Mach disk and the velocity at the same point decreased with the decrease of A_{EX}/A_{IN} . This qualitatively explains the experimental result that the value of Hfb for $A_{EX}/A_{IN} < 3.78$ ($p_{EX}/p_A > 2.45$) decreases with the decrease of A_{EX}/A_{IN} .

The mass flow rate required for the existence of stable flame is almost the same for $A_{EX}/A_{IN} \geq 3.78$ and the required flow rate for $A_{EX}/A_{IN} < 3.78$ decreases with the decrease of A_{EX}/A_{IN} . This observation could be qualitatively explained by considering the condition for stabilization of jet flame $Hw > Hfb$ regardless of the shock structures, where Hw is the distance from the nozzle axis to the maximum radius point on the stoichiometric contour.

REFERENCES

- [1] Acar C, Dincer I. Comparative assessment of hydrogen production methods from renewable and non-renewable sources. *Int J Hydrogen Energy* 2014;39:1–12.
- [2] Mazloomi K, Gomes C. Hydrogen as an energy carrier: prospects and challenges. *Renew Sustain Energy Rev* 2012;16:3024–33.
- [3] Kojima H, Matsumoto H, Tsujimura T. Development of large scale unified system for hydrogen energy carrier production and utilization: experimental analysis and systems modelling. *Int J Hydrogen Energy* 2017;42(19):13309–4044.
- [4] Annushkin YM, Sverdlov ED. Stability of submerged flames in subsonic and underexpanded supersonic gas-fuel streams. *Combust Explos Shock Waves* 1979;14(5):597–605.
- [5] Yoon Y, Donbar JM, Driscoll JF. Blow-out stability limits of a hydrogen jet flame in a supersonic heated coflowing air stream. *Combust Sci Technol* 1994;97(1–3):137–56.
- [6] Wu Y, Lu Y, Al-Rahbia IS, Kalghatgi GT. Prediction of the liftoff, blowout and blowoff stability limits of pure hydrogen and hydrogen/hydrocarbon mixture jet flames. *Int J Hydrogen Energy* 2009;34(14):5940–5.
- [7] Takeno K. Characteristics and safety for open-jet flame of high-pressurized hydrogen. *J Combust Society of Japan* 2010;52(160):121–9.
- [8] Takeno K, Okabayashi K, Hashiguchi K, Noguchi F, Chitose K. Experimental Study on open jet diffusion flame of 40MPa high-pressure hydrogen. *Environ Manag* 2005;41:33–40.
- [9] Takeno K, Hashiguchi K, Okabayashi K, Chitose K, Kushiyama M, Noguchi F. Experimental study on open jet diffusion flame and unconfined explosion for leaked high-pressurized hydrogen. *J Japan Society for Safety Eng* 2005;44:398–406.
- [10] Takeno K, Okabayashi K, Kouchi A, Nonaka T, Hashiguchi K, Chitose K. Dispersion and explosion field tests for 40MPa pressurized hydrogen. *Int J Hydrogen Energy* 2007;32:2144–53.
- [11] Kouchi, A., Okabayashi, K., Takeno, K. and Chitose, K. Dispersion tests on concentration and its fluctuation for 40MPa pressurized hydrogen. *Proceeding of international conference on hydrogen safety*, Sep. 8-10, 2007, Pisa, Italy.
- [12] Takeno K, Okabayashi K, Kouchi A, Misaka N, Hashiguchi K. Concentration fluctuation and ignition characteristics during atmospheric diffusion of hydrogen spouted from high pressure storage. *Int J Hydrogen Energy* 2017;42(22):15426–34.
- [13] Yamamoto S, Sakatsume R, Takeno K. Blow-off process of highly under-expanded hydrogen non-premixed jet flame. *Int J Hydrogen Energy* 2018;43(10):5199–205.
- [14] Crist S, Glass DR, Sherman PM. Study of the highly underexpanded sonic jet. *AIAA J* 1966;4(1):68–71.
- [15] Andre B, Castelain T, Bailly C. Experimental exploration of underexpanded supersonic jets. *Shock Waves* 2013;24(1):21–32.
- [16] Rogers T, Petersen P, Koopmans L, Lappas P, Boretti A. Structural characteristics of hydrogen and compressed natural gas fuel jets. *Int J Hydrogen Energy* 2015;40(3):1584–97.
- [17] Li X, Wu K, Yao W, Fan X. A comparative study of highly underexpanded nitrogen hydrogen jets using large eddy simulation. *Int J Hydrogen Energy* 2016;41(9):5151–61.
- [18] Franquet E, Perrier V, Gibout S, Bruel P. Free underexpanded jets in a quiescent medium: a review. *Prog Aero Sci* 2015;77:25–53.
- [19] Yakhot V, Orszag SA. Renormalization group Analysis of turbulence. I. Basic theory. *J Sci Comput* 1986;1(1):3–51.
- [20] Li X, Hecht ES, Christopher DM. Validation of a reduced-order jet model for subsonic and underexpanded hydrogen jets. *Int J Hydrogen Energy* 2016;41:1348–58.
- [21] Molkov V, Bragin M. High-pressure hydrogen leak through a narrow channel. In: *Nonequilibrium phenomena: plasma, combustion*. Moscow: Atmosphere; 2009. p. 332–8.

- [22] Chung SH. Stabilization, propagation and instability of tribrachial triple flames. *Proc Combust Inst* 2007;31:877–92.
- [23] Wu CY, Chao YC, Cheng TS, Li YH, Lee KY, Yuan T. The blowout mechanism of turbulent jet diffusion flames. *Combust Flame* 2006;145(3):481–94.
- [24] Birch AD, Brown DR, Dodson MG, Thomas JR. The turbulent concentration field of a methane jet. *J Fluid Mech* 1978;88(3):431–49.
- [25] Molkov V, Makarov D, Bragin M. Physics and modelling of under-expanded jets and hydrogen dispersion in atmosphere. *Physics of extreme state of matter* 2009:143–5.
- [26] Molkov V, Shentsov V, Brennan S, Makarov D. Hydrogen non-premixed combustion in enclosure with one vent and sustained release: numerical experiments. *Int J Hydrogen Energy* 2014;39:10788–801.

新規な金属クラスターの発生法と触媒機能

豊田工業大学
本山 幸弘

Metal Clusters: Novel Generation Methods and Their Catalytic Performances

Yukihiro Motoyama
Toyota Technological Institute, Tempaku, Nagoya, 468-8511, Japan
motoyama@toyota-ti.ac.jp

During the present program, three types of facile and efficient methods for generation of palladium and platinum clusters are developed. First is the combination of commercially available palladium on carbon (Pd/C) with 1,1,3,3-tetramethyldisiloxane (TMDS). The present Pd/C–TMDS system provides tertiary amines by deoxygenative silane-reduction of carboxamides. Detailed mechanistic studies revealed that the catalytically active species is the soluble palladium clusters leached from the palladium particles on the carbon support. By adding some copper compounds to this system as a co-catalyst, partial reduction of carboxylic esters or lactones proceeds to afford the corresponding silyl acetals. Similarly, treatment of PdCl₂ with TMDS gives quite small size of Pd clusters, which act as an effective catalyst for the cleavage reaction of C–O bond of *O*-*t*-Bu moieties. The present catalytic reaction offers a practical method for the deprotection of *tert*-butyl esters, *tert*-butyl ethers, *O*-Boc, and *N*-Boc derivatives under mild conditions. Platinum clusters, generated by treatment of zero-valent Pt complexes with molecular hydrogen in the presence of activated carbon, are found to act as an efficient catalyst for arene hydrogenation of aromatic compounds. The reaction proceeds at ambient temperature under atmospheric hydrogen pressure to afford the corresponding cyclic compounds without contamination of metallic residue. In addition, novel preparation method for supported palladium clusters is developed. The simply deposited palladium complexes on ZrO₂ are easily converted to the Pd clusters under atmospheric hydrogen pressure having unique activity towards hydrogenation of imines but other carbonyl groups remaining intact. The present catalytic property offers a practical synthetic method of functionalized secondary amines by reductive *N*-alkylation of amines with aldehydes or ketones: the reaction proceeds at ambient temperature under atmospheric hydrogen pressure by using only stoichiometric amounts of both substrates.

1. はじめに

従来のモノ作りは、化学製品の生産から廃棄までの全工程において生態系に与える影響を最小限にしつつ、経済的効率性を向上させる環境政策である「グリーンサステナブルケミストリー」が重視されてきた。さらに資源枯渇問題を見据え、近年は稀少・規制元素の原料、代替、循環、規制

に加え、新機能に基づく持続可能な社会の実現を目指した日本初の科学技術戦略である「元素戦略」に力点が置かれている。工業的な有機合成化学においては、回収・再利用性に優れた担持型の金属触媒(不均一系)が広く用いられており、その触媒機能のさらなる向上が求められている。

炭素-炭素および炭素-ヘテロ元素間の多重結合の還元反応は、有機合成上重要な官能基変換反応である。特に医薬品の製造において炭素-ヘテロ元素間の水素化分解を含めると、全工程の約15%が還元反応に分類される。それゆえ、これらの工程をより安全で効率的に行うことができる反応の開発、そのためには高機能で回収・再利用が容易な触媒の創製が必須となっている。

これまでに当研究室では、表面微細構造が制御された炭素ナノ繊維(CNF)に担持したナノサイズの金属クラスター(M/CNF)を合成し、これらが芳香環やニトロ基の水素化反応において市販の活性炭担持触媒と比較して高活性かつ高い再利用性を示すことを報告している。¹ 本プロジェクトではこれまでの知見を基盤とし、水素およびその関連化合物として取扱いが容易なヒドロシランを還元剤に用いる官能基変換反応を効率的に実現しうる「高機能性金属触媒の創製」を行ってきた。

本講演では、上記の成果について簡単に報告する。

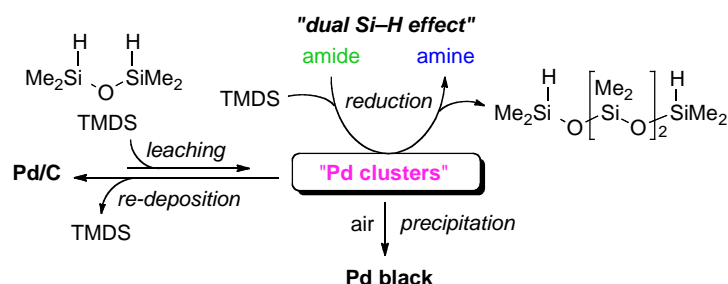
2. ヒドロシランによる Pd クラスターの発生と触媒反応

2-1. アミド化合物の脱酸素型還元反応²

一般にアミド化合物のアミンへの還元反応には広範にボラン化合物やアルミニウム反応剤が用いられているが、その禁水性ならびに発火性、さらには副生する還元剤残渣と生成物の分離における困難さから、特に大量スケールでの合成において改善が求められている。近年、安定で取扱いが容易なヒドロシランを還元剤として用いた触媒的反応が多数報告されているが、これらは均一系の錯体触媒を用いることが多く、担持型金属粒子を用いた反応例はほとんどない。しかしヒドロシランとして TMDS を用いると、担持型触媒でもアミド化合物の脱酸素型還元反応が進行することを見出した。驚くべきことに、水素化反応で高活性であった CNF 担持 Pd クラスターよりも、市販の活性炭担持パラジウム(Pd/C)の方が高い触媒活性を示した。一般に金属塩や金属錯体にヒドロシランを作用させるとコロイド状の金属種が生成する場合があることが知られている。³

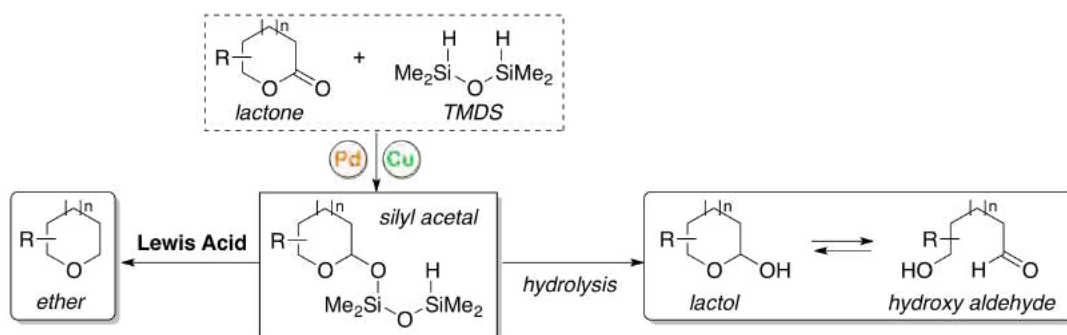
実際に本触媒系における反応溶液は Pd コロイドを示唆する黄茶色を呈していたことから、触媒活性種を含めた反応機構の解析を行った。まず、溶液中に存在する Pd 量を原子発光分析で測定したところ、

用いた Pd/C 上の 7-11% に相当する Pd が担体から溶出していることが明らかになった。さらに反応途中で Pd/C を除去しても反応が継続すること、この溶液に活性炭を添加すると溶液中の Pd 種のほぼすべてが活性炭上に担持されること、この Pd を含む活性炭はアミドに対し還元活性を示すことがわかった。これらの結果から、本 Pd/C-TMDS 系における触媒活性種は「可溶性の Pd クラスター」であり、反応系中に存在する活性炭に対して可逆的に再固定と溶液中への再溶出を繰り返すことが明らかになった。



2-2. 鎖状および環状エステルの部分還元⁴

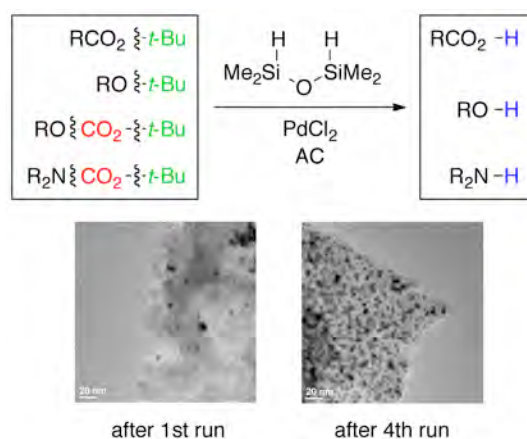
アミド化合物の脱酸素型還元にも有効であった Pd/C-TMDS 系は、エステル類の還元反応に触媒能を示さない。しかしながら、この反応系に銅化合物を触媒量添加すると、鎖状ならびに環状エステル(ラクトン)の部分還元反応が進行し、高い選択性で対応するシリルアセタール体が得られることを見出した。このシリルアセタール体は TMDS の一方の Si-H 基のみが反応した構造であり、加水分解により容易にラクトールやヒドロキシアルデヒドへと変換できる。さらにシリルアセタールに対しルイス酸を作用させることで、エステルの脱酸素型還元体であるエーテルが高選択的に得られることも見出した。なお、従来困難であった中員環から大員環のラクトンの変換においても、本触媒系は適用可能である。すなわち、同一の鎖状および環状エステルからシリルアセタールやアルデヒド、およびエーテルを高選択的に作り分ける手法を確立した。



2-3. *tert*-ブチル基の脱保護反応⁵

先の Pd/C-TMDS 系で *tert*-ブチルエステルの反応を行っていたところ、カルボン酸が生成していることに気がついた。これは反応系中で *tert*-ブトキシ基(*t*-BuO)の炭素-酸素結合を効率的に切断しうる触媒種が発生していることを示唆している。さらに反応溶液の ¹H NMR 測定下結果、系中ではシリルエステルとともにイソブテンが確認され、以前に 3 核ルテニウム錯体で報告した時と同様の機構で進行していることがわかった。⁶

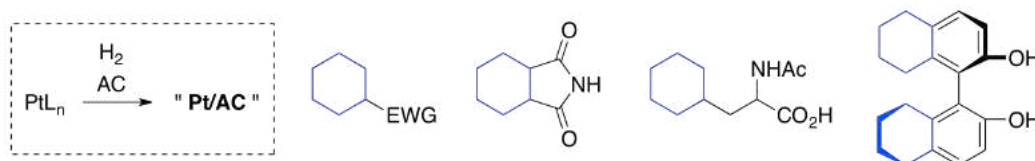
そこで反応条件を種々検討した結果、活性炭(AC)存在下、PdCl₂と TMDS を混合すると *tert*-ブチルエステル、*tert*-ブチルエーテル、*O*-Boc ならびに *N*-Boc 化合物の脱保護反応が穏和な条件下で進行し、対応するカルボン酸やアルコール、アミン体が収率良く得られた。さらに反応後の生成物中にはほとんど Pd 残渣は確認されず、Pd 種は活性炭上に存在しており、この Pd/AC は 3 回まで再利用可能である。反応後に回収した活性炭の TEM 画像から、触媒活性種は TEM で観測できない大きさのクラスターであることが示唆された。一般に Lewis 酸や Brønsted 酸を用いた酸性条件下で行われるこれらの脱保護反応が中性かつ 40 度程度で行えた要因は、この極微小なクラスターが有する特異な反応性によるものと考えられる。



3. 水素による金属クラスターの発生と触媒反応

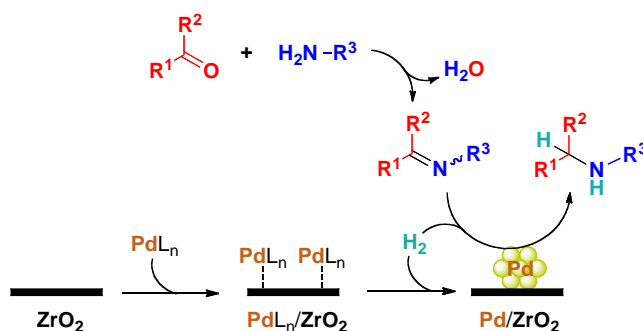
3-1. Pt クラスターによる芳香環の水素化反応⁷

これまでに我々は、CNF 担持 Ru および Rh ナノクラスターが芳香環の水素化に優れた触媒となることを報告している。¹ しかし Ru/CNF では 40 度以上、さらには 10 気圧以上の水素圧が必要であること、Rh/CNF は常温・常圧で活性を示すものを用いる溶媒や基質に大きな制限があった。ところが 0 価の白金錯体を用い、水素雰囲気下で炭素ナノ繊維に白金ナノクラスターを担持していたところ、配位子に含まれる芳香環部が常温・常圧下で環水素化されるが、担持された白金ナノクラスターの触媒活性はそれほど高くないことがわかった。これらの結果は、担持されたナノクラスターよりも高活性な触媒種が白金錯体から反応系中で発生していることを示唆している。そこで反応条件を種々検討した結果、同様に高活性な触媒種が安価な活性炭 (AC) 存在下でも発生することを見出した。この Pt-AC 系は常温・常圧下で様々な芳香環の水素化に有効であり、電子吸引基やアミノ基などを有する反応性の低い芳香族化合物や、多官能性化合物、さらには光学活性 BINOL などを、それぞれ対応する脂環式化合物へと穏和な条件下で変換できる。さらに Pt 種のほとんどは回収した AC 上に存在し、この回収した Pt/AC は再利用可能である。



3-2. Pd クラスターによるアミンの還元的 N-アルキル化反応⁸

活性炭は安価で高表面積を有し、かつ機械的強度や耐熱性、耐薬品性にも優れていることから、担持型金属種の担体として古くから用いられている。⁹ 材料と比較して表面や三次元立体構造、さらには電子構造が容易に制御可能なことから、近年になって炭素金属酸化物 (MO_x) が注目されている。そこで炭素材料と同様の手法でジルコニア (ZrO₂) 上への Pd 種の担持を行い、得られた Pd/ZrO₂ の基礎的な触媒活性を検討した。その結果、イミンの還元は速やかに進行するものの、一般に反応性が高いはずのアルデヒドやケトンに対しては水素化活性を示さないという、特異的な触媒活性を有していることを見出した。そこでこの特長を活かしてカルボニル化合物をアルキル化剤として用いるアミンの還元的 N-アルキル化を検討したところ、常温・常圧の水素雰囲気下、しかも等量のカルボニル化合物を用いるだけで、対応する 2 級アミンが高収率で得られることがわかった。本触媒系は反応開始時に誘導期があること、その間に Pd 担持 ZrO₂ の色が変わることから、反応系中で Pd 種が変化して活性種が発生していることが示唆された。実際、放射光を用いた構造・反応機構解析から、まず金属錯体が担体に吸着した後、水素雰囲気下で Pd クラスターを形成して反応が進行することが明らかとなった。



4. おわりに

以上のように、これまで先進触媒プロジェクトで行ってきた当研究室における研究の概略を紹介した。高活性な「金属クラスターの発生活」 という見方をすると、まず発生期の金属クラスターのトラップ法,そして固定化した金属錯体のクラスタリング法,という新規な2つの手法を開発した。二官能性のヒドロシランであるテトラメチルジシロキサン(TMDS)を用いた金属クラスターの発生および活性炭へのワンポット固定化においては、Pd以外にもRu, Rh, Pt等の金属種にも適用可能である。また、担体上でのクラスター発生についても、ZrO₂以外の金属酸化物や活性炭へと拡張できることも確認している。今後は担体や金属種の幅を広げて、様々な触媒反応への応用を行っていく予定である。

謝辞

本研究を進めるにあたり、炭素材料の提供とTEM解析を行って頂きました九州大学 先導物質化学研究所の尹 聖昊 教授と宮脇 仁 准教授、また、ZrO₂担持Pdの構造解析にご協力を頂きました九州大学大学院 理学研究院の徳永 信 教授と村山 美乃 准教授、および高輝度光科学研究センターの本間 徹生 博士に厚く御礼申し上げます。本研究の一部は文部科学省科学研究費、および公益財団法人 豊秋奨学会の助成の下で行なわれたものであり、ここに深く感謝いたします。

参考文献

- 1) a) Y. Moytoyama, S.-H. Yoon, H. Nagashima, *J. Synth. Org. Chem. Jpn.* **2009**, *67*, 724-734.
b) Y. Moytoyama, S. Hosokawa, *TANSO* **2015**, *266*, 35-40.
- 2) S. Hosokawa, K. Teramoto, Y. Motoyama, *ChemistrySelect* **2016**, *1*, 2594-2602.
- 3) L. N. Lewis, N. Lewis, *J. Am. Chem. Soc.* **1986**, *108*, 7228-7231.
- 4) S. Hosokawa, M. Toya, A. Noda, M. Morita, T. Ogawa, Y. Motoyama, *ChemistrySelect* **2018**, *3*, 2958-2961.
- 5) T. Ikeda, Z. Zhang, Y. Motoyama, *Adv. Synth. Catal.* **2019**, *361*, 673-677.
- 6) S. Hanada, A. Yuasa, H. Kuroiwa, Y. Motoyama, H. Nagashima, *Eur. J. Org. Chem.* **2010**, 1021-1025.
- 7) Manuscript in preparation.
- 8) Submitted for publication.
- 9) *Handbook of Heterogeneous Catalysis*, G. Ertl, H. Knözinger, J. Weitkamp, Eds., **1997**, VCH, Weinheim.

Specific Inhibition of the Hydrogenolysis of Benzylic C–O Bonds Using Palladium Nanoparticles Supported on Nitrogen-Doped Carbon Nanofibers

Yukihiro Motoyama,^{*[a]} Koshi Morii,^[a] Shoya Ishizuka,^[a] Sou Inomoto,^[b] Zhenzhong Zhang,^[a] and Seong-Ho Yoon^[c]

Palladium nanoparticles supported on 5%-nitrogen-doped, herringbone-type carbon nanofibers (Pd/N-CNF-H), which are prepared by thermally decomposing [Pd₂(dba)₃·CHCl₃] (dba = dibenzylideneacetone) in toluene in the presence of N-CNF-H, were found to be an efficient catalyst for the chemoselective hydrogenation of alkenyl and nitro moieties in benzyl-protected alcohols and carboxylic acid derivatives with high turnover frequencies: the hydrogenation reactions of these functional groups proceeded smoothly even at ambient temperature under atmospheric H₂ pressure, and the benzyl protecting groups in the molecules remained intact. Moreover, the recovered Pd/N-CNF-H catalyst could be reused without loss of its catalytic activity or chemoselectivity. The Pd/N-CNF-H catalyst also acted as an effective hydrogenation catalyst for the reduction of aromatic ketones to the corresponding benzyl alcohol derivatives with good to high product selectivity.

The benzyl moiety is widely used as a protecting group for the hydroxy, carboxyl, and amino functions in organic synthesis because of its stability under a variety of reaction conditions.^[1] These benzyl protecting groups are generally removed (deprotected) by commercially available palladium on carbon (Pd/C)-catalyzed hydrogenolysis under mild conditions.^[1] Therefore, much attention has recently been paid to the development of highly chemoselective hydrogenation methods with the use of heterogeneous Pd catalysts for the transformation of not only benzyl-protected organic molecules but also other multifunctionalized compounds.^[2] One solution for this subject is the chemical modification of Pd catalysts by using a catalyst poison. For example, Sajiki and Hirota reported the effectiveness of nitrogen-containing compounds as inhibitors of the

Pd/C-catalyzed hydrogenolysis of benzyl ethers.^[3] They also developed efficient catalyst systems, Pd-fibroin and Pd/C-SPh₂, for the chemoselective hydrogenation of functionalized organic molecules bearing benzyl ethers and esters.^[4,5] The product selectivity for the hydrogenation of the alkene moiety in the alkenyl benzyl esters and ethers over the Pd-fibroin or Pd/C-SPh₂ catalysts was quite high; however, the activities of these catalysts were not high enough at room temperature under ambient H₂ pressure: the turnover frequency (TOF) of these reactions was below 70 mol_{substrate} mol_{Pd}⁻¹ h⁻¹.^[4,5] In some cases, furthermore, the reactions required 3–10 atm pressure of H₂ (10 atm = 1.0 MPa).^[4]

The key to success in developing a novel chemoselective hydrogenation method with the use of heterogeneous catalysts is the choice of the catalyst support and the method used to prepare the metal nanoparticles. We previously reported that carbon nanofibers (CNFs)^[6] were good supports for the immobilization of metal nanoparticles with a narrow size distribution and that metal-supported CNFs (M/CNFs), which were prepared by pyrolysis of zero-valent organometallic complexes in the presence of CNFs, acted as efficient catalysts for some hydrogenation reactions.^[7] Recently, we also reported platinum and palladium nanoparticles supported on nitrogen-doped, herringbone-type CNFs^[8] (M/N-CNFs, M = Pt, Pd); the nitrogen atoms in CNF-H effectively acted as a catalyst poison, and the catalytic activity could be controlled by appropriate choice of the metal/nitrogen ratio, which led to the chemoselective and partial hydrogenation of nitroarenes and internal alkynes with high TOFs.^[9] We were interested in the application of Pd/N-CNF-H as a catalyst for hydrogenation without catalyzing the hydrogenolysis of benzylic carbon–oxygen (C–O) bonds.^[3–5,10] In this paper, we report the Pd/N-CNF-H-catalyzed selective hydrogenation of alkenes and nitroarenes without affecting the benzyl protecting groups present in the molecules.

The catalytic activity of Pd/N-CNF-H^[11] towards the hydrogenolysis of benzylic C–O bonds was compared with the that of commercially available Pd/C by using benzyl benzoate (**1a**) and benzyl phenyl ether (**1b**) as substrates. The reaction was performed by using **1a** or **1b** (0.5 mmol) and a Pd catalyst (substrate/catalyst molar ratio; S/C = 250) in toluene (1.5 mL) at 25 °C under a H₂ atmosphere (balloon). As shown in Figure 1, the 5% Pd/C-catalyzed hydrogenolysis of the benzylic C–O bond proceeded smoothly to afford corresponding carboxylic acid **2a** or alcohol **2b**; product **2a** was formed in 57.6% yield after 4 h, and the debenzilation reaction of **1a** was almost complete after 8 h (> 97% yield). In the case of the reaction of

[a] Prof. Dr. Y. Motoyama, K. Morii, S. Ishizuka, Dr. Z. Zhang
Department of Advanced Science and Technology
Toyota Technological Institute
Nagoya, Aichi 468-8511 (Japan)
E-mail: motoyama@toyota-ti.ac.jp

[b] S. Inomoto
Graduate School of Engineering Sciences
Kyushu University
Kasuga, Fukuoka 816-8580 (Japan)

[c] Prof. Dr. S.-H. Yoon
Institute for Materials Chemistry and Engineering
Kyushu University
Kasuga, Fukuoka 816-8580 (Japan)

Supporting Information for this article can be found under:
<https://doi.org/10.1002/cctc.201701326>.

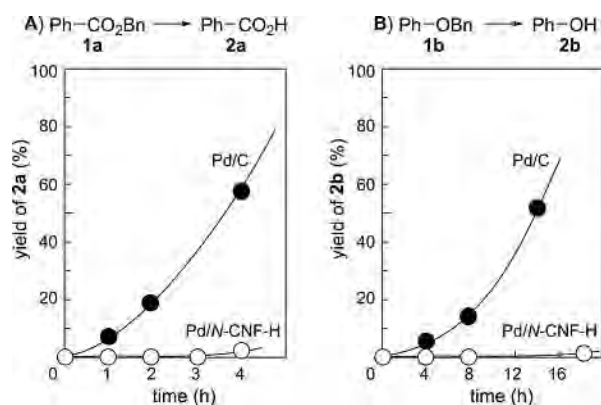


Figure 1. Plots of the products formed versus time in the hydrogenolysis over 5% Pd/C (●) and 2.5% Pd/N-CNF-H (○): A) reaction of benzyl benzoate (**1a**) and B) reaction of benzyl phenyl ether (**1b**).

1b, phenol (**2b**) was obtained in 51.7% yield after 14 h and in 81.6% after 24 h. In sharp contrast, treatment of **1a** with 2.5% Pd/N-CNF-H under these conditions gave only 2.8% of **2a** after 4 h. Similarly, 0.7% of **2b** was obtained after 8 h, and only 2.6% of **1b** was converted into **2b** after 24 h. Upon using normal CNF-H-immobilized Pd nanoparticles (3% Pd/CNF-H) as a catalyst, hydrogenolysis of the benzyl protecting group in **1b** proceeded to give the product in 2.2% yield after 8 h and in 5.3% yield after 24 h. These results clearly show that the catalytic activity of palladium nanoparticles on N-CNF-H towards cleavage of the benzylic C–O bond under a hydrogen atmosphere is eliminated effectively.

The use of Pd/N-CNF-H as a chemoselective hydrogenation catalyst was demonstrated by the reaction of benzyl esters and ethers containing other reducible functional groups. It is well known that benzyl esters are easily converted into the corresponding carboxylic acids under Pd-catalyzed hydrogenation conditions.^[1] Therefore, it is extremely difficult to achieve the selective transformation of other reducible functional groups in the presence of a benzyl-protected carboxylic acid under these conditions with the benzyl ester moiety remaining intact.^[4,5,10] So, we first investigated the Pd/N-CNF-H-catalyzed hydrogenation of alkenyl benzyl esters **3a–c**. The hydrogenation of a monosubstituted alkene, benzyl 10-undecenoate (**3a**), over 2.5% Pd/N-CNF-H (S/C=250) in ethyl acetate proceeded smoothly at 25 °C under a hydrogen atmosphere (balloon) to afford benzyl undecanoate (**6a**) in almost quantitative yield (97% yield of isolated compound after silica gel column chromatography) within 30 min: only a trace amount of undecanoic acid, which was formed by hydrogenation of the alkene moiety followed by hydrogenolysis of the benzyl protecting group, was detected by GC analysis, and the TOF of this reaction was 500 mol_{3a} mol_{Pd}⁻¹ h⁻¹ (Table 1, entry 1). It is well known that the reactivity of alkenes decreases in the order monosubstituted alkenes > 1,2-disubstituted alkenes > trisubstituted alkenes. For example, the hydrogenation of mono- and 1,2-disubstituted alkenes over the Pd-fibroin catalyst proceeded smoothly at room temperature under ambient H₂ pressure, but the reaction of trisubstituted (*E*)-benzyl tiglate, CH₃CH=C(CH₃)CO₂Bn, needed 5 atm pressure of H₂ to afford benzyl

Table 1. Selective hydrogenation of the alkenyl and nitro groups in benzyl esters **3a–d**, ethers **4a** and **4b**, and amide **5** by using Pd/N-CNF-H as a catalyst.^[a]

Entry	Substrate	Time [h]	Conversion [%] ^[b]	Selectivity [%] ^[b]
1		0.5	> 99	> 99 (97)
2		1	> 99	99 (99)
3 ^[c,d,e]		3	> 99	> 99
4		2	94	97
5 ^[f]		9	98	> 99 (91)
6		0.75	> 99	30
7 ^[e]		1.25	> 99	61
8 ^[c,d,e]		1.75	99	99 (96)
9 ^[c,d,e,f]		6	> 99	98
10		1	> 99	98
11 ^[c,d,e]		2	97	> 99 (91)
12		3	> 99	34
13 ^[e]		4	> 99	29
14 ^[c,d,e,f]		12	86	> 99
15 ^[c,d,e,f]		16	> 99	93 (91)
16		1	> 99	> 99

[a] Unless stated otherwise, all reactions were performed by using substrate (0.5 mmol) and 2.5% Pd/N-CNF-H (S/C=250–270) in ethyl acetate (1.5 mL) at 25 °C under a H₂ atmosphere (balloon). [b] Determined by analysis of the crude product by GC and ¹H NMR spectroscopy. The number in parentheses is the yield of the isolated product. [c] 1% Pd/N-CNF-H was used. [d] S/C=1000. [e] In toluene. [f] At 0 °C.

2-methylbutyrate, CH₃CH₂CH(CH₃)CO₂Bn, as the sole product in 77% yield after 18 h; the TOF of this reaction was approximately 18.^[3] In the Pd/N-CNF-H-catalyzed hydrogenation, however, 1,2-disubstituted alkene **3b** and trisubstituted alkene **3c** were smoothly converted into corresponding benzyl esters **6b** and **6c** in good yields with 97–99% selectivity within 1 or 2 h even under ambient pressure of H₂ (balloon); the TOFs of these reactions were 118 and 270, respectively (Table 1, entries 2 and 4). In these cases, hydrogenolytic cleavage of the benzylic C–O bond was inhibited by appropriate choice of the catalyst, solvent, and reaction temperature: the rate of the hydrogenolysis in protic and polar solvents, such as MeOH, THF, and ethyl acetate, is known to be faster than that in nonpolar solvents such as toluene.^[12] In addition, the catalytic activity of metal particles on N-CNF-H is highly dependent on the metal/nitrogen ratio.^[9] The hydrogenation of **3b** over 1% Pd/N-CNF-H in toluene gave **6b** in 99% yield with over 99% selectivity, and the TOF of this reaction was 333 (Table 1, entry 3). In the reaction of trisubstituted alkene **3c**, the reaction proceeded in ethyl acetate even at 0 °C, and product **6c** was obtained with over 99% selectivity (Table 1, entry 5). In the hydrogenation of benzyl ester **3d** bearing an aromatic nitro group over 2.5% Pd/N-CNF-H, however, the debenzilation reaction proceeded to give 4-aminobenzoic acid in yields of 70 and 39%, respectively (Table 1, entries 6 and 7). In this case, desired benzyl 4-aminobenzoate (**6d**) was obtained in high yield by using 1% Pd/N-CNF-H in toluene (Table 1, entries 8 and 9). The hydrogenation of the alkenyl group in benzyl ether derivative **4a** over 1% Pd/N-CNF-H (S/C=1000) in toluene at ambient

temperature for 2 h gave benzyl 3-phenylpropyl ether (**7a**) in high yield with over 99% selectivity: the calculated TOF of this reaction was 485 (Table 1, entry 11). Similar to the reaction of **3d**, some amount of a debenzylated product was formed in the reaction of 4-benzoyloxynitrobenzene (**4b**), but corresponding aniline derivative **7b** was obtained with 93% selectivity by using 1% Pd/N-CNF-H in toluene at 0 °C (Table 1, entries 12–15). In addition, hydrogenolytic cleavage of the benzylic N–O bond did not proceed under these conditions: the 2.5% Pd/N-CNF-H-catalyzed hydrogenation of *N*-benzylcinnamamide (**5**) in ethyl acetate afforded *N*-benzyl-3-phenylpropanamide (**8**) as the sole product in quantitative yield (Table 1, entry 16).

In developing a heterogeneous catalyst system, the reusability of the catalyst is important. Therefore, we next examined the durability of Pd/N-CNF-H in the present hydrogenation reaction. After the reaction of benzyl cinnamate (**3b**) in ethyl acetate under a H₂ atmosphere (balloon), as described in Table 1, entry 2 (S/C=250, 25 °C, 1 h), the 2.5% Pd/N-CNF-H catalyst was recovered by decantation and subjected to another catalytic run. As shown in Table 2, the recovered 2.5% Pd/N-CNF-H catalyst proved to be useful for five successive catalyst-recycling experiments: benzyl dihydrocinnamate (**6b**) was obtained in quantitative yields with high selectivities (97–99%). Microwave plasma-atomic emission spectroscopy (MP-AES) analysis of the crude product showed the existence of trace amounts of palladium species (288 ng, 2.40 ppm); the calculated catalyst leaching was 0.127% of the charged palladium (227 μg).

The above-described results clearly demonstrate that Pd/N-CNF-H is an efficient and recyclable catalyst for the chemoselective hydrogenation of alkenyl and nitro groups in various benzyl esters and ethers and an amide. Another application of Pd/N-CNF-H as a hydrogenation catalyst is the selective conversion of aromatic ketones into the corresponding secondary alcohols. Catalytic hydrogenation of ketones over heterogeneous catalysts is a simple method for the production of secondary alcohols.^[13] However, the application of conventional Pd/C systems to the hydrogenation of aromatic ketones is problematic, because hydrogenolytic cleavage of the benzylic C–O bond of the obtained alcohols often accompanies the hydrogenation reaction, resulting in the formation of the corresponding methylene compounds as the final products.^[14] For example, the hydrogenation of acetophenone (**9a**) over 5% Pd/C (S/C=270) in ethyl acetate at 25 °C for 5 h (99% conversion) gave 1-phenylethyl alcohol (**10a**) in 38% yield along with the formation of the hydrogenolysis product, ethylbenzene (**11a**), in 61% yield. In sharp contrast, the 2.5% Pd/N-CNF-H-catalyzed hydrogenation of **9a** under the same reaction conditions afforded desired alcohol **10a** with 98% selectivity (Table 3, entry 1). Comparing with the hydrogenation of alkenes and nitroarenes bearing benzyloxy groups, as shown in Table 1, the product selectivity decreased to 90% by using toluene as a solvent in the present reaction (Table 3, entry 2). In the

Table 2. Recycling experiments for the reaction of benzyl cinnamate (**3b**).^[a]

Run	Conversion [%] ^[b]	Selectivity to 6b [%] ^[b]
1	> 99	99
2	> 99	99
3	> 99	97
4	> 99	99
5	> 99	99

[a] All reactions were performed by using **3b** (0.5 mmol) and 2.5% Pd/N-CNF-H (S/C=250) in ethyl acetate (1.5 mL) at 25 °C for 1 h under a H₂ atmosphere (balloon). [b] Determined by analysis of the crude product by GC and ¹H NMR spectroscopy.

hydrogenation over 1% Pd/N-CNF-H, the product selectivity was high (99%), but the reaction was very slow (41% conversion after 10 h) (Table 3, entry 3). The reactivities of sterically hindered ketones **9b** and **9c**, which have β-naphthyl and isopropyl substituents on the carbonyl moiety, were lower than the reactivity of phenyl methyl ketone (**9a**), although application of a slightly higher temperature (40 °C) and/or the use of an increased amount of the catalyst (S/C=50–100) resulted in satisfactory yields within 2–3 h with selectivities of 98 and 99% (Table 3, entries 4 and 5). Similarly, the hydrogenation of keto ester **9d** over 2.5% Pd/N-CNF-H (S/C=100) at ambient temperature for 2 h gave methyl 2-hydroxy-2-phenylacetate (**10d**) in quantitative yield with 99% selectivity (Table 3, entry 6).

Table 3. Hydrogenation of aromatic ketones **9a–e** over Pd/N-CNF-H.^[a]

Entry	Substrate	Time [h]	Product	Conv. [%] ^[b]	Selectivity [%] ^[b,c]
1		5		> 99	98
2 ^[d]		24		> 99	90
3 ^[e]		10		41	99
4 ^[f]		2		> 99	98
5 ^[g]		3		> 99	99
6 ^[g]		2		> 99	99
7		11		97	96

[a] Unless stated otherwise, all reactions were performed by using substrate and 2.5% Pd/N-CNF-H (S/C=270) in ethyl acetate (1 mL) at 25 °C under a H₂ atmosphere (balloon). [b] Determined by analysis of the crude product by GC and ¹H NMR spectroscopy. [c] Product selectivity (**10/11**). [d] In toluene. [e] 1% Pd/N-CNF-H was used. [f] S/C=50 at 40 °C. [g] S/C=100.

Relative to alcohols derived from aryl alkyl ketones, alcohols derived from diaryl ketones are well known to be easily converted into the corresponding alkanes by hydrogenolytic cleavage of the C–O bond. Although the hydrogenation of diphenylketone (**9e**) over 2.5% Pd/N-CNF-H afforded a small amount of diphenylmethane after 11 h (97% conversion), desired diphenylmethanol (**10e**) was obtained with 96% selectivity (Table 3, entry 7).

In summary, we developed a new hydrogenation procedure for benzyl esters and ethers that contain other reducible functional groups such as alkenyl and nitro moieties. The Pd/N-CNF-H-catalyzed hydrogenation reactions proceeded smoothly at ambient temperature under atmospheric H₂ pressure with high turnover frequencies, and moreover, the benzyl protecting groups in the molecules remained intact. The present catalyst system was also effective for the hydrogenation of aromatic ketones by minimizing the hydrogenolysis of the benzylic C–O bond of the formed benzyl alcohol derivatives. We believe that the use of Pd/N-CNF-H as a hydrogenation catalyst provides a unique and practical protocol in organic synthesis. We are now investigating the use of N-CNF-H as an effective support to prepare other chemoselective hydrogenation catalysts.

Experimental Section

Hydrogenation of **3a** (Table 1, entry 1)

The hydrogenation was performed in a two-necked, 20 mL, round-bottomed flask equipped with a stopcock and containing **3a** (137.2 mg, 0.5 mmol), ethyl acetate (1.5 mL), and 2.5% Pd/N-CNF-H [S/C = 250 (mol_{3a}:mol_{pd}⁻¹)] at 25 °C under a H₂ atmosphere (balloon). After stirring for 30 min, the insoluble catalyst was removed by filtration, and the filtrate was concentrated under reduced pressure to give the crude material. The conversion of the substrate and the product selectivity were determined by using capillary GC and/or ¹H NMR spectroscopy analysis of the crude material. Product **6a** was isolated by column chromatography (silica gel, *n*-hexane/ether = 10:1) in 97% yield (134.1 mg).

Recycling Experiments (Table 2)

After the hydrogenation of benzyl cinnamate (**3b**) for 1 h, the catalyst was separated by decantation, and the supernatant was removed by using a membrane filter (DISMIC-13HP) under a nitrogen atmosphere. The 2.5% Pd/N-CNF-H recovered catalyst was washed with ethyl acetate (3 × 2 mL). After drying under reduced pressure, the catalyst was subjected to another hydrogenation run of **3b**.

Acknowledgements

Part of this work was supported by the Japan Society for the Promotion of Science through a Grants-in-Aid for Scientific Research (26390031) and the Ministry of Education, Culture, Sports, Science and Technology, Japan through the Strategic Research Foundation at Private Universities (S1511022). We are grateful to Prof. Hideo Nagashima (Kyusyu University) for helpful discussions. Help with the synthesis and characterization of N-CNF by Dr.

Jin Miyawaki and Mr. Kazunari Teshima (Kyushu University) is also acknowledged.

Conflict of interest

The authors declare no conflict of interest.

Keywords: heterogeneous catalysis · hydrogenation · hydrogenolysis · nanoparticles · palladium

- [1] P. G. M. Wuts, T. W. Green in *Protective Groups in Organic Synthesis*, 4th ed., Wiley, Hoboken, 2007, pp. 102–120; P. G. M. Wuts, T. W. Green in *Protective Groups in Organic Synthesis*, 4th ed., Wiley, Hoboken, 2007, pp. 396–402; P. G. M. Wuts, T. W. Green in *Protective Groups in Organic Synthesis*, 4th ed., Wiley, Hoboken, 2007, pp. 598–602; P. G. M. Wuts, T. W. Green in *Protective Groups in Organic Synthesis*, 4th ed., Wiley, Hoboken, 2007, pp. 814–818.
- [2] Review: a) Y. Monguchi, T. Ichikawa, H. Sajiki, *Chem. Pharm. Bull.* 2017, 65, 2–9. Recent representative papers: b) R. Singuru, K. Dhanalaxmi, S. C. Shit, B. M. Reddy, J. Mondal, *ChemCatChem* 2017, 9, 2550–2564; c) Z.-C. Ding, C.-Y. Li, J.-J. Chen, J.-H. Zeng, H.-T. Tang, Y.-J. Ding, Z.-P. Zhang, *Adv. Synth. Catal.* 2017, 359, 2280–2287; d) C. Zhang, Y. Leng, P. Jiang, J. Li, S. Du, *ChemistrySelect* 2017, 2, 5469–5474.
- [3] a) H. Sajiki, H. Kuno, K. Hirota, *Tetrahedron Lett.* 1998, 39, 7127–7130; b) H. Sajiki, K. Hirota, *Tetrahedron* 1998, 54, 13981–13996; c) H. Sajiki, K. Hattori, K. Hirota, *J. Org. Chem.* 1998, 63, 7990–7992. Pd/C-ethylenediamine catalyst, Pd/C(en), shows high chemo-selectivity in the hydrogenation of aromatic ketones to the corresponding benzyl alcohols: d) K. Hattori, H. Sajiki, K. Hirota, *Tetrahedron* 2001, 57, 4817–4824.
- [4] Pd-Fibroin catalyst: a) H. Sajiki, T. Ikawa, K. Hirota, *Tetrahedron Lett.* 2003, 44, 8437–8439; b) T. Ikawa, H. Sajiki, K. Hirota, *Tetrahedron* 2005, 61, 2217–2231.
- [5] Pd/C-SPh₂ catalyst: A. Mori, Y. Miyakawa, E. Ohashi, T. Haga, T. Maegawa, H. Sajiki, *Org. Lett.* 2006, 8, 3279–3280.
- [6] CNFs are classified into three types, where graphite layers are either perpendicular (platelet: CNF-P), parallel (tubular: CNF-T), or stacked obliquely (herringbone: CNF-H); see: a) H. Murayama, T. Maeda, *Nature* 1990, 345, 791–793; b) N. M. Rodriguez, *J. Mater. Res.* 1993, 8, 3233–3250; c) A. Tanaka, S.-H. Yoon, I. Mochida, *Carbon* 2004, 42, 591–597; d) A. Tanaka, S.-H. Yoon, I. Mochida, *Carbon* 2004, 42, 1291–1298.
- [7] a) M. Takasaki, Y. Motoyama, K. Higashi, S.-H. Yoon, I. Mochida, H. Nagashima, *Chem. Asian J.* 2007, 2, 1524–1533; b) M. Takasaki, Y. Motoyama, S.-H. Yoon, I. Mochida, H. Nagashima, *J. Org. Chem.* 2007, 72, 10291–10293; c) M. Takasaki, Y. Motoyama, K. Higashi, S.-H. Yoon, I. Mochida, H. Nagashima, *Org. Lett.* 2008, 10, 1601–1604; d) Y. Motoyama, M. Takasaki, S.-H. Yoon, I. Mochida, H. Nagashima, *Org. Lett.* 2009, 11, 5042–5045; e) Y. Motoyama, M. Taguchi, N. Desmira, S.-H. Yoon, I. Mochida, H. Nagashima, *Chem. Asian J.* 2014, 9, 71–74.
- [8] N-CNF-H was synthesized by chemical vapor deposition over MgO-supported Ni-Fe catalyst using acetonitrile and hydrogen at 530 °C. Elemental analysis of the N-CNF-H revealed the amount of nitrogen incorporated into the N-CNF-H to be ca. 5 wt%, and two N 1s peaks mainly appeared at binding energies of 398.6 (pyridinic units) and 400.1 eV (pyrrolic units) in the XPS spectrum of N-CNF-H with the area ratio of ca. 2:1, see: S. Lim, S.-H. Yoon, I. Mochida, D.-H. Jung, *Langmuir* 2009, 25, 8268–8273.
- [9] a) Y. Motoyama, Y. Lee, K. Tsuji, S.-H. Yoon, I. Mochida, H. Nagashima, *ChemCatChem* 2011, 3, 1578–1581; b) Y. Lee, Y. Motoyama, K. Tsuji, S.-H. Yoon, I. Mochida, H. Nagashima, *ChemCatChem* 2012, 4, 789–781.
- [10] Other representative papers for the Pd-catalyzed chemo-selective hydrogenation of alkenes in the presence of benzyloxy groups: a) J. Le Bras, D. K. Mukherjee, S. González, M. Tristany, B. Ganchev, M. Moreno-Mañas, R. Pleixats, F. Hénin, J. Muzart, *New J. Chem.* 2004, 28, 1550–1553; b) N. A. Soom, T. Thiemann, *Int. J. Org. Chem.* 2016, 6, 1–11.
- [11] 1%- and 2.5% Pd/N-CNF-Hs were synthesized by the method reported previously. Actual Pd amounts were 0.9–1.0 wt% for 1% Pd/N-CNF-H

(average diameter; d_{av} = 3.7 nm), and 2.4–2.6 wt% for 2.5% Pd/N-CNF-H (d_{av} = 3.6 nm), respectively. From the Pd 3d region of the XPS spectrum, the intensive doublet attributed to metallic Pd appears near 336 (Pd 3d_{5/2}) and 341 eV (Pd 3d_{3/2}). The shoulder region observed at 343–345 eV can be assigned to the Pd^{II} chemical state; Pd⁰/Pd^{II} = ca. 3:1, see Supporting Information.

- [12] A. P. G. Kieboom, F. van Rantwijk, *Hydrogenation and Hydrogenolysis in Synthetic Organic Chemistry*, Springer, Amsterdam, **1977**.
- [13] a) P. N. Rylander, *The Catalytic Hydrogenation in Organic Syntheses*, Academic Press, New York, **1979**, pp. 82–112; b) S. Nishimura, *Handbook of*

Heterogeneous Catalytic Hydrogenation for Organic Synthesis, Wiley, New York, **2001**, pp. 170–225.

- [14] S. Nishimura, *Handbook of Heterogeneous Catalytic Hydrogenation for Organic Synthesis*, Wiley, New York, **2001**, pp. 572–663.

Manuscript received: August 13, 2017

Revised manuscript received: August 30, 2017

Accepted manuscript online: September 4, 2017

Version of record online: December 12, 2017

Catalysis

Palladium on Carbon-Catalyzed Silane-Reduction of Tertiary Carboxamides: Soluble Palladium Colloids are an Active Catalyst Species

Satomi Hosokawa, Kazusue Teramoto, and Yukihiro Motoyama^{*[a]}

The combination of commercially available palladium on carbon (Pd/C) with 1,1,3,3-tetramethyldisiloxane (TMDS) was found to be an effective catalyst system for the production of tertiary amines by deoxygenative silane-reduction of carboxamides. Facile removal of both the metallic species and silane residues can be achieved by simple extraction, and the recovered Pd/C was reusable. Other palladium complexes and salts, Pd₂(dba)₃(CHCl₃) [dba = dibenzylideneacetone], Pd(OAc)₂, and

PdCl₂, were also effective for the reduction of tertiary carboxamides with TMDS. Detailed mechanistic studies of the present Pd/C–TMDS system revealed that the catalytically active species is the soluble palladium colloids leached from the palladium particles on the carbon support by treating with TMDS, and carboxamides, amine products, and TMDS act as a stabilizer for the generated palladium species in solution.

Introduction

In the metal-catalyzed organic transformations, easy separation of the metallic species from the product and reuse of the catalysts have been recently recognized as problems to be solved from an environmental point of view. The use of heterogeneous catalysts, e.g. immobilized molecular catalysts or metal particles on the solid supports, is a solution to these problems, and effective methods for attaching metal species to a variety of organic or inorganic materials have been actively investigated.^[1]

The deoxygenative reduction of carboxamides to amines is an important synthetic protocol in organic chemistry.^[2] Currently, there are many reports of catalytic silane-reduction processes using transition metal compounds as a catalyst or catalyst precursor because most hydrosilanes are stable and safe reducing reagents. In addition, the catalytic silane-reduction of carboxamides often proceeds under milder conditions with higher chemoselectivity in comparison to the conventional reactions using aluminohydrides and borohydrides.^[2,3] The above catalytic methods using metal salts or complexes are thus useful for the production of amines, and in some cases, facile isolation of the product from the reaction mixture can be achieved by the use of polymethylhydrosiloxanes (PMHS) as a reducing reagent.^[4] However, the available protocols for the silane-reduction of carboxamides using reusable catalysts are far fewer.

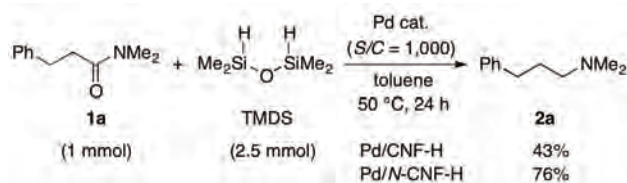
We previously reported that the carbon nanofibers (CNFs) are good supports for the immobilization of nano-sized metal

particles with a narrow size distribution by thermally decomposing the zero-valent organometallic complexes.^[5] CNFs are classified into three types, where graphite layers are either perpendicular (platelet, CNF-P), parallel (tubular, CNF-T), or stacked obliquely (herringbone, CNF-H) to the fiber axis.^[6] Comparing with the commercially available metal on carbon (M/C) catalysts, these carbon nanofiber-supported metal nanoparticles (M/CNFs; M = Ru, Rh, Ir, Pd, Pt) show efficient catalytic performances towards the hydrogenation of arenes to alicyclic compounds^[5a-c,e] and nitroarenes to aniline derivatives.^[5d,f] It is important that neither sintering nor leaching of metal nanoparticles on CNFs is observed after the hydrogenation reaction; this results in possible reuse of M/CNFs as a heterogeneous catalyst without loss of the catalytic activity. We recently synthesized the palladium- and platinum nanoparticles supported on the 5%-nitrogen-doped, herringbone-type CNF (M/N-CNF-H, M = Pd, Pt); the nitrogen atoms in the honeycomb lattice effectively act as a catalyst poison leading to decreasing the catalytic activity. Furthermore, the catalytic activity towards hydrogenation reactions can be controlled by an appropriate choice of the metal/nitrogen ratio leading to the chemoselective and partial hydrogenation of nitroarenes and internal alkynes.^[7] We also found that both the Pd/CNF-H and Pd/N-CNF-H catalyzed the deoxygenative silane-reduction of *N,N*-dimethyl-3-phenylpropanamide (**1a**) using 1,1,3,3-tetramethyldisiloxane (TMDS) as a reducing reagent. Surprisingly however, the catalytic activity of Pd/N-CNF-H towards silane-reduction of carboxamides was higher than that of the parent Pd/CNF-H: the reactions using the palladium catalyst (substrate/catalyst molar ratio, S/C = 1,000) in toluene at 50 °C for 24 h afforded *N,N*-dimethyl-3-phenylpropylamine (**2a**) in 43% for Pd/CNF-H and 76% for Pd/N-CNF-H, respectively (Scheme 1).

During the course of our continuous studies on the carbon-supported metal nanoparticles as a catalyst for silane-reduction of carboxamides, commercially available palladium on carbon

[a] Dr. S. Hosokawa, K. Teramoto, Prof. Dr. Y. Motoyama
Department of Advanced Science and Technology
Toyota Technological Institute
Nagoya, Aichi 468-8511, Japan
E-mail: motoyama@toyota-ti.ac.jp

Supporting information for this article is available on the WWW under <http://dx.doi.org/10.1002/slct.201600552>



Scheme 1. M/CNFs-catalyzed reduction of **1a** with TMDS.

(Pd/C) was found to be more effective catalyst for the silane-reduction than the CNF- and N-CNF-supported Pd nanoparticles. Herein, we wish to report on the novel catalytic system for the silane-reduction of tertiary carboxamides, using commercially available, heterogeneous Pd/C^[8–10] and TMDS.^[11] We also describe the detailed mechanistic studies of the present system including catalytically active species.

Results and Discussion

1. Silane-Reduction of Carboxamides. 1-1. Silane-Reduction of *N,N*-Dimethyl-3-phenylpropanamide (1a**).** For preliminary screening, the reduction of **1a** was investigated using various hydrosilanes (*Si*-H = 5 equivalents to **1a**) in the presence of Pd/C catalyst (substrate/catalyst molar ratio, *S/C* = 100) in toluene. Although no reaction took place using alkyl- or alkoxysilanes such as PhMe₂SiH, Me_n(EtO)_{3-n}SiH (*n* = 0–2), or polymethylhydrosiloxane (PMHS) as a reducing reagent, the reaction with 1,1,3,3,3-pentamethyldisiloxane proceeded at 50 °C to afford **2a** in 29% for 6 h and 99% for 24 h (Table 1, Entry 1). While using TMDS as a hydrosilane, the reaction of **1a** proceeded smoothly; the desired amine **2a** was obtained in 95–99% yields at 25 °C for 24 h and in almost quantitative yield at 50 °C within 6 h (Entries 2 and 3). Next, several commercially available metal on carbon catalysts (M/C; M = Rh, Ru, and Pt) and solvents were examined for their catalytic performances in the reduction of **1a** using TMDS. Comparing with the Pd/C catalyst, the catalytic activity of the other catalysts was lower: the yields of **2a** after 24 h were 35% for Rh/C and 57% for Ru/C, respectively (Entries 4 and 5). When the reaction was carried out using Pt/C as a catalyst, the substrate **1a** was completely consumed at 50 °C for 24 h but 6% of aldenamine, PhCH₂CH=CHNMe₂, was formed as a by-product *via* reductive dehydration (Entry 6).^[12] The amounts of TMDS used was also investigated in the Pd/C–TMDS system and found that the addition of 2.5 equivalents of TMDS (5 equivalents of *Si*-H group) to **1a** resulted in satisfactory yield; for examples, the chemical yields of **2a** after 6 h were 64% (2 equivalents of TMDS) and 45% (1.5 equivalents of TMDS), and those after 24 h were 70% (2 equivalents of TMDS) and 56% (1.5 equivalents of TMDS), respectively (Entry 3 vs. Entries 7 and 8). The rate of the reaction and product-selectivity in ethereal solvents such as 1,4-dioxane, dimethoxyethane (DME), and tetrahydrofuran (THF) were similar to those in toluene (Entry 3 vs. Entries 9–11), but small amount of side-product, formed by ring opening oligomerization of THF used as a solvent, was observed in the ¹H NMR

Table 1. Selected results of the reaction of **1a** and TMDS with various transition metal catalysts.^[a]

Entry	Catalyst	Solvent	Time [h]	Yield [%] ^[b]
1 ^[c]	Pd/C	toluene	6	29 (99) ^[d]
2 ^[e]	Pd/C	toluene	24	95–99
3	Pd/C	toluene	6	99
4	Rh/C	toluene	24	35
5	Ru/C	toluene	24	57
6	Pt/C	toluene	24	94 ^[f]
7 ^[g]	Pd/C	toluene	6	64 (70) ^[d]
8 ^[h]	Pd/C	toluene	6	45 (56) ^[d]
9	Pd/C	1,4-dioxane	6	97
10	Pd/C	DME	6	95
11	Pd/C	THF	6	94 ^[i]
12	Pd/C	hexane	6	91
13	Pd/C	AcOEt	6	80
14	Pd ₂ (dba) ₃ (CHCl ₃)	toluene	6	99
15	Pd(OAc) ₂	toluene	6	99
16	PdCl ₂	toluene	6	99

[a] All reactions were carried out with **1a** (1 mmol), TMDS (2.5 mmol), and catalyst (1 mol%; *S/C* = 100) in solvent (2 mL) at 50 °C. [b] Determined by ¹H NMR spectroscopy. [c] 5 mmol of 1,1,3,3,3-pentamethyldisiloxane was used. [d] The yield in parentheses was the yield after 24 h. [e] At 25 °C. [f] 6% of aldenamine was formed. [g] 2 mmol of TMDS was used. [h] 1.5 mmol of TMDS was used. [i] Oligomerization of THF was observed by ¹H NMR spectroscopy.

spectrum (Entry 11).^[13] Hexane and ethyl acetate (AcOEt) were also useful but the rate of the reduction in these solvents was slightly slow; 91% for hexane and 80% yields for AcOEt, respectively (Entries 12 and 13). As shown in Entries 14–16, other palladium complexes and salts such as Pd₂(dba)₃(CHCl₃) [dba = dibenzylideneacetone], Pd(OAc)₂, and PdCl₂ also catalyzed the silane-reduction of carboxamides using TMDS as a reducing reagent (details see Tables S3 in Supporting Information); the amide **1a** was completely converted to the amine **2a** in toluene at 50 °C within 6 h by using 1 mol% (*S/C* = 100) of the Pd species. It is worth noting that the addition order of TMDS and the carboxamide was a significant factor governing the catalytic activity in the present reaction using Pd₂(dba)₃(CHCl₃), Pd(OAc)₂, and PdCl₂; the reaction on adding TMDS to the mixture of the Pd species and the carboxamide **1a** proceeded smoothly at 50 °C, however, only trace amount of amine **2a** was obtained in the reaction by addition of **1a** to a mixture of Pd species and TMDS. While in the Pd/C-catalyzed reaction, the rate of the reaction was not affected by the addition order of the hydrosilane and the carboxamide. The details of these phenomena will be discussed later.

1-2. Silane-Reduction of Other Carboxamides using Pd/C.

To investigate the scope of the present catalyst system, a variety of carboxamides **1a–p** were subjected to the reduction using 5%-Pd/C (*S/C* = 50–100) and TMDS (2.5 equivalents to **1**) in toluene at 50–70 °C for 24 h, and the products formed were isolated by silica gel column chromatography (Table 2). As shown

Table 2. Reduction of various carboxamides by the Pd/C–TMDS system.^[a]

Entry	Amide	Product	Yield [%] ^[b]
1 ^[c]			98
2 ^[d]			98
3 ^[d,e]			95
4 ^[d,e]			85
5 ^[d,e]			< 5 ^[f]
6 ^[d]			83
7			97
8			94
9 ^[e]			92
10 ^[d,e]			81
11 ^[d,e]			73
12 ^[g]			99
13 ^[h]			92 ^[i]
14 ^[h]			99 ^[i]
15			0 ^[f]
16			0 ^[f]

[a] All reactions were carried out with **1** (1 mmol), TMDS (2.5 mmol), and Pd/C (*S/C* = 100) at 50 °C for 24 h. [b] Isolated yield by silica gel column chromatography. [c] For 6 h. [d] *S/C* = 50. [e] At 70 °C. [f] Determined by ¹H NMR spectroscopy. [g] 4 mmol of TMDS was used. [h] 5 mmol of TMDS was used. [i] Isolated yield by recrystallization.

in Entries 1–9, the silane-reduction of aliphatic tertiary carboxamides **1a–i** proceeded successively, affording their corresponding tertiary amines in good to high yields, except in the case of *N,N*-dimethyl-2,2-diphenylacetamide (**1e**). α -Aryl- or α,α -disubstituted acetamides are sometimes converted to the corresponding aldenamines *via* reductive dehydration under hydrosilylation conditions, because of their thermodynamic stability of alkenyl moiety formed.^[12] However, the reaction of *N,N*-dimethyl- α -phenylacetamide (**1c**) gave the desired amine **2c** as a sole product in 95% yield (Entry 3). Although α,α -disubstituted cyclohexanecarboxamide **1d** was also converted to the corresponding amine **2d** at 70 °C in the presence of 2 mol% (*S/C* = 50) of Pd/C, the reaction of acetamide **1e** having bulky two phenyl groups at the α -position gave the product below 5% yield (Entries 4 vs. 5). Reaction of 6- and 7-membered ring lactams **1g** and **1h** proceeded smoothly to afford

the corresponding cyclic amines **2g** and **2h** in 97% and 94% yields, respectively (Entries 7 and 8). While in the case of the less-reactive γ -lactam **1f**, the reaction using an increased amount of the Pd/C catalyst (*S/C* = 50) at 70 °C for 24 h gave **2f** in good yield (Entries 6–8). However, the reductions of non-protected lactams (secondary amides) did not proceed by the present catalyst system. In the reaction of amido ester **1i**, the amido group was selectively reduced to the amino moiety with ester group present in the molecule remaining intact (Entry 9). Comparing to the aliphatic carboxamides, the reactivity of aromatic ones were lower and some amounts of the starting materials remained under these conditions: the amines **2j** and **2k** were obtained in 81% and 73% yields, and the carboxamides **1j** and **1k** were recovered in 15% and 25% yields, respectively (Entries 10 and 11). When the reactions of *N,N*-dimethyl-4-bromo- and 4-nitrobenzamides (**1l** and **1m**), no reduction of amido moiety occurred even by using large excess amounts of TMDS (4–5 equivalents to **1**): **1l** was converted to the *N,N*-dimethylbenzamide (**1j**) quantitatively by the reduction of a Br atom on the benzene ring (reductive cleavage of the aromatic C–Br bond), and 4-aminobenzamide **4** was obtained in 92% yield by the NO₂-reduction of nitrobenzamide **1m**^[14] (Entries 12 and 13). It is well known that there are two reaction pathways in the hydride-reduction of α,β -unsaturated carbonyl compounds: one is the [1,2]-reduction and the other is the [1,4]-reduction (Michael addition). Attempted the reaction of *N,N*-dimethylcinnamamide (**1n**) gave *N,N*-dimethyldihydrocinnamamide (**1a**), as a sole compound in almost quantitative yield after usual workup, even by using 5 equivalent of TMDS to **1n**. This result indicated that the product formed in the reaction mixture is an *N,O*-ketene acetal derivative, PhCH₂CH=C(OSi)NMe₂, *via* [1,4]-hydride addition to **1n** and this *O*-silylated compound is stable under the reaction conditions (Entry 14).^[15] We also examined the reduction of secondary- and primary carboxamides such as *N*-methyl-3-phenylpropanamide (**1o**) and 3-phenylpropanamide (**1p**) by the present Pd/C–TMDS system. However, only hydrogen gas evolution was observed and the starting carboxamides were recovered almost quantitative yields; the dehydrogenative silylation of N–H moiety in the amido group proceeded to afford the corresponding silyl amides, PhCH₂CH₂C(=O)N(Me)Si and PhCH₂CH₂C(=O)NSi₂, or silyl imidates, PhCH₂CH₂(SiO)C=NMe and PhCH₂CH₂(SiO)C=NSi^[16] and starting carboxamides **1o** and **1p** were regenerated and then recovered quantitatively by hydrolysis of these silyl amides or silyl imidates during the workup process (Entries 15 and 16).^[17]

1-3. Catalyst Recycling in the Reaction using Pd/C. When developing a practical catalytic system using heterogeneous catalysts, it is important for the recyclability of the catalyst, determination of the metal leaching into the product, and scalability of the catalytic reaction. Therefore, we first investigated the durability of the commercially available Pd/C catalyst. After the reaction of **1a** as described in Table 2, Entry 1 (*S/C* = 100, 50 °C, 6 h), the Pd/C catalyst was recovered by decantation for 1 h under nitrogen atmosphere and subjected to the further catalytic runs (details see, Supporting Information). The catalytic activity of the recovered Pd/C gradually decreased: chemical yields of **2a** obtained in these experiments were > 99% (1st

run), 98% (2nd run), and 82% (3rd run), respectively (Table 3, left column). Microwave plasma-atomic emission spectrometer

Run	Yield [%] ^[b]	
	For 6 h	For 24 h
1st	> 99	> 99
2nd	98	> 99
3rd	82	> 99
4th	–	99 ^[c]

[a] All reactions were carried out with **1a** (1 mmol), TMDS (2.5 mmol), and Pd/C catalyst (1 mol%; *S/C* = 100) in toluene (2 mL) at 50 °C. [b] Determined by ¹H NMR spectroscopy. [c] Small amount of **1a** was observed.

(MP-AES) analysis of the supernatant including the product and siloxane waste, which was obtained by decantation for removing Pd/C followed by filtration through a pad of Celite, showed the existence of the Pd species; the calculated metal leaching was 0.8% of the Pd/C catalyst used in the first run. While extension of the reaction time from 6 h to 24 h, the catalyst recovery/reuse cycle was successfully repeated four times in almost quantitative yields (Table 3, right column). From the MP-AES analysis, palladium-leaching from the carbon support to the supernatant obtained in each cycle was found below the detection limit. The calculated palladium amount in the crude product contained was below 1.6 µg: this corresponds to <0.15% of the Pd species used. The details of the palladium leaching during the reaction will be discussed later.

1-4. Scale-up Reactions. It also allowed a decrease of the catalyst loading to 0.1–0.2 mol% (*S/C* = 500–1,000) without affecting the efficiency for the reaction of **1a**. For example, amine **2a** was obtained in 98% yield (820 mg) after purification by silica gel column chromatography by using 906 mg of **1a** (5.14 mmol) and only 10.6 mg of 5%-Pd/C catalyst ([Pd] = 530 µg): the turnover number (TON) of the reaction reached 980 [mol (product)/mol (Pd)]. The Pd content in the crude product obtained by filtration through a pad of Celite was also shown below the detection limit (<1.2 ppm) (Table 4, Entry 2). In addition,

Entry	<i>S/C</i>	1a [mmol]	Time [h]	Yield of 2a [%]
1	500	5.01	6	99 (0.81 g) ^[b]
2	1,000	5.14	24	98 (0.82 g) ^[b]
3	500	10.01	6	98 (1.61 g) ^[c]
4	1,000	9.74	24	89 (1.42 g) ^[c]

[a] All reactions were carried out with TMDS (2.5 equivalents to **1a**) in toluene at 50 °C. [b] Isolated yield by silica gel column chromatography. [c] Isolated yield by a workup process using conc. HCl and aqueous NaOH solution.

tion, the present procedure was adaptable to a gram-scale reaction (Entries 3 and 4). For example, the reaction of 1.77 g (10.01 mmol) of **1a** and 4.42 mL of TMDS (25.0 mmol) in the

presence of Pd/C catalyst (42.3 mg, *S/C* = 500) afforded 1.61 g (9.80 mmol, 98% yield) of pure **2a** without silica gel column purification: after separation of the Pd/C catalyst by filtration, the siloxane waste in the filtrate could be removed from the amine **2a** by a workup process using conc. HCl and aqueous NaOH solution through the corresponding water-soluble ammonium salts of **2a**, Ph(CH₂)₃NMe₂•HCl, formed. NMR analysis of **2a** thus obtained showed no contamination of the siloxane wastes, and no Pd species was detected by MP-AES analysis.

2. Mechanistic Studies. 2-1. Reaction using Palladium Salts or Complexes. In some hydrosilylation reactions, it is well known that the metal colloids are formed from the transition metal salts or complexes with hydrosilanes during the course of an induction period.^[18] Therefore, we first investigated the actual catalytic species of the present silane-reduction by using palladium salts and complexes. When TMDS was added to the mixture of **1a** and 1 mol% of Pd(OAc)₂, the color of the initial orange solution (Figure 1, A) gradually became dark brown

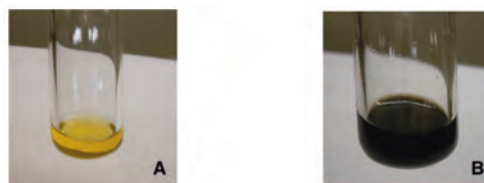
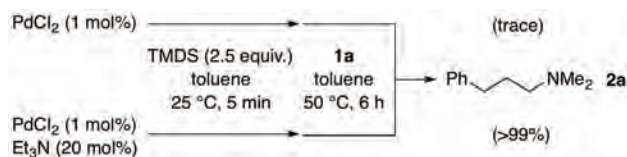


Figure 1. Photos of the reaction using Pd(OAc)₂. A: Before adding TMDS; B: During the reaction.

(Figure 1, B). After it was stirred at 50 °C for 6 h, the carboxamide **1a** was completely consumed to afford the amine **2a** in 99% yield along with the formation of palladium residues as black precipitates.

As described above, the addition order of TMDS and the carboxamide **1a** was crucial for the present catalytic system using PdCl₂, Pd(OAc)₂, and Pd₂(dba)₃(CHCl₃). For example, addition of TMDS (2.5 equivalent to **1a**) to the yellow suspension of PdCl₂ (1 mol%) in toluene resulted in evolution of small amounts of hydrogen gas and formation of the black precipitates immediately. Then the carboxamide **1a** was added to this suspension thus obtained and the resultant mixture was stirred at 50 °C, however, only trace amount of the amine product **2a** formed. When adding TMDS to a mixture of PdCl₂ (1 mol%) and a catalytic amount of triethylamine (Et₃N, 20 mol%) at 25 °C, small amounts of gas evolution was observed and the color of the solution turned to dark brown instantly. After addition of **1a** to this solution and stirring the resultant mixture at 50 °C, the silane-reduction proceeded smoothly to afford the amine **2a** in almost quantitative yield within 6 h (Scheme 2). It is also well known that the color of the colloidal Pd species is brown-yellow to dark brown.^[19] These results imply that the colloidal palladium species is generated by treatment of TMDS with Pd(OAc)₂ or PdCl₂, and amines, Et₃N and presumably **2a** formed, act as a stabilizer for preventing the agglomeration of unstable and highly reactive palladium colloids in solution.



Scheme 2. PdCl₂-catalyzed reduction of **1a** with TMDS.

2-2. Reaction using Pd/C. In contrast to the reaction using palladium salts and complexes as a catalyst precursor, there is no effect of the addition order of TMDS and the carboxamide on the catalytic activity in the Pd/C-catalyzed reaction. For example, adding TMDS to the suspension of Pd/C in toluene followed by the addition of carboxamide **1a** afforded the amine **2a** in over 99% yield within 6 h. Therefore, we examined the generation of colloidal palladium species in the reaction of **1a** and TMDS (2.5 equivalents to **1a**) in the presence of 5%-Pd/C (S/C = 100) as shown in Scheme 4. After the reaction at 50 °C for 30 min, the solid Pd/C was removed by filtration with membrane filters (Durapore HV, 0.45 μm) to afford the clear, brown-yellow solution (Figure 2, C), in which contained silane residue,

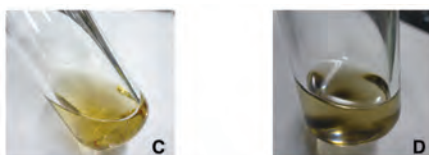
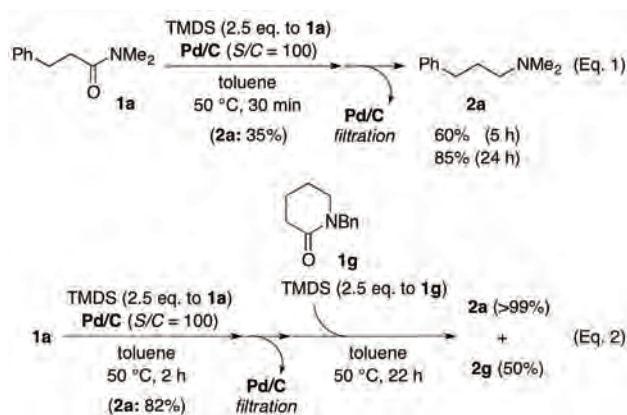


Figure 2. Photos of the reaction mixtures in Scheme 4. C: After removal of the Pd/C by filtration in Eq 1; D: After exposure of the resultant mixture to air at 25 °C for 5 min in Eq 2.

unreacted TMDS, 35% of **2a** formed, and 65% of **1a** remained. The filtrate thus obtained was continuously stirred at 50 °C resulting in the further formation of **2a**: total yields of **2a** were 60% for 5 h and 85% for 24 h, respectively (Scheme 3, Eq. 1).



Scheme 3. Pd/C-catalyzed reduction after removal of the solid Pd/C.

Furthermore, there was no black precipitate and the color of the solution was still brown-yellow after the reaction. Similarly, the Pd/C charged was filtered out after stirring at 50 °C for 2 h then another carboxamide **1g** and TMDS (2.5 equivalents to **1g**) were added to the filtrate including 82% of **2a** and 18% of **1a**. After the resultant mixture was stirred at 50 °C for further 22 h, the amide **1a** charged firstly was completely converted to the amine **2a** (over 99% yield), and the reduction of *N*-benzylpiperidone (**1g**) added after removing Pd/C catalyst proceeded smoothly to afford the corresponding amine **2g** in 50% yield (Scheme 3, Eq. 2). These results clearly showed that some palladium atoms were leached out from the support into the solution under the reaction conditions,^[20] and the dissolved palladium species acts as an active catalyst for the present Pd/C-TMDS system. It is worth noting that the colloidal palladium species (brown-yellow solution) formed under the reaction conditions is stable under inert atmosphere at 25 °C for a few days, but small amount of black precipitates was instantly formed by exposure of the reaction mixture to air (Figure 2, D).

2-3. Palladium Leaching during the Reaction using Pd/C. For calculating the value of palladium leaching from the Pd/C used during the present reaction system, we first checked the exact palladium amount on the commercially available 5%-Pd/C used, and MP-AES analysis revealed that 4.4–4.5 wt% of palladium is loaded. It means that 937–959 μg of palladium is charged in the standard reactions as shown in Table 2 (1 mmol scale of reaction using 21.3 mg of Pd/C). Next, we investigated the amounts of palladium species in the solution obtained by the Pd/C-catalyzed reaction of **1a** with TMDS (2.5 equivalent to **1a**) as shown in Table 2, Entry 1. All determinations of the palladium concentration in the solution at each time of the reaction were performed by MP-AES analysis after filtration of the Pd/C from the reaction mixture with membrane filters (Durapore HV, 0.45 μm).^[21] These results and the reaction profile were shown in Figure 3 (details see Table S4 in Supporting Information). The

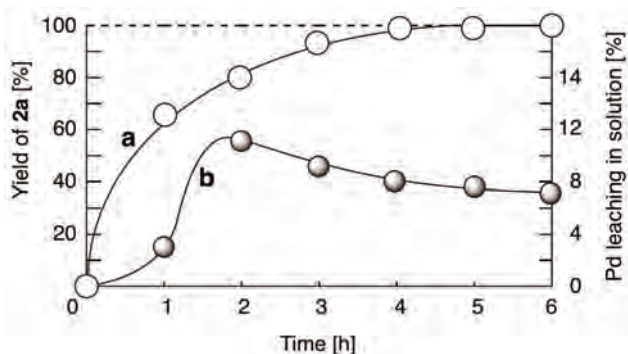
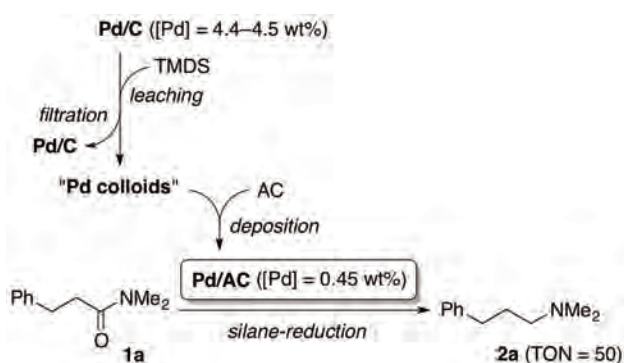


Figure 3. Kinetic investigations of catalytic activity and palladium leaching: (a) the plots of formed **2a** [%] versus time [h] (○); (b) the plots of palladium leaching [%] versus time [h] (●).

palladium content in solution was the highest after stirring the mixture at 50 °C for 2 h (104.4 μg) and the calculated palladium leaching from Pd/C charged was about 11%. Then the palla-

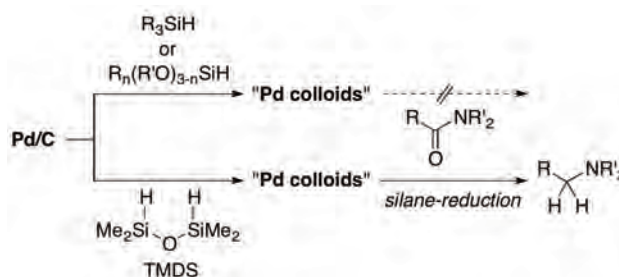
dium amount in solution gradually decreased but 67.7 μg (7.1–7.2% leaching) of palladium was still observed in solution when the reaction was just finished (after 6 h). We also investigated the temperature effect on the palladium leaching from Pd/C. Generation of the palladium colloids from the Pd/C and TMDS was also occurred even at ambient temperature (25 $^{\circ}\text{C}$) in the presence of carboxamide **1a**, or in the absence of carboxamides and/or amines at 50 $^{\circ}\text{C}$. However, the value of palladium leaching from the Pd/C charged was only 1.20–1.23% (11.5 μg) after the reaction at 25 $^{\circ}\text{C}$ for 6 h, and 0.60–0.61% (5.7 μg) after treatment of Pd/C with TMDS at 50 $^{\circ}\text{C}$ for 2 h.

In the Pd/C-catalyzed Heck reactions of haloarenes, it is well known that the palladium colloids are generated from the Pd/C and the soluble palladium species formed act as a catalyst.^[20] In these cases, the quantity of catalytically active palladium colloids in solution decreased when the reaction was completed.^[19d] While in the present Pd/C-catalyzed silane-reduction of carboxamides with TMDS, ca. 7% of palladium colloids were still existed in solution after the reaction completed (Figure 3). As described above, the palladium colloids in solution containing the product amine and TMDS were stable under inert atmosphere, but the palladium content in the reaction mixture in the presence of Pd/C was gradually decreased from 68 μg (after 6 h) to 17 μg (after 24 h) (see Table S4 in Supporting Information). These results suggested that palladium colloids once formed are anchored to the carbon surface of the Pd/C used. Indeed, the treatment of the brown-yellow solution, in which palladium quantity was ca. 104 μg (see Table S4 in Supporting Information), with 20 mg of palladium-free activated carbon (AC) at 50 $^{\circ}\text{C}$ followed by removal of the carbon materials afforded the clear, colorless solution. From MP-AES analysis, the concentration of the palladium species in the filtrate thus obtained was under the detection limit. Furthermore, 109 μg of palladium species was loaded on the recovered AC. These results clearly showed that almost all the dissolved palladium species redeposit on the carbon support. It is worth noting that the palladium on activated carbon thus obtained (Pd/AC) also acts as a catalyst precursor for the silane-reduction of carboxamide with TMDS (Scheme 4).



Scheme 4. Palladium leaching from and deposition onto carbon support.

2-4. Effects of Hydrosilanes. First of all, the use of TMDS, $\text{HSiMe}_2\text{OSiMe}_2\text{H}$, is crucial for the present palladium-catalyzed silane-reduction of tertiary carboxamides; no reaction proceeded by using other hydrosilanes such as alkyl- or alkoxy-silanes (details see Tables S2 and S3 in Supporting Information). In addition, the colloidal palladium species, leached from Pd/C in the presence of TMDS, is an actual catalytic species. Therefore, we also investigated the generation of soluble palladium species from Pd/C by treatment of other hydrosilanes, and found that small amount of palladium species is formed in the reaction mixture. For examples, the palladium contents in brown-yellow solutions, which were obtained by filtration after the reaction of **1a** with PhMe_2SiH or $\text{Me}(\text{EtO})_2\text{SiH}$ (5 equivalents to **1a**) in the presence of Pd/C ($[\text{Pd}] = 937\text{--}959 \mu\text{g}$) at 50 $^{\circ}\text{C}$ for 2 h, were 6.6 μg for PhMe_2SiH and 13.3 μg for $(\text{EtO})_2\text{MeSiH}$, respectively: calculated palladium leachings from Pd/C used were ca. 0.7% for PhMe_2SiH and 1.4% for $(\text{EtO})_2\text{MeSiH}$, respectively. However, there was no product in the solution and the starting amide **1a** was recovered in quantitative yield. These results clearly showed that the palladium colloids are generated by the reaction of Pd/C with a variety of hydrosilanes, but TMDS containing two proximate Si–H groups in the molecule is crucial for the deoxygenative reduction of carboxamides (Scheme 5).



Scheme 5. Active vs. inactive hydrosilanes in the silane-reduction using Pd/C.

In the present catalyst system, 2.5 equivalent (5 equivalents Si–H) of TMDS to the tertiary carboxamides is necessary for complete conversion to the corresponding amines. In the reactions using below 2.5 equivalents of TMDS, the reduction of carboxamide stopped within 24 h but 0.3 equivalent of TMDS still remained in the reaction mixture (Table 5, Entries 2 and 3). From the ^1H NMR spectra of the crude materials obtained in Table 5, Entries 1–3, there were mainly two hydrosilane compounds observed: one is the remaining TMDS [δ 0.18 (d, $J = 2.7$ Hz, 12H), 4.68 (sep, $J = 2.7$ Hz, 2H)], and the other is a symmetrical structure. Newly formed compound, which could be isolated by silica gel chromatography, was $\text{HMe}_2\text{Si}(\text{OSiMe}_2)_2\text{-OSiMe}_2\text{H}$ [^1H NMR: δ 0.08 (s, 12H), 0.196 (d, $J = 2.9$ Hz, 12H), 4.71 (sep, $J = 2.9$ Hz, 2H); ^{13}C NMR: δ 0.78, 1.12; IR $\nu_{\text{Si-H}}$ 2128 cm^{-1}].^[22,23] These results clearly showed that the only one of the Si–H group in TMDS reacts with the carboxamide and the other one remains intact. Similar “dual Si–H effects” were reported in some silane-reduction of carbonyl compounds: the use of bi-

Entry	Yield [%] ^[b]	TMDS [mmol]		
		Charged	Consumed ^[b]	Remained ^[b]
1	>99 (6 h)	2.5	2.2 (2.0) ^[c]	0.3
2	70 (24 h)	2.0	1.7 (1.4) ^[c]	0.3
3	56 (24 h)	1.5	1.2 (1.1) ^[c]	0.3

[a] All reactions were carried out with **1a** (1 mmol), TMDS, and Pd/C (S/C = 100) in toluene at 50 °C. [b] Determined by ¹H NMR spectroscopy. [c] The amount in parentheses was the calculated value from the yield of **2a** formed.

functional hydrosilanes having dual, closely located Si-H groups accelerates the silane-reduction of carbonyl compounds such as ketones and carboxamides.^[24]

2-5. Minimization of Palladium Leaching into the Product. As described above, the palladium content in the solution obtained in Table 2, Entry 1 was 68 µg (7.1–7.2% leaching from the Pd/C used), and these palladium colloids were readily converted to the insoluble black precipitates by exposure of the reaction mixture to air at ambient temperature (Figure 4, E).

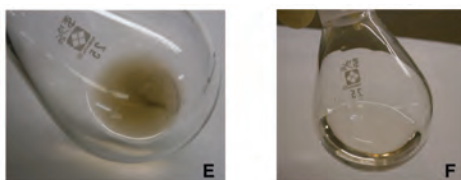
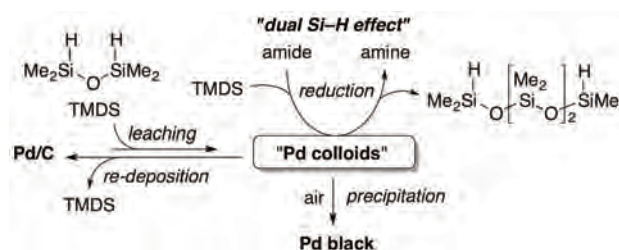


Figure 4. Photos of the crude materials. **E:** After filtration followed by exposure to air; **F:** After quenching with MeOH followed by filtration.

The separation of black precipitates thus formed by filtration enabled removal of the palladium residues from the crude material: only 7.2 µg of palladium (0.75–0.77% leaching from the Pd/C used) was detected in the filtrate after the reaction. These results were in good agreement with the recycling experiments as shown in Table 3, left column: the yields of **2a** in the recycling experiments gradually decreased, but calculated metal leaching in the crude material obtained after filtration was only 0.8%. While after stirring the reaction mixture for 24 h, which were the same conditions as shown in Table 3, right column, the palladium content in solution was reduced to 17 µg (ca. 1.8% leaching from the Pd/C used). As shown in Table 5, Entry 1, 0.3 equivalent of TMDS was still existed in the reaction mixture after the reaction. Therefore, we investigated the effect of the remaining TMDS on the quantity of the palladium colloids in solution, and the minimization of the palladium leaching into the crude material was achieved by treatment of the reaction mixture with MeOH. When adding excess amounts of MeOH (250 µL) to the mixture including the product amine, TMDS and Pd/C, hydrogen gas evolution was observed and TMDS was completely consumed by palladium-catalyzed dehydrogenative silylation of MeOH. The filtrate thus obtained

was clear solution (Figure 4, F) and MP-AES analysis revealed that the content of the palladium species in this filtrate was only 4.4 µg.

2-6. Possible Reaction Mechanism. A possible reaction mechanism of the present palladium on carbon (Pd/C)-catalyzed reduction of carboxamides with TMDS is shown in Scheme 6. The solid Pd/C is treated with hydrosilanes to gen-



Scheme 6. Possible reaction mechanism.

erate brown-yellow palladium colloids, which act as a catalyst for the deoxygenative reduction of carboxamides to afford the corresponding amines only by using TMDS as a hydrosilane ("dual Si-H effect"). TMDS is a bi-functional hydrosilane having two proximate Si-H groups in the molecule, and one Si-H group is consumed through the deoxygenative reduction of carboxamides but the other one remains intact. Finally, amine products and HMe₂Si-(OSiMe₂)₂-OSiMe₂H are formed. The palladium colloids formed in solution are stabilized with the product amine, carboxamide, and TMDS, and such colloidal species are stable under inert atmosphere for a few days. While in the presence of the activated carbon, the palladium colloids re-deposit gradually on the carbon support. In addition, the palladium species in solution is instantly turned into black precipitates by exposure to air, and the resultant palladium residues are easily separable by filtration.

Conclusions

A novel activity of heterogeneous palladium on carbon (Pd/C) catalyst for the deoxygenative silane-reduction of carboxamides to the corresponding amines is demonstrated. The combination of Pd/C and 1,1,3,3-tetramethyldisiloxane (TMDS) effectively catalyzes the reaction of tertiary carboxamides under mild conditions. It is of practical importance that commercially available Pd/C and inexpensive TMDS can be used, and the present system is tolerant of a variety of solvents used. In addition, the present procedure can be scaled up to a gram-quantity reaction and the product amine is obtained in good to high yields without contamination of both the siloxane wastes and palladium species by simple filtration followed by extraction. Detailed mechanistic studies revealed that the palladium colloids are the catalytically active species, and the reversible transfer of palladium species between solvent and the carbon support is occurred in the presence of hydrosilanes.

Details of experimental procedures, spectral data for all the synthesized compounds and the copies of NMR spectra and other supporting experimental data can be found in the Supporting Information.

Acknowledgements

A part of this work was supported by a Grants-in-Aid for Scientific Research (C) (26390031) from Japan Society for the Promotion of Science, and for the Strategic Research Foundation at Private Universities (S1511022) from Ministry of Education, Culture, Sports, Science and Technology, Japan.

Keywords: Amides · heterogeneous catalysis · hydrosilylation · palladium · reduction

- [1] a) *Catalyst Supports and Supported Catalysts* (Ed.: A. B. Stiles), Butterworths, Boston, **1987**; b) *Handbook of Heterogeneous Catalysis* (Eds.: G. Ertl, H. Knözinger, J. Weitkamp), VCH, Weinheim, **1997**; c) J. A. Grady, *Pure Appl. Chem.* **2001**, *73*, 1319-1324; d) D. L. Feldheim, C. A. Foss, Jr., *Metal Nanoparticles: Synthesis, Characterization, and Application*, Marcel Dekker, New York, **2002**; e) C. A. McNamara, M. J. Dixon, M. Bradley, *Chem. Rev.* **2002**, *102*, 3275-3300; f) D. J. Cole-Hamilton, *Science* **2003**, *299*, 1702-1706; g) P. McMorn, G. J. Hutchings, *Chem. Soc. Rev.* **2004**, *33*, 108-122; h) *Catalyst Separation, Recovery and Recycling* (Eds.: D. J. Cole-Hamilton, R. Tooze), *Catalysis by Metal Complexes Book Series*, No. 30, Springer, The Netherlands, **2006**; i) *Nanoparticles: From Theory to Application* (Ed.: G. Schmid), Wiley-VCH, Weinheim, **2010**.
- [2] Reviews: a) J. Seyden-Penne, *Reductions by the Alumino- and Borohydrides in Organic Synthesis, 2nd Ed.*, Wiley-VCH, Canada, **1997**; b) D. Addis, S. Das, K. Junge, M. Beller, *Angew. Chem. Int. Ed.* **2011**, *50*, 6004-6011; c) H. Nagashima, *Synlett* **2015**, *26*, 866-890.
- [3] Representative papers: Rh catalyst: a) R. Kuwano, M. Takahashi, Y. Ito, *Tetrahedron Lett.* **1998**, *39*, 1017-1020; Ru catalyst: b) Y. Motoyama, C. Itonaga, T. Ishida, M. Takasaki, H. Nagashima, *Org. Synth.* **2005**, *82*, 188-195; c) S. Hanada, T. Ishida, Y. Motoyama, H. Nagashima, *J. Org. Chem.* **2007**, *72*, 7551-7559; d) J. T. Reeves, Z. Tan, M. A. Marsini, Z. S. Han, Y. Xu, D. C. Reeves, H. Lee, B. Z. Lu, C. H. Senanayake, *Adv. Synth. Catal.* **2013**, *355*, 47-52; Pt catalyst: e) S. Hanada, E. Tsutsumi, Y. Motoyama, H. Nagashima, *J. Am. Chem. Soc.* **2009**, *131*, 15032-15040; Fe catalysts: f) S. Zhou, K. Junge, D. Addis, S. Das, M. Beller, *Angew. Chem. Int. Ed.* **2009**, *48*, 9507-9510; g) Y. Sunada, H. Kawakami, T. Imaoka, Y. Motoyama, H. Nagashima, *Angew. Chem. Int. Ed.* **2009**, *48*, 9511-9514; h) S. Das, B. Wendt, K. Möller, K. Junge, M. Beller, *Angew. Chem. Int. Ed.* **2012**, *51*, 1662-1666; Zn catalyst: i) S. Das, D. Addis, S. Zhou, K. Junge, M. Beller, *J. Am. Chem. Soc.* **2010**, *132*, 1770-1771; j) O. O. Kovalenko, A. Volkov, H. Adolffson, *Org. Lett.* **2015**, *17*, 446-449; Ir catalyst: k) S. Park, M. Brookhart, *J. Am. Chem. Soc.* **2012**, *134*, 640-653; l) C. Cheng, M. Brookhart, *J. Am. Chem. Soc.* **2012**, *134*, 11304-11307; Cu catalyst: m) S. Das, B. Join, K. Junge, M. Beller, *Chem. Commun.* **2012**, *48*, 2683-2685; Co catalyst: n) T. Dombay, C. Helleu, C. Darcel, J.-B. Sortais, *Adv. Synth. Catal.* **2013**, *355*, 3358-3362.
- [4] a) Y. Motoyama, K. Mitsui, T. Ishida, H. Nagashima, *J. Am. Chem. Soc.* **2005**, *127*, 13150-13151; b) S. Hanada, Y. Motoyama, H. Nagashima, *Tetrahedron Lett.* **2006**, *47*, 6173-6177. Also see Refs 3c, 3e, 3g.
- [5] a) Y. Motoyama, M. Takasaki, K. Higashi, S.-H. Yoon, I. Mochida, H. Nagashima, *Chem. Lett.* **2006**, *35*, 876-877; b) M. Takasaki, Y. Motoyama, K. Higashi, S.-H. Yoon, I. Mochida, H. Nagashima, *Chem. Asian J.* **2007**, *2*, 1524-1533; c) M. Takasaki, Y. Motoyama, S.-H. Yoon, I. Mochida, H. Nagashima, *J. Org. Chem.* **2007**, *72*, 10291-10293; d) M. Takasaki, Y. Motoyama, K. Higashi, S.-H. Yoon, I. Mochida, H. Nagashima, *Org. Lett.* **2008**, *10*, 1601-1604; e) Y. Motoyama, M. Takasaki, S.-H. Yoon, I. Mochida, H. Nagashima, *Org. Lett.* **2009**, *11*, 5042-5045; f) Y. Motoyama, M. Taguchi, N. Desmira, S.-H. Yoon, I. Mochida, H. Nagashima, *Chem. Asian J.* **2014**, *9*, 71-74.
- [6] a) H. Murayama, T. Maeda, *Nature* **1990**, *345*, 791-793; b) N. M. Rodriguez, *J. Mater. Res.* **1993**, *8*, 3233-3250; c) A. Tanaka, S.-H. Yoon, I. Mochida, *Carbon* **2004**, *42*, 591-597; d) A. Tanaka, S.-H. Yoon, I. Mochida, *Carbon* **2004**, *42*, 1291-1298; e) S. Lim, S.-H. Yoon, I. Mochida, D.-H. Jung, *Langmuir* **2009**, *25*, 8268-8273.
- [7] a) Y. Motoyama, Y. Lee, K. Tsuji, S.-H. Yoon, I. Mochida, H. Nagashima, *ChemCatChem* **2011**, *3*, 1578-1581; b) Y. Lee, Y. Motoyama, K. Tsuji, S.-H. Yoon, I. Mochida, H. Nagashima, *ChemCatChem* **2012**, *4*, 778-781.
- [8] Reviews: a) P. N. Rylander, *Hydrogenation Methods*, Academic Press, New York, **1985**; b) S. Siegel in *Comprehensive Organic Synthesis, Vol. 8* (Eds.: B. M. Trost, I. Fleming), Pergamon Press, Oxford, **1991**, pp. 417-442; c) M. Hudlicky, *Reductions in Organic Chemistry*, ACS, Washington DC, **1996**; d) S. Nishimura, *Handbook of Heterogeneous Catalytic Hydrogenation for Organic Synthesis*, Wiley, New York, **2001**.
- [9] It is reported that Pd/C-Et₃SiH systems catalyze the hydrosilylation and transfer hydrogenation, see: reduction of S-ethylthioesters: a) L. Leping, S.-C. Lin, T. Fukuyama, *J. Am. Chem. Soc.* **1990**, *112*, 7050-7051; b) H. Tokuyama, T. Fukuyama, *Aldrichim. Acta* **2004**, *37*, 87-96; c) T. H. Graham, W. Liu, D.-M. Shen, *Org. Lett.* **2011**, *13*, 6232-6235; [1,4]-reduction of enones and enals: d) S. Tuokko, P. M. Pihko, *Org. Process Res. Dev.* **2014**, *18*, 1740-1751; reduction of multiple bonds, nitro groups, azides, and deprotection of allyl- and benzyl groups: e) P. K. Mandal, J. S. McMurray, *J. Org. Chem.* **2007**, *72*, 6599-6601.
- [10] Very recently, Verho, Bäckvall and Adolffson reported the mild deoxygenation of benzylic ketones and aldehydes by Pd/C-polymethylhydrosiloxane (PMHS) system, see: A. Volkov, K. P. J. Gustafson, C.-W. Tai, O. Verho, J.-E. Bäckvall, H. Adolffson, *Angew. Chem. Int. Ed.* **2015**, *54*, 5122-5126.
- [11] We also examined the reactions of other carbonyl compounds by Pd/C-TMDS system and found that benzaldehyde and acetophenone were smoothly converted to the corresponding alcohols at 50 °C for 24 h, but no reaction proceeds even at 80 °C using esters and an imine as a substrate. Details about these reactions and results of the reactions of other functional groups were listed in Table S1 in the supporting information.
- [12] Reports for the formation of aldenamines from tertiary carboxamides under hydrosilylation conditions, see: a) R. J. P. Corriu, J. J. E. Moreau, M. Pataud-Sat, *J. Organomet. Chem.* **1982**, *228*, 301-308; b) S. Bower, K. A. Kreuzter, S. L. Buchwald, *Angew. Chem. Int. Ed. Engl.* **1996**, *35*, 1515-1516; c) Y. Motoyama, M. Aoki, N. Takaoka, R. Aoto, H. Nagashima, *Chem. Commun.* **2009**, 1574-1576; d) A. Volkov, F. Tinnis, H. Adolffson, *Org. Lett.* **2014**, *16*, 680-683. Also see Refs. 3c and 3e.
- [13] Selected papers for the ring-opening polymerization of cyclic ethers under hydrosilylation conditions see: a) A. J. Chalk, *J. Chem. Soc. D* **1970**, 847-848; b) J. V. Crivello, M. Fan, *J. Polym. Sci. A: Polym. Chem.* **1991**, *29*, 1853-1863; c) J. V. Crivello, M. Fan, *J. Polym. Sci. A: Polym. Chem.* **1992**, *30*, 1-11, 31-39; d) H. Nagashima, A. Suzuki, T. Iura, K. Ryu, K. Matsubara, *Organometallics* **2000**, *19*, 3579-3590; e) N. Harada, J. Yasuhara, Y. Motoyama, O. Fujimura, T. Tsuji, T. Takahashi, Y. Takahashi, H. Nagashima, *Bull. Chem. Soc. Jpn.* **2011**, *84*, 26-39.
- [14] Representative papers for the silane-reduction of nitro groups: Pd/C: a) J. Lipowitz, S. A. Bowman, *J. Org. Chem.* **1973**, *38*, 162-165, and Ref 9e; RhCl(PPh₃)₃: b) H. R. Brinkman, W. H. Miles, M. D. Hillborn, M. C. Smith, *Synth. Commun.* **1996**, *26*, 973-980; Pd(OAc)₂: c) R. J. Rahaim, Jr., R. E. Maleczka, *Org. Lett.* **2005**, *7*, 5087-5090; Fe₃(CO)₁₂: d) Y. Sunada, H. Kawakami, T. Imaoka, Y. Motoyama, H. Nagashima, *Angew. Chem. Int. Ed.* **2009**, *48*, 9511-9514.
- [15] [1,4]-Reduction of α,β -unsaturated compounds by Pd/C-Et₃SiH system were reported, see Refs 9d and 9e.
- [16] Pd/C-catalyzed dehydrogenative silylation of secondary carboxamides with *t*-BuMe₂SiH was reported, see: K. Yamamoto, M. Takemae, *Bull. Chem. Soc. Jpn.* **1989**, *62*, 2111-2113.
- [17] Secondary amines can be obtained from tertiary *N*-benzylamides by the Pd/C-catalyzed sequential reactions; deoxygenative reduction with TMDS followed by hydrogenolytic cleavage of benzylic C-N bond. Details see Supporting Information.
- [18] Representative papers: a) L. N. Lewis, N. Lewis, *J. Am. Chem. Soc.* **1986**, *108*, 7228-7231; b) L. N. Lewis, N. Lewis, *Chem. Mater.* **1989**, *1*, 106-114; c) L. N. Lewis, R. J. Uriarte, *Organometallics* **1990**, *9*, 621-625; d) B. P. S. Chauhan, J. S. Rathore, M. Chauhan, A. Krawicz, *J. Am. Chem. Soc.* **2003**, *125*, 2876-2877; e) B. P. S. Chauhan, J. Rathore, R. Sardar, P. Tewari, U. Latif, *J. Organomet. Chem.* **2003**, *686*, 24-31; f) B. P. S. Chauhan, J. S. Rathore, *J. Am. Chem. Soc.* **2005**, *127*, 5790-5791.
- [19] a) J. Turkevich, G. Kim, *Science* **1970**, *169*, 873-879; b) H. Bönemann, W. Brijoux, *Angew. Chem. Int. Ed. Engl.* **1991**, *30*, 1312-1314; c) L. A. Fowley,

- D. Michos, X.-L. Luo, R. H. Crabtree, *Tetrahedron Lett.* **1993**, *34*, 3075-3078; d) M. Beller, H. Fischer, K. Kühlein, C.-P. Reisinger, W. A. Herrmann, *J. Organomet. Chem.* **1996**, *520*, 257-259; e) G. Schmid, H. West, H. Mehles, A. Lehnert, *Inorg. Chem.* **1997**, *36*, 891-895; f) I. Pryjomaska-Ray, A. Gniewek, A. M. Trzeciak, J. J. Ziółkowski, W. Tylus, *Top. Catal.* **2006**, *40*, 173-184.
- [20] Similar Pd leaching was reported in the Heck reaction, see Review: a) A. M. Trzeciak, J. J. Ziółkowski, *Coord. Chem. Rev.* **2007**, *251*, 1281-1293. Representative papers: b) F. Zhao, M. Shirai, M. Arai, *J. Mol. Catal. A: Chem.* **2000**, *154*, 39-44; c) F. Zhao, K. Murakami, M. Shirai, M. Arai, *J. Catal.* **2000**, *194*, 479-483; d) R. G. Heidenreich, J. G. E. Krauter, J. Pietsch, K. Köhler, *J. Mol. Catal. A: Chem.* **2002**, *182-183*, 499-509; e) F. Zhao, M. Arai, *React. Kinet. Catal. Lett.* **2004**, *81*, 281-289; f) K. Köhler, W. Kleist, S. S. Pröckl, *Inorg. Chem.* **2007**, *46*, 1876-1883.
- [21] Similarly, soluble metal species were generated in the reactions using other metal on carbons (Rh/C, Ru/C, and Pt/C) and TMDS; Rh: light brown solution (after 24 h) including 11.6% of Rh was leached from 3.7–4.0 wt% Rh/C, Ru: light brown solution (after 24 h) including 4.0% of Ru was leached from 4.1–4.3 wt% Ru/C, and Pt: yellow solution (after 6 h) including 1.9% of Pt was leached from 4.3 wt% Pt/C, respectively.
- [22] Similar siloxane chain extension in the Pt-catalyzed reduction of DMF with TMDS was reported, see: J. L. Martinez, H. K. Sharma, R. Arias-Ugarte, K. H. Pannell, *Organometallics* **2014**, *33*, 2964-2967.
- [23] In the reaction using 1,1,3,3,3-pentamethyldisiloxane, there were at least three hydrosilanes existed in the crude materials [$^1\text{Si-H}$: δ 4.62 ($J = 1.6$ Hz), 4.65 ($J = 2.0$ Hz), 4.70 ($J = 2.8$ Hz); $^1\text{SiCH}_3$: 0.19 ($J = 2.8$ Hz), 0.24 ($J = 2.0$ Hz)]. These results suggested that the Si–O bond cleavage and reformation occurred.
- [24] a) H. Nagashima, K. Tatebe, T. Ishibashi, A. Nakaoka, J. Sakakibara, K. Itoh, *Organometallics* **1995**, *14*, 2868-2879; b) Y. Sunada, Y. Fujimura, H. Nagashima, *Organometallics* **2008**, *27*, 3502-3513; c) H. Tsutsumi, Y. Sunada, H. Nagashima, *Organometallics* **2011**, *30*, 68-76; d) Y. Sunada, H. Tsutsumi, K. Shigeta, R. Yoshida, T. Hashimoto, H. Nagashima, *Dalton Trans.* **2013**, *42*, 16687-16692; e) N. Nakatani, J. Hasegawa, Y. Sunada, H. Nagashima, *Dalton Trans.* **2015**, *44*, 19344-19356, and also see Refs 3e, 3g, and 12c

Submitted: May 19, 2016

Accepted: June 20, 2016

Organic & Supramolecular Chemistry

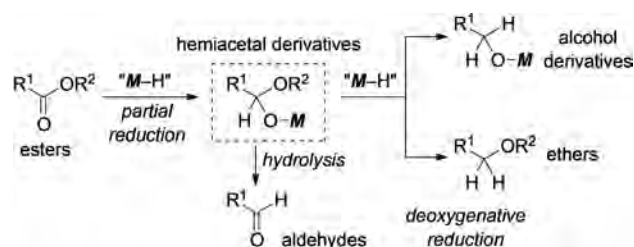
Catalytic Silane-Reduction of Carboxylic Esters and Lactones: Selective Synthetic Methods to Aldehydes, Lactols, and Ethers via Silyl Acetal Intermediates

Satomi Hosokawa, Motoki Toya, Arika Noda, Masato Morita, Takaki Ogawa, and Yukihiro Motoyama*^[a]

Practical procedures for the production of aldehydes, lactols, and ethers are offered by the palladium-catalyzed silane-reduction of carboxylic esters and lactones. The partial reduction of carboxylic esters or lactones with 1,1,3,3-tetramethyldisiloxane in the presence of commercially available palladium on carbon (Pd/C) and some copper compounds as a co-catalyst smoothly proceeds under mild conditions to afford the silyl acetal derivatives in high yields, which are easily converted to the corresponding aldehydes or lactols by hydrolysis of silyloxy group. On the other hand, deoxygenated ethers are obtained with high selectivity by treatment of silyl acetals with catalytic amounts of Me₃SiOTf at -78 °C or stoichiometric amounts of BF₃•OEt₂ at ambient temperature.

Simple and selective transformations of a molecule to a variety of compounds by virtue of catalysis are a challenge to be developed in modern organic synthesis. Among the organic compounds, carboxylic esters and lactones are quite useful because they have reactive functions such as acidic α -protons and carbonyl groups: enolates formed by α -deprotonation act as a nucleophile, whereas their carbonyl carbons react with various nucleophiles. As shown in Scheme 1, reduction of ester carbonyls by nucleophilic addition of one equivalent of hydride species affords hemiacetal derivatives. These partial reduction products can be converted to the corresponding aldehydes by hydrolysis, while further addition of hydride species gives alcohol derivatives or ethers. Comparing with the traditional methods using stoichiometric amounts of metal hydride reagents,^[1] catalytic reduction using hydrosilanes as a hydride source is much more attractive from a selectivity, safety and environmental points of view.^[2] In general, transition metal-catalyzed hydrosilylation of carboxylic esters give alcohols after hydrolysis of silyl ethers formed.^[3] In some catalyst systems, deoxygenative reduction of acyclic esters proceeded to afford the corresponding ethers as a major product in good yields.^[4]

However, chemical yields of cyclic ethers by the reaction of 5 to 7-membered ring lactones were not satisfactory,^[5] except in the case of two-step silane-reduction of γ - and δ -lactones reported by Buchwald.^[6] On the other hand, aldehydes are obtained by partial reduction of carboxylic esters to silyl acetals (hemiacetal silyl ethers) followed by hydrolysis of their silyloxy group.^[7] Similarly, Buchwald reported the efficient preparation method of lactols by titanocene-catalyzed partial reduction of 5- and 6-membered ring lactones.^[8] However, hydrosilylation of larger ring-size lactones generally gives the corresponding diols; only one example was reported by Darcel for the selective reduction of ϵ -decanolactone to the hydroxy aldehyde,^[7e] which is the acyclic equivalent to the corresponding lactol.



Scheme 1. Hydride-Reduction of Esters.

We have recently reported that the combination of 1,1,3,3-tetramethyldisiloxane (TMDS)^[9] and commercially available palladium on carbon (Pd/C) was effective catalyst system for the reduction of tertiary carboxamides to amines.^[10] In that case, the reaction of carboxylic esters did not proceed leading to the selective formation of amino esters from amido esters. Our continuous efforts to achieve the reduction of carboxylic esters resulted in the discovery that the addition of some copper species to the Pd/C–TMDS system provides an efficient synthetic process for the silyl acetals in high selectivity by partial reduction of carboxylic esters and lactones. We also found that the silyl acetals formed are easily converted to the corresponding aldehydes or lactols by hydrolysis of silyloxy group, and to ethers *via* further silane-reduction by treatment with Lewis acids.

First, the reaction of ethyl dihydrocinnamate (**1a**) with TMDS was investigated using various metal salts as an additive

[a] Dr. S. Hosokawa, M. Toya, A. Noda, M. Morita, T. Ogawa, Prof. Dr. Y. Motoyama

Department of Advanced Science and Technology, Toyota Technological Institute, Nagoya, Aichi 468–8511, Japan
E-mail: motoyama@toyota-ti.ac.jp

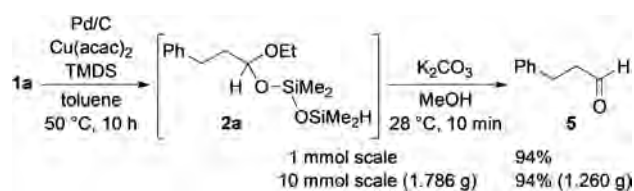
Supporting information for this article is available on the WWW under <https://doi.org/10.1002/slct.201703033>

in the presence of Pd/C in toluene. Although no reaction took place at 50 °C by the addition of Li, Ag, Zn, Fe, Co, and Ni salts,^[11] the starting material was completely consumed by using Cu(OAc)₂(H₂O) or Cu(acac)₂ to afford the corresponding partial reduction product, silyl acetal **2a**, preferentially in quantitative yields (Table 1, Entries 2 and 3).^[12] Other copper salts were not effective for the partial reduction of ester **1a**; the reaction using Cu(OTf)₂^[13] gave a mixture of ethyl 3-phenylpropyl ether (**3a**) via the deoxygenative reduction of **1a**, and 3-phenylpropanol silyl ether (**4a**) (77% conversion, **3a/4a** = 85:15), whereas most of all ester **1a** was recovered by the addition of CuSO₄(H₂O)₅ and [Cu(MeCN)₄](PF₆) (Entries 5 and 6). The amounts of Cu salts were also examined and found that the reaction using 0.02 equivalent of Cu(acac)₂ (Pd/Cu = 1:2) proceeded smoothly under the same conditions to afford **2a** in quantitative yield (Entry 7). We also checked the reaction in other solvents and found that the silyl acetal **2a** was obtained in quantitative yield in hexane, however, only trace amount of **2a** was formed in dichloroethane and dimethoxyethane.^[11] It is noteworthy that silyl acetal **2a** could be isolated in pure form by silica gel chromatography at 0 °C (Entry 7: 70% yield), and its structure proved to be Ph(CH₂)₂CH(OEt)(OSiMe₂OSiMe₂H) by ¹H- and ¹³CNMR, IR, and elemental analysis. Similarly, the silyl ether **4a** proved to be Ph(CH₂)₃OSiMe₂OSiMe₂H.^[11] These results clearly showed that the only one of the Si–H group in TMDS reacts with ester **1a**, and the other one remains intact.

Table 1. Pd/C–Catalyzed reduction of **1a** with TMDS.^[a]

Entry	Additive	Conversion [%] ^[b]	Ratio (2a/3a/4a) ^[b]
1	–	0	–
2	Cu(OAc) ₂ (H ₂ O)	> 99	100 : 0 : 0
3	Cu(acac) ₂	> 99	100 : 0 : 0
4	Cu(OTf) ₂	77	0 : 85 : 15
5	CuSO ₄ (H ₂ O) ₅	trace	100 : 0 : 0
6	[Cu(MeCN) ₄](PF ₆)	trace	0 : 100 : 0
7 ^[c]	Cu(acac) ₂	> 99 (70) ^[d]	100 : 0 : 0

[a] Reaction conditions: **1a** (1 mmol), TMDS (2.5 mmol), Pd/C (0.01 equiv), additive (0.05 equiv), toluene (2 mL). [b] Determined by ¹HNMR. [c] Cu(acac)₂ (0.02 equiv). [d] Isolated yield of **2a**.



Scheme 2. Synthesis of Aldehyde **5** from Ester **1a**.

The silyl acetal **2a** was easily converted to the aldehyde **5** in high yield by hydrolysis of silyloxy group (Scheme 2). After the reaction as shown in Table 1, entry 7, Pd/C catalyst was filtered off and the remaining TMDS was removed under reduced pressure. The resultant mixture was then treated with K₂CO₃ in MeOH to afford **5** in 94% yield after column chromatography. In addition, the present procedure is adaptable to a gram-scale reaction; the reaction of 1.786 g (10 mmol) of **1a** under the same conditions afforded 1.260 g (94%) of **5**.

It is well known that acetals are easily converted to the corresponding ethers by treatment with hydrosilanes in the presence of Brønsted- or Lewis acids.^[14] Therefore, we next examined the conversion of silyl acetal **2a** to ether **3a**. The crude silyl acetal **2a**, which was obtained after removal of solid Pd/C catalyst and the remaining TMDS by filtration followed by evaporation, was treated with several Lewis acids. As shown in Table 2, the reactions with 0.05 equivalent of Cu(OTf)₂ and

Table 2. Conversion of ester **1** to ether **3** via silyl acetal **2**.^[a]

Entry	Ester 1	Reagent (equiv.)	Conditions (Step ii)	Conv. [%] ^[b]	Ratio (3/6) ^[b]
1	1a	Cu(OTf) ₂ (0.05)	25 °C, 1 h	> 99	87 : 13
2	1a	TMSOTf (0.05)	25 °C, 1 h	> 99	85 : 15
3	1a	BF ₃ •OEt ₂ (1.10)	25 °C, 1 h	> 99	96 : 4
4	1a	TMSOTf (0.05)	–78 °C, 1 h	> 99	96 : 4
5	1a	BF ₃ •OEt ₂ (1.10)	–78 °C, 1 h	> 99	96 : 4
6 ^[c]	1a	TMSOTf (0.05)	–78 °C, 1 h	> 99 (87) ^[d]	95 : 5
7 ^[c]	1b	BF ₃ •OEt ₂ (1.10)	–78 °C, 1 h	> 99 (92) ^[d]	> 99 : < 1
8 ^[c,e]	1c	BF ₃ •OEt ₂ (1.10)	–78 °C, 1 h	> 99 (86) ^[d]	94 : 1 ^[f]

[a] Reaction conditions: i) **1a** (1 mmol), TMDS (2.5 mmol), Pd/C (0.01 equiv), Cu(acac)₂ (0.02 equiv), toluene (2 mL), 50 °C, 10 h; ii) reagent (0.05 or 1.1 equiv); iii) TBAF (1.5 mmol). [b] Determined by ¹HNMR. [c] One-pot reaction. [d] Isolated yield of ether **3**. [e] Step i): Pd/C (0.02 equiv), Cu(acac)₂ (0.05 equiv), toluene (3 mL), 24 h. [f] 5% of aldehyde **5** was formed.

Me₃SiOTf (TMSOTf) at 25 °C afforded the ether **3a** as a major product with 87 and 85% selectivity (Entries 1 and 2). The product selectivity of **3a** reached up to 96% in the reaction with TMSOTf (0.05 equivalent) at –78 °C or BF₃•OEt₂ (1.1 equivalent) at both –78 and 25 °C (Entries 3–5). These results indicated that the Si–H group in the silyl acetal **2a** reacts with Lewis acid resulting in the formation of ether **3a** without further addition of hydrosilanes, and the product selectivity was highly dependent on the reaction temperature and Lewis acid used. The present transformation from **1a** to **3a** was successfully achieved without removal of the catalyst and remaining TMDS (one-pot reaction); after the reaction of **1a** with TMDS as shown in Table 1, entry 7, the resultant mixture was treated with 0.05 equivalent of TMSOTf at –78 °C for 1 h gave **3a** with 95% selectivity, and **3a** could be isolated in 87% yield by silica gel chromatography (Entry 6). Similarly, the reactions of silyl acetals **2b** and **2c**, which were obtained by

Table 3. Results of the Reaction of Various Lactones **7a–g** to Lactol **8a–c**, Hydroxyaldehydes **8d–g**, and Cyclic Ethers **9a–g**.^[a]

Substrate	Conditions (silyl acetal)	Product (<i>Method A</i>)	Conversion [%] ^[b]	Selectivity ^[b]	Product (<i>Method B</i>)	Conversion [%] ^[b]	Selectivity ^[b]
	25 °C, 3 h		> 99 (82)	94% ^[c] (diol 10a : 6%)		> 99 (84)	94% (diol 10a : 6%)
	25 °C, 6 h ^[d]		> 99 (86)	97% ^[e] (diol 10b : 3%)		> 99 (86)	97% (diol 10b : 3%)
	50 °C, 18 h		> 99 (82)	92% ^[e] (diol 10c : 8%)		> 99 (86) ^[f]	> 99%
	25 °C, 6 h ^[d]		> 99 (76)	> 99%		> 99 (99) ^[f,g]	> 99%
	25 °C, 3 h		> 99 (86)	> 99%		> 99 (78) ^[f]	> 99%
	50 °C, 24 h		> 99 (76)	> 99%		> 99 (88)	97% (diol 10f : 3%)
	50 °C, 24 h		> 99 (71)	> 99%		> 99 (80)	93% (diol 10g : 7%)

[a] Reaction conditions: lactone **7** (1 mmol), TMSD (2.5 mmol), Pd/C (0.01 equiv), Cu(acac)₂ (0.02 equiv), toluene (2 mL). **Method A**) K₂CO₃/MeOH at 25 °C for 10 min. **Method B**) TMSOTf (0.05 equiv) at –78 °C for 1 h. [b] Determined by ¹HNMR. The numbers in parentheses are the isolated yield. [c] 1.4:1 diastereomixture. [d] Without Cu(acac)₂. [e] 1:1 diastereomixture. [f] Cu(OTf)₂ (5 mol%) was used instead of Cu(acac)₂; **7c**: 25 °C for 24 h, **7d**: 25 °C, 2 h, **7e**: 25 °C for 1 h. [g] Determined by GC because **9d** is highly volatile compound.

the silane-reduction of *iso*-propyl and benzyl dihydrocinnamate (**1b** and **1c**), with BF₃•OEt₂ at –78 °C afforded the corresponding ethers with high selectivity: >99% selectivity for **3b** and 94% selectivity for **3c** (Entries 7 and 8).

The present partial reduction and deoxygenative reduction of carboxylic esters were also effective for the preparation of lactols, hydroxyaldehydes, and cyclic ethers from cyclic esters (lactones). Lactols and their ring-chain tautomers, hydroxy aldehydes, can participate in a variety of chemical reactions. Partial reduction products of 5- and 6-membered ring lactones are known to be relatively stable in a cyclic form (lactols), whereas those of large ring-size lactones are generally existed in a acyclic equivalent, hydroxy aldehydes.^[15] Therefore, partial reduction of large ring-size lactones is quite difficult; when desilylation of lactol silyl ethers occurs in the reaction mixture, thermodynamically more stable and reactive hydroxy aldehydes are generated, and then subsequent hydride-reduction of formyl group smoothly proceeds to afford diols (over-reduction products). As shown in Table 3, not only the 5- and 6-membered ring lactones **7a–c** but also the middle to large ring-size (7, 16, and 17-membered ring) lactones **7d–g** were completely consumed at 25–50 °C.^[11] Although small amounts of over-reduction products, diols **10a–c**, were formed using 5- and 6-membered ring lactones **7a–c** as a substrate (92–97% selectivity), the reaction of other lactones **7d–g** afforded the corresponding silyl acetals preferentially. Among these lactones, the reaction of ϵ -caprolactone (**7d**) proceeded at ambient

temperature without addition of Cu salts. In all cases, the silyl acetals formed were smoothly converted to the corresponding lactols **8a–c** and hydroxy aldehydes **8d–g** by treatment with K₂CO₃ in MeOH at 25 °C (**Method A**).^[11] In the reactions of substituted lactones **7a** and **7b**, the diastereomer ratios of the lactols formed were *ca.* 1.4:1 for **8a** and 1:1 for **8b**, respectively. While treatment of crude silyl acetals with 0.05 equivalent of TMSOTf at –78 °C (**Method B**)^[11] gave the corresponding cyclic ethers with over 93% selectivity. In contrast to the synthesis of hydroxy aldehydes **8f** and **8g**, the reactions of lactol silyl ethers derived from 16- and 17-membered ring lactones afforded small amounts of diols **10f** and **10g** (3% and 7%, respectively). In some cases, the deoxygenative reduction of lactones directly proceeded by using Pd/C (0.01 equivalent to lactones) and Cu(OTf)₂ (0.05 equivalent to lactones) to afford the desired ethers as a sole product in good yields (cyclic ethers **9c**, **9d**, and **9e**).^[11] It is noteworthy that *the Pd/C recovered from the reaction media acts as a catalyst for the reaction of 1a without further addition of Cu species*. However, chemical yields of the product decreased slightly (original: >99%, 1st: 95%, 2nd: 85%, 3rd: 93% after 10 h) because of the leaching of both Pd and Cu species (0.71% of Pd/C and 0.87% of Cu(acac)₂ used, respectively) into the crude material.^[16]

In summary, we have developed the simple catalytic process for the Pd-catalyzed partial reduction of carboxylic esters to the corresponding silyl acetals under mild conditions using 1,1,3,3-tetramethyldisiloxane (TMSD) as a reducing agent.

The addition of some copper salts was found to be crucial for the present silane-reduction of carboxylic esters. Silyl acetals obtained were easily converted to the corresponding aldehydes, lactols, and ethers in good to high yields. To the best of our knowledge, the present procedure is the first example of the preparation of hydroxy aldehydes and cyclic ethers from middle to large ring-size of lactones with high selectivity. It is of practical importance that commercially available Pd/C and inexpensive TMDS can be used, and the present procedure can be scaled up to a gram-quantity reaction. Detailed mechanistic studies on the catalytically active species, and further application of the present catalyst systems are now actively being investigated.

Supporting Information Summary

The Supporting Information contains detailed experimental procedures, compound data and characterization, spectra (^1H and ^{13}C NMR), other supporting experimental data, and references.

Acknowledgements

Part of this work was supported by the Japan Society for the Promotion of Science through a Grants-in-Aid for Scientific Research (26390031) and the Ministry of Education, Culture, Sports, Science and Technology, Japan through the Strategic Research Foundation at Private Universities (S1511022).

Conflict of Interest

The authors declare no conflict of interest.

Keywords: lactone · palladium · reduction · silane · silyl acetal

- [1] a) J. Seyden-Penne, *Reductions by the Almino- and Borohydrides in Organic Synthesis*, 2nd Ed., Wiley, New York, **1997**; b) G. M. Barrett, In *Comprehensive Organic Synthesis*, (Eds.: B. M. Trost, I. Fleming), Pergamon Press, Oxford, U. K., **1991**; Vol. 8, Part 1.10, pp. 235–257.
- [2] Reviews: a) D. Addis, S. Das, K. Junge, M. Beller, *Angew. Chem. Int. Ed.* **2011**, *50*, 6004–6011; b) H. Nagashima, *Synlett* **2015**, *26*, 866–890.
- [3] Representative papers: a) S. C. Berk, K. A. Kreutzer, S. L. Buchwald, *J. Am. Chem. Soc.* **1991**, *113*, 5093–5095; b) S. C. Berk, S. L. Buchwald, *J. Org. Chem.* **1992**, *57*, 3751–3753; c) T. Ohta, M. Kamiya, K. Kusui, T. Michibata, M. Nobutomo, I. Furukawa, *Tetrahedron Lett.* **1999**, *40*, 6963–6966; d) H. Mimoun, *J. Org. Chem.* **1999**, *64*, 2582–2589; e) K. Matsubara, T. Iura, T. Maki, H. Nagashima, *J. Org. Chem.* **2002**, *67*, 4985–4988; f) A. C. Fernandes, C. C. Romão, *J. Mol. Catal. A: Chem.* **2006**, *253*, 96–98; g) K. Junge, B. Wendt, S. Zhou, M. Beller, *Eur. J. Org. Chem.* **2013**, 2061–2065; h) D. Bézier, G. T. Venkanna, L. C. M. Castro, J. Zheng, T. Roisnel, J.-B. Sortais, C. Darcel, *Adv. Synth. Catal.* **2012**, *354*, 1879–1884; i) K. Jung, B. Wendt, S. Zhou, M. Beller, *Eur. J. Org. Chem.* **2013**, 2061–2065; j) O. O. Kovalenko, H. Adolfsson, *Chem. Eur. J.* **2015**, *21*, 2785–2788. Other methods: k) K. Revunova, G. Nikonov, *Eur. J. Org. Chem.* **2014**, *20*, 839–845; l) D. Peng, M. Zhang, Z. Huang, *Chem. Eur. J.* **2015**, *21*, 14737–14741.
- [4] Representative papers: a) Z. Mao, B. T. Gregg, A. R. Cutler, *J. Am. Chem. Soc.* **1995**, *117*, 10139–10140; b) N. Sakai, T. Moriya, T. Konakahara, *J. Org. Chem.* **2007**, *72*, 5920–5922; c) S. Das, Y. Li, K. Junge, M. Beller, *Chem. Commun.* **2012**, *48*, 10742–10744; d) S. Xu, J. S. Boschen, A. Biswas, T. Kobayashi, M. Pruski, T. L. Windus, A. Sadow, *Dalton Trans.* **2015**, *44*, 15897–15904.
- [5] TiCl_4 (1.5 equiv.) and Me_3SiOTf (3 equiv.) were used, see: M. Yato, K. Homma, A. Ishida, *Tetrahedron* **2001**, *57*, 5353–5359. Also see Refs. 3e, 4a, 4b, 4d.
- [6] M. C. Hansen, X. Verdaguer, S. L. Buchwald, *J. Org. Chem.* **1998**, *63*, 2360–2361.
- [7] Representative papers: a) D. J. Parks, W. E. Piers, *J. Am. Chem. Soc.* **1996**, *118*, 9440–9441; b) M. Igarashi, R. Mizuno, T. Fuchikami, *Tetrahedron Lett.* **2001**, *42*, 2149–2151; c) J. Nakanishi, H. Tatamidani, Y. Fukumoto, N. Chatani, *Synlett* **2006**, 869–872; d) C. Cheng, M. Brookhart, *Angew. Chem. Int. Ed.* **2012**, *51*, 9422–9424; e) H. Li, L. C. Misal Castro, J. Zheng, T. Roisnel, V. Dorcet, B. Sortais, C. Darcel, *Angew. Chem. Int. Ed.* **2013**, *52*, 8045–8049. From tertiary amides: f) F. Tinnis, A. Volkov, T. Slagbrand, H. Adolfsson, *Angew. Chem. Int. Ed.* **2016**, *55*, 4562–4566.
- [8] a) X. Verdaguer, S. C. Berk, S. L. Buchwald, *J. Am. Chem. Soc.* **1995**, *117*, 12641–12642; b) X. Verdaguer, M. C. Hansen, S. C. Berk, S. L. Buchwald, *J. Org. Chem.* **1997**, *62*, 8522–8528. Also see Refs. 3d, 7e.
- [9] J. Pesti, G. L. Larson, *Org. Process Res. Dev.* **2016**, *20*, 1164–1181.
- [10] S. Hosokawa, K. Teramoto, Y. Motoyama, *ChemistrySelect* **2016**, *1*, 2594–2602.
- [11] Details see: Supporting Information.
- [12] Other metal on carbon (M/C) catalysts also showed the catalytic activity towards silane-reduction of **1a** under the same conditions. Pt/C: 70% conversion, 100% selectivity; Ru/C: 91% conversion, 100% selectivity; Rh/C: > 99% conversion, 100% selectivity, see Supporting Information.
- [13] $\text{Cu}(\text{OTf})_2$ showed catalytic activity towards silane-reduction of **1a** without Pd/C catalyst: 50% conversion at 50 °C for 10 h, **2a/3a/4a** = 0:12:1. We also examined the reaction with $\text{Cu}(\text{acac})_2$ and TMSOTf (without Pd/C catalyst), but no reaction proceeded at 50 °C.
- [14] a) J. H. Brewster, In *Comprehensive Organic Synthesis*, (Eds.: B. M. Trost, I. Fleming), Pergamon Press, Oxford, U. K., **1991**; Vol. 8, Part 1.9, pp. 211–234; b) H. Vorbrüggen, In *Silicon-Mediated Transformations of Functional Groups*, Wiley-VCH, Weinheim, **2004**, pp. 267–276.
- [15] a) C. D. Hurd, W. H. Saunders, Jr., *J. Am. Chem. Soc.* **1952**, *74*, 5324–5329. Also see: b) P. R. Jones, *Chem. Rev.* **1963**, *63*, 464–487.
- [16] From the MP-AES analysis, both Pd and Cu species were existed in the solution during the reaction (Pd/Cu = ca. 0.8–1.5; initial ratio was Pd/Cu = 0.5).

Submitted: December 13, 2017

Revised: February 27, 2018

Accepted: March 2, 2018

VIP Very Important Publication

Hydrosilane-Promoted Facile Deprotection of *tert*-Butyl Groups in Esters, Ethers, Carbonates, and CarbamatesTakuya Ikeda,^a Zhenzhong Zhang,^a and Yukihiro Motoyama^{a,*}

^a Department of Advanced Science and Technology, Toyota Technological Institute, Nagoya, Aichi 468-8511, Japan
Phone: (+81)-52-809-1807
Fax: (+81)-52-809-1721
E-mail: motoyama@toyota-ti.ac.jp

Manuscript received: September 25, 2018; Revised manuscript received: November 15, 2018;
Version of record online: December 11, 2018

Supporting information for this article is available on the WWW under <https://doi.org/10.1002/adsc.201801279>

Abstract: Combination of PdCl₂ with 1,1,3,3-tetramethyldisiloxane in the presence of activated carbon was found to be an effective catalyst system for the cleavage reaction of C–O bond of *O*-*t*-Bu moieties. The present catalytic reaction offers a practical method for the deprotection of *tert*-butyl esters, *tert*-butyl ethers, *O*-Boc, and *N*-Boc derivatives under mild conditions. The addition of activated carbon in the reaction mixture was proved to be crucial for not only sustaining the catalytic activity but also trapping the palladium species after the reaction.

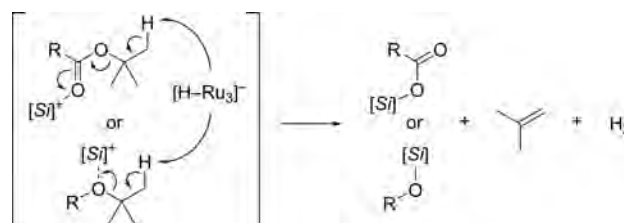
Keywords: activated carbon; deprotection; hydrosilane; palladium; *tert*-butyl group

The development of novel transformation method of organic molecules, especially by virtue of catalysis, is one of the most challenging and formidable endeavours in organic synthesis. In addition, facile removal of the metallic species from the product is quite important for the design of the metal-catalyzed reaction systems.^[1]

The *tert*-butyl substituent (*t*-Bu), which possesses prominent stability under a variety of reaction conditions, is widely recognized as one of the most powerful protecting groups for alcohols and carboxylic acids.^[2] However, the harsh conditions are commonly required to cleave the C–O bond of *tert*-butoxy moiety (deprotection) by using strong Brønsted- or Lewis acids.^[2,3] In the past decades, Jaime-Figueroa *et al.* developed a new deprotection method of *tert*-butyl esters and carbonates using fluorinated alcohols as a solvent at 100 °C.^[4] Bartoli and Sambri also developed a simple procedure for the deprotection of *tert*-butyl

esters and ethers: the reaction proceeded smoothly in CH₃CN at 40–70 °C by using stoichiometric amounts of CeCl₃ and NaI.^[5]

In 2010, Nagashima and co-workers firstly reported a catalytic method for C–O bond cleavage of *tert*-butoxy moiety (*O*-*t*-Bu) using (μ³,η²,η³,η⁵-acenaphthylene)Ru₃(CO)₇ complex and Me₂PhSiH.^[6] In this reaction, heterolytic cleavage of the Si–H bond of hydrosilane is induced by the triruthenium cluster to form an ionic intermediates, [Si]⁺⋯[Ru₃-H]⁻, then the Lewis acidic [Si]⁺ species interacts with carbonyl- or ether oxygen atom followed by deprotonation of the *t*-Bu group by the [Ru₃-H]⁻ species resulting in the formation of silyl ester, isobutene, and hydrogen gas (Scheme 1).^[7] This catalytic system is attractive because the procedure is simple and reaction proceeds under neutral conditions, but the preparation of triruthenium cluster complex is unavoidable.^[8] In addition, this system is not compatible towards a compound having other ester groups in a molecule because they are reduced under reaction conditions to afford the corresponding silyl ethers.



Scheme 1. Reaction mechanisms for the silane-induced deprotection of *tert*-butyl esters and ethers by using triruthenium cluster as a catalyst.

We have recently reported the catalytic silane-reduction of carbonyl compounds using commercially available palladium on carbon (Pd/C) as a catalyst.^[9] During the course of these studies, we became aware of the gas evolution and formation of silyl esters and isobutene as a by-product in the Pd-catalyzed reaction of *tert*-butyl esters with hydrosilanes.^[10] Similar to the triruthenium cluster system, the present Pd-hydrosilane system also initiates the ring-opening oligomerization of THF^[7] (details see, Supporting Information). Our efforts to achieve the selective conversion of *tert*-butyl esters to the corresponding carboxylic acids resulting the discovery that the combination of 1,1,3,3-tetramethyldisiloxane (TMDS)^[11] and PdCl₂ in the presence of activated carbon provides an efficient deprotection process of *tert*-butyl groups in not only esters but also ethers, carbonates, and carbamates under mild conditions.

Table 1 summarizes the results when *tert*-butyl 3-phenylpropionate (**1a**) was treated with several palladium compounds^[12] and hydrosilanes in dimethoxyethane (DME) at 40 °C for 24 h followed by workup with methanol. Although the chemical yield of the reaction of **1a** and Me₂PhSiH using Pd/C as a catalyst was quite low, the reaction with palladium salts or complexes proceeded smoothly in the presence of activated carbon (AC) to give 3-phenylpropionic acid (**5a**) in good to high yields (Entries 1 vs. 2–5). The presence of AC in the reaction mixture was crucial for the present deprotection: when the reaction was

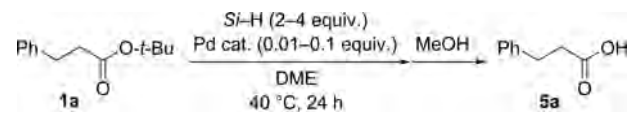
carried out without addition of AC, only trace amount of **5a** was obtained along with the formation of palladium residues as black precipitates (Entry 6). As shown in Entries 7–10, TMDS and alkoxy silanes were also effective for the present reaction; Me₂PhSiH and TMDS gave the best results among them by the reaction using 1 mol% of PdCl₂ in the presence of AC (details, see Supporting Information). It is noteworthy that the present reaction was highly dependent on the solvent used: no reaction took place in toluene and hexane, however, the C–O bond cleavage reaction smoothly proceeded in DME and dichloromethane (see, Supporting Information).

The combination of TMDS and a catalytic amount of PdCl₂ (1–2 mol%) in the presence of AC also induced deprotection of other *tert*-butyl esters **1** as well as *tert*-butyl ethers **2**, *O*-Boc and *N*-Boc derivatives **3** and **4** in DME at 40 °C (Table 2). Conversion of both aliphatic and aromatic *tert*-butyl esters **1** to the corresponding carboxylic acids **5** was accomplished within 6 h (Entries 1–3). Similarly, deprotection of *O*-Boc derivatives **3a** and **3b** proceeded smoothly under the same conditions (Entries 6 and 7). Comparing with the *tert*-butyl esters and *O*-Boc derivatives, the reaction of *tert*-butyl ethers **2a** and **2b** required prolonged reaction time (20–24 h) to afford the desired alcohols **6a** and **6b** in high yields (Entries 4 and 5). Although the reactivity of the *N*-Boc derivatives **4a**, **4c** and **4d** were relatively lower than that of the others, using 2 mol% of PdCl₂ led to satisfactory yields (Entries 8, 10, and 11). Finally, the present procedure is adaptable to a gram-scale reaction. For example, the reaction of 1.782 g (10 mmol) of **1c** with TMDS (10 mmol) in the presence of PdCl₂ (0.5 mol% to **1c**) at 40 °C for 24 h afforded 1.118 g (92%) of **5c**.

Hydrolysis of esters is generally performed by treatment with strong bases, but *tert*-butyl esters are not hydrolyzed under these conditions.^[2] One aspect of the present hydrosilane-promoted reaction system is the preparation of half esters from mixed esters by the selective deprotection of *t*-Bu group. For example, *tert*-butyl ethyl succinate (**8**) was selectively converted to mono-*tert*-butyl succinate (**10**) in 81% isolated yield by treatment with NaOH in methanol. In sharp contrast, the reaction of **8** with TMDS (1 equiv. to **8**) in the presence of PdCl₂ (1 mol%) and activated carbon in DME at 40 °C for 6 h afforded monoethyl succinate (**9**) in 89% isolated yield as a single product (Scheme 2).^[13]

Another interesting application of the present system is the preparation of esters from *t*-butyl esters or carboxylic acids (Scheme 3). The reaction of *t*-butyl ester **1a** with Me₂PhSiH followed by the addition of MeOH gave methyl ester **11a** in quantitative yield.^[14] Similarly, dehydrogenative silylation of carboxylic acid **5a** with Me₂PhSiH gave the corresponding silyl ester, which then was treated with alcohols to afford esters

Table 1. Catalytic deprotection of *t*-Bu group in **1a**.^[a]



Entry	Catalyst	Si-H	Yield [%] ^[b]
1	Pd/C	Me ₂ PhSiH	10
2	Pd(OAc) ₂ -AC	Me ₂ PhSiH	82
3	Pd(dba) ₂ (H ₂ O)-AC	Me ₂ PhSiH	> 99
4	Pd(acac) ₂ -AC	Me ₂ PhSiH	> 99
5	PdCl ₂ -AC	Me ₂ PhSiH	> 99
6	PdCl ₂	Me ₂ PhSiH	< 1
7 ^[c]	PdCl ₂ -AC	Me ₂ PhSiH	> 99
8 ^[c,d]	PdCl ₂ -AC	TMDS	> 99
9 ^[c]	PdCl ₂ -AC	(EtO)Me ₂ SiH	65
10 ^[c]	PdCl ₂ -AC	(EtO) ₂ MeSiH	39

^[a] All reactions were carried out by using **1a** (0.5 mmol), hydrosilane (2 mmol), catalyst (0.1 equivalent to **1a**), activated carbon (AC: 100 mg) in DME (0.5 mL) at 40 °C for 24 h.

^[b] Determined by ¹H NMR analysis of the crude material.

^[c] **1a** (1 mmol), PdCl₂ (0.01 mmol), AC (50 mg), and DME (2 mL) was used.

^[d] TMDS (1 mmol) was used.

Table 2. Deprotection of *tert*-butyl esters, *tert*-butyl ethers, *O*-Boc, and *N*-Boc derivatives.^[a]

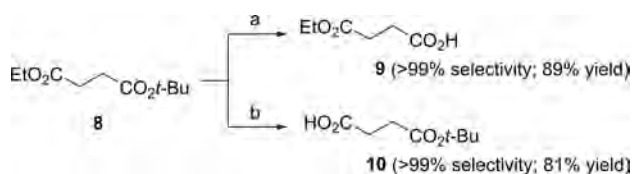
Entry	Substrate	Time [h]	Product	Yield [%] ^[b]
1		4	5a	> 99 (97)
2		6	5b	> 99 (95)
3		6	5c	> 99 (97)
4		24	6a	> 99 (86)
5		20	6b	> 99 (98)
6		6	6a	> 99 (84)
7		6	6b	> 99 (99)
8 ^[c]		24	7a	> 99 (80) ^[d]
9		6	7b	> 99 (90)
10 ^[c]		24	7c	> 99 (72) ^[d]
11 ^[c]		24	7d	> 99 (92)

^[a] All reactions were carried out by using substrate (1 mmol), TMDS (1 mmol), PdCl₂ (0.01 mmol), AC (50 mg) in DME (2 mL) at 40 °C followed by workup with methanol or *n*-Bu₄NF.

^[b] Determined by ¹H NMR analysis of the crude material. The yield in parentheses was the isolated yield.

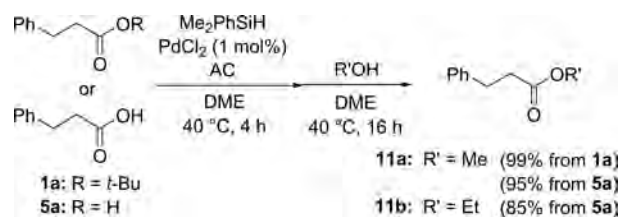
^[c] 0.5 mmol of substrate was used.

^[d] The product was isolated as the corresponding acetamide.



Scheme 2. Selective conversion of *tert*-butyl ethyl succinate (**8**) to monoethyl succinate (**9**). Conditions: a) PdCl₂/TMDS/DME/40 °C; b) NaOH/MeOH/25 °C

11 in good yields. The source of alkyl groups of **11** was determined as alcohols by the formation of PhCH₂CH₂CO₂CD₃ from CD₃OD (see, Supporting Information).



Scheme 3. Esterification or transesterification of **5a** and **1a**.

When developing a practical synthetic process using metal catalyst, it is important for removal of metal residues from the reactions, especially in pharmaceutical synthesis.^[15] Therefore, we checked the amounts of residual palladium species in the crude material obtained by the reaction of **1a** as described in Table 2, Entry 1 followed by workup process. Microwave plasma-atomic emission spectrometer (MP-AES) analysis revealed that only 0.121 μg of Pd exists in the crude materials: this corresponds to 0.01% of the Pd species used (calculated amounts of charged Pd was 1.08 mg). The remaining Pd species was trapped on the recovered activated carbon (*ca.* 1 mg, 92% of the Pd species used). *It is noteworthy that the palladium on activated carbon thus obtained (Pd/AC) showed catalytic activity towards silane-induced deprotection of tert-butyl groups.* After the reaction of **1a** as described in Table 2, Entry 1 (at 40 °C for 4 h), the carbon material was recovered by decantation and subjected to another catalytic run (Table 3). Although the catalytic activity of the recovered Pd/AC gradually decreased, the catalyst recovery/reuse cycle was successfully repeated three times in almost quantitative yields by extension of the reaction time to 24 h. We also checked the transmission electron microscopy (TEM) images of the recovered Pd/AC and found that there is only trace amount of Pd nanoparticles observed after the reaction as shown in Table 2, Entry 1 (Figure 1, left). In sharp contrast, many nano-sized particles were existed on the AC after four recycling experiment (Figure 1, right).

Table 3. Recycle experiments of recovered Pd/AC in the reaction of **1a**.^[a]

Run	Yield [%] ^[b]		
	4 h	10 h	24 h
1st	> 99	–	–
2nd	99	–	–
3rd	49	89	> 99
4th	20	–	60

^[a] All reactions were carried out by using **1a** (1 mmol), TMDS (1 mmol), recovered Pd/AC in DME (2 mL) at 40 °C followed by workup with methanol.

^[b] Determined by ¹H NMR analysis of the crude material.

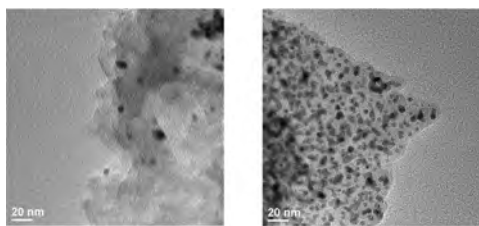
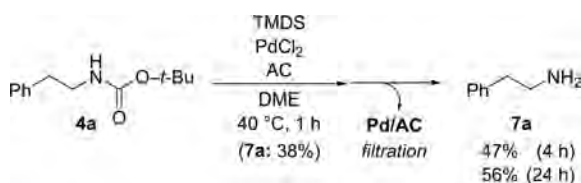


Figure 1. TEM images of the recovered Pd/AC: after the reaction as shown in Table 1, Entry 1 (left), and after four recycling experiment (right).

In the Pd/C-catalyzed Heck reaction, it is well known that the soluble Pd species, which is generated by the reaction of Pd/C with aryl halides, is the catalytically active species.^[16] Therefore, we next examined the amounts of palladium species in the solution obtained by the reaction of *N*-Boc compound **4a** as shown in Table 2, Entry 8. After the reaction at 40 °C for 1 h, the solid AC was removed by filtration with membrane filters (Durapore HV, 0.45 μm) to afford the brown solution, in which contained silane residue, unreacted TMDS, 38% of the product, 62% of **4a** remained, and 41.9 μg of Pd species (3.9% of charged Pd). In addition, the filtrate thus obtained was continuously stirred at 40 °C resulting in the further formation of the product **7a**: 47% for 4 h, and 56% for 24 h (Scheme 4). These results and the TEM images suggested that the catalytically active species of the present reaction is the small-sized, soluble Pd clusters, which are initially formed by the reaction of PdCl₂ with TMDS. In the absence of carbon materials, these Pd clusters are in contact with each other to form black precipitates. While in the presence of activated carbon, such palladium species is immobilized on the AC and regenerates by the reaction with TMDS.^[17] During such reversible immobilization-regeneration step, the Pd species on the AC was gradually aggregated resulting in the formation of large-size of palladium particles.



Scheme 4. Deprotection of **4a** after removal of the solid carbon materials.

In conclusion, we have developed a simple process for the Pd-catalyzed cleavage reaction of C–O bond of *O*-*t*-Bu groups leading to the facile deprotection of *tert*-butyl esters, *tert*-butyl ethers, *O*-Boc, and *N*-Boc

derivatives under mild conditions. The addition of activated carbon was found to be crucial for the present silane-induced deprotection. It is of practical importance that inexpensive PdCl₂ and 1,1,3,3-tetra-methyl-disiloxane (TMDS) can be used, and the present procedure can be scaled up to a gram-quantity reaction. Further mechanistic studies on the catalytically active species and detailed reaction pathway are now under investigation.

Experimental Section

Deprotection of 1c (10 mmol Scale). To a suspension of AC (250 mg), **1c** (1.782 g, 10 mmol), and PdCl₂ (8.9 mg, 0.5 mol%) in DME (0.5 mL) was added a 0.83 mol·L⁻¹ solution of TMDS in DME (12 mL, 10 mmol) at 25 °C. After it was stirred at 40 °C for 24 h, the reaction was quenched by the addition of MeOH (3 mL). Following stirring at 25 °C for 30 min, the reaction mixture was filtered and the filtrate was concentrated. Purification by silica gel chromatography gave **5c** in 92% yield (1.118 g).

Acknowledgements

The authors are grateful to Prof. S.-H. Yoon and Dr. J. Miyawaki (Kyushu University) for their help in the TEM analysis. Part of this work was supported by JSPS through a Grants-in-Aid for Scientific Research (C) (26390031) and MEXT through the Strategic Research Foundation at Private Universities (S1511022).

References

- [1] a) C. E. Garrett, K. Prasad, *Adv. Synth. Catal.* **2004**, *346*, 889–900; b) C. J. Welch, J. Albaneze-Walker, W. R. Leonard, M. Biba, J. DaSilva, D. Henderson, B. Laing, D. J. Mathre, S. Spencer, X. Bu, T. Wang, *Org. Process Res. Dev.* **2005**, *9*, 198–205; c) N. Galaffu, S. P. Man, R. D. Wilkes, J. R. H. Wilson, *Org. Process Res. Dev.* **2007**, *11*, 406–413.
- [2] P. G. M. Wuts in *Greene's Protective Groups in Organic Synthesis*, 5th ed., John Wiley & Sons, New Jersey, **2014**, pp. 97–99, 750–758.
- [3] L. Sambri, G. Bartoli, G. Bencivenni, R. Dalpozzo, *Curr. Org. Synth.* **2012**, *9*, 137–148.
- [4] a) J. Choy, S. Jaime-Figueroa, L. Jiang, P. Wagner, *Synth. Commun.* **2008**, *38*, 3840–3853; b) J. Choy, S. Jaime-Figueroa, T. Lara-Jaime, *Tetrahedron Lett.* **2010**, *51*, 2244–2246.
- [5] a) E. Marcantoni, M. Massaccesi, E. Torregiani, G. Bartoli, M. Bosco, L. Sambri, *J. Org. Chem.* **2001**, *66*, 4430–4432; b) G. Bartoli, M. Bosco, A. Carlone, M. Locatelli, E. Marcantoni, P. Melchiorre, L. Sambri, *Adv. Synth. Catal.* **2006**, *348*, 905–910.
- [6] S. Hanada, A. Yuasa, H. Kuroiwa, Y. Motoyama, H. Nagashima, *Eur. J. Org. Chem.* **2010**, 1021–1025.
- [7] Nagashima *et al.* reported that the formed ionic intermediates, [Si]⁺...[Ru₅-H]⁻, initiates cationic ring-open-

- ing polymerization of cyclic ethers and addition polymerization of vinyl ethers, see a) H. Nagashima, A. Suzuki, T. Iura, K. Ryu, K. Matsubara, *Organometallics* **2000**, *19*, 3579–3590; b) H. Nagashima, C. Itonaga, J. Yasuhara, Y. Motoyama, K. Matsubara, *Organometallics* **2004**, *23*, 5779–5786.
- [8] Y. Motoyama, C. Itonaga, T. Ishida, M. Takasaki, H. Nagashima, *Org. Synth.* **2005**, *82*, 188–195.
- [9] a) S. Hosokawa, K. Teramoto, Y. Motoyama, *ChemistrySelect* **2016**, *1*, 2594–2602; b) S. Hosokawa, M. Toya, A. Noda, M. Morita, T. Ogawa, Y. Motoyama, *ChemistrySelect* **2018**, *3*, 2958–2961.
- [10] ¹H NMR (CDCl₃) of isobutene in the reaction mixture: δ = 1.72 (bs, 6H, CH₃) and 4.65 (bs, 2H, vinylic proton).
- [11] Review: J. Pesti, G. L. Larson, *Org. Process Res. Dev.* **2016**, *20*, 1164–1181.
- [12] For preliminary screening, we found some Ru, Rh, Ir, and Pt compounds show catalytic activity towards the deprotection reaction of **1a**, see Supporting Information.
- [13] We also examined the reactions of some compounds having other functional groups and found that reduction of formyl-, keto-, amido-, imino-, and nitro groups proceeded smoothly, but methyl ether and nitrile groups were tolerant under the present conditions. Details see Supporting Information.
- [14] Interestingly, the present Pd-catalyzed esterification and transesterification did not proceed with TMDS.
- [15] a) Guideline for Elemental Impurities: http://www.ich.org/fileadmin/Public_Web_Site/ICH_Products/Guidelines/Quality/Q3D/Q3D_Step2b.pdf; b) Implementing the Guideline on the Specification Limits for Metal Residues of Metal Catalysts or Metal Reagents: http://www.dgra.de/media/pdf/studium/masterthesis/master_reichert_u.pdf.
- [16] Review: a) A. M. Trzeciak, J. J. Ziolkowski, *Coord. Chem. Rev.* **2007**, *251*, 1281–1293. Representative papers: b) F. Zhao, M. Shirai, M. Arai, *J. Mol. Catal. A: Chem.* **2000**, *154*, 39–44; c) F. Zhao, K. Murakami, M. Shirai, M. Arai, *J. Catal.* **2000**, *194*, 479–483; d) R. G. Heidenreich, J. G. E. Krauter, J. Pietsch, K. Köhler, *J. Mol. Catal. A* **2002**, *182–183*, 499–509; e) F. Zhao, M. Arai, *React. Kinet. Catal. Lett.* **2004**, *81*, 281–289; f) K. Köhler, W. Kleist, S. S. Pröckl, *Inorg. Chem.* **2007**, *46*, 1876–1883.
- [17] We previously reported that the catalytically active species in the Pd/C-catalyzed silane-reduction of carboxamides is the soluble palladium species leached out from the carbon support, see: ref. 9a.

放射光 X 線および中性子回折技術に基づく合成高分子の結晶構造解析： 電子レベルからの構造物性相関解明を目指した新しい挑戦

(豊田工業大学) ○田代 孝二 (茨城大学フロンティア応用原子科学) 日下勝弘
(あいちシンクロトロン光センター) 山元博子 (SPring-8) 杉本邦久

Crystal Structure Analysis of Synthetic Polymers on the Basis of Organizedly-Combined Synchrotron X-ray and Neutron Diffraction Techniques

(Toyota Technological Institute) *Kohji Tashiro (ktashiro@toyota-ti.ac.jp)

(Ibaraki University) Katsuhiko Kusaka

(Aichi Synchrotron Radiation Center) Hiroko Yamamoto, (SPring-8) Kuniyoshi Sugimoto

Crystal structure information is basically important for the study of structure-property relation of synthetic polymers. In particular, the extraction of H atomic positions in the crystal lattice is indispensable for the theoretical prediction of physical property. In addition, the evaluation of bonded electron density distribution along polymer chain can make it possible to discuss the physical property of polymer from the electron level. In order to determine the H atomic positions and to estimate the electron density distribution, we have been challenged to combine the X-ray and neutron diffraction methods in highly quantitative manner.

合成高分子の究極の状態として結晶領域の構造を見極めることは、高分子の構造物性相関解明のための最も基本的に重要な情報である。特に、高分子鎖の外に張り出している水素原子の座標を決定することは、分子鎖間の水素原子間相互作用を知り、それに基づいて物理的性質を理論的に予測する上で不可欠である。また、電気伝導性や光学的性質の議論に際しては電子密度分布の情報が必要となる。密度汎関数法などの量子科学的計算に基づく予測がなされてはいるが、それを実験の立場から精密に決定した例は皆無である。このように高分子物質の水素原子位置や電子密度分布の様子を定量的に決定することは、今後の高分子科学の展開の上でも極めて大事な課題である。我々は、X線回折データと中性子回折データを有機的に結合し、これまで不可能と信じられてきたこれらの課題に挑戦した。

(1) 電子共役系高分子ポリジアセチレンにおける結合電子密度分布の定量的解明

この物質はモノマー結晶の光固相重合で得られる高分子巨大単結晶である。高輝度放射光研究センター (SPring-8) および日本原子力研究機構 J-PARC (MLF, i-BIX) において得られた X 線および中性子回折データを精細に解析し、両者のフーリエ変換の差として (X-N 法)、共有結合形成に際して偏位する電子密度分布の様子を合成高分子の分野で初めて描出することに成功した。密度汎関数法による計算結果と極めて良い一致を得ることが出来た (図 1)。

Kohji Tashiro et al., "Structure Analysis and Derivation of Deformed Electron Density Distribution of Polydiacetylene Giant Single Crystal by the Combination of X-ray and Neutron Diffraction Data", *Macromolecules*, 51, 3911–3922 (2018).

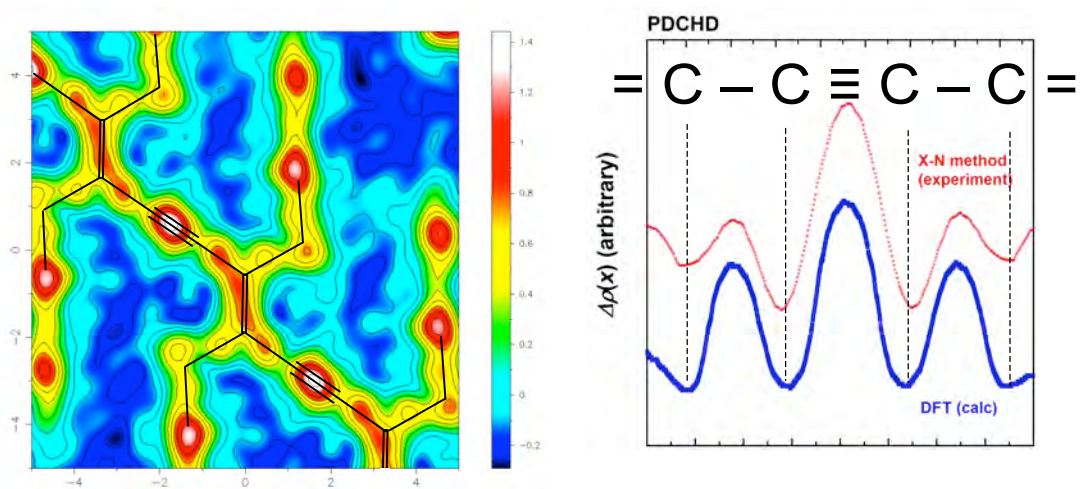


Figure 1. Bonded electron density distribution of polydiacetylene and its comparison with the density functional calculation result

(2) ポリビニルアルコールならびにそのヨウ素錯体の精密構造解析

ポリビニルアルコールおよびそのヨウ素錯体は工業的に極めて重要な物質であるが、それらの結晶構造は未確定のまま今日に至っている。我々は、これまでに、両者について X 線結晶構造解析を行い、「結晶構造を決定できた」...と想着てきたが、残念ながら、最近測定した中性子回折データを決して満足していないことが判明した。これら X 線と中性子回折データを併せた詳細な定量解析を行い、結晶構造への乱れ概念を新たに導入することで (図 2)、両者のデータを矛盾なく再現できることを見出した。高分子科学の黎明期に登場したポリビニルアルコールではあるが、その結晶構造は、およそ一世紀が経ってようやく確定させることが出来たことになる。

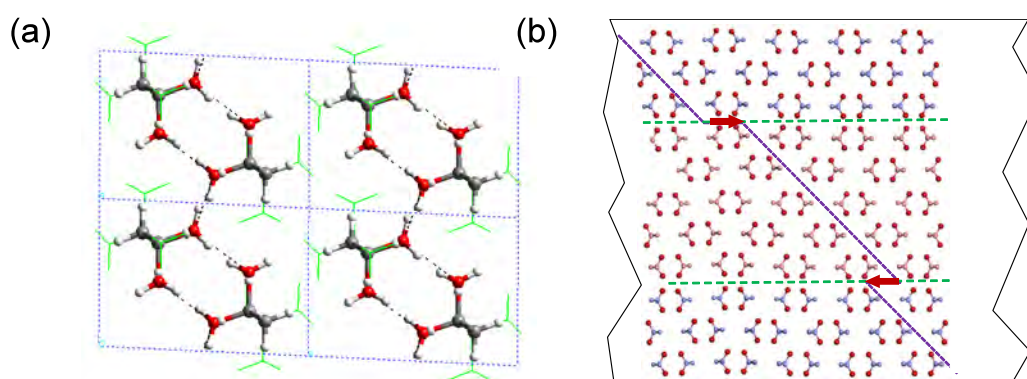


Figure 2. (a) Statistically-disordered crystal structure of PVA, (b) Schematic illustration of aggregation state of domains in the crystalline region of PVA.

田代孝二ら、「X 線および中性子回折データの統合的解析に基づくポリビニルアルコールおよびヨウ素錯体の結晶構造への乱れ概念導入」、第 69 回高分子学会年次大会にて発表予定 (2020 年 5 月)。

X-ray Crystal Structure Analysis of Poly(3-hydroxybutyrate) β -Form and the Proposition of a Mechanism of the Stress-Induced α -to- β Phase Transition

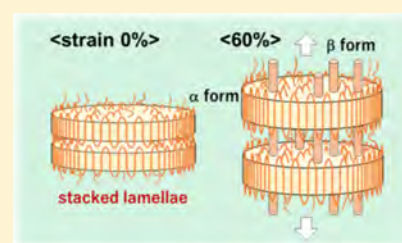
Suttinun Phongtamrug[†] and Kohji Tashiro^{*,‡}

[†]Department of Industrial Chemistry, Faculty of Applied Science, King Mongkut's University of Technology North Bangkok, Bangkok 10800, Thailand

[‡]Department of Future Industry-Oriented Basic Science and Materials, Toyota Technological Institute, Tempaku, Nagoya 468-8511, Japan

S Supporting Information

ABSTRACT: The crystal structure of poly(3-hydroxybutyrate) β crystal form has been analyzed on the basis of two-dimensional X-ray diffraction data. The all-trans zigzag chains are packed in the hexagonal unit cell of $a = b = 9.22$ Å, c (chain axis) = 4.66 Å, and $\gamma = 120^\circ$ with the space group $P3_221$. The upward and downward chains are statistically located at one lattice site at 50% probability. By combining the thus-analyzed structure information of the β -form with the previously reported structure information of the α -form, the geometrical relation between these two crystalline phases has been clarified in detail. The tension-induced α -to- β phase transition affects the higher-order structural change, as known from the small-angle X-ray scattering (SAXS) data collected in the tensile deformation process. By analyzing all experimentally obtained wide-angle X-ray diffraction and SAXS data, the following transition model has been proposed: the high tension to the oriented sample causes the increase of the long period of the α -form lamellae. As the tensile force is increased, the local stress concentration starts to occur at the short tie chain segmental parts in the amorphous region sandwiched between the stacked lamellae. These highly tensioned tie chains induce the α -to- β structural change in both amorphous and directly connected crystalline regions and generate the 40 Å-wide bundles of zigzag chain segments passing through several neighboring lamellae along the draw direction. These bundles are repeated with the averaged period of about 90 Å in the lateral direction perpendicular to the draw axis. Further stretching causes the cut of the highly tensioned extended chain parts, resulting in the formation of voids and finally the breakage of the whole sample before the completion of the phase transition from the α - to β -form.



1. INTRODUCTION

Poly(3-hydroxybutyrate) (PHB, $[-\text{CH}(\text{CH}_3)\text{-CH}_2\text{COO-}]_n$) is one of the representative biodegradable polymers produced naturally by microorganisms.^{1–4} The crystal structure is the most important basic knowledge for the study of the structure–physical property of this polymer from the microscopic point of view. PHB is known to crystallize into two crystal modifications, that is, the α -form and the β -form.^{5–10}

The α -form is normally obtained by cooling from the melt. The drawing of this sample gives the uniaxially oriented α -form sample. About forty years ago, Cornibert and Marchessault^{5,7,8} and Yokouchi et al.⁶ reported the crystal structure models of the α -form by performing the X-ray diffraction data analysis. Sato et al. studied the structure of the α -form from the viewpoint of vibrational spectroscopy.^{11–14} Using a maximum entropy method, Sasaki et al.¹⁵ estimated the electron density distribution of the α -form by utilizing these previously proposed crystal structures. However, these X-ray-analyzed crystal structure models are difficult to assume as accurate models, judging from the relatively small number of observed X-ray diffraction spots: 24 (Cornibert and Marchessault⁵) and 42 (Yokouchi et al.⁶). Wang and Tashiro¹⁶ collected two-

dimensional (2D) X-ray diffraction data of the oriented α sample using a Mo $K\alpha$ X-ray beam of short wavelength ($\lambda = 0.71$ Å), different from the previous reports using a Cu $K\alpha$ X-ray beam of 1.54 Å wavelength. The observed diffraction spots were 70 at room temperature and 94 at -190 °C, much more than the abovementioned two cases, making it possible to deduce more accurate structural parameters. The unit cell of the α -form is of the orthorhombic type with $a = 5.73 \pm 0.01$ Å, $b = 13.15 \pm 0.02$ Å, and c (fiber axis) = 5.93 ± 0.01 Å at 23 °C, and $a = 5.67 \pm 0.01$ Å, $b = 13.02 \pm 0.01$ Å, and c (fiber axis) = 5.91 ± 0.01 Å at -140 °C. Two T_2G_2 chains are packed in the cell with the space group $P2_12_12_1-D_2^4$, as shown in Figure 10 in a later section.

On the other hand, the details of the crystal structure of the β -form have not yet been determined. The β -form is obtained by applying a tensile force to the oriented α -form.^{4–10} However, the transition does not occur completely, and the α - and β -forms coexist even in the sample tensioned strongly just before the occurrence of the breakage.^{17–27} The reason for such an

Received: February 1, 2019

Revised: March 7, 2019

Published: April 4, 2019

incomplete transition behavior must be understood from the structural point of view, including the higher-order structural change.

First of all, however, it is indispensable to clarify the crystal structure of the β -form as a basic and significant knowledge for the discussion. When the literature was searched thoroughly, we found only the symposium abstracts by Sato et al.^{28,29} They prepared the α , β -mixed sample by applying a high tensile force to the oriented α -form sample and measured the X-ray diffraction pattern. Because the X-ray diffraction peaks of the β -form are located between the layer lines of the α -form (see a later section), the positions of the β -form diffraction spots were read out on the observed 2D diffraction pattern. The thus-detected β -form diffraction peaks were indexed using an orthorhombic unit cell with $a = 5.28$ Å, $b = 9.20$ Å, and c (fiber axis) = 4.69 Å. The c -axial length corresponds to the zigzag conformation of the molecular chain as already pointed out in the literature.^{6,7,28,29} Unfortunately, however, the chain packing structure could not be analyzed by those authors. During the preparation of the present report, we had found out their abstract.^{28,29} That is to say, without any information, we measured the 2D X-ray diffraction pattern and analyzed the data independently of them. As will be reported in the present paper, we have obtained the 2D X-ray diffraction pattern of the β -form by subtracting the diffraction pattern of the α -form from the observed 2D diffraction pattern, from which the peak positions and the one-dimensional (1D) diffraction profiles along the layer lines were read out. The thus-extracted β -form spots were indexed using the various possible unit cell parameters including the orthorhombic cell reported in the literature.^{28,29} The zigzag chains were packed in these unit cells, and the crystal structural models were built up by employing various possible space group symmetries. These structure models were modified so that all of the observed layer line profiles were reproduced as well as possible. Finally, the hexagonal packing mode was found to give the best reproduction of the observed data. In the first part of the present paper, we will describe the details of the structure analysis of the β -form.

The polarized infrared (IR) spectral data of the α - and β -forms are also presented here, which are useful for the characterization of the α - and β -forms using the spectroscopic data in addition to the Raman data reported in the literature.¹⁴

As will be described in the second half of the present paper, the thus-determined crystal structure information of the two crystalline forms allows us to discuss the characteristic behavior of the α -to- β phase transition by using the wide-angle X-ray diffraction (WAXD) and small-angle X-ray scattering (SAXS) data. Several papers were reported already to describe the change of WAXD and SAXS patterns during the strain-induced transition.^{17–27} However, the structural images derived in those papers are not necessarily consistent with each other. We need to interpret the SAXS data again by combining with the crystal structure information of both the α - and β -forms. The anisotropic X-ray diffraction pattern measured for the doubly oriented sample was useful to know the spatial relation between the α and β crystalline regions. As already pointed out, the α -to- β transition of PHB is not completed before the sample breakage. This might be a good hint for the discussion of the phase transition behavior. One model is proposed here by combining all of the observed information consistently.

PHB is one of the most important biodegradable polymers, but the behavior under the externally applied mechanical force is still ambiguous. The clarification of the chain aggregation

structure in the β -form crystallites and its role in the mechanical deformation behavior may be a key point for understanding the essential feature of PHB.

2. EXPERIMENTAL SECTION

2.1. Samples. Bacterially synthesized PHB sample was obtained from Dr. Kumar Sudesh, Malaysia. The molecular weight of the PHB sample used here was $M_w \approx 500\,000$ g/mol and $M_n \approx 160\,000$ g/mol, which was determined by the gel permeation chromatography analysis in chloroform at 40 °C using polystyrene as a standard. The uniaxially oriented samples were prepared by stretching the melt-quenched samples (mp 175 °C) about 10 times the original length at 0 °C in ice–water bath. PHB is quite brittle and easy to break at a high temperature. The hot drawing mostly causes breakage of the sample.³⁰ The stretching at around the glass transition (0–4 °C) makes it relatively easy to get the highly oriented sample as reported in the literature.^{17–27} For the IR measurement, the film was prepared by casting from the chloroform solution, followed by the melt (180 °C) and quenching into ice–water bath. The thus-obtained amorphous film was stretched by 10 times the original length at 0 °C to prepare the uniaxially oriented film of about 20 μ m thickness, which was annealed at 160 °C in a hot air oven under tension. The doubly oriented sample was prepared by rolling the uniaxially oriented sample by about 2 times the original length at room temperature, followed by heat treatment at 100 °C for 30 min.

2.2. Measurements. The 2D WAXD patterns of the uniaxially oriented samples were measured using a Rapid-2 and an R-axis VII X-ray diffractometers (Rigaku, Tokyo), both of which possess the imaging plate detector of a cylindrical camera type (radius 127.4 mm) and that of a flat camera type (a sample-to-detector distance 110 mm), respectively. The incident X-ray beam was a graphite-monochromatized Mo $K\alpha$ with 0.711 Å wavelength. The uniaxially oriented α -form sample was set on a small homemade stretcher. A series of 2D WAXD patterns were measured at the stepwise-changed constant strains. The half-width of the diffraction spots along the 2θ direction was evaluated quantitatively after the correction of the slit width using the aluminum powder as a standard. The 2D SAXS patterns were measured for the sample set on a small homemade stretching holder installed on a Rigaku NANO-Viewer X-ray diffractometer, where a Cu $K\alpha$ X-ray beam (the wavelength 1.542 Å) was focused on the sample position by a confocal mirror (Max-Flux optical system³¹).

The polarized IR spectra were measured for the oriented films in the stepwise stretching process at room temperature using an Agilent FTS7000 Fourier transform infrared (FTIR) spectrometer with a resolution of 2 cm^{-1} .

2.3. X-ray Crystal Structure Analysis. The 2D WAXD pattern measured for the highly tensioned sample was found to consist of the reflections originated from the mixed α and β crystals. The WAXD pattern of the highly oriented α -form was also measured. The 2D WAXD pattern of the highly oriented β -form was extracted by subtracting the 2D diffraction pattern of the pure α -form sample from the observed diffraction pattern of the α , β -mixed sample. The peak positions and the diffraction profiles along the layer lines were obtained from the thus-extracted 2D diffraction pattern. The indexing of these observed spots was made by a trial and error method, and the unit cell parameters were estimated. The repeating period along the chain axis was estimated using a Polanyi's equation for the spacings between the layer and equatorial lines.^{32–34} The molecular chain conformation was estimated using a conformational analysis (energy minimization), with the repeating period fixed to the experimental value. The calculation was performed using a commercial software Cerius² (BIOVIA, version 4.10). These energetically minimized chains were packed in the unit cell. The relative positions and orientations of the chains were modified in various ways so that the calculated X-ray diffraction profiles reproduced the observed data as best as possible. At the same time, the packing energy was calculated to check the reasonableness of the packing structure, in particular, the nonbonded H···H distances between the neighboring chains. Because the total number of the observed X-ray diffraction spots was too small to perform the structural

refinement, the best candidate obtained in the abovementioned analyzing process was proposed as the most plausible crystal structure of the β -form.

3. RESULTS AND DISCUSSION

3.1. X-ray Diffraction Measurement in the α -to- β Phase Transition. Figure 1 shows the 2D WAXD patterns measured for the uniaxially oriented PHB samples in the stepwise stretching process starting from the oriented α -form. Figure 2a shows the 1D diffraction profile obtained along the equatorial line. In the case of the thermally annealed sample [Figure 1a], the WAXD pattern at 0% strain is that of the typical highly oriented α -form. As indicated by arrows, at around 10–15% strain, the β -form peaks started to appear and increased in intensity. The peaks are broader but spotlike, suggesting the highly oriented crystallites of small size. In parallel to the generation of the β -form, the relative intensity of the α -form peaks decreased, but the decreasing rate was not very fast. The half-width of the α diffraction peaks along the 2θ direction became wider, indicating the decrease of the α crystallite size along the lateral direction, as evaluated using the Scherrer's equation^{32,33} [see Figure 2b]. Contrarily, the β -form peak became relatively sharper, indicating an increase of the crystallite size. It must be noted that the crystallite size itself was only about 40 Å, 1 order smaller compared with that of the α -form, ca. 270 Å. The latter became smaller gradually with an increase of tensile strain. Another point to notice is that, as the sample was

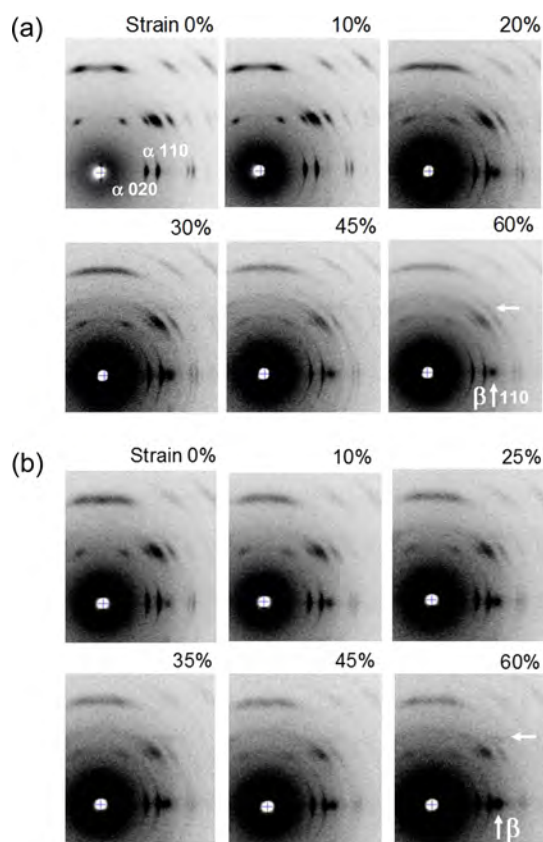


Figure 1. 2D X-ray diffraction patterns measured in the tensile deformation process of the uniaxially oriented PHB sample: (a) the annealed sample at 160 °C under tension and (b) the as-stretched sample. The measurement was performed using a flat imaging plate (Rigaku R-axis VII with Mo K α line).

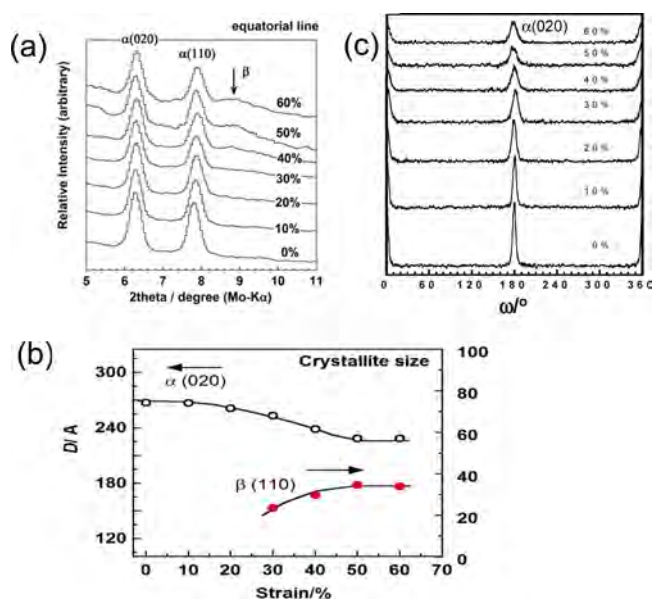


Figure 2. (a) Strain-dependent X-ray diffraction profiles of PHB scanned along the equatorial line [see Figure 1a], (b) X-ray coherent crystallite size estimated from the half-width of the diffraction spots, and (c) ω -scanned profile of the α -form 020 peak, where ω is the angle measured from the equatorial line along the arc. The wider profile corresponds to the lower degree of crystal orientation.

stretched to higher strain, some portions of the α -form crystallites show a slight reduction of the orientation, which look to overlap with the spots of still highly oriented α -form crystallites. Figure 2c shows this situation clearly, where the intensity distribution along the azimuthal angle ω is plotted for the α -form 020 diffraction (ω is the angle measured from the equatorial line axis). As the sample was tensioned, the ω -scanned peak profile became broader, indicating the lower degree of the α -crystal orientation (see Figure 1).

In contrast to the thermally annealed α -form sample [Figure 1a], the as-drawn sample contained the β -form even at the starting point [Figure 1b], suggesting that a residual tensile strain in the sample is appreciably large. The arc length of the diffraction spots intrinsic to the α -form did not decrease remarkably, different from the case of the annealed sample. The β -form diffraction spots along the equatorial and layer lines were spotlike, indicating a higher degree of the β crystalline region.

By summarizing the experimental data, the following information is extracted about the behavior of the α - and β -form crystallites in the stretching process:

- (i) The α -form exists in large crystallites (along the equatorial line). These crystallites are highly oriented at the starting point. With an increase of tension, the crystallite size of the α -form becomes smaller, and the degree of orientation in some parts of the α -form crystallites becomes lower, though slightly. These observations are more remarkable for the annealed sample compared with the as-drawn sample.
- (ii) By stretching the sample strongly, the β -form starts to appear and coexists with the α -form. The degree of orientation of the β -form crystallite is high, but the crystallite size is quite small, about 40 Å.
- (iii) The transition from the α - to β -form is not completed at around the strain 70%, beyond which the sample is broken.

(iv) As mentioned in (i), the thermally annealed α sample has larger crystallite size, but the crystallites become smaller and their orientation is slightly poorer as the sample is tensioned. The as-drawn sample contains both of the α - and β -forms even at the starting point of stretching. The orientation of the α -form does not become lower even by high stretching. The residual strain may be larger in the sample without any heat treatment.

3.2. Crystal Structure Analysis. **3.2.1. Unit Cell of the β -Form.** The 2D X-ray diffraction pattern of the β -form was obtained by subtracting the α -form diffraction pattern from that of the 60%-tensioned sample containing both of these crystal forms [Figure 1b]. The thus-extracted X-ray diffraction pattern of the highly oriented β -form is shown in Figure 3. As a whole,

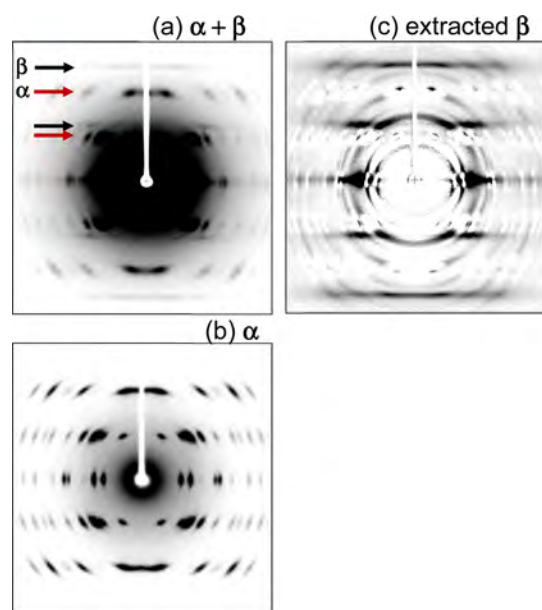


Figure 3. 2D X-ray diffraction patterns of PHB measured for (a) the mixture of α - and β -forms, (b) the pure α -form, and (c) the β -form pattern obtained by subtracting (b) from (a).

the diffraction spots are broad and the diffuse scatterings overlap these Bragg spots. The equatorial and layer lines were obtained up to the third line. The 1D profiles were calculated by integrating the individual layer lines with some span. The obtained profiles are shown in Figure 4. The repeating period along the chain axis was estimated from the observed spacings between the equatorial and various layer lines on the basis of the so-called Polanyi's equation.^{32–34} The c -axial length is 4.66 Å. This value suggests the zigzag chain conformation for the β -form, as reported in the literature.^{6–8,28,29}

The various candidates of the unit cell parameters were checked for indexing the observed diffraction spots, and the following two types of cells were obtained:

- (i) $a = 5.33 \text{ \AA}$, $b = 9.22 \text{ \AA}$, c (chain axis) = 4.66 Å, $\alpha = \beta = \gamma = 90^\circ$
- (ii) $a = b = 9.22 \text{ \AA}$, c (chain axis) = 4.66 Å, $\alpha = \beta = 90^\circ$, $\gamma = 120^\circ$

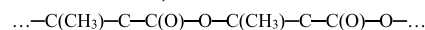
The ratio b/a in the candidate (i) is $\sqrt{3}$, and the unit cell (i) is apparently the same as that of the pseudo-hexagonal cell (ii). However, the space group symmetry should be different between them. The observed density of a bulk PHB sample was about 1.2 g/cm³.⁸ The crystal density of the α -form is 1.28

g/cm³.¹⁶ If a similar density is assumed for the β -form, the two zigzag chains are packed in the unit cell (i). In the unit cell (ii), three zigzag chains are contained. The calculated density of the β -form is 1.25 g/cm³.

3.2.2. Chain-Packing Mode of the β -Form. Now let us estimate the most plausible space group symmetry for the β crystal form. All possible space groups were checked³⁵ to know whether they could reproduce the observed X-ray diffraction data as a whole. By referring to the packing density of the chains in the cell, as mentioned above, and the energy stability calculated with a commercial software Cerius² (BIOVIA), where the potential function parameters used were COMPASS force field,³⁶ the plausible candidates of the space group were extracted as follows: $P2_12_12_1$, $Pnma$, $P12_1/n1$, $P112_1/n$, $P3$, $\bar{P}3$, and $P3_221$. The structure models of these space groups and the corresponding X-ray diffraction profiles along the layer lines are shown in the Supporting Information. By comparing the observed X-ray diffraction profiles along the $hk0$, $hk1$, $hk2$, and $hk3$ layer lines with those calculated for the models, the crystal structure model of the space group $P3_221$ was found to reproduce all diffraction profiles totally, as seen in Figure 4. In the calculation of these X-ray diffraction patterns with a software of Cerius², the following parameters were used: the crystallite size 70 Å × 70 Å × 70 Å, the crystal strain 0.5% × 0.5% × 0.5%, the isotropic temperature factor for C, O, and H atoms commonly 10 Å², and the degree of chain orientation 3.0°. The comparison of the 2D X-ray diffraction pattern is made in Figure 5. The crystal structure is shown in Figure 6. The atomic fractional coordinates are listed in Table 1. The geometrical parameters are listed in Table 2. As seen in Figure 6, the three chains and their counter chains with the opposite chain direction are packed at the probability 50% at each lattice site.

3.2.3. Introduction of Disorder. In the X-ray diffraction pattern of the β -form (Figure 5), the streaks are detected along the layer lines, suggesting the disorder of the relative height between the neighboring chains. As a trial, the structure model shown in Figure 6 was extended by 5 × 5 times along the a and b axes of the original unit cell, in which 75 chains were contained. The relative height along the c -axis was randomly shifted by 0 to ±0.25 c for all chains. The X-ray diffraction pattern was calculated as shown in Figure 5c, where the streaks were detected along the layer lines. The calculated X-ray diffraction profiles along the layer lines were slightly modified because of this streak effect, but the agreement with the observed profiles is almost the same even after the introduction of streaks [see Figure 4b] since the streak intensity was not very strong.

3.2.4. Comparison of Packing Structure between α - and β -Forms. Figure 7 compares the chain conformation between the α - and β -forms. The chain conformation of the α -form consists of a repetition of two monomeric units with the approximate (TTGG)₂ helical segment in a period 5.93 Å.¹⁶ These two units are related by the 2₁ screw symmetry along the c -axis. The conformation of the β -form is almost fully extended with the TTT... sequence (more strictly speaking, T'T'T' for T' = 152° and T = 172°). The repeating period 4.66 Å is for one monomeric unit, which is much longer than that of the α -form (=5.93 Å/2 units = 2.97 Å).



α	-52° -47° -175° 152°	-52° -47° -175° 152°
β	171° 152° -173° -152°	171° 152° -173° -152°

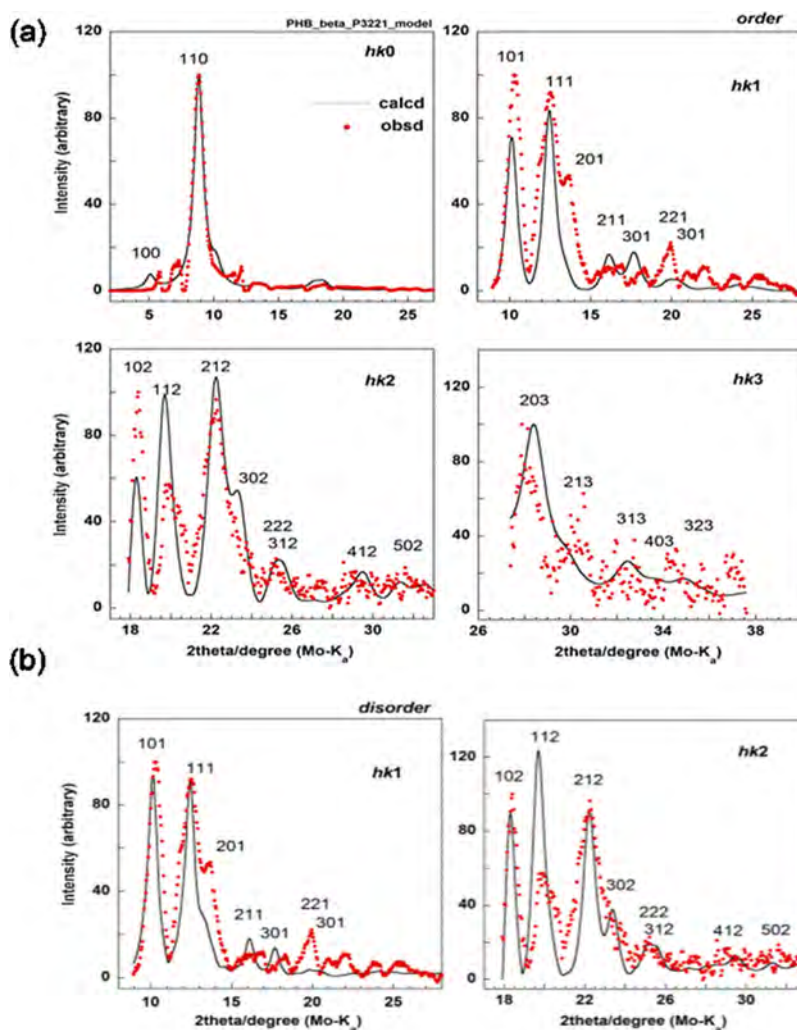


Figure 4. Comparison of the X-ray diffraction profiles along the various layer lines observed for PHB β form with those calculated for the model with the space group $P3_221$: (a) the regular packing model and (b) the disordered model with the random relative height of the neighboring chains along the c -axis.

As shown in Figure 10, for the α -form, the two chains are packed in the ab plane of the unit cell size $a = 5.73 \text{ \AA}$ and $b = 13.15 \text{ \AA}$; then, the effective cross-sectional area of one chain is 37.7 \AA^2 . On the other hand, the hexagonal unit cell of the β -form contains three chains in the area of $ab \cdot \sin(\gamma) = 73.6 \text{ \AA}^2$. The effective cross-section of one chain, 24.5 \AA^2 , is about 65% of that of the α -form. For one monomeric unit, the effective volume of the α -form, $111.7 \text{ \AA}^3 (= 37.7 \text{ \AA}^2 \times 2.97 \text{ \AA})$, is almost equal to that of the β -form, $114.4 \text{ \AA}^3 (= 24.5 \text{ \AA}^2 \times 4.66 \text{ \AA})$. In this way, the β -form takes the effective monomer volume similar to that of the α -form, but the conformation of one monomeric unit changes remarkably by the strong tension along the chain axis: from the transversely long shape of the α -form to the longitudinally long shape of the β -form, attended with the contraction in the lateral direction.

3.2.5. Transition from the α - to β -Form. Once we know the crystal structures of the α - and β -forms, we may be able to investigate the structural transition from the α - to β -form. The spatial relation of these unit cells must be clarified at first. The X-ray diffraction pattern measured in the end direction or along the draw axis is useful. For this purpose, the doubly oriented sample was prepared by rolling the uniaxially oriented α sample at room temperature. The rolled sample contained both of the diffraction

spots of the α - and β -forms. The X-ray diffraction patterns measured in the end, through, and edge directions of the doubly oriented sample is shown in Figure 8. Figure 9 gives the information deduced from the end pattern or about the a^*b^* reciprocal lattice plane. As shown in (a), the azimuthal scan of the (110) diffraction of the β -form shows the repeated intensity change at every 60° around the c^* axis (the draw axis). The 020 diffraction of the α -form shows mainly the four peaks, indicating the twin structure directing toward the four directions (the small peaks are detected at the azimuthal angle $\phi = 90^\circ$ and 270° in Figure 9, which means the existence of the α -form crystallites directing into these directions, but the relative content is small and neglected in the present discussion). By combining the reciprocal lattices between the α - and β -forms, as seen in Figure 9b,c, we can know the spatial relation in the doubly oriented sample as follows: the b^* axis of the α -form orients at an angle of ca. $\pm 30^\circ$ from the normal to the rolled plane, and the b^* (a^*) axis of the hexagonal β -form directs to 0° , 60° , and 120° from the rolled plane. This indicates that the b -axis is common to these two phases in the doubly oriented sample [Figure 9d].

As shown in Figure 10b, by overlapping the unit cell structures of the α - and β -forms so that the b -axis becomes common, we notice that the individual chain in the α crystal lattice can be

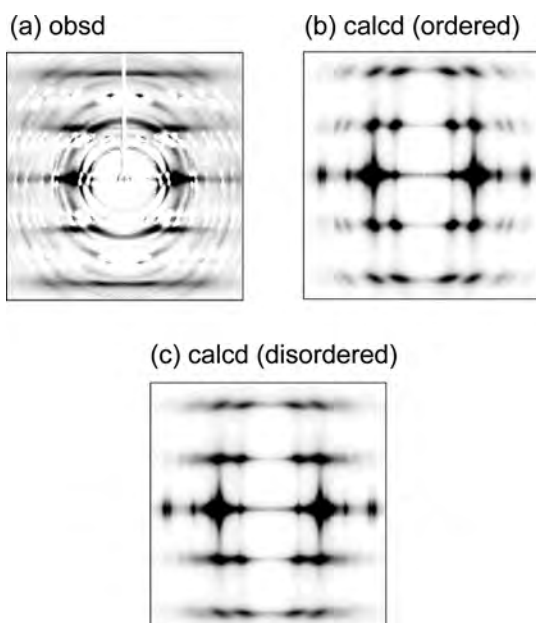


Figure 5. 2D X-ray diffraction pattern of the uniaxially oriented PHB β -form. (a) Observed, (b) calculated for the regular $P3_221$ model, and (c) calculated for the disordered model.

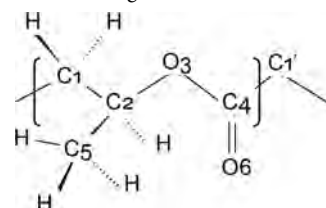
connected to that of the β crystal lattice in one-to-one relation. The application of a tensile force causes the translational shift of the α chains to the positions of the β chains: the shift direction is preferentially parallel to the b -axial direction with a small shift to the a -axial direction also. The shift size is proportional to the distance from the arbitrarily chosen central chain, that is, the translational movement occurs approximately in an *affine* mode, as indicated by red arrows in Figure 10b. Because the effective cross-sectional area of the β zigzag chain is only 65% of that of the α helical chain, such *affine* deformation causes the reduction of the crystallite size in the lateral direction.

3.2.6. IR Spectra of the α - and β -Forms. The Raman bands of the β -form were reported in a literature;¹⁴ but the IR spectral information of the β -form had not been obtained. The IR spectra of the β -form are also sensitive to the chain conformation and so useful for the structural study from the vibrational spectroscopic point of view. Figure 11a shows the polarized IR spectra measured for the oriented PHB films of the pure α -form and the mixture of α - and β -forms. In Figure 11b, the strain dependence of the polarized IR spectra is shown. Several new bands

Table 1. Atomic Fractional Coordinates of PHB β -Form^a

no.	element	x	y	z
1	C	0.46	-0.01	0.67
2	C	0.35	-0.03	0.92
3	O	0.44	0.01	1.18
4	C	0.35	-0.07	1.41
5	C	0.28	0.09	0.90
6	O	0.20	-0.17	1.41
1-H1	H	0.56	0.12	0.64
1-H2	H	0.52	-0.09	0.71
2-H	H	0.24	-0.16	0.92
5-H1	H	0.19	0.06	0.72
5-H2	H	0.21	0.09	1.10
5-H3	H	0.38	0.22	0.87

^aThe unit cell parameters are $a = b = 9.22 \text{ \AA}$, c (chain axis) = 4.66 \AA , and $\gamma = 120^\circ$. The numbering of atoms is shown below.



increased in intensity with an increase of the tensile strain, from which the IR bands characteristic of the β -form are picked up at $446 (\parallel)$, $857 (\parallel, \perp)$, $969 (\parallel)$, $1082 (\parallel)$, $1185 (\parallel)$, $1291 (\parallel)$, and $1310 (\parallel) \text{ cm}^{-1}$, where \parallel and \perp indicate the band with the stronger intensity when the electric vector of the IR beam is parallel and perpendicular to the draw axis, respectively. The bands with the red arrows in Figure 11a are assigned to these β -form bands. The factor group of the zigzag chain is isomorphous to the point group C_1 . All of the possible bands are predicted to be active in the IR and Raman spectra, and so the vibrational modes are coupled together, giving the complicated spectral profiles.

Using the data of strain-dependent IR spectral change shown in Figure 11b, the integrated absorbance of the IR bands was evaluated and plotted against the stress. Figure 12 shows the results. The strain dependence of the integrated intensity is plotted in (a) for the IR bands at $954 (\alpha)$ and $970 (\beta) \text{ cm}^{-1}$. The relative content of the α -form decreases and that of the β -form increases as the sample is stretched. Figure 12c shows the stress dependence of the intensity ratio between the α and β IR bands,

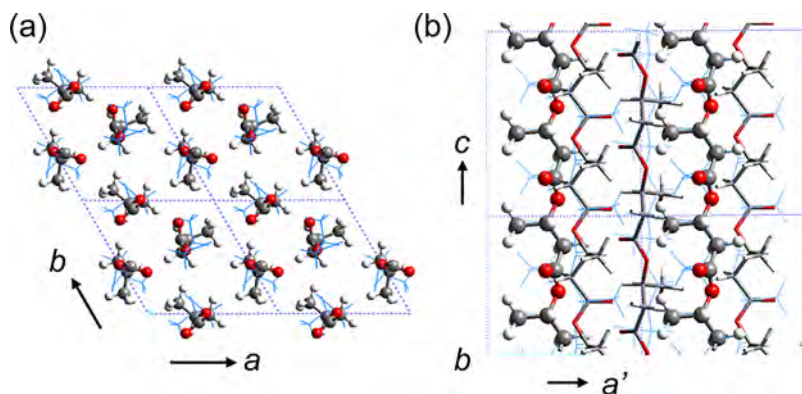
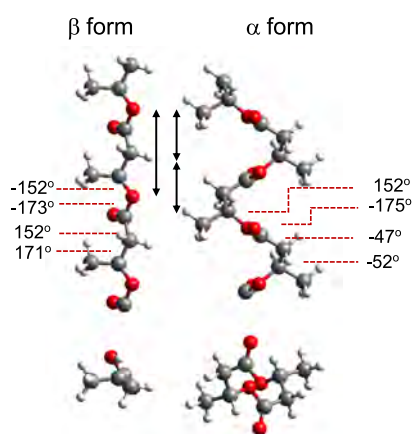


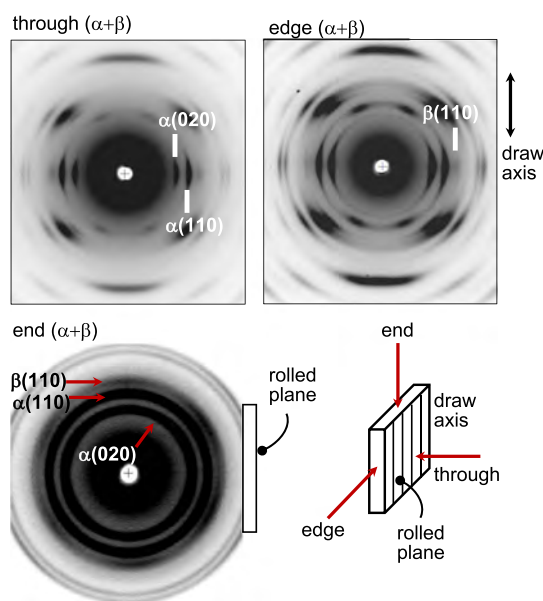
Figure 6. Crystal structure of the PHB β -form. The solid line and blue thin-line chains are positioned at the same lattice site at the statistical probability of 50%.

Table 2. Internal Structure Parameters of the β -Form Chain

bond length/Å	bond angle/deg	internal rotation angle/deg	intermolecular H...H distance/Å
C1C2 1.51	C1C2C3 107.9	C1C2O3C4 -151.6	CH ₂ ...CH ₃ 1.97, 2.47, 2.99
C2O3 1.42	C2O3C4 113.9	C2O3C4C1' -172.5	CH ₃ ...CH ₃ 2.11, 2.59, 2.16, 2.87, 2.99,...
O3C4 1.35	O3C4C1' 108.1	O3C4C1'C2' 151.7	
C4C1' 1.52	C1C2C5 112.7	C4C1'C2'O3 170.6	
C4=C6 1.21	O3C2C5 110.3	C4C1C2C5 -67.4	
C2C5 1.53	O3C4O6 124.9	C1C2C5H 68.1, -171.7, -52.9	
CH 1.10	C1'C4O6 126.9	C2O3C4O6 4.1	
	HC1H 109.2	C2C1C4O6 -24.8	
	HCSH 107.8, 107.5, 108.2		
	CCH		
	CH ₃ 110.2, 110.7, 112.3		
	CH ₂ 110.1, 111.4, 110.4, 109.7		

**Figure 7.** Chain conformation of PHB β -form (left) and PHB α -form.¹⁶

where the ratio was used because the film thickness decreased with stretching. A similar plot was also made for the X-ray 020 (α) and 110 (β) diffraction peaks. The β/α intensity ratio increases almost linearly with the stress. Besides, this increment occurs in parallel to the strain because the stress and strain change almost linearly, as seen in Figure 12b, except the early stage of deformation. It must be noted here that the α -to- β transition started for the first time when the stress increased beyond a critical stress σ^* , about 70 MPa [see Figure 12c]. The same behavior was detected also for the X-ray diffraction data [Figure 12d]. These observations suggest that the α -to- β phase transition occurs following the concept of the stress-induced transition mechanism. Such a stress-induced transition was reported for the α -to- β phase transition of poly(tetramethylene terephthalate) (PTMT),^{37–42} poly(tetramethylene nathalate),⁴³ and poly(tetramethylene succinate),^{44–47} which occurs at a critical stress value; but, one different point is observed between the cases of PTMT and PHB. In the former case, the transition is completed at an almost constant stress (σ^*), during which the sample strain increases remarkably. As a result, the stress–strain curve shows a clear plateau region corresponding to the transition process. In the PHB case, the transition occurs

**Figure 8.** X-ray diffraction patterns of the doubly oriented PHB sample of the α - and β -form mixture measured along the through, edge, and end directions. In the end pattern, the diffraction intensity is not homogeneous but changes along the circles (refer to Figure 9).

beyond a critical stress, but the stress in the transition process is not kept constant, whereas it increases gradually as seen in Figure 12b. This difference might come from the difference in the degree of homogeneity of the stress distribution in the sample.^{43,47} In the PHB case, the stress may be appreciably heterogeneously distributed, and the timing to attain the critical stress is different depending on the position. This concept of the heterogeneous stress distribution will be utilized in the later discussion about the phase transition behavior of PHB.

3.3. The α -to- β Phase Transition and Higher-Order Structural Change. **3.3.1. SAXS Data.** The large tensile deformation of the oriented α sample causes the partial transition from the α -form to the β -form. The stress relaxation causes the return to the original α -form, although some amount of the β -form remains because of the residual strain in the sample. Some literature suggest that the β -form can be crystallized directly from the amorphous phase.^{7,19,22} However, the tensile stretching decreases the relative content of the α -form crystal and increases that of the β form crystal, as observed in both of WAXD and FTIR spectral data (Figures 2, 11, and 12). As will be discussed later, the crystallization of the β -form from the amorphous region might also occur at the same time in addition to the transition from the α -form. In the present study, therefore, the solid-state transformation to the β form is assumed to occur in *both* of the α crystalline and amorphous regions.

In many polymers, the phase transition occurring in the crystalline region is known to affect the higher-order structure composed of the crystalline and amorphous phases.^{48–51} The present PHB case is one of them.^{4,17–27} Once we know the details of the crystal structural change, the discussion becomes possible about the relation between the structural change in the crystalline region and the higher-order structural change.

The WAXD and SAXS patterns were traced in detail in the tensile deformation process. The 2D WAXD pattern change has already been shown in Figure 1, where the X-ray diffraction peaks of the α -form decreased in intensity and those of the β -

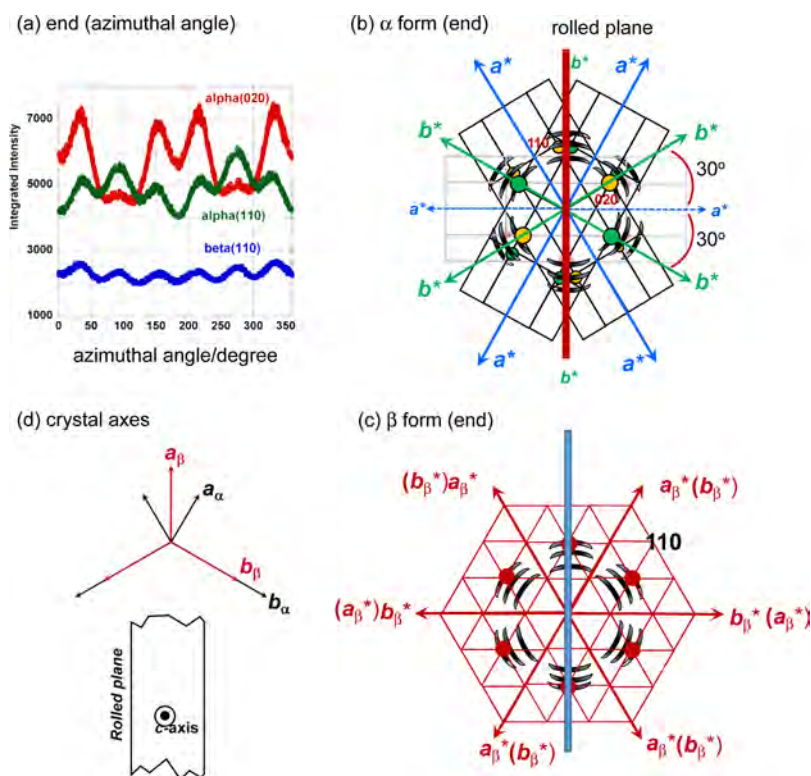


Figure 9. (a) Intensity distribution traced along the ω angle for the X-ray end diffraction pattern of the doubly oriented PHB $\alpha + \beta$ mixed sample (refer to Figure 8). (b,c) Indexing of the observed diffraction spots for the α - and β -forms, respectively. They are the twinned structures. (d) Spatial relation of the real lattices of the α - and β -forms in the doubly oriented sample. The b -axis is common to these forms.

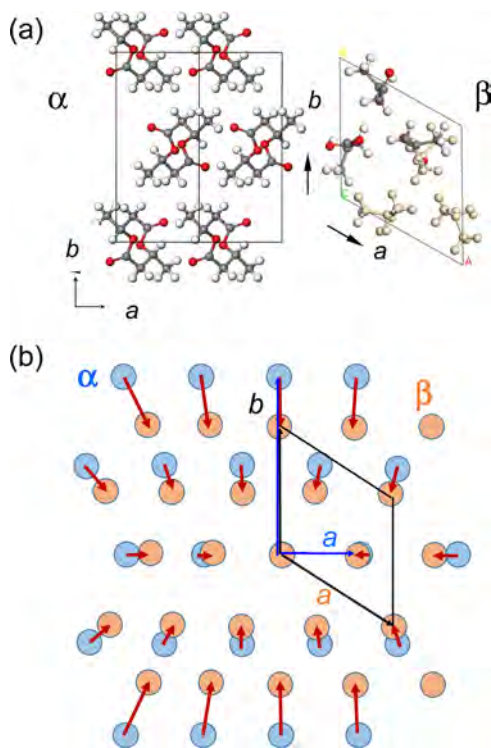


Figure 10. Geometrical relation between PHB α - and β -forms: (a) the unit cell and (b) the positions of the chains. The chains of the α -form (light blue) transform to the positions of the β -form chains, as indicated by the red arrows with an *affine* deformation mode mainly along the b -axis.

form increased instead. However, the sample was broken at around $\sim 70\%$ strain before the completion of the transformation to the β -form. Another important X-ray observation is the overlap of the spots coming from the still highly oriented α -form crystallites and the spots with slightly longer arc corresponding to some portion of the α -form crystallites of the lower degree orientation. The sample measured after the breakage regained the X-ray diffraction pattern with the comparatively higher degree of orientation. The reflections of the β -form are spotlike, although they are, as a whole, broader than the α -form, suggesting the highly oriented β crystallites with a small size.

Figure 13 shows the SAXS pattern change in the stretching process. The initial α sample shows the sharp 2-point scattering in the meridional direction, indicating the existence of the regularly stacked lamellar structure. The calculation of the stacked lamellar correlation function⁵² revealed the long period (LP) of ca. 110 Å. The lamellar thickness along the draw direction is about 50 Å. The X-ray coherent lateral size of the crystalline domain is about 270 Å, as estimated using the Scherrer's equation for the WAXD 020 reflection width of the α -form. As the sample was tensioned along the chain axis, the meridional scattering peak of the α phase was observed to shift to the lower q direction, and at the same time, a new peak was detected near the beam stopper, as shown in Figure 13. These overlapped peaks were separated into the components, and the lamellar correlation functions were calculated. The result is shown in Figure 13b. The LP value of the β phase was about 220 Å at around 10% strain, which increased almost linearly with strain up to ~ 400 Å. In parallel, the lamellar thickness of the β -form was also found to increase in parallel from 90 to 160 Å. In addition, it is noticed that the weak and diffuse scattering started

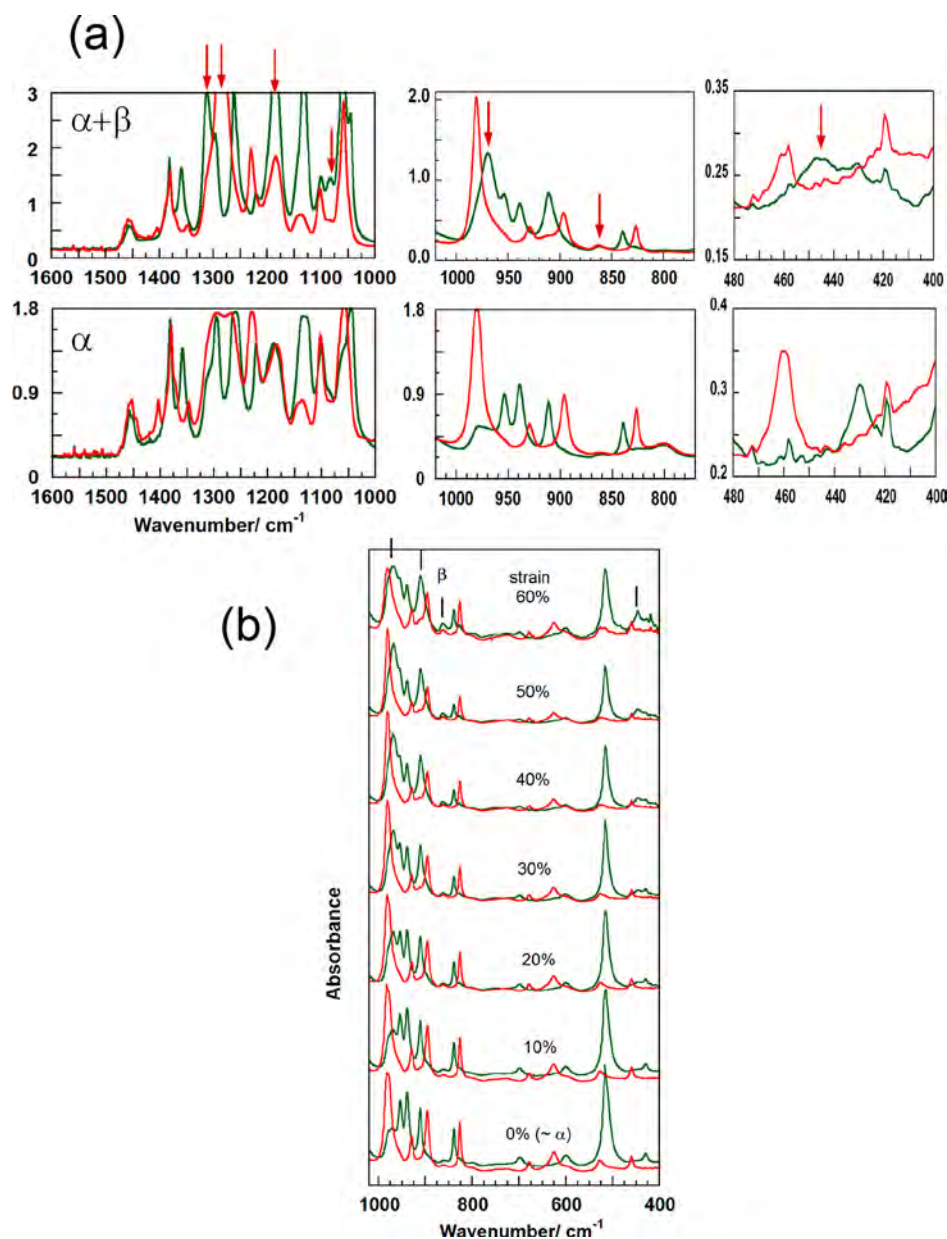


Figure 11. (a) Polarized IR spectra measured for the α -form (lower) and $\alpha + \beta$ mixed forms (upper) of the oriented PHB films. The latter data were obtained for the sample subjected to tensile deformation, as reproduced in (b). The \parallel (green) and \perp (red) indicate the spectra taken with the electric vector of the incident IR beam parallel and perpendicular to the draw direction.

to appear along the *horizontal* direction or along the direction perpendicular to the stretching direction [see Figure 13a,c]. The averaged repeating period was about 90 Å, but the period distributes in a wide range of ± 90 Å. As the tensile deformation proceeded, the distribution became relatively sharp (± 70 Å).

All of these observations are summarized in the following ways.

- (#1) In the transition from the oriented α -form to the oriented β -form, the relative content of the α -form decreases and that of the β -form increases with an increase of strain. The critical stress σ^* may exist, beyond which the transition occurs. The stress does not distribute very homogeneously, and the attainment to the critical stress cannot be made at the same timing at all positions. The transition does not finish completely, but the sample is broken before it. As well known, an increment of the molecular

weight may improve the brittleness of the sample, as already reported in refs.^{17–27,30} However, even when the PHB sample of an ultrahigh molecular weight of 10^6 g/mol order is stretched, the transition from the α - to β -form is still not perfect.^{17–27} This origin must be found out.

- (#2) The α -form shows the comparatively sharp WAXD reflections corresponding to the X-ray coherent crystallite size (ca. 270 Å) in the lateral direction and 50 Å (lamellar thickness) in the chain direction, whereas the β -form exhibits the smaller crystallite size (ca. 40 and 90 Å). The crystallite size of the α -form decreases gradually as known from the increase in the half-width of the WAXD diffraction peaks.
- (#3) The tensile force causes the *affine* deformation of the chain positions mainly along the *b*-axis common to both α and β lattices (Figure 10).

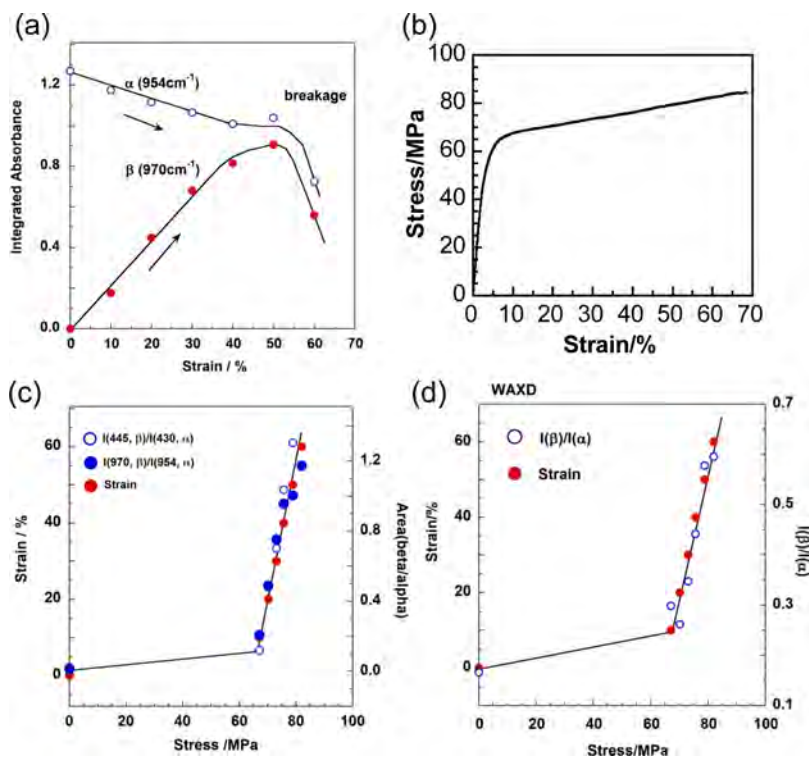


Figure 12. (a) Strain dependence of the integrated intensity of the IR bands characteristic of the α -form (954 cm^{-1}) and β -form (970 cm^{-1}). (b) Stress–strain curve measured in the experiment of (a). (c) Stress dependence of the integrated intensity of the IR band intensity ratio between the α - and β -forms. (d) Stress dependence of the integrated intensity of the X-ray diffraction intensity ratio between the α - and β -forms, where the 020 (α) and 110 (β) reflections were used.

- (#4) The SAXS pattern is interpreted to consist of the overlap of the crystalline lamellae of the α - and β -forms. Some parts of the regularly stacked lamellar structure of the α -form (LP ~ 110 Å) change to the lamellar structure of the β -form with the longer LP of 220 Å (at 10–20% strain). The LP values increase in an *affine* mode with an increase of strain up to 240 Å (α -form) and 400 Å (β -form). It must be noted that the LP of the β -form is remarkably longer than that of the α lamellae.
- (#5) The diffuse and weak SAXS peak is observed along the equatorial line, showing the existence of the repeated structure in the lateral direction. The period is about 90 Å in average and distributes in a wide range.
- (#6) In the tensile deformation process, the crystallite orientation of the α -form becomes worse, whereas the β -form crystallites exist with the high degree of chain orientation (see Figure 1).

3.3.2. Model of Higher-Order Structural Change. We have to build up the deformation model of the higher-order structure in the α -to- β transition so that all experimental data (#1)–(#6) can be explained without any contradiction. There might be various models to show the structural change in the higher-order structure level. Figure 14 shows the several possible models.

- (i) Model A: The crystalline lamellae of the α -form change to the β -form, but the amorphous region does not show any change except for the large extension. In this case, the LP (LP1) changes in an *affine* mode with strain, and the two different LPs do not generate since the electron density is not very much different between the α and β lamellae ($\rho_\alpha = 1.28$ g/cm^3 and $\rho_\beta = 1.25$ g/cm^3). This is against the experimental fact #4. Since the lamellar size remains large,

the SAXS peak does not appear along the lateral direction (#5). (The change of crystallinity may be an important point, but it cannot be judged here since the exact estimation of the crystallinity during the deformation is actually difficult because of the low intensity of the X-ray amorphous halo peak).

- (ii) Model B: The transition to the β -form occurs in the amorphous region only. This model was proposed in ref 7. The two LP peaks may exist, which come from the lamellar stacking of the α -form and that of the β -form. However, the α -form content is kept unchanged since no effect occurs in the α -form crystalline part, being inconsistent with the result #1.
- (iii) Model C: The β -form is created totally in the amorphous region sandwiched between the lamellae of the α -form. The α -form is not affected by this event. This model was proposed in refs. ^{17–24} The LP becomes shorter since the daughter lamella (β) is inserted into the original mother lamellae of the α -form, the density of which is almost the same between them. The shortening of LP is against the experimental fact #4. The α -form content has no change, not consistent with #1.
- (iv) Model D: This is the modification of model C. Some parts of the α -form lamellae are stressed and change to the β -form. The relative contents of the α - and β -forms are exchanged, but the α -form exists overwhelmingly since the transition occurs only locally (#1). The amorphous region connected to these local parts also causes the transition to the β -form. That is to say, some columns of the β crystallite are formed and pass through the several lamellae. The length of the column may be random. As a result, the two (or more) types of LPs will be generated as

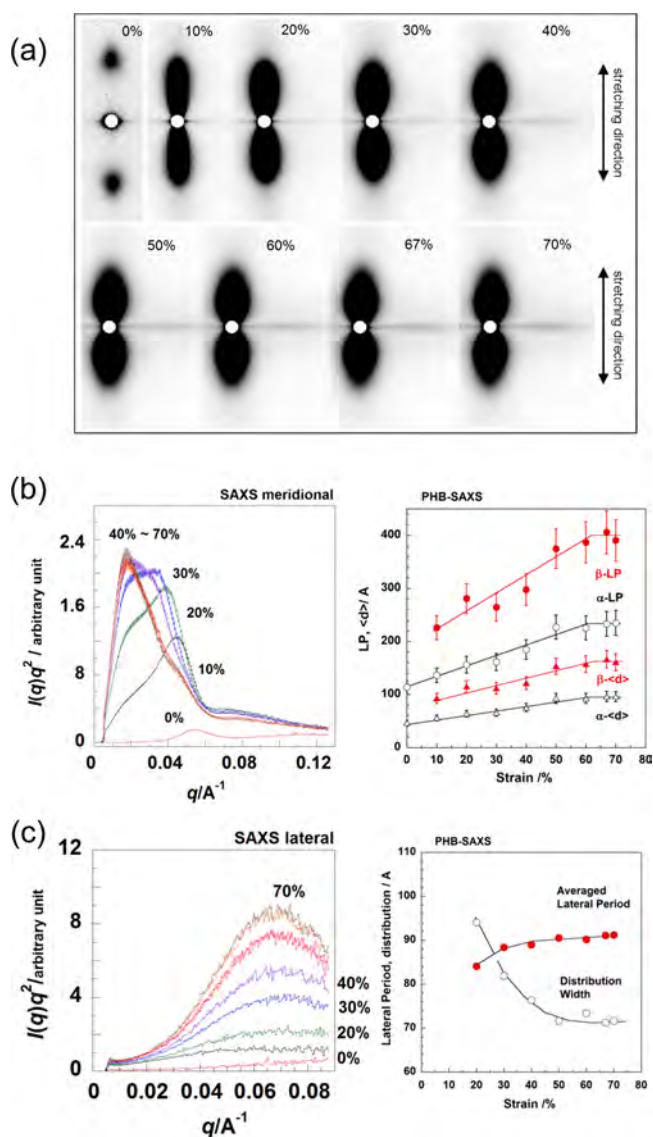


Figure 13. (a) SAXS patterns measured for the uniaxially oriented PHB sample under tension. (b) 1D profiles scanned along the meridional direction. (c) 1D profiles scanned along the horizontal line.

detected in the SAXS data (#4). This model requires the existence of some locally stressed tie chain segments, which pass through the neighboring lamellae along the drawing axis.

Conclusively speaking, our model proposed here is model D, though the other models A–C may also occur in parallel with some contributions. A more detailed structure model is illustrated in Figure 15. The mechanical deformation and the phase transition may be related in the following manners.

- The initial α crystallites form the regular lamellar stacking structure [Figure 15(2a)].
- As the tensile deformation is applied, the short tie chain segments start to be tensioned strongly, and the locally high stress is generated in these tie chain parts. Once the local stress exceeds a critical value σ^* , the transformation to the zigzag chain conformation of the β -form starts to occur in the highly strained tie chains and in the chain segments in the crystalline lamellae connected directly to these tie chains [Figure 15(1,2b)]. Because the tie chain

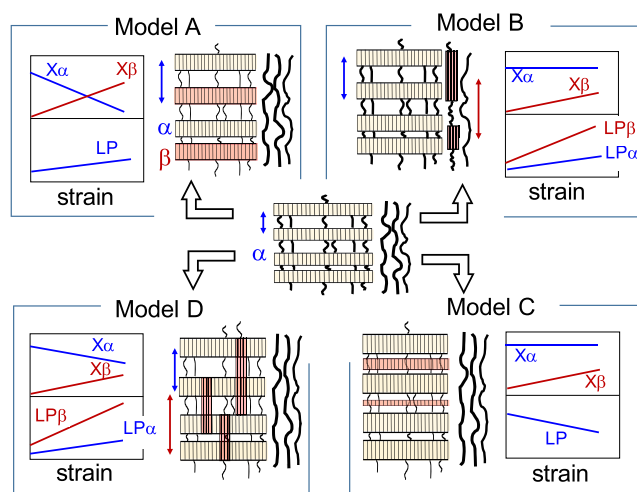


Figure 14. Illustrations of the various models showing the higher-order structural change induced by the tensile deformation of the oriented PHB sample. The higher-order structure was assumed to consist of the sacked lamellae and the parallel amorphous region. The predicted changes of the relative contents (X_α and X_β) and the averaged LPs (LP_α and LP_β) of the α - and β -forms are also illustrated.

lengths may distribute widely, the tensioning of the short tie chains may occur gradually and widely over the various positions (#1).

- The thus-created β crystalline bundles exist at various positions with the averaged period of about 90 Å, giving the streaky SAXS peak along the equatorial line [LP2 in Figure 15(1,2b)]. The width of the bundle is 40 Å (WAXD) to 70 Å (SAXS) in a and b directions. In the bundle of the β -form, the zigzag chains are packed together, but they are slipped irregularly along the drawing axis to cause the diffuse scattering in the WAXD pattern. As a result of this structural formation, cavities may be created between the β crystal bundles. The electron density difference between the crystallites and the cavities is higher than that between the crystalline and amorphous regions, causing a remarkable increase of the SAXS intensity along the meridional direction.
- Some shrinkage of the cross-sectional area may occur in the structural change from the α - to β -chain conformation. As a result, the α -chain segments located near the β crystalline bundles are pulled into the stressed part, and the tilting of the α chain segments may be induced [Figure 15(2b)], which is detected as the overlap of the longer arc with the original spotlike diffractions of the α -form in Figure 1.
- By increasing the stress furthermore, the highly tensioned tie chain segments cannot bear anymore against the too-high local stress, and they are finally broken to generate the radicals. These radicals react with the neighboring chain segments and accelerate the breakage of the surrounding chain segments.^{53–55} As a result, microvoids are generated. In the corresponding crystalline region, the contracted α -chain conformation is recovered [Figure 15(2c)]. These microvoids are fused into further larger macrovoids, which induce the rupture of the whole sample.^{53,54} Once the sample is broken, the stress is relaxed, and the whole system returns to the α -form quickly. The detection of some amount of the β -form in

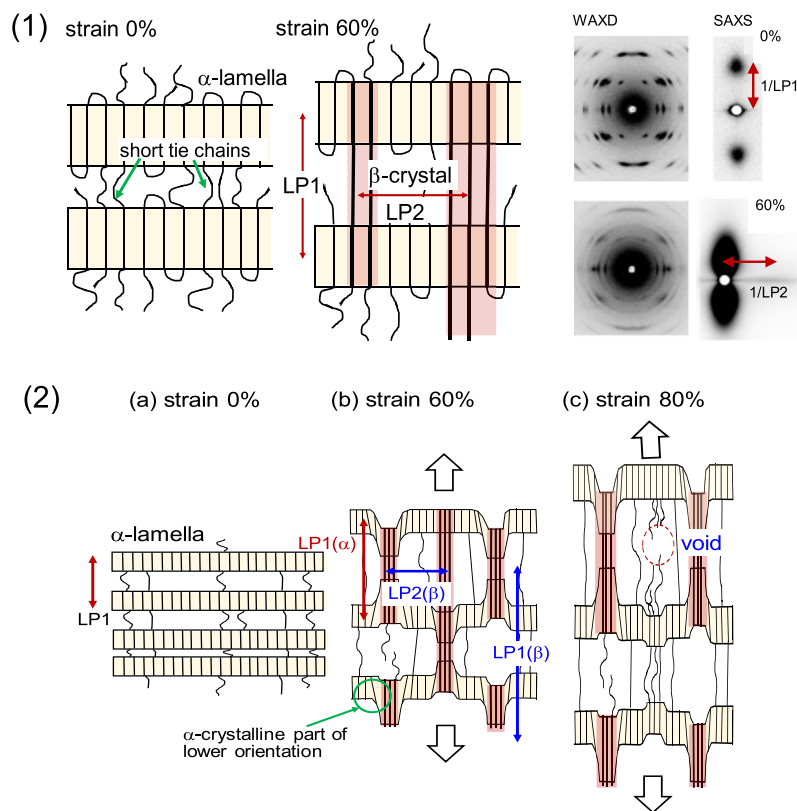


Figure 15. (1) Images of the higher-order structure of the a and b forms of the oriented PHB sample. The LPs LP1 and LP2 are defined as shown in the SAXS patterns. The short tie chains are assumed to exist in the amorphous region between the neighboring lamellae. (2) The mode-detailed illustration of the higher-order structure change in the tensile deformation of the oriented PHB sample. (a) Stacked lamellar structure of the α -form with short and long tie chains. (b) Tensile deformation induces the high extension of short tie chain segments. The lamellar domain connected to these strained tie chains transforms to the β -form structure. The LP, LP1, of the β bundle parts is much longer than that of the α -form. The β -form bundles are arrayed horizontally with the averaged LP, LP2. The α -form region adjacent to the β -form bundle is pulled toward the bundle, and the orientation becomes lower slightly. (c) Further tension causes breakage of these short tie chains and generates microscopic voids. The β -form parts return to the α -form.

the broken sample may be due to the imperfect relaxation or the residual strain in the local part of the sample.

These phenomena are detected more clearly for the sample annealed at a high temperature. The as-drawn (unannealed) sample contains higher amount of the β crystallites. This may come from the smaller lamellae and from the existence of the residual strain in the unannealed sample.

Another point to be noticed is that the spatial relation between these two crystalline phases is not random but they are related with the common b -axis (of course, the twin structure must be taken into account). If the β phase is generated simply in the amorphous phase (including the amorphous region between the neighboring lamellae), there may no spatial relation, but the crystal lattice of these two phases may direct toward arbitrary directions. Actually, they are oriented not randomly but with the abovementioned relative orientation. As illustrated in Figure 10b, the β phase is considered to be generated in the α -phase lattice with the common b -axis. This transition may affect the preferential orientation of the β phase generated in the tie chain segments in the highly tensioned amorphous phase.

3.3.3. Complete and Incomplete Phase Transitions. The stress-induced phase transition is observed for the various polymers. For example, poly(vinylidene fluoride) crystalline form II (TGT \bar{G} conformation) and form III (TTTGT $\bar{T}\bar{G}$) transform to form I of all-trans zigzag conformation by applying tensile force at a relatively low temperature.⁵⁶ These transitions are *irreversible*. Similar transitions were reported for poly-

(pivalolactone),⁵⁷ polypeptide (α -helix to β -pleated sheet),⁵⁸ α -to- β keratin,⁵⁹ and so forth. As already mentioned, the *reversible* transition is observed for PTMT^{37–42} and poly(tetramethylene succinate),^{44–47} in which the α -form of the contracted chain conformation transforms *reversibly* to the β -form of the fully extended conformation at a critical stress. The phase transition occurring in the crystallite affects the lamellar stacking structure, but the change is not very remarkable in the strain region of the transition, as known from the simultaneous measurement of WAXD, SAXS, and FTIR spectral data.⁶⁰ Different from the present case of PHB, the phase transition of PTMT occurs almost *completely* between the two crystalline phases. The sample rupture occurs *after the sample changes totally to the β -form*. The incomplete transition is observed for the uniaxially oriented poly(ethylene oxide) sample.^{61,62} The original monoclinic phase constructed by the (7/2) helical chains⁶³ transforms *reversibly but only partially* to the triclinic phase of the fully extended zigzag chain conformation⁶¹ by the application of a tensile force. Similarly to the present PHB case, the existence of short tie chains in the amorphous region between the neighboring lamellae might play an important role to cause such a partial transformation in the lamellae, as illustrated in Figure 15(2).

3.3.4. Existence of Tie Chains. The existence of short tie chains passing through the stacked lamellae is an assumption made in the present PHB study as the most important factor for the partial transition from the α - to β -form. The important role

of tie chains is discussed in the literature.⁶⁴ How can we verify the existence of the tie chains?

3.3.4.1. Heterogeneous Stress Distribution. The heterogeneous stress distribution in the mechanically deformed polymer sample may tell us the existence of such tie chains.^{65–68} The apparent Young's modulus in the crystalline region (or the crystallite modulus) is evaluated by the measurement of the X-ray diffraction peak shift under the application of constant macroscopic stresses by assuming that the local stress working in the crystalline region is equal to the macroscopic sample stress (the assumption of the homogeneous stress distribution).⁶⁹ However, the apparent crystallite modulus is not always the same, but it changes depending on the sample preparation condition.^{67,68,70} In an extreme case, the apparent crystallite modulus is lower than the Young's modulus of the bulk sample consisting of the crystalline and amorphous phases.⁷⁰ These observations indicate the breakage of such an assumption of homogeneous stress distribution. The quantitative analysis of the apparent crystallite modulus is made using a complex mechanical model, from which the degree of local stress concentration and the fraction of the corresponding mechanical component (the parallel crystalline component in the parallel-series crystalline model^{65,67,68}) are evaluated. The parallel component is quite small in the fraction but owes high stress, which is similar to the tie chains passing through the neighboring lamellae.

3.3.4.2. Formation of Tie Chains. Another experimental check of the tie chains was made by tracing the structural evolution in the isothermal crystallization process from the molten state of poly(oxyethylene).⁷¹ The creation of the long extended chain segments was detected in the isothermal crystallization process by the time-resolved IR spectral measurement. On the other hand, the lamellar insertion phenomenon (or the generation of a daughter lamella between the original mother lamellae) was detected in the time-resolved SAXS data. The key point is that the formation of the daughter lamellae in addition to the mother lamellae and the crystallization of the long extended chain segments occur at the same time. This can be interpreted by assuming the existence of fully extended tie chain segments passing through several lamellae.

The utilization of these experimental methods to catch the concept of tie chains in the case of PHB is difficult at present. This should be an important future theme for checking the reasonableness of the present interpretation of the characteristic phase transition behavior of PHB.

4. CONCLUSIONS

In addition to the previously reported crystal structure of the PHB α -form,¹⁶ we have analyzed the crystal structure of the β crystal form for the first time on the basis of the 2D X-ray diffraction data collected for the uniaxially oriented sample under the application of high tensile stress. The fully extended trans-zigzag chains are packed in the hexagonal cell with the upward and downward disordering along the chain axis. The doubly oriented PHB sample was useful for the clarification of the spatial relation between the α and β crystal lattices. The b -axis is common to these two crystals. The *affine* deformation-like translational shift of the chains preferentially along the b -axis can move the helical chains of the α -form to the extended chains of the β -form in one-to-one correspondence.

To know the higher-order structural change in relation to the change of the inner structure of the crystalline region, the WAXD and SAXS patterns were measured in the tensile

deformation process. An introduction of the concept of the locally tensioned tie chains can help us to interpret these experimental data: the strong stress works on the short tie chains between the neighboring lamellae, and the bundles of the β crystalline region are formed passing through both the extended tie chain segments and the local parts of the α crystalline lamellae in series. The transition is not completed, but the sample breakage occurs at around 70% strain, which may be related to the high stress concentration to these extended parts and the resultant scission of the extended chains. Even when the ultrahigh-molecular-weight sample is used in the experiment, the transition does not occur completely since the PHB chains are easier to break, probably because of their chemical characteristics containing the ester units. In this way, the present study has revealed the relation between the hierarchical structure change and the mechanical deformation behavior of PHB from the microscopic point of view.

PHB is one of the typical environmentally friendly aliphatic polyesters including poly(lactic acid) [PLLA]. Both PHB and PLLA show stress-induced phase transitions from the helical chain conformation of the α -form to the fully extended β -form (PHB) or from the helical chain conformation of the α -form to the another helical β -form (PLLA).^{72–74} The α -to- β transition mechanism of PLLA was proposed,⁷⁵ in which the slippage of the helical chains attended with the chain conformational change was speculated as a key factor of the transition. In such a point, the transition mechanism of these two polymers is similar to each other, although the resultant β -form possesses a different chain conformation. The β -form of PHB (and also PLLA) is said to possess higher mechanical property than the α -form because of the more highly extended chain conformation.^{4,21,24,76} The present structural study may encourage us to study such a mechanical property of PHB from the atomic level, once we know the concrete crystal structure of the PHB β -form.

■ ASSOCIATED CONTENT

Supporting Information

The Supporting Information is available free of charge on the ACS Publications website at DOI: [10.1021/acs.macromol.9b00225](https://doi.org/10.1021/acs.macromol.9b00225).

Extraction of the most suitable crystal structure model of PHB β -form (PDF)

■ AUTHOR INFORMATION

Corresponding Author

*E-mail: ktashiro@toyota-ti.ac.jp.

ORCID

Kohji Tashiro: [0000-0002-7543-2778](https://orcid.org/0000-0002-7543-2778)

Notes

The authors declare no competing financial interest.

■ ACKNOWLEDGMENTS

The author (S.P.) thanks Prof. Kumar Sudesh (Universiti Sains Malaysia, Malaysia) for supplying the PHB samples. This study was supported financially by the MEXT, Japan "Strategic Project to Support the Formation of Research Bases at Private Universities (2010-2014) and also (2015-2019)."

■ REFERENCES

- (1) Dawes, E. A.; Senior, P. J. The Role and Regulation of Energy Reserve Polymers in Micro-organisms. *Advances in Microbial Physiology*; Academic Press, 1973; Vol. 10, pp 135–266.

- (2) Anderson, A. J.; Dawes, E. A. Occurrence, metabolism, metabolic role, and industrial uses of bacterial polyhydroxyalkanoates. *Microbiol. Rev.* **1990**, *54*, 450–472.
- (3) Sudesh, K.; Abe, H.; Doi, Y. Synthesis, structure and properties of polyhydroxyalkanoates: biological polyesters. *Prog. Polym. Sci.* **2000**, *25*, 1503–1555.
- (4) Iwata, T. Strong fibers and films of microbial polyesters. *Macromol. Biosci.* **2005**, *5*, 689–701.
- (5) Cornibert, J.; Marchessault, R. H. Physical properties of poly- β -hydroxybutyrate: IV. Conformational analysis and crystalline structure. *J. Mol. Biol.* **1972**, *71*, 735–756.
- (6) Yokouchi, M.; Chatani, Y.; Tadokoro, H.; Teranishi, K.; Tani, H. Structural studies of polyesters: 5. Molecular and crystal structures of optically active and racemic poly (β -hydroxybutyrate). *Polymer* **1973**, *14*, 267–272.
- (7) Orts, W. J.; Marchessault, R. H.; Bluhm, T. L.; Hamer, G. K. Observation of strain-induced β form in poly(β -hydroxyalkanoates). *Macromolecules* **1990**, *23*, 5368–5370.
- (8) Pazur, R. J.; Hocking, P. J.; Raymond, S.; Marchessault, R. H. Crystal Structure of Syndiotactic Poly(β -hydroxybutyrate) from X-ray Fiber and Powder Diffraction Analyses and Molecular Modeling. *Macromolecules* **1998**, *31*, 6585–6592.
- (9) Sudesh, K.; Abe, H. *Practical Guide to Microbial Polyhydroxyalkanoates*; iSmithers: UK, 2010; pp 25–49.
- (10) Iwata, T.; Tanaka, T. Manufacturing of PHA as Fibers. In *Plastics from Bacteria: Natural Functions and Applications*; Chen, G.-Q., Ed.; Microbiology Monographs; Springer-Verlag Berlin Heidelberg, 2010; Vol.14, pp 257–282.
- (11) Sato, H.; Nakamura, M.; Padermshoke, A.; Yamaguchi, H.; Terauchi, H.; Ekgasit, S.; Noda, I.; Ozaki, Y. Thermal behavior and molecular interaction of poly(3-hydroxybutyrate-co-3-hydroxyhexanoate) studied by wide-angle X-ray diffraction. *Macromolecules* **2004**, *37*, 3763–3769.
- (12) Sato, H.; Mori, K.; Murakami, R.; Ando, Y.; Takahashi, I.; Zhang, J.; Terauchi, H.; Hirose, F.; Senda, K.; Tashiro, K.; Noda, I.; Ozaki, Y. Crystal and Lamella Structure and C–H \cdots O=C Hydrogen Bonding of Poly(3-hydroxyalkanoate) Studied by X-ray Diffraction and Infrared Spectroscopy. *Macromolecules* **2006**, *39*, 1525–1531.
- (13) Sato, H.; Ando, Y.; Dybal, J.; Iwata, T.; Noda, I.; Ozaki, Y. Crystal Structures, Thermal Behaviors, and C–H \cdots O=C Hydrogen Bondings of Poly(3-hydroxyvalerate) and Poly(3-hydroxybutyrate) Studied by Infrared Spectroscopy and X-ray Diffraction. *Macromolecules* **2008**, *41*, 4305–4312.
- (14) Murakami, R.; Sato, H.; Dybal, J.; Iwata, T.; Ozaki, Y. Formation and stability of β -structure in biodegradable ultra-high-molecular-weight poly(3-hydroxybutyrate) by infrared, Raman, and quantum chemical calculation studies. *Polymer* **2007**, *48*, 2672–2680.
- (15) Sasaki, S.; Ishii, Y.; Sakurai, S.; Iwata, T.; Sugimoto, K.; Takata, M. Investigation of Electron-density distribution imaging for poly(3-hydroxybutyrate) crystal by maximum entropy method to visualize weak hydrogen bonding. *Fiber Prepr. Jpn.* **2013**, *68*, 87.
- (16) Wang, H.; Tashiro, K. Reinvestigation of Crystal Structure and Intermolecular Interactions of Biodegradable Poly(3-Hydroxybutyrate) α -Form and the Prediction of Its Mechanical Property. *Macromolecules* **2016**, *49*, 581–594.
- (17) Aoyagi, Y.; Doi, Y.; Iwata, T. Mechanical properties and highly ordered structure of ultra-high-molecular-weight poly[(R)-3-hydroxybutyrate] films: Effects of annealing and two-step drawing. *Polym. Degrad. Stab.* **2003**, *79*, 209–216.
- (18) Iwata, T.; Aoyagi, Y.; Fujita, M.; Yamane, H.; Doi, Y.; Suzuki, Y.; Takeuchi, A.; Uesugi, K. Processing of a Strong Biodegradable Poly[(R)-3-hydroxybutyrate] Fiber and a New Fiber Structure Revealed by Micro-Beam X-Ray Diffraction with Synchrotron Radiation. *Macromol. Rapid Commun.* **2004**, *25*, 1100–1104.
- (19) Iwata, T.; Fujita, M.; Aoyagi, Y.; Doi, Y.; Fujisawa, T. Time-Resolved X-ray Diffraction Study on Poly[(R)-3-hydroxybutyrate] Films during Two-Step-Drawing: Generation Mechanism of Planar Zigzag Structure. *Biomacromolecules* **2005**, *6*, 1803–1809.
- (20) Tanaka, T.; Fujita, M.; Takeuchi, A.; Suzuki, Y.; Uesugi, K.; Ito, K.; Fujisawa, T.; Doi, Y.; Iwata, T. Formation of highly ordered structure in poly[(R)-3-hydroxybutyrate-co-(R)-3-hydroxyvalerate] high-strength fibers. *Macromolecules* **2006**, *39*, 2940–2946.
- (21) Tanaka, T.; Yabe, T.; Teramachi, S.; Iwata, T. Mechanical properties and enzymatic degradation of poly[(R)-3-hydroxybutyrate] fibers stretched after isothermal crystallization near T_g. *Polym. Degrad. Stab.* **2007**, *92*, 1016–1024.
- (22) Kabe, T.; Tanaka, T.; Marubayashi, H.; Hikima, T.; Takata, M.; Iwata, T. Investigating thermal properties of and melting-induced structural changes in cold-drawn P(3HB) films with α - and β -structures using real-time X-ray measurements and high-speed DSC. *Polymer* **2016**, *93*, 181–188.
- (23) Kabe, T.; Tsuge, T.; Kasuya, K.-i.; Takemura, A.; Hikima, T.; Takata, M.; Iwata, T. Physical and Structural Effects of Adding Ultrahigh-Molecular-Weight Poly[(R)-3-hydroxybutyrate] to Wild-Type Poly[(R)-3-hydroxybutyrate]. *Macromolecules* **2012**, *45*, 1858–1865.
- (24) Yang, J.; Zhu, H.; Zhao, Y.; Jiang, Q.; Chen, H.; Liu, G.; Chen, P.; Wang, D. New insights into the beta-form crystal toughening mechanism in pre-oriented PHBV films. *Eur. Polym. J.* **2017**, *91*, 81–91.
- (25) Zhang, J.; Kasuya, K.; Hikima, T.; Takata, M.; Takemura, A.; Iwata, T. Mechanical properties, structure analysis and enzymatic degradation of uniaxially cold-drawn films of poly[(R)-3-hydroxybutyrate-co-4-hydroxybutyrate]. *Polym. Degrad. Stab.* **2011**, *96*, 2130–2138.
- (26) Furuhashi, Y.; Imamura, Y.; Jikihara, Y.; Yamane, H. Higher order structures and mechanical properties of bacterial homo poly(3-hydroxybutyrate) fibers prepared by cold-drawing and annealing processes. *Polymer* **2004**, *45*, 5703–5712.
- (27) Yamane, H.; Terao, K.; Hiki, S.; Kimura, Y. Mechanical properties and higher order structure of bacterial homo poly(3-hydroxybutyrate) melt spun fibers. *Polymer* **2001**, *42*, 3241–3248.
- (28) Iwata, T.; Sato, S.; Park, J. W.; Tanaka, T. Beta structure and unique crystalline orientation analysis of PHB fibers and films. *Abstract of International Symposium on Biological Polyesters 2008, New Zealand, 2008*; p 101.
- (29) Sato, S.; Tanaka, T.; Yoshida, Y.; Iwata, T. Crystal Structure Analysis of Poly[(R)-3-hydroxybutyrate] with Planar Zigzag Conformation. *Polym. Prepr. Jpn* **2007**, *56*, 2280.
- (30) Barham, P. J.; Keller, A. The relationship between microstructure and mode of fracture in polyhydroxybutyrate. *J. Polym. Sci., Polym. Phys. Ed.* **1986**, *24*, 69–77.
- (31) Verman, B.; Jiang, L.; Kim, B.; Smith, R.; Grupido, N. Confocal graded d-spacing multilayer beam conditioning optics. *Adv. X-Ray Anal.* **2000**, *42*, 321–332.
- (32) Alexander, L. L. *X-ray Diffraction Methods in Polymer Science*; John Wiley & Sons: New York, 1969.
- (33) Tadokoro, H. *Structure of Crystalline Polymers*; John Wiley & Sons: New York, 1990.
- (34) Polanyi, M. Das Röntgen-Faserdiagramm (Erste Mitteilung). *Z. Physik* **1921**, *7*, 149–180.
- (35) *International Table for Crystallography, Volume A: Space Group Symmetry*, 5th ed.; Hahn, T., Ed.; Springer: Dordrecht, 2005.
- (36) Sun, H. COMPASS: An ab Initio Force-Field Optimized for Condensed-Phase Applications Overview with Details on Alkane and Benzene Compounds. *J. Phys. Chem. B* **1998**, *102*, 7338–7364.
- (37) Jakeways, R.; Ward, I. M.; Wilding, M. A.; Hall, I. H.; Desborough, I. J.; Pass, M. G. Crystal deformation in aromatic polyesters. *J. Polym. Sci., Polym. Phys. Ed.* **1975**, *13*, 799–813.
- (38) Ward, I. M.; Wilding, M. A.; Brody, H. The mechanical properties and structure of poly(m-methylene terephthalate) fibers. *J. Polym. Sci., Polym. Phys. Ed.* **1976**, *14*, 263–274.
- (39) Jakeways, R.; Smith, T.; Ward, I. M.; Wilding, M. A. Reversible crystal deformation and conformational changes in poly-(tetramethylene terephthalate). *J. Polym. Sci., Polym. Lett. Ed.* **1976**, *14*, 41–46.

- (40) Tashiro, K.; Nakai, Y.; Kobayashi, M.; Tadokoro, H. Solid-State Transition of Poly(butylene Terephthalate) Induced by Mechanical Deformation. *Macromolecules* **1980**, *13*, 137–145.
- (41) Tashiro, K.; Hiramatsu, M.; Ii, T.; Kobayashi, M.; Tadokoro, H. Stress-induced crystalline phase transition in block copolymers of poly(tetramethylene terephthalate) and poly(tetramethylene oxide). I Dependence of transitional behavior on hard/soft segmental ratio. *Sen'i Gakkaishi* **1986**, *42*, T597–T605.
- (42) Tashiro, K.; Hiramatsu, M.; Ii, T.; Kobayashi, M.; Tadokoro, H. Stress-induced crystalline phase transition in block copolymers of poly(tetramethylene terephthalate) and poly(tetramethylene oxide). II Phase transition and inhomogeneous deformation. *Sen'i Gakkaishi* **1986**, *42*, T659–T664.
- (43) Tashiro, K.; Cheng, J.; Ike, M. Stress-Induced Reversible Phase Transition of Poly(tetramethylene naphthalate). *Macromolecules* **2003**, *36*, 359–367.
- (44) Ichikawa, Y.; Suzuki, J.; Washiyama, J.; Moteki, Y.; Noguchi, K.; Okuyama, K. Strain-induced crystal modification in poly(tetramethylene succinate). *Polymer* **1994**, *35*, 3338–3339.
- (45) Ichikawa, Y.; Kondo, H.; Igarashi, Y.; Noguchi, K.; Okuyama, K.; Washiyama, J. Crystal structures of α and β forms of poly(tetramethylene succinate). *Polymer* **2000**, *41*, 4719–4727.
- (46) Liu, G.; Zheng, L.; Zhang, X.; Li, C.; Jiang, S.; Wang, D. Reversible Lamellar Thickening Induced by Crystal Transition in Poly(butylene succinate). *Macromolecules* **2012**, *45*, 5487–5493.
- (47) Liu, G.; Zheng, L.; Zhang, X.; Li, C.; Wang, D. Critical Stress for Crystal Transition in Poly(butylene succinate)-Based Crystalline-Amorphous Multiblock Copolymers. *Macromolecules* **2014**, *47*, 7533–7539.
- (48) Hashida, T.; Tashiro, K.; Ito, K.; Takata, M.; Sasaki, S.; Masunaga, H. Correlation of Structure Changes in the Water-Induced Phase Transitions of Poly(ethylenimine) Viewed from Molecular, Crystal, and Higher-Order Levels As Studied by Simultaneous WAXD/SAXS/Raman Measurements. *Macromolecules* **2010**, *43*, 402–408.
- (49) Gowd, E. B.; Tashiro, K.; Ramesh, C. Structural phase transitions of syndiotactic polystyrene. *Prog. Polym. Sci.* **2009**, *34*, 280–315.
- (50) Tashiro, K.; Tanaka, R. Structural correlation between crystal lattice and lamellar morphology in the ferroelectric phase transition of vinylidene fluoride-trifluoroethylene copolymers as revealed by the simultaneous measurements of wide-angle and small-angle X-ray scatterings. *Polymer* **2006**, *47*, 5433–5444.
- (51) Tashiro, K. Structural Phase Transition of Aliphatic Nylons Viewed from the WAXD/SAXS and Vibrational Spectral Measurements and Molecular Dynamics Calculation. *Chin. J. Polym. Sci.* **2007**, *25*, 73–82.
- (52) Roe, R.-J. *Methods of X-ray and Neutron Scattering in Polymer Science*; Oxford University Press: New York, 2000.
- (53) Zhurkov, S. N.; Zakrevskiy, V. A.; Korsukov, V. E.; Kuksenko, V. S. Mechanism of submicrocrack generation in stressed polymers. *J. Polym. Sci., Part A-1: Polym. Chem.* **1972**, *10*, 1509–1520.
- (54) Vettegren, V. I.; Novak, I. I.; Friedland, K. J. Overstressed interatomic bonds in stressed polymers. *Int. J. Fract.* **1975**, *11*, 789–801.
- (55) Kausch, H. H. *Polymer Fracture*; Springer-Verlag: Berlin, 1978.
- (56) Tashiro, K. *Crystal Structure and Phase Transition of PVDF and Related Copolymers, Ferroelectric Polymers: Chemistry, Physics, and Technology*; Nalwa, H. S., Ed.; Marcel Dekker Inc., 1995; pp 63–182.
- (57) Suehiro, K.; Chatani, Y.; Tadokoro, H. Structural Studies of Polyesters. VI. Disordered Crystal Structure (Form II) of Poly(β -propiolactone). *Polym. J.* **1975**, *7*, 352–358.
- (58) Fraser, R. D. B.; MacRae, T. P. *Conformation in Fibrous Proteins and Related Synthetic Polypeptides*; Academic Press Inc.: New York, 1973.
- (59) Kreplak, L.; Doucet, J.; Dumas, P.; Briki, F. New Aspects of the α -Helix to β -Sheet Transition in Stretched Hard α -Keratin Fibers. *Biophys. J.* **2004**, *87*, 640–647.
- (60) Tashiro, K.; Yamamoto, H.; Yoshioka, T.; Ninh, T. H.; Tasaki, M.; Shimada, S.; Nakatani, T.; Iwamoto, H.; Ohta, N.; Masunaga, H. Hierarchical Structural Change in the Stress-Induced Phase Transition of Poly(tetramethylene terephthalate) As Studied by the Simultaneous Measurement of FTIR Spectra and 2D Synchrotron Undulator WAXD/SAXS Data. *Macromolecules* **2014**, *47*, 2052–2061.
- (61) Takahashi, Y.; Sumita, I.; Tadokoro, H. Structural studies of polyethers. IX. Planar zigzag modification of poly(ethylene oxide). *J. Polym. Sci., Part B: Polym. Phys.* **1973**, *11*, 2113–2122.
- (62) Tashiro, K.; Tadokoro, H. Vibrational Spectra of Planar-zigzag Poly(ethylene Oxide). *Rep. Prog. Polym. Phys. Jpn.* **1978**, *21*, 417–420.
- (63) Takahashi, Y.; Tadokoro, H. Structural Studies of Polyethers, $(-(\text{CH}_2)_m\text{-O})_n$. X. Crystal Structure of Poly(ethylene oxide). *Macromolecules* **1973**, *6*, 672–675.
- (64) Gedde, U. W. *Polymer Physics*; Springer-Science + Business Media, B. V.: Berlin, 1995.
- (65) Clements, J.; Jakeways, R.; Ward, I. M. Lattice modulus and crystallite thickness measurements in ultra-high modulus linear polyethylene. *Polymer* **1978**, *19*, 639–644.
- (66) Prasad, K.; Grubb, D. T. X-ray modulus and strain distribution in single fibers of polyethylene. *J. Polym. Sci., Part B: Polym. Phys.* **1990**, *28*, 2199–2212.
- (67) Nakamoto, S.; Tashiro, K.; Matsumoto, A. Quantitative Evaluation of Stress Distribution in Bulk Polymer Samples through the Comparison of Mechanical Behaviors between Giant Single-Crystal and Semicrystalline Samples of Poly(trans-1,4-diethyl muconate). *J. Polym. Sci., Part B: Polym. Phys.* **2003**, *41*, 444–453.
- (68) Funaki, A.; Tashiro, K. Influence of the third monomer component on the temperature-dependent crystallite modulus and tie chain fraction evaluated for ethylene-tetrafluoroethylene copolymers. *Polymer* **2012**, *53*, 740–746.
- (69) Sakurada, I.; Ito, Y.; Nakamae, K. Elastic moduli of the crystal lattices of polymers. *J. Polym. Sci.* **1967**, *15*, 75–91.
- (70) Tashiro, K.; Wu, G.; Kobayashi, M. Morphological Effect on the Raman Frequency Shift Induced by Tensile Stress Applied to Crystalline Polyoxymethylene and Polyethylene: Spectroscopic Support for the Idea of an Inhomogeneous Stress Distribution in Polymer Material. *Polymer* **1988**, *29*, 1768–1778.
- (71) Hama, H.; Tashiro, K. Structural Changes in Isothermal Crystallization Process of Polyoxymethylene Investigated by Time-Resolved FTIR, SAXS and WAXS Measurements. *Polymer* **2003**, *44*, 6973–6988.
- (72) Sawai, D.; Takahashi, K.; Imamura, T.; Nakamura, K.; Kanamoto, T.; Hyon, S.-H. Preparation of oriented β -form poly(L-lactic acid) by solid-state extrusion. *J. Polym. Sci., Part B: Polym. Phys.* **2002**, *40*, 95–104.
- (73) Sawai, D.; Yokoyama, T.; Kanamoto, T.; Sungil, M.; Hyon, S.-H.; Myasnikova, L. P. Crystal Transformation and Development of Tensile Properties upon Drawing of Poly(L-lactic Acid) by Solid-State Coextrusion: Effects of Molecular Weight. *Macromol. Symp.* **2006**, *242*, 93–103.
- (74) Zhang, J.; Tashiro, K.; Tsuji, H.; Domb, A. J. Investigation of phase transitional behavior of poly(L-lactide)/poly(D-lactide) blend used to prepare the highly-oriented stereocomplex. *Macromolecules* **2007**, *40*, 1049–1054.
- (75) Wang, H.; Zhang, J.; Tashiro, K. Phase Transition Mechanism of Poly(L-lactic acid) among the α , δ , and β Forms on the Basis of the Reinvestigated Crystal Structure of the β Form. *Macromolecules* **2017**, *50*, 3285–3300.
- (76) Iwata, T.; Tsunoda, K.; Aoyagi, Y.; Kusaka, S.; Yonezawa, N.; Doi, Y. Mechanical properties of uniaxially cold-drawn films of poly([R]-3-hydroxybutyrate). *Polym. Degrad. Stab.* **2003**, *79*, 217–224.

ARTICLE

<https://doi.org/10.1038/s41467-019-09350-3>

OPEN

A study of the extraordinarily strong and tough silk produced by bagworms

Taiyo Yoshioka¹, Takuya Tsubota², Kohji Tashiro³, Akiya Jouraku⁴ & Tsunenori Kameda¹

Global ecological damage has heightened the demand for silk as ‘a structural material made from sustainable resources’. Scientists have earnestly searched for stronger and tougher silks. Bagworm silk might be a promising candidate considering its superior capacity to dangle a heavy weight, summed up by the weights of the larva and its house. However, detailed mechanical and structural studies on bagworm silks have been lacking. Herein, we show the superior potential of the silk produced by Japan’s largest bagworm, *Eumeta variegata*. This bagworm silk is extraordinarily strong and tough, and its tensile deformation behaviour is quite elastic. The outstanding mechanical property is the result of a highly ordered hierarchical structure, which remains unchanged until fracture. Our findings demonstrate how the hierarchical structure of silk proteins plays an important role in the mechanical property of silk fibres.

¹Silk Materials Research Unit, National Agriculture and Food Research Organization (NARO), 1-2 Owashi, Tsukuba, Ibaraki 305-8634, Japan. ²Transgenic Silkworm Research Unit, National Agriculture and Food Research Organization (NARO), 1-2 Owashi, Tsukuba, Ibaraki 305-8634, Japan. ³Department of Future Industry-Oriented Basic Science and Materials, Graduate School of Engineering, Toyota Technological Institute, Tempaku, Nagoya 468-8511, Japan. ⁴Insect Genome Research and Engineering Unit, National Agriculture and Food Research Organization (NARO), 1-2 Owashi, Tsukuba, Ibaraki 305-8634, Japan. Correspondence and requests for materials should be addressed to T.K. (email: kamedat@affrc.go.jp)

Severe global concerns about growing ecological damage and depletion of non-renewable resources have heightened the demand for silk as a structural material made from renewable resources^{1–3}. More than 200,000 different silks are known to exist in nature⁴. When we focus on toughness, i.e., a balance of strength and extensibility, we find the dragline silks of some kinds of spiders, such as those of the *Araneus*, *Nephila*, and *Latrodectus* genera, to be among the most attractive^{5–7}. Particularly, the *Caerostris darwini* (*C. darwini*) (aka *Darwin's bark*) spider dragline silk had been considered the toughest silk in nature, showing five times higher toughness than that of the *Bombyx mori* (*B. mori*) silkworm silk⁸ (see Table 1). However, many spider dragline silks, especially that of *C. darwini*, show typical plastic deformation in their tensile behaviours, showing a distinct yield point after the initial elastic region, followed by a subsequent levelling-off or plateau region before strain-hardening^{8,9}. To realise their practical application as structural materials, stronger and tougher silks with more elastic deformation behaviours are required. Towards this goal, many trials are being conducted worldwide to produce ideal silk products, for instance, by controlling the hierarchical structure of regenerated silk proteins^{10,11}, producing transgenic (or genome-edited) artificial silk proteins^{12–14}, and searching for superior un-explored silks in nature^{8,15,16}. When we search for superior un-explored silks, spiders provide a major hint that the silks used for dangling should be strong and tough^{17–19}. Bagworm silk, produced by larvae of bagworm moths (*Lepidoptera* order and *Psychidae* family)²⁰ especially of the largest and heaviest Japanese bagworm *Eumeta variegata* (*E. variegata*) (a synonym for *Eumeta japonica* and *Clania variegata*)^{21,22}, might be a promising candidate, considering its superior capacity to dangle a heavy weight, summed up by the weights of the larva and its house (generally called larval case, bag, or nest). However, little is known about the mechanical and physical properties of bagworm silks^{23–25}.

In this report, based on the detailed analyses of the fibre morphology and mechanical properties, we reveal that the *E. variegata* bagworm silk is extraordinarily strong and tough compared to other known silks, and that its tensile deformation behaviour is quite elastic. To investigate the relationship between the structure and the outstanding mechanical properties of this bagworm silk, a comprehensive analysis of the hierarchical structure, made up of crystalline and amorphous phases, is conducted by in situ time-resolved simultaneous measurements of synchrotron wide-angle X-ray diffraction (WAXD) and small-angle X-ray scattering (SAXS) during tensile deformation.

Results

Morphology of bagworm silk. While the exterior of the nest of *E. variegata* bagworms is covered with dead branches and leaves (Fig. 1a), the interior is made of fine, densely stacked nest silk fibres, like a nonwoven fabric (Fig. 1b, c). It is well-recognised that bagworms use their silk also as lifeline for dangling. Furthermore, we found that they use it as a foothold as well, by

spinning it in a zigzag manner with slightly greater widths than that of the space between their legs, in which folded points are attached with adhesive glue. While spiders have plural pairs of silk glands and spinnerets for different purposes, the multi-task thread is produced by a pair of silk glands via a single spinneret in the case of bagworms. The individual silk threads are composed of a pair of thin filaments, as in the cases of silkworm silks and spider dragline silks, and their cross-sections were revealed to be rather elliptical, and not circular (Fig. 1d). The fact that *E. variegata* bagworms spin silk over several tenths of a metre to several hundreds of metres is worthy of mention; therefore, one can wound it on a bobbin (Fig. 1e) or twist it into multiple threads (Fig. 1f).

Mechanical properties. In the estimation of the tensile properties, the cross-sectional area of the sample filament should be evaluated as accurately as possible. Our detailed morphological observation revealed that the cross-sections were well-approximated by an ellipse, with a pair of major and minor axes L_a and L_b , satisfying an axial ratio (L_a/L_b) of 1.7 (Fig. 1g–j; Table 2). This axial ratio was used to estimate the cross-sectional area of the single filaments, needed for converting the tensile force to stress values in the tensile test (further details in the Methods section).

A typical stress–strain curve of *E. variegata* bagworm silk is shown in Fig. 1k, and the average tensile properties of modulus, strength, extensibility, and toughness are summarised in Table 3. The values of modulus, strength, and toughness are extraordinarily high compared to other known silks (note that the toughness is almost comparable with that of *C. darwini* silk⁸). In addition, the *E. variegata* bagworm silk exhibits an ideal stress–strain behaviour, without a levelled-off stress after the yield point, but followed by a linear and steep strain-hardening just after elastic deformation.

Amino acid sequence. The structural and mechanical properties of the silk produced by *Lepidoptera* are predominantly attributable to the contribution of heavy-chain silk fibroin (H-Fib). An analysis of the amino acid composition, carried out for *E. variegata* bagworm silk, revealed that the molar ratios of Gly and Ala are approximately equal, and their sum accounts for about 80% (Supplementary Fig. 1), which is consistent with the results in earlier reports^{26,27}. In accordance with this, we found, via silk gland transcriptomic analysis, that the bagworm *h-fib* gene hypothetically encodes the Gly and Ala-rich protein. The molecular structure of the H-Fib was investigated by a long-read transcriptomic analysis. At least 5 tandem repeat motifs were identified, each of which is composed of polyalanine block (PAB) and non-polyalanine block (NPAB) sequences (Fig. 2). This kind of combination motif of PAB and NPAB sequences is widely observed in the *Saturniidae* silkworm and spider dragline silks^{28–30}. However, one can find several decisive distinctions from their motifs. Firstly, the length of each sequence motif,

Table 1 Tensile properties of various silks

		Young's modulus (GPa)	Fracture strength (GPa)	Extensibility	Toughness (MJ m ⁻³)	Ref.
<i>Araneus diadematus</i>	Spider silk (MA)	10	1.1	0.27	160	54
<i>Nephila clavipes</i>	Spider silk (MA)	13.8	1	0.20	111.2	61
<i>Latrodectus hesperus</i>	Spider silk (MA)	10.2	1	0.45	180.9	61
<i>Caerostris darwini</i>	Spider silk (MA)	11.5	1.7 (1.0) ^a	0.52 (0.69) ^b	354	8
<i>Bombyx mori</i>	Silkworm silk	7	0.6	0.18	70	54
<i>Eumeta minuscula</i>	Bagworm silk	25	–	–	–	24

^aThe true stress and ^btrue strain values from the original paper were converted into engineering stress and strain and are given in parentheses

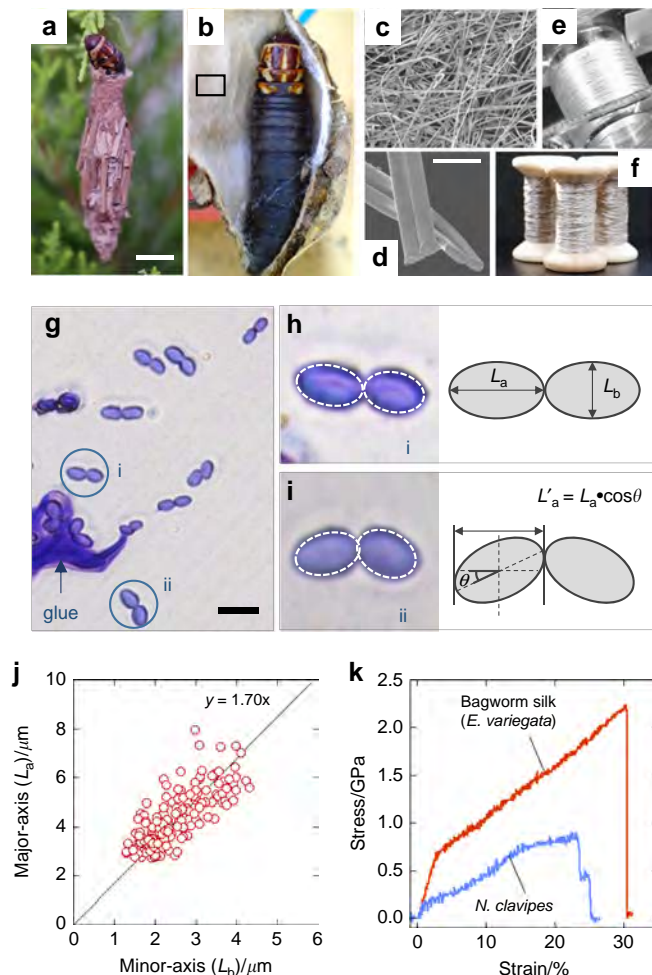


Fig. 1 Morphological and mechanical characteristics of the bagworm silk. Photographs of **a** exterior and **b** interior of larval house (or nest) of a last-instar female larva of *E. variegata*. **c** SEM image of inner surface of the larval house (from rectangular part in **b**). **d** Magnified SEM image of single fibres with their cross-sections. **e** Continuous bagworm silk wound on a bobbin, and **f** its twisted yarn. **g** Optical micrograph of cross-sections of bagworm silks. Typical cross-sections of a single fibre composed of **h**, a pair of straight conjugated filaments, and **i** a pair of filaments conjugated with a tilting angle θ , are shown together with schematic illustrations. In each filament in **h**, **i**, the cross-section is traced by an elliptical shape with a broken line. **j** Plot of axial ratios of lengths of major and minor axes in elliptical cross-sections of bagworm silk. The straight line with a slope of 1.70 was obtained by linear regression for the plots. **k** Typical stress-strain curve of single bagworm silks. For comparison, a typical stress-strain curve of *N. clavipes* dragline silk, measured in this study using the same procedure and instruments used for bagworm silks, is included. The average tensile properties of *N. clavipes* ($n = 5$) were as follows: modulus = 8.13 GPa, strength = 0.9 GPa, extensibility = 0.26, and toughness = 139.7 MJ m⁻³. Scale bars; 10 mm (**a**), 10 μ m (**d**), and 10 μ m (**g**)

composed of ~160 amino acid units, is remarkably longer than the repeating units of ~20–40 known for the *Saturniidae* silkworm silks²⁸, and of ~30–60 for the spider dragline silks^{29,30}. Secondly, the NPAB sequence is found to be made up of a combination of the long Gly-X dipeptide sequences (X is mainly Ala or Ser) observed characteristically in the *B. mori* silkworm silk³¹, and the Gly-Gly-X tripeptide sequences (X is mainly Ala or Tyr) observed characteristically in the *Saturniidae* silkworm and spider dragline silks^{28–30}. The long sequence of over 20 Ala

residues in the PAB is also very unique, compared to that of the *Saturniidae* silkworm (~3–15 repeats) and spider dragline silks (~5–8 repeats)^{28–30}. It should be noticed that a short non-repeated sequence of ~5–8 residues, made up of the relatively bulky residues of mainly Ser, Val, and Tyr, is characteristically inserted in each NPAB sequence (coloured blue).

Crystal modification and hierarchical structure. To understand the structural origin of the outstanding mechanical properties of the bagworm silk, the crystal modification and hierarchical structure, which is a combination of crystal and amorphous phases, were investigated. The two-dimensional (2D) WAXD fibre diagram shows a typical β -sheet pattern³² (Fig. 3a) widely observed in the silkworm and spider dragline silks. Although the β -sheet crystals formed in a variety of silks are commonly indexed with the orthogonal unit cell, the detailed unit cell parameters differ slightly among the silks depending on their amino acid composition^{33,34}. The β -sheet unit cell parameters of the bagworm silk were evaluated, using the 200, 210, and 002 reflections, under the assumption of a rectangular unit cell, to be $a = 9.39$ Å, $b = 9.50$ Å, and c (fibre axis) = 6.98 ± 0.05 Å, which are quite similar to those of the *B. mori* silk ($a = 9.38$ Å, $b = 9.49$ Å, and $c = 6.98$ Å)³². The crystallinity was estimated to be about 44% by peak fitting the crystalline and amorphous diffraction peaks (Fig. 3b).

The meridional 1D-SAXS Kratky profile ($q^2I(q)$ vs. q plot)³⁵ (Fig. 3d) (the original $I(q)$ vs. q plot is shown in Supplementary Fig. 2) obtained from synchrotron SAXS measurement (Fig. 3c) clearly revealed at least five scattering peaks, the peak positions of which approximately satisfy an integer ratio of 1:2:3:4:5. This relation revealed the existence of a well-ordered repeating structure, composed of alternating crystal and amorphous phases. The first-order long period, that is, the real period (L_p^{1st}), was estimated to be about 38.5 nm. Analysis of the correlation function $K(z)$ ^{36,37} (Fig. 3e) for the electron density distribution $\eta(z)$ of the repeating system made up of phases I and II (Fig. 3f) revealed that the 38.5 nm periodic structure consists of phase I with thickness of 15.7 nm and phase II with a thickness of 22.8 nm. The meridional periodic scatterings in SAXS are observed not only in this bagworm silk, but also in many kinds of spider dragline and wild silkworm silks. However, to the best of our knowledge, such a clear periodicity for fifth-order scattering has never been reported in any kind of β -sheet silk. In addition, the long period is roughly five times longer than those (~6–8 nm) reported for spider dragline silks and wild silkworm silks^{38–43} (see Supplementary Fig. 3). This highly ordered and long-range hierarchical structure is considered to contribute significantly to the outstanding mechanical properties, and might be directly related to the amino acid sequence.

The SAXS data also revealed two-point scatterings on the equatorial line, indicating the presence of a nanofibril bundle with a neighbouring fibril distance of 4.7 nm (Fig. 3g). This periodicity is approximately the same as the periodicities observed for *B. mori* silkworm silk, *A. assama* wild-silkworm silk³⁸, and (*N. clavipes*) spider dragline silk³⁹ (Supplementary Fig. 3a, b). It is interesting that the fibre diameters of these silks considerably differ from each other, but the diameter of each minimum constituent nanofibril entity is similar. This is probably determined by the lateral spacing of the β -sheet crystallite³⁹. The significantly sharper peak width of bagworm silk, compared to that of other silks, indicates a well-developed nanofibril bundle thickness. The nanofibril bundle thickness was estimated using the Scherrer equation and was around 150 nm, which is considerably thicker than those of other silks (Supplementary Fig. 3c).

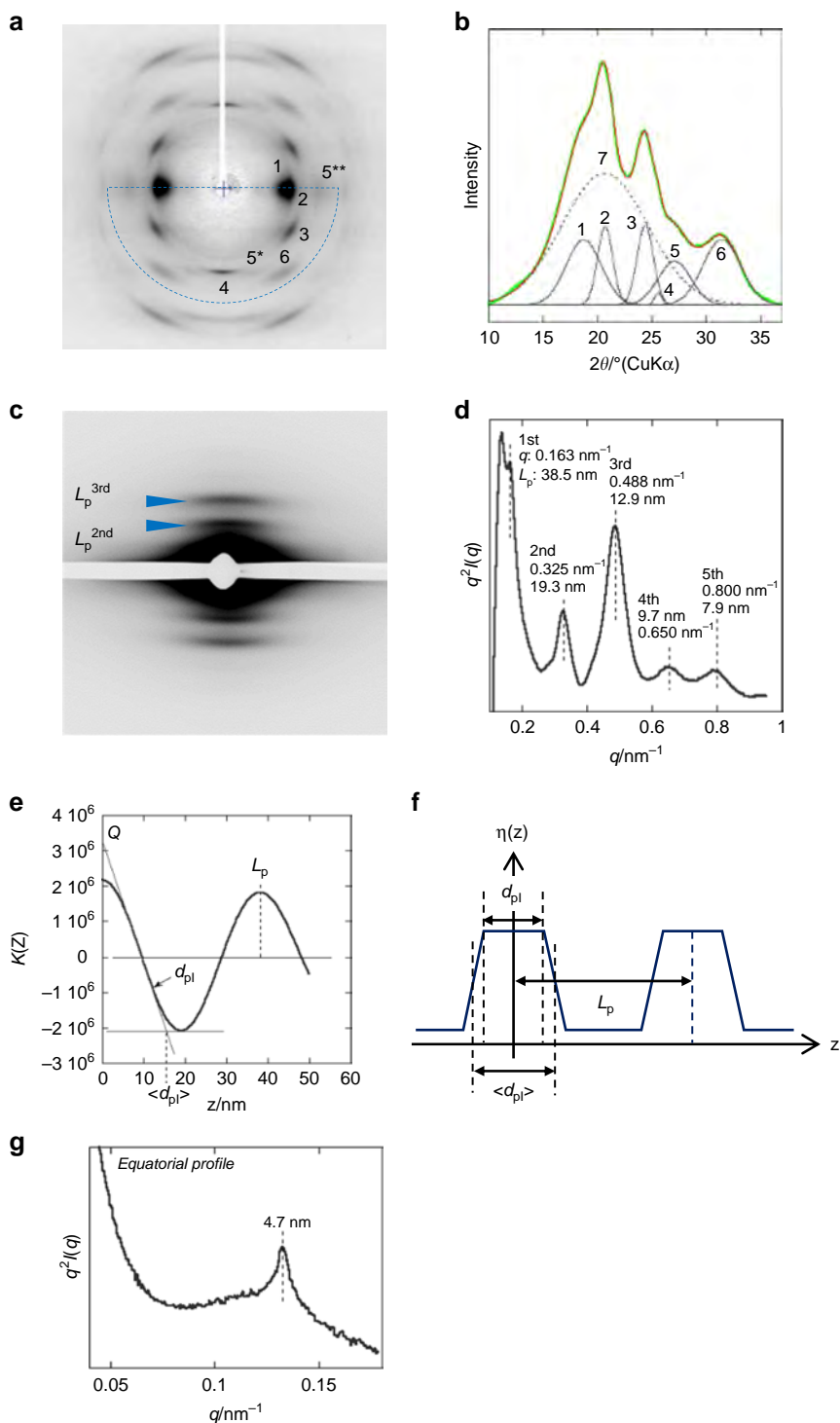


Fig. 3 Structural information of the bagworm silk. **a** WAXD fibre diagram obtained from the bagworm silk and **b** its 2θ profile scanned in the 2θ range from 10° to 37° , and for the azimuthal angle range from 0° to -180° , which is enclosed by the broken blue line in **a**. The crystallinity was evaluated from the 2θ profile by peak fitting. Each peak number corresponds to the following. 1: (200) crystalline reflection, 2: (210), 3: (211), 4: (002), 5: $(102)^* + (300)^{**}$, 6: (202), and 7: amorphous peak. The peak fitting was performed using the spectroscopy software Grams Suite 9.3 (Thermo Fisher Scientific Inc., USA) by fixing the peak positions for the crystalline reflections at -1 – 6 . **c** Synchrotron SAXS pattern and **d** its meridional q -profile ($q^2I(q)$ vs. q Kratky plot). To avoid beam damage of the detector due to the strong equatorial-streak scattering, a narrow metal plate was attached on the detector surface along the equatorial line, and it appears as the white gap running along the equatorial line in the SAXS pattern **c**. **e** The electron density correlation function $K(z)$ and **f** the corresponding electron density distribution $\eta(z)$, for the repeating phases. Q , L_p , d_{pl} , and $\langle d_{pl} \rangle$ denote the invariant, long period (phase I + II), core thickness of phase I, and mean thickness of phase I, respectively. The L_p , d_{pl} , and $\langle d_{pl} \rangle$ were estimated to be 38.2, 12.5, and 15.7 nm, respectively. **g** Equatorial SAXS q -profile ($q^2I(q)$ vs. q Kratky plot) scanned from the 2D pattern shown in Supplementary Fig. 3a-(1)

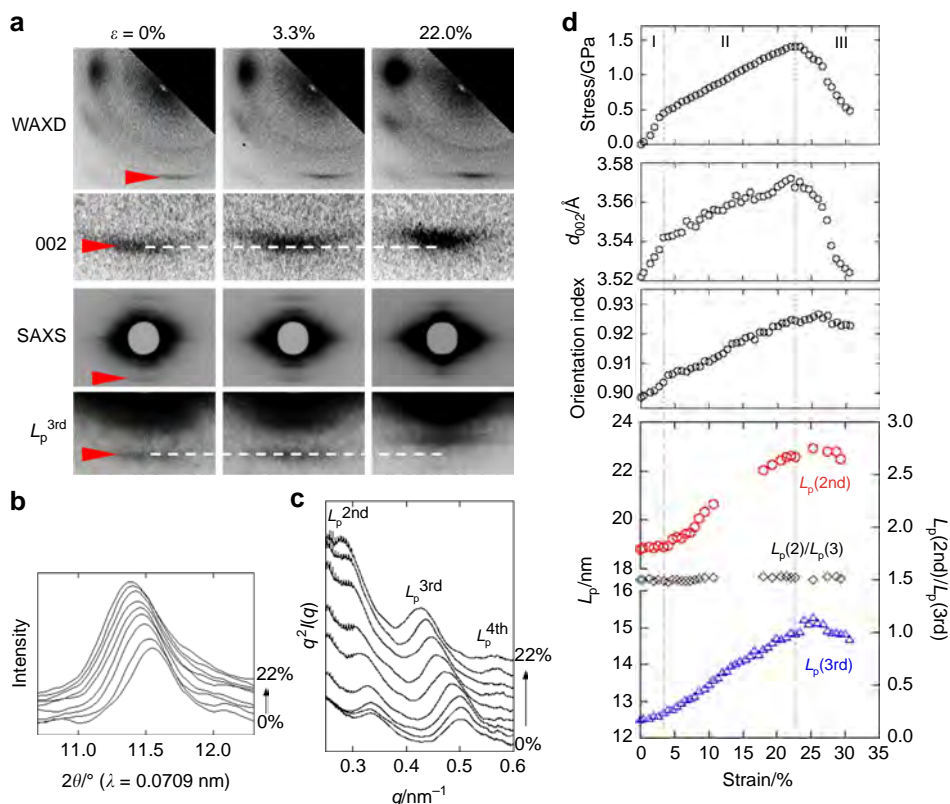


Fig. 4 Time-resolved tracing of structural changes during tensile deformation. **a** Changes in time-resolved synchrotron WAXD and SAXS patterns during the tensile deformation process. The corresponding stress-strain curve is shown at the top of **d**. **b** The selective meridional WAXD 2θ profiles and **c** the meridional SAXS $q^2 I(q)$ vs. q profiles, both of which were obtained from the strains at 0, 1.3, 3.3, 6.0, 8.7, 12.0, 14.7, 18.0, and 22.0% in the stress-strain curve shown at the top of **d**. **d** Summary of the time-resolved simultaneous measurement. From top to bottom, the changes in the tensile stress, crystal unit cell dimension along the c -axis direction (d_{002}), crystalline orientation index, and meridional long periods (L_p^{2nd} and L_p^{3rd}), estimated from the 2nd and 3rd periodic scatterings, are plotted against the bulk strain. In the bottom plots of the long periods, the ratio of L_p^{2nd}/L_p^{3rd} is also plotted

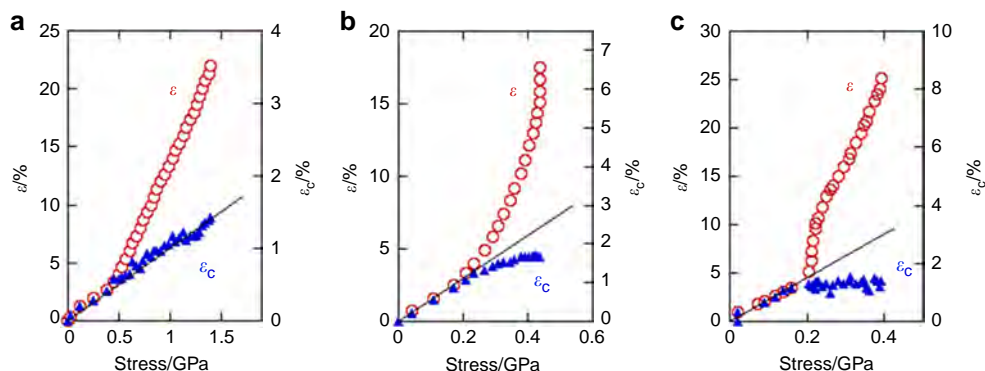


Fig. 5 Relationships between crystal strain and tensile stress in different kinds of silk. The changes in bulk strain (ϵ) and of crystal strain (ϵ_c) against the tensile stress in the time-resolved simultaneous synchrotron X-ray analysis for **a** *E. variegata* bagworm silk, **b** *B. mori* (*Bombycidae*) silkworm silk, and **c** *A. assama* (*Saturniidae*) silkworm silk. The changes in tensile stress and crystal strain against the bulk strain, using the same experimental data, are shown in Supplementary Fig. 5

Table 4 Summary of the dimensional changes observed in the bulk sample, crystal unit cell, and hierarchical structure

	Stage I (Initial elastic region)	Stage II (Strain hardening)	Total (I + II)	Stage III (After fracturing)
Sample length (mm)	15.0 → 15.5	15.5 → 18.3	15.0 → 18.3	not evaluated
Bulk strain (ϵ) (%)	3.3	18.7	22.0	not evaluated
d_{002} (Å)	3.52 → 3.54	3.54 → 3.57	3.52 → 3.57	3.57 → 3.52
Crystal strain (ϵ_c) (%)	0.57	0.85	1.41	-1.40
Long period (L_p^{1st}) (nm)	37.5 → 38.1	38.1 → 44.7	37.5 → 44.7	44.7 → 44.0
Strain of long period (ϵ_l) (%)	1.6	17.6	19.2	-1.6

superior mechanical properties and their quite elastic tensile-deformation behaviour. While the β -sheet crystal modification revealed by WAXD analysis is common in the other kinds of silkworm and spider silks, the hierarchical structure was found to be quite unique. The SAXS analysis revealed a highly ordered and long-range repeating structure. Additionally, while the *B. mori* silk does not show the meridional long period, many *Saturniidae* silkworm and spider dragline silks show it. In other words, such ordered structure is considered to be constructed only in the silks having a PAB sequence, and the PAB plays an important role in the formation of the periodic structure. The PAB of the *Saturniidae* silkworm or spider dragline silks is considered to form a helical conformation in their silk glands^{44,45}. It is reasonably speculated that the polyalanine helices in the neighbouring H-Fib proteins (or spidroins) are gathered around each other, probably forming a hexagonal packing via hydrophobic–hydrophobic self-assembly interactions^{10,46,47}. The long PAB sequence of 22 residues (corresponding to 6 helical pitches) in the bagworm silk (Fig. 6a, b) may gather together more effectively compared to the shorter alanine repeats of the *Saturniidae* and spider dragline

silks. This self-assembly of the helical polyalanine sequences occurs at approximately constant intervals determined by the amino acid residues of the tandem repeat motifs (~160 residues in the case of the *E. variegata* bagworm silk) (Fig. 6c), and these intervals are speculated to correspond to the long period detected by SAXS measurement (Fig. 6d). Here, the question is: how many amino acid sequence units contribute to the β -sheet crystal formation from the end of the PAB sequence? We paid attention to the presence of the non-repeated short sequences inserted in each NPAB sequence region. It was found that around 45 residues exist between the PAB and non-repeated short unit. The 67 residues (22 in PAB and 45 in NPAB) were calculated to measure 23.5 nm (~0.35 nm/residue in the β -sheet crystal³²), which is consistent with the length of phase II (22.8 nm) experimentally estimated by SAXS analysis (Fig. 6d). We made an assumption, which is widely believed, that the polyalanine helical conformation changes to β -sheet crystals due to the stress-induced helix-sheet transition^{10,47}. We can assign the lengths of phases I and II to the amorphous and crystalline phases, respectively (Supplementary Note 1). The remaining NPAB sequence of around 90 residues should behave

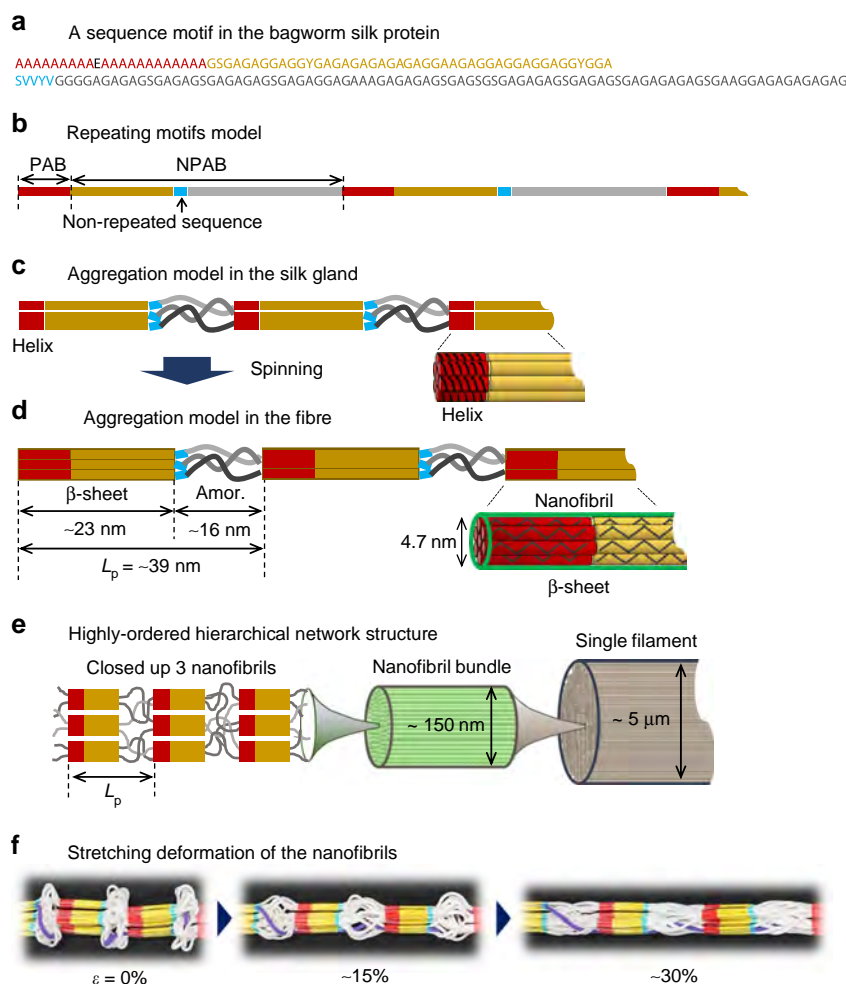


Fig. 6 Relationship between primary structure and hierarchical structure. **a** A representative sequence motif, corresponding to the top of Fig. 2, identified in the H-Fib protein of the *E. variegata* bagworm silk, and **b** the repeating model of the motifs. **c** Assumed aggregation model of the motifs in the silk gland, and **d** after spinning. In the silk gland, the PAB has a helical conformation, and the neighbouring helical PABs gather together to form the aggregation bundle (or nanofibril) with 4.7 nm thickness and hexagonal packing, as shown in **c**. During the spinning process, the neighbouring NPAB sequences between the PAB and blue-coloured non-repeated sequences crystallise with β -sheet modification as shown in **d**. Simultaneously, the helical PAB bundle exhibited a stress-induced structural transition from helix to β -sheet crystals (as shown in **d**). SAXS analysis revealed a well-developed nanofibril bundle with a thickness of around 150 nm for a single filament, as shown in **e**. A stretching deformation model of the nanofibrils, during which the ordered repeating structure is maintained, is proposed in **f**. In situ X-ray analysis revealed that the deformations of the crystal and amorphous phases are reversible and irreversible modes, respectively

as amorphous, by shrinking about 50% from the β -sheet conformation ($(90 \times 0.35 - 15.7)/(90 \times 0.35) \times 100$ (%)) (picture on the left in Fig. 6d).

The tensile deformation behaviours of the different silks differ significantly among the species. The in situ time-resolved synchrotron X-ray measurement during the tensile deformation of the bagworm silk successfully revealed a remarkable structural feature, wherein the crystal strain increased linearly against the tensile stress throughout the stretching, up to the fracture point (Fig. 5a). For comparison, we conducted the same measurements for the *B. mori* and *A. assama* silks, which yielded different types of stress–strain curves. All the three kinds of silk initially show a linear increase in the crystal strain for a low tensile stress, as reported by Seydel et al. for the *B. mori* silk⁴⁸, but saturated at a later stage in the *B. mori* and *A. assama* silks (Fig. 5b, c, and Supplementary Fig. 5). This indicates that the stress distribution to the crystal phases in the bagworm silk is more homogeneous throughout the tensile process than that in the other two silks. This superior stress distribution mode should be realised owing to the continuous and highly ordered periodic structure revealed by SAXS analysis. By combining all the experimental results obtained in the present study, we have proposed a hierarchical structure model for bagworm silks (Fig. 6e). The ellipsoidal single filament is made up of the 150 nm-thick bundles of nanofibrils, each of which has a diameter of about 4.7 nm. These nanofibrils are considered to be assembled together and form the repeatedly-arranged structure with the amorphous phases. It is reasonably speculated that the amorphous chain segments gather together randomly and the entire system of nanofibrils appears like a network of nanofibrils (image on the left in Fig. 6e). The tension-induced structural deformation of the nanofibril bundle is schematically illustrated in Fig. 6f, where the ordered repeating structure is maintained in this process. Our findings obtained by X-ray scattering techniques are consistent with the intrinsic nanofibrillar nature of silkworm and spider silks revealed by nanoscale imaging techniques^{49,50}. Verification of the proposed structural model and the deformation process of bagworm silks using nanoscale imaging and spectroscopy techniques remains an avenue for further study.

Our experimental results presented an important fact: the mechanical property of the crystal phase of silk β -sheets is considerably higher than what we had considered so far. The slope of the stress vs. crystal strain plot of the bagworm silk gave a crystal modulus of 106 GPa (Fig. 5a), which is four times higher than the values for *B. mori* silkworm silks estimated by the X-ray diffraction method^{51,52}. The methodology for the measurement of the crystal modulus is established, but it is made under an assumption of homogeneous stress distribution (Supplementary Note 2). The high modulus of the bagworm silk proposed a possibility that the true crystal modulus of the β -sheet crystal is much higher than what we had considered⁵³, and that the stress distribution to the crystal phases is far from an ideal homogeneous stress distribution, but quite heterogeneous, in natural silks (Supplementary Note 3). In contrast, the highly ordered network structure of bagworm silk results in a highly homogeneous stress distribution mode and gives the crystal modulus approximately close to the true ultimate modulus.

In summary, we found that the bagworm silk is extraordinarily strong and tough compared to other known natural silks, and its tensile deformation behaviour is quite elastic. Although a variety of silks with different mechanical properties should be candidates for various practical applications, bagworm silk seems especially appropriate for use as a structural material. The detailed structural analyses, from amino acid sequence to hierarchical structure level, clarified that the outstanding mechanical properties originated from a highly ordered hierarchical network structure,

which remains unchanged up to fracture in the tensile deformation process. Such unique structural and mechanical functions are largely attributed to the requirements of protecting and supporting the larva, where the former requirement is crucial for silkworm cocoon silks and the latter for spider dragline silks. Silkworm cocoon silks have evolved to protect the larva during their pupal stage, and therefore stiffness is a crucial aspect¹⁸. On the other hand, spider dragline silks, the web-frame silk, have evolved to bring rapidly flying prey as well as to support the spider's body as her lifeline. Therefore, spider dragline silks are tougher, which enables absorption of the kinetic energy of the prey or the spider itself without breaking^{18,54,55} (the architectures of spider webs are also sophisticated to the requirements^{55,56}). The tandem repeat motifs of the H-Fib protein of bagworm silk show an ideal sequence composition to produce this hybrid silk from a pair of glands, combining the functions of silkworm and spider dragline silks. Our findings clearly demonstrate how the hierarchical structure of silk proteins plays an important role in the mechanical properties of the resultant bulk fibres, and how it is closely related to the primary structure of the amino acid sequence. We believe that the knowledge obtained through this will lead to fruitful strategies for designing the primary structures, resulting in stronger and tougher artificial silks, based on genome-editing technology⁵⁷. It should be emphasised here that the strong potential of bagworm silks is not only owing to the superior mechanical properties, but also the promising possibilities for practical applications. We have successfully developed a mass rearing technique and fibre collection method for bagworms, with a continuous and long scale over several hundreds of metres, without sacrificing the animals (Fig. 1e, f). This strong, tough, and long silk thread is anticipated to be applicable to various kinds of material fields, such as modern apparel, and biomedical and opto-electrical fields, and an especially promising candidate for the next generation of structural materials made from renewable resources, conforming to the spirit of animal welfare.

Methods

Silk fibre collection. *E. variegata* bagworm larvae of the last instar, within a size distribution reported by Sugimoto²¹, were collected in Tsukuba City, Ibaraki (Japan) in October 2015. Single fibres for the tensile test were collected from the wall of the rearing cage on which bagworms spun their silk as footholds. The fibre bundles for X-ray analysis and for time-resolved simultaneous measurement of X-ray diffraction and tensile tests were also collected from the wall of the rearing cage. Once stress is loaded, the initial long period irreversibly changes, as revealed in this study; therefore, all the sample fibres were carefully corrected without loading excessive tension.

Observation of surface morphology. Observations of the fibre surface morphology were made using a digital camera (Stylus Tough, Olympus Co., Japan), fluorescence microscope in optical microscopy mode (BZ-X700, Keyence Co., Japan), and scanning electron microscope (SEM) (JSM-6301F, JEOL Ltd., Japan).

Observation of cross-sections. Cross-sections of the bagworm silks were prepared as described below and examined using the BZ-X700 microscope in optical mode. The silk fibres were gently aligned in a parallel fashion and embedded in an epoxy resin (Quetol 812, Nisshin EM Co. Ltd., Japan). Thereafter, the resin was polymerised at 60 °C for 48 h and the samples were sliced across the fibre axis to thicknesses ranging from 1.0 to 2.0 μm using an ultra-microtome (LKB 2088, LKB Produkter, Sweden). The resultant thin sections were stained with a 1% (w/v) aqueous solution of toluidine blue containing 1% (w/v) borax.

Evaluation of cross-sectional area. While most of the fibres are made up of a pair of conjugated filaments with an almost linear relation between their major axes as schematically illustrated in Fig. 1h, for some fibres, the major axes of the pair of filaments were found to be conjugated at an angle of $180 - 2\theta$ (°), where the angle θ is defined as the tilt angle of each major axis from the linear relation, as schematically illustrated in Fig. 1i. The θ for each fibre was evaluated using the ImageJ open-source software to be approximately 10.37°.

The cross-sectional area of each fibre was estimated as follows. Firstly, the cross-sectional shape of each thin filament was assumed to be a perfect ellipse with an

axial ratio (L_a/L_b) of 1.7, as described in the main text. By this approximation, one can calculate the cross-sectional area by measuring the length of the major axis of the filament using a well-calibrated BZ-X700 instrument. At this stage, the θ should be taken into account, because the length of the major axis measured using the optical microscope (L'_a) is $L_a \cdot \cos\theta$, as illustrated schematically in Fig. 1i. Therefore, the actual cross-sectional area of a single filament is $\frac{\pi}{4 \times 1.70 \times \cos^2\theta} \cdot L_a^2$. The average tilt angle of 10.37° was used as the value of θ .

Tensile test. The tensile properties of the individual fibres of *E. variegata* bagworm silk were measured at 22–25 °C and 40–60% relative humidity, using a mechanical tensile stage (EZ Test/CE, Shimadzu Co., Japan) equipped with a 5 N load cell. All the measurements were carried out at a cross-head speed of 10 mm min⁻¹. A single fibre made up of a pair of thin filaments with an elliptical cross section was attached to a handmade paper flame using epoxy glue, with a window distance (i.e., sample distance) of 15 mm. After positioning the paper flame holding a single fibre in the tensile stage, both sides of the flame were cut gently, and then the measurement was started. The cross-sectional area of each fibre was estimated for every sample, based on optical microscope observations. The procedure for estimating the elliptical cross-sectional area of bagworm silks was described in the previous section. In all, 19 measurements (4 or 5 measurements each for 4 different bagworms) were carried out and averaged (Supplementary Fig. 6).

Analysis of amino acid composition. The amino acid composition of the bagworm silk fibres was analysed with a Shimadzu amino acid analysis system using a high-performance liquid chromatography CBM-20A controller (Shimadzu Co., Japan), equipped with the columns Shim-pack Amino-Na (100 mm (L) × 6.0 mm (φ)) and ISC-30 (Na) (50 mm (L) × 4.0 mm (φ)) (Shimadzu Co., Japan). The degummed fibres were dissolved in 6 N hydrochloric acid under vacuum at 110 °C for 22 h. The sample was dried under nitrogen gas purging, re-dissolved in pH 2.2 sodium citrate buffer, and examined, for the amino acid analysis.

RNA sequencing and bioinformatics analysis. The larvae of the bagworm moth were collected in Abiko City, Chiba (Japan) in September 2015. The silk gland was dissected from one larva and the total RNA was extracted from the posterior region of the silk gland using the ISOGEN (NIPPON GENE, Tokyo, Japan) and SV Total RNA Isolation System (Promega, Madison, WI). The long-read sequencing analysis (Isoform Sequencing) was carried out using a PacBio RS II sequencer. The library was prepared using the Clontech SMARTer PCR cDNA Synthesis Kit (TaKaRa, Kusatsu, Japan), and the ~5–10 kb libraries were selected using the BluePippin Size-Selection System (NIPPON Genetics, Tokyo, Japan). After purification and end-repair, the blunt-end SMARTbell adaptors were ligated. The libraries were quantified using a Quant-IT PicoGreen kit (Thermo Fisher Scientific, Waltham, MA), and qualified using the Agilent Technologies 2100 Bioanalyzer (Agilent Technologies, Waldbronn, Germany). Subsequently, the libraries were sequenced using the PacBio P6C4 chemistry in an 8-well SMART Cell v3 with a PacBio RS II system. For sequence correction, the Illumina short-read sequence was used. The total RNA extracted from the posterior region of the silk gland was applied for the RNA library construction using a TruSeq RNA Sample Prep Kit v2 (Illumina, San Diego, CA), and the 101 bp paired-end reads were obtained using an Illumina HiSeq 2500 sequencer. Adaptor sequences and low quality bases in the Illumina short reads were trimmed using the Trimmomatic version 0.32⁵⁸, and the cleaned short reads were used for the long-read correction with CoLoRMap⁵⁹. The raw sequence data have been deposited in the DNA Data Bank of Japan (DDBJ) Centre (<https://www.ddbj.nig.ac.jp/index-e.html>) and can be accessed via accession numbers, DRA007344 (short-reads) and DRA007345 (long-reads).

Static structural analysis by WAXD and SAXS. A parallel-aligned fibre bundle with a thickness of about 0.1 mm was prepared, and the surface adhesive was washed with a 0.05 M sodium carbonate boiled aqueous solution for 3 min. The fibre bundle was then thoroughly rinsed and dried, and transferred as samples for the subsequent X-ray analyses.

For references, the de-gummed *B. mori* and Indian *Antheraea assama* (*A. assama*) (aka *Muga* silk) (*Saturniidae*) silks were also gently collected in a parallel-aligned fibre bundle with a bundle thickness of about 0.5 mm, and used for the subsequent X-ray analyses during the tensile deformation test. The cross-sectional area for each fibre bundle, needed for the data conversion from the force-strain to the stress-strain curves, was estimated from the length and weight of the initial fibre bundle and the density for each silk. The values of density, 1.35 and 1.31 g cm⁻³, reported by Gupta et al. for *B. mori* and *A. assama* silks, respectively, were used⁶⁰.

The crystalline modification of the bagworm silk was investigated by WAXD analysis, using an R-Axis Rapid II X-ray diffractometer (Mo-Kα) (Rigaku Co., Japan) equipped with a cylindrical-type imaging plate camera. The hierarchical structure was investigated by SAXS analysis, using a synchrotron X-ray beam in the SPring-8 40B2 beamline or using a NANOPIX 3.5 M X-ray diffractometer (Cu-Kα) (Rigaku Co., Japan) equipped with the highly sensitive single-photon-counting pixel detector HyPix-6000 (Rigaku Co., Japan). Cerium oxide and silver behenate were used to calibrate the camera distances for the WAXD and SAXS

measurements, respectively. All X-ray measurements were performed at 22–25 °C and 40–60% relative humidity.

Time-resolved synchrotron X-ray scattering investigation. The structural changes in the bagworm silk, occurring in the stretching processes, were investigated by time-resolved simultaneous measurements of the force-strain curve and synchrotron WAXD and SAXS patterns. The fibre bundle with a bundle thickness of about 0.1 mm was set on a stretching device, the Micro-stretcher (Linkam Scientific Instruments Ltd., UK), which was set in a SPring-8 40B2 synchrotron X-ray beamline (Hyogo, Japan). The setup geometry is shown in Supplementary Fig. 4. The WAXD and SAXS data were measured every 9 s (8 s exposure time + 1 s interval) during the continuous stretching process, with a stretching rate of 10 μm s⁻¹. The wavelength of the incident X-ray beam was 0.0709 nm, and the sample-to-camera distances for the WAXD and SAXS measurements were 95 and 763 mm, respectively. The beam size at the sample position was around 0.4 × 0.8 mm². Tuning of the best beam intensity, which yields the best quality of scattering without serious sample damage during the repetitive measurements, was carefully performed using the attenuator system. A flat panel detector with a pixel size of 50 × 50 μm² (Hamamatsu Photonics K. K., Japan) and CMOS detector with a pixel size of 43.1 × 43.1 μm² (Hamamatsu Photonics K. K., Japan) were used for the WAXD and SAXS measurements, respectively. For the accurate calibration of the WAXD camera distance, silicon powder was dusted onto the fibre bundle. The force-strain data obtained from the tensile test was approximately converted to a stress-strain curve on the basis of the stress-strain curves obtained from the single fibres. The sample strain (%) was estimated as Δl (mm)/ l_0 (mm) × 100 (%), where l_0 is the initial sample length of 15 mm between the tensile clamps, and Δl is the stretched length.

WAXD data analysis. For all the cases of WAXD analysis, air scattering was subtracted from the original 2D-WAXD pattern. The crystallinity was estimated from the WAXD 2θ profile. The 2θ profile was scanned from the 2D-WAXD fibre diagram, and ranged from 10 to 37°. For the 2θ profile obtained, peak fitting analysis was performed to separate the contributions from the crystalline reflections and amorphous halo-scattering. For the peak fitting, the contributions from the 6 crystalline lattice planes, (200), (210), (211), (002), (102) + (300), and (202), and that from the single amorphous scattering, were considered. Each 2θ position of the crystalline reflections was calculated on the basis of the unit cell parameters of the β-sheet crystal determined for the bagworm silk in this study. The peaks were fitted with Gaussian functions, using a “non-linear least squares fitting”, in the spectroscopy software Grams Suite 9.3 (Thermo Fisher Scientific Inc., USA). The crystallinity X_c was calculated using Eq. (1):

$$X_c(\%) = \frac{I_c}{(I_c + I_a)} \times 100, \quad (1)$$

where I_c and I_a are the total intensities from the crystal and amorphous phases, respectively.

The crystal strain (ϵ_c) along the *c*-axis direction at each bulk strain (ϵ) was evaluated from the changes in the 2θ position of the 002 meridional reflection. The ϵ_c was defined as shown in Eq. (2).

$$\epsilon_c(\%) = (d_{002}(\epsilon) - d_{002}(\text{initial})) / d_{002}(\text{initial}) \times 100 \quad (2)$$

The crystalline orientation index was evaluated using the definition (180-FWHM)/180, where FWHM is the full width at half maximum of the azimuthal angular distribution of the WAXD equatorial 200 reflection.

SAXS data analysis. For all the cases of SAXS analysis, air scattering was subtracted from the original 2D-SAXS pattern. The meridional or equatorial *q*-profiles were scanned from the meridional and equatorial lines with an azimuthal angle range of ±10°, where *q* is the scattering vector, defined as $(4\pi/\lambda) \sin\theta$, where λ is the wavelength of the X-ray beam used. Thus, the obtained 1d-*q*-profile ($I(q)$ vs. *q* plot) was replotted as a Kratky plot ($q^2I(q)$ vs. *q* plot) to enhance the peak features more evidently³⁵.

The one-dimensional electron density correlation function $K(z)$ between a periodic structure made of phases I and II, which gives an electron density distribution $\eta(z)$, as depicted in Fig. 3f, was calculated from the SAXS data. The correlation function $K(z)$ is defined as shown in Eq. (3)³⁶.

$$K(z) \propto \int_0^\infty q^2 I(q) \cos(zq) dq \quad (3)$$

Q , L_p , d_{p1} , and $\langle d_{p1} \rangle$, shown in Fig. 3e, f, denote the invariant, long period, core thickness of domain I, and mean thickness of phase I, respectively.

The strain (ϵ_l) in the long period was estimated using Eq. (4).

$$\epsilon_l(\%) = (L_p^{1st}(\epsilon) - L_p^{1st}(\text{initial})) / L_p^{1st}(\text{initial}) \times 100 \quad (4)$$

The thickness of the nanofibril bundle was evaluated from the broadening of the equatorial SAXS peak, using the Scherrer Eq. (5)¹⁰:

$$d = \frac{K\lambda}{\beta \cos \theta}, \quad (5)$$

where d is the thickness of the nanofibre bundle, λ is the wavelength of the incident X-ray beam (CuK α 0.15418 nm radiation), θ is the angle of the considered reflection, β is the line broadening at half-maximum intensity of the considered reflection, and K is a dimension-less shape factor (Scherrer factor). For the shape factor K , a value of 0.9 was used. The β was corrected for the instrumental broadening, which was estimated by measuring the powder diffraction profile of silver behenate, on the basis of the Eq. (6).

$$\beta = \sqrt{\beta_{\text{obs}}^2 - \beta_{\text{AgBeh}}^2} \quad (6)$$

Data availability

The raw sequence data of the next generation sequencer have been deposited in the DNA Data Bank of Japan (DDBJ) Centre (<https://www.ddbj.nig.ac.jp/index-e.html>) and can be accessed via accession numbers, DRA007344 (short-reads), and DRA007345 (long-reads). The same raw sequence data is available from the Open Science Framework: <https://doi.org/10.17605/OSF.IO/3GYSU>. Data supporting the findings of this study are available from the authors upon reasonable request.

Received: 18 September 2018 Accepted: 27 February 2019

Published online: 01 April 2019

References

- Nickel, J. & Riedel, U. in *Biorelated Polymers: Sustainable Polymer Science and Technology*. 27–40 (Kluwer Academic/Plenum Publishers, New York, 2001).
- Mathijssen, D. Beyond carbon fiber: what will be the fibers of choice for future composites? *Reinf. Plast.* **60**, 38–44 (2016).
- Gosline, J. M. in *Mechanical Design of Structural Materials in Animals*. 103–180 (Princeton University Press, Princeton and Oxford, 2018).
- Craig, C. L. Evolution of arthropod silks. *Annu. Rev. Entomol.* **42**, 231–267 (1997).
- Harmer, A. M. T., Blackledge, T. A., Madin, J. S. & Herverstein, M. E. High-performance spider webs: integrating biomechanics, ecology and behaviour. *J. R. Soc. Interface* **8**, 457–471 (2011).
- Dalton, A. B. et al. Super-tough carbon-nanotube fibers. *Nature* **423**, 703 (2003).
- Wegst, U. G. K., Bai, H., Saiz, E., Tomsia, A. P. & Ritchie, R. O. Bioinspired structural materials. *Nat. Mater.* **14**, 23–36 (2015).
- Agnarsson, I., Kuntner, M. & Blackledge, T. A. Bioprospecting finds the toughest biological material: extraordinary silk from a giant riverine orb spider. *PLoS One* **5**, e11234 (2010).
- Cranford, S. W., Tarakanova, A., Pugno, N. M. & Buehler, M. J. Nonlinear material behaviour of spider silk yields robust webs. *Nature* **482**, 72–76 (2012).
- Yoshioka, T., Tashiro, K. & Ohta, N. Molecular orientation enhancement of silk by the hot-stretching-induced transition from α -helix-HFIP complex to β -sheet. *Biomacromolecules* **17**, 1437–1448 (2016).
- Koepfel, A. & Holland, C. Progress and trends in artificial silk spinning: A systematic review. *ACS Biomater. Sci. Eng.* **3**, 226–237 (2017).
- Bourzac, K. Spiders: web of intrigue. *Nature* **519**, s4–s6 (2015).
- Lazaris, A. et al. Spider silk fibers spun from soluble recombinant silk produced in mammalian cells. *Science* **295**, 472–476 (2002).
- Kuwana, Y. et al. High-toughness silk produced by a transgenic silkworm expressing spider (*Araneus ventricosus*) dragline silk protein. *PLoS One* **9**, e105325 (2014).
- Malay, A. D. et al. Relationships between physical properties and sequence in silkworm silks. *Sci. Rep.* **6**, 27573 (2016).
- Yoshioka, T., Kameda, T., Tashiro, K., Ohta, N. & Schaper, A. K. Transformation of coiled α -helices into cross- β -sheets superstructure. *Biomacromolecules* **18**, 3892–3903 (2017).
- Osaki, S. Spider silk as mechanical lifeline. *Nature* **384**, 419 (1996).
- Vollrath, F. & Knight, D. P. Liquid crystalline spinning of spider silk. *Nature* **410**, 541–548 (2001).
- Vollrath, F. & Porter, D. Spider silk as archetypal protein elastomer. *Soft Matter* **2**, 377–385 (2006).
- Rhainds, M., Davis, R. D. & Price, P. W. Bionomics of bagworms (Lepidoptera: Psychidae). *Annu. Rev. Entomol.* **54**, 209–226 (2009).
- Sugimoto, M. A comparative study of larval cases of Japanese Psychidae (Lepidoptera) (2). *Jpn J. Ent.* **12**, 17–29 (2009).
- Nishida, E. Biologies and parasite complexes of two bagworms, *Eumeta variegata* and *Eumeta minuscula* (Lepidoptera, Psychidae) in Japan. *Kontyû, Tokyo* **51**, 394–411 (1983).
- Reddy, N. & Yang, Y. Structure and properties of ultrafine silk fibers produced by Theriodopteryx ephemeraeformis. *J. Mater. Sci.* **45**, 6617–6622 (2010).
- Osaki, S. Animals teach science on natural fibers: spider's silks, bagworm's silks, collagen fibers. *Sen'i Gakkaishi* **58**, p74–p78 (2002).
- Wolff, J. O. et al. Strength of silk attachment to Ilex chinensis leaves in the tea bagworm *Eumeta minuscula* (Lepidoptera, Psychidae). *J. R. Soc. Interface* **14**, 20170007 (2017).
- Lucas, F., Shaw, J. T. B. & Smith, S. G. Comparative studies of fibroins I. The amino acid composition of various fibroins and its significance in relation to their crystal structure and taxonomy. *J. Mol. Biol.* **2**, 239–349 (1960).
- Suyama, Y. & Kawamura, S. Studies on the silk fibroins of insects I. Amino acid composition of silk fibroins from a moth (*Clania variegata*) and a Sawfly (*Arge similis*). *Annu. Rep. Meiji Univ.* **38**, 55–59 (1977).
- Yukhiro, K. et al. in *Extracellular Composite Matrices in Arthropods*. 515–555 (Springer, Cham, 2016).
- Malay, A. D., Arakawa, K. & Numata, K. Analysis of repetitive amino acid motifs reveals the essential features of spider dragline silk proteins. *PLoS One* **12**, e0183397 (2017).
- Fu, C., Shao, Z. & Vollrath, F. Animal silks: their structure, properties and artificial production. *Chem. Commun.* 6515–6529 (2009).
- Zhou, C. Z. et al. Fine organization of Bombyx mori fibroin heavy chain gene. *Nucleic Acids Res.* **28**, 2413–2419 (2000).
- Takahashi, Y., Gehoh, M. & Yuzuriha, K. Structure refinement and diffuse streak scattering of silk (Bombyx mori). *Int. J. Biol. Macromol.* **24**, 127–138 (1999).
- Fraser, R. D. B. & MacRae, T. P. in *Conformation in Fibrous Proteins and Related Synthetic Polypeptides*. 293–343 (Academic Press, New York and London, 1973).
- Warwicker, J. O. Comparative studies of fibroins II. The crystal structures of various fibroins. *J. Mol. Biol.* **2**, 350–362 (1960).
- Roe, R. J. in *Methods of X-ray and Neutron Scattering in Polymer Science*. 155–209 (Oxford University Press, New York, 2000).
- Strobl, G. R. & Schneider, M. Direct evaluation of the electron density correlation function of partially crystalline polymers. *J. Polym. Sci.* **18**, 1343–1359 (1980).
- Sasaki, S. et al. Microscopically viewed structural change of PE during the isothermal crystallization from the melt II. Conformational ordering and lamellar formation mechanism derived from the coupled interpretation of time-resolved SAXS and FTIR data. *Polymer* **40**, 7125–7135 (1999).
- Yoshioka, T. & Kameda, T. X-ray scattering analyses quantitatively revealed periodic hierarchical structure of polyalanine β -sheet and non-polyalanine amorphous domains in *Antheraea assamensis* (Muga) silk. *J. Silk Sci. Tech. Jpn* **27**, 95–101 (2019).
- Miller, L. D. & Eby, R. K. A 45 Å equatorial long period in dry dragline silk of *Nephila clavipes*. *Polymer* **41**, 3487–3490 (2000).
- Wagner, J. A. et al. Stress-induced long-range ordering in spider silk. *Sci. Rep.* **7**, 15273 (2017).
- Riekel, C. & Vollrath, F. Spider silk fiber extrusion: combined wide- and small-angle X-ray microdiffraction experiments. *Int. J. Biol. Macromol.* **29**, 203–210 (2001).
- Yang, Z., Grubb, D. T. & Jelinski, L. W. Small-angle X-ray scattering of spider dragline silk. *Macromolecules* **30**, 8254–8261 (1997).
- Riekel, C. et al. Nanoscale structural features in major ampullate spider silk. *Biomacromolecules* **18**, 231–241 (2017).
- Nakazawa, Y. & Asakura, T. Structure determination of a peptide model of the repeated helical domain in *Samia cynthia ricini* silk fibroin before spinning by a combination of advanced solid-state NMR methods. *J. Am. Chem. Soc.* **125**, 7230–7237 (2003).
- Giesa, T., Perry, C. C. & Buehler, M. J. Secondary structure transition and critical stress for a model of spider silk assembly. *Biomacromolecules* **17**, 427–436 (2016).
- Drummy, L. F. et al. Thermally induced α -helix to β -sheet transition in regenerated silk fibers and films. *Biomacromolecules* **6**, 3328–3333 (2005).
- Giesa, T., Arslan, Melis, Pugno, N. M. & Buehler, M. J. Nanoconfinement of spider silk fibrils begets superior strength, extensibility, and toughness. *Nano Lett.* **11**, 5038–5046 (2011).
- Seydel, T. et al. Silkworm silk under tensile strain investigated by synchrotron X-ray diffraction and neutron spectroscopy. *Macromolecules* **40**, 1035–1042 (2007).
- Du, N. et al. Design of superior spider silk: from nanostructure to mechanical properties. *Biophys. J.* **91**, 4528–4535 (2006).
- Putthanarat, S., Stribeck, N., Fossey, S. A., Eby, R. K. & Adams, W. W. Investigation of the nanofibrils of silk fibers. *Polymer* **41**, 7735–7747 (2000).
- Nakamae, K., Nishino, T. & Ohkubo, H. Elastic modulus of the crystalline regions of silk fibroin. *Polymer* **30**, 1243–1246 (1989).

52. Sinsawat, A. et al. The crystal modulus of silk (*Bombyx mori*). *Polymer* **44**, 909–910 (2003).
53. Nakamoto, S., Tashiro, K. & Matsumoto, A. Quantitative evaluation of stress distribution in bulk polymer samples through the comparison of mechanical behaviours between giant single-crystal and semicrystalline samples of poly (trans-1,4-diethyl muconate). *J. Polym. Sci. Part B* **41**, 444–453 (2003).
54. Gosline, J. M., Guerette, P. A., Ortlepp, C. S. & Savage, K. N. The mechanical design of spider silks: from fibroin sequence to mechanical function. *J. Exp. Biol.* **202**, 3295–3303 (1999).
55. Gosline, J. M., DeMont, M. E. & Denny, M. W. The structure and properties of spider silk. *Endeavour* **10**, 37–43 (1986).
56. Qin, Z., Compton, B. G., Lewis, J. A. & Buehler, M. J. Structural optimization of 3D-printed synthetic spider webs for high strength. *Nat. Commun.* **6**, 7038 (2015).
57. Yoshioka, T., Takasu, Y., Sezutsu, H. & Kameda, T. Genome editing advances the structural study of silk. *ACS Biomater. Sci. Eng.* **4**, 832–835 (2018).
58. Bolger, A. M., Lohse, M. & Usadel, B. Trimmomatic: a flexible trimmer for Illumina sequence data. *Bioinformatics* **30**, 2114–2120 (2014).
59. Haghshenas, E., Hach, F., Sahinalp, S. C. & Chauve, C. CoLoRMap: Correcting long reads by mapping short reads. *Bioinformatics* **32**, i545–i551 (2016).
60. Gupta, A. K., Mita, K., Arunkumar, K. P. & Nagaraju, J. Molecular architecture of silk fibroin of Indian golden silkmoth, *Antheraea assama*. *Sci. Rep.* **5**, 12706 (2015).
61. Swanson, B. O., Blackledge, T. A., Beltran, J. & Hayashi, C. Y. Variation in the material properties of spider dragline silk across species. *Appl. Phys. A* **82**, 213–218 (2006).

Acknowledgements

This research was partly supported by Science and Technology Research Partnership for Sustainable Development (SATREPS), Japan Science and Technology Agency (JST) / Japan International Cooperation Agency (JICA) (T.K.). K.T. thanks MEXT, Japan for their support through the “Strategic Project to Support the Formation of Research Bases at Private Universities (2015–2019)”. The synchrotron radiation experiments were performed using the SPring-8 BL40B2 with the approval of Japan Synchrotron Radiation Research Institute (JASRI) (Proposal Nos 2015B1184 and 2016A1440) (T.Y.). The authors thank Dr. N. Ohta (JASRI) for his professional support in the synchrotron X-ray experiments, and Ms. F. Yukuhiro of the National Agriculture and Food Research Organisation (NARO) for the sample preparation related to the cross-sections. The authors also thank Dr. S. Niitsu and Mr. O. Saito for providing the bagworm moth.

Author contributions

All the authors (T.Y., T.T., K.T., A.J., and T.K.) contributed equally to the work and manuscript preparation.

Additional information

Supplementary Information accompanies this paper at <https://doi.org/10.1038/s41467-019-09350-3>.

Competing interests: Patent applications have been filed for the findings described in this publication (PCT/JP2017/023839 and PCT/JP2017/037327). While the research was done in an academic/institutional environment, since then the material has been taken up by a company to develop for commercialisation.

Reprints and permission information is available online at <http://npg.nature.com/reprintsandpermissions/>

Journal peer review information: *Nature Communications* thanks Konstantin Kornev, Christian Riekel and the anonymous reviewer for their contribution to the peer review of this work.

Publisher’s note: Springer Nature remains neutral with regard to jurisdictional claims in published maps and institutional affiliations.



Open Access This article is licensed under a Creative Commons Attribution 4.0 International License, which permits use, sharing, adaptation, distribution and reproduction in any medium or format, as long as you give appropriate credit to the original author(s) and the source, provide a link to the Creative Commons license, and indicate if changes were made. The images or other third party material in this article are included in the article’s Creative Commons license, unless indicated otherwise in a credit line to the material. If material is not included in the article’s Creative Commons license and your intended use is not permitted by statutory regulation or exceeds the permitted use, you will need to obtain permission directly from the copyright holder. To view a copy of this license, visit <http://creativecommons.org/licenses/by/4.0/>.

© The Author(s) 2019

Structure Analysis and Derivation of Deformed Electron Density Distribution of Polydiacetylene Giant Single Crystal by the Combination of X-ray and Neutron Diffraction Data

Kohji Tashiro,^{*,†} Katsuhiko Kusaka,[‡] Takaaki Hosoya,[§] Takashi Ohhara,^{||} Makoto Hanesaka,[†] Yoshinori Yoshizawa,[†] Hiroko Yamamoto,[⊥] Nobuo Niimura,[§] Ichiro Tanaka,[§] Kazuo Kurihara,^{||} Ryota Kuroki,^{||,#} and Taro Tamada^{||}

[†]Department of Future Industry-Oriented Basic Science and Materials, Toyota Technological Institute, Tempaku, Nagoya 468-8511, Japan

[‡]Frontier Research Center for Applied Atomic Sciences, Ibaraki University, Tokai, Naka-gun, Ibaraki 319-1106, Japan

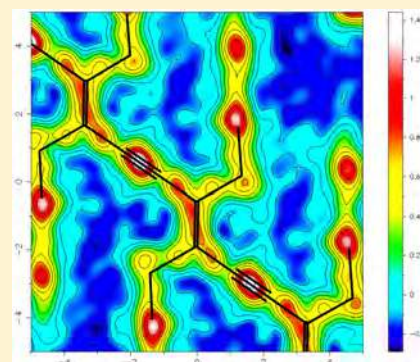
[§]Department of Biomolecular Functional Engineering, College of Engineering, Ibaraki University, Hitachi 316-8511, Japan

^{||}Research Unit for Quantum Beam Science Initiative, Japan Atomic Energy Agency, Tokai, Naka-gun, Ibaraki 319-1195, Japan

[⊥]Aichi Synchrotron Radiation Center, Aichi Science and Technology Foundation, 250-3 minamiyamaguchi, Seto 489-0965, Japan

Supporting Information

ABSTRACT: The crystal structure of polydiacetylene giant single crystal has been analyzed on the basis of the two different methods of wide-angle neutron diffraction and X-ray diffraction. The X-ray result gives us the total electron density distribution [$\rho(\mathbf{x})$] of polymer chain. The neutron result tells the positions of atomic nuclei, which can allow us to speculate the electron density distributions [$\rho_0(\mathbf{x})$] around the nonbonded isolated atoms. As a result, the so-called bonded (or deformed) electron density $\Delta\rho(\mathbf{x})$ [$\equiv \rho(\mathbf{x}) - \rho_0(\mathbf{x}) = \rho_X(\mathbf{x}) - \rho_N(\mathbf{x})$], i.e., the electron density distribution due to the conjugation among the covalently bonded atoms along the polymer chain, can be estimated using the two information obtained by the X-ray and neutron data analyses (the so-called X-ray–neutron subtraction (X–N) method). The present report is the first example of the application of X–N method to the synthetic polymer species. The $\Delta\rho(\mathbf{x})$ derived for polydiacetylene was found similar to that of the low-molecular-weight model compound having the similar electronically conjugated chemical formula. The $\Delta\rho(\mathbf{x})$ was calculated by the density functional theory, which was in a good agreement with the experimental result qualitatively.

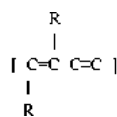


1. INTRODUCTION

1.1. Giant Single Crystals of Synthetic Polymers.

Different from the general partially crystalline polymers, in which the tiny crystallites of several tens to hundreds nanometer size are aggregated together, we sometimes have a chance to get a giant single crystal of polymer substance with the length and width of several millimeters to centimeters order. Most of these giant single crystals are obtained by the solid-state polymerization reactions of the original monomer single crystals under the irradiation of photons (γ -rays, etc.).^{1–25}

One of the well-known examples is polydiacetylene with the following chemical formula:^{6–9}



where the side chain R is, for example, a carbazoyl group, an amide group with long alkyl chain, and so on. These giant single crystals give more than 5000 sharp diffraction spots in

the X-ray diffraction measurement, allowing us to perform the highly accurate crystal structure analysis, different from the general synthetic polymer cases. (In the latter case, only several tens broad reflections are collected and the detailed crystal structure analysis is hard to do.^{26–29}) Several structural studies were reported about the polydiacetylene single crystals.^{6–9,30,31} For example, the comparison in the molecular packing structure between the original monomer crystal and the resultant polymer crystal revealed that the space group symmetry is kept unchanged before and after the solid-state polymerization reaction. Among the many photoinduced chemical reactions (topochemical reaction),^{32–36} the photoinduced chemical reaction with the space group symmetry reservation is called the topotactic reaction, which is quite limited to only a few kinds of polymer species including poly(distyrylpyrazine),^{4,5} polydiacetylene,^{6–9} *cis,cis*-poly(diethyl muconate),^{10–25} etc.

Received: March 27, 2018

Revised: May 5, 2018

Published: May 15, 2018

Since such a giant single crystal of mm size can be treated manually, the atomic displacements caused by the mechanical deformation can be traced by measuring the X-ray diffraction patterns under the application of tensile force and so the discussion can be made about the mechanical deformation mechanism of polymer chain viewed from the atomic scale.³¹ The structural deformation occurring in the photoinduced solid-state polymerization reaction process can be traced also through the simultaneous measurement of X-ray diffraction and Raman scattering.^{20,25} The Raman spectra gave the information on polymer/monomer ratio and also the strain of the polymer chain created in the monomer matrix. The X-ray data gave the strain of the crystal lattice during the reaction. These information makes it possible to know the mechanism of the photoinduced polymerization reaction in detail. In this way, the usage of giant single crystal of polymer is quite useful to reveal the details of the behaviors of polymer chains in the various processes.

1.2. Deformed Electron Density Distribution. By the way, as understood from the chemical formula of polydiacetylene, this polymer species is electronically conjugated among the single, double, and triple CC skeletal bonds. We can expect to clarify the details of the effect of electronic conjugation on the electron density distribution along the skeletal chain. Such an information should be useful for the study of the physical property from the viewpoint of electron level. For example, the highly developed π -electron conjugate system is related strongly to such characteristic physical property as a nonlinear optical property.

How can we quantitatively evaluate the electron density distribution $\rho(\mathbf{x})$ at a position \mathbf{x} ? The X-ray structure analysis may be one of the most useful and direct methods for the evaluation of $\rho(\mathbf{x})$.^{37–43} The Fourier transform of structure factors $F_{\text{obs}}^X(\mathbf{q})$, which are obtained from the observed X-ray diffraction intensities and the corresponding phase angle information, gives the electron density distribution as follows:

$$\rho(\mathbf{x}) = (1/V) \int F_{\text{obs}}^X(\mathbf{q}) e^{i\mathbf{q}\mathbf{x}} d\mathbf{q} \quad (1)$$

where \mathbf{q} is a scattering vector and V is the volume of the unit cell. Before the chemical bonds are formed, the electron clouds distribute homogeneously around the individual atoms, but they are deformed once when the atoms are bonded to form the molecule. In other words, the originally spherical electron density distribution is deformed and electron density becomes preferentially high on the middle position of the bonds. The part of electron density concentrated to the bond is called the “bonded” or “deformed” electron density distribution. The information on the density distribution of the bonded electrons $\Delta\rho(\mathbf{x})$ can be obtained by subtracting the density $\rho_0(\mathbf{x})$ of isolated atoms

$$\Delta\rho(\mathbf{x}) = \rho(\mathbf{x}) - \rho_0(\mathbf{x}) \quad (2)$$

where the $\rho_0(\mathbf{x})$ is generally assumed to be spherical. The centers of electron density clouds might be assumed approximately as the atomic nucleus positions.

$$\rho_0(\mathbf{x}) = (1/V) \int F_{\text{calc}}^X(\mathbf{q}) e^{i\mathbf{q}\mathbf{x}} d\mathbf{q} \quad (3)$$

$F_{\text{calc}}^X(\mathbf{q})$ is the structure factor calculated for the crystal structure by assuming that the atomic positions \mathbf{x}_j^X and the thermal parameters \mathbf{U}_j^X determined by the X-ray analysis (or the gravity centers of electron clouds) are equal to those of the

nuclei where the atomic scattering factors $f_j^X(\mathbf{q})$ of the isolated and noninteracting atoms without bondings are used:

$$F_{\text{calc}}^X(\mathbf{q}) = \sum_j f_j^X(\mathbf{q}) \exp(-i\mathbf{q}\mathbf{x}_j^X) \exp(-i\mathbf{q}\mathbf{U}_j^X) \quad (4)$$

Then, the $\Delta\rho(\mathbf{x})$ is calculated as

$$\Delta\rho(\mathbf{x}) = \rho(\mathbf{x}) - \rho_0(\mathbf{x}) = (1/V) \int [F_{\text{obs}}^X(\mathbf{q}) - F_{\text{calc}}^X(\mathbf{q})] e^{i\mathbf{q}\mathbf{x}} d\mathbf{q} \quad (5)$$

In the actual analysis, the continuous integration in eq 5 is changed to the discrete summation over the observed \mathbf{q} vectors.

$$\Delta\rho(\mathbf{x}) = (1/V) \sum_j \mathbf{q}_j [F_{\text{obs}}^X(\mathbf{q}_j) - F_{\text{calc}}^X(\mathbf{q}_j)] e^{i\mathbf{q}_j\mathbf{x}} \quad (6)$$

Unfortunately, however, this calculation gives sometimes a curious result of $\Delta\rho(\mathbf{x})$ due to the so-called asphericity shift effect or the deformation shift effect as mentioned above. The X-ray diffractions originating mainly from the valence (or the outer-side) electrons do not give the exact positions of the nuclei in general, but they give the center of gravity of electron clouds. In the above calculation of $F_{\text{calc}}^X(\mathbf{q}_j)$, these gravity centers of electron clouds are assumed to be equal to those of atomic nuclear positions (see eq 4). But strictly speaking, the molecular geometry given by the coordinates of atomic nuclei and that by the electron clouds are not necessarily the same. It is needed to use directly the exact positions of atomic nuclei themselves, which can be obtained experimentally by performing the wide-angle neutron diffraction analysis of the same substance. That is to say

$$\Delta\rho(\mathbf{x}) = (1/V) \sum_j \mathbf{q}_j [F_{\text{obs}}^X(\mathbf{q}_j) - F_{\text{calc}}^N(\mathbf{q}_j)] e^{i\mathbf{q}_j\mathbf{x}} \quad (7)$$

where $F_{\text{calc}}^N(\mathbf{q}_j)$ is the structure factor calculated from the isolated-atom X-ray scattering factors $f_j^X(\mathbf{q})$ combined with the parameters of nuclear positions \mathbf{x}_j^N and thermal parameters \mathbf{U}_j^N determined by neutron diffraction data analysis.

$$F_{\text{calc}}^N(\mathbf{q}) = \sum_j f_j^X(\mathbf{q}) \exp(-i\mathbf{q}\mathbf{x}_j^N) \exp(-i\mathbf{q}\mathbf{U}_j^N) \quad (8)$$

This method is called the X–N method.

The reports using this method are quite limited in number, since it is as a whole the hard work to perform both the X-ray and neutron diffraction experiments in parallel. So far, the experimental evaluation of $\Delta\rho(\mathbf{x})$ on the basis of the X–N method was reported mainly for low-molecular-weight organic compounds and metal complexes.^{44–49} As mentioned above, $\Delta\rho(\mathbf{x})$ is important also for the study of electron conjugation system of such a polymer substance as polyacetylene and electronically conductive polymer.⁵⁰ There had been, however, no experimental report to estimate the $\Delta\rho(\mathbf{x})$ along the skeletal chain of polymer substance. Because of the poor X-ray diffraction data of small number of broad reflections, the detailed analysis of the 3-dimensional crystal structure is difficult for the general synthetic polymer crystal.^{26–29} The evaluation of $\Delta\rho(\mathbf{x})$ is further more difficult or rather impossible for these general synthetic polymers! If we can find a single crystal of synthetic polymer giving as many sharp reflections as possible in both of the X-ray and neutron diffraction experiments, the accurate structural information and $\Delta\rho(\mathbf{x})$ may be obtained successfully. Of course, we must be careful in the easy usage of the term “single crystal” for the synthetic polymers. In general, a semicrystalline polymer can give a “single crystal” from the dilute solution, the size of which

is however only of submicrometer order and contains irregular structure on the surfaces.⁵¹ It is impossible to use such an extremely tiny and imperfect “single crystal” for our present purpose. Fortunately, as already mentioned above, we know some special polymers, which give the “giant single crystals” of several centimeters length and so can be treated manually for the X-ray and neutron diffraction study. Polydiacetylene is one of the most hopeful candidates for the purpose of $\Delta\rho(\mathbf{x})$ estimation.

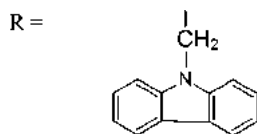
In our previous paper,⁵² we reported a preliminary research result to estimate the $\Delta\rho(\mathbf{x})$ based on the observed X-ray and neutron diffraction data. However, the neutron diffraction data were collected using the neutron beam source of relatively weak intensity from the nuclear reactor [JRR-3 (Japan Research Reactor) of JAEA (Japan Atomic Energy Agency)] although the sensitive 2D imaging plate camera was used for the collection of as many reflections as possible.^{53–55} In the present paper, we have challenged again to obtain more accurate structure information on the atomic nuclear positions by combining the two different types of the neutron diffraction experiments: (i) the diffraction data from the newly developed neutron facility *i*-BIX system in J-PARC (Japan Proton Accelerator Research Complex) and (ii) the data obtained by the JRR-3 neutron source as mentioned above. In case i, the incident neutron beams are pulse signals composed of the components with the various wavelengths, and the collection and analysis of the observed diffraction data must be performed by the TOF (time-of-flight) method.^{56–60} The experimental results obtained by these two methods are compared with each other, from which the atomic nuclear positions have been established more accurately. By combining the X-ray and neutron structure analysis results, the $\Delta\rho(\mathbf{x})$ information was obtained with high accuracy, as will be described in the first half part of the present paper.

In the second half part of the paper, the thus-derived $\Delta\rho(\mathbf{x})$ information was compared with the experimental result obtained for the low-molecular-weight model compound and also with the result obtained by the density functional theoretical calculation.

This is the first application of the X–N method to the synthetic polymer. So far, the study of electron state of polymer substance has been made mainly by using the electron spectroscopy⁶¹ and quantum chemical calculation method.⁶² The information on the electron density distribution, in particular, the bonded (or deformed) electron density distribution derived by the X–N method, may play an important role in these research also.

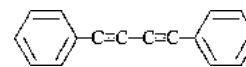
2. EXPERIMENTAL SECTION

2.1. Samples. The giant polymer single crystal used here was poly(1,4-dicarbazoryldiacetylene) (PDCHD). The side group R is a carbazoyl group:



The PDCHD single crystal was prepared by irradiating 40 Mrad γ -rays onto the single crystal of 1,4-dicarbazoryldiacetylene (DCHD) monomer at room temperature. The size of the single crystals used was about $0.5 \times 0.3 \times 10 \text{ mm}^3$ (for the X-ray diffraction measurement), about $3 \times 1 \times 5 \text{ mm}^3$

(for the neutron diffraction measurement by BIX-3 system), and about $2 \times 0.6 \times 5 \text{ mm}^3$ (for the neutron diffraction measurement by the *i*-BIX system). The single crystals of the model compound 1,6-biphenyl-2,4-butadiyne (BPBD) were also used for the check of the usefulness of the X–N method.



The single crystals of BPBD were grown from the *p*-xylene solution at room temperature.

2.2. Measurements.

(1) *X-ray Diffraction.* The X-ray diffraction measurements were performed at room temperature by utilizing a Rigaku R-Axis Rapid II X-ray diffractometer with a graphite-monochromatized Mo $K\alpha$ line as an incident X-ray beam and with a cylindrical imaging plate camera as the 2-dimensional X-ray detector. The oscillation angle $\Delta\omega = 1^\circ$ in the range of $\omega = 130\text{--}260^\circ$ at $\chi = 45^\circ$ and $\phi = 90^\circ$ and $\omega = 0\text{--}180^\circ$ at $\chi = 45^\circ$ and $\phi = 270^\circ$. The exposure rate was 120 s/deg. No detectable damage occurred for the sample due to the incident X-ray beam.

(2) *Neutron Diffraction.* The neutron diffraction measurement was performed at room temperature by using the two systems.

(A) *BIX-3.* The formal name of BIX-3 is a high-resolution neutron diffractometer dedicated to biological macromolecules, which is installed at the JRR-3 reactor hall of the JAEA in Tokaimura, Japan.^{53–55} A schematic illustration of the BIX-3 cylindrical camera is shown in Figure 1. The sample was amounted on a goniometer head, which was set downward on the top of the cylindrical imaging plate camera of 40 cm diameter. The oscillation angle of the sample was $\Delta\omega = 2^\circ$ ($0.4^\circ/\text{min}$) in the ranges of $\omega = 0\text{--}180^\circ$ at $\chi = 30^\circ$, $\omega = 0\text{--}90^\circ$ at $\chi = 50^\circ$, and $\omega = 0\text{--}90^\circ$ at $\chi = 70^\circ$. The exposure time was 25 min per shot. The monochromatized neutron beam with a wavelength 1.51 Å was incident on the sample through a slit of 5 mm diameter. The imaging plate was used as the 2-dimensional neutron detector, which is a thick polyethylene plate containing Gd_2O_3 , Ba_2BF , and Eu^{2+} . The film was defended from γ -rays by covering with a lead plate and from neutron scatterings originated from outer sources by covering with a B4C plate. The 2D scattering images were read by irradiating a rotating He–Ne laser beam on the imaging plate moved continuously along the vertical direction.

(B) *i*-BIX. Another measurement system was an *i*-BIX or the Ibaraki Biological crystal diffractometer installed in the beamline 03 at the Material and Life Science Experimental Facility (MLF), J-PARC, Tokaimura, Japan.^{56–60} The pulsed neutron beam, which was generated from the fission decay (or spallation) of mercury by shooting the highly accelerated proton particles, was incident to the sample at 25 Hz through the collimator of 5 mm ϕ . The proton acceleration power was 200 kW. The wavelength range of the thus-generated neutron was 0.7–4 Å. The 20 2-dimensional position-sensitive detectors were set around the sample. The detector was a scintillation counter composed of ZnS scintillator with the dopants Ag and $^{10}\text{B}_2\text{O}_3$, and the emitted photons were collected using the photomultiplier. The TOF measurement for one sample orientation was made for about 2.4 h by shooting the 183 600 proton pulses to the mercury target at 25 Hz. As shown in Figure 2, the sample was set on a goniometer head, and the diffraction data were collected for the 54 different sample orientations at ϕ (0° , -90° , and $+90^\circ$) and ω angles (every 25° in the range of -90° to $+85^\circ$). The total collection time was about 6 days. The thus-collected data were processed using a software STARGazer developed there.^{59,60} The details of the

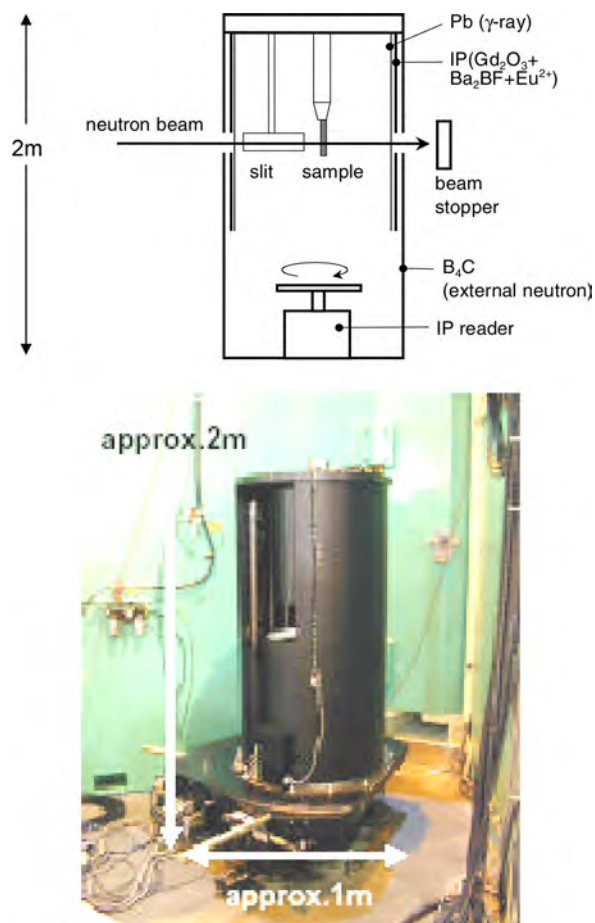


Figure 1. BIX-3 system. The cylindrical imaging plate is used as the 2-dimensional detector, which is covered with Pb and B₄C to guard the imaging plate from the external γ -rays and neutron signals. The diffraction image is read out by irradiating a red laser beam onto the whole part of the plate.^{53–55}

treatment of the TOF data are described in the Supporting Information 1.

2.3. X-ray Structure Analysis. The X-ray diffraction data were analyzed to obtain the unit cell parameters and the diffraction indices by using a software Rapid Auto (Rigaku, Tokyo). The 12 620 diffraction spots were collected with the correction of Lorentz and polarization factors as well as the absorption effect, among which 2375 were unique ($R_{\text{int}} = 2.55\%$), and the equivalent reflections were merged. The crystal structure was analyzed using a Rigaku software Crystal Structure (version 3.7.0) with the direct method (SIR⁶³) and the full-matrix least-squares method. The non-hydrogen atoms were refined anisotropically. Hydrogen atoms were refined using the riding model (i.e., by putting H atoms on the C atoms with the standard geometries). The full-matrix least-squares refinement on $|F(hkl)|^2$ was based on 1882 observed reflections [$|F_o(hkl)| > 2\sigma(|F_o(hkl)|)$] and 186 variable parameters and converged (largest parameter shift was 0.08 times its esd) with unweighted and weighted agreement factors of $R_1 = \frac{\sum ||F_o| - |F_c||}{\sum |F_o|} = 4.29\%$ [$|F_o(hkl)| > 2\sigma(|F_o(hkl)|)$] and $wR_2 = \frac{[\sum (w(|F_o|^2 - |F_c|^2))^2 / \sum w(|F_o|^2)^2]^{1/2}}{\sum w(|F_o|^2)^2} = 11.5\%$, where hkl is the reflection index and $|F(hkl)|^2$ is the square of the absolute value of the corresponding structure factor. The Robust-resistant weighting scheme was used. Neutral atom scattering factors were taken from International Tables for X-ray Crystallography.⁶⁴

2.4. Neutron Structure Analysis.

- (A) *BIX-3 Data Analysis.* The observed intensity data were corrected for the Lorentz factor and the extinction effect to obtain the set of hkl and $|F(hkl)|^2$ using the software DENZO. The total number of the observed spots was 5958. $R_{\text{int}} = 4.5\%$. The thus-treated diffraction data were analyzed for all the atoms including H atoms using SHLEX software⁶⁵ to derive the crystal structure. The reliable factor was 11.4% for the unique 1654 reflections with $F_o > 2\sigma(F_o)$ where F_o is a structure factor and σ is the standard deviation.
- (B) *i-BIX Data Analysis.* The total number of the observed spots was 13 730, among which the unique diffractions was 3027 for $F_o > 2\sigma(F_o)$. The R_{int} factor for the equivalent spots was 14.4%. (This value looks relatively high compared with that of the normal diffraction data analysis, about 3–10%. In the present TOF experiment, the wide range of wavelength was covered

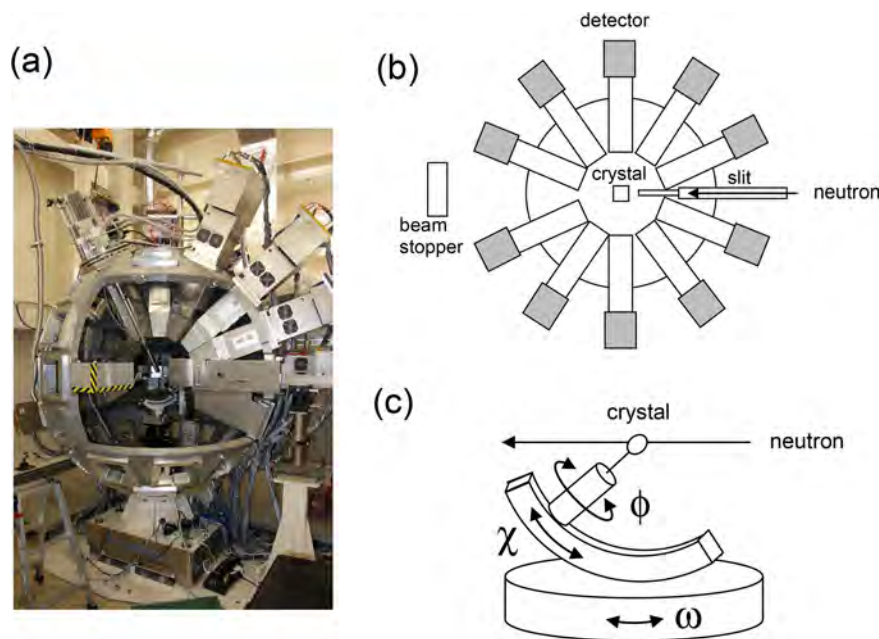


Figure 2. i-BIX system. Neutrons are incident to the sample set on a goniometer head at the center position, and the diffracted signals are measured by 20 detectors surrounding the crystal.^{56–60} (a) A snapshot of the system, (b) an illustration of the system, and (c) the sample setting angles ϕ , χ , and ω .

(0.7–4 Å). The incident neutron beam of the shortest wavelength 0.7 Å is relatively weak, and the intensity estimation is less accurate compared with the neutron components of the longer wavelength. As a result, the relatively poor coincidence was obtained among the observed equivalent spots. However, since many setting data were collected using the different detectors, the accuracy of the averaged intensity itself of the observed diffraction spots is enough high.) The structure factors were estimated from the thus-collected integrated intensity data after the Lorentz factor correction. The crystal structure analysis was performed using a program SHELX-2018 to refine the coordinates and anisotropic temperature factors of all the atoms including hydrogen atoms. The *R* factor of the final structure was 10.45% for the data of $F_o > 2\sigma(F_o)$ and 17.26% for all the observed diffraction spots.

2.5. Density Functional Theoretical Calculation. The electron density distribution was calculated using the DMol³ program (Materials Studio 8.0, Biovia). The X-ray analyzed structure was optimized energetically, and the total electron density $\rho(\mathbf{x})$ and the bonded electron density (or the deformation density) $\Delta\rho(\mathbf{x})$ were calculated. In the calculation of $\Delta\rho(\mathbf{x})$, the $\rho_0(\mathbf{x})$ or the electron density distributions of the isolated atoms were calculated and subtracted from the total electron density $\rho(\mathbf{x})$. The GGA-PBE was used as the functionals. The DFT semicore pseudopotentials were used for the core electrons. The basis set was DNP (double-numerical plus polarization, version 4.4).

3. RESULTS AND DISCUSSION

3.1. X-ray-Analyzed Crystal Structure. Figure 3 shows the crystal structure and molecular conformation of PDCHD obtained by the X-ray data analysis. The unit cell parameters are as follows: $a = 12.8525(4)$ Å, $b = 4.88680(10)$ Å, $c = 17.3393(6)$ Å, and $\beta = 108.3690(10)^\circ$. The space group is $P2_1/c-C_{2h}^5$. The atomic fractional coordinates, thermal parameters, and structure factors are shown in Supporting Information 2.

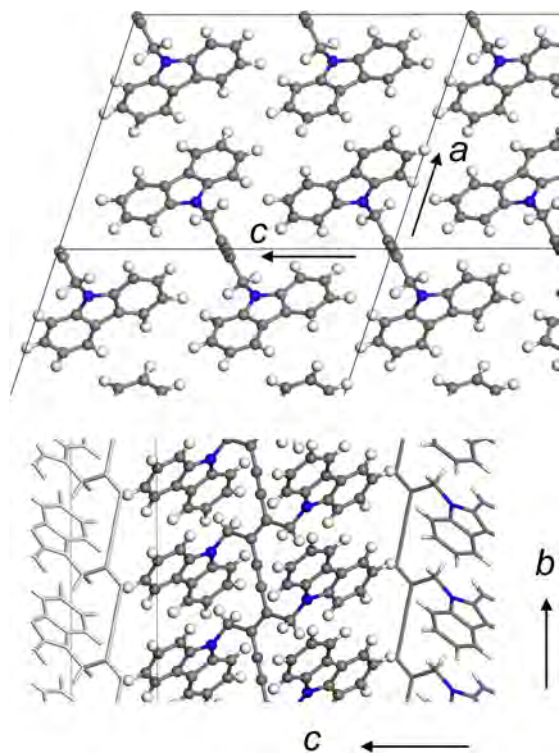


Figure 3. Crystal structure of PDCHD revealed by the X-ray structure analysis.

The thus-derived crystal structure is consistent with that reported already in the literatures including ours.^{6–9,31,52} As seen in Figure 3, the almost fully extended chains of planar-zigzag conformation with the bulky carbazolyl groups are packed side by side in the unit cell. The bond lengths are C–C 1.4176(14) Å, C = C 1.3608(19) Å, and C≡C 1.203(2) Å. The single bond is shorter and the double bond is longer than the normal values of single (1.53 Å) and double (1.34 Å) bonds, reflecting the electronic conjugation of the PDCHD skeletal chain. The triple bond is close to the normal value (1.21 Å). However, this type of comparison is not very meaningful since the apparent bond length determined by the X-ray diffraction data analysis is that derived from the center of gravity of the total electron density distribution $\rho(\mathbf{x})$. A more detailed discussion is made in a later section.

3.2. Neutron-Analyzed Crystal Structure. As already mentioned in the Experimental Section, the structure analysis of PDCHD was performed separately using the two different types of neutron diffraction data collected with BIX-3 and i-BIX systems, from which the positions of atomic nuclei were determined.

- For the BIX-3 data: the total number of the observed reflections was 5958. The *R* factor was 11.4% for the 1654 unique diffraction spots. The unit cell parameters were transferred from those determined by the X-ray data analysis since the sample size used for the neutron diffraction measurement was too large.
- For the i-BIX data: the total number of the observed reflections was 13 730, among which the number of the unique reflections with $F_o > 2\sigma(F_o)$ was 2124. The *R* factor was 10.45%. The unit cell parameters evaluated by the X-ray analysis were used.

The result of the structure analysis is compared between these methods as shown in the Supporting Information 3 (the cif files for BIX-3 and i-BIX). Table 1 compares the bond lengths between these methods as well as the X-ray result. The crystal structures derived by these two methods were essentially the same in the accuracy of the atomic nuclear coordinates. Figure 4 shows the thus-obtained atomic nuclear density distribution of PDCHD in comparison with the electron density distribution derived from the X-ray data analysis, where the data derived by the BIX-3 were used for the calculation. The electron clouds (X-ray) distribute more widely than the nuclear density (neutron), indicating that the originally locally distributed electron clouds are overlapped, hybridized, and deformed more or less. The bonded electron clouds between the adjacent carbon nuclei may be extracted by performing the X–N calculation, as will be described in the next section.

3.3. Estimation of Bonded Electron Density Distribution. X–N Method. Utilizing the results of both the X-ray and neutron data analyses, the X–N method was applied to derive the $\Delta\rho(\mathbf{x})$ on the basis of eq 8. The $F_{\text{calc}}^N(\mathbf{q}_j)$ in eq 8 was calculated using the X-ray isotropic atomic scattering factors with the fractional coordinates and thermal parameters of atomic nuclei estimated by the neutron analysis. The thus-calculated $\Delta\rho(\mathbf{x})$ is shown in Figure 5a. Figure 5b shows the 1-dimensional bonded-electron-density distribution curve traced along the skeletal chain axis. The electron density is highly distributed around the center positions of triple bonds. The lower but similar maxima are detected also on the single and double bonds.

Table 1. Comparison of Bond Lengths Evaluated by X-ray and Neutron Data Analyses

bonds	X-rays		BIX-3		i-BIX	
	length (Å)	U_{eq}	length (Å)	U_{eq}	length (Å)	U_{eq}
	PDCHD $-C_2=C_2-C_3\equiv C_3-C_2=C_2-$					
$C_3\equiv C_3$	1.203(2)	C_3 0.0427(3)	1.238(8)	C_3 0.0289 (3)	1.216(3)	C_3 0.0347(7)
C_2-C_3	1.418(1)	C_2 0.0407(3)	1.404(5)	C_2 0.0269(3)	1.410(2)	C_2 0.0318(7)
$C_2=C_2$	1.361(2)		1.372(7)		1.366(3)	
	BPBD $-C_2\equiv C_1-C_1\equiv C_2-$					
$C_1\equiv C_2$	1.1996(14)	C_2 0.0555(3)	1.212(8)	C_2 0.0479(15)		
C_1-C_1	1.376(2)	C_1 0.0568(3)	1.374(11)	C_1 0.0549(16)		

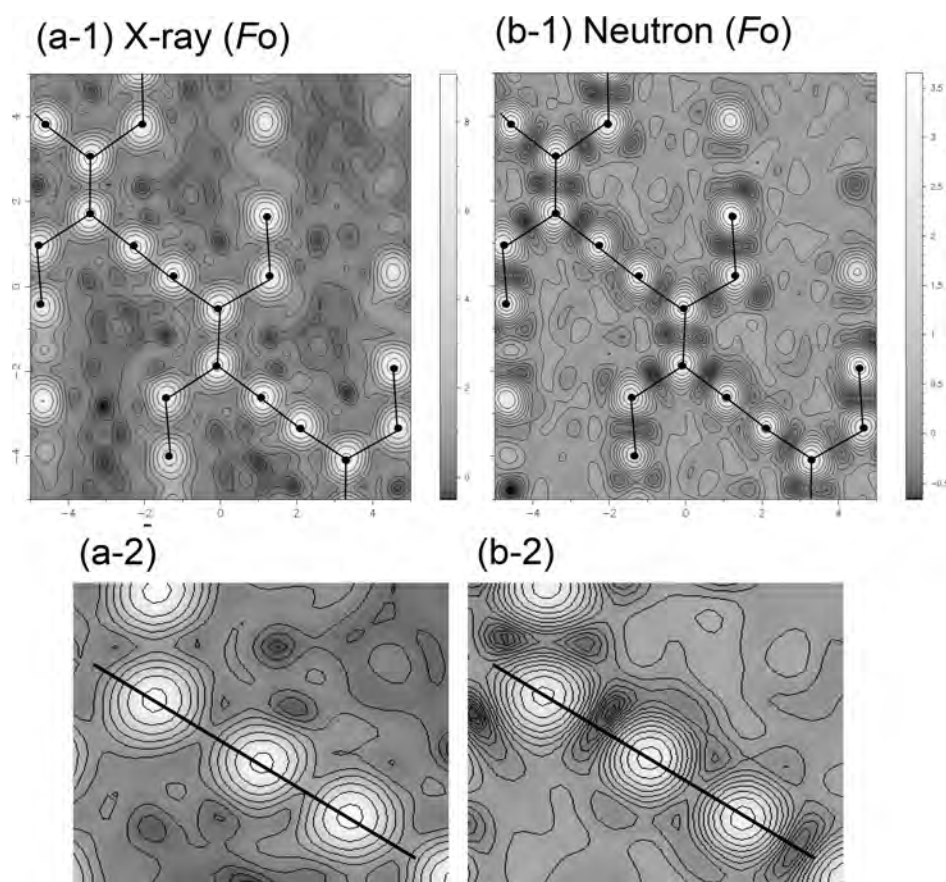


Figure 4. (a) Electron density distribution derived by the X-ray structure analysis and (b) nuclear density distribution by the neutron structure analysis. The expanded pictures shown in (a-2) and (b-2) show clearly the difference in the density distribution between the electron and nuclei.

Similar calculation of $\Delta\rho(\mathbf{x})$ was performed with the X–N method for the crystal structure of the model compound BPBD using the results of the X-ray and neutron diffraction data analyses, the details of which are given in [Supporting Information 4](#) (X-ray and neutron analysis). As shown in [Figure 6](#), the bonded electron density peaks are detected in a similar way to those of PDCHD. In the case of BPBD, the two $C\equiv C$ bonds are connected by one $C-C$ bond and the bonded electron density is relatively low at the $C-C$ bond, and the peaks with some shoulders are detected on the CC triple bond centers.

Density Functional Theoretical Calculation. The $\Delta\rho(\mathbf{x})$ obtained by the X–N method is now compared with the calculated results by the density functional theory (DFT). The electron density distributions were calculated in the two different ways: one was the total density distribution with the conjugation between electron clouds taken into account, and

another was the density distribution by assuming the spherical orbitals for the isolated atoms. The $\Delta\rho(\mathbf{x})$ was obtained by subtracting the latter from the former. [Figure 7](#) shows the $\Delta\rho(\mathbf{x})$ and $\rho(\mathbf{x})$ calculated for PDCHD and BPBD. [Figures 5b](#) and [6b](#) compare the 1-dimensional $\Delta\rho(\mathbf{x})$ curves obtained by the DFT calculation with those by the X–N method.

The agreement of $\Delta\rho(\mathbf{x})$ between the observed and calculated results is good for PDCHD. In the BPBD case, the whole pattern is similar between the observed and calculated ones. But the calculated curve is relatively sharper than the observed one. As will be demonstrated later, only a slight change of the molecular geometry results sensitively in the change of the $\Delta\rho(\mathbf{x})$ profile, giving a relatively broad experimental curve due to the errors of the atomic coordinates. On the other hand, the DFT calculation seems so sharp, where the choice of such various parameters as the basis set, etc., might affect the result sensitively. The effect of the electronic

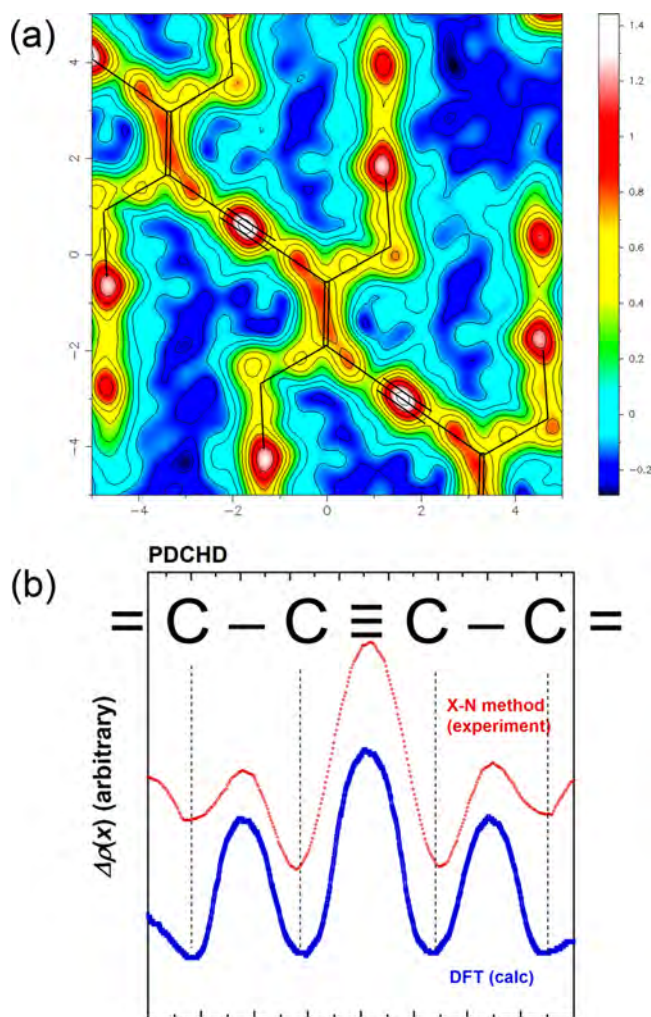


Figure 5. (a) Bonded electron density distribution revealed for PDCHD crystal. (b) 1D distribution curve traced along the skeletal chain axis. The experimentally obtained curve (X–N method) is compared with the DFT calculated result.

conjugation system between PDCHD and BPBD might be different depending on such parameters. In this way, the comparison between the observed and calculated $\Delta\rho(x)$ may be a good chance to check the quality of the experimental data and also the reasonableness of the DFT calculation.

$\Delta\rho(x)$ by Only the X-ray Data Analysis. As a trial we calculated the $\Delta\rho(x)$ using only the X-ray analyzed results. That is to say, eq 3 is used for the estimation of $\rho_o(x)$ by using the atomic coordinates and thermal parameters derived by the X-ray analysis. This method may be called the X–X method. The results obtained for PDCHD and BPBD are shown in Figures 8a and 8b, respectively. The abnormal electron density distribution is observed, in particular, around the CC triple bond. The similar curious distribution is observed also for the BPBD.

What is the reason why the $\Delta\rho(x)$ becomes abnormal when only the X-ray diffraction data are used? In the present study we analyzed the crystal structure by the Fourier transform using the limited number of the observed reflections (see eq 6). This causes the so-called “cutoff” effect, which might be one possibility to give the anomalous electron density distribution. However, the cutoff effect should occur commonly to both the X-ray and neutron analyses.

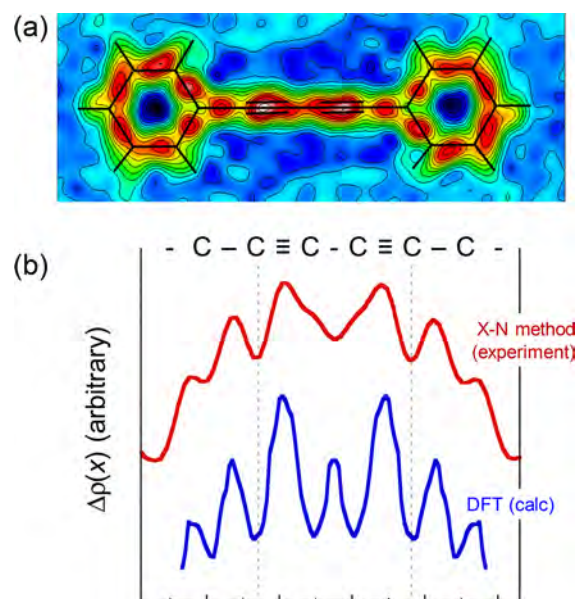


Figure 6. (a) Bonded electron density distribution revealed for BPBD crystal. (b) 1D distribution curve traced along the main axis. The experimentally obtained curve (X–N method) is compared with the DFT calculated result.

It is noticed in Table 1 and the Supporting Information that the atomic coordinates obtained by the X-ray and neutron data analysis are slightly different, and the bond lengths of C–C, C=C, and C≡C are also slightly different between these two methods. These results generate the slight discrepancy of the center positions of the electron clouds and the atomic nuclear positions. At the same time the thermal parameters are larger for the X-ray results than the neutron results. As illustrated in Figure 9b, when the comparatively small electron density spheres are drawn at the centers of nuclear positions and subtracted from the whole electron density, then the density maxima are generated on the centers of the bonds, which correspond well to the result shown in Figures 5 and 6. If the spheres are drawn at the centers of the X-ray-derived electron density centers and the radii of these spheres are relatively larger because of the larger thermal parameters, the overlaps between the neighboring spheres are more remarkable. As a result, the rest of electron density after the subtraction becomes almost zero in the middle part of C≡C bond and it is rather higher in the center of C–C bond, as illustrated in Figure 9c. This result corresponds well to the abnormal distribution obtained by the $\Delta\rho(x)$ calculation using only the X-ray data shown in Figure 8. The illustrations in Figure 9 indicate clearly the significance of the usage of atomic nucleus positions revealed by the neutron data analysis in the calculation of $\Delta\rho(x)$.

This type of interpretation convinces us about the apparently normal $\Delta\rho(x)$ results on the C–C and C=C bonds. As seen in the comparison between Figures 5, 6, and 8, the abnormal distribution is not detected remarkably for these bonds. The reason might come from their relatively long bond distances. As understood in Figure 9, the aftereffect by the subtraction of spherical electron density distribution is smaller for these bonds compared with the case of the shorter C≡C bond.

We need to consider the reason why the X-ray data analysis gives the apparently shorter C≡C distance from the different point of view. The atomic scattering factor consists of the

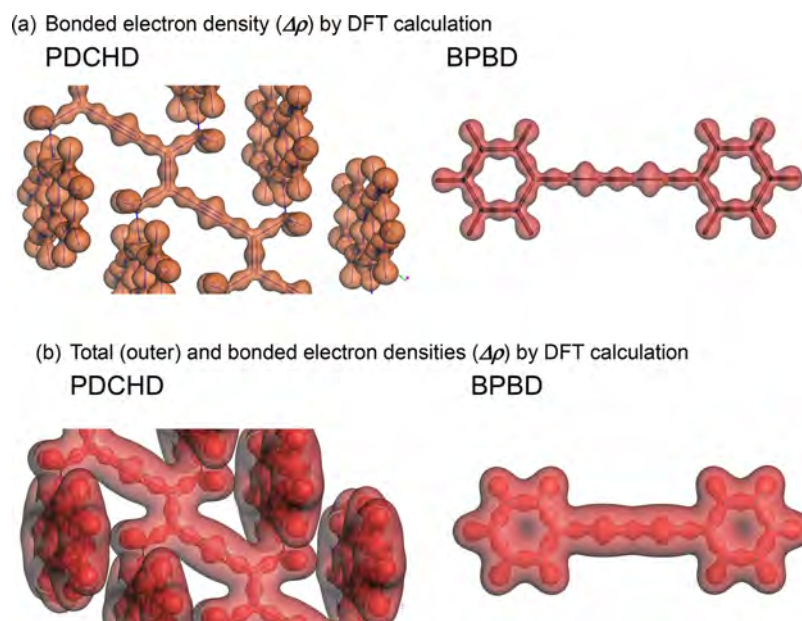


Figure 7. (a) Bonded electron density distributions $\Delta\rho(\mathbf{x})$ calculated by DFT for PDCHD and BPBD molecules. (b) Overlap of the total and bonded electron density distributions calculated by DFT for these two molecules. The whole shape of molecule is represented by the total electron density distribution $\rho(\mathbf{x})$. The bonded electron density distribution $\Delta\rho(\mathbf{x})$ is shown inside the $\rho(\mathbf{x})$.

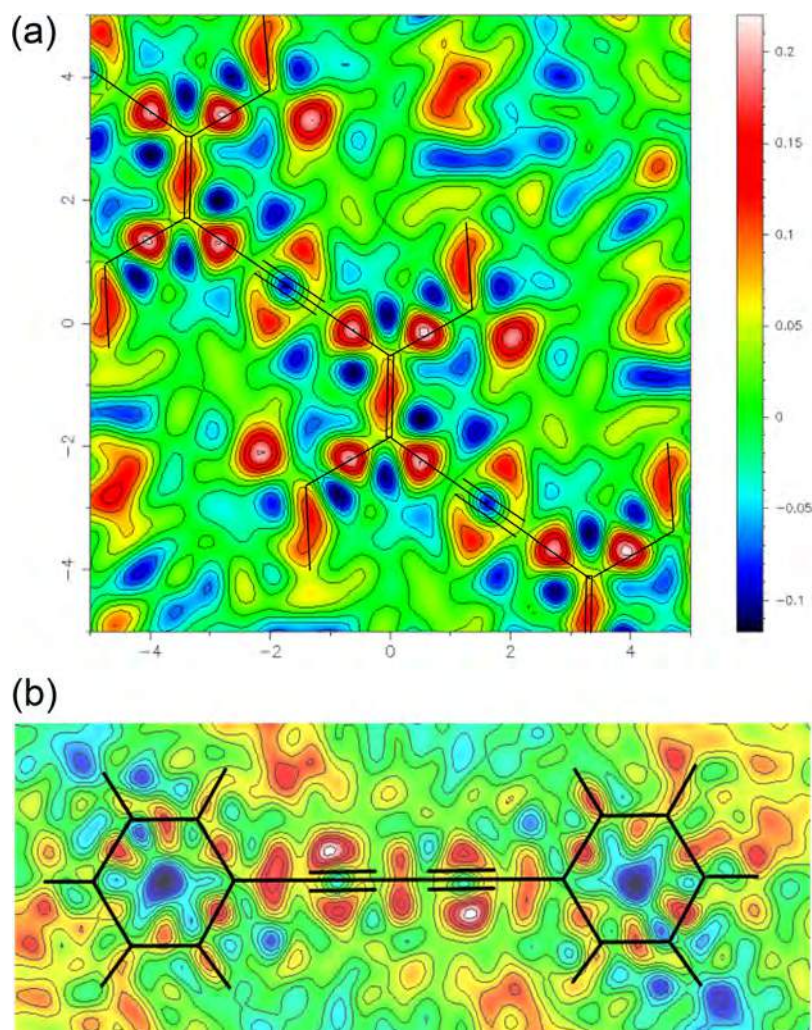


Figure 8. Bonded electron density distribution estimated by using only the X-ray analyzed data (a) for PDCHD crystal and (b) for BPBD crystal.

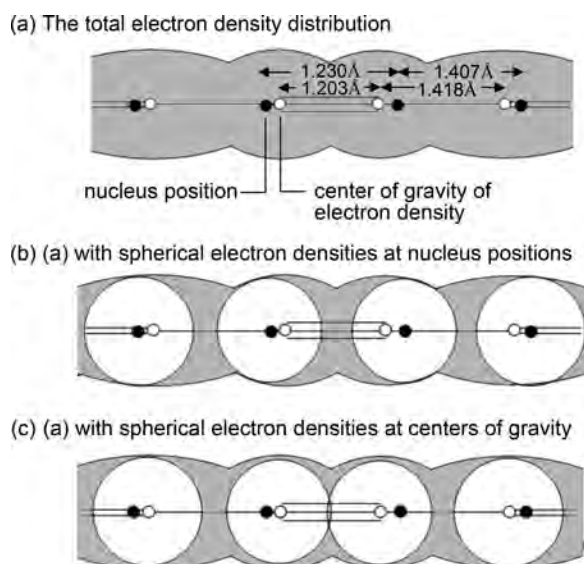


Figure 9. (a) Total electron density distribution obtained by the X-ray analyzed data analysis. (b, c) Residual electron density distribution calculated by subtracting the spherical density distributions of the isolated atoms located (b) at the nuclear positions and (c) at the center of gravity of electron density in (a). The subtracted results can be compared with the results shown in Figures 5, 6, and 8. The slight difference in the center position of the sphere resulted in the remarkable difference of the bonded electron density distribution.

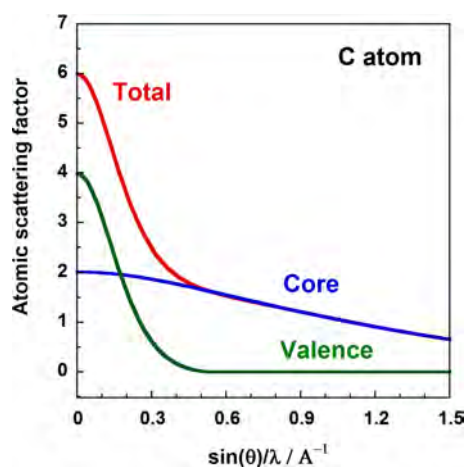


Figure 10. X-ray atomic scattering factor of neutral C atom separated to the contributions of the core and valence electrons.^{66,67}

contributions from the core and valence electron clouds.^{41–43,66,67} As shown in Figure 10, the contribution of the outer-shell electrons or the valence electrons is relatively large in the low scattering angle region, while that of the core electron changes slowly in a wide-angle range. The core electron contribution is overwhelmingly large in the higher angle region. From such a point of view, the asphericity shifts might be removed if *enough* higher order reflections are measured *accurately*. In an extreme case the utilization of only the higher-order reflection data may give us the atomic positions much closer to the nuclear positions, since the contribution of valence electrons to the X-ray scattering decreases more rapidly than that of core electrons as the scattering angle increases, as mentioned above.^{41–43,66,67} That is to say, even the X–X method may give us the reasonable evaluation of $\Delta\rho(\mathbf{x})$ by using the electron density distribution

information derived by the analyses of the X-ray diffraction data collected in the lower angle range (the whole electron density distribution $\rho(\mathbf{x})$) and those in the higher angle range (the positions of the atomic cores and $\rho_o(\mathbf{x})$). Of course, we need to separate the contribution of the atomic displacements due to the thermal vibrations from the effect of the deformed electron density in the X-ray diffraction data analysis. In such a sense the diffraction measurement at enough low temperature is required. In summary, the quantitatively accurate evaluation of the deformed electron density distribution by the X–X method needs the highly accurate X-ray diffraction analysis on the basis of the accurate data collection in a wide diffraction angle and at a low temperature. Actually, such an accurate collection of higher-order reflections has been made successfully at a low temperature for PDCHD single crystal by our group using a synchrotron X-ray diffraction system at SPring-8, Japan.⁶⁸ The asphericity shift effect has been erased successfully, and the stereochemically reasonable $\Delta\rho(\mathbf{x})$ was obtained.

CONCLUSIONS

We have succeeded for the first time to evaluate the $\Delta\rho(\mathbf{x})$ for electronically conjugated polydiacetylene (PDCHD) and its model compound (BPBD) on the basis of the X–N method. The obtained $\Delta\rho(\mathbf{x})$ is reasonable when compared with the DFT calculation result. So far, the structure analysis of polymer substance has been made with the purpose to discuss the structure–property relationship on the basis of classical mechanics utilizing the atomic positions and interatomic interactions. It can be expected hopefully that the experimentally evaluated electron density distribution along the skeletal chain allows us to predict the structure and physicochemical properties of polymer substances viewed from the electron level or from the quantum-chemical point. At the same time the experimental data of $\Delta\rho(\mathbf{x})$ can be used also for checking the reasonableness of the theoretical prediction of $\Delta\rho(\mathbf{x})$ by the DFT method.

Of course, the X–N method (and X–X method) cannot be applied to the general partially crystalline polymer substances with tiny crystallites of several hundred angstroms size, since the total number of the observed reflections is quite small compared with the present special case of polydiacetylene giant single crystal. But even for the general synthetic polymers, there may be still some cases which can give the several hundreds of observed reflections: for example, poly(L-lactic acid)⁶⁹ and polyoxymethylene⁷⁰ give the several hundreds of reflections when the high-energy X-ray beam from the synchrotron source is used as an incident beam. The more or less serious problem might be seen rather in the side of wide-angle neutron diffraction experiment. The reactor gives the less powerful neutron beam of relatively long wavelength of 1 Å, which cannot give a large enough number of the observed reflections. The utilization of pulsed neutron beam from the J-PARC facility might be one good candidate for this purpose since it gives the appreciably intense diffraction signals in a wide diffraction angle range.

In many literatures the structure and physical property of synthetic polymers have been studied on the basis of atomic coordinates and intra- and interatomic interactions which are obtained by the X-ray (and neutron or electron) structure analysis mainly. The recent development of quantum chemical theory makes it possible to discuss the structure and physical property from the electron level. In a future, the physicochemical research might be shifted toward that viewed from the

electron level. For this purpose, we will be challenged by the experimental estimation of the bonded electron density distribution for the general partially crystalline polymer substances.

■ ASSOCIATED CONTENT

📄 Supporting Information

The Supporting Information is available free of charge on the ACS Publications website at DOI: 10.1021/acs.macromol.8b00650.

Treatment of TOF neutron data (PDF)

Crystallographic data of PDCHD by the X-ray structure analysis (PDF)

Crystallographic data of PDCHD by the neutron structure analysis (PDF)

Crystallographic data of BPBD by the X-ray and neutron structure analyses (PDF)

■ AUTHOR INFORMATION

Corresponding Author

*E-mail: ktashiro@toyota-ti.ac.jp (K.T.).

ORCID

Kohji Tashiro: 0000-0002-7543-2778

Notes

The authors declare no competing financial interest.

#Deceased.

■ ACKNOWLEDGMENTS

The authors thank Dr. Daisuke Hashizume of RIKEN Harima Institute/SPring-8 and Dr. Yuji Ohashi, Professor Emeritus, Tokyo Institute of Technology, for their kind discussion about the electron density distribution. K.T. thanks also Dr. Tomohiko Takahama of Toyota Technological Institute for his kind suggestion about the DFT calculation. This work was performed with the kind support by the staff of the BIX-3 and i-BIX facilities at JAEA, Tokai, Japan. The TOF experiments were performed under the proposals 2014PX0008, 2015PX0009, 2016PX0006, and 2017PX0016 of the Ibaraki Prefecture Project. This work was supported also by “the Strategic Project to Support the Formation of Research Base at Private University (2010-2014) and (2015-2019)” of MEXT, Japan.

■ REFERENCES

- (1) Hayashi, K.; Okamura, S. Kinetics of radiation-induced solid-state polymerization of cyclic monomers. *Makromol. Chem.* **1961**, *47*, 230–236.
- (2) Chatani, Y.; Uchida, T.; Tadokoro, H.; et al. X-ray crystallographic study of solid-state polymerization of trioxane and tetraoxymethylene. *J. Macromol. Sci., Part B: Phys.* **1968**, *2*, 567–590.
- (3) Uchida, T.; Tadokoro, H. Structural studies of polyethers. IV. Structure analysis of the polyoxymethylene molecule by three-dimensional Fourier syntheses. *J. Polym. Sci. Part A-2* **1967**, *5*, 63–81.
- (4) Hasegawa, M.; Suzuki, Y. Four-center type photopolymerization in the solid state: Poly-2,5-distyrylpyrazine. *J. Polym. Sci., Part B: Polym. Lett.* **1967**, *5*, 813–815.
- (5) Nakanishi, H.; Hasegawa, M.; Sasada, Y. Four-center type photopolymerization in the crystalline state. V. X-ray crystallographic study of the polymerization of 2,5-distyrylpyrazine. *J. Polym. Sci.* **1972**, *10*, 1537–1553.
- (6) Wegner, G. Solid-State Polymerization Mechanisms. *Pure Appl. Chem.* **1977**, *49*, 443–453.

(7) Bässler, H. Photopolymerization of Polydiacetylenes. *Adv. Polym. Sci.* **1984**, *63*, 1–48.

(8) Sixl, H. Spectroscopy of the intermediate states of the solid state polymerization reaction in diacetylene crystals. *Adv. Polym. Sci.* **1984**, *63*, 49–90.

(9) Enkelmann, V. Structural aspects of the topochemical polymerization of diacetylenes. *Adv. Polym. Sci.* **1984**, *63*, 91–136.

(10) Matsumoto, A.; Matsumura, T.; Aoki, S. Stereospecific polymerization of diethyl (Z,Z)-hexa-2,4-dienedioate in the crystalline state. *J. Chem. Soc., Chem. Commun.* **1994**, 1389–1390.

(11) Matsumoto, A.; Matsumura, T.; Aoki, S. Stereospecific Polymerization of Dialkyl Muconates through Free Radical Polymerization: Isotropic Polymerization and Topochemical Polymerization. *Macromolecules* **1996**, *29*, 423–432.

(12) Matsumoto, A.; Yokoi, K.; Aoki, S.; Tashiro, K.; Kamae, T.; Kobayashi, M. Crystalline-State Polymerization of Diethyl(Z,Z)-2,4-Hexadienedioate via a Radical Chain Reaction Mechanism to Yield an Ultrahigh-Molecular-Weight and Stereoregular Polymer. *Macromolecules* **1998**, *31*, 2129–2136.

(13) Tashiro, K.; Kamae, T.; Kobayashi, M.; Matsumoto, A.; Yokoi, K.; Aoki, S. Structural Change in the Topochemical Solid-State Polymerization Process of Diethyl cis, cis-Muconate Crystal. I. Investigation of Polymerization Process by Means of X-ray Diffraction, Infrared/Raman Spectra, and DSC. *Macromolecules* **1999**, *32*, 2449–2454.

(14) Tashiro, K.; Zadorin, A. N.; Saragai, S.; Kamae, T.; Matsumoto, A.; Yokoi, K.; Aoki, S. Structure Analysis of Monomer and Polymer Crystals in the Photoinduced Solid-State Polymerization Reaction of Diethyl cis,cis-Muconate. *Macromolecules* **1999**, *32*, 7946–7950.

(15) Matsumoto, A.; Katayama, K.; Odani, T.; Oka, K.; Tashiro, K.; Saragai, S.; Nakamoto, S. Feature of γ -Radiation Polymerization of Muconic Acid Derivatives in the Crystalline State. *Macromolecules* **2000**, *33*, 7786–7792.

(16) Matsumoto, A.; Odani, T.; Sada, K.; Miyata, M.; Tashiro, K. Intercalation of Alkylamines into an Organic Polymer Crystal. *Nature* **2000**, *405*, 328–330.

(17) Tashiro, K.; Nakamoto, S.; Saragai, S.; Matsumoto, A.; Tsubouchi, T. Vibrational Spectroscopic Study on the Photo-Induced Solid-State Reactions of a Series of Muconate Diesters with Various Side Groups. *Polymer* **2001**, *42*, 6747–6757.

(18) Saragai, S.; Tashiro, K.; Nakamoto, S.; Kamae, T.; Matsumoto, A.; Tsubouchi, T. Comparison of Crystal Structure between Low- and High-Temperature Phases of Diethyl (Z,Z)-muconate: A Trial to Investigate the Reasons Why the Solid-State Polymerization Reaction is Ceased at Low Temperature. *Polym. J.* **2001**, *33*, 199–203.

(19) Saragai, S.; Tashiro, K.; Nakamoto, S.; Matsumoto, A.; Tsubouchi, T. Relationship between Packing Structure and Monomer Reactivity in the Photo-induced Solid-State Polymerizations of Muconic Diesters with Different Side Groups. *J. Phys. Chem. B* **2001**, *105*, 4155–4165.

(20) Tashiro, K.; Kariyo, S.; Nishimori, A.; Fujii, T.; Saragai, S.; Nakamoto, S.; Kawaguchi, T.; Matsumoto, A.; Rangsiman, O. Development of a Simultaneous Measurement System of X-ray Diffraction and Raman Spectra: Application to Structural Study of Crystalline-Phase Transitions of Chain Molecules. *J. Polym. Sci., Part B: Polym. Phys.* **2002**, *40*, 495–506.

(21) Matsumoto, A.; Sada, K.; Tashiro, K.; Miyata, M.; Tsubouchi, T.; Tanaka, T.; Odani, T.; Nagahama, S.; Tanaka, T.; Inoue, K.; Saragai, S.; Nakamoto, S. Reaction Principles and Crystal Structure Design for the Topochemical Polymerization of 1,3-Dienes. *Angew. Chem., Int. Ed.* **2002**, *41*, 2502–2505.

(22) Matsumoto, A.; Tanaka, T.; Tsubouchi, T.; Tashiro, K.; Saragai, S.; Nakamoto, S. Crystal Engineering for Topochemical Polymerization of Muconic Esters Using Halogen-Halogen and CH/ π Interactions as Weak Intermolecular Interactions. *J. Am. Chem. Soc.* **2002**, *124*, 8891–8902.

(23) Nakamoto, S.; Tashiro, K.; Matsumoto, A. Vibrational Spectroscopic Study on the Molecular Deformation Mechanism of a

Poly(trans-1,4-diethyl muconate) Single Crystal Subjected to Tensile Stress. *Macromolecules* **2003**, *36*, 109–117.

(24) Nakamoto, S.; Tashiro, K.; Matsumoto, A. Quantitative Evaluation of Stress Distribution in Bulk Polymer Samples through the Comparison of Mechanical Behaviors between Giant Single-Crystal and Semicrystalline Samples of Poly(trans-1,4-diethyl muconate). *J. Polym. Sci., Part B: Polym. Phys.* **2003**, *41*, 444–453.

(25) Tashiro, K.; Nakamoto, S.; Fujii, T.; Matsumoto, A. Generation and Relaxation of Large Stress in the Photoinduced Solid-State Polymerization Reaction of Diethyl Muconate Detected by Simultaneous Time-Resolved Measurement of X-ray Diffraction and Raman Spectra. *Polymer* **2003**, *44*, 6043–6049.

(26) Tadokoro, H. *Structure of Crystalline Polymers*; John Wiley & Sons: New York, 1990.

(27) Alexander, L. L. *X-ray Diffraction Methods in Polymer Science*; John Wiley & Sons: New York, 1969.

(28) Tashiro, K.; Yamamoto, H.; Hanesaka, M. Recent Progress in Static and Dynamic Structure Analysis of Crystalline Polymers Studied from a Microscopic Point of View. In *Encyclopedia of Polymers and Composites*; Springer-Verlag: Berlin, 2013.

(29) Tashiro, K.; Hanesaka, M.; Yamamoto, H.; Wasanasuk, K.; Jayaratri, P.; Yoshizawa, Y.; Tanaka, I.; Niimura, N.; Kusaka, K.; Hosoya, T.; Ohhara, T.; Kurihara, K.; Kuroki, R.; Tamada, T.; Fujiwara, S.; Katsube, K.; Morikawa, K.; Komiyama, Y.; Kitano, T.; Nishu, T.; Ozeki, T. Accurate Structure Analyses of Polymer Crystals on the Basis of Wide-Angle X-ray and Neutron Diffractions. *Kobunshi Ronbunshu* **2014**, *71*, 508–526.

(30) Wu, G.; Tashiro, K.; Kobayashi, M. Vibrational Spectroscopic Study on Molecular Deformation of Polydiacetylene Single Crystal: Stress and Temperature Dependence of Young's Modulus. *Macromolecules* **1989**, *22*, 188–196.

(31) Tashiro, K.; Nishimura, H.; Kobayashi, M. First Success in Direct Analysis of Microscopic Deformation Mechanism of Polydiacetylene Single Crystal by the X-ray Imaging-Plate System. *Macromolecules* **1996**, *29*, 8188–8196.

(32) Kohlshutter, H. Z. Zur Kenntnis des Graphitischen Kohlenstoffs und der Graphitsäure. *Z. Anorg. Allg. Chem.* **1919**, *105*, 121–144.

(33) Cohen, M. D.; Schmidt, J. M. G. In *Reactivity of Solids*; DeBoer, J. H., Ed.; Elsevier Pub. Co.: Amsterdam, 1961; pp 556–656.

(34) Cohen, M. D.; Schmidt, G. M. J. Topochemistry. Part I. A Survey. *J. Chem. Soc.* **1964**, 1996–2000.

(35) Schmidt, G. M. J. Photodimerization in the solid state. *Pure Appl. Chem.* **1971**, *27*, 647–678.

(36) Ramamurthy, V.; Venkatesan, K. Photochemical reactions of organic crystals. *Chem. Rev.* **1987**, *87*, 433–481.

(37) Coppens, P. Electron Density from X-Ray Diffraction. *Annu. Rev. Phys. Chem.* **1992**, *43*, 663–692.

(38) Helmholdt, R. B.; Ruysink, A. F. J.; Reynaers, H.; Kemper, G. Electron density distributions on single, double and triple C-C bonds. *Acta Crystallogr., Sect. B: Struct. Crystallogr. Cryst. Chem.* **1972**, *28*, 318–319.

(39) Hirshfeld, F. L. Hellmann-Feynman Constraint on Charge Densities, An Experimental Test. *Acta Crystallogr., Sect. B: Struct. Sci.* **1984**, *40*, 613–615.

(40) Antipin, M. Y.; Chernega, A. N.; Lysenko, K. A.; Struchkov, Y. T.; Nixon, J. F. J. Electron distribution in *tert*-butyl phosphoethyne Bu⁺C≡P. *J. Chem. Soc., Chem. Commun.* **1995**, 505–506.

(41) *Accurate Molecular Structures. Their Determination and Importance*; Domenicano, A., Gargittai, I., Eds.; Oxford Science Publ.: Oxford, UK, 1991.

(42) Coppens, P. *X-ray Charge Densities and Chemical Bonding*; Oxford University Press Inc.: Oxford, UK, 1997.

(43) Coppens, P.; Iversen, B.; Larsen, F. K. The Use of Synchrotron Radiation in X-ray Charge Density Analysis of Coordination Complexes. *Coord. Chem. Rev.* **2005**, *249*, 179–195.

(44) Figgis, B. N.; Sobolev, A. N.; Young, D. M.; Schultz, A. J.; Reynolds, P. A. Bonding Effects and the Crystal Structures of (NH₄)₂[Cu(H₂O)(6)](SO₄)₂ and Its (H₂O)-O-18 Substituted Form at 9.5 K. *J. Am. Chem. Soc.* **1998**, *120*, 8715–8723.

(45) Mallinson, P. R.; Woźniak, K.; Wilson, C. C.; McCormack, K. L.; Yufit, D. S. Charge density distribution in the 'proton sponge' compound 1,8-bis(dimethylamino)naphthalene. *J. Am. Chem. Soc.* **1999**, *121*, 4640–4646.

(46) Wilson, C. C. *Single Crystal Neutron Diffraction From Molecular Materials*; Series on Neutron Techniques and Applications; World Scientific Publishing Co.: New York, 2000; Vol. 2.

(47) Kiyonagi, R.; Kimura, H.; Watanabe, M.; Noda, Y.; Mochida, T.; Sugawara, T. Hydrogen-Bond Nature Studied by X-ray and Neutron Structure Analyses of MeHPLN at Room Temperature. *J. Phys. Soc. Jpn.* **2003**, *72*, 2816–2821.

(48) Kiyonagi, R.; Kojima, A.; Kimura, H.; Watanabe, M.; Noda, Y.; Mochida, T.; Sugawara, T. Phase Transition Scheme of the Isolated Hydrogen-bonded Material h-MeHPLN studied by Neutron and X-ray Diffraction. *J. Phys. Soc. Jpn.* **2005**, *74*, 613–620.

(49) Taniguchi, H.; Machida, M.; Koyano, N. Neutron Diffraction Study of Crystal Structures of Glycinium Phosphite H₃NCH₂COOH·H₂PO₃ in Paraelectric and Ferroelectric Phase. *J. Phys. Soc. Jpn.* **2003**, *72*, 1111–1117.

(50) *One-Dimensional Metals: Conjugated Polymers, Organic Crystals, Carbon Nanotubes and Graphene*; Siegmund, R., David, C., Eds.; Wiley-VCH Verlag GmbH & Co. KGaA: 2015.

(51) Wunderlich, B. *Macromolecular Physics*; Academic Press: New York, 1973; Vol. 1.

(52) Tashiro, K.; Hanesaka, M.; Yoshizawa, Y.; Ohhara, T.; Kuroki, R.; Kitano, T.; Nishu, T.; Sasaki, S.; Takata, M. Combinatory Usage of X-ray and Neutron Diffraction Techniques for the Refined Structure Analysis of Polymer Crystals: From Hydrogen Atoms to Bonded Electron Density Distribution. *J. Phys.: Conf. Ser.* **2009**, *184*, 012012.

(53) Niimura, N.; Karasawa, Y.; Tanaka, I.; Miyahara, J.; Takahashi, K.; Saito, H.; Koizumi, S.; Hidaka, M. An imaging plate neutron detector. *Nucl. Instrum. Methods Phys. Res., Sect. A* **1994**, *349*, 521–525.

(54) Tanaka, I.; Kurihara, K.; Chatake, T.; Niimura, N. A High-Performance Neutron Diffractometer for Biological Crystallography (BIX-3). *J. Appl. Crystallogr.* **2002**, *35*, 34–40.

(55) Niimura, N.; Chatake, T.; Ostermann, A.; Kurihara, K.; Tanaka, I. High Resolution Neutron Protein Crystallography Hydrogen and Hydration in Proteins. *Z. Kristallogr. - Cryst. Mater.* **2003**, *218*, 96–107.

(56) Kusaka, K.; Hosoya, T.; Yamada, T.; Tomoyori, K.; Ohhara, T.; Katagiri, M.; Kurihara, K.; Tanaka, I.; Niimura, N. Evaluation of performance for IBARAKI biological crystal diffractometer iBIX with new detectors. *J. Synchrotron Radiat.* **2013**, *20*, 994–998.

(57) Kusaka, K.; Hosoya, T.; Tanaka, I.; Niimura, N.; Kurihara, K.; Ohhara, T. Current Status of Ibaraki Biological Crystal Diffractometer iBIX - Several Examples of the Measurement. *J. Phys.: Conf. Ser.* **2010**, *251*, 012031.

(58) Kusaka, K.; Ohhara, T.; Tanaka, I.; Niimura, N.; Ozeki, T.; Kurihara, K.; Aizawa, K.; Morii, Y.; Arai, M.; Ebata, K.; Takano, Y. Peak Overlapping and its De-convolution in TOF Diffraction Data from Neutron Biological Diffractometer in J-PARC. *Phys. B* **2006**, *385*–386, 1062–1065.

(59) Ohhara, T.; Kusaka, K.; Hosoya, T.; Kurihara, K.; Tomoyori, K.; Niimura, N.; Tanaka, I.; Suzuki, J.; Nakatani, T.; Otomo, T.; Matsuoka, S.; Tomita, K.; Nishimaki, Y.; Ajima, T.; Ryufuku, S. Development of Data Processing Software for a New TOF Single Crystal Neutron Diffractometer at J-PARC. *Nucl. Instrum. Methods Phys. Res., Sect. A* **2009**, *600*, 195–197.

(60) Hosoya, T.; Nakamura, T.; Katagiri, M.; Birumachi, A.; Ebine, M.; Soyama, K. Development of a New Detector and DAQ Systems for iBIX. *Nucl. Instrum. Methods Phys. Res., Sect. A* **2009**, *600*, 217–219.

(61) Pireaux, J. J.; Riga, J.; Boulanger, P.; Snauwaert, P.; Novis, Y.; Chtai, M.; Gregoire, C.; Fally, F.; Beelen, E.; Caudano, R.; Verbist, J. Electron Spectroscopy of Polymers. *J. Electron Spectrosc. Relat. Phenom.* **1990**, *52*, 423–445.

(62) Koch, W.; Holthaus, M. C. *A Chemist's Guide to Density Functional Theory*; Wiley-VCH: 2001.

(63) Giacobuzzo, C.; Siliqi, D. Direct Methods for Solving Macromolecular Structures. Integration of Direct Methods with SIR Techniques. *NATO Sci. Ser. C: Math. Phys. Sci.* **1998**, 285–295.

(64) *International Tables for Crystallography*; Kluwer Academic Publ.: 2001; Vol. B: Reciprocal Space.

(65) Sheldrick, G. M. A Short History of SHELX. *Acta Crystallogr., Sect. A: Found. Crystallogr.* **2008**, *64*, 112–122.

(66) Coppens, P. The structure factor. In *International Tables for Crystallography*; Kluwer Academic Publ.: 2001; Vol. B: Reciprocal Space, pp 10–24.

(67) Su, Z.; Coppens, P. Relativistic X-ray Elastic Scattering Factors for Neutral Atoms $Z = 1-54$ from Multiconfiguration Dirac-Fock Wavefunctions in the $0-12\text{\AA}^{-1} \sin \theta/\lambda$ Range, and Six-Gaussian Analytical Expressions in the $0-6\text{\AA}^{-1}$ Range. *Acta Crystallogr., Sect. A: Found. Crystallogr.* **1997**, *53*, 749–762.

(68) Bagautdinov, B.; Tanaka, H.; Shih, C.-H.; Sugimoto, K.; Sasaki, S.; Tashiro, K.; Takata, M. New Insight into the Polymerization and Structural Mechanisms of Polydiacetylene DCHD: an X-ray/MEM Study. *Acta Crystallogr., Sect. A: Found. Crystallogr.* **2011**, *67*, C27–C28.

(69) Wasanasuk, K.; Tashiro, K.; Hanesaka, M.; Ohhara, T.; Kurihara, K.; Kuroki, R.; Tamada, T.; Ozeki, T.; Kanamoto, T. Crystal Structure Analysis of Poly(L-lactic Acid) α Form Based on the 2-Dimensional Wide-Angle Synchrotron X-ray and Neutron Diffraction Measurements. *Macromolecules* **2011**, *44*, 6441–6452.

(70) Tashiro, K.; Hanesaka, M.; Ohhara, T.; Ozeki, T.; Kitano, T.; Nishu, T.; Kurihara, K.; Tamada, T.; Kuroki, R.; Fujiwara, S.; Tanaka, I.; Niimura, N. Structural Refinement and Extraction of Hydrogen Atomic Positions in Polyoxymethylene Crystal Based on the First Successful Measurements of 2-Dimensional High-Energy Synchrotron X-ray Diffraction and Wide-Angle Neutron Diffraction Patterns of Hydrogenated and Deuterated Species. *Polym. J.* **2007**, *39*, 1253–1273.

ポリビニルアルコール=ヨウ素錯体型偏光板の内部構造

(豊田工大院工) 田代孝二、高濱智彦、Wang MengFan

我々はこれまでに、ポリビニルアルコール (PVA) 延伸フィルムをヨウ化カリウム/ヨウ素水溶液に浸漬し作成される PVA=ヨウ素錯体について、水溶液の濃度 0.1~0.8 mol/L 程度では I 型結晶相が、0.8~3mol/L 圏では II 型結晶相が形成されることを見出してき (ヨウ化水素の場合、3mol/L 以上では III 型も形成される) [Macromolecules, 48, 2138 (2015); Macromolecules, 48, 8867 (2015); Polymer, 89, 81 (2016); Polymer, 99, 566 (2016)]. PVA=ヨウ素錯体コンピュータディスプレイなどの偏光板として利用されており、膨大な量が工業的に製造されている。その場合、ヨウ素濃度は上記の場合よりも圧倒的に低い 0.1~0.01mol/L の数種類のヨウ素水溶液に多段階浸漬ロール延伸する工程に加えてホウ酸水溶液中での延伸工程も含まれている。これらの「ヨウ素染色」「ホウ架橋」「ロール延伸」過程が色調の整った優れた偏光製造上の重要な因子となっている。我々は、これまで蓄積してきた PVA=ヨウ素錯体における PVA 分子鎖とヨウ素イオンの集合状態に関する知見に基づき、偏光板の内部構造を明らかにすることに挑戦した。その研究結果は偏光板の更なる性能向上を狙う上の基本的指導指針になると考えている。

(1) まず上記の種々の要因が構造に及ぼす効果を解明するために、高度延伸 PVA フィルムを 0.001mol/L~3mol/L と非常に広い範囲のヨウ素水溶液に 1 秒から 2 週間にわたる種々の時間浸漬し、夫々の試料の 2 次元 X 線回折図形を測定した。この場合、PVA フィルムは未熱処理、および 160°C 熱処理の両方を用いたが、後者の場合、ヨウ素錯体形成に時間はかかるものの、得られた結果は基本的には同じであった。図 1 に、種々の濃度の水溶液に 2 日間浸漬した場合の X 線回折赤道線プロファイルの変化を示す。このデータから上記の I 型、II 型に加えて濃度 0.001~0.05mol/L の範囲で新しい結晶変態が発現していることが判明した。これを仮に I' 型と呼ぶことにする。浸漬時間に関しては、0.01mol/L 以下の濃度の場合、数十分から数時間かけて非常にゆっくりと I' 型の出現してくることが X 線回折測定から判明した。これらの試料の子午線回折プロファイルおよびラマン散スペクトルを解析することで、I' 型では I_5^- イオン、II 型では I_3^- イオン、そして I 型では I_3^- と I_5^- の共存状態にあることが分かった。

(2) ホウ酸水溶液 (0.05mol/L) 中で PVA フィルムを延伸し、その配向試料を種々の濃度のヨウ素水溶液に

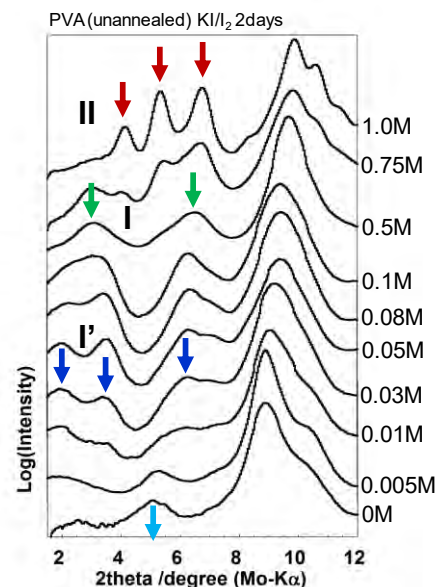


Figure 1. X-ray diffraction profiles of PVA=iodine complexes prepared at the different iodine concentrations.

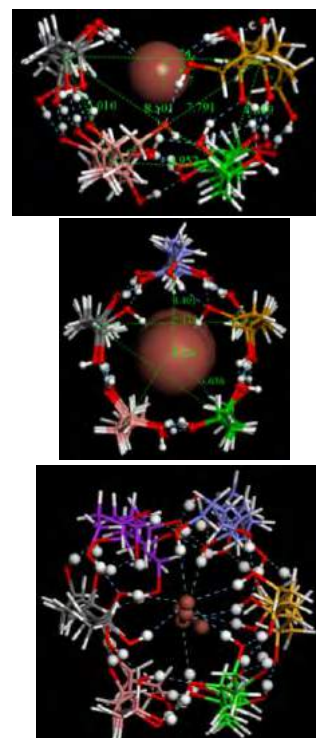


Figure 2. PVA-iodine complex models assumed in the amorphous region

様々の時間浸漬した。その X 線回折図形を (1) の場合と比較すると、同一のヨウ素水溶液に同じ時間浸漬した場合、ホウ酸中での延伸フィルムでは、例え濃度が 0.01~0.03mol/L と希薄であっても、長時間の後には I 型が優先的に生じることが分かった。ホウ酸は PVA 分子鎖セグメント間に共有結合型の架橋を与え、その結果、結晶化し得る PVA セグメント長が短くなり、微結晶サイズが極めて小さくなる。事実、X 線回折図形に於いて広角の反射は殆ど検出できなくなっている。結晶サイズが微小であるが故に、ヨウ素イオンの結晶相への侵入が容易になり、I' 型に留まることなく I 型にまで進行したと考えられる。1 時間程の短時間では I' 型に落ち着いている点は忘れてはならない。

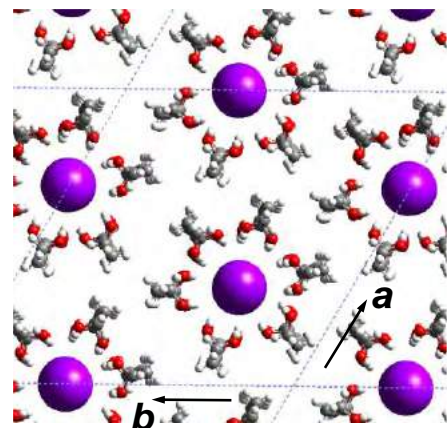


Figure 3. Crystal structure model of form I'

(3) I' 型の X 線回折データを解析した結果、 $a = b = 22.85 \text{ \AA}$ 、 c (fiber axis) = 2.55 \AA 、 $\gamma = 120^\circ$ の六方晶型単位格子を取っていることが判明した。I 型や II 型での直方晶型単位格子とは異なっている。X 線回折図形から PVA 分子鎖は平面ジグザグ型コンフォーメーションを取っていると考えられるが、六方晶型格子の場合、それらの分子鎖平面が 60 度毎に向いた充填構造の生じる可能性がある。I' 型の場合、濃度が極めて希薄であり、I' 型反射に加えて PVA 結晶由来の X 線回折パターンも混在していることから、一つの可能性として配向非晶部分で I' 型が出来ている可能性もある。宮坂らは 4 本のジグザグ PVA 鎖が I_5^- イオンを取り囲んでいるモデルを非晶中での錯体として提案しているが [Adv. Polym. Sci., 108, 91 (1993)]、残念ながらそれを支持する実験データは全くなかった。今回得られた I' 型 X 線回折データが、そのような複数の PVA 分子鎖で囲まれた錯体構造で説明可能かどうかを調べてみた。密度汎関数法に基づくエネルギー最小化計算を行ったところ (図 2)、4 本鎖ではヨウ素イオンを保持しきれないが、5 本あるいは 6 本では安定な構造が形成されている。充填構造の有利な六角形構造モデルを上記の格子に充填させ (図 3)、X 線赤道線回折パターンを計算したところ実測データを比較的上手く再現できた。詳細はさらに検討中である。

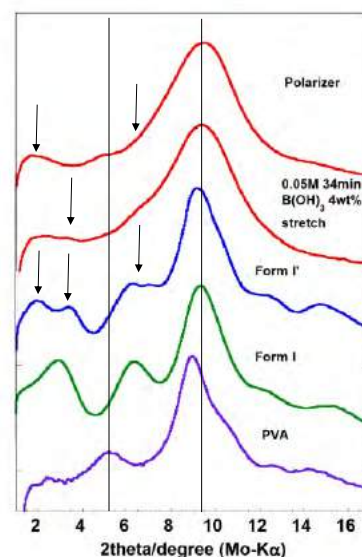


Figure 4. Comparison of X-ray diffraction profiles between the polarizer and the various crystalline forms.

(4) 以上の如く得られた種々の知見を基に、偏光板の内部構造について考察を加えた。市販の偏光板の X 線回折図形は、ホウ酸中での延伸や種々の低濃度のヨウ素溶液中での延伸を短時間施しているために、全体に曖昧であるが、低角側の反射などは検出できる。それらを上述の種々の濃度の X 線パターンと比較すると、PVA の反射に加え、I' 型パターンに I 型を多少重ねたように見られる。ホウ酸液中で延伸したのち 0.05mol/L ヨウ素溶液中 30 分程度浸漬した試料の X 線パターンに似ている (図 4)。偏光板は PVA 結晶 + 非晶中での I' 型形成が主なる構造成分と考えられる。

X線および中性子回折データの統合的解析に基づく
ポリビニルアルコールおよびヨウ素錯体の結晶構造への乱れ概念導入

(豊田工大院工) ○田代孝二 (茨城大フロンティア) 日下勝弘(あいちシンクロトロン) 山元博子
(茨城大工) 田中伊知朗 (原研 J-PARC) 大原高志 (量子科学技術研) 玉田太郎

合成高分子の結晶構造は物性の議論の上で不可欠な情報であるが、一般の合成高分子においては実測可能な X 線反射数が少なく、物性の定量的予測に要する高精度構造情報を得るには限界がある。特に、隣接分子鎖間相互作用の中で最も大きな貢献をする水素原子について、その位置座標を得ることは事実上不可能である。また、高機能性を賦与させるべく有機高分子に無機物をブレンドして生成される錯体についても、炭素など軽元素に比べ重元素からの X 線散乱強度が圧倒的に強く、周辺の高分子鎖との位置関係について詳細を知ることは極めて困難である。その点では、時には軽原子の散乱強度が重原子よりも圧倒的に強い中性子回折が有利であるが、中性子ビームの弱さ、重水素化合物の必要性など様々の課題がある。

このような、高分子の結晶構造解析にまつわる様々の状況が原因して、X 線構造解析によって提案されてきた過去の結晶構造に変更を迫らざるを得ない場合も起こり得る。中でも、新たに測定した中性子回折データを再現できないケースは深刻である。本発表では、最近、我々が体験したポリビニルアルコール(PVA)およびそのヨウ素錯体の結晶構造に関する事情を報告するとともに、結晶構造に「乱れ」を新たに導入することで、X 線回折データと中性子回折データの両方を矛盾なく解釈できることを示す。

<ポリビニルアルコール> 我々は、この高分子について、まず X 線回折データの再現を試みた。これまでに提案されてきた結晶構造の中で、C. W. Bunn の構造 [*Nature*, **161**, 929 (1965); I. Nitta *et al.*, 阪大繊維研年報, **10**, 1 (1957)] が X 線データをほぼ完全に再現できることを確認した。ところが、この構造に基づいて広角中性子回折パターンを計算したところ、実測(全重水素化一軸配向試料について J-PARC の i-BIX を使用)を説明できないことが判明した。この結晶構造の場合、二本のジグザグ鎖が向かい合わせに水素結合で結ばれているが、図1のように、この一対を 110 面に沿って約 1/2 シフトさせた状況も確率 50% で存在し得るとした統計構造を想定することで、X 線、中性子回折データを矛盾なく再現することが出来た。PVA の水素結合はロール面(つまり 110 面)に沿って形成されているが、この統計構造は、ある範囲のドメインが、この面に沿って互いにズれて共存していることを示している。

<ポリビニルアルコール・ヨウ素錯体> このような分子鎖充填の乱れは、PVA 結晶にヨウ素イオン分子が侵入して形成される錯体についても引きずっているはずである。事実、X 線回折データをほぼ完璧に再現できていた構造モデル [*Macromolecules*, **48**, 2138, 8867 (2015); *Polymer*, **99**, 566; 89, 81 (2016)] が、実測の中性子回折データをまったく説明できないことが、今回、判明した。上記の PVA と同様に、これまでに提案した構造に加えて、それを 1/2 シフトさせた統計的に乱れたモデルを組み立てることで、この矛盾を解消することが出来た。

このように、新たに中性子回折データを取得して X 線回折データの貧弱さをカバーしようとする場合、従来、X 線構造解析によって提案されてきた結晶構造を修正あるいは破棄せざるを得ない状況に遭遇することがある。我々は、合成高分子の結晶構造を X 線、中性子、電子線、振動分光、計算機シミュレーションなど可能な限り数多くの観点からの確認の重要性を強調してきたが、今回のケースはそれを如実に示したと言える。

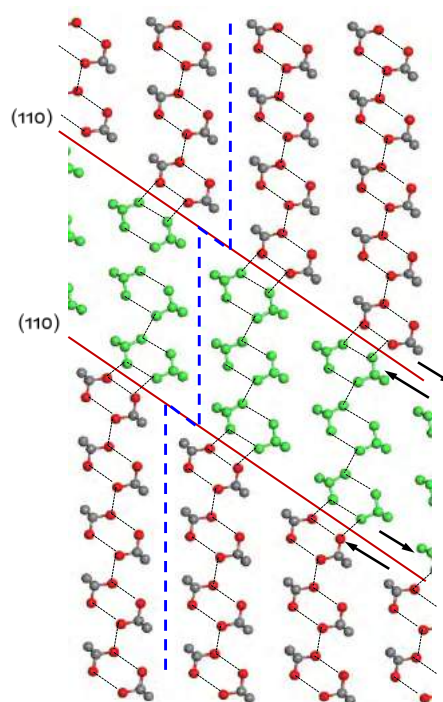


Figure 1. Statistically- disordered structure of at-PVA crystal

Integrated Analysis of X-ray and Neutron Diffraction Data of Poly(vinyl Alcohol) and its Iodine Complex and the Introduction of New Concept to their Crystal Structures or the Disorder Kohji Tashiro, (Graduate School of Engineering, Toyota Technological Institute, Nagoya 468-8511, Japan), Katsuhiro Kusaka (Ibaraki Univ), Hiroko Yamamoto (Aichi Synchrotron), Ichiro Tanaka (Ibaraki Univ), Takashi Ohhara (J-PARC, JAEA), and Taro Tamada (Quantum Beam Science, JAEA) Tel: +81-52-809-1790, Fax: +81-52-809-1793, E-mail:ktashiro@toyota-ti.ac.jp